Transactions of the ASME®

Editor, **DAVID C. WISLER (2008)**
Assistant to the Editor: **ELIZABETH WISLER**
Associate Editors
Gas Turbine (Review Chair)
H. SIMMONS (2003)
Heat Transfer
T. ARTS (2005)
R. BUNKER (2006)
Structures and Dynamics
M. MIGNOLET (2006)
Turbomachinery
R. DAVIS (2005)
S. SJOLANDER (2005)

BOARD ON COMMUNICATIONS
Chair and Vice-President
OZDEN OCHOA

OFFICERS OF THE ASME
President, **REGINALD VACHON**

Executive Director, **VIRGIL R. CARTER**

Treasurer, **R. E. NICKELL**

PUBLISHING STAFF
Managing Director, Engineering
THOMAS G. LOUGHLIN
Director, Technical Publishing
PHILIP DI VIETRO
Manager, Journals
JOAN MERANZE
Production Coordinator
JUDITH SIERANT
Production Assistant
MARISOL ANDINO

Transactions of the ASME, Journal of Turbomachinery (ISSN 0889-504X) is published quarterly (Jan., Apr., July, Oct.) by The American Society of Mechanical Engineers, Three Park Avenue, New York, NY 10016. Periodicals postage paid at New York, NY and additional mailing offices. POSTMASTER: Send address changes to Transactions of the ASME, Journal of Turbomachinery, c/o THE AMERICAN SOCIETY OF MECHANICAL ENGINEERS, 22 Law Drive, Box 2300, Fairfield, NJ 07007-2300.
CHANGES OF ADDRESS must be received at Society headquarters seven weeks before they are to be effective. Please send old label and new address.
STATEMENT from By-Laws. The Society shall not be responsible for statements or opinions advanced in papers or ... printed in its publications (B7.1, Par. 3).

INDEXED by Applied Mechanics Reviews and Engineering Information, Inc. Canadian Goods & Services Tax Registration #126148048

Journal of Turbomachinery

Published Quarterly by The American Society of Mechanical Engineers

VOLUME 125 • NUMBER 4 • OCTOBER 2003

TECHNICAL PAPERS

(**Contents continued on inside back cover**)

This journal is printed on acid-free paper, which exceeds the ANSI Z39.48-1992 specification for permanence of paper and library materials. ♾™
♻ 85% recycled content, including 10% post-consumer fibers.

Journal of Turbomachinery Volume 125, Number 4 OCTOBER 2003

TECHNICAL BRIEF

ANNOUNCEMENTS AND SPECIAL NOTES

Shou-Shing Hsieh
Sun Yat-Sen Professor of
Mechanical and
Electromechanical Engineering
Fellow ASME

Hsiang-Jung Chin
Graduate Student

Department of Mechanical and
Electro-Mechanical Engineering,
National Sun Yat-Sen University,
Kaohsiung, Taiwan 80424,
Republic of China

Turbulent Flow in a Rotating Two Pass Ribbed Rectangular Channel

Laser-Doppler anemometry has been applied to approximately two-dimensional turbulent air flow in rotating two pass channel with turbulator of rectangular cross section (AR =3:1). The axis of rotation is normal to the axis of the duct, and the flow is radially outward/inward. The duct is of finite length and the walls are isothermal. Two sided oppositely ribbed channel including one sided ribbed U bend of $p/e=8$ at $e/D_H=0.27$ are experimentally conducted with $Re_D=5000$ and 10,000. The main features of the flow, reattachment length, recirculation zone, and mean velocity as well as turbulent intensity and shear stress distributions are presented in ribbed ducts. The measured flow field is found to be quite complex, consisting of secondary cross-stream flows due to the Coriolis effects and centrifugal forces with rib-roughened surfaces. [DOI: 10.1115/1.1622714]

1 Introduction

Effective turbine blade cooling is necessary to enhance the efficiency of advanced aircraft engines. In general, convective cooling is used inside the blades by means of cooling passages. The internal cooling passages are connected at the ends, which lead to a serpentine flow path consisting of alternate channels of radially outward and inward flow. In addition, to promote turbulence and enhance heat transfer, roughened surfaces like the rib type are the most commonly used on the walls of these internal passages.

Rotation of turbine blade cooling passages gives rise to Coriolis and buoyancy forces that can significantly alter the local heat transfer in the inward coolant passage from the development of cross stream (Coriolis), as well as radial (buoyant) secondary flows. Consequently, the flow, and hence the heat transfer, in these rotating passages are quite different as compared to that in stationary channels. It is therefore recognized that comprehensive data as well as accurate methods for predicting flow and heat transfer are necessary.

A number of investigators have studied the phenomena of the Coriolis force induced secondary flow. These include the analytical works by Hart [1], Moore [2], and Rothe and Johnston [3], and the experimental works by Wagner and Velkoff [4] and Johnston et al. [5]. They all came to the same conclusion that, when a channel is being rotated, there would be strong secondary flows and have identified aspects of flow stability that produce streamwise-oriented vortexlike structures in the flow of rotating radial passage. The cross-section aspect ratio effect on turbine blade cooling passages was also mentioned in Moore's [2] paper.

Although plenty of papers reported the results for the effect of centrifugal buoyancy or combined effects of Coriolis and buoyancy effects on heat transfer or temperature fields, it seems quite few papers dealt with velocity fields especially for LDV (Laser Doppler Velocimetry)/or LDV-like measurements [6] in rotating ducts with cross section aspect ratio different from unity. Only several papers have so far been found reporting such results either experimentally or numerically with/without the aspect ratio effect. Prakash and Zerkle [7] reported a numerical prediction of turbulent flow and heat transfer in a radially rotating square duct. Hsieh et al. [8,9] using LDV techniques measured velocity fields in a rotating two pass square channel with/without rib roughened walls, respectively. Recently, Dutta et al. [10] numerically studied turbulent flow and heat transfer in rotating channels where five different aspect ratios of the coolant passages were examined. Cheah et al. [11] experimentally studied the flow pattern in a rotating U-bend smooth channel using LDV measurements and, more recently, the subsequent work was done by Iacovides et al. [12] for a ribbed channel. Liou and Chen [13] used LDV measurements for developing flow in a rotating smooth duct with an aspect ratio of 1.1. Bons and Kerrebrock [14] experimentally studied complementary velocity and heat transfer in a radially outward rotating cooling passage with smooth walls.

Here the results of a subsequent study of Hsieh et al. [8,9] are presented in which the effects of discrete ribs and a large aspect ratio (AR=3:1) of the duct have been included. As shown in Fig. 1, two-dimensional transverse square ribs have been added to the first/second straight channels as well as within the U bend (two rib arrangements considered) in an inline arrangement. The objectives for the study are further examination of Coriolis and centrifugal forces induced by inward and outward flow using LDV techniques for the mean velocity as well as turbulent intensity distribution and turbulent shear stress in a ribbed channel during the rotation. Such data should not only improve our fundamental understanding of blade cooling flow, but would also provide challenging test cases for further assessment of turbulence models used in the computation of blade-cooling flows.

2 Experimental Apparatus and Procedure

2.1 Rotating Facility. Figure 1 depicts the present physical geometry and relevant parameters as well as flow variables considered. The present test facility initially was followed by Hsieh et al. [9] with a slight modification in flow passage for rib roughened geometry. It is almost the same as that of Hsieh et al. [15] and the extension for LDV measurements. It was comprised of a blower, a motor, a heat source, two slip ring assemblies, a LDV, and a datalogger.

Experimental data were taken on the leading and trailing surface of the test section in both rotating and stationary channels. Rotational speeds of 100, 200, and 300 rpm were set either in the counterclockwise or clockwise direction. The test channel geometry and operating conditions for velocity measurements are also shown in Fig. 1. A stereographic view of the present experimental setup schematic was similar to that of Hsieh et al. [9]. Figure 2 depicts the test channels with rib arrangements and temperature as well as LDV measurement positions. With the present roughened geometry, an increase in friction factor as compared to that of smooth channel is expected.

2.2 LDV Measurements. The present system is a commercial two color, four beam DANTEC fringe-type LDV system, operated in the backward scatter mode, with the general layout similar to that of Hsieh et al. [9]. The relevant optical system parameters are listed in Table 1. Standard DANTEC 55× modular optics and a model Stabilite 2016 4 W Spectral Physics Ar^+ laser are mounted on a two-dimensional (2D), traversing system. Two

Contributed by the International Gas Turbine Institute for publication in the JOURNAL OF TURBOMACHINERY. Manuscript received by the IGTI Aug. 1998, revised manuscript received May 2003. Associate Editor: R. S. Bunker.

	W (mm)	H (mm)	D_H (mm)	AR (H:W)	e/H	e/D_H	p/e
geometries	10	30	15	3:1	0.135	0.27	8

	Re_D	Re_Ω	Ro
relevent parameters	5000 -10000	0 -451	0-0.0902

	First pass	Second pass	U-bend
boundary conditions	isothermal	isothermal	isothermal

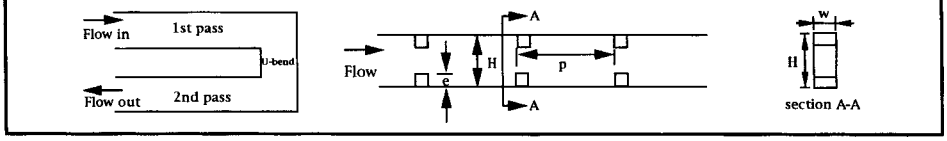

Fig. 1 Geometries and operating conditions in the channel

separate LDV channels are formed by use of color separation. They are 514.5-nm (green light) and 488.0-nm (blue light) wavelength beams. These two beams form orthogonal fringes by means of a standard DANTEC two channels optical train. These two sets of fringes allow the simultaneous measurement of two orthogonal components. The transverse velocity component is measured using a 488.0-nm beam, while the 514.5-nm beam measures a streamwise velocity component. A combined counter-type signal processor (Dantec model 57H00) with functions of counter, buffer interface, and coincidence filter, which is interfaced with a LEO (Intel-486) PC in the direct access mode, was employed for data processing. Statistical data were based on a sample size of 320,000 measurements with a sampling frequency of approximately 400 samples/s, from which the time averaged values were determined.

For the present system, the link consisted of four fiber manipulators and four single mode fibers. Each fiber manipulator was used as a launch unit to couple the beam onto the fiber. The single mode polarization preserving fiber produced a beam diameter of 1.35 mm, and a beam divergence angle of 0.5–0.6 mrad. It was fitted with two plugs at each end, which included the microlens for focusing (at the receiving end) and/or resetting the divergence angle of the beam (at the probe end).

The selection of seed particles for laser Doppler measurements

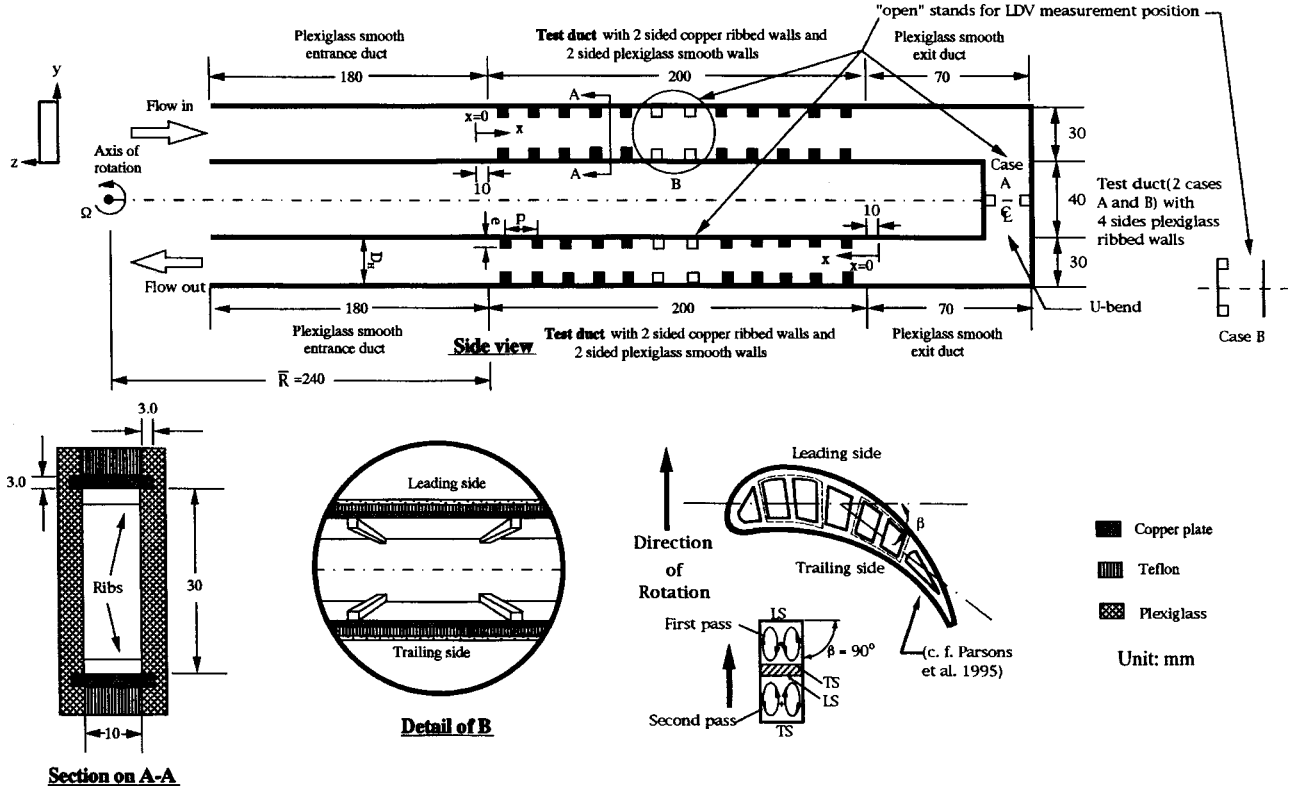

Fig. 2 The measurement positions and dimensions of the test section

Table 1 Laser-Doppler velocimeter optical parameter

Laser power	4 W
Laser wavelength	
green beam	514.5 nm
blue beam	488.0 nm
Beam-diameter at e^{-2} (major and minor axes of ellipsoid)	
green	3.98×0.189 mm
blue	3.98×0.189 mm
Beam half angle	
green	2.72°
blue	2.72°
Focal length	
green	400 mm
blue	400 mm
Fringe opening	
green	5.27 μm
blue	5.27 μm
Number of fringes	36

Table 2 Maximum possible measurement errors

Quantity	System error	Random error
Measured quantity		
x	±0.5 mm	±0.01 mm
y	±0.5 mm	±0.01 mm
z	±0.5 mm	±0.01 mm
u_0	±2.5%	±0.25%
u	±2%	±2.5%
u'	±2.5%	±3%
v	±2.5%	±3%
v'	±3%	±2%
Ω	±1 rpm	±0.5 rpm
Derived quantity		
u/u_0	±1%	±1.5%
u'/u	±4%	±3%

represents a compromise between large particles (diameter>10 μm), which are good light scatterers, and small particles (diameter<1 μm), which follow the air flow very accurately. A satisfactory compromise could be obtained by 4–5-μm diameter soot droplets from a straw smoke generator. Since the flow was forced convection dominated, velocity measurements were made without heating.

3 Data Reduction and Analysis

The laser-Doppler signal from the photomultiplier was fed to a signal processor and, then, measured with a frequency counter. The digital value of the Doppler frequency shift f_d, the characteristic wavelength of the laser λ, and the half angle between the beams $\theta/2$ are translated to horizontal (streamwise) u and vertical (transverse) v velocity components, respectively, by the equation

$$u/\text{or}\ \ v = \frac{\lambda_{u/or} f_d}{2\sin(\theta/2)}. \tag{1}$$

Once a valid laser velocimeter signal is generated, the test section angular position is recorded with a shaft encoder. The encoder divides each revolution into 3600 parts. The two velocity signal and the shaft position are simultaneously recorded onto floppy disks by a PC. A typical test had 40 data points in each measured downstream station. This zone's two-dimensional velocity and angular position data for the measured point were analyzed after the test.

In addition, various sources of uncertainty contribute to the random and system errors in the mean velocity measurements. These include index of refraction effects that alter the half angle between the beams and the optical probe volume location; velocity bias, filter bias, and velocity gradient broadening; particle seeding and particle deposition considerations; finite size of the data samples; rotating channel wobble and vibrations in rotational speeds of the channel. The visual optical probe volume positioning uncertainty was kept less than ±0.01 mm by the careful determination of an initial reference location and using stepping motors with incremental steps equal to 50 μm.

The nonuniform axial deposition of soot droplets on the glass window contributed to the random uncertainty of all the velocity measurements as well as to the symmetric uncertainty of these measurements made along axial traverses. Of the uncertainties specifically attributable to the LDA technique, filter bias, velocity bias, and gradient broadening were carefully examined. Filter bias was avoided. The maximum velocity bias was estimated to be less than 10% but typically, it was about 10%. The effect of gradient broadening seems negligible. In the flow region measured, typical uncertainties in the mean velocities and turbulent intensities due to this effect were 3–4% and 3–5%, respectively.

As mentioned before, the small size (4–5 μm) of the soot droplets used guaranteed the tracking of velocity fluctuation higher than 1 kHz to better than 1% speed accuracy. Similarly, particle drift velocity due to the centrifugal force can be shown to be negligibly small. Calculation of the mean and turbulent intensity results in statistical uncertainties of ±12% for mean velocity and ±15% for turbulent intensity at the maximum rotational speed. In this study, channel rotation was maintained constant within ±0.3%. Table 2 summarizes the estimates of maximum measured error and derived error associated with each measurement presented in Sec. 2.

4 Results and Discussion

The forced flow mechanism present in the rotating channel is influenced mainly by the presence of Coriolis and centrifugal forces. The tests are conducted for two channel Reynolds numbers (Re_D=5000 and 10,000) and three rotational speeds (Ω=100, 200, and 300 rpm). The parameters apparent for this type of flow in rotating ribbed roughened channels are the flow rates (Re_D), rotational numbers (Ro) with fixed rib geometry e/D_H =0.27 (e/H=0.135), and given size of p/e=8. The time average u circumferential velocity (streamwise/axial direction in the test channel) was measured along a radial line at midplane (z =10 mm) and downstream distance (shown in Fig. 2) at rotational Reynolds numbers of 150, 301, and 451, and at the corresponding rotational numbers (Ro) from 0.015 to 0.0902. The temperature of the air was maintained at 25±1°C for all the experiments. Based on the definition of Ro, it is found that Ro of the channel at Re_D=10,000 would be half of that channel at Re_D=5000 for the same rotational speed.

4.1 Qualification Test and Assessment. Verification of the experimental procedure and its accuracy for the mean velocity were made for smooth duct without rotation at various streamwise locations, and the results were also compared with the known one-seventh law for turbulent flow velocity profile. It was found (not shown) that the rms deviations were less than ±1.5% and 2% at $x/D_H \leqq 9.73$ (9.67) in the first (second) channel, respectively. To examine the conservation of the mean flow rate, the mean streamwise velocities were also integrated over each cross section at specified stations. The results showed that the mass continuity was valid within ±3% in two entire channels. The ratios of u_{max}/u_0 for this particular case (Re_D=10,000) at downstream of the first channel and the second channel were found to be about 1.18 and 1.14, respectively. This coincided adequately (≦6%) with the conventional one-seventh result (=1.233). The good agreement served to establish the validity of the measurements and data reduction method. There is no discernable trend and the flow may be regarded as symmetric without rotation. Moreover,

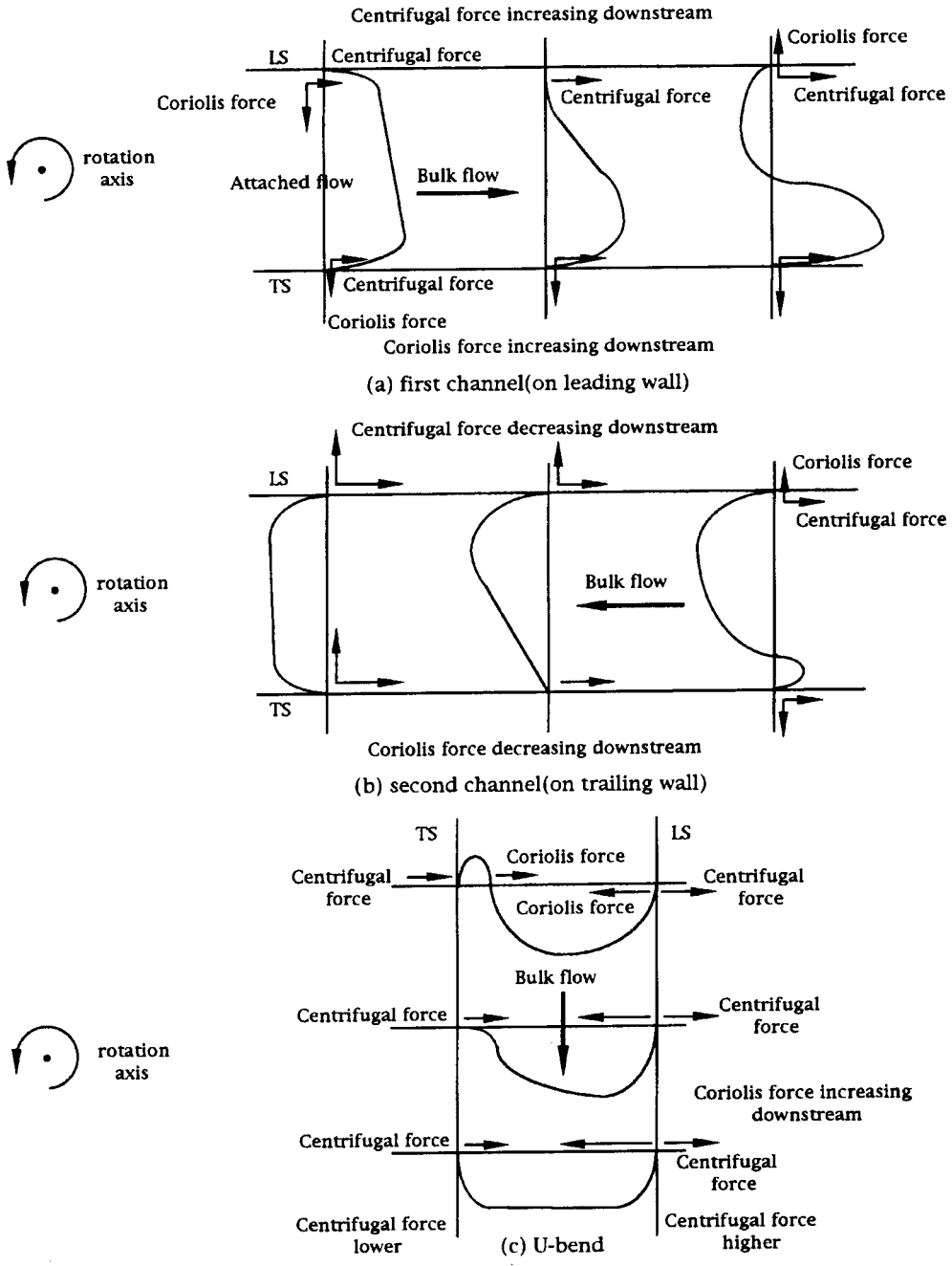

Fig. 3 Schematic of the possible separation mechanisms in the ribbed channel (followed by Dutta et al. [16])

streamwise velocity and turbulent intensity distribution at the entrance within the midplane for the cases under study were also measured which demonstrate the degree of uniformity and symmetry produced by the entry arrangements.

4.2 Mean Velocity Distribution. The possible flow separation mechanisms [16] in both the first/second channels including the U bend with rotation are depicted in Fig. 3. The balance of the centrifugal buoyancy due to radial pressure variation and Coriolis force is discussed later in related figures and, with reference to this figure, the details of flow development in the present two rotating roughened channels can be discussed. Within the first/second channel, after the flow passing over the seventh rib the present measurements show that the flow is fully developed with the same flow pattern being repeated over successive rib intervals. This finding is the same as reported by Iacovides et al. [12]. Therefore the following figures will only show the flow characteristics near the vicinity of two consecutive ribs for periodic fully developed flow.

Figure 4 illustrates the mean flow distribution at various streamwise stations for $Re_D = 5000$ under various rotating speeds. A dependence of rotating speeds on the velocity profiles was found. The axial velocity profiles obtained for eight downstream stations in each channel with/without rotation are shown in Fig. 4. The distortion of the profiles in Fig. 4 appears clearly. Generally, the flow pattern with rotation is skewed continuously from the typical one-seventh law turbulent velocity profile. The mean velocity profiles show the presence of a nearly uniform velocity core region in which the velocity gradient is small, along the entire

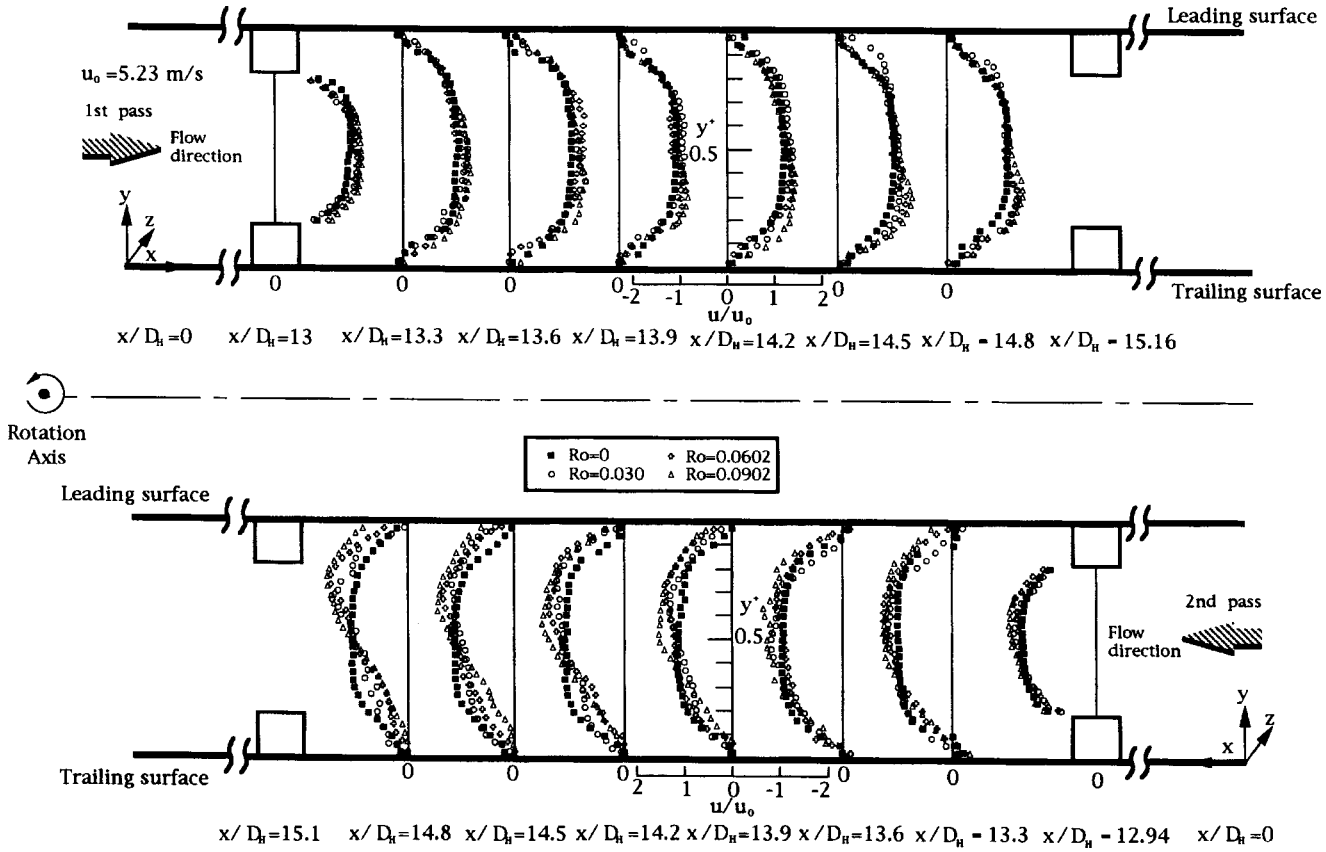

Fig. 4 LDV measurements for streamwise velocity along the channels between two consecutive ribs (Re_D=5000) at z^+=0.5 and u_0=5.23 m/s

length of the duct which isolates the boundary layers adjacent to the duct wall except for the region in the U bend. In spite of this, the flow structure redistributes slightly with rotation due to the Coriolis force. With the assistance of Fig. 3, it is found that the Coriolis force acts toward the trailing (leading) wall, while it is in the first (second) channel as the channel rotates. Since the present flow is isothermal, rotational (centrifugal force due to density variations) buoyancy is not found. This can also be seen later in Fig. 5. Moreover, the flow shown in Fig. 4 is significantly accelerated by the presence of the channel obstruction presented by the opposite ribs. Mean velocities at the central portion at Ro=0 are observed somewhat higher. A large recirculation happens downstream of the upstream rib occupying the entire zone in between two consecutive ribs is evident for both channels. This reverse flow region extends from x/D_H=13 to x/D_H=13.9 (first channel) and from x/D_H=12.94 to x/D_H=13.6 (second channel). These strongly indicate that flow separation occurs between two consecutive ribs in both channels. The reattachment length seems not changed a bit (from $0.9D_H$ to $0.86D_H$) after the flow makes 180° U turn. In addition, the separation in both first/second pass will delay with rotation. The distortion of the mean velocity profile from traditional nearly flat shape appears to be shifted toward the trailing side (first channel) and leading side (second channel) because the secondary flow exists in the plane of test section due to Coriolis forces with rotation. While the centrifugal force acts toward the same (opposite) direction as the flow proceeds in the first (second) channel. This causes that the mean flow would accelerate (decelerate) in the first (second) channel, respectively, with rotation. All behaviors stated above will become significant as Ro increases.

Figure 5 shows the corresponding of Fig. 4 except for Re_D =10,000. In fact, the Ro in Fig. 5 is half that in Fig. 4 for the same rotational speed. Since the inertia force becomes strong, the findings in Fig. 4 become less noted as one would expect. However, the change in reattachment length with Re_D seems significant (e.g., $0.9D_H$–$0.7D_H$) from Fig. 5 after the flow makes a 180° U turn. In contrast to the smooth wall case (see Hsieh et al. [9]), there is now a region of flow separation along both leading and trailing walls in the first and second channel with rib turbulators. The symmetric nature holds without rotation. However, the position of the peak value of streamwise velocity distribution along the channel moves from y/D_H=0.5 to y/D_H=0.3 (0.8) when Ro becomes higher as the flow proceeds downstream in the first (second) channel in Fig. 4. In fact, in Figs. 4 and 5 the velocity peak in the streamwise direction increases and converges toward the downstream rib on trailing (leading) surface in the first (second) channel.

A typical vector plot of streamwise velocity at the region between two consecutive ribs at Re_D=5000 is shown in Fig. 6 in both channels. This gives a clear picture of the flow. The value of $|V_{max}|$ as well as the flow behavior seems not changed much (6.5–6.73 m/s) in both channels different rotational speeds even after the flow makes a 180° sharp U turn. However, the influences of the present rib, rotational speed and Re_D on reattachment length, were clearly noted. In addition, the effects of rotation on the mean flow are clearly seen in Fig. 6. As stated before, in the first (second) channel when repeating flow conditions are in evidence (not shown here), rotation displaces the faster fluid toward the trailing (leading) side in the first (second) channel. This situation shown in Fig. 6 becomes more noted as Ro increases. These effects are consistent with the rotation effects observed in flow through ribbed (staggeredly roughened in straight tangent parts only) U bends measured by Iacovides [12]. The Coriolis-induced secondary motion convects high momentum fluid toward trailing (leading) side in the first (second) channel.

To quantify flow development and downstream behavior in tur-

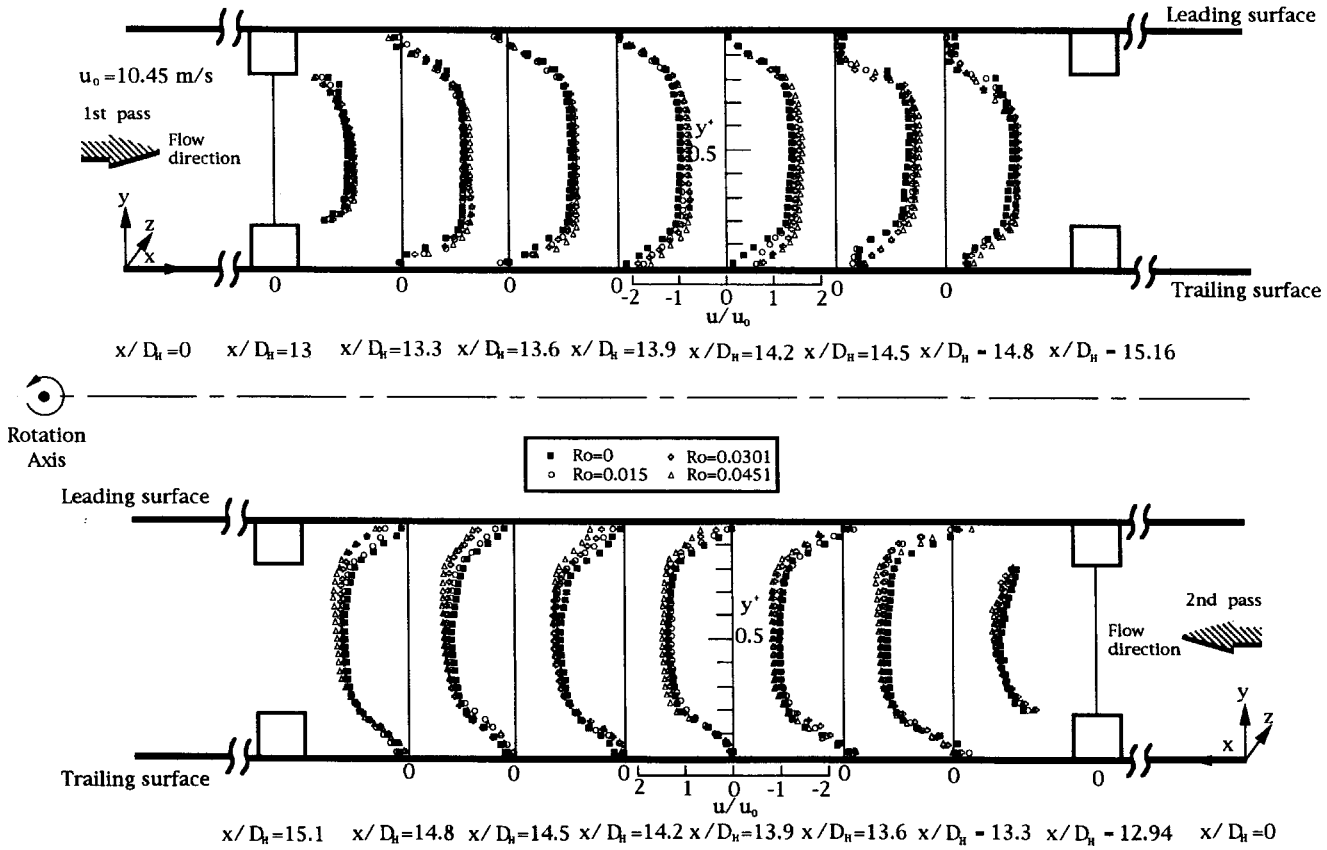

Fig. 5 LDV measurements for streamwise velocity along the channels between two consecutive ribs (Re_D=10000) at z^+=0.5 at u_0=10.45 m/s

bulent flow over ribbed geometry/or roughed surfaces (case A and B for two different rib arrangements), velocity measurements were taken for the region of 180° U bend (not including the up/downstream elbow regions) at Re_D=5000 and 10,000 with rotational speeds of 100, 200, and 300 rpm. In Fig. 7 for case A (here the ribs were positioned oppositely), the streamwise velocity profiles at midplane are shown in the 180° U bend channels for Reynolds number of Re_D=5000 and 10,000, respectively. In every channel, based on the Kutta condition, the separation should occur at a 90° sharp corner. In fact, at y/D_H=1.08 the flow has separated for a while on the trailing side of the first half of the U bend. Keeping this separation and passing over the ribs, the flow, eventually, reattached on the wall of the second half of the U bend at y/D_H=−0.84. This gives the reattachment length bigger than $1.92D_H$. Furthermore, how the flow evolves in the streamwise region downstream can be observed. Like the smooth channel (Hsieh et al. [9]), the flow at the U bend is still developing and the boundary layers are thin except that the migration of the flow to the trailing side changed a little bit. Moreover, the separated flow seems never reattached because of the presence of the ribs (see Fig. 7 for case A). After the flow passed over the rib, the flow reattached at y/D_H=−0.84 (second half of U bend). This behavior was totally changed when case B arrangement was placed instead (see Fig. 7).

In contrast to case A, there is now a small region of flow separation at y/D_H=0.93 along the top floor of the upstream rib right after the bend entry (first half of the U bend) first and then, the flow starts to separate from the trailing wall when it passes over the upstream rib (first half) and this situation preserves until touching the downstream rib (second half). However, at y/D_H =−0.93 (second half), there is no more separation region on the top floor of the downstream rib (second half) which is different from the phenomena mentioned above. Another important feature of Fig. 7 is that the velocity peak can reach $1.85u_0$ (much bigger than those of smooth ducts) for both rib arrangements in the U bend and it seems the mean velocity distribution in the first half of the U bend is more uniform than that in the second half of the U bend.

Figure 8 further deciphered the rotation and rib effects on the vector velocity within the U bend. For the case-A rib arrangement, rotation displaces the faster fluid toward the trailing wall (see Figs. 8(*b*)–(*d*). This is a consequence of Coriolis force-induced secondary flow. Rotation also has a noticeable effect on the flow development within the U bend. Moreover, as can be seen in Figs. 8(*b*)–(*d*), rotation leads to a more uniform velocity distribution. The upstream separation of the rib is about 1.6 diameters long and 0.4 diameters high. This situation becomes less distinct as Ro increase. While for the case-B rib arrangement, the separation bubble almost occupies the entire space of the two consecutive ribs as shown in Figs. 8(*e*)–(*h*). Again, rotation leads to a more uniform velocity distribution which can be seen in Figs. 8(*g*) and (*h*). The size of the separation bubble becomes smaller especially for its height as Ro increases. For instance, at Ro=0.0451 (300 rpm) the bubble is 1.4 diameters long and 0.15 diameters high. Further inspection of Figs. 8(*b*)–(*d*), shows that there are two co-rotating vortices existing right up/downstream from the rib on trailing wall, respectively. The one upstream is rotating in a clockwise direction and strong; and the one downstream seems not clear and weak. However, this situation seems to never occur for the rib on the leading wall for the cases under study. In contrast to this finding, the case-B rib arrangement exhibited a different behavior (see Figs. 8(*e*)–(*h*)). Only one big vortex exists in between two consecutive ribs. The strength of the vortex becomes weaker as Ro increases.

These figures strongly support the flow pattern shown in the corresponding results as illustrated in Fig. 7. It is important to

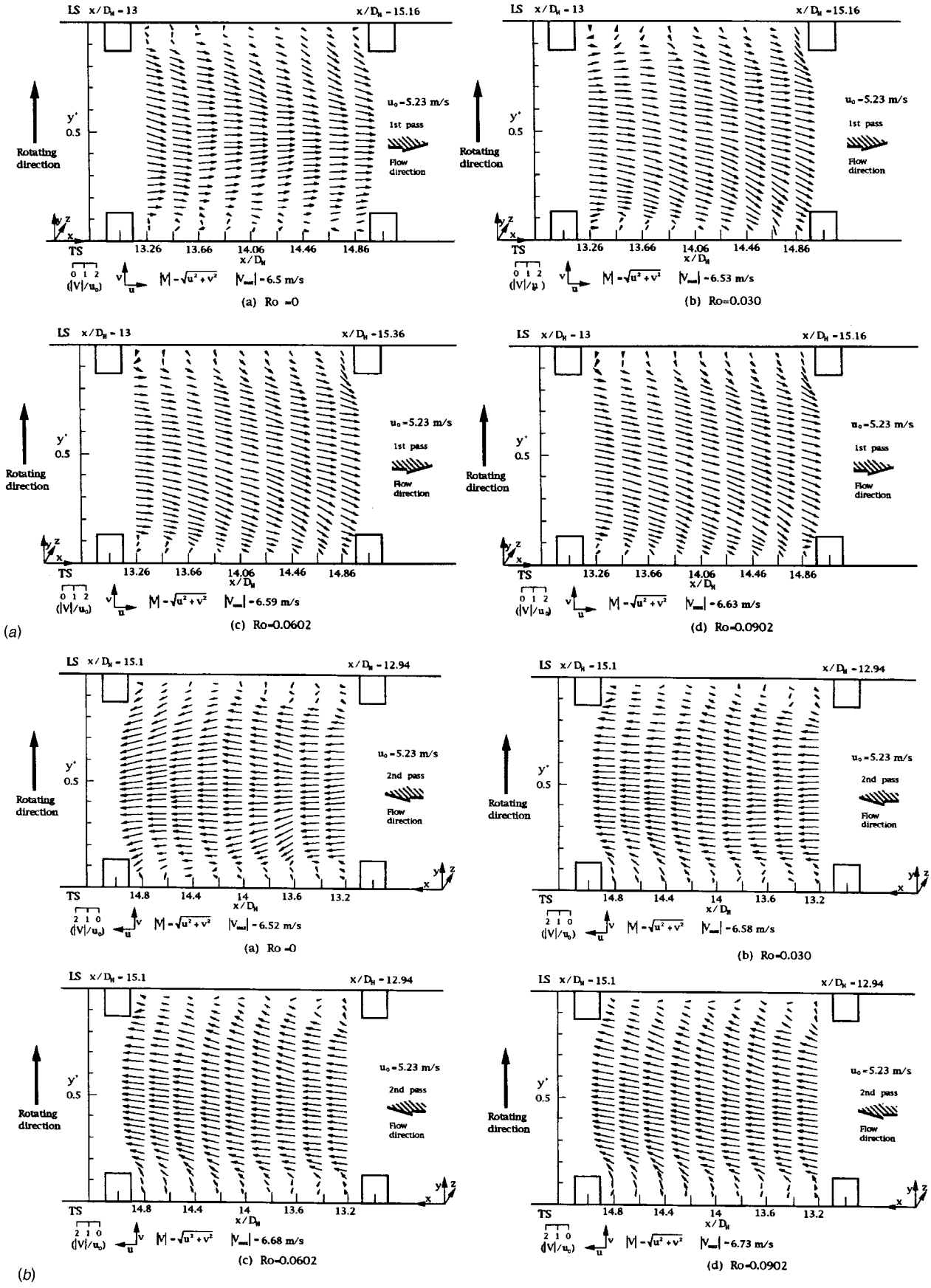

Fig. 6 Streamwise vector plots between two consecutive ribs in first channel at different Ro at $Re_D = 5000$ at $u_0 = 5.23$ m/s Streamwise vector plots between two consecutive ribs in second channel at different Ro at $Re_D = 5000$ at $u_0 = 5.23$ m/s

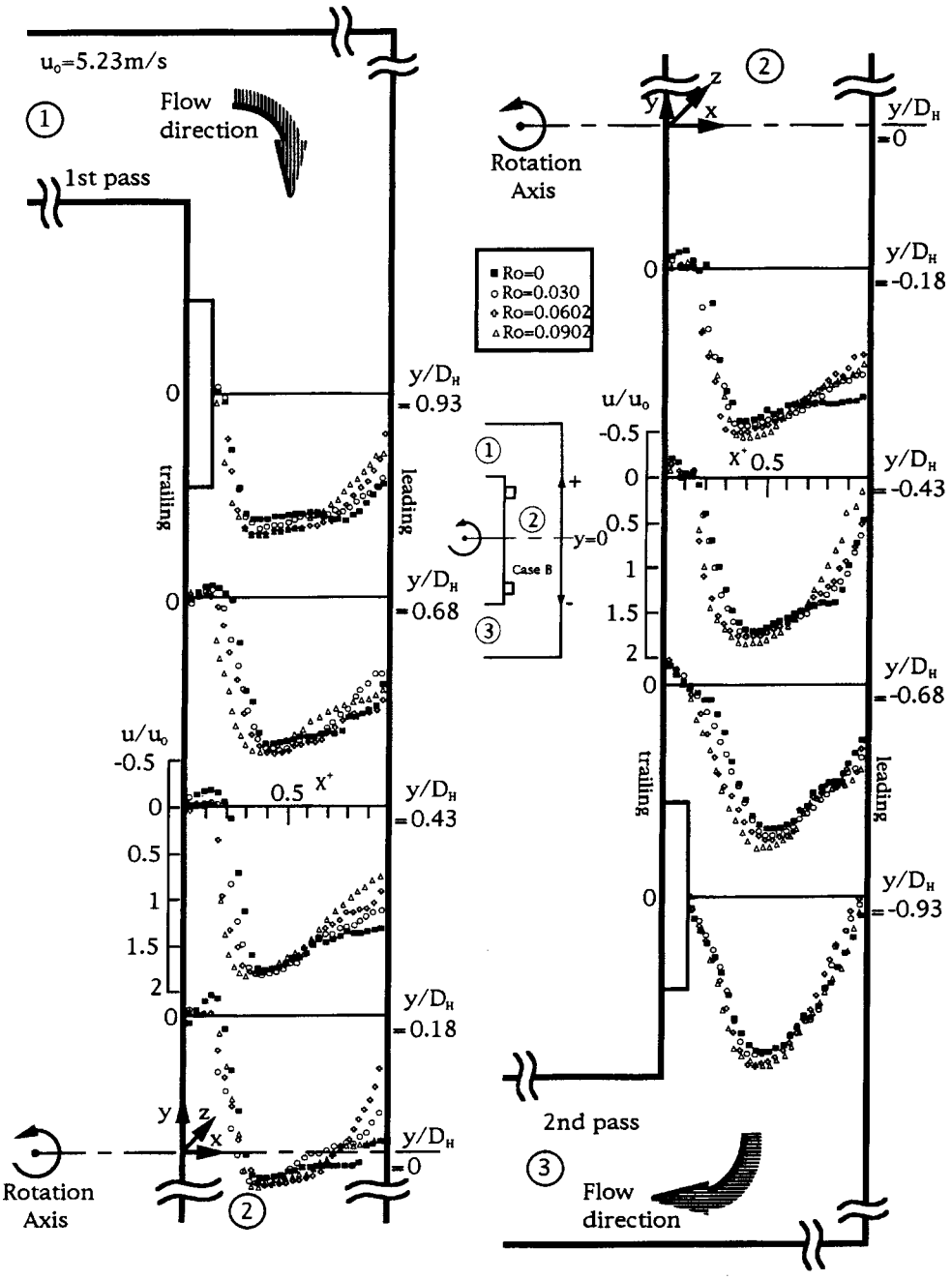

Fig. 7 LDV measurements for the streamwise velocity distribution in U bend at $Re_D=10000$ and $z^+=0.5$ at $u_0=10.45$ m/s LDV measurements for the streamwise velocity distribution in U bend at $Re_D=5000$ and $z^+=0.5$ at $u_0=5.23$ m/s

remark that the size of the core flow (defined as fluid of velocity greater than about $0.5u_0$ at each downstream station) shown in Figs. 7 and 8 in the U bend, rather than the degrees of distortion of the streamwise distribution adjacent to the trailing wall, indicates the importance of the secondary flow: the smaller the core, the larger the magnitude of the secondary velocities. This can be seen in Figs. 8(*d*) and (*h*) at which they all have the highest Ro.

In general, Fig. 8 shows that for both case-A and -B rib arrangements, the core is found progressively towards the trailing wall and along the side wall with a corresponding low velocity region adjacent to both the leading and trailing wall due to the presence of the ribs. However, with case B, the situation of the low velocity region near the leading wall is getting less strong due to the absence of the rib. The development of the streamwise velocity is influenced by a streamwise pressure gradient. Although wall pressures were not measured, their form can be expected.

4.3 Turbulent Intensity and Shear Stress Distributions. The effect of rib and rotation on the boundary layers on the trailing and leading walls for both channels on the midplane of symmetry of the channel and the possible three dimensionality associated with the flow separation on both walls were already evident from the mean velocity fields as shown in Figs. 4 and 5. These three effects (rib, rotation, and 3D effect) combine to produce a quite complex distribution of the turbulent intensity and shear stress.

The results of turbulent intensity measurements are shown in Fig. 9. The normalized turbulence intensity u'/u has been plotted

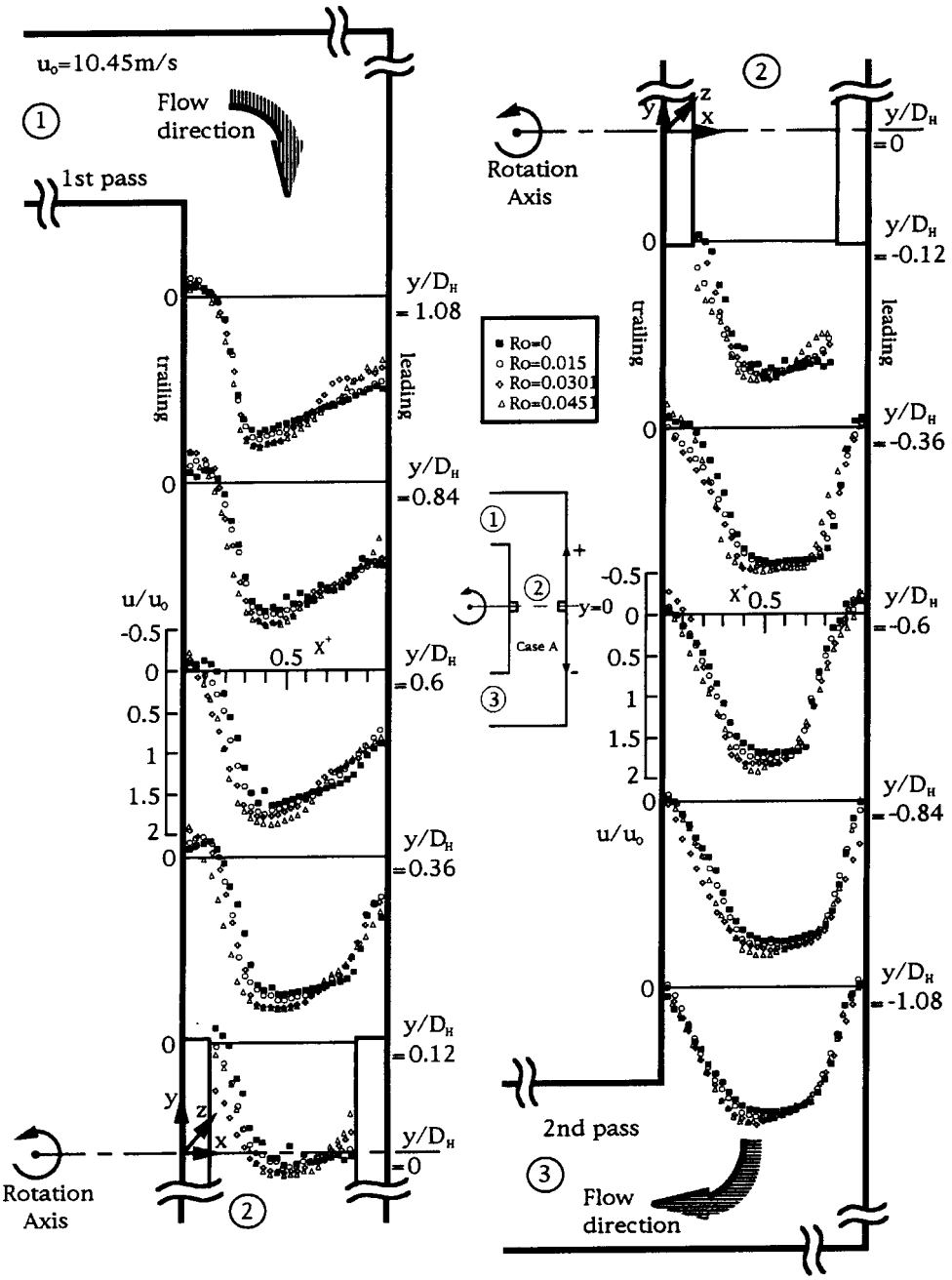

Fig. 7 (***continued***)

in the transverse direction. At $x/D_H=7.6$ (first channel) and 7.54 (second channel), a nearly uniform turbulence intensity of 10% is observed all across where the flow was accelerated except near the rib top floor where it is higher at 120%. Further downstream, for instance, $x/D_H=7.9$ in the first channel, the profiles show an increase in the turbulence levels in the recirculation zone close to trailing wall, going up to 120% near to edge of the dividing stream line and up to 60% near the leading wall. Figure 9 also shows profiles of streamwise turbulence intensities in the vicinity of two consecutive ribs in both the first and second channels at different rotational speeds and $Re_D=5000$ which stands for the corresponding developments in the turbulence levels of Fig. 4. The increase in turbulence intensities along the ribs is expected due to the growth of the boundary layer shear layer where the flow was decelerated. The intensity of shear layer is greater in the vicinity of the ribs as the flow tries to retain in flow direction and hence a higher turbulence intensity is seen there. The increase in intensity along the rib top floor can be seen. This is because of flow development against the adverse pressure gradient along the upstream and downstream corner and hence higher shear levels as high as 100% at $x/D_H=8.8$ (first channel) and 200% at $x/D_H=7.9$ (second channel). As the flow moves downstream, the distortion of the turbulence intensity distribution close to the center reduces a bit (only about 10%) due to the bulk movement of the flow and self-imposed favorable pressure gradient by the flow as the flow proceeds further downstream after passing over the ribs as shown in Fig. 9.

The higher turbulence intensity levels shown in Fig. 9 due to rotation serves to reaffirm the existence of more disturbed flow with ribs. It shows that higher turbulence levels (about 100%) near the walls and in the shear layer separating the mean flow from the circulation zone as shown in Fig. 9 for $x/D_H=13-14.8$ in both the first/second channel. Upon further inspec-

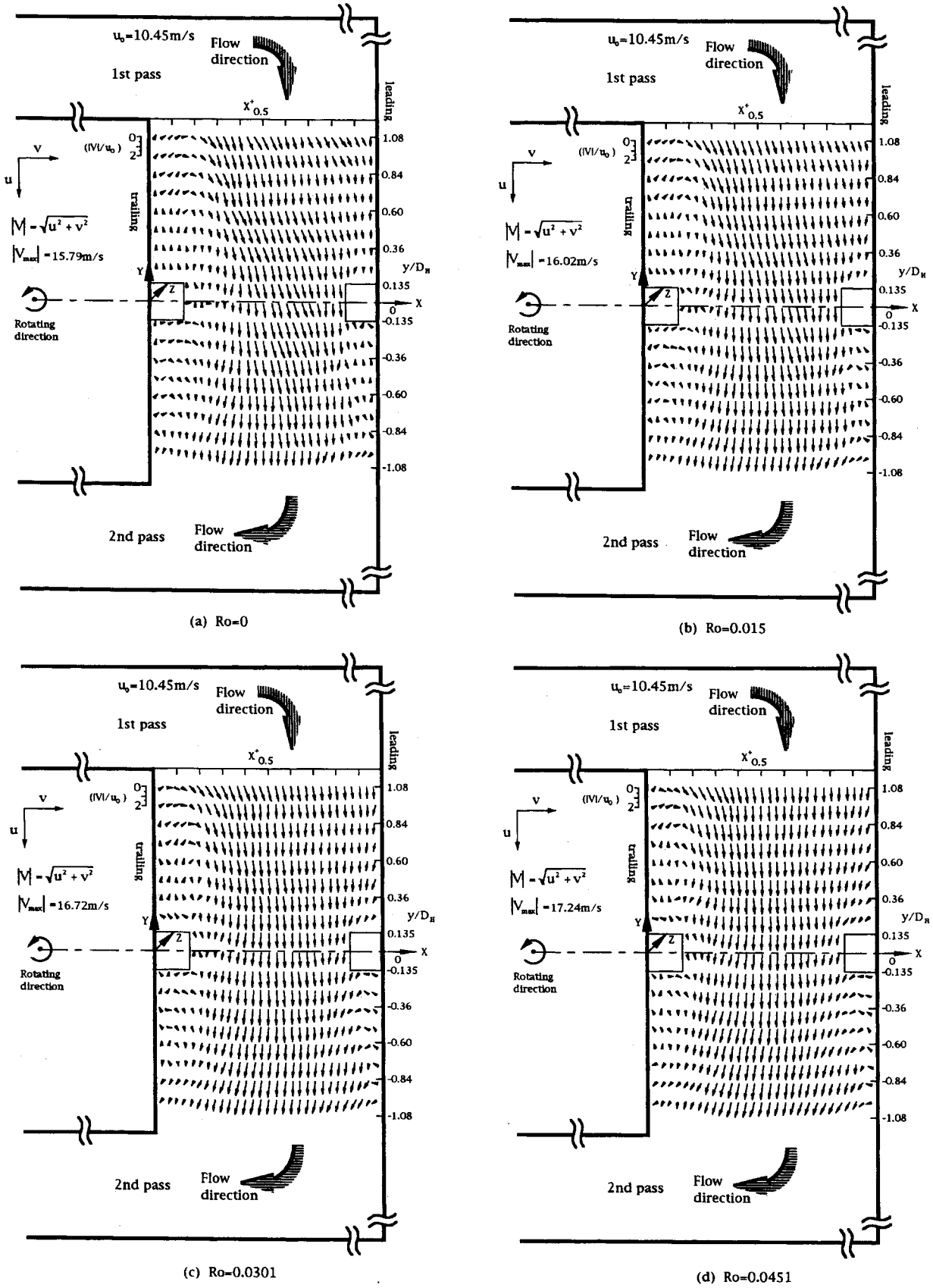

Fig. 8 Velocity vector plots in U bend (rib arrangement; Case A) at $Re_D=10000$ ($u_0=10.45$ m/s) and $z^+=0.5$ under different Re Velocity vector plots in U bend (rib arrangement; Case A) at $Re_D=10000$ ($u_0=10.45$ m/s) and $z^+=0.5$ under different Ro

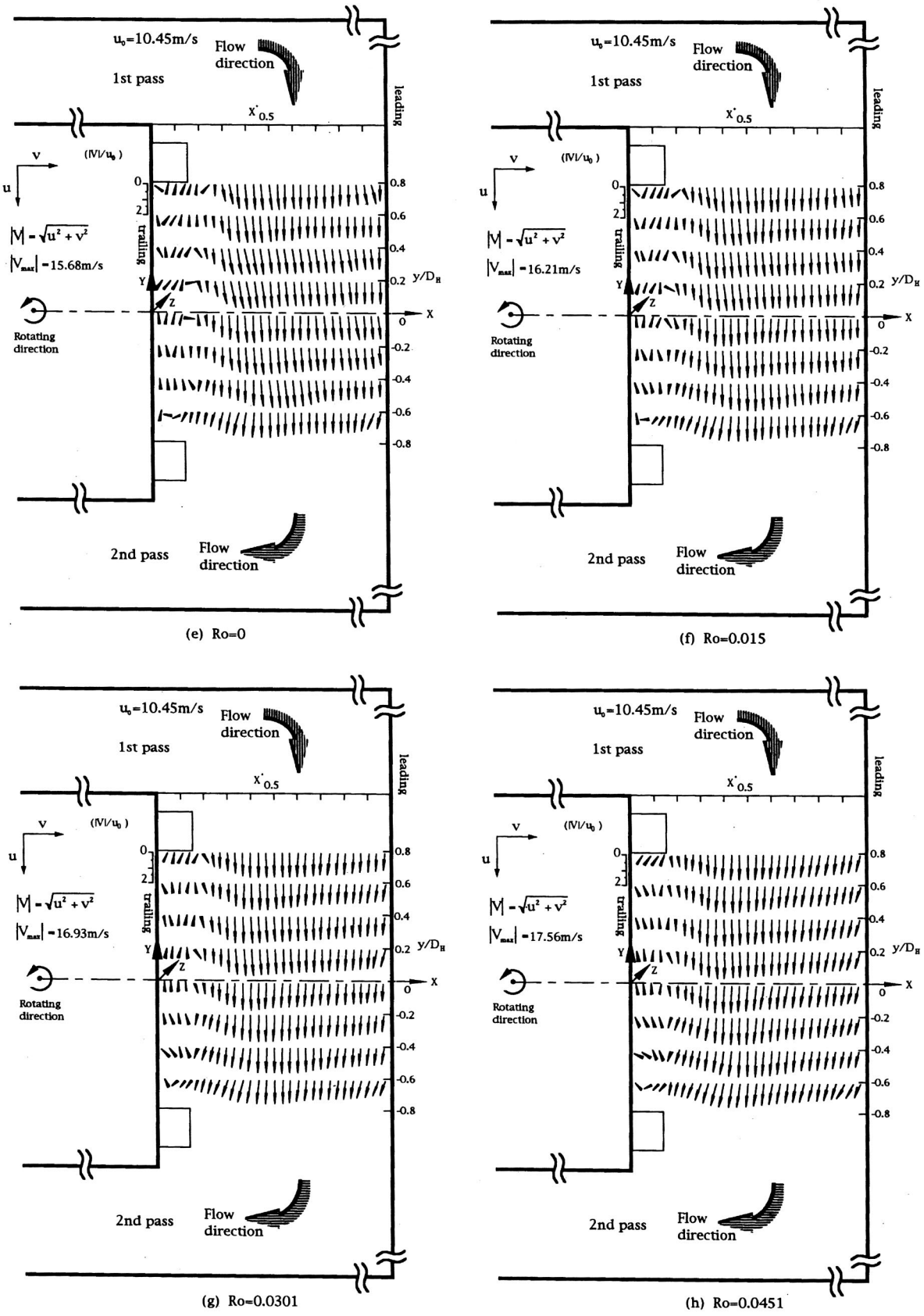

Fig. 8 (*continued*)

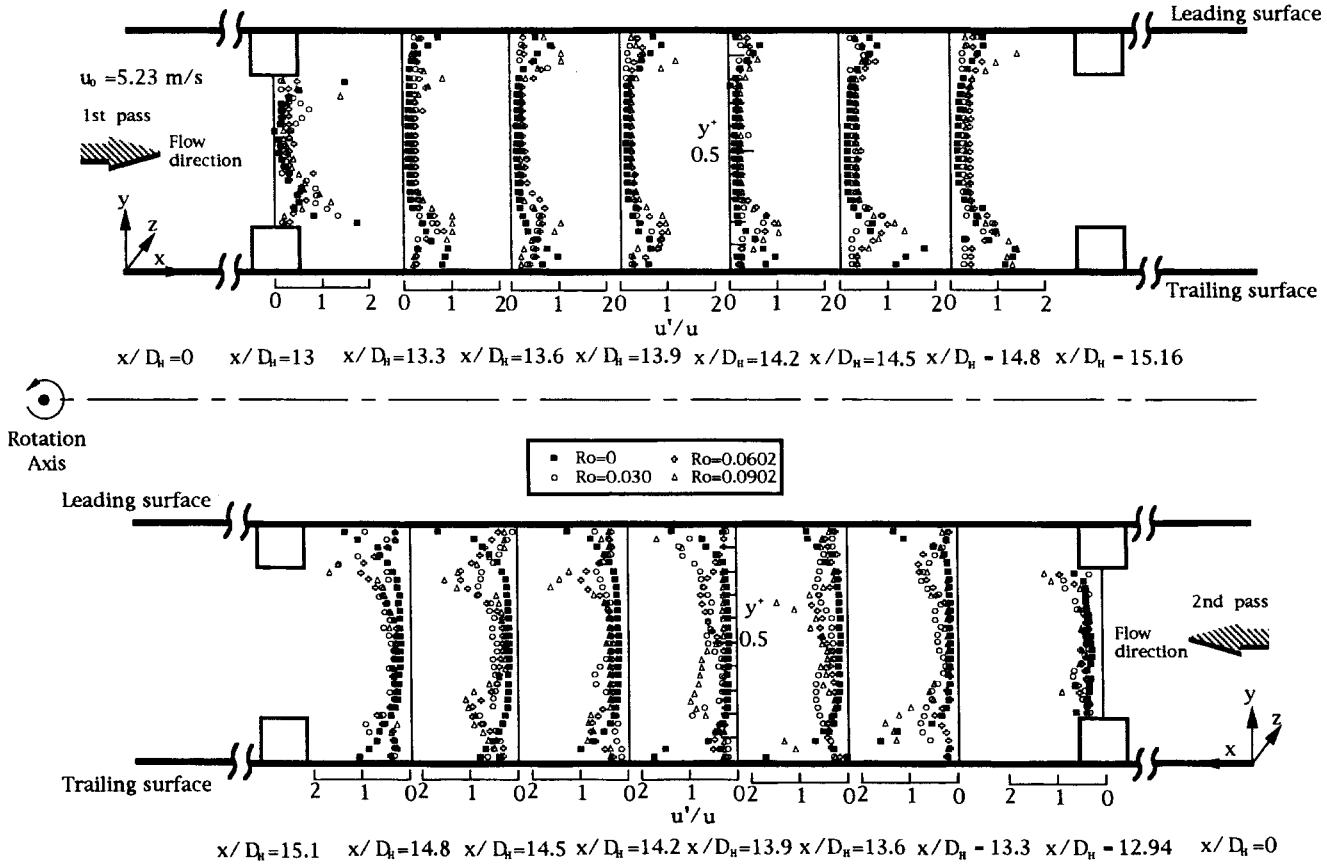

Fig. 9 LDV measurements for streamwise turbulence intensity at Re_D=5000 and u_0=5.23 m/s

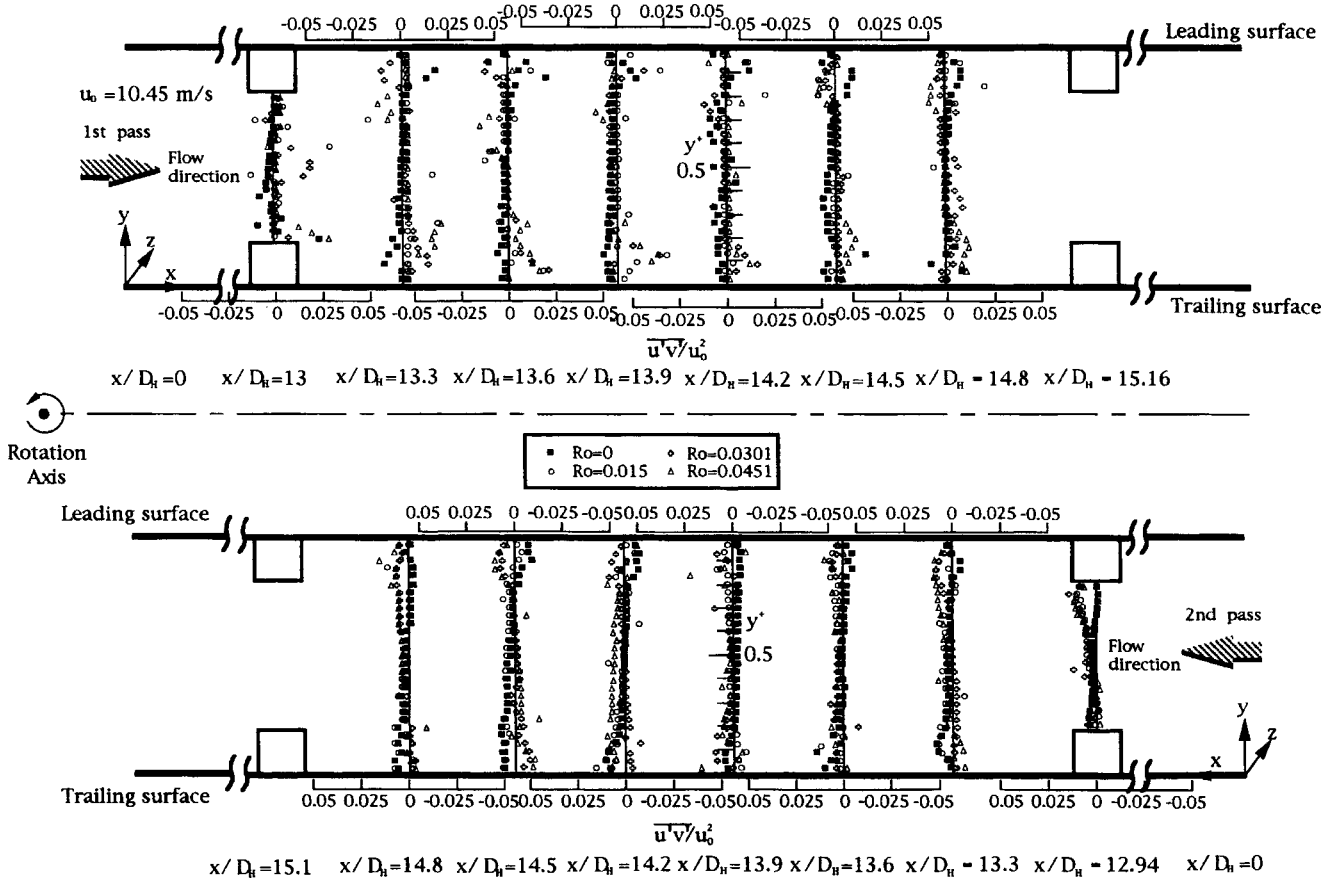

Fig. 10 Profiles of the Reynolds shear stress at Re_D=10000 and u_0=10.45 m/s

tion of Fig. 9, it is found that most of the significant shear stress variation occurs downstream of the U turn. These measurements in the second pass indicate that, at $x/D_H = 12.94-14.5$, turbulence levels vary significantly with separation region's growth and decay. Unlike the behavior in the first pass, the region of high turbulence randomly expands from leading/trailing walls towards the duct center, which are also significantly affected by rotation. Even so, the effects of rotation on turbulence are not strong, perhaps because of the present low rotation speed ($Ro \leqslant 0.0902$). By contrast, the flow along the smooth channel has stabilized somewhat.

The distribution of the turbulent shear stress component at $Re_D = 10{,}000$ within the mid-plane $\overline{u'v'}$ along the downstream in both the first pass and the second pass is shown in Fig. 10. These measurements indicate that the shear stress distribution is significantly affected by ribs and rotation as well as the U bend. The shear stress is small ($\leqslant \pm 5\%$) as expected due to low rotation speeds of the present study, with peak values near the leading/trailing walls. The ribs and rotation increase shear stress. However, the effect of rotation seems different in the first and second pass, in which the peak value was shifted toward the trailing wall in the first pass and the leading wall in the second pass due to the Coriolis forces. Unlike the turbulent intensity distribution in the second pass as shown in Fig. 10, the U turn has a weak effect on $\overline{u'v'}$ values. Also shown in Fig. 10 are the profiles of the turbulent shear stresses measured within two consecutive ribs. As expected, the levels of turbulence are considerably higher and become even higher over the ribs. At successive streamwise stations, large values of $\overline{u'v'}$ are found near the trailing and leading walls in both channels indicating that the momentum transport is large in the region coinciding with large streamwise velocity gradients. The change in the sign of $\overline{u'v'}$ is closely associated with changes in the sign of transverse velocity gradients due to rotation and the rib. Upon approaching the rib, $\overline{u'v'}$ values are low, corresponding to the small boundary layer thickness and in the core along the downstream $\overline{u'v'}$ seems not changed a bit indicating a weak mixing in the center of the core.

5 Conclusions

The measurements presented and discussed provide more insight into the flow structure within a two pass rotating ribbed roughened 180° U bend of rectangular cross section duct (AR =3:1) for $Re_D = 5000$ and 10,000 and $Ro = 0-0.0902$, simulating that encountered in internal cooling passages of gas turbine blades. Detailed streamwise mean velocity distribution as well as turbulence intensity and shear stress in the vicinity of two consecutive ribs in both channel pass and U bend are reported. The following specific features are observed.

1. A steamwise-periodic fully developed flow is approximately achieved after sufficient distance (about the seventh rib before/after the U turn).
2. Separation is observed in both the first and second channels between two consecutive ribs, and in the U-bend region as well. However, the size of separation region is smaller than that of the stationary duct as Ro increases which are consistent with the previous studies of Iacovides et al. [12]. In addition, the separation delayed effect in straight channels (first/second pass) is noted and becomes more significant as Ro increases.
3. Secondary flow observed due to Coriolis force in the (first) second channel and Coriolis as well as centrifugal force in the U bend becomes strong as Ro increases.
4. The intensity of the shear layer is greater in the vicinity of the ribs as compared to that in the smooth surface. The rib as well as the U-bend region effect on turbulent intensity and shear stress are dominant over that of rotation.
5. Despite remark 4, the effect of rotation is still noted. It is found that the rotation makes the turbulent intensity and shear stress distribution more random in transverse direction along the midplane as compared to those without rotation.

Acknowledgments

This work was supported by a research grant (NSC 87-2212-E-110-026) from the National Science Council, Taiwan, ROC. Special thanks go to one of the leading author's Ph.D. graduate students, Mr. H. H. Tsai, for his assistance during the manuscript preparation of this paper.

Nomenclature

- AR = aspect ratio, H:W=3:1
- D_H = hydraulic diameter, 2WH/(W+H)
- e = rib height
- H = height of channel
- L = test channel length
- p = pitch
- R = mean rotation radius
- Re_D = Reynolds number, $u_0 D_H/\nu$
- Re_Ω = rotational Reynolds number, $\Omega D_H^2/\nu$
- Ro = rotional number, $\Omega D_H/u_0$
- u = horizontal velocity (streamwise)
- u' = horizontal velocity fluctuation
- u_0 = inlet mean velocity
- v = vertical velocity (transverse)
- v' = vertical velocity fluctuation
- W = width of channel
- x = x ordinate (streamwise) direction
- y = y ordinate (transverse) direction
- y^+ = y/D_H
- z = z ordinate (spanwise) direction
- z^+ = z/D_H

Greek Symbols

- β = model orientation
- λ = wavelength
- θ = intersection angle of laser beams
- Ω = rotational speed

References

[1] Hart, J. E., 1971, "Instability and Secondary Motion in a Rotating Channel Flow," J. Fluid Mech., **45**, pp. 341–351.
[2] Moore, J., 1967, "Effects of Coriolis on Turbulent Flow in Rotating Rectangular Channels," MIT Gas Turbine Laboratory Report, No. 89.
[3] Rothe, P. H., and Johnson, J. P., 1979, "Free Shear Layer Behavior in Rotating Systems," ASME J. Fluids Eng., **101**, pp. 117–120.
[4] Wagner, R. E., and Velkoff, H. R., 1972, "Measurements of Secondary Flows in a Rotating Duct," ASME J. Eng. Power, **94**, pp. 261–270.
[5] Johnston, J. P., Halleen, R. M., and Lezius, D. K., 1972, "Effects of Spanwise Rotation on the Structure of Two-Dimensional Fully Developed Turbulent Channel Flow," J. Fluid Mech., **56**, Part 3, pp. 533–557.
[6] Guidez, J., 1989, "Study of the Convective Heat Transfer in Rotating Coolant Channel," ASME J. Turbomach., **111**, pp. 43–50.
[7] Prakash, C., and Zerkle, R., 1992, "Prediction of Turbulent Flow and Heat Transfer in a Radially Rotating Square Duct," ASME J. Turbomach., **114**, pp. 835–846.
[8] Hsieh, S. S., Wang, Y. S., and Chiang, M. H., 1997, "Local Heat Transfer and Velocity Measurements in a Rotating Ribbed Two Pass Square Channel With Uneven Wall Temperatures," ASME J. Heat Transfer, **119**, pp. 843–848.
[9] Hsieh, S. S., Chen, P. J., and Chin, H. J., 1999, "Turbulent Flow in a Rotating Two Pass Smooth Channel," ASME J. Fluids Eng., **121**, pp. 725–734.
[10] Dutta, S., Andrews, M. J., and Han, J. C., 1997, "Turbulent Flow and Heat Transfer in Rotating Different Aspect Ratio Channels," J. Thermophys. Heat Transfer, **11**, pp. 318–319.
[11] Cheah, S. C., Iacovides, H., Jackson, D. C., Ji, H., and Launder, B. E., 1996, "LDA Investigation of the Flow Development Through Rotating U-ducts," ASME J. Turbomach., **118**, pp. 590–596.
[12] Iacovides, H., Jackson, D. C., Ji, H., Kelemenis, G., Launder, B. E., and Nikas, K., 1998, "LDA Study of the Flow Development Through an Orthogonally Rotating U-Bend or Strong Curvature and Rib-Roughened Walls," ASME J. Turbomach., **120**, pp. 386–391.

[13] Liou, T. M., and Chen, C. C., 1999, ''LDV Study of Developing Flows Through a Smooth Duct With a 180° Straight-Corner Turn,'' ASME J. Turbomach., **121**, pp. 167–174.
[14] Bons, J. P., and Kerrebrock, J. L., 1999, ''Complementary Velocity and Heat Transfer Measurements in a Rotating Cooling Passage With Smooth Walls,'' ASME J. Turbomach., **121**, pp. 651–662.
[15] Hsieh, S. S., and Liu, W. J., 1996, ''Uneven Wall Flux Effect on Local Heat Transfer in Rotating Two-Pass Channels With Two Oppositely Ribbed Walls,'' ASME J. Heat Transfer, **118**, pp. 864–876.
[16] Dutta, S., Andrews, M. J., and Han, J. C., 1996, ''Prediction of Turbulent Heat Transfer in Rotating Smooth Square Ducts,'' Int. J. Heat Mass Transfer, **39**, pp. 2505–2514.

Analysis of the Worst Mistuning Patterns in Bladed Disk Assemblies

E. P. Petrov

D. J. Ewins

Imperial College of Science, Technology & Medicine,
Center of Vibration Engineering,
Mechanical Engineering Department,
Exhibition Road,
London SW7 2BX, UK

The problem of determining the worst mistuning patterns is formulated and solved as an optimization problem. Maximum resonant amplitudes searched across the many nodes of a large-scale finite element model of a mistuned bladed disk and across all the excitation frequencies in a given range are combined into an objective function. Individual blade mistuning is controlled by varying design parameters, whose variation range is constrained by manufacture tolerances. Detailed realistic finite element models, which have so far only been used for analyzing tuned bladed disks, are used for calculation of the forced resonant response of mistuned assemblies and for determination of its sensitivity coefficients with respect to mistuning variation. Results of the optimum search of mistuning patterns for some practical bladed disks are analyzed and reveal higher worst cases than those found in previous studies. [DOI: 10.1115/1.1622710]

Introduction

Blade mistuning is inevitable in practical bladed disks and is usually caused by small imperfections in their manufacture and assembly process. Stress levels and vibration amplitude distributions are highly sensitive to mistuning variations even in the small ranges restricted by manufacture tolerances.

The problem assessing the mistuning worsening effect on resonance response levels has been studied so far mostly as a problem of analysis of response levels for some given mistuning patterns. These mistuning patterns, can be consciously chosen by the investigator, as was done in Refs. [1–4], can be randomly generated, as in Refs. [5–7], or presented as superposition of both as in Ref. [8]. In some references (Refs. [9–11]) attempts are made to determine directly statistical characteristics of response levels variation in respect blade mistuning. More complete lists of references on studies of mistuned bladed disks can be found in Refs. [12] and [13].

There are wide variations in predictions of what the maximum response level increase can be, e.g., 21% in Ref. [2], 82% in Ref. [14], 63% in Ref. [3], 105% in Ref. [5], 110% in Ref. [7], less than 50% in Ref. [6], 90% in Ref. [8]. Although such results can give some estimate for the mistuning worsening effect, they do not guarantee that the trial mistuning patterns used are the worst (as in the case of deliberately chosen patterns) or they require generation and analyzing a very large number of random mistuning patterns, which can be used only with very simplified models (and, moreover, it is unknown *a priori* how large this number of trials has to be). The theoretical limit for the maximum magnification of the forced response that can be caused by mistuning is presented by Whitehead [15,16], where it is found to be equal to $\frac{1}{2}(1+\sqrt{N_B})$, where N_B is number of blades. Although helpful as an estimate this limit does not allow us to answer whether it can be achieved under prescribed forcing and damping for a particular bladed disk design with specific design parameters and for a given range of mistuning. Knowledge of the largest response level increase caused by the mistuning and of the arrangements of blades that are the most favorable, and those which are the most dangerous, is very important for design practice. The answers can and should be obtained only for some specific bladed disk assemblies and under specific forcing conditions since it is very case specific.

The problem of searching for the worst and best mistuning patterns has been formulated as an optimization problem first by Petrov [17,18], where the blades of a mistuned bladed disk were modeled by pretwisted beams with many degrees of freedom connected by shrouds, and the search was carried out by optimization methods which do not require sensitivity coefficients. Several optimization algorithms using sensitivity coefficients have been developed and used for this problem in Ref. [19]. An attempt to use the direct optimization search has been made in Ref. [20], although use of the maximum coefficient of the dynamic stiffness matrix of the system as a rough estimate for the maximum amplitude and absence of determination of resonances for a mistuned system make application of the proposed approach for practical purposes doubtful. Possibilities of using a simulated annealing algorithm for a combinatorial problem to determine the best arrangement of mistuned blades on a bladed disk have been explored in Ref. [21]. The problem of search for the best arrangement of mistuned blades with prescribed mistuning values has been solved by genetic algorithms using gradient-based response surface approximations in Ref. [22]. Recently, a new method for analysis of mistuned bladed disks has been developed [23], which allows use of detailed, realistic, finite element models, such as were applied only for analysis of tuned bladed disks to date. The method is based on an exact relationship between the response of tuned and mistuned assemblies. It allows us to reduce exactly a large finite element model and to overcome excessive computational expense inherent usually to the analysis of mistuning.

In the present paper the problem of determining the worst mistuning patterns is formulated and solved as an optimization problem for large finite element models. Further development of the method is made to solve the optimization problem for such models. An effective method is developed for calculation of the sensitivity coefficients for maximum forced response with respect to blade mistuning. The effectiveness and accuracy of the sensitivity coefficient computations are based on an analytical derivation of the expressions for their calculation. Numerical studies are carried out for a finite element model of a realistic bladed disk.

Contributed by the International Gas Turbine Institute (IGTI) of THE AMERICAN SOCIETY OF MECHANICAL ENGINEERS for publication in the ASME JOURNAL OF TURBOMACHINERY. Paper presented at the International Gas Turbine and Aeroengine Congress and Exhibition, New Orleans, LA, June 4–7, 2001; Paper 2001-GT-0292. Manuscript received by IGTI, December 2000, final revision, March 2001. Associate Editor: R. Natole.

Problem Formulation

Usually, in service conditions, bladed disks are subjected to excitations of the so-called ''engine-order type,'' i.e., the ampli-

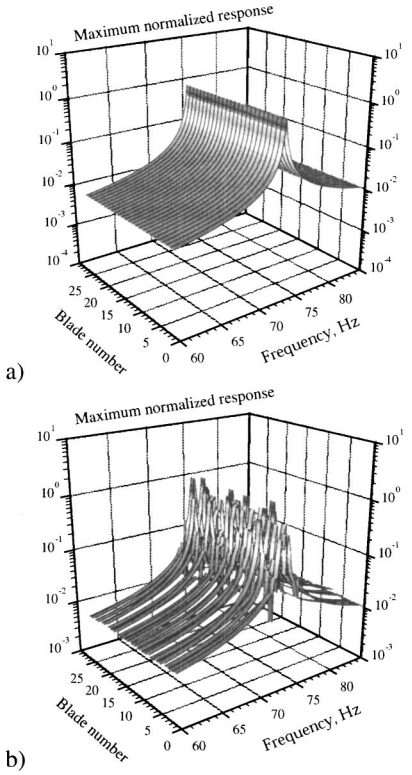

Fig. 1 Forced response of each from 26 blades of the fan bladed disk: (*a*) the case of tuned blades; (*b*) the case of mistuned blades

tudes of vibration forces acting on different blades are identical but there is a fixed phase shift between forces on adjacent blades of the assembly.

A perfectly tuned bladed disk subjected to such excitation generates the same amplitudes for all blades. Moreover, for such a bladed disk, the only modes that can be excited from a large variety of natural modes are those that have the same number of displacement waves around the circumference of the bladed disk as the engine order forcing.

Even small mistuning can change the vibration response characteristics of a bladed disk to a large extent. Amplitudes become different for the blades of a bladed disk and their distribution becomes very irregular. Many closely spaced resonance peaks are excited. An example of the mistuning influence on the amplitudes of a bladed disk is shown in Fig. 1.

In the derivation of the proposed method attention is focused on maximum displacements, since the worsening effect of mistuning is estimated here from an increase of the maximum displacement amplitude level in the system compared with one of the tuned system. Although mode shape variation caused by mistuning can also change the ratios between stresses and displacements, in many cases these changes are secondary compared with the amplitude increase, and because of that, the effect of mistuning on stresses can be expected to be similar to the effect on displacements. Direct formulation of the problem with respect to stresses can be conducted analogously to the one presented here using expressions obtained in Ref. [19] for sensitivity coefficients of stress intensity with respect to mistuning.

The maximum displacement response $\mathfrak{M}$ is found by searching over all points of the bladed disk, over all excitation frequencies and over all time instants during a vibration period, and is represented by the following expression:

$$\mathfrak{M}=\max_{\omega}\ \max_{x}\ \max_{t}\|\tilde{\boldsymbol{u}}(\omega,\boldsymbol{x},t)\|, \tag{1}$$

where $\tilde{\boldsymbol{u}}=\{u_x,u_y,u_z\}^T$ is a vector of displacements at a considered point; ω is the excitation frequency, which can admit values from a frequency range given, i.e., $\omega\in[\omega^-,\omega^+]$; $\boldsymbol{x}=\{x,y,z\}^T$ is a vector of co-ordinates of the point, which can be any point of the volume V occupied by the bladed assembly, i.e., $\boldsymbol{x}\in V$; t is time, which can be considered over one period of vibration only, i.e., $t\in[0,2\pi/\omega]$.

We characterize a mistuning pattern by a vector of mistuning parameters $\boldsymbol{b}$:

$$\boldsymbol{b}=\{b_1,b_2,\ldots,b_{N_B}\}^T, \tag{2}$$

where N_B is a total number of blades in the assembly.

The method proposed does not impose restrictions on a choice of parameters that characterize blade mistuning. In practice, however, blade mistuning is usually measured by values of individual natural frequencies of blades, which can be assembled into a bladed disk or manufactured together with a disk as in the case of a blisk. Because of that, it is convenient to assume that the jth component of the vector is determined as the relative difference between the ith natural frequency of the jth blade $f_j^{(i)}$ and natural frequency of the perfectly tuned, standard blade $f_0^{(i)}$, i.e.,

$$b_j=(f_j^{(i)}-f_0^{(i)})/f_0^{(i)}. \tag{3}$$

The choice of the particular mode used for the mistuning estimate is determined by the excitation frequency range of interest and the available experimental data.

The maximum displacement response is dependent on the mistuning pattern. In order to find the worst mistuning pattern (the one that provides the maximum displacement when acceptable mistuning is restricted by manufacture tolerances), the following constrained optimization problem is formulated:

$$\mathfrak{M}(\boldsymbol{b})\rightarrow\max \tag{4}$$

with the bound constraints

$$\boldsymbol{b}^-\leqslant\boldsymbol{b}\leqslant\boldsymbol{b}^+. \tag{5}$$

Calculation of the Maximum Displacement

Bladed-Disc Modeling and Amplitude Calculation. The equation of motion for forced vibration of a bladed disk can be written, accounting for stress stiffening and spin softening effects occurring due to the bladed disk rotation, in a frequency-domain form as

$$[\boldsymbol{K}+\boldsymbol{K}_S(\Omega)-\Omega^2\boldsymbol{M}_\Omega-\omega^2\boldsymbol{M}+i\boldsymbol{D}]\boldsymbol{q}=\boldsymbol{Z}(\omega)\boldsymbol{q}=\boldsymbol{f}, \tag{6}$$

where $\boldsymbol{q}$ is a vector of complex response amplitudes for nodal displacements along co-ordinate axes; $\boldsymbol{f}$ is a vector of complex amplitudes of harmonic nodal loads; ω is the excitation frequency; $\Omega=\omega/m$ is rotation speed (where m is an engine order number); $\boldsymbol{K}$, $\boldsymbol{M}$, and $\boldsymbol{D}$ are stiffness, mass, and structural damping matrices of the system respectively; $\boldsymbol{K}_S$ is a stress stiffening matrix determined by action of centrifugal forces; $\boldsymbol{M}_\Omega$ is the so-called ''pseudomass'' matrix reflecting spin softening; $\boldsymbol{Z}(\omega)$ is the dynamic stiffness matrix; and $i=\sqrt{-1}$.

For mistuned bladed disks the matrices in Eq. (6) are too large to allow direct solution when a detailed enough finite element model is applied. Because of that, an effective method for calculation of vibration amplitudes of mistuned bladed disks has been developed in Ref. [23], which allows the use of large detailed finite element models that have previously been applied to the analysis of tuned bladed disks only. The method, together with a new technique for the analytical calculation of sensitivity coefficients of the maximum displacement with respect to mistuning, constitutes a basis for the optimization search of the worst mistuning pattern. The formulation given below for the method for amplitude calculation is modified to increase its efficiency for the optimization problem considered here.

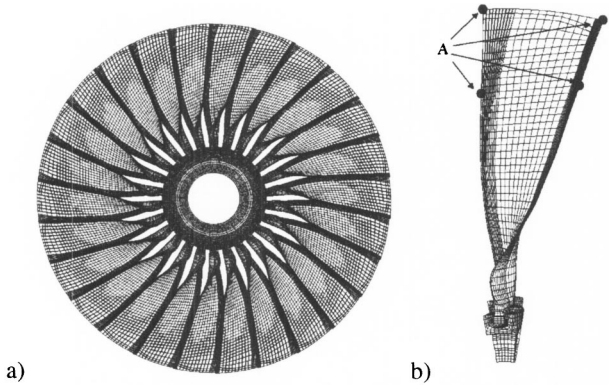

Fig. 2 Finite element model and active nodes: (*a*) a bladed disk; (*b*) a sector of the bladed disk

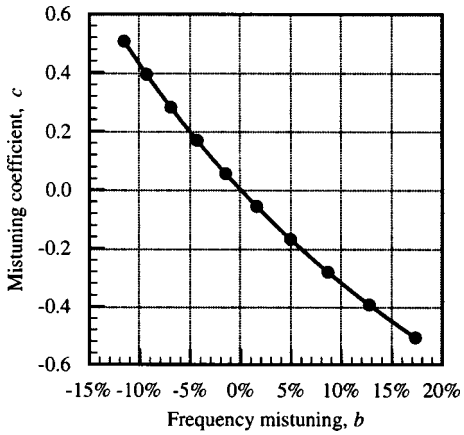

Fig. 3 Correspondence calculated between the mistuning coefficient and frequency mistuning

In accordance with the method, the dynamic stiffness matrix for a mistuned system can be represented by a sum of the matrix for tuned system $\boldsymbol{Z}_0$ and a mistuning matrix $\Delta\boldsymbol{Z}$, characterizing distinctions of the mistuned system from a tuned one, i.e.,

$$\boldsymbol{Z}=\boldsymbol{Z}_0+\Delta\boldsymbol{Z}. \tag{7}$$

It can be shown that any mistuning matrix $\Delta\boldsymbol{Z}$ can be expressed as the multiplication of two matrices $\boldsymbol{E}$ and $\boldsymbol{V}$ as follows:

$$\Delta\boldsymbol{Z}=\sum_{i,j=1}^{N}\Delta z_{ij}\boldsymbol{e}_i\boldsymbol{e}_j^T=\sum_{i=1}^{N}\boldsymbol{e}_i\left(\sum_{i=1}^{N}\Delta z_{ij}\boldsymbol{e}_j^T\right)=\underset{(N\times n)}{\boldsymbol{E}}\ \underset{(n\times N)}{\boldsymbol{V}}, \tag{8}$$

where $\boldsymbol{e}$, is a vector whose ith component is equal to 1 and the others are equal 0; $\boldsymbol{V}$ is a matrix, in which each row is constructed of the nonzero rows of the mistuning matrix $\Delta\boldsymbol{Z}$; $\boldsymbol{E}$ is a matrix consisting of vectors $\boldsymbol{e}_i$ corresponding to these nonzero rows; N is the number of degrees of freedom (DOF's) in the considered system, and n is the number of nonzero rows in $\Delta\boldsymbol{Z}$.

Then, the complex amplitudes $\boldsymbol{q}$ can be determined from Eqs. (6)–(8). In order to calculate the amplitudes we apply the Sherman-Morrison-Woodbury formula derived in Refs. [24] and [25] for inversion of special structure, which allows us to obtain the following expression for amplitude determination:

$$\boldsymbol{q}=(\boldsymbol{Z}_0+\Delta\boldsymbol{Z})^{-1}\boldsymbol{f}=[\boldsymbol{A}-\boldsymbol{AE}(\boldsymbol{I}+\boldsymbol{VAE})^{-1}\boldsymbol{VA}]\boldsymbol{f}, \tag{9}$$

where $\boldsymbol{A}=\boldsymbol{Z}_0^{-1}$ is the FRF matrix of the tuned system and $\boldsymbol{I}(n\times n)$ is an identity matrix.

The main advantage of Eq. (9) is that it is exact and valid for any subset of the so-called ''active'' nodes and DOF's selected. The active nodes are those where one wishes to determine amplitude response levels and where mistuning is applied. The number of active nodes can be chosen to be small enough to enable effective calculations. Moreover, the FRF matrix of a tuned bladed disk used in Eq. (9) can be generated from the mode shapes and natural frequencies calculated from a finite element model of one its sector only, having taken into account the cyclic symmetry properties of the tuned assembly. The effective method for calculation of the FRF matrix for a tuned bladed disk is described in Ref. [23]. An example of the finite element model for a bladed disk, its sector, and active nodes chosen, are shown in Fig. 2.

The blade frequency mistuning is modeled by applying the mistuning matrix $\boldsymbol{V}_0(n/N_B\times N/N_B)$ of the same structure to each blade of the assembly. The differences in mistuning between blades are described by coefficients $c(b_j)$, which are used as a multiplier for matrix $\boldsymbol{V}_0$. Owing to this, the mistuning matrix for the whole bladed assembly $\boldsymbol{V}$ can be expressed in the following block-diagonal form:

$$\boldsymbol{V}(\boldsymbol{b})=\mathrm{diag}\{c(b_1)\boldsymbol{V}_0,c(b_2)\boldsymbol{V}_0,\ldots,c(b_{N_B})\boldsymbol{V}_0\}. \tag{10}$$

The coefficient $c(b_j)$ establishes correspondence between the mistuning parameters of the blade-alone natural frequencies defined in Eq. (3) and magnitudes of the components of the mistuning matrix.

In order to determine this coefficient, calculations of forced response for a lone blade is performed for a set of trial values c_j $(j=1,n_c)$, when mistuning matrix $c(b_j)\boldsymbol{V}_0$ is applied to the blade. As a result of these calculations for each trial value of the mistuning coefficient c_j, ith resonance frequency of a single blade $f^{(i)}$ and hence the mistuning parameter b are determined. Then using this set of points spline approximation $c(b)$ with respect to the introduced mistuning parameters b provides a possibility to obtain the mistuning coefficient for any frequency mistuning (Fig. 3).

Although there is no restriction on the structure and values of components of the matrix $\boldsymbol{V}_0$, it is useful to define some mistuning elements which have a physical interpretation and which help to form $\boldsymbol{V}_0$. Simple examples of such elements can be: lumped masses, dampers, or springs applied to nodes of the finite element model.

Equation (9) can be rewritten in the following set of two equations, which are much more effective for computation:

$$\boldsymbol{q}=\boldsymbol{q}_0-\boldsymbol{A}_E\boldsymbol{p}, \tag{11}$$

where $\boldsymbol{A}_E(N\times n)=\boldsymbol{A}(N\times N)\boldsymbol{E}(N\times n)$ is the FRF matrix of the tuned system with excluded columns corresponding to zero rows of matrix $\Delta\boldsymbol{Z}$ and $\boldsymbol{q}_0$ is vector of response amplitudes for the tuned bladed disk. An auxiliary vector $\boldsymbol{p}(\mathrm{n}\times 1)$ is determined from the solution of the following equation:

$$(\boldsymbol{I}+\boldsymbol{VA}_E)\boldsymbol{p}=\boldsymbol{Vq}_0. \tag{12}$$

Maximum Displacement Over Vibration Period. Each component of the nodal displacement vector can have its own phase, which results in an elliptical in space orbit of a node during vibration. Because of that, the maximum displacement at a node cannot be obtained simply as the sum of the squares of the amplitude of all its co-ordinate components. The analytical formula has been derived in Ref. [19] to express the maximum displacements using complex amplitudes of co-ordinate displacements and it has the following form:

$$\max_t\|\tilde{\boldsymbol{u}}_k\|=\max_t\|\mathrm{Re}(e^{i\omega t}\boldsymbol{u}_k)\|=\sqrt{\frac{1}{2}(\boldsymbol{u}_k^*\boldsymbol{u}_k+|\boldsymbol{u}_k^T\boldsymbol{u}_k|)}, \tag{13}$$

where $\boldsymbol{u}_k$ is a vector of complex amplitudes of co-ordinate components at the kth node considered, and * represents the Hermitian conjugate.

Maximum Displacement Over a Bladed Disk Assembly. The maximum displacement over all nodes of the system and the corresponding node number $k_{\mathfrak{M}}$ are determined by a simple comparison of $\max_t \|\tilde{\boldsymbol{u}}_k\|$ at all nodes analyzed.

Maximum Displacement in a Given Excitation Frequency Range. Near resonance peaks, the amplitude levels of systems with small damping (which is typical of bladed disks) vary abruptly. Because of that, an accurate calculation of resonance amplitudes requires a very small excitation frequency step in order to locate the resonance frequencies precisely. Mistuned bladed disks have many resonance peaks, which are sometimes spread over a rather wide frequency range. To make the search for the maximum displacement $\mathfrak{M}$ efficient, it is performed as the solution of an optimization problem with excitation frequency considered as an optimization parameter varied in a given range. Frequency stepping is applied to separate the resonance peaks and the step size can be chosen to be reasonably large for this goal. A combination of the golden section method and the inverse quadratic approximation method (for description of these methods see, for example, Ref. [26]) is then used for precise determination of the resonance amplitudes. The displacements found at all resonance peaks are compared and the largest value gives $\mathfrak{M}$ and a value of the corresponding excitation frequency $\omega_{\mathfrak{M}}$.

Sensitivity Coefficients With Respect to Mistuning

The number of variable parameters in the proposed optimization search of the worst mistuning patterns is equal to the number of blades in the assembly. This number is always large enough to make it necessary to use optimization methods based on the gradient of the maximum displacement with respect to the mistuning parameters. Because of this, determination of this gradient, where components are the sensitivity coefficients for the maximum displacement with respect to the mistuning parameters, is one of the most important tasks which determines the effectiveness of the developed method.

The sensitivity coefficients could be calculated using finite difference approximations for the derivatives. However, even the simplest first-order finite-difference formulas require calculating $\mathfrak{M}(\boldsymbol{b}+\Delta b\boldsymbol{e}_j)$ $(j=\overline{1,N_B})$ at least N_B times for small increments Δb. This is a very time-consuming process and makes this approach too expensive for the problem of analyzing mistuned bladed disks, leaving apart inevitable approximation errors. The method proposed below for analytical determination of the sensitivity coefficients of the maximum displacement in a mistuned bladed disk with respect to the mistuning parameters provides a fast and exact calculation.

Sensitivity Coefficients for Complex Nodal Amplitudes. Expressions for determination of the sensitivity coefficients for the complex nodal amplitudes can be obtained by differentiating Eqs. (11) and (12) with respect to the jth mistuning parameter analyzed:

$$\frac{\partial \boldsymbol{q}}{\partial b_j} = -\boldsymbol{A}_E \frac{\partial \boldsymbol{p}}{\partial b_j}, \tag{14}$$

$$(\boldsymbol{I}+\boldsymbol{V}\boldsymbol{A}_E)\frac{\partial \boldsymbol{p}}{\partial b_j} = \frac{\partial \boldsymbol{V}}{\partial b_j}\boldsymbol{q}, \tag{15}$$

where all matrices are calculated at the previously found excitation frequency $\omega_{\mathfrak{M}}$, corresponding to the maximum displacement, and the vector of complex amplitudes $\boldsymbol{q}$ is determined from Eqs. (11) and (12).

Matrix $\partial \boldsymbol{V}/\partial b_j$ is determined by differentiation of Eq. (10), which results in the following expression:

$$\frac{\partial \boldsymbol{V}}{\partial b_j} = \mathrm{diag}\left\{\boldsymbol{0},\boldsymbol{0},\ldots,\frac{\partial c(b_j)}{\partial b}\boldsymbol{V}_0,\ldots,\boldsymbol{0}\right\}, \tag{16}$$

where only the jth block on the main diagonal of the matrix is nonzero. Smooth character of the function $c(b)$ (see Fig. 3) allows calculating derivatives $\partial c/\partial b$ without difficulty and with high accuracy using the spline approximation.

It should be noted that the calculation of the sensitivity coefficients for all the introduced mistuning parameters is not time consuming, compared with the calculation of the maximum displacement, since all calculations are performed for only one excitation frequency $\omega_{\mathfrak{M}}$. Moreover, the matrix $\boldsymbol{I}+\boldsymbol{V}\boldsymbol{A}_E$ in Eq. (15) is identical for derivatives with respect to all the mistuning parameters b_j $(j=\overline{1,N_B})$. Taking this into account also allows us to save the computation time by decomposing the matrix in a Gauss elimination solution of Eq. (15) only once.

Sensitivity Coefficients for the Maximum Displacement. To use the derivatives of the complex amplitudes obtained in the previous section, we derive an expression for the sensitivity coefficients of the maximum displacement with respect to the mistuning parameters having taken into account the dependence of the maximum displacement on the real and imaginary parts of the complex amplitudes. This results in the following formula:

$$\frac{\partial \mathfrak{M}}{\partial b_j} = \left(\frac{\partial \mathfrak{M}}{\partial \boldsymbol{u}^{\mathrm{Re}}}\right)^T \frac{\partial \boldsymbol{u}^{\mathrm{Re}}}{\partial b_j} + \left(\frac{\partial \mathfrak{M}}{\partial \boldsymbol{u}^{\mathrm{Im}}}\right)^T \frac{\partial \boldsymbol{u}^{\mathrm{Im}}}{\partial b_j} = \mathrm{Re}\left(\frac{\partial \boldsymbol{u}^*}{\partial b_j}\frac{\partial \mathfrak{M}}{\partial \boldsymbol{u}}\right), \tag{17}$$

where three components of the vector $\partial \boldsymbol{u}/\partial b_j$ are selected from the vector of sensitivity coefficients for complex nodal amplitudes, $\partial \boldsymbol{q}/\partial b_j$, for the node $k_{\mathfrak{M}}$, where the maximum of displacements is achieved.

The complex vector $\partial \mathfrak{M}/\partial \boldsymbol{u}$ is introduced in Eq. (17) to facilitate the use of derivatives of complex amplitudes with respect to the mistuning parameters. It is defined by the following expression: $\partial \mathfrak{M}/\partial \boldsymbol{u} = \partial \mathfrak{M}/\partial \boldsymbol{u}^{\mathrm{Re}} + i\partial \mathfrak{M}/\partial \boldsymbol{u}^{\mathrm{Im}}$. Having differentiated Eq. (13), this can be expressed through the complex amplitudes in the following form:

$$\frac{\partial \mathfrak{M}}{\partial \boldsymbol{u}} = \frac{1}{2\mathfrak{M}}\left(\boldsymbol{u}+\bar{\boldsymbol{u}}\frac{\boldsymbol{u}^T\boldsymbol{u}}{|\boldsymbol{u}^T\boldsymbol{u}|}\right), \tag{18}$$

where a bar above a symbol $\boldsymbol{u}$ means a complex conjugate.

Expressions (17) and (18) are calculated jointly with Eqs. (14) and (15) for all mistuning parameters b_j to obtain all components of the vector of the sensitivity coefficients:

$$\nabla \mathfrak{M} = \left\{\frac{\partial \mathfrak{M}}{\partial b_1}, \frac{\partial \mathfrak{M}}{\partial b_2}, \ldots, \frac{\partial \mathfrak{M}}{\partial b_{N_B}}\right\}^T. \tag{19}$$

The calculations are performed at the excitation frequency corresponding to maximum displacement $\omega_{\mathfrak{M}}$.

The chosen objective function $\mathfrak{M}$ is continuous but the gradient $\nabla \mathfrak{M}$ can be diskontinuous when the number of a blade where the amplitudes are maximum is changed with a variation of the mistuning parameters. There is no difficulty to smooth the gradient without influence on the optimal solution, for example, as shown in Ref. [19] but there was no need to do this for the bladed assemblies investigated. This occasional gradient diskontinuity does not affect significantly the robustness of the optimal search for the worst mistuning patterns since the location of the point of maximum amplitude is usually not changed in the vicinity of the optimal solution for the considered problem, and, moreover, the developed optimization algorithm can withstand occasional gradient diskontinuity.

Optimization Search of the Worst Mistuning Pattern

The efficient method developed above for calculation of the sensitivity coefficients $\nabla \mathfrak{M}$ and the objective function $\mathfrak{M}$ allows us to make a search for the worst mistuning pattern using the derivatives. The most efficient optimization methods using the sensitivity coefficients belong to the family of quasi-Newton methods. An effective algorithm also based on the quasi-Newton method has been developed and applied in Ref. [19] for the opti-

mal search of worst and best mistuning patterns of bladed disks for the case when blades are modeled by pretwisted beams. The algorithm allows us to take into account the bound constraints imposed by manufacturing tolerances on mistuning variations. It has been used for the multi-degrees-of-freedom finite element models of the bladed disks analyzed here with some minor modifications.

Numerical Results

A Fan Bladed Disc. The presented method has been applied to the analysis of a bladed fan disk containing 26 blades, which is shown in Fig. 2. A detailed finite element model was used for determination of the FRF matrix of the tuned assembly. It contains above 120,000 DOF's in each sector of the finite element model and the full bladed disk comprises above 3,000,000 DOF's. Direct implementation of this model, comprising more than three million DOF's for the mistuned assembly, would be impractical even for a simple response analysis, leaving apart the optimization search. Because of that, just four nodes were selected (marked by letter "A" in Fig. 2) as the active nodes for each blade, namely the nodes where amplitudes are expected to be maximum and displacements were determined and controlled at these nodes. The proposed method provides exact calculation of the amplitudes at these nodes and, moreover, a realistic distribution of excitation forces over nodes of the blade surface can also be accounted for. Because the use of such a relatively small number of active nodes allows very fast calculations, and does not affect the accuracy of the calculations, this permits the determination of the maximum amplitudes occurring in the bladed disk analyzed. The number of DOF's analyzed, n, in vector $\boldsymbol{q}$ equals 468, which is quite acceptable for our purposes. The values of possible blade frequency mistuning were assumed to be located within the range $[-5\%\cdots+5\%]$ and the damping loss factor was taken to be 0.003. Natural frequencies of the bladed fan disk for all nodal diameter numbers are shown in Fig. 4, where they are normalized with respect to the first blade-alone frequency.

When mistuning is introduced into the system, resonance frequencies corresponding to nodal diameter numbers other than 0 and $N/2$ split into pairs; and for a frequency range corresponding to one family of modes all N resonance frequencies can potentially be observed even under excitation by a single engine-order harmonic. Because of this, the frequency range studied is presented in Fig. 4 by a rectangular area between two dashed horizontal lines. The frequency range corresponds to a family of first flap-wise mode and excitation by sixth engine-order harmonic is considered while excitation loads are distributed over the blade surface.

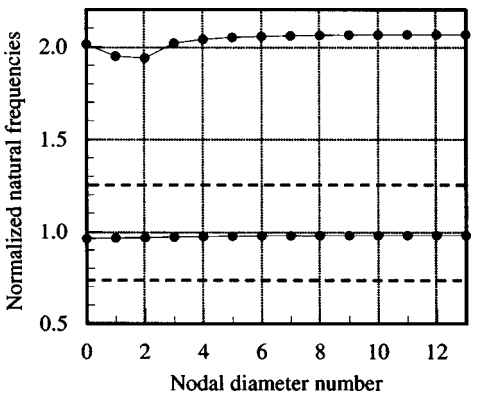

Fig. 4 Natural frequencies of a tuned bladed fan disk and the analyzed frequency range

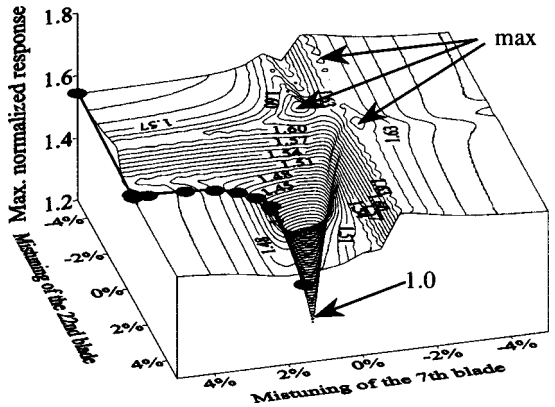

Fig. 5 Dependence the envelope of maximum response $\mathfrak{M}$ on mistuning parameter variation for two blades of the assembly

Illustrative Case: Mistuning Variation for Two Blades. The behavior of the objective function in the developed optimization search is demonstrated on a relatively simple example, which can be visualized easily. In this example only two mistuning parameters are varied (namely b_1 and b_{22}) and mistuning parameters for all the other blades are not varied and are assumed to be zero (i.e., these blades are tuned). The objective function normalized by its value for the perfectly tuned assembly, $\mathfrak{M}(\boldsymbol{0})$, i.e., $\hat{\mathfrak{M}}(\boldsymbol{b}) = \mathfrak{M}(\boldsymbol{b})/\mathfrak{M}(\boldsymbol{0})$, is shown in Fig. 5. It is evident that the objective function has a complex character with several local maxima. Moreover, restrictions imposed on the mistuning variation provide the possibility of finding the maximum response on the boundaries of the area of acceptable mistuning values. The points corresponding to sequential iterations of the optimization search are shown in this figure by circles. Initial values for the mistuning vector $\boldsymbol{b}$ were close to the tuned values, where the objective function has a minimum ($\hat{\mathfrak{M}}(\boldsymbol{0})=1$). After nine iterations the worst mistuning pattern was found, which for the considered case locates on the boundary of the area of acceptable mistuning, namely it has values $b_1=5\%$, $b_{22}=-5\%$, and the other 24 parameters are zero.

The Realistic Case: Mistuning Values for All Blades are Varied. The increase in the maximum response levels with the number of iterations when all 26 mistuning parameters are varied is demonstrated in Fig. 6 where results of the optimization search

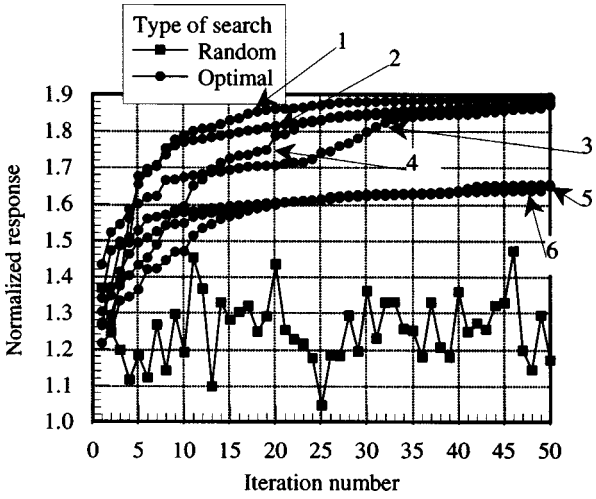

Fig. 6 Increase of the maximum amplitude with the number of iteration for the optimization search starting from different initial configurations and for random search

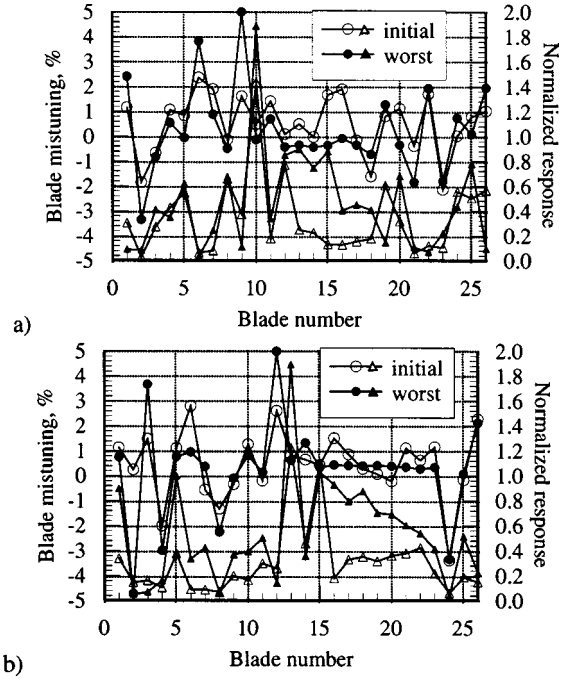

Fig. 7 Comparison of initial and worst mistuning patterns (circles) and amplitude distributions (triangles) for two of the optimization searches

starting with six different initial values of the vector of mistuning parameters are shown. As one can see from the figure, first iterations usually give a larger increase rate for the maximum response normalized with respect to the tuned response $\hat{\mathfrak{M}}$ than later iterations. Furthermore, results of a search for the worst mistuning with the random search (or called sometimes ''statistical'' or Monte Carlo simulations) are displayed. In the random search, the vector of mistuning parameters was generated randomly at each iteration and the corresponding value of $\hat{\mathfrak{M}}$ was calculated. Comparison of both methods demonstrates the superiority of the optimization search proposed in this paper. Due to the existence of many local maxima of the objective function $\hat{\mathfrak{M}}$, starting the optimization search from different initial points can lead to different final values for maximum response. Because of that several different initial patterns are used in the analysis to find the largest local maximum. The initial mistuning patterns were generated by a random number generator providing mistuning values within the given mistuning range. The maximum magnification factor found for all initial patterns is equal to 1.89 which is lower than the limit 3.05 given by the formula $1/2(1+\sqrt{N_B})$ derived in Refs. [15] and [16].

In Fig. 7 mistuning patterns and amplitude distributions found as a result of the optimization search are compared with their initial counterparts for two different starting patterns. Both found mistuning patterns give the same maximum response value of 1.89. Although maximum amplitude is located at different blades, there is some resemblance between the amplitude distribution and mistuning patterns when one simply rotates the obtained amplitude distribution relative to the bladed disk. This effect is also found in Ref. [19] and is explained by the independence of the maximum response to the orientation of the worst mistuning pattern (and amplitude distribution correspondingly) relative to the bladed disk, since for blade numbering, any blade can be chosen as the first one. In Ref. [19] using a study based on a shrouded bladed disk with higher blade-to-blade vibration coupling, this effect was much more evident and accurately calculated in contrast to the unshrouded fan bladed disk considered here.

Table 1 Normalized difference between the excitation frequency of maximum response and resonance frequency of a tuned lone blade

Number of search	1	2	3	4	5	6
Initial, %	−1.96	−2.87	−2.21	−2.61	−2.49	−2.51
Worst, %	−2.05	−3.01	−2.78	−2.05	−2.43	−2.51

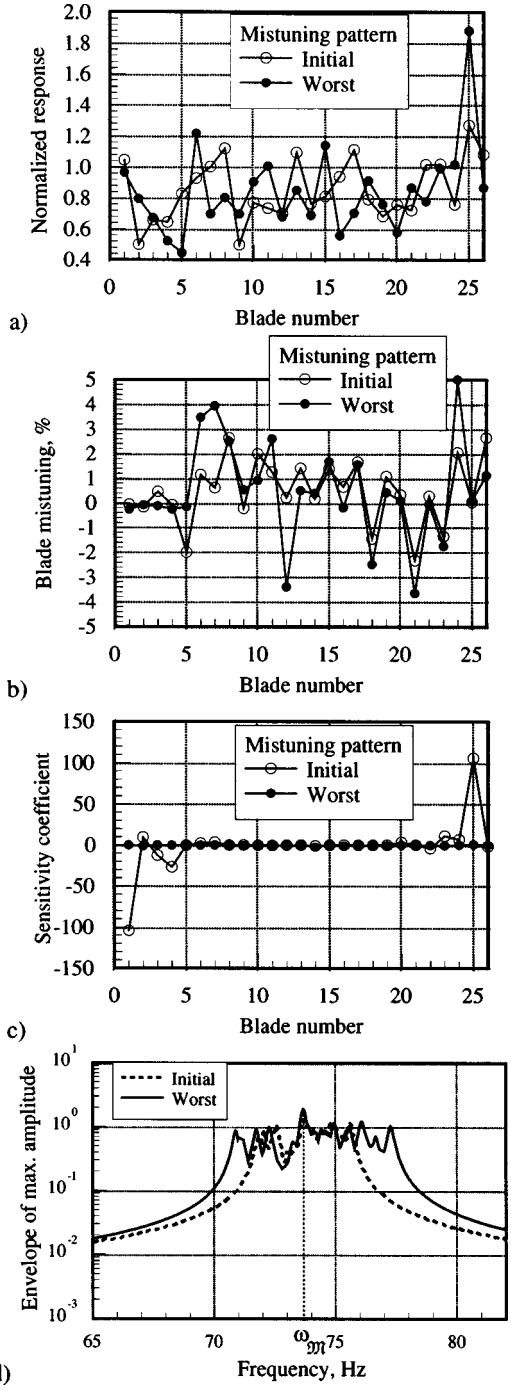

Fig. 8 Initial and found worst mistuning patterns, (*a*); maximum amplitude distributions corresponding to these patterns, (*b*); sensitivity coefficients, (*c*); an envelope of maximum amplitudes calculated for the patterns, (*d*).

As expected, for different initial patterns and the patterns found as a result of optimization search, the excitation frequencies at

which the responses are maximum are different. The excitation frequencies providing maximum forced response for given mistuning patterns are presented in Table 1 for all six different initial mistuning patterns and patterns found after the optimization search. In the table the difference between the resonance frequencies of maximum response and resonance frequency of a single tuned blade $\tilde{\omega}$ is normalized with respect to first blade-alone frequency ω_0 using the following formula: $\tilde{\omega}=(\omega_{\mathfrak{M}}-\omega_0)/\omega_0$. All the normalized differences are negative because the disk vibration is accounted for in the mistuning analysis. In the cases considered, changes in the excitation frequency of maximum response are not very large for different patterns and are located within a 1% band. For some cases, as, for example, for the sixth optimization search, the initial and the worst patterns provide practically indistinguishable excitation frequencies of maximum response.

For the worst mistuning pattern found over all used initial values maximum response levels for each of the blades, and envelopes of maximum forced response function corresponding to the initial and worst patterns, are compared in Fig. 8 with initial values. Sensitivity coefficients for maximum response levels with respect to variation of mistuning of each blade are shown in Fig. 8(*c*) for the initial pattern and the found worst mistuning pattern. As one can see, the sensitivity coefficients are close to zero for the worst mistuning patterns, which indicates that the found mistuning pattern is close to a point of local maximum of the maximum response as a function of the mistuning, since the conventional necessary condition for the function extremum point is $\partial\hat{\mathfrak{M}}/\partial b_j=0$.

In the case demonstrated here, and other worst mistuning patterns found as a result of the optimization search, mistuning for some of the blades reaches the limits imposed by restrictions on the range of acceptable mistuning variation. It is evident that small changes in the mistuning pattern can change many very important vibration characteristics of the bladed assembly, namely: (i) distribution of amplitudes over blades of the bladed assembly; (ii) range of resonance amplitudes; and (iii) maximum response levels.

A High-Pressure Turbine Bladed Disc. The optimization search has also been applied to the analysis of a high-pressure turbine bladed disk shown in Fig. 9.

The bladed disk analyzed comprises 92 shrouded blades although due to gaps between the shrouds they do not touch each other during vibrations. The full bladed disk finite element model comprises about 15 millions DOF's and its finite single-sector model contains 162,708 degrees of freedom (DOF's). The sector model is used for determination the first 24 natural frequencies and mode shapes of the tuned bladed-disk assembly for all their cyclic indices (nodal diameters) that are possible for the considered assembly in the range from 0 to 46. These modes of the tuned system are used for generating the FRF matrix of the tuned assembly. The damping loss factor is set to 0.003 and excitation by sixth engine order is considered in the analysis.

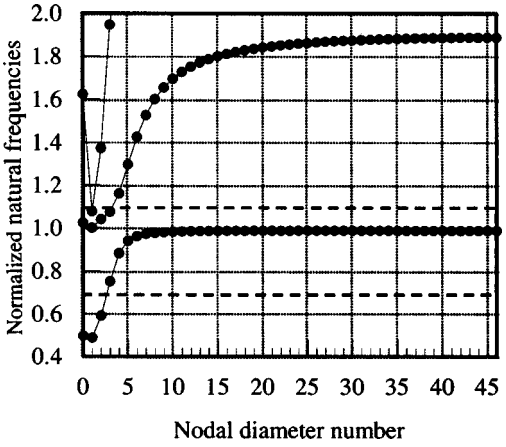

Fig. 10 Natural frequencies of a tuned bladed high-pressure turbine disk and the analyzed frequency range

Natural frequencies of the high-pressure turbine disk normalized with respect to the first blade-alone frequency are shown in Fig. 10 for all possible nodal diameter numbers. The frequency range in which the maximum forced response is searched is presented in Fig. 10 by a rectangular area between dashed lines. This frequency range corresponds to a family of first predominantly flap-wise modes, although several natural frequencies of second family of modes are also located within the range.

As active nodes in the optimization search for the worst mistuning patterns, the amplitudes at two nodes chosen at the blade tip (see nodes marked by letter A in Fig. 9) were calculated for each blade, and the total number of DOF's analyzed was thus 552. As for the preceding case of the bladed fan disk, a choice of the two nodes as the active nodes for each blade of the bladed turbine disk does not reduce the accuracy of the maximum amplitude calculations.

Results of the optimization search for the worst mistuning patterns for this bladed disk are shown in Figs. 11 and 12. The increase in the maximum response levels with the number of iterations is shown in Fig. 11. The optimization search was started

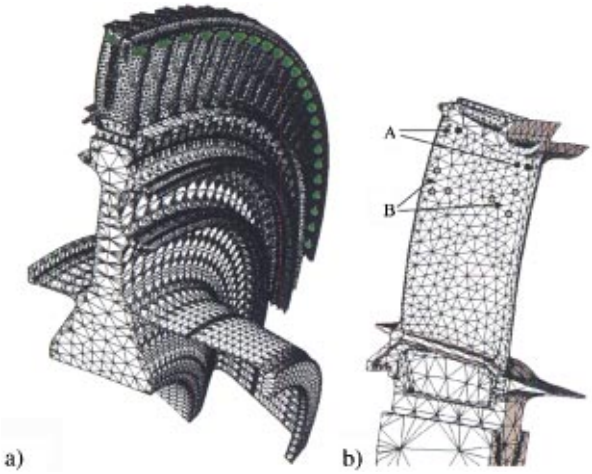

Fig. 9 A quarter of the high-pressure turbine bladed disk analyzed (*a*); and the active nodes chosen (*b*)

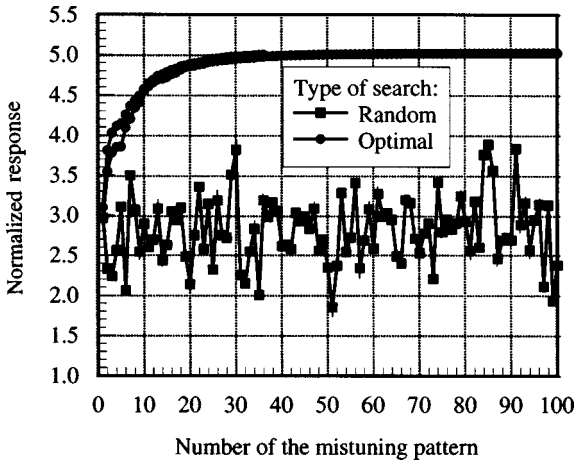

Fig. 11 Increase of the maximum amplitude with the number of iteration for the optimization and random search

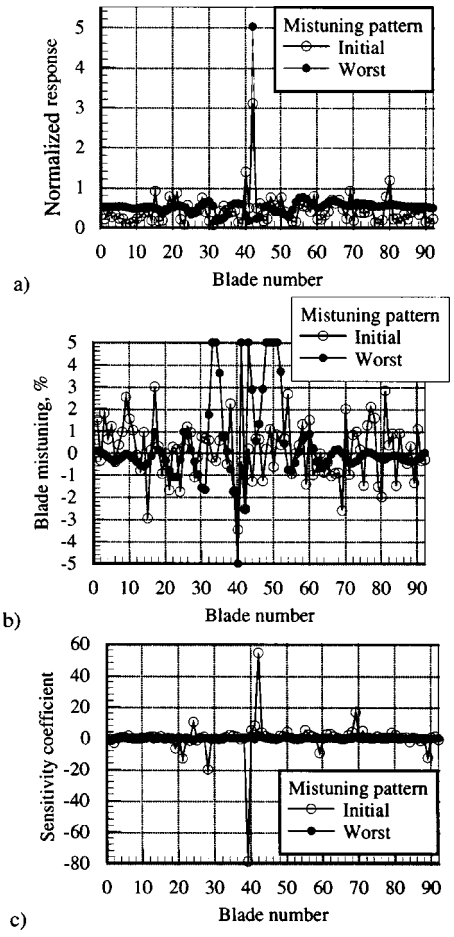

Fig. 12 Comparison of amplitude distributions (*a*); mistuning patterns (*b*); and sensitivity coefficients for initial and the found worst mistuning pattern (*c*)

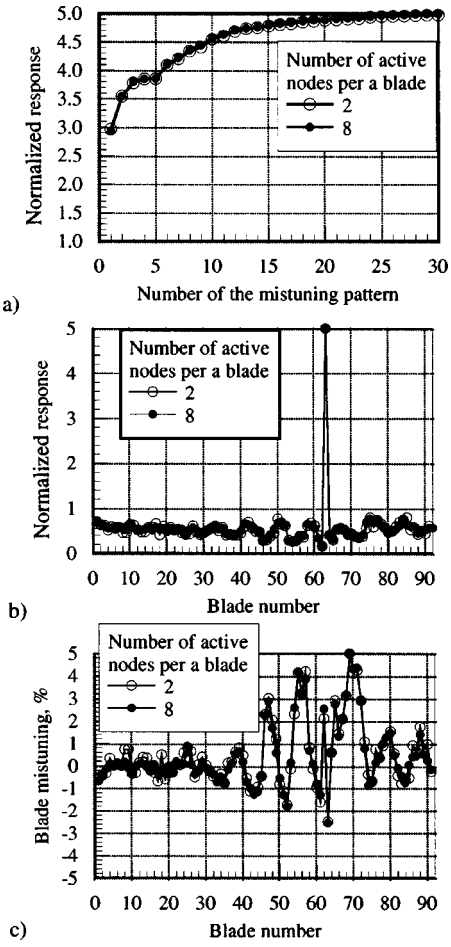

Fig. 13 Comparison of results obtained with different numbers of active nodes: (*a*) increase of the maximum amplitude with the number of iteration; (*b*) worst amplitude distribution; (*c*) worst mistuning pattern

from two different initial mistuning patterns, generated randomly, and two curves can be seen corresponding to optimization search, although these curves become be close after several iterations. Mistuning parameters are varied for all 92 blades of the bladed disk. For comparison results obtained by random search are plotted also. The maximum magnification factor for the peak forced response level for the considered bladed disks was found as a result of the optimization search to be equal 5.02, which is significantly higher than all values obtained in the referenced papers and other papers known to the authors. This value is close to the theoretical limit of 5.296 obtained using Whitehead's formula.

Distribution of maximum amplitudes over blades of the bladed disk for initial and the found worst mistuning patterns are shown in Fig. 12(*a*). One can see that the optimization process has tendency to increase the response level for the most stressed blade. In Fig. 12(*b*) the found worst mistuning patterns are presented. Some of blades in the worst mistuning patterns have mistuning parameter values that are equal to limits imposed on mistuning variation, i.e., $\pm 5\%$. In Fig. 12(*c*) sensitivity coefficients for maximum response levels with respect to variation of mistuning of each blade are plotted for the initial and the found worst mistuning patterns. At initial configurations, which is far from the worst, the sensitivity coefficients of the maximum response for blades can differ significantly. At the found worst configuration sensitivity coefficients are close to zero which is indication that at least the local maximum for forced response as function of mistuning parameters has been found.

On the Choice for the Number and Positions of the Active Nodes. The proposed method and formulas derived above do not impose restrictions on the number or positions of nodes where modifications of mass, stiffness, and/or damping properties of the tuned bladed disk can be applied, or where amplitudes have to be determined. However, in practical computations, in order to take full advantage of fast computations it is desirable to choose the number of active nodes to be as small as possible.

The set of active nodes consists of two subsets: (i) nodes where mistuning elements are applied; (ii) nodes where one wants to have maximum level of forced response calculated. These two subsets can be partly or wholly the same although there is some difference in criteria for their choice.

For the subset of mistuning elements when there is design or other information about the locations where the blade properties can differ mostly from standard ones, e.g., due to higher manufacturing tolerances or due to blade wear during service, the mistuning elements should be placed in this location. When, as happens often in industrial practice, blade mistuning is estimated simply by natural frequencies of individual blades and there is no more specific data, it is appropriate to locate the mistuning elements at the nodes where blade mode shape corresponding to the natural frequency analyzed have higher amplitudes. This allows control of the desired natural frequency of an individual mistuned blade efficiently, while keeping the corresponding mode shape close enough to the initial one, and without imposing redundant changes on mode shapes and natural frequencies of the other modes.

The choice of the subset of nodes where amplitudes are to be calculated is dictated by the needs of the investigation, and in the examples shown above these nodes were selected at locations where amplitudes were expected to be maximum.

In order to check the influence of the choice of active nodes on the results, the optimization search has been applied to the high-pressure turbine bladed disk with different numbers of active nodes. The results obtained for two and eight active nodes (with mistuning elements applied to the all active nodes and maximum amplitudes searched among the all active nodes) are compared in Fig. 13. A set of two nodes marked in Fig. 9 by the letter A and a set of eight nodes comprising nodes marked by letters A and B are used for the comparison. The optimization search is started for both cases from the same initial distribution of individual blade natural frequencies. As can be seen, the results are close enough, especially for the maximum level of forced response.

Concluding Remarks

A method has been developed to calculate for practical mistuned bladed disks the mistuning patterns that provide the highest response levels.

The method uses an optimization approach in a search for the worst mistuning pattern and is based on the developed effective algorithm for analytical calculation of the sensitivity coefficients for the maximum response level in respect to blade mistuning. It is intended for use with finite element models having a large number of degrees of freedom, which could be used only for tuned bladed disks so far. It takes full advantage of the use of an exact condensation method based on the Sherman-Morrison-Woodbury formula for the finite element model.

Case studies carried out for realistic finite element models of fan and turbine bladed disk assemblies have demonstrated the efficiency of the proposed method for seeking the worst mistuning patterns and the highest response levels that are possible in specific excitation conditions and design of bladed disks. The proposed method is much superior to the random, ''statistical'' search used in the past both in terms of computational expense and in terms of response levels provided by the identified worst mistuning patterns.

Acknowledgment

The authors are grateful to Rolls-Royce plc. for providing the financial support for this project and for giving permission to publish this work.

References

[1] Castanier, M. P., Óttarsson, G., and Pierre, C., 1999, ''Reduced Order Modelling and Vibration Analysis of Mistuned Bladed Disk Assemblies with Shrouds,'' ASME J. Eng. Gas Turbines Power, **121**, pp. 515–522.

[2] Ewins, D. J., 1969, ''Effect of Detuning upon the Forced Vibration of Bladed Discs,'' J. Sound Vib., **9**, pp. 65–79.

[3] Ewins, D. J., and Han, Z. C., 1984, ''Resonant Vibration Levels of a Mistuned Bladed Disk,'' ASME J. Vibr. Acoust., **106**, pp. 211–217.

[4] Yang, M.-T., and Griffin, J. H., 1999, ''A Reduced Order Model of Mistuning using a Subset of Nominal System Modes,'' presented at the ASME TURBO EXPO'99, Indianapolis, USA, ASME Paper 99-GT-288.

[5] Griffin, J. H., and Hoosac, T. M., 1984, ''Model Development and Statistical Investigation of Turbine Blade Mistuning,'' ASME J. Vibr. Acoust., **106**, pp. 204–210.

[6] Griffin, J. H., 1992, ''Optimizing Instrumentation when Measuring Jet Engine Blade Vibration,'' ASME J. Eng. Gas Turbines Power, **114**, pp. 217–221.

[7] Sanliturk, K. Y., Imregun, M., and Ewins, D. J., 1992, ''Statistical Analysis of Random Mistuning of Bladed Assemblies,'' J. Mech. Eng., **C432/110**, pp. 51–57.

[8] Castanier, M. P., and Pierre, C., 1998, ''Investigation of the Combined Effects of Intentional and Randomm Mistuning on the Forced Response of Bladed Disks,'' *Proc. 34th AIAA/ASME/SAE/ASEE Joint Propulsion Conf. & Exhibit*, July 13–15, Cleveland, AIAA 98-3720.

[9] Mignolet, M. P., and Lin, C.-C., 1993, ''The Combined Closed Form–Perturbation Approach to the Analysis of Mistuned Bladed Disks,'' ASME J. Turbomach., **115**, pp. 771–780.

[10] Lin, C.-C., and Mignolet, M. P., 1997, ''An Adaptive Perturbation Scheme for the Analysis of Mistuned Bladed Discs,'' ASME J. Eng. Gas Turbines Power, **119**, pp. 153–160.

[11] Sinha, A., and Chen, S., 1989, ''A Higher Order Technique to Compute the Statistics of Forced Response of a Mistuned Bladed Disc Assembly,'' J. Sound Vib., **130**, pp. 207–221.

[12] Ewins, D. J., 1991, ''The Effects of Blade Mistuning on Vibration Response—A Survey,'' *IFToMM 4th International Conference on Rotordynamics*, Prague, Czechoslovakia.

[13] Slater, J. S., Minkiewicz, G. R., and Blair, A. J., 1999, ''Forced Response of Bladed Disk Assemblies—A Survey,'' Shock Vib. Dig., **31**(1), pp. 17–24.

[14] Dye, R. C. F., and Henry, T. A., 1969, ''Vibration Amplitudes of Compressor Blades Resulting from Scatter in Blade Natural Frequencies,'' ASME J. Eng. Power, **91**, pp. 182–187.

[15] Whitehead, D. S., 1966, ''Effect of Mistuning on the Vibration of Turbomachine Blades Induced by Wakes,'' J. Mech. Eng. Sci., **8**(1), pp. 15–21.

[16] Whitehead, D. S., 1998, ''The Maximum Factor by Which Forced Vibration of Blades can Increase due to Mistuning,'' ASME J. Eng. Gas Turbines Power, **120**, pp. 115–119.

[17] Petrov, E. P., 1988, ''Determination the Worst Blade Mistuning upon Forced Vibration of Impellers using the Nonlinear Programming Methods,'' Abstracts of the Conference *Mathematical Simulation of Processes and Structures of Power and Transport Turbines in CAD-CAM Systems*, Gotvald, Ukraine, Vol. 3, pp. 71–72.

[18] Petrov, E. P., 1993, ''Optimization of Perturbation Parameters for Forced Vibration Stress Levels of Turbomachine Blade Assemblies,'' *Proc. of the IUTAM Symposium on Discrete Structural Optimization*, Zakopane, Poland, pp. 108–117.

[19] Petrov, E. P., and Iglin, S. P., 1999, ''Search of the Worst and Best Mistuning Patterns for Vibration Amplitudes of Bladed Disks by the Optimization Methods using Sensitivity Coefficients,'' *Proc. of 1st ASSMO UK Conf. Engineering Design Optimization*, llkley, UK, pp. 303–310.

[20] Sinha, A., 1997, ''Computing the Maximum Amplitude of a Mistuned Bladed Disk Assembly via Infinity Norm,'' Proc. of the ASME Aerospace Division, AD- **55**, pp. 427–432.

[21] Thompson, E. A., and Becus, G. A., 1993, ''Optimization of Blade Arrangement in a Randomly Mistuned Cascade using Simulated Annealing,'' *AIAA/SAE/ASME/ASEE 29th Joint Propulsion Conference and Exhibit*, CA, USA, AIAA 93-2254.

[22] Petrov, E. P., Vitali, R., and Haftka, R., 2000, ''Optimization of Mistuned Bladed Discs using Gradient-Based Response Surface Approximations,'' *Proc. 41st AIAA/ASME/ASCE/AHS/ASC Structures, Struct. Dynamics and Materials Conf. and Exhibit*, Atlanta, USA, Paper AIAA-2000-1522, p. 11.

[23] Petrov, E. P., Sanliturk, K. Y., and Ewins, D. J., 2002, ''A New Method for Dynamic Analysis of Mistuned Bladed Disks Based on Exact Relationship Between Tuned and Mistuned Systems,'' ASME J. Eng. for Gas Turbines Power, **122**, pp. 586–597.

[24] Sherman, J., and Morrison, W. J., 1949, ''Adjustment of an Inverse Matrix Corresponding to Changes in the Elements of a Given Column or a Given Row of the Original Matrix,'' Ann. Math. Stat., **20**, p. 621.

[25] Woodbury, M., 1950, ''Inverting Modified Matrices,'' Memorandum Report 42, Statistical Research Group, Princeton University, Princeton, NJ.

[26] Forsythe, G. E., and Malcolm, M. A., 1977, *Computer Methods for Mathematical Computations*, Prentice-Hall Inc., Englewood Cliffs, NJ.

Blade Count and Clocking Effects on Three-Bladerow Interaction in a Transonic Turbine

H. D. Li
e-mail: Haidong.Li@durham.ac.uk

L. He
e-mail: Li.He@durham.ac.uk

School of Engineering,
University of Durham,
South Road,
Durham DH1 3LE, UK

A computational study of the multirow interaction mechanisms has been carried out for a one-and-a-half stage (NGV-rotor-stator) transonic turbine. In addition to measurable subharmonic unsteadiness on the rotor blades induced by two fundamental stator passing frequencies, a significant aperiodic ("mistuned") circumferential variation of unsteady forcing magnitude by about three times has been observed in the downstream stator blades. Further parametric studies with various stator blade counts illustrate that the circumferential variation pattern of the unsteady forcing is dictated by the NGV-stator blade count difference, while the local stator forcing magnitude is affected by its circumferential clocking position relative to the upstream NGV blades. The present work suggests that the circumferential clocking together with the choice of blade count should be considered as an aeromechanical design parameter. For cases with stator-stator (or rotor-rotor) blade counts resulting in a tuned (or nearly tuned) unsteady forcing pattern, the clocking position should be chosen to minimize the unsteady forcing. On the other hand, if the choice of blade counts leads to a significant aerodynamic aperiodicity (mistuning), the clocking-forcing analysis can be used to identify the most vulnerable blade that is subject to the maximum forcing.
[DOI: 10.1115/1.1622711]

1 Introduction

In multistage turbines, wake disturbances (entropy/vorticity distortions) from the upstream blade row and potential disturbances from the adjacent downstream blade row are the primary unsteady sources for any blade rows embedded in the middle. The influence from immediate upstream row's trailing edge shock waves is another important unsteady source for transonic turbines. For a downstream blade row, there are more complicated interactions among the unsteady wakes and shock waves from the immediate upstream row, and the chopped (and hence also unsteady) wakes and/or shocks from the relatively stationary further upstream row. All these upstream interactions may significantly influence the unsteady loading on the downstream blade row under consideration. To minimize this unsteady blade forcing is of obvious importance to blade fatigue life. Therefore understanding of blade rows interaction mechanism and identification of controlling parameters of unsteady forcing are of general interest to aeromechanic designs.

Various previous researches have been conducted in the relation to unsteady blade row interaction effects on aeromechanics and aerothermal performance in axial turbomachines. Stator-stator and/or rotor-rotor interactions exist when the wakes and shock waves passing through adjacent downstream blade row have not been completely mixed out. Capece et al. [1] reported that multiple stage interaction effects have a significant influence on the unsteady aerodynamic forces to the first and second stage vane rows of a three-stage compressor. In a low-speed compressor experiment, Hsu and Wo [2] found an optimal clocking position under influence of rotor-rotor interaction, which can reduce the unsteady loading of the middle row stator by 60%. Huber et al. [3] measured an increase of efficiency by about 0.8% in a two-stage turbine for an optimized second stator clocking position. Griffin et al. [4] predicted the same trend in a mid-span simulation of the same turbine. Dorney and Sharma [5] and Cizmas and Dorney [6] found that the minimum pressure fluctuation on the downstream stator blade indicates an optimal clocking position of efficiency. Similar findings were obtained by Arnone et al. [7] and Reinmoller et al. [8]. In a two-dimensional (2D) computational analysis of a transonic turbine stage, Hummel [9] found that interactions between chopped upstream stator wakes and rotor wakes/trailing edge shocks could generate strong nonuniformity at different circumferential positions in the downstream absolute frame of reference, leading to a significant potential for a stator-stator clocking. All the previous work closely relevant to the effects of stator-stator (rotor-rotor) interaction on blade aeromechanics seems to point to two related issues:

i. Does the clocking affect unsteady forcing to such an extent so that it can be used as a design parameter to control blade forced responses?
ii. How is the clocking effect influenced by blade counts?

The second issue is of particular interest here, as it is appreciated that different blade counts can lead to completely different clocking effects as far as averaged aerothermal performances are concerned. For a case with the same NGV and stator blade count, one should give the maximum clocking effect on the flow loss/efficiency. While if the difference between NGV and the stator blade numbers is 1 for instance, the passage-averaged flow loss will remain virtually the same, when clocked.

From the aeromechanics viewpoint, the fatigue life of a blade row is dictated by the blade subject to the maximum forcing (minimum damping). Blade aeromechanic models typically assume a ''tuned'' cascade/blade row, in which all blades in the row oscillate in the same frequency with the same amplitude and a constant blade-to-blade phase shift (interblade phase angle). The corresponding unsteady flow satisfies the phase-shifted periodicity. Any difference from this tuned blade row model can be regarded as ''mistuning.'' Mistuning effects due to nonuniformity in blade structural dynamic properties have been extensively studied (e.g., Kielb and Kaza [10]). However, mistuning behavior and effects of purely aerodynamic origins have rarely been reported.

Contributed by the International Gas Turbine Institute (IGTI) of THE AMERICAN SOCIETY OF MECHANICAL ENGINEERS for publication in the ASME JOURNAL OF TURBOMACHINERY. Paper presented at the International Gas Turbine and Aeroengine Congress and Exhibition, Amsterdam, The Netherlands, June 3–6, 2002; Paper No. 2002-GT-30310. Manuscript received by IGTI, December 2001, final revision, March 2002. Associate Editor: E. Benvenuti.

The present work was started with a numerical study of steady and unsteady flows for a one-and-a-half stage transonic H.P. turbine under a nominal operation condition, which has been experimentally studied by Miller et al. [11]. Based on the observation of a significant, but unreported aperiodic (mistuned) flow pattern in the downstream stator, the authors further investigated how the NGV-stator blade count affects the blade forcing and more interestingly how this effect can be linked to the clocking and the corresponding practical implications on blade aeromechanics.

2 Methodology

In simulations of unsteady turbomachinery flows with moving boundaries, an integral form of three-dimensional Navier-Stokes equations written in the absolute cylindrical coordinate system is usually used,

$$\frac{\partial}{\partial t}\int\int\int_{\delta V} U dV + \oint\oint_{\delta A} [Fn_x + (G - U\nu_{mg})n_\theta + Hn_r]\cdot dA = \int\int\int_{\delta V} S_i dV + \oint\oint_{\delta A} [V_x n_x + V_\theta n_\theta + V_r n_r]\cdot dA, \quad (1)$$

where U is the vector of conservative variables, F, G, and H are inviscid flux vectors, ν_{mg} is mesh moving velocity due to blade rotation if the mesh is attached to a rotor. The extra inviscid flux term $U\nu_{mg}$ counts for the contribution to the fluxes due to grid movement. S_i is the inviscid source term. Full viscous stress terms (V_x, V_θ, and V_r) are adopted in the current work. The system equations are closed by the equation of state and the mixing length turbulence model by Baldwin and Lomax [12].

The above governing equations are discretized in space using the cell centered finite volume scheme, together with the blend second-order and fourth-order artificial dissipations [13]. Temporal integration of the discretized equations is carried out using the second order four-step explicit Runge-Kutta scheme. A time-consistent multigrid technique [14] has been adopted to speed up convergence procedure.

The computational domain consists of multiple passages with a blade being at the center of each passage. The direct periodic conditions are applied on the lower periodic boundary of the first passage and upper boundary of the last passage. On blade and end-wall surfaces, a log law is applied to determine the surface shear stress and the tangential velocity is left to slip. At the inlet, stagnation parameters and flow angles are specified. At the exit, pitch-wise mean static pressure at each spanwise section is specified. The 1D nonreflective procedure [15] has been implemented at both inlet and exit to shorten extension domains. On the interfaces of adjacent blade rows, mixing plane treatment was adapted for steady calculations, while a direct interpolation on sliding meshes was applied to unsteady computations.

3 Case Study on Experimental Configuration

The case concerns a one-and-a-half stage transonic turbine. The experimental measurement was carried out by Miller et al. [11] and Moss et al. [16]. The numerical simulation conducted here is based on a quasi-three-dimensional section near the mid span with the stream-tube height varying from inlet to exit to match the experimental diffusing ducting geometry on the meridional plane.

3.1 Steady Flow. The operation condition of the steady flow is derived from Ref. [16] and the major parameters are listed in Table 1. The purpose of this calculation is to match the experimental rotor operation condition as close as possible. 100×40 computational cells in each NGV passage, 130×30 cells in each rotor passage, and 140×60 cells in each stator passage were used. Figure 1 shows the mesh distribution for the current steady calculation and the same mesh was thereafter used for unsteady simulations.

Table 1 Turbine operating condition

	NGV	Rotor	Stator
Blade number	36	60	21
Relative exit Mach number	0.95	0.98	0.86
Rotational speed		8910 rpm	
Blade Reynolds number		1.56e6	

Figure 2 shows the isentropic Mach number distribution on the rotor blade in comparison with the experimental time-mean data. The overall agreement is regarded as satisfactory for the purposes of the present work, though some numerical oscillations appear at the rear part of the suction surface.

3.2 Unsteady Flow. A validation calculation of the unsteady flow was carried out based on the nominal operation condition listed in Table 1. In all the unsteady computations, a multipassage domain was adopted with a direct periodic/repeating

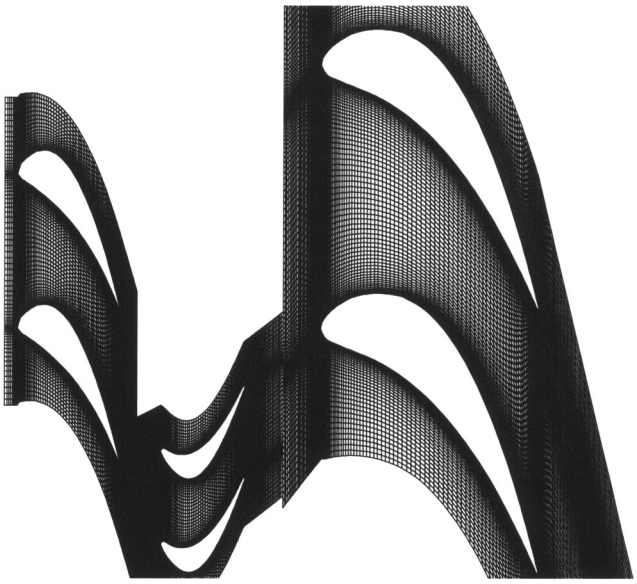

Fig. 1 Computational mesh (original experimental configuration)

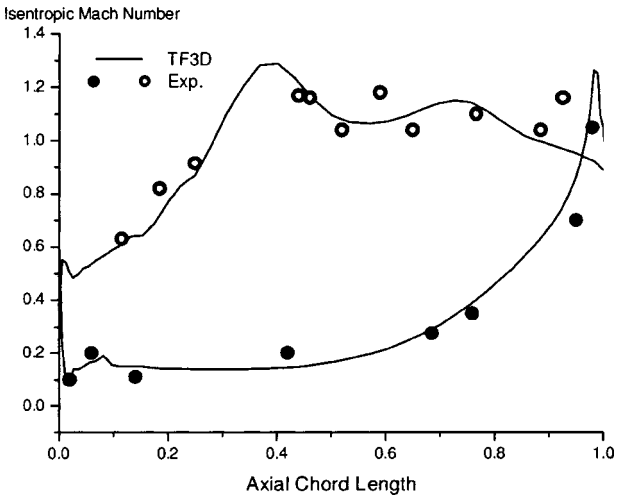

Fig. 2 Isentropic Mach number distribution

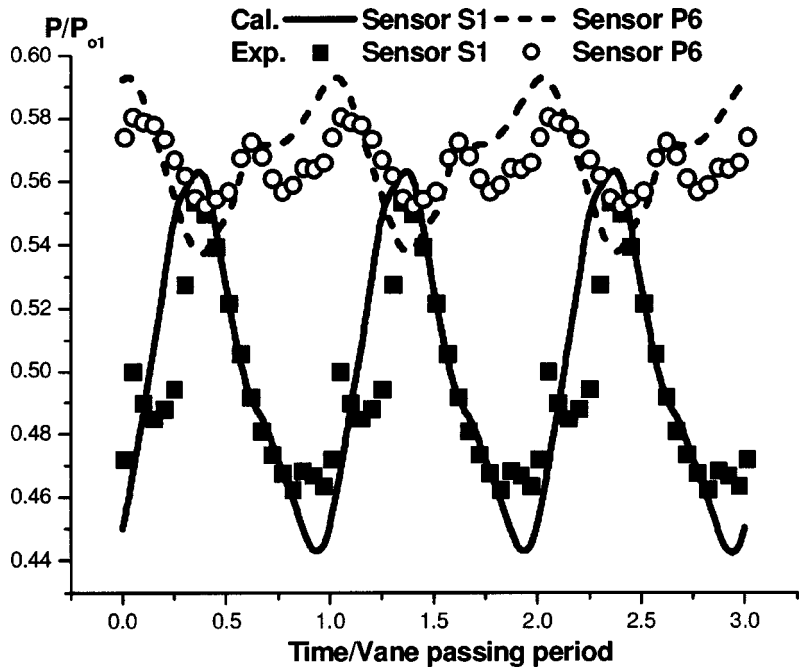

Fig. 3 Pressure time histories at sensor positions S1 and P6 (S1: suction surface 5% axial chord; P6: pressure surface 67% axial chord)

condition. The numbers of passages in the three blade row computational domain for the original configuration were taken to be 12/20/7 to match 1/3 of the annulus. The calculated results are compared with the experiment on two rotor surface points (sensor S1 and P6) where unsteady experimental data are available [11]. Sensor S1 is at about 5% axial chord length from the leading edge on the suction surface. Sensor P6 is at about 67% axial chord length on the pressure surface. Figure 3 shows the time traces of static pressure on these measured points. The predicted suction surface data (S1) agree with the experiment very well. The pressure surface prediction (P6) captures the main feature of the experiment data, though the amplitude is overpredicted. A significant difference between the pressure surface and the suction surface is that the NGV trailing-edge shock does not directly sweep across the pressure surface. Therefore the amplitude of the pressure fluctuation on the pressure surface is much smaller than that on the suction surface near the leading edge. Note that the downstream stator is of a different blade count compared to the NGV. But the unsteady pressure traces at these two rotor surface points hardly show any sign of the stator frequency, which suggests that potential effects from the downstream stator is much weaker compared to the effects from the upstream NGV flow distortions.

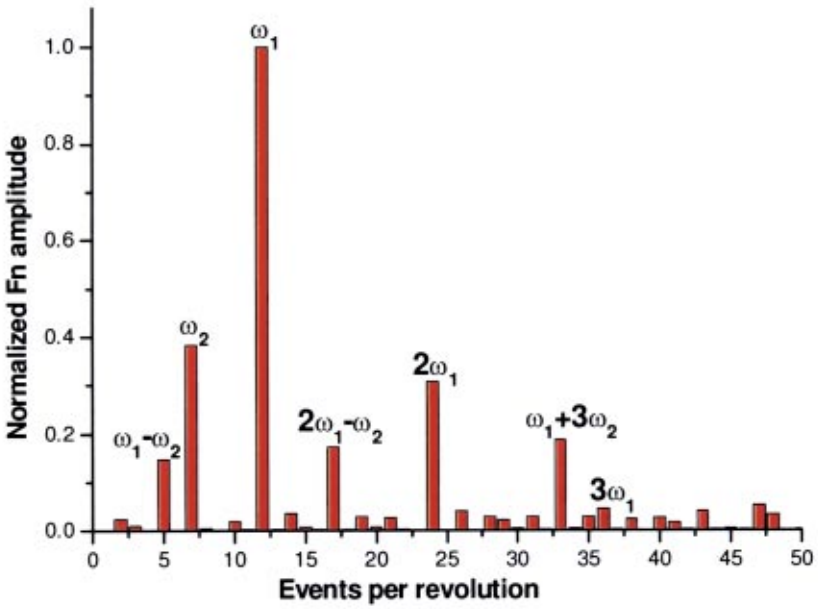

Fig. 4 Spectrum of normal force on a rotor blade (normalized by the first harmonic component, experimental condition, blade counts 12/20/7)

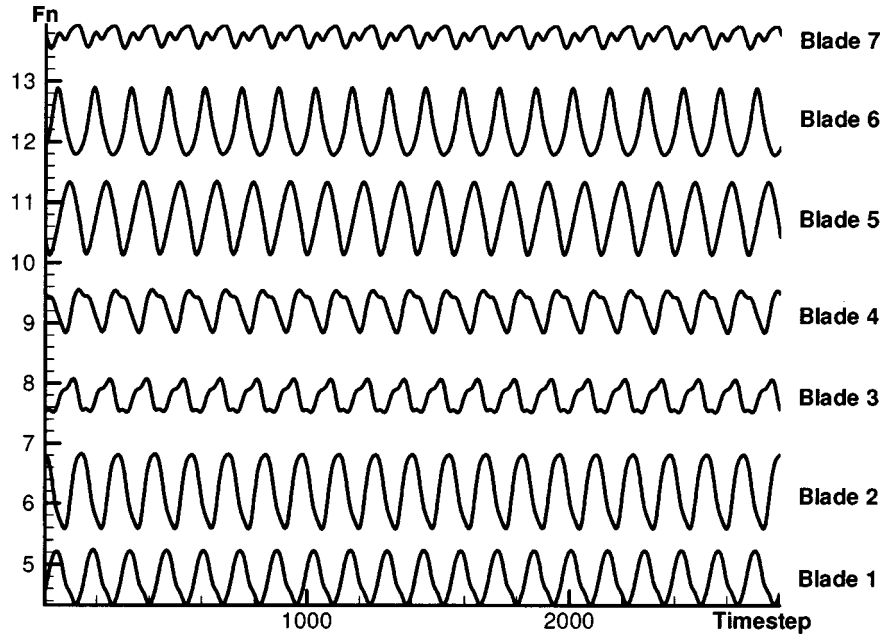

Fig. 5 Time histories of unsteady normal force on stator blades (experimental condition, blade counts: 12/20/7)

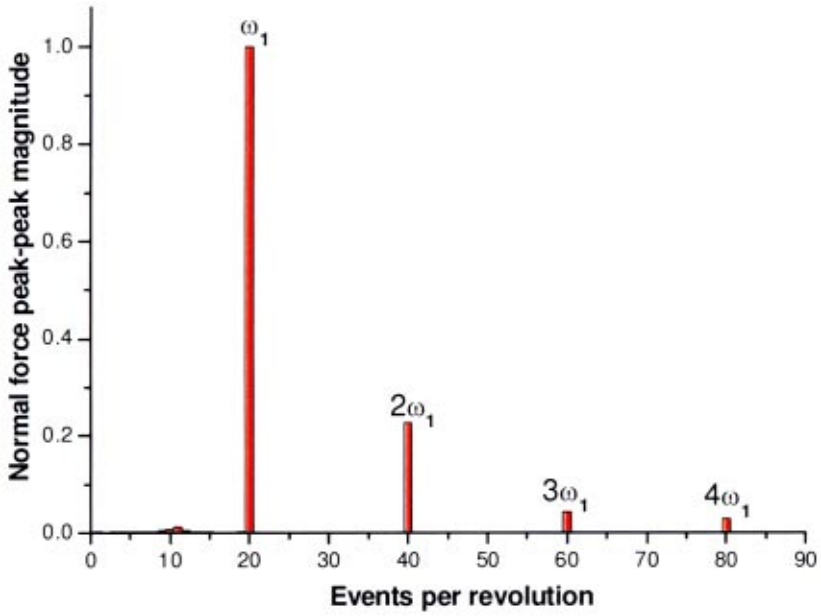

Fig. 6 Spectrum of normal force on stator blade 5 (normalized by the first harmonic component, experimental condition, blade counts: 12/20/7)

3.2.1 Subharmonics on Rotor. In principle, when two primary harmonic disturbances with frequencies ω_1 and ω_2 coexist, flow responses may contain subharmonics with frequencies like $n\omega_1+m\omega_2$ or $n\omega_1-m\omega_2$, where n and m are positive integer numbers, due to nonlinear interactions. The embedded rotor row is predominately affected by the upstream NGV flow distortion and downstream stator potential disturbance. These two disturbances at different frequencies (due to different NGV-stator blade counts) interact with each other and generate subharmonic modes. As shown on Fig. 4, the spectrum of the rotor blade normal force (i.e., the force component in the direction normal to the blade chord) indicates measurable subharmonics at frequencies of $\omega_1-\omega_2$, $2\omega_1-\omega_2$, and $\omega 1+3\omega_2$. The subharmonic component at $\omega_1-\omega_2$ is about 12% of the magnitude of the primary NGV flow disturbance, which is comparable to the experimental observation [11].

3.2.2 Aperiodic Flow in Downstream Stator. When the number of NGV blade is different from that of the stator, the NGV-stator interaction will induce an aperiodic flow pattern in both stator rows. First of all, it was noted that the aperiodic variation of unsteady forcing magnitude on the NGV blades is very small (less than 5%) due to very weak upstream running potential influences. But on the other hand, the flow in the downstream stator row turns out to be strikingly different. Figure 5 shows time histories of the unsteady normal forces on the seven stator blades at the nominal

Table 2 Number of passages used in calculations

Case index	NGV	Rotor	Stator
1 (nominal)	12	20	***7***
2	12	20	***10***
3	12	20	***11***
4	12	20	***12***
5	12	20	***13***
6	12	20	***14***

condition (note these time traces are vertically shifted for clarity). One can easily see that the unsteady flow around the stator blades is markedly aperiodic or mistuned. There is neither a constant magnitude, nor a constant phase shift. The maximum magnitude of the unsteady force (blade 2) is about three times of the minimum one (blade 7).

Before discussing the stator aperiodicity further, the authors would make a comment regarding the frequency of the unsteadiness. Figure 6 shows the spectrum of the normal blade force on one of these stator blades. It is clear that only the unsteadiness at the rotor blade passing frequency and its higher-order harmonics have been detected. All the present computational results consistently show that the interference between the rotor row and NGV-stator interaction does not introduce any other temporal disturbances with frequencies other than that of the rotor blade-passing one. The NGV wakes are chopped by the rotor blades, and are seen by the stator as unsteady disturbances. But the frequency remains to be the rotor passing frequency. Hence the term ''mistuning'' or ''mistuned'' should be used with this frequency characteristic in mind. This is in contrast to a ''tuned'' blade row situation, where unsteady forcing on each blade has the same amplitude but with a constant blade-to-blade phase shift.

Also it should be pointed out that although the unsteady stator loading is largely different from blade to blade in terms of both phase and amplitude, the time averaged blade loading values are very similar (with a blade-blade variation of less than 5%). This is in line with relatively small influences on averaged aerothermal performances due to stator-stator interactions, as commonly observed.

4 Case Study With Variable Blade Counts

With the strikingly large aperiodic unsteady forcing pattern observed in the downstream stator row, one would naturally ask about corresponding mechanisms and controlling parameters if any. A number of computations were thus conducted with different NGV-stator blade counts and clocking positions. All the cases studied have the same number of blades in the NGV and rotor rows as in the original experimental configuration, i.e., 12 NGV blades and 20 rotor blades. Only the stator blade count was changed over a range from 7 to 14, as listed in Table 2. When changing the stator blade count, the dimensions of the stator blades were scaled accordingly to keep the same solidity in order to achieve the same steady loading coefficients on the blade surface as the original one. Therefore the overall loading of the stator row was kept the same as the original configuration. Meanwhile, the gap between the rotor and the stator was kept the same for all the cases, so the time-averaged loading on the rotor remained roughly the same when the downstream stator blade count was changed.

4.1 Rotor Unsteady Loading. A general observation regarding the rotor unsteady forcing is that the magnitudes of subharmonics can be changed considerably depending upon the stator blade count and rotor-stator gap distance. Nevertheless, in all cases studied, all rotor blades consistently exhibit unsteady loading with the same amplitude and a constant phase shift, indicating the phase-shifted periodicity. The time histories of unsteady normal forces on different rotor blades of case 3 (blade count ratio 12/20/11) is shown on Fig. 7. Each blade is subject to two primary disturbances and the sub-harmonics. Thus the time traces do not appear simply periodic in time. However, a detailed examination confirms that the phase-shifted periodicity exists among the rotor blades. This implies that even under induced subharmonic interactions, as discussed in Sec. 3.2.1, each harmonic component still can be directly traced back to the two primary disturbances, i.e., those from the upstream flow distortions and the downstream stator potential waves, respectively. Hence the rotor blades under consideration are still aerodynamically tuned. Therefore regardless of NGV-stator blade counts, periodically unsteady results (computational or experimental) in one *single rotor blade passage* would be sufficient for reconstructing the unsteady flow field for the whole rotor annulus.

4.2 Stator Unsteady Loading. The computational results suggest the NGV-stator blade counts have a key influence on the aperiodic unsteady forcing of the downstream stator row. Figure 8 shows the distributions of peak-to-peak unsteady normal force magnitudes (normalized by the time-averaged normal force on the stator blade) for five different NGV-stator blade counts.

First for the case with an equal NGV-stator blade count (12/20/12), the unsteady forcing magnitude is constant for all blades in the stator row. Hence the stator is tuned for this configuration. All the other cases exhibit clearly a mistuned unsteady forcing on the stator blades. The circumferential variation of the unsteady loading magnitude corresponds to exactly the NGV-stator interference mode with its circumferential wavelength dictated by the blade count difference. If the NGV-stator blade count difference is one, the wavelength covers the whole circumference. The wavelength is a half of a circumference when the blade-count difference is 2. Alternatively, the aperiodic patterns can be directly linked to the corresponding clocking positions, as the same local clocking position will repeat *Nd* times, where *Nd* is the difference of blade numbers between the NGV and the stator.

It is also noted from Fig. 8 that a NGV-stator interaction with a longer interference wavelength seems to generate a larger forcing magnitude difference among the stator blades. As we can see, the maximum normal force magnitude of case 3 (blade count 12/20/11) is higher than case 2 (blade count 12/20/10). The same trend can be found between case 5 (blade count 12/20/13) and case 6 (blade count 12/20/14). Furthermore, for the same interference wavelength, the case with a smaller number of stator blades tends to have a smaller aperiodic forcing variation. For instance, case 3 (blade counts 12/20/11) and case 5 (blade counts 12/20/13) both have a count difference of 1 and thus the same NGV-stator interference wavelength. But the circumferential aperiodic forcing variation in case 3 is considerably smaller than that in case 5. This might be attributed to the number of NGV wakes ''seen'' by a stator passage. In case 3, the stator pitch is larger than that of the NGV. Hence each stator passage sees either 1 or 2 NGV wakes. But in the case 5, each stator passage would see either 1 NGV wake or nothing at all. The latter one with a smaller stator pitch (case 5) seems to be subject to a bigger difference in the NGV wake effect on the blade forcing.

4.3 Link Between Clocking and Forcing. Given the significant aperiodic forcing distributions in the stator blades for unequal NGV-stator blade counts, it is interesting to explore the correlation between the stator forcing magnitude and the NGV-stator clocking. The clocking is defined by the relative circumferential position at blade leading edge (see Fig. 11):

$$\theta_{\text{stator}} - \theta_{\text{NGV}}. \tag{2}$$

Unsteady normal force magnitudes of all the stator blades for the cases with different blade counts are plotted against each blade's local clocking position, as shown in Fig. 9. Although the results for different blade count cases are different quantitatively, there is a clear overall trend of the unsteady force magnitudes in relation to the clocking. Regardless of blade counts, the maximum forcing appears when a stator blade is clocked in a region of

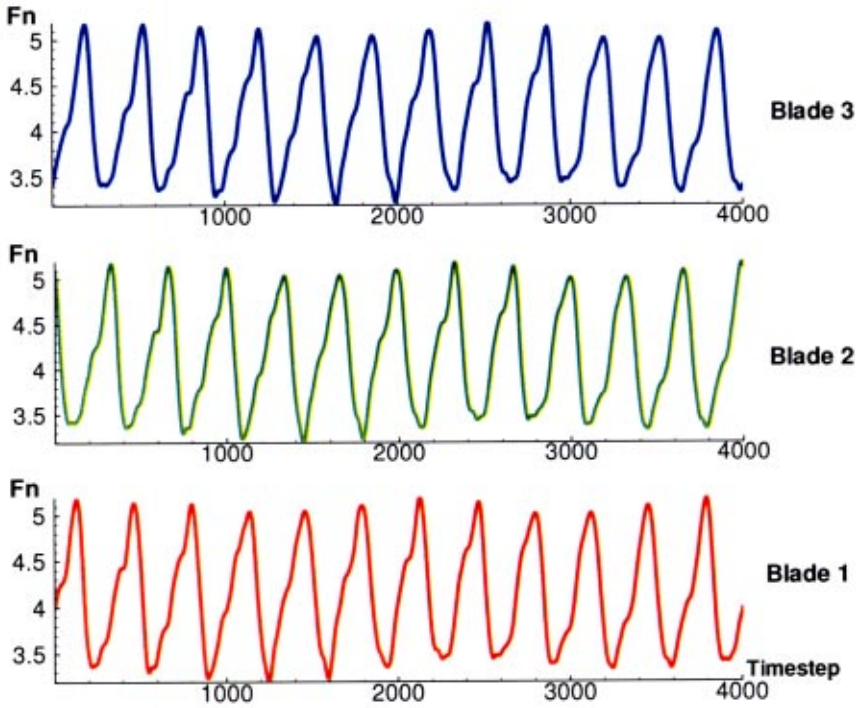

Fig. 7 Time histories of normal force on rotor blades (Blade counts: 12/20/11)

0.2–0.5 NGV blade pitch relative to its corresponding NGV blade. And the minimum forcing happens when a stator blade is clocked to around 0.8 NGV pitch.

Also plotted in Fig. 9 is that of the equal NGV-stator blade count (12/20/12). In this case, the local clocking positions are the same for all the blades. The forcing dependence on clocking was generated by several separate calculations at specified clocking positions. We can see that the result of the equal NGV-stator count case follows the same trend as others with unequal NGV-stator blade counts.

A further confirmation of the clocking-forcing correlation is provided by the results for case 3 (blade counts 12/20/11) when the stator row is clocked to four different clocking positions (0, 1/11, 2/11, and 3/11 NGV pitch). Figure 10 shows the stator force magnitudes versus the clocking positions from the four calculations. All the points from the calculations collapse to one single curve, meaning that the aperiodic unsteady forcing is solely caused and determined by the local clocking position for a given blade configuration.

For both situations with equal and unequal blade counts, a com-

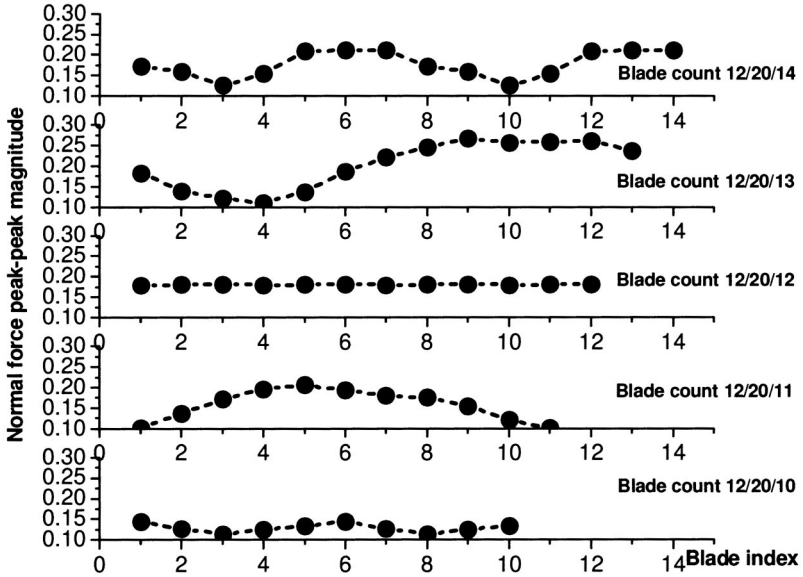

Fig. 8 Unsteady normal force magnitudes of the stator row for five different blade counts

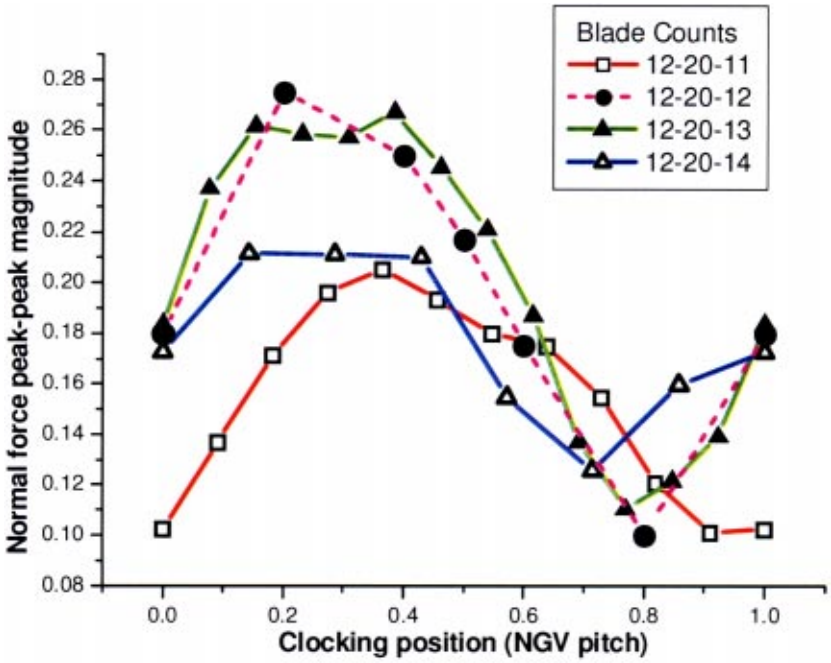

Fig. 9 Unsteady normal force magnitudes variation with local clocking position

mon feature seems to emerge. Unsteady forcing can be linked to the clocking position, either inherently determined by an aperiodic flow distribution or artificially determined by clocking the stator. The effectiveness of the clocking on the forcing can be explained in a simple and fundamental manner as follows.

As illustrated in the sketch on Fig. 11, NGV wakes are chopped and turned by rotor blades. A chopped NGV wake will be seen as an unsteady disturbance by the downstream stator at the rotor passing frequency. So the stator blades are effectively subject to two separately primary sources of periodic disturbances at the same frequency. As a result, the phasing between the two disturbances can either enhance or suppress each other. The kinematical relation between a NGV wake and a rotor blade that chops the wake tells us that the instantaneous *phase angle of the chopped NGV wake* is given by

$$\theta_{\text{rotor}} - \theta_{\text{NGV}}, \tag{3}$$

where θ_{rotor} is the *instantaneous* circumferential position of the rotor. On the other hand if we look at a stator blade subject to the

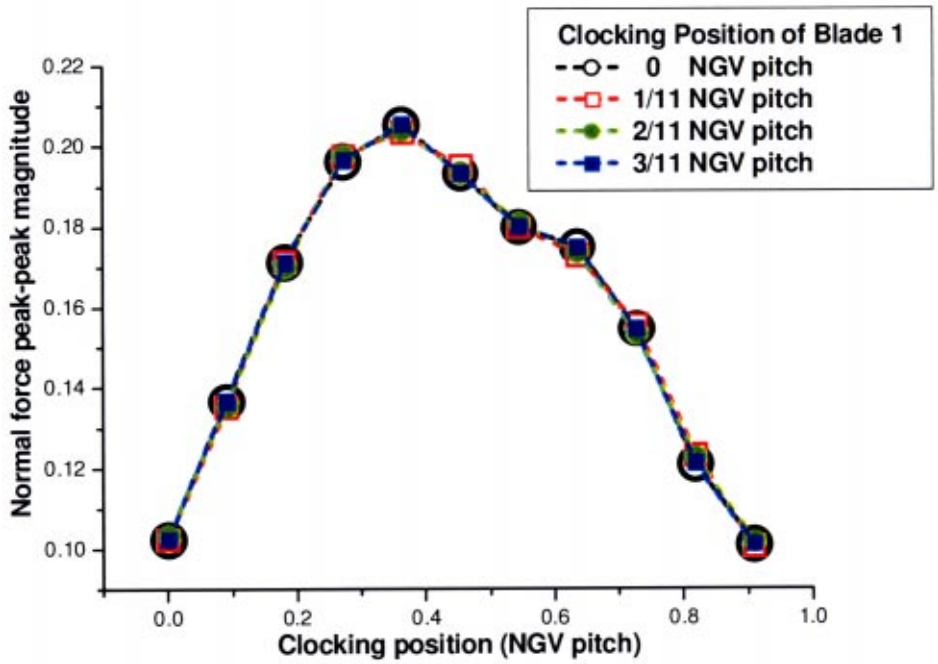

Fig. 10 Unsteady normal force magnitude on stator blades at different clocking positions of blade 1 (blade counts: 12/20/11)

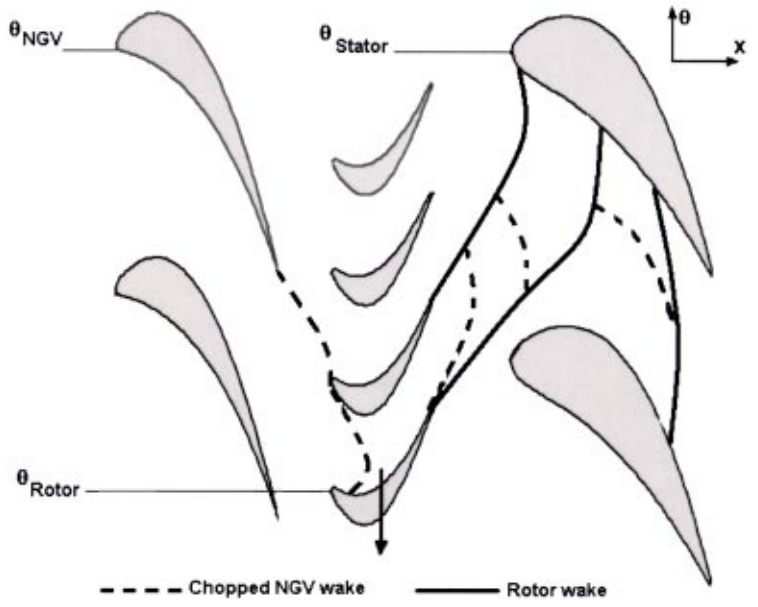

Fig. 11 Sketch showing NGV wake-rotor wake interference (both phases of chopped NGV and rotor wakes seen by stator are determined by instantaneous rotor phase θ_{rotor})

moving wake (and/or trailing edge shock waves) from this rotor blade, then *the phase angle of the rotor unsteadiness seen in that stator blade* is given by

$$\theta_{rotor} - \theta_{stator}. \tag{4}$$

The above two phase angles given by Eqs. (3) and (4) simply mean that the instantaneous rotor blade position (movement) dictates the events. It then must follow that the relative phasing between the chopped NGV wake and the rotor unsteadiness (moving wake and/or shock wave) is given by the difference of the two phase angles, i.e.,

$$\theta_{NGV} - \theta_{stator}. \tag{5}$$

In other words, the above proves that the phasing between unsteady chopped NGV wakes and unsteady rotor wakes (and/or shock waves) is solely determined by the stationary NGV-stator clocking position. It should be emphasized that the above argument is purely based on a generic kinematics of a single blade in each row and does not involve blade count.

It is noted that some possible phasing mechanisms have been discussed in detail by Hummel [9], which might lead to a more specific determination of the clocking positions with the maximum and minimum forcing. Here we may get some indication of the NGV wake paths in the stator by looking at the time-averaged entropy contours. For the case with an equal NGV-stator blade

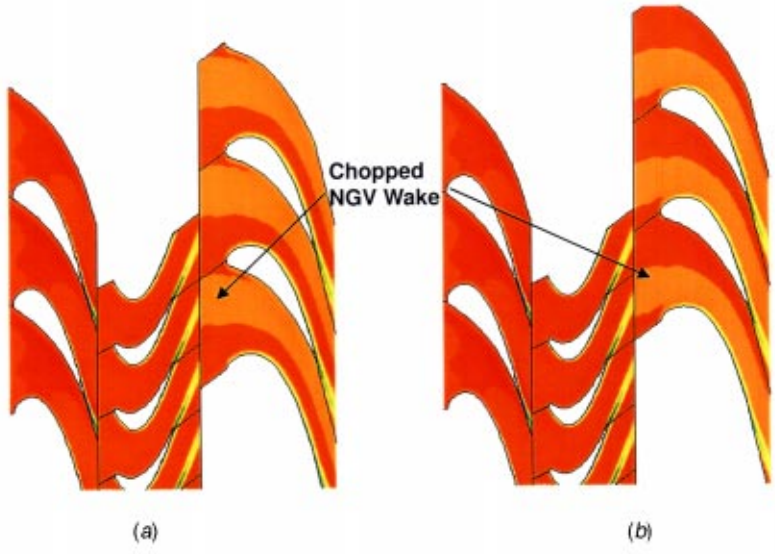

Fig. 12 Time averaged entropy contours at different clocking positions (stator L.E. relative to NGV L.E.) (equal NGV stator blade count: 12/20/12); (*a*) clocking at 0.2 NGV pitch, near maximum forcing, (*b*) clocking at 0.8 NGV pitch, near minimum forcing.

count, the time-averaged flow is the same for all stator passages. The results for the two clocking positions roughly corresponding to the maximum and the minimum forcing magnitudes are shown in Fig. 12. The stator blade subject to the maximum forcing is located in a position where a time averaged NGV wake passes through the pressure side stator surfaces (Fig. 12(*a*)). The minimum unsteady forcing appears at the position where a NGV wake passes over the suction side of the stator blades (Fig. 12(*b*)).

It should be cautioned that the exact clocking positions corresponding to the forcing extrema may well depend on blading design and the intra row gap. This is because that the clocking at which the chopped NGV wake and the rotor unsteadiness enhance (or cancel) each other will be largely dependent on the propagation of the rotor unsteadiness. For a transonic turbine, it should be noted that downstream propagation of rotor wakes is determined by the convection following the relative flow direction, while the pressure waves associated with the rotor trailing edge shock wave will propagate to downstream in completely different directions. As such, a stator blade at a different rotor-stator gap should sense a different phasing between the rotor wake and shock disturbances. Given that the phase of the rotor unsteadiness seen by the stator changes with the rotor-stator gap for different configurations, the NGV-rotor phasing effect should also be dependent on the rotor-stator gap.

On practical relevance and implications, the present results indicate that clocking together with blade counts should be relevant to aeromechanical design consideration. In terms of controlling unsteady blade forcing, stator-stator (or rotor-rotor) blade counts should be chosen as such that all blades in a row are aerodynamically tuned or nearly so. Then the designer may select the optimum clocking position (Fig. 12(*b*) for the present cases) to have a minimum forcing. If the choice of blade counts is such that a significantly aperiodic (mistuned) forcing pattern is unavoidable, the clocking-forcing analysis may be carried out to identify the most vulnerable blade subject to the maximum forcing. The clear identification of the least safe blade is very useful as it may be used as a basis for a circumferentially preferential damping treatment. The understanding of this aerodynamic mistuning may be utilized in combination with selective structural mistuning to optimize aeromechanical designs.

5 Concluding Remarks

The present work was started with a study of unsteady flow for a one-and-a-half stage transonic turbine with comparison to the experimental data. The effort was then focused on examining the NGV-stator blade count effect in junction with clocking-forcing correlation. The following conclusions might be drawn:

Rotor: Subharmonic effects on the rotor blade row, as observed in the experiment, have been identified. Although the magnitudes of the rotor subharmonic components are influenced by the NGV-stator interactions, a clearly defined phase-shifted periodicity is found to be valid for rotor blades in all cases studied.

Downstream stator: A significant aperiodic (mistuned) unsteady forcing variation by as much as three times in magnitude has been observed in the stator row for the experimental configuration. The circumferential variation pattern of the unsteady forcing magnitude corresponds exactly to the NGV-stator interference mode, dictated by the blade count difference. The relative phasing between chopped NGV wakes and rotor unsteadiness is shown to be solely determined by the NGV-stator clocking position for any given blade configurations.

The outcomes of the present work suggest that a careful choice of NGV-stator blade counts together with selective clocking during design can serve to control the maximum stator blade forced response. For a given design, if the stator-stator (rotor-rotor) blade counts lead to a significantly aperiodic forcing variation, the clocking-forcing analysis should be used to identify the aeromechanically most vulnerable blade, which is under the maximum forcing.

Acknowledgments

The authors wish to thank the Engineering and Physical Sciences Research Council (EPSRC) of U.K. for sponsoring this work under Grant No. GR/M43821. This paper is a substantially modified version of that presented at the 2002 ASME Gas Turbine conference at Amsterdam. The valuable comments on clocking by Dr. Matt Montgomery (Siemens Westinghouse) and Professor Ted Okiishi (Iowa State University) are much appreciated.

Nomenclature

dA = mesh cell face area
dV = mesh cell volume
F, G, H = inviscid flux vector
Fn = force component in the direction normal to blade chord
n_x, n_θ, n_r = unit normal vectors of cell face
U = conservative variable vector
V_x, V_θ, V_r = viscous terms
ω = angular frequency
θ = circumferential position

References

[1] Capece, V. R., Manwaring, S. R., and Fleeter, S., 1986, ''Unsteady Blade Row Interactions in a Multi-stage Compressor,'' AIAA J., Propul. Power **2**(2), pp. 168–174.
[2] Hsu, S. T., and Wo, A. M., 1998, ''Reduction of Unsteady Blade Loading by Beneficial Use of Vortical and Potential Disturbances in an Axial Compressor with Rotor Clocking,'' ASME J. Turbomach., **120**, pp. 705–713.
[3] Huber, F. W., Johnson, P. D., Sharma, O. P., Staubach, J. B., and Goddis, S. W., 1996, ''Performance Improvement Through Indexing of Turbine Airfoils: Part I-Experimental Investigation,'' ASME J. Turbomach., **118**, pp. 630–635.
[4] Griffin, L. W., Huber, F. W., and Sharma, O. P., 1996, ''Performance Improvement Through Indexing of Turbine Airfoils: Part II-Numerical Simulation,'' ASME J. Turbomach., **118**, pp. 636–642.
[5] Dorney, D. J., and Sharma, O. P., 1996, ''A Study of Turbine Performance Increase Through Airfoil Clocking,'' AIAA Paper No. 96-2816.
[6] Cizmas, P., and Dorney, D. J., 1998, ''Parallel Computation of Turbine Blade Clocking,'' AIAA Paper No. 98-3598.
[7] Arnone, A., Marconcini, M., Pacciani, R., Schipani, C., and Spano, E., 2002, ''Numerical Investigation of Airfoil Clocking in a Three-Stage Low-Pressure Turbine,'' ASME J. Turbomach., **124**, pp. 61–68.
[8] Reinmoller, U., Stephan, B., Schmidt, S., and Niehuis, R., 2002, ''Clocking Effects in 1 1.5 Stage Axial Turbine-Steady and Unsteady Experimental Investigations Supported by Numerical Simulations,'' ASME J. Turbomach., **124**, pp. 52–60.
[9] Hummel, F., 2002, ''Wake-Wake Interaction and Its Potential for Clocking in A Transonic High Pressure Turbine,'' ASME J. Turbomach., **124**, pp. 69–76.
[10] Kielb, R. E., and Kaza, K. R. V., 1984, ''Effects of Structural Coupling on Mistuning Cascade Flutter and Response,'' ASME J. Eng. Gas Turbines Power, **106**, pp. 17–24.
[11] Miller, R. J., Moss, R. W., Ainsworth, R. W., and Harvey, N. W., 2001, ''Time-Resolved Vane-Rotor-Vane Interaction in A Transonic One and A Half Stage Turbine,'' Proc. of IMechE, Part A, J. of Power and Energy, **215**, pp. 675–685.
[12] Baldwin, B. S., and Lomax, H., 1978, ''Thin Layer Approximation and Algebraic Model for Separated Turbulent Flows,'' AIAA Paper 78-0257.
[13] Jameson, A., Schmidt, W., and Turkel, E., 1981, ''Numerical Solutions of the Euler Equations by Finite Volume Method using Runge-Kutta Time-Stepping Scheme,'' AIAA Paper 81-1259.
[14] He, L., 2000, ''Three-Dimensional Unsteady Navier-Stokes Analysis of Stator-Rotor Interaction in Axial-Flow Turbines,'' Proc. of IMechE, Part A, J. of Power and Energy, **214**, pp. 13–22.
[15] Giles, M. B., 1990, ''Nonreflecting Boundary Conditions for Euler Equation Calculations,'' AIAA J., **28**, No. 12, pp. 2050–2058.
[16] Moss, R. W., Ainsworth, R. W., Sheldrake C. D., and Miller, R., 1997, ''The Unsteady Pressure Field Over a Turbine Blade Surface: Visualisation and Interpretation of Experimental Data,'' ASME Paper 97-GT-474.

Fluid Dynamics of a Pre-Swirl Rotor-Stator System

Youyou Yan
Aero, Civil and Mechanical Engineering,
City University, London,
Northampton Square,
London EC1V 0HB, UK

Mahmood Farzaneh Gord

Gary D. Lock

Michael Wilson

J. Michael Owen

Department of Mechanical Engineering,
University of Bath,
Bath BA2 7AY, UK

In a "direct-transfer" pre-swirl supply system, cooling air flows axially across the wheelspace from stationary pre-swirl nozzles to receiver holes located at a similar radius in the rotating turbine disc. This paper describes a combined computational and experimental study of the fluid dynamics of such a system. Measurements of total and static pressures have been made using a purpose-built rotor-stator rig, with 24 pre-swirl nozzles on the stator and 60 receiver holes in the rotor. The number of pre-swirl nozzles could be reduced, and it was possible to calculate C_D*, the discharge coefficient of the receiver holes. Information on the flowfield was also obtained from three-dimensional, incompressible steady turbulent flow computations. The measurements showed that there was a significant loss of total pressure between the outlet from the pre-swirl nozzles and the rotating core of fluid in the wheel-space. This loss increased as the pre-swirl flow-rate and inlet swirl ratio increased, and as the number of nozzles decreased.* C_D *increased as the swirl ratio at the receiver hole radius approached unity; also* C_D *decreased as the number of nozzles decreased. Computed pressures and tangential velocities were in mainly good agreement with the measurements. The computations help to explain the reasons for the significant losses in total pressure and for the relatively low values of* C_D *in this pre-swirl system.* [DOI: 10.1115/1.1578502]

Keywords: Pre-Swirl, Rotor-Stator Systems, Fluid Dynamics, Discharge Coefficients

Introduction

The air used for internal cooling of turbine blades in engines is supplied through receiver holes near the periphery of the rotating turbine disc. The air is delivered across the wheelspace from ''pre-swirl'' nozzles, in the stator, angled to impart swirl to the air in the direction of rotation, thus reducing the relative temperature of the air entering the receiver holes. Fluid dynamics parameters of interest to the designer include the *effective* pre-swirl ratio, the loss of total pressure in the system and the discharge coefficients.

In some engines, as illustrated in Fig. 1(*a*), the pre-swirl nozzles are located at a low radius on the stator, and the cooling air flows radially outward to the receiver holes through the rotating cavity between the disc and a rotating cover-plate attached to it. The flow in cover-plate systems has been studied computationally by Popp et al. [1] and both experimentally and computationally by Karabay et al. [2,3]. Popp et al. studied the geometric factors affecting the collection of the pre-swirl air at the base of the cover-plate, and made comparisons with system efficiencies measured by Meierhofer and Franklin [4]. Karabay et al. found that, at the high cooling air flow rates expected in engines, free-vortex flow occurs in the rotating cavity between the cover-plate and the disk; the adiabatic effectiveness of the system is then amenable to simplified theoretical analysis. The most important parameters affecting the flow structure were found to be the inlet pre-swirl ratio, $\beta_p = V_{\phi,p}/\Omega r_p$ (the ratio of the tangential component of velocity of the pre-swirl air to the speed of the rotating disk at the same radius) and the turbulent flow parameter, $\lambda_T = C_{W,p}\,\mathrm{Re}_\phi^{-0.8}$, where $C_{W,p}$ is the nondimensional flow rate of the pre-swirl air and Re_ϕ is the rotational Reynolds number for the disk.

Karabay et al. [2,3] found that the ''effective'' pre-swirl ratio, $\beta_{p,\mathrm{eff}}$, for the radial outflow at the base of the cavity (at radius a close to that of the nozzles) was less than β_p. The difference is caused by mixing losses, which in cover-plate systems occur mainly as the inlet flow is turned radially as it enters the cavity. Karabay et al. found that the ratio $\beta_{\mathrm{p,eff}}/\beta_{\mathrm{p}}$ reduces as β_{p} increases, and the free-vortex flow in the cover-plate cavity could then be represented by

$$\frac{V_\phi}{\Omega r} = \beta_{p,\mathrm{eff}}\left(\frac{x_P}{x}\right)^2 = \beta_p\left(\frac{\beta_{p,\mathrm{eff}}}{\beta_p}\right)\left(\frac{x_p}{x}\right)^2 \tag{1}$$

An alternative ''direct-transfer'' pre-swirl arrangement is used in other engines, as shown in Fig. 1(*b*). In this system the stationary pre-swirl nozzles are located at a higher radius, compared with cover-plate systems, and the pre-swirl air is confined, by the seals, to a compact rotor-stator chamber in the outer part of the wheelspace. The flow and heat transfer in a model pre-swirl rotor-stator system was studied by Wilson et al. [5], who found that the pre-swirl flow mixed fully with a superposed radial outflow of disk-cooling air before entering the receiver holes. Dittman et al. [6] measured discharge coefficients for both the pre-swirl nozzles and the receiver holes in a direct transfer pre-swirl rig. Greater losses in total pressures are expected for direct transfer systems compared with the free-vortex flow found in cover-plate systems, due to strong mixing between the pre-swirl flow and the recirculating rotor-stator flow in the chamber. Earlier research into direct transfer systems, and rotor-stator systems in general, is described by Owen and Rogers [7].

This paper describes a combined experimental and computational study of the fluid dynamics of the idealized pre-swirl rotor-stator chamber shown schematically in Fig. 2. The results are used to describe the flow structure in the chamber and the effects of the parameters β_p and $\lambda_{T,p}$, and N, the number of pre-swirl nozzles. Discharge coefficients for the rotating receiver holes are also presented and discussed.

Designers are also interested in the total temperature of the cooling air that enters the turbine blade-cooling passages, and this will be affected by heat transfer from the turbine disk to the air. Heat transfer in the system considered here will be discussed in a future publication.

Contributed by the International Gas Turbine Institute and presented at the International Gas Turbine and Aeroengine Congress and Exhibition, Amsterdam, The Netherlands, June 3–6, 2002. Manuscript received by the IGTI November 14, 2001; revised manuscript received January 25, 2003. Paper No. 2002-GT-30415. Review Chair: E. Benvenuti.

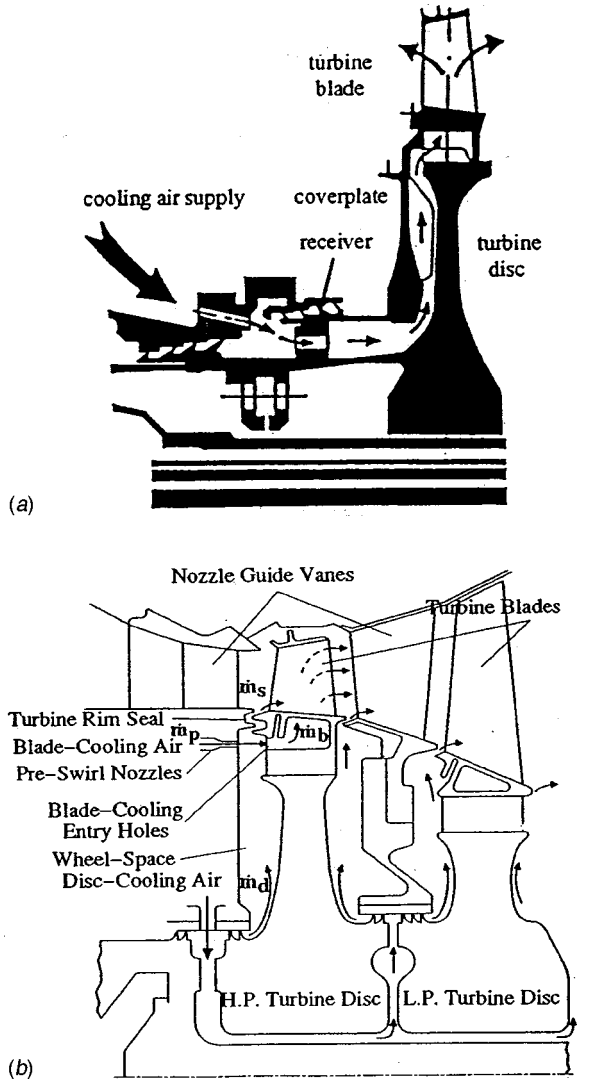

Fig. 1 (*a*) A cover-plate pre-swirl system (reproduced from [1]); (*b*) a direct-transfer pre-swirl system (reproduced from [5])

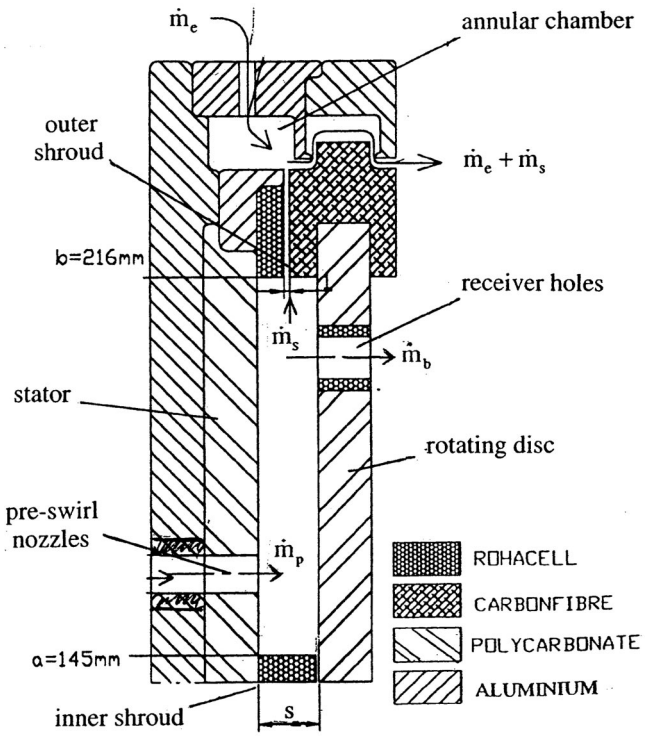

Fig. 2 Schematic diagram of the rotor-stator experimental rig (not to scale)

Experimental Apparatus

A rotor-stator rig, purpose-built for both flow and heat transfer studies, was used for the measurements. The geometry, which was based on information obtained for existing engine designs, is illustrated schematically in Fig. 2.

The disc radius was $b=216$ mm, and the principal dimensions gave the inner-to-outer radius ratio (a/b) as 0.67 and the gap ratio (s/b) as 0.051. The rotating disc was made from transparent polycarbonate, for the subsequent application of optical heat transfer measurements using liquid crystal techniques. There were 24 circular pre-swirl nozzles, angled at $\theta=20°$ to the tangential direction, in the stator, and 60 axial receiver holes in the rotor; the receiver holes were square-edged with a length-to-diameter ratio of 1.25. The radial location of the nozzles, for which $x_p=r_p/b=0.74$, was less than the centreline radius of the holes at $x_b=r_b/b=0.93$ (Fig. 2). The number of pre-swirl nozzles, N, could be reduced from $N=24$ to 12 by blocking every other nozzle, and this allowed higher inlet swirl ratios to be tested for the preswirl flow rates available. The ratio of the area of the receiver holes to that of the nozzles (A_R/A_N) was 2.9 for $N=24$ and 5.8 for $N=12$. The inlet swirl ratio, β_p, was calculated from:

$$\beta_{\mathrm{p}}=\frac{\mathrm{C}}{\mathrm{N}}\left(\frac{\mathrm{C_{W,p}}}{\mathrm{Re}_\phi}\right)=\frac{\mathrm{C}}{\mathrm{N}}\lambda_{\mathrm{T,p}}\mathrm{Re}_\phi^{-0.2} \tag{2}$$

where

$$\mathrm{C}=\frac{4b^3\cos\theta}{\pi d^2 \mathrm{r_p}} \tag{3}$$

The outer shroud was in two sections, one attached to the stator and the other to the rotor; the inner shroud was stationary. A stationary annular chamber was fitted around the periphery of the system, and this chamber could be pressurized (by an external flow rate, $\dot{m}_e$) to control the seal flow rate, $\dot{m}_s$, through the peripheral seals. The value of $\dot{m}_s$ was determined from calibration tests of the seal assembly.

The rig could be rotated at speeds giving rotational Reynolds numbers Re_ϕ (based on the disc radius) up to around 1.2×10^6. It was possible to control independently $\dot{m}_p$, m_b, and $\dot{m}_s$, the pre-swirl, blade-cooling and sealing flow rates, respectively (see Fig. 2), and the mass flow rates were measured using British Standard orifice plates. Tests were carried out for sealing flow rates $C_{w,s}$ of zero and $C_{w,s}/C_{w,b}\approx0.1$; only results for the former are included here.

A total-temperature probe and pitot-tube located in the outlet from the nozzles, together with a static-pressure tap between the nozzles, were used to measure the total and static temperature and the velocity of the inlet flow. (Equation (2), rather than the measured inlet velocity, was used to calculate β_{p}.) Static pressure taps were located at nine radial stations in the stator, and nine pitot-tubes were located at the same radii on the mid-axial plane $(z/s=0.5)$ in the wheel-space. This enabled the measurement of the radial distribution of p, the static pressure, $\mathrm{p_o}$, the total pressure, and $V_{\phi,\infty}$, the tangential velocity of the air in the core outside the boundary layers. As the blade-cooling air discharged directly into the atmosphere, it was also possible to calculate C_D, the discharge coefficient of the receiver holes.

It should be noted that the above measurements were made at only one angular location. However, the pitot-tubes in the mid-axial plane were subject to a rotating core of fluid, which would tend to average-out any circumferential variation in total pressure.

The parameter range tested in the experiments was

$$0.77\times 10^6 < \mathrm{Re}_\phi < 1.2\times 10^6$$

$$0.6\times 10^4 < C_{w,p} < 2.8\times 10^4$$

$$(\text{giving } 0.12 < \lambda_{T,p} = C_{W,p}\,\mathrm{Re}_\phi^{-0.8} < 0.4).$$

$$0.5 < \beta_p < 3.$$

Owen and Rogers [7] have shown that the flow structure depends principally on β_p and λ_T and only weakly on Re_ϕ, and this result has been confirmed by Karabay et al. [2,3] for cover-plate pre-swirl systems. Hence, although the values of Re_ϕ used here are lower than those (typically around 10^7) found in gas turbines, the flow structures are considered to be representative of those found in the cooling systems of engines.

It was not possible to vary β_p, $C_{w,p}$, Re_ϕ, and N independently (see Eq. (2)); for $\beta_p \leqslant 1$, 24 nozzles were used, while tests with $\beta_p > 1.5$ were carried out using the 12-nozzle configuration. (Tests were carried out for $\beta_p \approx 1$ for both 12 and 24 nozzles; however, in these cases there was also a factor of two difference in flow rate.)

Computational Model

Computations were carried out using a 3-D incompressible flow model, with one discrete pre-swirl nozzle on the stator and cyclic-symmetry boundary conditions applied at the tangential faces of the domain. Computations were carried out only for $N=24$ (i.e. a 15 deg segment).

The structured cylindrical-polar mesh used is illustrated in Fig. 3. To permit steady-state computations, an annular outlet was used on the rotor that matched the centreline radius, r_b, and total flow area of the receiver holes. The Reynolds-averaged Navier-Stokes equations were solved in primitive-variable form using the finite-volume method, hybrid differencing and the SIMPLEC pressure-correction scheme. The low-Reynolds-number Launder-Sharma [8] k-ε turbulence model was used; this model has been used successfully in previous pre-swirl research where both flow and heat transfer is to be considered (see, for example, Pilbrow et al. [9]). Grid distribution tests showed that a $140\times211\times40$ (axial $\times$radial$\times$tangential) grid was required. Near wall grid points satisfied the condition $y+<1$, and a convergence condition that total absolute residuals be less than 10^{-4} when normalized by inlet mass flux and tangential velocity values was used.

Boundary conditions for the axial and tangential velocity components were prescribed for the angled flow at the inlet (which was square but having the same area as the circular nozzles in the rig), using the flow rates recorded in the experiments. The radial velocity component at inlet was zero. The angular velocity of the disc was also set to match the measured disc speed. At the annular outlet boundary on the rotating disc, a uniform normal velocity component based on measured flow rates was imposed to ensure continuity, and tangential velocities were computed from a zero normal derivative condition. (At the seal clearances, see Fig. 2, a linear variation in angular velocity between rotating and stationary components was used for the zero sealing flow cases.)

Results

Computed Flow Structure. Figures 4(*a*) and 4(*b*) show computed vector velocity fields, for $\mathrm{Re}_\phi = 0.78\times 10^6$, $\lambda_{T,p}=0.236$, and $\beta_p = 0.96$, for the flow in two planes: one through the middle of the pre-swirl inlet nozzle (Fig. 4(*a*)), and the other midway between nozzles (Fig. 4(*b*)). Figure 4(*a*) shows that the axial flow of pre-swirl air impinges on the rotor and flows outward over the rotating disk; the disk boundary layer supplies the blade-cooling flow leaving the system at the annular outlet at $x=0.93$. Figure 4(*b*) shows very similar characteristics except at low radius in the region of the axial pre-swirl flow; in this plane, midway between the inlet nozzles, the flow close to the stator at around $x=0.74$ (the nozzle radius) is affected by entrainment into the pre-swirl flow. There is mixing between the pre-swirl flow, the recirculating flow inward of the nozzles and the radially inward flow on the stator; this reduces the effective pre-swirl ratio. For $z/s > 0.5$ approx., the velocity fields in the two planes are very similar, indicating that the discrete-inlet flows have merged. Under the influence of the rotating disk, the flow becomes very nearly axisymmetric prior to turning radially to form the disk boundary layer.

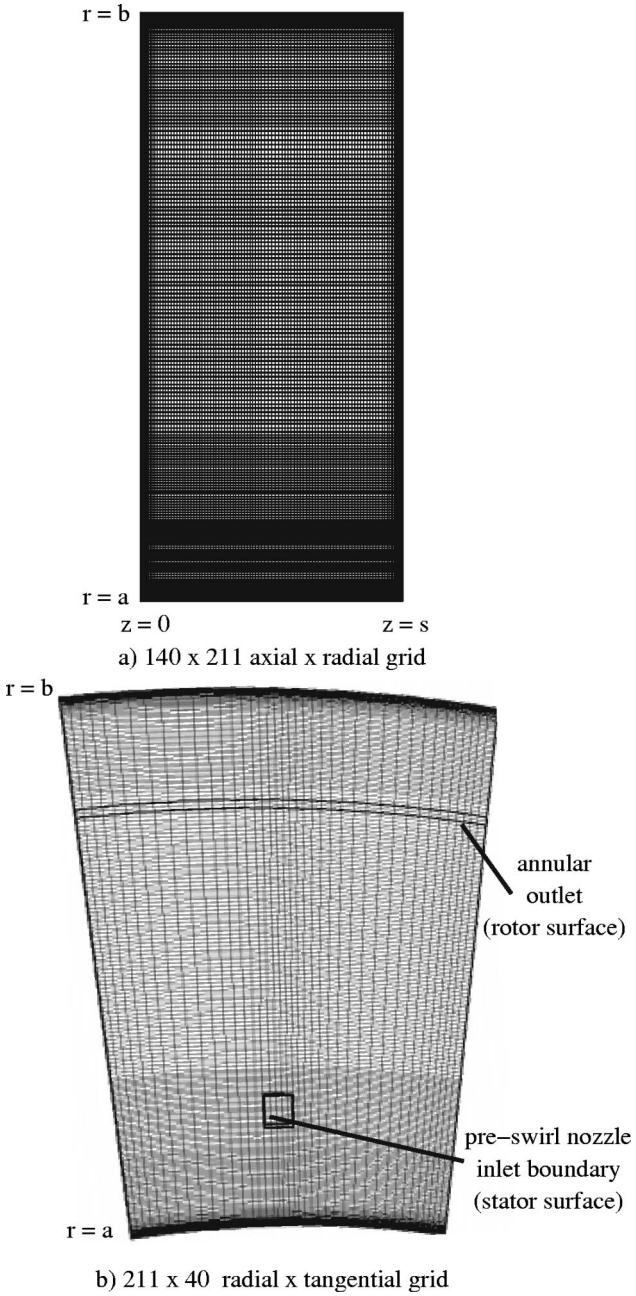

Fig. 3 140×211×40 computational grid—(*a*) 140×211 axial ×radial grid (*b*) 211×40 radial×tangential grid

Comparison Between Computations and Measurements. Figure 5(*a*) shows measured and computed stator-surface ($z/s=0$) static pressures for three cases at $\mathrm{Re}_\phi \approx 0.8\times 10^6$, with $\beta_p = 0.52$ (for which $\lambda_{T,p}=0.127$) and $\beta_p = 0.96$ ($\lambda_{T,p}=0.236$), both for $N=24$, and $\beta_p = 1.86$ ($\lambda_{T,p}=0.229$) for $N=12$. (The computations shown for the latter case are for $N=24$ at the same flow conditions; reliable solutions for $N=12$ were not obtained

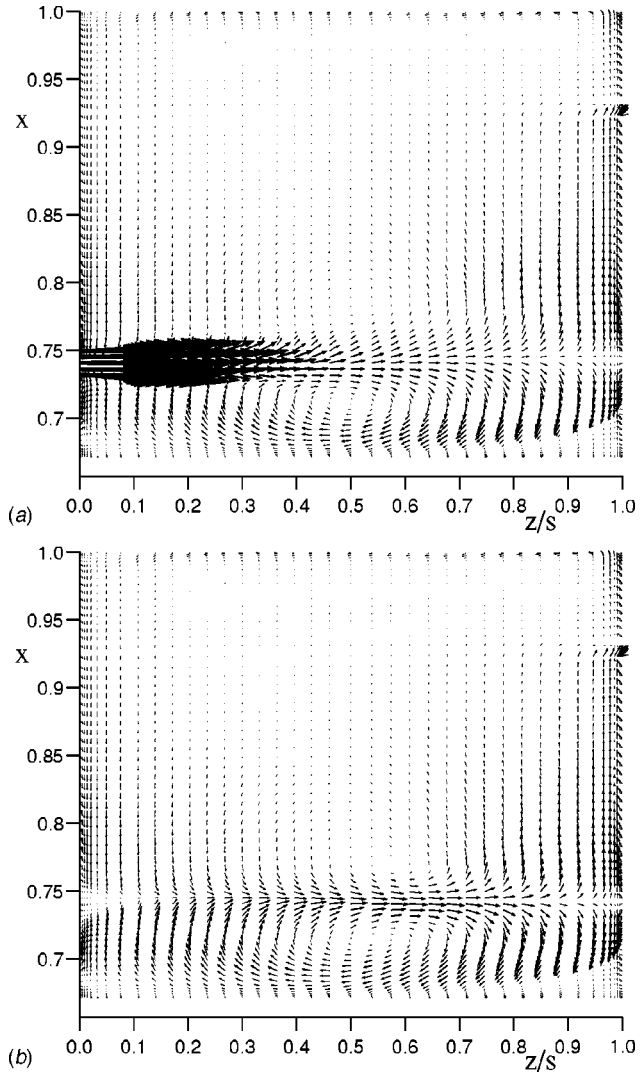

Fig. 4 Computed velocity vectors in two tangential planes for $Re_\phi = 0.78\times10^6$, $\lambda_{T,p} = 0.236$ and $\beta_p = 0.96$—(*a*) inlet nozzle midplane, (*b*) midway between nozzles

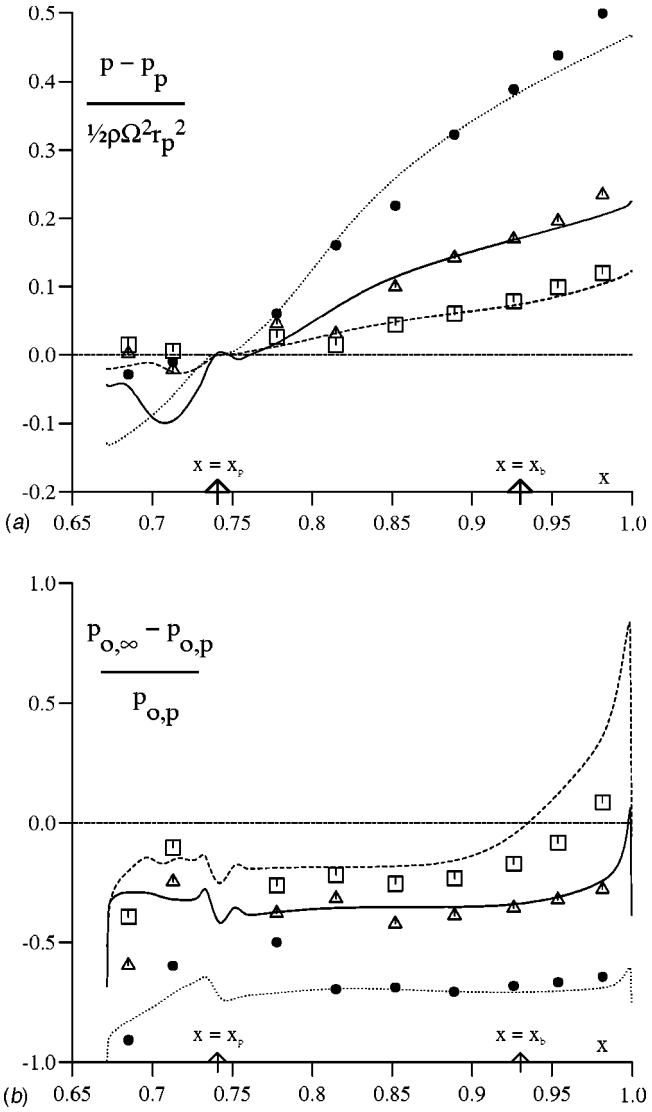

Fig. 5 Measured and computed radial variation of pressure, $Re_\phi = 0.78\times10^6$—(*a*) static pressure at stator surface, (*b*) total pressure at axial midplane ($z/s = 0.5$) measured computed ($N = 24$) □ $\lambda_{T,p} = 0.127$, $\beta_p \approx 0.52$, N=24 — — —△ $\lambda_{T,p} = 0.236$, $\beta_p \approx 0.96$, N=24 —— ● $\lambda_{T,p} = 0.229$, $\beta_p \approx 1.86$, N=12 · · · ·

due to increased gridding requirements.) Corresponding total pressures at the axial midplane ($z/s = 0.5$) are shown in Fig. 5(*b*). The computed static pressures are the values obtained midway between inlet nozzles; the reference pressure for these incompressible flow results was chosen arbitrarily as the measured static pressure at $x = 0.9$. There is reasonably good agreement between computed and measured values radially outward of the pre-swirl nozzles; inward of this location, the static pressure field is affected by the three-dimensional flow around the discrete nozzles. (Measurements were made on a radial line through the nozzle midplane.)

The midplane total pressure results, shown in Fig. 5(*b*), are relative to the total pressure measured at the pre-swirl nozzle outlet. There are three noteworthy points: (i) owing to mixing losses, there is a significant drop in total pressure near the inlet (where $p_{0,\infty} < p_{0,p}$); (ii) except at the smaller or larger radii, $p_{0,\infty}$ is approximately constant, which is consistent with free-vortex flow; (iii) at the larger radii, the increase in $p_{0,\infty}$ is associated with work done on the air by the rotating disk and shroud. The tangentially averaged computations generally show less variation with x than the data.

Figure 6 shows measured distributions of $\beta_\infty (= V_{\phi,\infty}/\Omega r)$ at z/s=0.5, obtained from the total and static pressure measurements, and computational results for the three inlet pre-swirl ratio cases discussed in the foregoing (the values of β_p are indicated on the figure) at $Re_\phi \approx 0.8\times10^6$. Figure 6 also shows measured results for similar values of β_p obtained at a higher rotational Reynolds number, $Re_\phi \approx 1.18\times10^6$, with the flow rate C_w adjusted so that $\lambda_{T,p}$ remained approximately constant for similar values of β_p. The measured results show that, as expected, there is no significant effect of Re_ϕ on the radial distribution of β_∞ for the lower values of β_p, and only a small effect on the magnitude of β_∞.

Not surprisingly, the results for β_∞ in Fig. 6 are consistent with those for $p_{0,\infty}$ in Fig. 5(*b*). (i) The mixing losses near the inlet mean that $\beta_\infty < \beta_p$ at $x = x_p$ such that $\beta_{p,\text{eff}} < \beta_p$; (ii) except at the smaller or larger radii, β_∞ decreases as x increases: this is consistent with free-vortex flow in which $p_{0,\infty}$ is constant; (iii) at the larger radii, β_∞ increases as x increases as a consequence of work input from the rotating disk and shroud. (The tangential velocity at the boundary at $z/s = 0.5$, $x = 1$, in the computed results is less than that of the disc, as this point lies within the small clearance between the rotating and stationary sections of the shroud.)

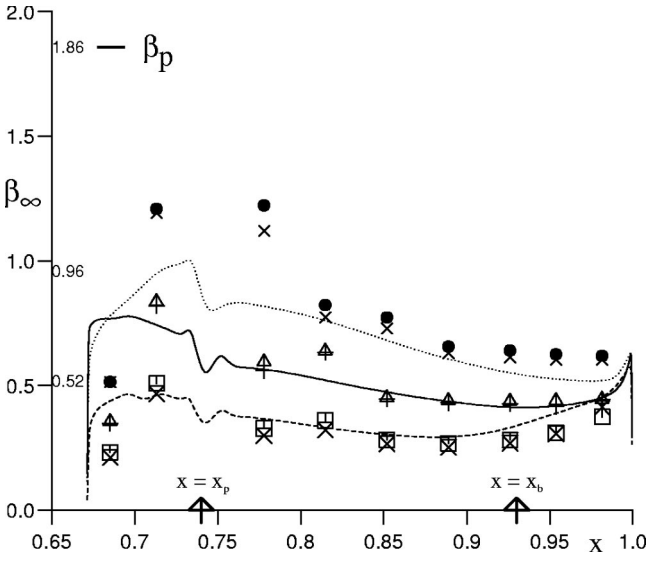

Fig. 6 Effect of β_p and $\lambda_{T,p}$ on measured and computed variation of β_∞ ($z/s=0.5$) measured computed ($N=24$) ($Re_\phi \approx 0.78\times10^6$, 1.2×10^6) □, ⧖ $\lambda_{T,p}\approx0.127$, $\beta_p\approx0.52$, N=24 — — — △, + $\lambda_{T,p}\approx0.236$, $\beta_p\approx0.96$, N=24 —— ●, × $\lambda_{T,p}\approx0.229$, $\beta_p\approx1.86$, N=12 · · · ·

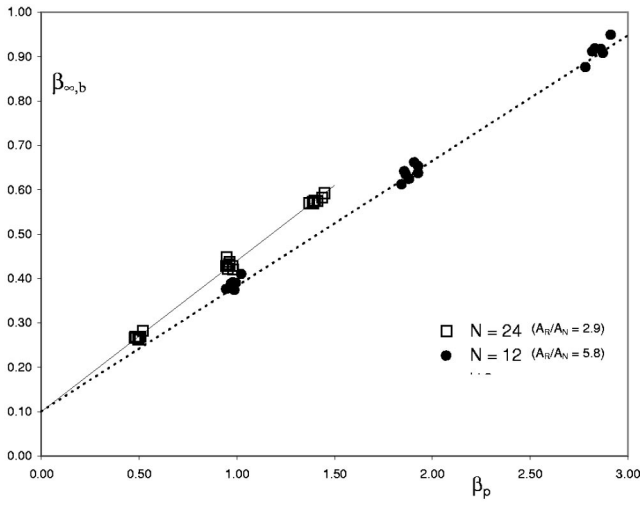

Fig. 7 Measured variation of $\beta_{\infty,b}$ with β_p (— — — Eq. (4*a*), —— Eq. (4*b*))

The tangentially averaged computed values of β_∞ for $\beta_p=0.52$ in Fig. 6 show similar behavior to the measurements. The computed level of β_∞ is in reasonable agreement with the data for $x<0.9$, however the increase in β_∞ in the outer part of the system is overpredicted. The computational results are in good agreement with the data for $\beta_p=0.96$ outward of the nozzle radius, $x_p=0.74$. For $\beta_p=1.86$, the computed distribution is qualitatively correct but the level of β_∞ is underpredicted. (As described in the foregoing, this computation was carried out for N=24, while the measurements correspond to $N=12$.) The local minimum in β_∞ seen in the computed results at x≈0.74 occurs in the region just outward of the pre-swirl flow, where there is strong shear and entrainment into the jet flow (as illustrated in Fig. 4). For all the computed results, circumferential variations from the tangentially averaged behavior shown in Fig. 6 were very small except around the nozzle radius $x_p=0.74$, where peak values of β_∞ for $\beta_p=1.86$ were up to around 50% higher than the average values. No measurements were made of β_∞ at $z/s=0.5$ at $x=x_p$.

The discharge coefficients for the receiver holes are expected to be affected by conditions near $x=x_b$ ($x_b=0.93$), and Fig. 7 shows the measured variation of $\beta_{\infty,b}$ (i.e. at β_∞ at $x=x_b$), with β_p for $N=12$ and $N=24$; the measurements were made over a range of values of Re_ϕ and $\lambda_{T,p}$. The distributions are approximately linear:

$$N=12(0.9<\beta_p<2.9): \quad \beta_{\infty,b}\approx0.1+0.28\beta_p \tag{4a}$$

$$N=24(0.5<\beta_p<1.5): \quad \beta_{\infty,b}\approx0.1+0.34\beta_p \tag{4b}$$

Referring to Eq. (2), it should be remembered that β_p depends strongly on $\lambda_{T,p}$ and N and only weakly on Re_ϕ. For a given value of β_p, $\lambda_{T,p}$ doubles when N is increased from 12 to 24. Figure 7 shows that, for a given value of β_p, $\beta_{\infty,b}$ decreases as N decreases. Larger numbers of nozzles and larger values of flow rate are expected to reduce the mixing losses, but it is not possible here to differentiate between the effects of N and $\lambda_{T,p}$.

Measured Discharge Coefficients

Definition of CD for Receiver Holes. C_D is defined here as

$$C_D=\frac{\dot{m}_b}{\dot{m}_i} \tag{5}$$

where $\dot{m}_b$ is the measured mass flow rate through the receiver holes and $\dot{m}_i$ is the isentropic value.

Consider the isentropic flow in a stream tube from station 1 to station 2 in a rotating fluid. The work done *by* the air, $\dot{W}_{12}$, is given by

$$-\frac{\dot{W}_{12}}{\dot{m}_i}=\Omega(r_2V_{\phi,2}-r_1V_{\phi,1})=c_p(T_{0,2}-T_{0,1}) \tag{6}$$

where T_0, the total temperature in a *stationary* frame of reference, is

$$c_pT_0=c_pT+\frac{1}{2}U^2 \tag{7}$$

T being the static temperature and U the magnitude of the velocity in a stationary frame.

It is convenient to locate station 1 in the rotating core of fluid and station 2 at the outlet of the receiver holes, such that $r_2=r_b$. It can be shown from Eq. (6) that, for isentropic flow of a perfect gas,

$$\frac{\dot{m}_i}{A_2}=\rho_{0,1}\left(\frac{p_2}{p_{0,1}}\right)^{1/\gamma}\left\{\left(\frac{2\gamma}{\gamma-1}\right)\frac{p_{0,1}}{\rho_{0,1}}\left[1-\left(\frac{p_2}{p_{0,1}}\right)^{\gamma-1/\gamma}\right]+2\Omega(r_2V_{\phi,2}-r_1V_{\phi,1})-V_{\phi,2}^2\right\}^{1/2} \tag{8}$$

For the case where $V_{\phi,1}=V_{\phi,2}=0$, Eq. (8) reduces to the standard result for flow through a stationary nozzle. When $r_1=r_2$, Eq. (8) is equivalent to the result used by those authors (see, for example Dittmann et al. [6]) who base C_D on *relative* total pressure rather than the *absolute* value used here. It should be emphasised that the use of relative pressures is *only* valid if $r_1=r_2$, which may not be true in all cases. It can also be shown that, for any value of $V_{\phi,1}$, $\dot{m}_i$ will have a maximum value when $V_{\phi,2}=\Omega r_2$.

Measurement of CD. It should be noted that, owing to an error in processing the experimental data, the versions of Figs. 8(*a*) and 8(*b*) presented in the conference paper GT-2002-30415 are incorrect. The corrected versions of these figures are presented here, and the following text has been modified accordingly.

In the results discussed here, $p_{0,1}$ and $V_{\phi,1}$ were respectively taken as the total pressure and tangential component of velocity

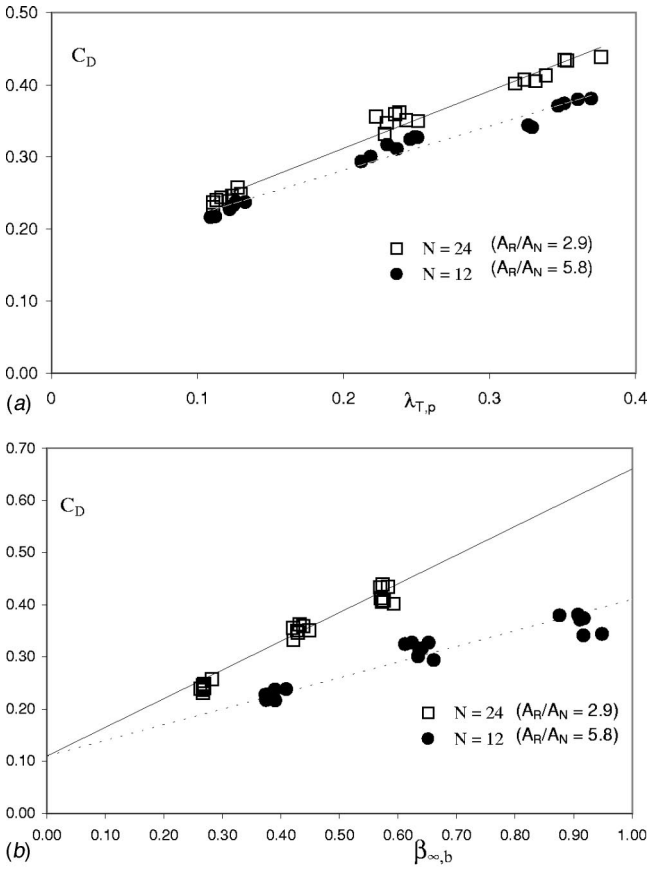

Fig. 8 Measured variation of C_D with (*a*) $\lambda_{T,p}$, (*b*) $\beta_{\infty,b}$

measured by the pitot tube at $r=r_b$. Also, $V_{\phi,2}$ was assumed to be equal to Ωr_b (the rotational speed of the receiver holes), and p_2 was taken as the atmospheric pressure.

In measurements of C_D in rotating disks, experimenters usually assume, explicitly or implicitly, that the swirling air achieves solid-body rotation at exit from the receiver holes, as is assumed here. If the length-to-diameter ratio of the receiver holes is sufficiently large then this assumption will be valid; in the rig used here, the length-to-diameter ratio is 1.25 and so the assumption is questionable. As noted in the foregoing, $\dot{m}_i$ calculated from Eq. (8) will be a maximum when $V_{\phi,2}=\Omega r_2$. That is, the assumption that $V_{\phi,2}=\Omega r_2$ will produce a lower bound for the true value of C_D; an upper bound could be found by setting $V_{\phi,2}=V_{\phi,1}$ in Eq. (8).

It is expected that C_D will be a maximum when the air near the receiver holes is in synchronous rotation with the disk, i.e., when $\beta_{\infty,b}=1$; the air will then enter the holes with minimum shear. It is also expected that higher values of C_D will occur the more uniform is the distribution of flow between the receiver holes. As the number N of inlet pre-swirl nozzles is reduced (hence as the ratio A_R/A_N increases), the distribution of the discrete inlet flows to the receiver holes is likely to become less uniform, and values of C_D would be expected to decrease.

Figures 8(*a*) and (*b*) respectively, show the variation of C_D with $\lambda_{T,p}$ and with $\beta_{\infty,b}$. Figure 8(*a*) shows that C_D increases as $\lambda_{T,p}$ increases and, for any value of $\lambda_{T,p}$, C_D is larger for $N=12$ than for $N=24$. It should be remembered that, for a given value of $\lambda_{T,p}$, β_p increases as N decreases: the effects of N and β_p are therefore coupled in the experiments.

Figure 8(*b*) shows that, as expected, C_D increases as $\beta_{\infty,b}$ increases; also, for a given value of $\beta_{\infty,b}$, C_D decreases as N decreases. Linear extrapolation (which may not be appropriate) to $\beta_{\infty,b}=1$ suggests that $C_D\approx 0.7$ for $N=12\,(A_R/A_N=5.8)$, and $C_D\approx 0.9$ for $N=24\,(A_R/A_N=2.9)$. These values are consistent with the results of Popp et al. [1], who also found that C_D decreases as A_R/A_N increases. Their maximum values of C_D, at $\beta_{\infty,b}=1$, were 0.53 and 0.8 for $A_R/A_N=7$ and 2, respectively.

Dittman et al. [6] found that, for a given number of nozzles ($N=11$ or 12), C_D increased as the number of receiver holes increased (from 4 to 24), which is consistent with the ''uniformity'' argument. They also showed that, as expected, radiusing the inlet of the receiver holes increased C_D. It is difficult to make quantitative comparisons with their measurements, as they based their values of C_D on predicted rather than measured values of pressure in the core.

Conclusions

Measurements and three-dimensional steady computations have been carried out for the fluid dynamics of a compact pre-swirl rotor-stator chamber, simulating part of the blade-cooling air supply system used in some gas-turbine engines. The effects of rotational speed, flow rate, pre-swirl ratio and number of pre-swirl nozzles on the flow field and on the total pressure losses in the system were investigated.

Turbulent flow computations, carried out using a simplified 3-D steady model of the system, gave results for total pressure and tangential velocity which were in mostly good agreement with measurements in the outer part of the system (including the radial location of the receiver holes). It was shown that, owing to mixing losses, there is a significant drop in total pressure between the pre-swirl nozzles and the core of rotating fluid. Consequently, the measured and computed values of swirl ratio, β_∞ (outside the boundary layers on the disc surfaces), were significantly lower than the inlet pre-swirl ratio, β_p. Measurements showed that, at the radius r_b of the receiver holes in the rotating disk, $\beta_{\infty,b}$ increased linearly with increasing β_p, and the ratio was higher for $N=24$ pre-swirl nozzles than for $N=12$; it should be noted that, for the same value of β_p, the flow rate for $N=24$ is double that for $N=12$. Discharge-coefficients, C_D, were measured assuming solid-body rotation for the flow inside the receiver holes. As expected, C_D increased as $\beta_{\infty,b}$ increased. For a given value of $\beta_{\infty,b}$, C_D decreased as N decreased.

Acknowledgments

The experimental work described here was funded by Alstom Power Ltd and the UK Engineering and Physical Sciences Research Council (EPSRC). Mr Farzaneh-Gord is a PhD student funded by the Iranian Government.

Nomenclature

A = area
a = inner radius of cavity
b = outer radius of cavity
c = constant for calculation of β_p
C = constant (in Eq. (3))
C_D = discharge coefficient of receiver holes
c_p, c_v = specific heat at constant pressure and constant volume, respectively
C_w = nondimensional mass flow rate ($=\dot{m}\mu b$)
d = pre-swirl nozzle diameter
G = gap ratio ($=s/b$)
k = turbulence kinetic energy
$\dot{m}$ = mass flow rate
N = no. of pre-swirl nozzles
p = static pressure
p_0 = total pressure in stationary frame
r, ϕ, z = radial, tangential, and axial coordinates
Re_ϕ = rotational Reynolds no. ($=\rho\Omega b^2/\mu$)

s = axial spacing between rotor and stator
T = temperature
U = total velocity in stationary frame
U_τ = friction velocity ($=\sqrt{\tau_w/\rho}$)
V_r, V_ϕ, V_z = time-averaged radial, circumferential, axial components of velocity in stationary frame
$\dot{W}$ = work done by fluid
x = nondimensional radius ($=r/b$)
y, y^+ = distance normal to wall, nondimensional distance ($=\rho y U_\tau/\mu$)
β = swirl ratio ($=V_\phi/\Omega r$)
β_p = pre-swirl ratio ($=V_{\phi,p}/\Omega r_p$)
ε = turbulent energy dissipation rate
γ = ratio of specific heats ($=c_p/c_v$)
λ_T = turbulent flow parameter ($=C_w/\mathrm{Re}_\phi^{0.8}$)
θ = angle of pre-swirl nozzle to tangential direction
μ = dynamic viscosity
ρ = density
τ = shear stress
Ω = angular speed of disk

Subscripts

b = blade-cooling air, receiver hole radius
e = external air
eff = effective value
i = isentropic value
N = nozzles
o = total value in stationary frame of reference
p = pre-swirl air
R = receiver holes
s = sealing air
t = total value in rotating frame of reference
∞ = value in core outside boundary layers
1, 2 = upstream, downstream stations in stream tube

References

[1] Popp, O., Zimmerman, H., and Kutz, J., 1998, "CFD Analysis of Cover-Plate Receiver Flow," ASME J. Turbomach., **120**, pp. 43–49.
[2] Karabay, H., Chen, J. X., Pilbrow, R., Wilson, M., and Owen, J. M., 1999, "Flow in a "Cover-Plate" Pre-Swirl Rotor-Stator System," ASME J. Turbomach., **121**, pp. 160–166.
[3] Karabay, H., Wilson, M., and Owen, J. M., 2001, "Predictions of Effect of Swirl on Flow and Heat Transfer in a Rotating Cavity," Int. J. Heat Fluid Flow, **22**(2), pp. 143–155.
[4] Meierhofer, B., and Franklin, C. J., 1981, "An Investigation of a Pre-swirled Cooling Airflow to a Gas Turbine Disk by Measuring the Air Temperature in the Rotating Channels," ASME Paper 81-GT-132.
[5] Wilson, M., Pilbrow, R., and Owen, J. M., 1997, "Flow and Heat Transfer in a Pre-Swirl Rotor-Stator System," ASME J. Turbomach., **119**, pp. 364–373.
[6] Dittmann, M., Geis, T., Schramm, V., Kim, S., and Wittig S., 2001, "Discharge Coefficients of a Pre-Swirl System in Secondary Air Systems," ASME Paper 2001-GT-122.
[7] Owen, J. M., and Rogers, R. H., 1989, *Flow and Heat Transfer in Rotating Disc Systems: Vol. 1, Rotor-Stator Systems*, Research Studies Press, Taunton, UK and John Wiley, NY.
[8] Launder, B. E., and Sharma, B. I., 1974, "Application of the Energy-Dissipation Model of Turbulence to Flow Near a Spinning Disc," Lett. Heat Mass Transfer, **1**, pp. 131–138.
[9] Pilbrow, R., Karabay, H., Wilson, M., and Owen, J. M., 1999, "Heat Transfer in a "Cover-Plate" Pre-Swirl Rotating-Disc System," ASME J. Turbomach., **121**, pp. 249–256.

Heat Transfer Coefficients and Film Cooling Effectiveness on the Squealer Tip of a Gas Turbine Blade

Jae Su Kwak[1]

Je-Chin Han
e-mail: jchan@mengr.tamu.edu

Turbine Heat Transfer Laboratory,
Department of Mechanical Engineering,
Texas A&M University,
College Station, TX 77843-3123

Experimental investigations were performed to measure the detailed heat transfer coefficients and film cooling effectiveness on the squealer tip of a gas turbine blade in a five-bladed linear cascade. The blade was a two-dimensional model of a first stage gas turbine rotor blade with a profile of the GE-E^3 aircraft gas turbine engine rotor blade. The test blade had a squealer (recessed) tip with a 4.22% recess. The blade model was equipped with a single row of film cooling holes on the pressure side near the tip region and the tip surface along the camber line. Hue detection based transient liquid crystals technique was used to measure heat transfer coefficients and film cooling effectiveness. All measurements were done for the three tip gap clearances of 1.0%, 1.5%, and 2.5% of blade span at the two blowing ratios of 1.0 and 2.0. The Reynolds number based on cascade exit velocity and axial chord length was 1.1×10^6 and the total turning angle of the blade was 97.9 deg. The overall pressure ratio was 1.2 and the inlet and exit Mach numbers were 0.25 and 0.59, respectively. The turbulence intensity level at the cascade inlet was 9.7%. Results showed that the overall heat transfer coefficients increased with increasing tip gap clearance, but decreased with increasing blowing ratio. However, the overall film cooling effectiveness increased with increasing blowing ratio. Results also showed that the overall film cooling effectiveness increased but heat transfer coefficients decreased for the squealer tip when compared to the plane tip at the same tip gap clearance and blowing ratio conditions. [DOI: 10.1115/1.1622712]

Introduction

In modern gas turbine engines, inlet temperatures have begun to exceed the allowable temperature of turbine component materials, thus creating a need for turbine components to be cooled properly in order to maintain the desired performance. Among the turbine components, the blade tip is one of the most critical regions because of the high heat load caused by hot leakage flow through the tip gap. For the unshrouded blade, there is a gap between the blade tip and shroud, and flow leaks through the gap due to the pressure difference between the blade's pressure side and suction side. This hot leakage flow is the major cause of blade tip failures. Because of the complex flow field and heat transfer distribution, sophisticated cooling technology must be applied to cool the blade tip.

Figure 1 shows typical cooling methods for the modern gas turbine blade. Inside the blade, impingement cooling, pin-fin cooling, and rib turbulated cooling are employed to remove heat from blade's interior. Outside the blade, film cooling, which is a common method for cooling the external surface of blades, is applied by ejecting cooler air from the internal cooling passage through discrete holes. The cooler air provides a protective film on the surface and prevents the blade surface from being exposed to the hot gas. Due to the decreased film-to-wall temperature difference, heat transfer rates can be reduced substantially. Detailed turbine cooling methods are described by Han et al. [1].

To reduce the leakage flow and heat transfer coefficient on the tip, the blades of modern gas turbines are typically grooved chordwise. The groove acts as a labyrinth seal to increase flow resistance and thus reduces leakage flow and heat transfer coefficient on the tip. It is therefore very important to know the distribution of the heat transfer coefficient and film cooling effectiveness on the squealer tip of film cooled blade.

In the open literature, there is limited information on the flow field and heat transfer of a grooved blade tip. Metzger et al. [2] and Chyu et al. [3] investigated heat transfer in a rectangular grooved tip model. Their work included the effect of the depth-to-width ratio and the tip gap to width ratio of a cavity with both moving and standing shrouds over the stationary grooved tip model. The result showed that the local heat transfer coefficient upstream of the grooved cavity was greatly reduced compared to a rectangular plane tip model, while the coefficient downstream of the grooved cavity was enhanced because of the flow reattachment at that region. They concluded that there was an optimum value of depth-to-width ratio for a given pressure difference across the gap. Heyes et al. [4] studied tip leakage flow on plane and squealer tips in a linear cascade and concluded that the use of a squealer tip, especially a suction side squealer tip, was more beneficial than a flat tip. Yang and Diller [5] studied local heat coefficients on a turbine blade tip model with a recessed cavity (squealer tip) in a stationary linear cascade. Based on the measurement at a single point on the cavity floor, they reported that the convection coefficients were insensitive to the tip gap height. Ameri et al. [6] computed the flow and heat transfer on the squealer tip of a GE-E^3 first stage gas turbine blade. They observed higher heat transfer in the bottom of the cavity compared to the plane tip. The heat transfer on the pressure side rim was comparable to the plane tip case but was higher on the suction side rim. They concluded that the large heat transfer in the bottom of the cavity was due to flow impingement containing hot gas. Dunn and Haldeman [7] measured time averaged heat flux at a

[1]Currently Senior Researcher, Aeropropulsion Department, Korea Aerospace Research Institute, Daejeon, Korea.

Contributed by the International Gas Turbine Institute (IGTI) of THE AMERICAN SOCIETY OF MECHANICAL ENGINEERS for publication in the ASME JOURNAL OF TURBOMACHINERY. Paper presented at the International Gas Turbine and Aeroengine Congress and Exhibition, Amsterdam, The Netherlands, June 3–6, 2002; Paper No. 2002-GT-30555. Manuscript received by IGTI, Dec. 2001, final revision, Mar. 2002. Associate Editor: E. Benvenuti.

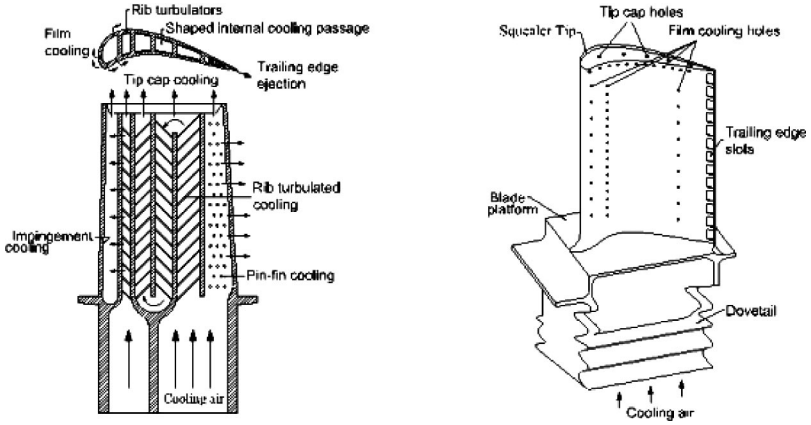

Fig. 1 Schematic of a modern gas turbine blade with common cooling techniques

recessed blade tip for a full-scale rotating turbine stage at transonic vane exit conditions. They found that the Nusselt number on the suction side lip and on the floor of the recess near the leading edge of the blade was higher than that of the blade stagnation value. Azad et al. [8,9] studied the flow and heat transfer on the first stage blade tip gap of an aircraft engine turbine (GE-E^3). They presented the effects of tip gap clearance and free-stream turbulence intensity level on the detailed heat transfer coefficient distributions for both plane and squealer tips under engine representative flow conditions. They used transient liquid crystals technique and found that the overall heat transfer coefficients on the squealer tip were lower than those on the plane tip. Azad et al. [10] also studied the effect of squealer geometry arrangement on gas turbine blade tip heat transfer. They found that a blade tip with the suction side squealer was more effective to reduce heat transfer than that with pressure side squealer.

Some literature for the plane tip case is also available in the open domain. Mayle and Metzger [11] used a two-dimensional (2D) rectangular tip model with and without rotating shroud to find the rotating effect on blade tip heat transfer. They noted that the rotating effect could be neglected in order to access the blade tip heat transfer over the entire range of parameters considered in the study. Metzger et al. [12] measured local heat flux using heat flux sensors in a rotating turbine rig with two different tip gaps. Bunker et al. [13] used a hue detection based liquid crystals technique to investigate the detailed heat transfer coefficient distribution on the blade tip surface. Their result was obtained at three different tip gap sizes and two free-stream turbulence levels with sharp or rounded edges. Bunker and Bailey [14] studied the effect of squealer cavity depth and oxidation on turbine blade tip heat transfer. Teng et al. [15] measured the heat transfer coefficients and static pressure distributions of a turbine blade tip region in a large-scale low-speed wind tunnel facility using a transient liquid crystals technique. They concluded that a major leakage flow existed in the mid-chord region, and the unsteady wake augmented the Nusselt number at a large tip gap (3%), while the effect of the unsteady wake disappeared with decreasing tip gap clearance.

Some researchers conducted numerical approaches to investigate blade tip heat transfer. Ameri and Steinthorsson [16,17] predicted heat transfer on the tip of the SSME (Space Shuttle Main Engine) rotor blade. Ameri et al. [18] also predicted the effects of tip gap clearance and casing recess on heat transfer and stage efficiency for several squealer blade tip geometries. Ameri and Bunker [19] performed a computational study to investigate the detailed heat transfer distributions on blade tip surfaces for a large power generation turbine and compared the result with the experimental data of Bunker et al. [13]. Ameri and Rigby [20] also calculated heat transfer and film cooling effectiveness on film cooled turbine blade models. Ameri [21] predicted heat transfer and flow on the blade tip of a gas turbine equipped with a mean-camber line strip.

There are limited experimental data on the blade tip film cooling. Kim et al. [22] and Kim and Metzger [23] used a 2D rectangular tip model to simulate leakage flow. A transient liquid crystals technique was used to investigate heat transfer coefficients and film cooling effectiveness with various film cooling configurations. In the authors' knowledge, however, there is no literature for a squealer tip film cooling test available, and this study might be the first experimental data for the squealer tip film cooling test.

The present study applied a hue detection based transient liquid crystals technique to obtain the heat-transfer coefficient and film cooling effectiveness distributions on the squealer tip, and the results were compared with the plane tip case (Kwak and Han [24]). A five-bladed linear cascade was used as a test section and the blade profile was that of the first stage rotor blade of a modern aircraft gas turbine engine (GE-E^3). The experiments were performed for the tip clearances of 1.0%, 1.5%, and 2.5% of blade span with the averaged blowing ratios of 1.0 and 2.0.

Experimental Setup

Figure 2 shows the schematic of the test facility. The test section consisted of a stationary blow-down facility with a five-bladed linear cascade. The definition of blade tip and shroud are also shown in the upper side of Fig. 3. Compressed air stored in the tanks entered a high flow pneumatic control valve that was designed to receive feedback from the downstream pressure to

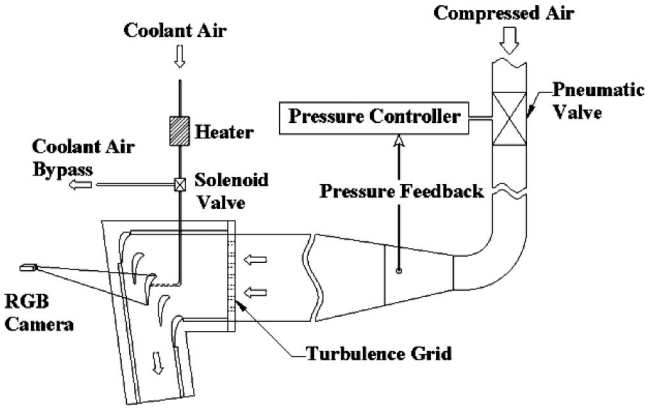

Fig. 2 Schematic of blow down facility

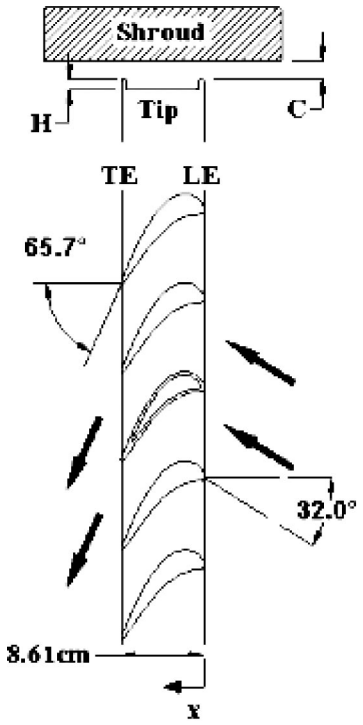

Fig. 3 Definition of blade tip and shroud

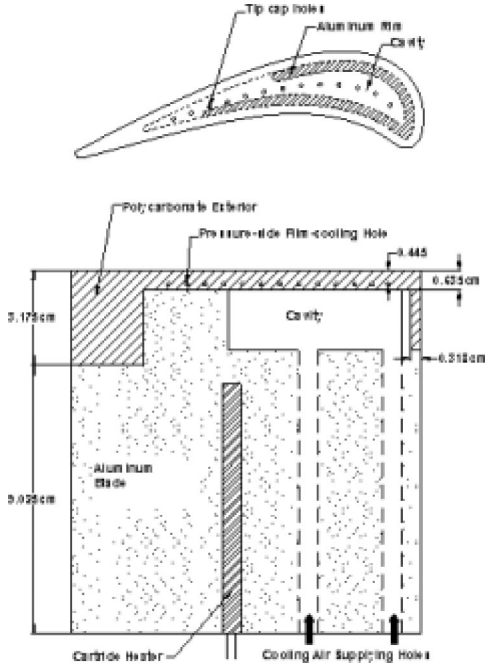

Fig. 4 Film-cooling measurement blade

maintain a velocity within ±3% of the desired value. The inlet of the test section was 31.1 cm wide and 12.2 cm high, and its top, bottom, and sides were made of 1.27-cm-thick polycarbonate plates for the pressure measurement test. In the heat transfer test, however, the top plate was replaced with a 1.27-cm-thick clear acrylic plate for better optical access to the blade tip. Two adjustable trailing edge tailboards were used to provide identical flow conditions through the two passages adjacent to the center blade. For the heated coolant air case, the coolant air was bypassed until the desired temperature was achieved. Once the temperature reached the desired value, the heated coolant air was diverted to the test blade by a three-way solenoid valve. A turbulence-generating grid of 57% porosity was placed 26.7 cm upstream of the center blade. The turbulence intensity was measured 6 cm upstream of the center blade with a TSI IFA-100 unit. In this test, the turbulence intensity at that location was 9.7%. The turbulence length scale was estimated to be 1.5 cm, which is slightly larger than the grid size. The tip gaps used for this study were 1.31, 1.97, and 3.29 mm, which correspond to about 1.0%, 1.5%, and 2.5% of the blade span (12.2 cm). Hard gaskets of desired thickness were placed on top of the side walls, the trailing edge tailboard, and two outer guide blades to create tip gaps of desired height.

During the blow-down test, the cascade inlet air velocity and exit velocity were 85 and 199 m/s, respectively. The Reynolds number based on axial chord length and exit velocity was 1.1×10^6. Azad et al. [8,9] described the detailed flow conditions, including the flow periodicity in cascade and the pressure distribution along the blade.

The blades were made of aluminum and finished with electrical discharge machining (EDM) machine. The blade had a 12.2-cm span and an 8.61-cm axial chord length, which are three times the dimensions of a GE-E^3 blade tip profile. Each blade had a constant cross section for the entire span as shown in the lower side of Fig. 3. Figure 4 shows the film cooling measurement blade. The lower portion of the blade was made of aluminum with two holes for supplying coolant air and one hole for a cartridge heater. The upper portion consisted of an inner aluminum rim with a cavity and an outer shell made of a polycarbonate with low thermal conductivity. A cartridge heater was inserted into the blade to heat the aluminum core and, consequently, to heat the outer polycarbonate shell. Thirteen film cooling holes were instrumented on both the blade tip and the pressure side, respectively. Tip holes were located along the camber line while the pressure side holes were located 0.444 cm below the squealer tip surface at an angle of 30 deg with respect to the blade pressure surface. Each hole had a diameter (d) of 0.127 cm, and the distance between each hole was 0.635 cm ($5d$). Figure 5 shows the geometry of the film cooling holes on the pressure side and the tip of blade.

The experiments were conducted for two different blowing ratios (M) of 1.0 and 2.0. Because the actual velocity of leakage flow and coolant air could vary with the location and the flow rate of the coolant, blowing ratio was defined as $M = \rho_c V_c / \rho_m V_{avg}$. Here, V_c and V_{avg} are the averaged coolant air velocity and the averaged velocity of cascade inlet and exit velocity while, ρ_m and ρ_c are the densities of mainstream and coolant air, respectively. Two separate tests were required in order to obtain both heat transfer coefficients and film cooling effectiveness. In the first test, unheated cooling air was injected and the coolant-to-mainstream density ratio was around 0.99. In the second test, heated cooing air was injected and the coolant-to-mainstream density ratio was around 0.92. It is noted that the coolant-to-mainstream density

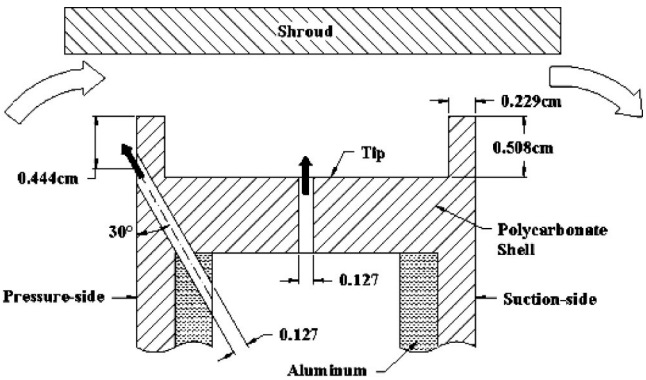

Fig. 5 Geometry of film-cooling holes

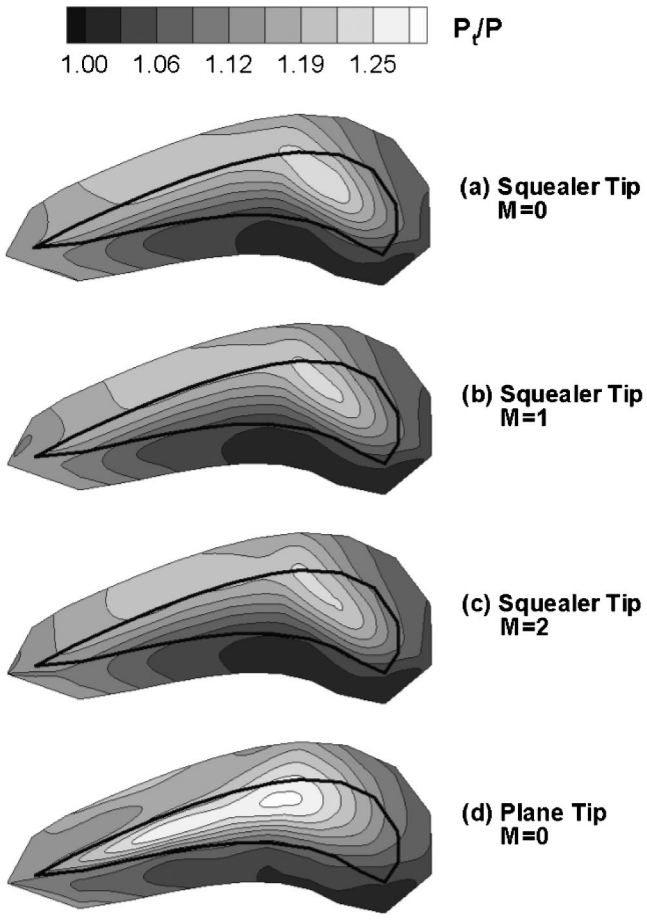

Fig. 6 Pressure distribution on the shroud surface for C =1.5% and injection from tip hole only case

ratio could be varied around 1.5–2.5 for the typical film cooled blades in real gas turbine engines. The effect of coolant-to-mainstream density ratio on heat transfer coefficients and film cooling effectiveness is not considered in this study.

Pressure Measurement and Results

To investigate the pressure distribution on the tip with film cooling, a total of 46 pressure taps were equipped on the shroud surface. Pressure was measured with the Scanivalve system with Labview software. The pressure side film cooling holes were covered with duct tape, and coolant was injected through the tip holes only.

Figure 6 shows the pressure distribution on the shroud surface for the injection from tip holes only. Figures 6(a)–(c) present the pressure distribution for the squealer tip, and Fig. 6(d) shows the plane tip without injection. The black curves indicate the blade tip location under the shroud. High P_t/P indicates low static pressure (high velocity) while low P_t/P corresponds to high static pressure (low velocity).

Comparing the squealer tip cases (Figs. 6(a)–(c)) with the plane tip case (Fig. 6(d), Kwak and Han [24]), results show that the overall P_t/P of the plane tip case is much higher than that of the squealer tip cases. This indicates that leakage flow is significantly reduced by the squealer tip. The maximum P_t/P location also moves from near the suction side at about 35% of chord for the plane tip case to near the camber line at about 20% of chord for the squealer tip cases. Thus the path of leakage flow is shifted towards the leading edge, and this may result in a higher heat transfer coefficient in the cavity near the leading edge.

Results also show that overall P_t/P decreases slightly as blowing ratio increases. The possible reason for this trend is that leakage flow may be blocked by the film injection. Coolant injected into the narrow tip gap can work as flow resistance, and thus reduce leakage flow. As blowing ratio increased from $M=0$ to $M=2$, P_t/P decreased by about 7% at the maximum P_t/P region.

Heat Transfer Measurement Theory

Hue detection based transient liquid crystals technique was used to measure heat transfer and film cooling effectiveness on the blade tip. The local heat transfer coefficient over a liquid crystals coated surface without film injection can be obtained using a one-dimensional semi-infinite solid assumption for the test surface. The 1D transient conduction equation, the initial condition, and the convective boundary condition are

$$k\frac{\partial^2 T}{\partial x^2}=\rho c_p\frac{\partial T}{\partial t}, \tag{1}$$

$$\text{at } t=0,\ T=T_i, \tag{2}$$

$$\text{at } x=0,\ -k\frac{\partial T}{\partial X}=h(T_w-T_m);\ \text{as } x\to\infty,\ T=T_i. \tag{3}$$

The solution of above equations at the convective boundary surface ($x=0$) is the following:

$$\frac{T_w-T_i}{T_m-T_i}=1-\exp\left(\frac{h^2\alpha t}{k^2}\right)\text{erfc}\left(\frac{h\sqrt{\alpha t}}{k}\right). \tag{4}$$

By knowing the initial temperature (T_i) of the test surface, the mainstream temperature (T_m) at the cascade inlet and the color change temperature (T_w) at time t, the local heat transfer coefficient (h) can be calculated from Eq. (4). For the film cooling test, the mainstream temperature (T_m) in Eq. (4) is replaced by the local film temperature (T_f), which is a mixture of the coolant (T_c) and mainstream temperature (T_m). The film temperature is defined in terms of the film cooling effectiveness η,

$$\eta=\frac{T_f-T_m}{T_c-T_m}\ \text{ or }\ T_f=\eta T_c+(1-\eta)T_m. \tag{5}$$

Then, Eqs. (4) and (5) can be combined as follows:

$$\frac{T_w-T_i}{T_f-T_i}=\frac{T_w-T_i}{\eta T_c+(1-\eta)T_m-T_i}=\left[1-\exp\left(\frac{h^2\alpha t}{k^2}\right)\text{erfc}\left(\frac{h\sqrt{\alpha t}}{k}\right)\right]. \tag{6}$$

Two similar transient tests were run to obtain the heat transfer coefficient (h) and film cooling effectiveness (η). In the first test, the surface of the test model was heated while the coolant was not. In the second test, both surface and coolant air were heated. Because both mainstream and coolant air temperature changed with time, the gradual change of the temperatures was recorded on the chart recorder. In this study, the temperature of the mainstream at the cascade inlet varied from 20 °C to 24 °C. The temperature of the cooling air varied from 20 °C to 22 °C for the unheated and from 40 °C to 50 °C for the heated coolant case, respectively. The varying temperatures were represented as a series of time step changes ($\tau_i, i=1,2\ldots N$). Using Duhamel's superposition theorem (Ekkad et al. [25]), Eq. (6) can be written as follows:

$$T_{w1}-T_{i1}=\{\eta(T_{c1,0}-T_{m1,0})+T_{m1,0}-T_{i1}\}F\left(\frac{h\sqrt{\alpha t_1}}{k}\right)+\sum_{i=1}^{n}\left[\{\eta(\Delta T_{c1,i}-\Delta T_{m1,i})+\Delta T_{m1,i}\}\times F\left(\frac{h\sqrt{\alpha(t_1-\tau_i)}}{k}\right)\right], \tag{7}$$

$$T_{w2}-T_{i2}=\{\eta(T_{c2,0}-T_{m2,0})+T_{m2,0}-T_{i2}\}F\left(\frac{h\sqrt{\alpha t_2}}{k}\right)+\sum_{i=1}^{n}\left[\{\eta(\Delta T_{c2,i}-\Delta T_{m2,i})+\Delta T_{m2,i}\}\times F\left(\frac{h\sqrt{\alpha(t_2-\tau_i)}}{k}\right)\right] \quad (8)$$

where $F(x)=1-\exp(x^2)\mathrm{erfc}(x)$. ΔT_m and ΔT_c are step changes in the mainstream and coolant air temperatures, respectively. Subscripts 1 and 2 indicate separate tests.

Equations (7) and (8) were solved iteratively at each pixel to obtain the detailed heat transfer coefficient and film effectiveness distributions.

The experimental uncertainty was calculated by the Kline and McClintock method [26]. The uncertainty for the local heat transfer coefficient and film cooling effectiveness was estimated to be 8% and 10%, respectively. However, the uncertainty near the squealer tip edge and film-hole edge might be much greater than 10% due to the 2D/3D heat conduction effect. The uncertainty near the blade-tip trailing edge cavity region also might be higher than 10% due to the longer color change time (25 sec). The researchers must be cautious in applying the present 1D transient film-cooled blade tip model for measuring local heat transfer coefficients. Since the blade tip is exposed to both internal and external convection, the thickness of the blade-tip model should be sufficient, in order to not violate the transient 1D semi-infinite assumption. The estimated mid-plane temperature of the present 0.64-cm thickness blade-tip model, near the leading edge cavity with the highest heat transfer coefficient, could be deviated from the initial temperature (at 60 °C) by 0.2 °C only. However, the estimated mid-plane temperature of the blade-tip model, near the trailing edge cavity with the lowest heat transfer coefficient, could be lower than the initial temperature (at 50 °C) by 5 °C due to both internal and external convection effects during the 25-sec transient time. It is imperative that a thicker blade-tip model with a less number of film cooling holes should be used in order to reduce the potential internal cooling effects and the 2D/3D conduction effects due to the holes. It is also desirable to have a uniform initial temperature of the blade-tip model to reduce axial temperature gradients that develop during the transient periods. Overall, the present 1D transient semi-infinite model is acceptable except near the trailing edge cavity region.

Heat-Transfer Measurement and Results

Two different liquid crystals were used in this study. The 20 °C bandwidth liquid crystals (R34C20W, Hallcrest) was used to measure the initial temperature of the tip surface, and the 5 °C bandwidth liquid crystals (R30C5W, Hallcrest) was used to measure the color changing time.

Calibration was performed to find the hue versus temperature relation. A foil heater was placed at the bottom of a 0.635-cm-thick copper plate. Above the copper plate, a 0.32-cm-thick black polycarbonate plate was attached with high conductivity glue. Because the color display of liquid crystals depends on the background color, the same black polycarbonate material was used for the calibration and for the blade tips heat-transfer tests. Input voltage to the foil heater was set properly in order to increase the surface temperature by 0.6 °C, and enough time was allowed for the temperature to be steady at each temperature step. The surface temperature was read by a thermocouple that was attached at the surface of the black polycarbonate plate and the color of the liquid crystals was recorded to a computer. At each temperature step, the hue was calculated from the stored image, and the relationship between hue and temperature was obtained. Figure 7(*a*) shows the results of the calibration for both liquid crystals.

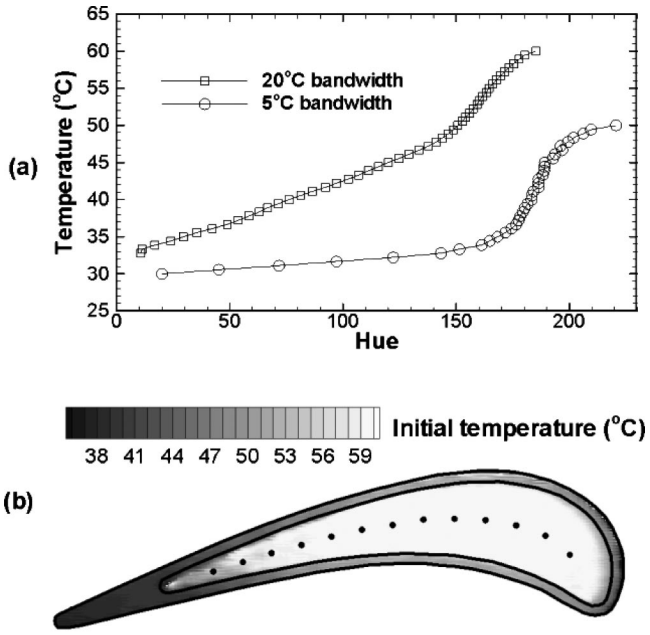

Fig. 7 (*a*) Relation between hue and temperature for both liquid crystals (*b*) Initial temperature distribution for $C=1.5\%$

Before the transient test, the 20 °C bandwidth liquid crystals was sprayed uniformly on the blade tip, and the blade tip was heated for about two hours. After the surface temperature reached the desired temperature (about 60 °C), the color of the liquid crystals on the tip surface was recorded by a RGB color charge-coupled device (CCD) camera with 24-bit color frame grabber board. From every pixel of the stored image, hue was calculated using the single hexcone color model (Foley et al. [27]), and the initial temperature of the blade tip was determined using the calibrated hue versus temperature relation. Figure 7(*b*) shows the distribution of the initial temperature for the $C=1.5\%$ case.

After the initial temperature measurement on the blade tip, the 20 °C bandwidth liquid crystals was removed and the 5 °C bandwidth liquid crystals was sprayed on. The blade tip was heated for about two hours until the reference temperatures became the same as those of the initial temperature measurement test. Reference temperatures were measured by two thermocouples located at the blade trailing edge surface and inside the cavity to ensure the same temperature conditions for the initial temperature measurement and the transient tests. After temperatures reached the desired value, the compressed air was allowed to flow by turning on the flow controller. When the mainstream velocity reached the preset value, the color change of the liquid crystals was recorded at the speed of 30 frames per second. The test duration time was short enough (10–30 sec) to make a semi-infinite solid assumption. From every pixel at each stored image, hue was evaluated and used to calculate the time from the initial condition (about 40–60 °C, depending on location) to a given hue value (50), which corresponded to the temperature of 30.6 °C in this test. Two similar tests were done with different coolant air temperatures. Then, the local heat-transfer coefficient and film cooling effectiveness on every pixel were calculated using Eqs. (7) and (8).

Heat Transfer Coefficient Results for Coolant Injection From Tip Holes Only. Figure 8 shows the heat transfer coefficient distribution for the coolant injection from tip holes only. Due to the shadow of the squealer rim, data near the leading edge cavity could not be acquired. The plane tip result (Fig. 8(*d*)) is presented for comparison. Detailed results of the plane tip heat transfer with film cooling are discussed by Kwak and Han [24]. Compared to the plane tip case (Fig. 8(*d*)), the squealer tip cases (Figs. 8(*a*)–(*c*)) show a much lower heat-transfer coefficient. The maximum heat transfer region also moves from 30–40% of chord

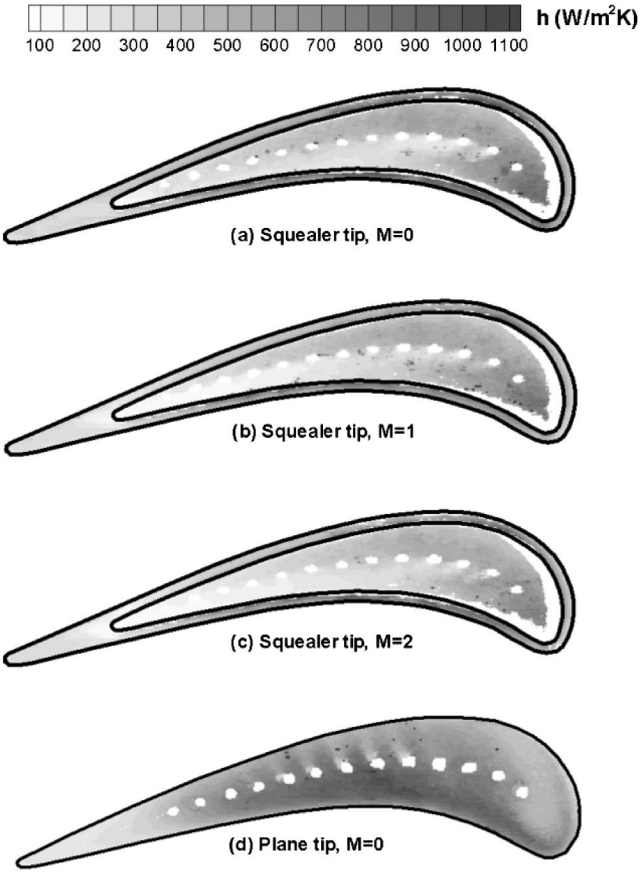

Fig. 8 Heat transfer coefficient for $C=1.5\%$ and coolant injection from tip holes only

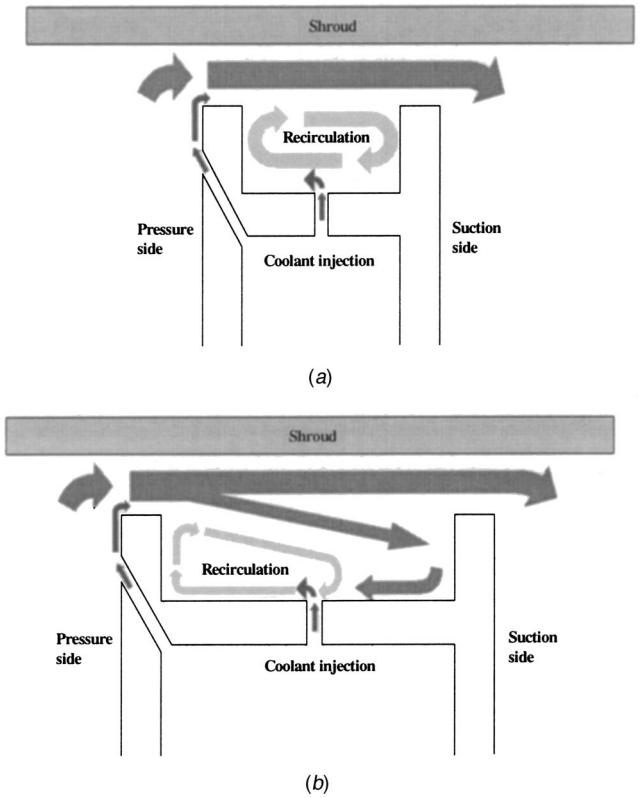

Fig. 9 Conceptual view of flow in the cavity, (*a*) cavity closer to the trailing edge, (*b*) cavity closer to the leading edge

(plane tip case) to the leading edge portion of the cavity (squealer tip cases). These trends correspond to the pressure distribution shown in Fig. 6.

The heat transfer coefficient in the cavity decreases as blowing ratio increases. However, the heat transfer coefficient on the squealer rim does not change much with changing blowing ratios. These also agree with the pressure distribution shown in Fig. 6. In the pressure distribution (Fig. 6), the maximum P_t/P near the leading edge decreases as the blowing ratio increases. However, the P_t/P at the pressure and suction side squealer rims does not change much as the blowing ratio changes. The overall heat transfer coefficient decreases by 7% as the blowing ratio increases from $M=0$ to $M=2$.

For the squealer tip cases, heat transfer coefficients on the suction side rim near 10–20% of chord and the pressure side rim near 10–40% of chord show relatively high values. Generally, heat transfer coefficients on the rim are higher than those in the cavity except near the leading edge. The distribution of heat transfer coefficients in the cavity shows the highest value near the leading edge portion due to reattachment of the leakage flow. Relatively high heat transfer coefficients appear near the suction side cavity also due to reattachment of the leakage flow. However, heat transfer coefficients near the pressure side cavity show lower values. It seems that after leakage flow reattaches to the cavity surface, flow moves from the suction side to the pressure side of the cavity and forms a recirculation region near the pressure side of the cavity as illustrated in Fig. 9. Figure 9 presents the conceptual view of flow in the cavity. If the width of the cavity is relatively small, leakage flow may not go into the cavity, and recirculation may occur in the cavity as shown in Fig. 9(*a*). Therefore heat transfer near the trailing edge of the cavity is minimal due to the recirculation as shown in Fig. 9(*a*). However, if the width of cavity is relatively large, leakage flow may reattach to the suction side rim or the cavity surface and form a recirculation region near the pressure side of the cavity as shown in Fig. 9(*b*). This may happen near the

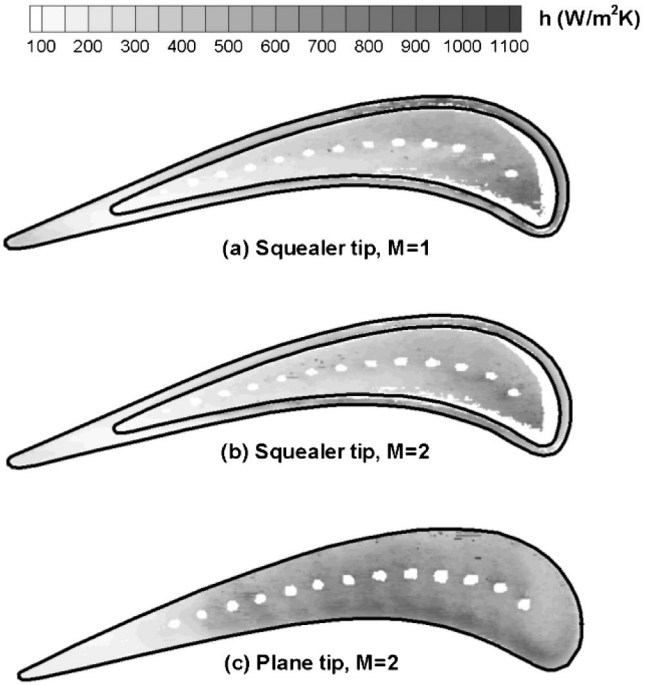

Fig. 10 Heat transfer coefficient for $C=1.5\%$ and coolant injection from both tip and pressure side holes

leading edge of the cavity. Due to the recirculation in the cavity, heat transfer coefficients near the pressure side of the cavity may be lower than on the suction side.

Effects of Pressure Side Injection. Figure 10 presents the heat transfer coefficient distribution for $C=1.5\%$ and coolant injection from both tip and pressure side holes. The plane tip result (Fig. 10(*c*), Kwak and Han [24]) is presented for comparison. Compared to the plane tip case (Fig. 10(*c*)), heat transfer coefficients for the squealer tip cases (Figs. 10(*a*) and (*b*)) show lower values.

For the squealer tip cases, compared to the injection from tip holes only, overall heat transfer coefficient decreases by about 5%. This may be caused by the additional blockage effect of the pressure side injection.

At $M=1$, a high heat transfer coefficient is observed on the suction side rim near 20–40% of chord. At $M=2$, however, the heat transfer coefficient on the suction side rim decreases, while the heat transfer coefficient on the pressure side rim near 10–50% of chord increases. The overall heat transfer coefficient decreases by 9% as blowing ratio increases from $M=1$ to $M=2$.

Figures 11(*a*) and (*b*) show the averaged heat transfer coefficient for the coolant injection from tip holes only and the coolant injection from both tip and pressure side holes, respectively. The local heat transfer coefficients on the pressure side rim, suction side rim, and cavity are averaged at a given x/C_x location. In both cases, the averaged heat transfer coefficient in the cavity continuously decreases as x/C_x increases. Generally, the heat transfer coefficient on the squealer rim is higher than that on the cavity.

Compared with the injection from tip holes only (Fig. 11(*a*)), the injection from both tip and pressure side holes (Fig. 11(*b*)) shows a slightly smaller value of the overall averaged heat transfer coefficient for each blowing ratio. This may be caused by the additional blockage effect of the pressure side injection.

Effects of Tip Gap Clearance. Figures 11(*b*) and 12(*a*) and (*b*) present the averaged heat transfer coefficient for $C=1.5\%$, $C=1.0\%$, and $C=2.5\%$, respectively. All cases have injection from both tip and pressure side holes.

All cases show a decreasing trend of the averaged heat transfer coefficient in the cavity as x/C_x increases. For all tip gap clearance cases, the overall averaged heat transfer coefficient slightly decreases as blowing ratio increases. The overall averaged heat transfer coefficient slightly increases as tip gap clearance increases for each blowing ratio.

As blowing ratio increases, the heat transfer coefficient on the suction side rim generally decreases, while the heat transfer coefficient on the pressure side rim generally increases. This may be caused by the pressure side injection. As blowing ratio increases, pressure side injected coolant may mix with leakage flow and enhance heat transfer on the pressure side rim. Because of different interactions between leakage flow and injected coolant for each tip gap, the effects of film cooling on heat transfer coefficient distributions appear differently.

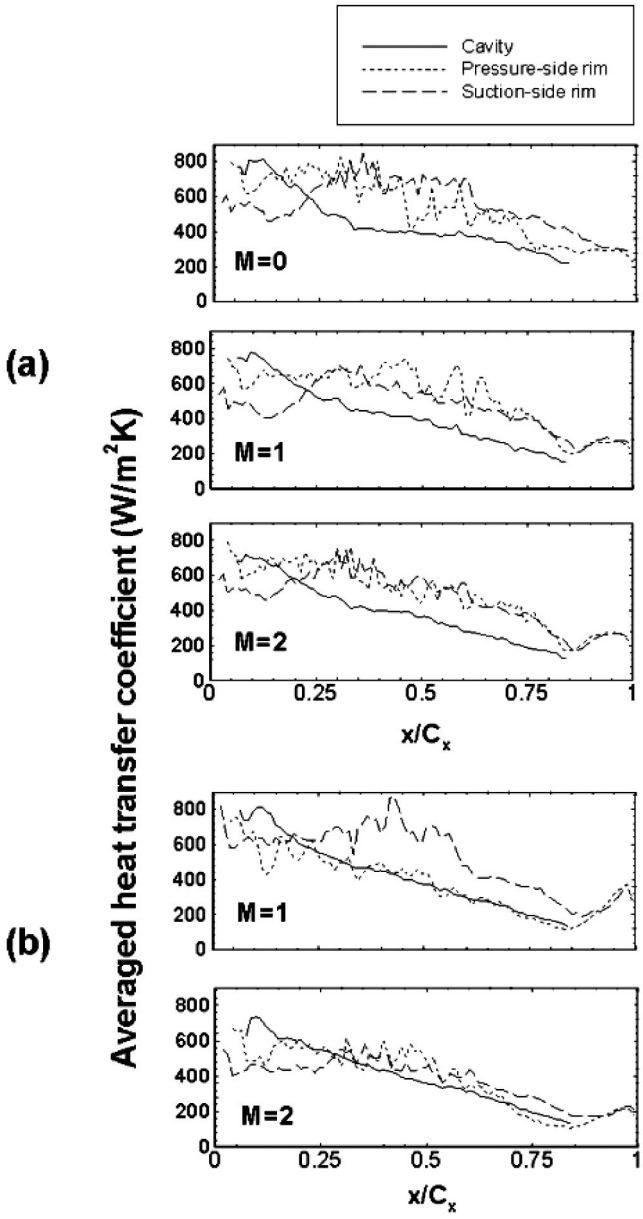

Fig. 11 Averaged heat transfer coefficient for $C=1.5\%$ and (*a*) coolant injection from tip holes only (*b*) coolant injection from both tip and pressure side holes

Film Cooling Effectiveness Results

Film cooling effectiveness was calculated simultaneously with the heat transfer coefficient from Eqs. (7) and (8) for three tip gap clearances with two different blowing ratios.

Film Cooling Effectiveness Results for Coolant Injection From Tip Holes Only. Figure 13 presents the film cooling effectiveness distribution for $C=1.5\%$ and coolant injection from tip holes only. Again, the plane tip result (Fig. 13(*c*)) is presented for comparison. Detailed results of the film cooling effectiveness on the plane tip are discussed by Kwak and Han [24]. Compared with the plane tip case (Fig. 13(*c*)), the squealer tip cases (Figs. 13(*a*) and (*b*)) show a much higher film cooling effectiveness.

The squealer tip cases show high film cooling effectiveness between the camber line and the pressure side rim. As reattached leakage flow recirculates in the cavity as described in Fig. 9, the coolant injected from the tip holes may be pushed towards the pressure side and accumulate there. Thus high film cooling effectiveness can be observed between the camber line and the pressure side, while film cooling effectiveness near the cavity suction side is very low. On the suction side rim, higher film cooling effectiveness appears near the trailing edge, as accumulated coolant exits near the trailing edge of the cavity. As blowing ratio increases, film cooling effectiveness and the film covered area also increase.

Effects of Pressure Side Injection. Figure 14 shows the film cooling effectiveness distribution for $C=1.5\%$ and coolant injection from both tip and pressure side holes. The plane tip result (Fig. 14(*c*), Kwak and Han [24]) is presented for comparison. Compared with the plane tip case (Fig. 14(*c*)), the squealer tip cases (Figs. 14(*a*) and (*b*)) show a higher film cooling effectiveness.

For the squealer tip cases, film cooling effectiveness and the

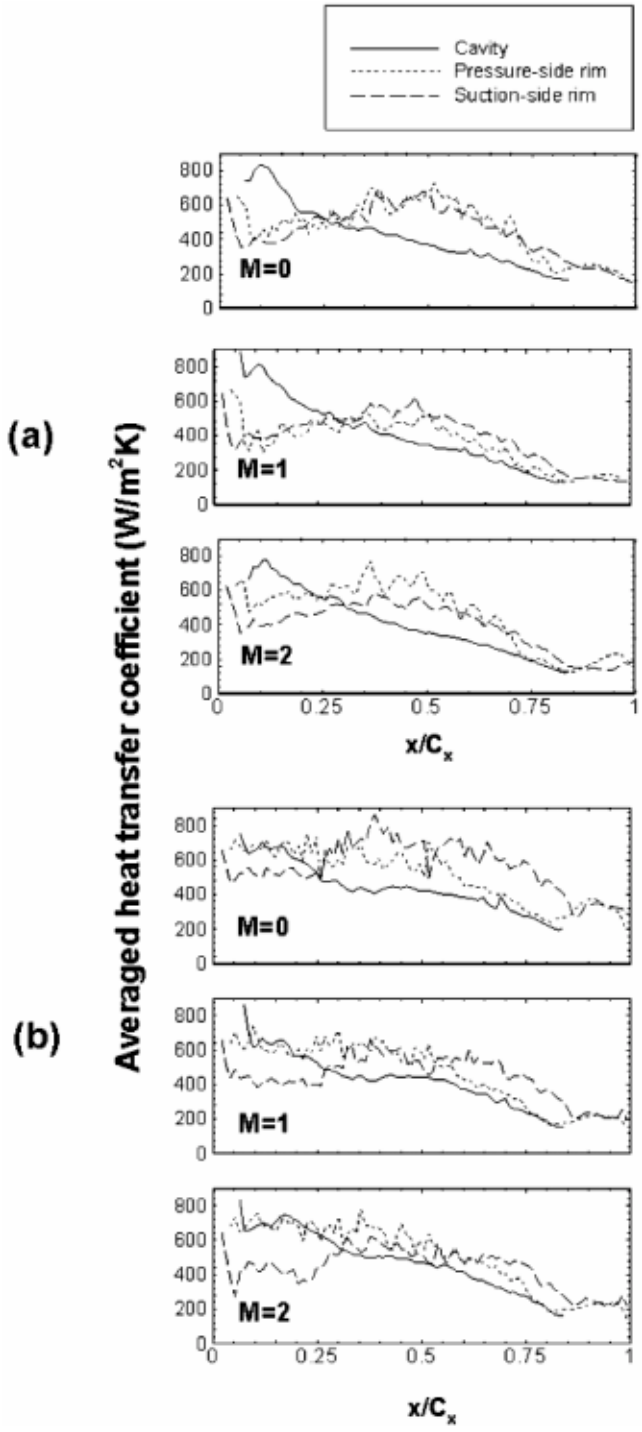

Fig. 12 Averaged heat transfer coefficient for coolant injection from both tip and pressure side holes and (*a*) $C=1.0\%$, (*b*) $C=2.5\%$

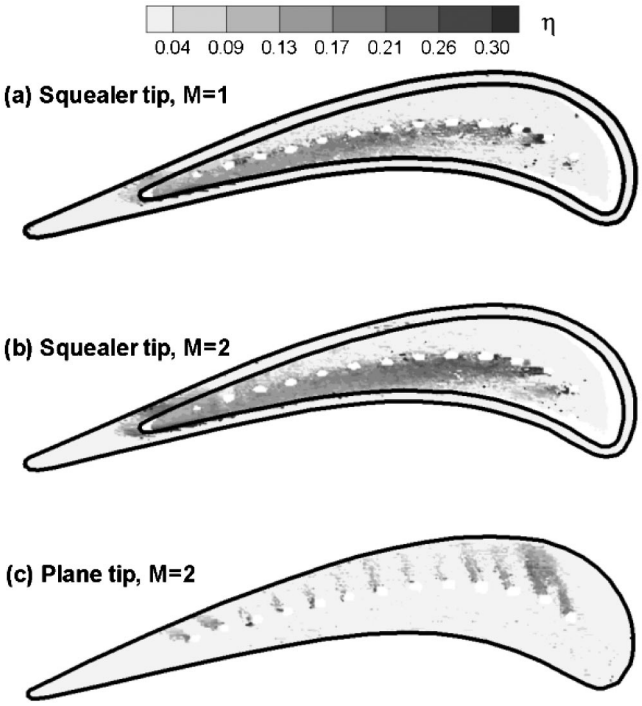

Fig. 13 Film cooling effectiveness for $C=1.5\%$ and coolant injection from tip holes only

film-covered area increase as blowing ratio increases. For the $M=1$ case (Fig. 14(*a*)), film cooling effectiveness on the pressure side and suction side rims from 50% of chord to trailing edge show a higher value than that of the injection from tip holes only (Fig. 13(*a*)). This may be caused by the pressure side injected coolant. As the pressure side coolant is carried over the pressure side rim, film cooling effectiveness on the pressure side rim increases. Some part of the pressure side coolant may go directly to the suction side rim and may accumulate in the cavity. Thus film cooling effectiveness on the suction side rim and in the cavity also increase for the injection from both tip and pressure side holes case.

Results show that coolant injected from the tip holes is pushed towards the pressure side and exits from the cavity near the trailing edge. At this location, coolant injected from the pressure side holes and the tip holes accumulates, and results in high film cool-

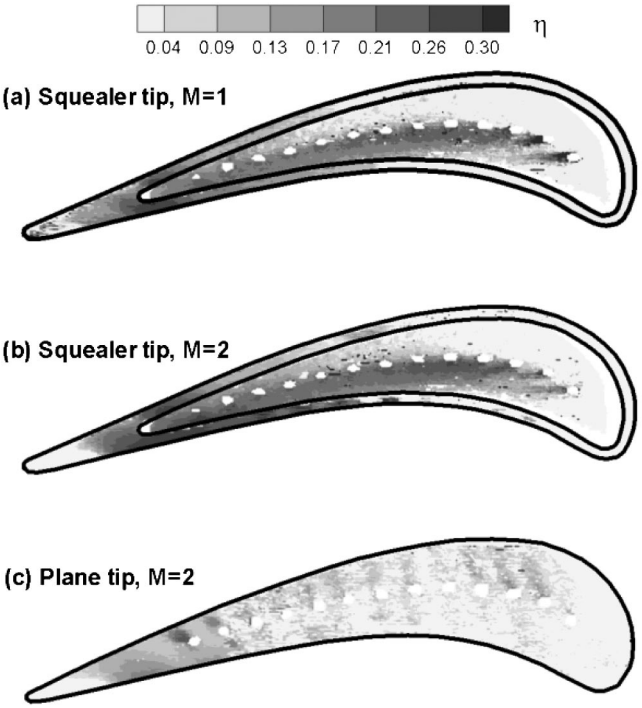

Fig. 14 Film cooling effectiveness for $C=1.5\%$ and coolant injection from both tip and pressure side holes

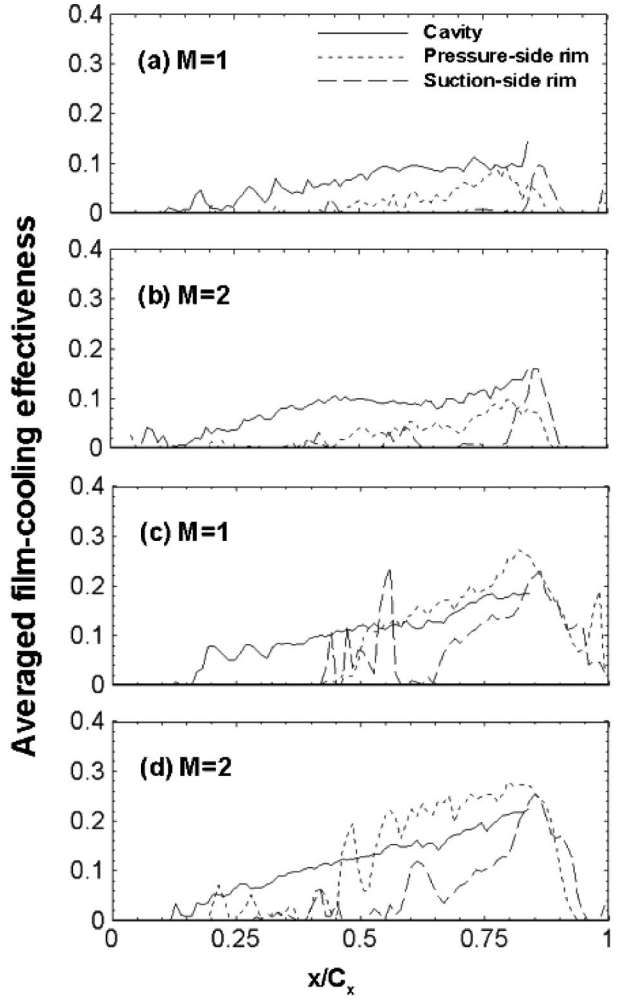

Fig. 15 Averaged film cooling effectiveness for (*a*) and (*b*): $C=1.5\%$, injection from tip holes only (*c*) and (*d*): $C=1.5\%$, injection from both tip and pressure side holes

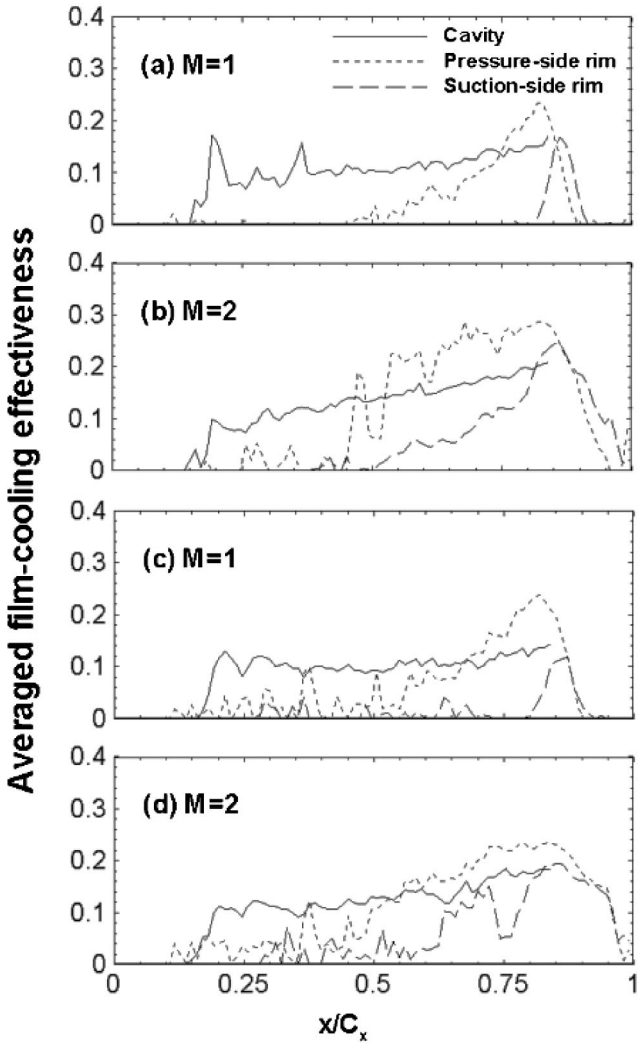

Fig. 16 Averaged film cooling effectiveness for injection from both tip and pressure side holes, (*a*) and (*b*): $C=1.0\%$; (*c*) and (*d*): $C=2.5\%$

ing effectiveness near 85% of chord. As blowing ratio increases to $M=2$, the film covered area increases and film cooling effectiveness also increase.

Figure 15 shows averaged film cooling effectiveness at a given x/C_x location for $C=1.5\%$ and coolant injection from tip holes only and both tip and pressure side holes. Both cases show that film cooling effectiveness increases as x/C_x increases in the cavity and on both the pressure side and the suction side rims due to the coolant accumulation. For the coolant injection from tip holes only case (Figs. 15(*a*) and (*b*)), the averaged film cooling effectiveness in the cavity is higher than on the rims. For the both tip and pressure side holes injection case (Figs. 15(*c*) and (*d*)), the averaged film cooling effectiveness on the pressure side rim is the highest at $x/C_x>0.5$ due to the pressure side injected coolant, which is carried over.

Effects of Tip Gap Clearance. Figures 15(*c*) and (*d*, 16(*a*) and (*b*), and 16(*c*) and (*d*) show the averaged film cooling effectiveness for $C=1.5\%$, $C=1.0\%$, and $C=2.5\%$, respectively. All cases have coolant injection from both tip and pressure side holes.

All cases show that the averaged film cooling effectiveness increases as blowing ratio increases, and the maximum averaged film cooling effectiveness exists at about $x/C_x=0.8$ due to the accumulated coolant in the cavity and the pressure side coolant carrying over. For $M=1$, the $C=1.5\%$ case gives the best overall averaged film cooling effectiveness. For $M=2$, however, the $C=1.0\%$ shows the highest overall averaged film cooling effectiveness. The high blowing rate of coolant to the narrow tip gap may cause a large amount of accumulation and recirculation of coolant in the cavity, which result in high film cooling effectiveness. For $C=2.5\%$, coolant may dilute well with leakage flow and result in relatively low film cooling effectiveness compared with narrower tip gap clearance cases. Because of the different interactions/mixings between coolant and leakage flow for each tip gap clearance, blowing ratio effects on film cooling effectiveness appears differently.

Conclusions

The major findings based on the experimental results are as follows:

1. Pressure and heat transfer coefficient measurements showed that tip leakage flow and heat transfer coefficient on the tip surface were reduced by using a squealer tip blade.
2. For all cases, the heat transfer coefficient in the cavity showed the high value near the leading edge and the suction side of the cavity due to leakage flow reattachment. However, the heat transfer coefficient was lower near the pressure side and the trailing edge of the cavity due to possible flow recirculation.
3. Coolant injection from both tip and pressure side holes showed a slightly reduced heat transfer coefficient compared

to the injection from tip holes only, due to the additional blockage effect of the pressure side injected coolant.

4. For all cases, the heat transfer coefficient on the pressure side and suction side squealer rims was higher than that in the cavity at all x/C_x locations except the cavity leading edge region.
5. As blowing ratio increased, static pressure on the shroud slightly increased and the overall heat transfer coefficient on the blade tip slightly decreased.
6. For all cases, because film coolant was pushed towards the pressure side by the recirculation of cavity flow, film cooling effectiveness in the cavity showed a higher value between the camber line and the pressure side of the cavity and a lower value between the camber line and the suction side of cavity.
7. Film cooling effectiveness increased as blowing ratio increased for all cases.
8. High film cooling effectiveness appeared near the trailing edge cavity due to the coolant accumulation.
9. Compared with the coolant injection from tip holes only case, film cooling effectiveness for the coolant injection from both tip and pressure side holes case showed higher film cooling effectiveness due to the potential carrying over of pressure side coolant.
10. The overall averaged heat transfer coefficient slightly increased as the tip gap increased. However, film cooling effectiveness did not show a constant trend.
11. Compared to the plane tip at the same tip gap clearance and blowing ratio, the overall film cooling effectiveness increased but heat transfer coefficient decreased for the squealer tip case.

Acknowledgments

This work was prepared with the support of the NASA Glenn Research Center under Grant No. NAG3-2002. The NASA technical team is Mr. Robert Boyle and Dr. Raymond Gaugler. Their support is greatly appreciated. Technical discussions with Dr. C. Pang Lee of GE Aircraft Engines, Dr. Ron Bunker of GE R&D Center, and Dr. GM S. Azad of Siemens-Westinghouse were helpful and are acknowledged.

Nomenclature

C = Tip clearance gap (% of span or mm)
C_x = Axial chord length of the blade (8.61 cm)
d = Diameter of film cooling holes (0.127 cm)
h = Local convective heat transfer coefficient ($W/m^2 K$)
H = Cavity depth (recess) (0.508 cm)
k = Thermal conductivity of blade tip material (0.18 W/m K)
M = Averaged blowing ratio ($=\rho_c V_c/\rho_m V_{avg}$)
LE = Leading edge of the blade
P = Local static pressure (kPa)
P_t = Total pressure at the cascade inlet (kPa)
PS = Blade pressure side
t = Transition time for liquid crystals color change (second)
TE = Trailing edge of the blade
T_c = Coolant air temperature (°C)
T_i = Initial temperature of the blade tip surface (°C)
T_m = Temperature of the mainstream at the cascade inlet (recovery temperature) (°C)
T_w = Color change temperature of the liquid crystals (°C)
Tu = Turbulence intensity level at the cascade inlet (%)
x = Axial distance (cm)
V_{avg} = Averaged velocity of mainstream air between cascade inlet and exit (m/s)
V_c = Averaged velocity of coolant from all film cooling holes (m/s)
α = Thermal diffusivity of blade tip material (1.25×10^{-7} m^2/s)
η = Local film cooling effectiveness
ρ_c = Density of coolant air (kg/m^3)
ρ_m = Density of mainstream air (kg/m^3)
τ_i = Step change of time (sec)

References

[1] Han, J. C., Dutta, S., and Ekkad, S. V., 2000, *Gas Turbine Heat Transfer and Cooling Technology*, Taylor & Francis, New York.
[2] Metzger, D. E., Bunker, R. S., and Chyu, M. K., 1989, "Cavity Heat Transfer on a Transverse Grooved Wall in a Narrow Flow Channel," ASME J. Heat Transfer, **111**, pp. 73–79.
[3] Chyu, M. K., Moon, H. K., and Metzger, D. E., 1989, "Heat Transfer in the Tip Region of Grooved Turbine Blades," ASME J. Turbomach., **111**, pp. 131–138.
[4] Heyes, F. J. G., Hodson, H. P., and Dailey, G. M., 1991, "The Effect of Blade Tip Geometry on the Tip Leakage Flow in Axial Turbine Cascades," ASME Paper 91-GT-135.
[5] Yang, T. T., and Diller, T. E., 1995, "Heat Transfer and Flow for a Grooved Turbine Blade Tip in a Transonic Cascade," ASME Paper 95-WA/HT-29.
[6] Ameri, A. A., Steinthorsson, E., and Rigby, L. David, 1997, "Effect of Squealer Tip on Rotor Heat Transfer and Efficiency," ASME Paper 97-GT-128.
[7] Dunn, M. G., and Haldeman, C. W., 2000, "Time-Averaged Heat Flux for a Recessed Tip, Lip, and Platform of a Transonic Turbine Blade," ASME J. Turbomach., **122**, pp. 692–697.
[8] Azad, GM S., Han, J. C., Teng, S., and Boyle, R., 2000, "Heat Transfer and Pressure Distributions on a Gas Turbine Blade Tip," ASME J. Turbomach., **122**, pp. 717–724.
[9] Azad, GM S., Han, J. C., and Boyle, R., 2000, "Heat Transfer and Pressure Distributions on the Squealer Tip of a Gas Turbine Blade," ASME J. Turbomach., **122**, pp. 725–732.
[10] Azad, GM S., Han, J. C., Lee, C. P., and Bunker, R. S., 2001, "Effect of Squealer Geometry Arrangement on Gas Turbine Blade Heat Transfer," ASME J. Heat Transfer, **124**, pp. 452–459.
[11] Mayle, R. E., and Metzger, D. E., 1982, "Heat Transfer at the Tip of an Unshrouded Turbine Blade," *Proc. Seventh Int. Heat Transfer Conf.*, Hemisphere Publishing, Washington, DC, pp. 87–92.
[12] Metzger, D. E., Dunn, M. G., and Hah, C., 1991, "Turbine Tip and Shroud Heat Transfer," ASME J. Turbomach., **113**, pp. 502–507.
[13] Bunker, R. S., Baily, J. C., and Ameri, A. A., 2000, "Heat Transfer and Flow on the First Stage Blade Tip of a Power Generation Gas Turbine: Part 1: Experimental Results," ASME J. Turbomach., **122**, pp. 263–271.
[14] Bunker, R. S., and Baily, J. C., 2001, "Effect of Squealer Cavity Depth and Oxidation on Turbine Blade Tip Heat Transfer," ASME Paper 2001-GT-0155.
[15] Teng, S., Han, J. C., and Azad, GM S., 2001, "Derailed Heat Transfer Coefficient Distributions on a Large-Scale Gas Turbine Blade Tip," ASME J. Heat Transfer, **123**, pp. 803–809.
[16] Ameri, A. A., and Steinthorsson, E., 1995, "Prediction of Unshrouded Rotor Blade Tip Heat Transfer," ASME Paper 95-GT-142.
[17] Ameri, A. A., and Steinthorsson, E., 1996, "Analysis of Gas Turbine Rotor Blade Tip and Shroud Heat Transfer," ASME Paper 96-GT-189.
[18] Ameri, A. A., Steinthorsson, E., and Rigby, L. David, 1999, "Effects of Tip Clearance and Casing Recess on Heat Transfer and Stage Efficiency in Axial Turbines," ASME J. Turbomach., **121**, pp. 683–693.
[19] Ameri, A. A., and Bunker, R. S., 2000, "Heat Transfer and Flow on the First Stage Blade Tip of a Power Generation Gas Turbine: Part 2: Simulation Results," ASME J. Turbomach., **122**, pp. 272–277.
[20] Ameri, A. A., and Rigby, D. L., 1999, "A Numerical Analysis of Heat Transfer and Effectiveness on Film Cooled Turbine Blade Tip Models," NASA/CR 1999-209165.
[21] Ameri, A. A., 2001, "Heat Transfer and Flow on the Blade Tip of a Gas Turbine Equipped With a Mean-Camberline Strip," ASME J. Turbomach., **123**, pp. 704–708.
[22] Kim, Y. W., Downs, J. P., Soechting, F. O., Abdel-Messeh, W., Steuber, G. D., and Tanrikut, S., 1995, "A Summary of the Cooled Turbine Blade Tip Heat Transfer and Film Effectiveness Investigations Performed by Dr. D. E. Metzger," ASME J. Turbomach., **117**, pp. 1–11.
[23] Kim, Y. W., and Metzger, D. E., 1995, "Heat Transfer and Effectiveness on Film Cooled Turbine Blade Tip Model," ASME J. Turbomach., **117**, pp. 12–21.
[24] Kwak, J. S., and Han, J. C., 2003, "Heat Transfer Coefficients and Film Cooling Effectiveness on a Gas Turbine Blade Tip," ASME J. Heat Transfer, **125**, pp. 494–502.
[25] Ekkad, S. V., Zapata, D., and Han, J. C., 1997, "Heat Transfer Coefficients Over a Flat Surface With Air and CO2 Injection Through Compound Angle Holes Using a Transient Liquid Crystal Image Method," ASME J. Turbomach., **119**, pp. 580–586.
[26] Kline, S. J., and McClintock, F. A., 1953, "Describing Uncertainties in Single Sample Experiments," Mech. Eng. (Am. Soc. Mech. Eng.), **75**, pp. 3–8.
[27] Foley, J. D., van Dam, A., Feiner, S. K., and Huyghes, J. F., 1990, *Computer Graphics: Principles and Practice*, Addison-Wesley Publishing Company, Reading, MA, p. 592.

An Overview of High-Temperature Electronics and Sensor Development at NASA Glenn Research Center

Gary W. Hunter
Philip G. Neudeck
Robert S. Okojie
Glenn M. Beheim
J. A. Powell

NASA Glenn Research Center at Lewis Field,
Cleveland, OH 44135

Liangyu Chen
OAI,
Cleveland, OH 44142

This paper gives a brief overview of the status of high-temperature electronics and sensor development at NASA Glenn Research Center supported in part or in whole by the Ultra Efficient Engine Technology Program. These activities contribute to the long-term development of an intelligent engine by providing information on engine conditions even in high temperature, harsh environments. The technology areas discussed are: 1) high-temperature electronics, 2) sensor technology development (pressure sensor and high-temperature electronic nose), 3) packaging of harsh environment devices and sensors, and 4) improved silicon carbide electronic materials. A description of the state-of-the-art and technology challenges is given for each area. It is concluded that the realization of a future intelligent engine depends on the development of both hardware and software including electronics and sensors to make smart components. When such smart components become available, an intelligent engine composed of smart components may become a reality. [DOI: 10.1115/1.1579508]

Introduction

In order for future aeronautic engines to meet the increasing requirements for reduced emissions, reduced fuel burn, and increased safety, the inclusion of intelligence into the engine design and operation becomes necessary. As has been seen in the automotive industry's inclusion of improved intelligence in internal combustion engines, the aeronautic engine will have to incorporate technology that will allow the internal systems to monitor engine conditions, analyze the incoming data, and modify operating parameters to optimize engine operations to achieve improved performance. This implies the development of sensors, actuators, control logic, signal conditioning, communications, and packaging that will be able to operate under the harsh environments present in an engine. However, given the harsh environments inherent in an engine, the development of engine-compatible electronics and sensors is not straightforward.

The use of complex electronics to enhance the capabilities and efficiency of modern jet aircraft implies operation at temperatures above 300°C. However, since today's conventional silicon-based electronics technology cannot function at such high temperatures, these electronics must reside in environmentally controlled areas. This necessitates either the use of long wire runs between sheltered electronics and hot-area sensors and controls, or the fuel cooling of electronics and sensors located in high-temperature areas. Such low-temperature electronics approaches suffer from serious drawbacks in terms of increased weight, decreased fuel efficiency, and reduction of aircraft reliability. A family of high-temperature electronics and sensors that could function in hot areas as high as 600°C would enable substantial aircraft performance gains through weight reduction and active controls.

In addition, the electronics and sensors do not need to be part of the flight systems on the aircraft to contribute to the development of an intelligent engine. Three envisioned uses of electronic and sensor technology in aeronautic engine applications are: 1) system development and ground testing where the sensor provides information on the state of a system that does not fly (this information would be used for the design and advanced modeling of systems that are used in flight); 2) vehicle health monitoring (VHM) which involves the long-term monitoring of a system in operation to determine the health of the vehicle system (e.g., is the engine increasing fuel burn or increasing emissions). This information could be used to change engine parameters to improve performance; 3) active control of the vehicle in a feedback mode where information from a sensor and possibly accompanying electronics is used to change a system parameter in real-time (e.g., fuel flow to the engine changed due to system measurements). Each application has its own requirements for electronics and sensor technology.

This paper gives a brief overview of the electronics and sensor development at NASA Glenn Research Center (NASA GRC) supported, in part or in full, by the Ultra Efficient Engine Technology program. Four major technology areas are discussed: 1) high-temperature electronics, 2) sensor technology development, 3) packaging of harsh environment devices and sensors, and 4) improved silicon carbide electronic materials. A description of the state-of-the-art and remaining technology challenges is given for each area.

High-Temperature Electronics

Silicon carbide (SiC) presently appears to be the strongest candidate semiconductor for implementing 500–600°C integrated electronics in the nearer term, as competing high-temperature electronics technologies are either physically incapable of functioning at this high of a temperature range (silicon and silicon-on-insulator), or are significantly less-developed (GaN, diamond, etc.). Discrete SiC devices such as pn junction diodes, junction field effect transistors (JFETs), and metal-oxide-semiconductor field effect transistors (MOSFETs) have previously demonstrated excellent electrical functionality at 600°C for relatively short time periods [1]. However, for such electronics to be useful in crucial turbine-engine applications, much longer 600°C harsh-environment lifetimes must eventually be realized. Between 500 to 5000 h of operation is needed for various jet engine ground tests, while many years of reliable operation is required for insertion into everyday passenger aircraft.

Contributed by the International Gas Turbine Institute and presented at the International Gas Turbine and Aeroengine Congress and Exhibition, Amsterdam, The Netherlands, June 3–6, 2002. Manuscript received by the IGTI February 28, 2002. Paper No. 2002-GT-30624. Review Chair: E. Benvenuti.

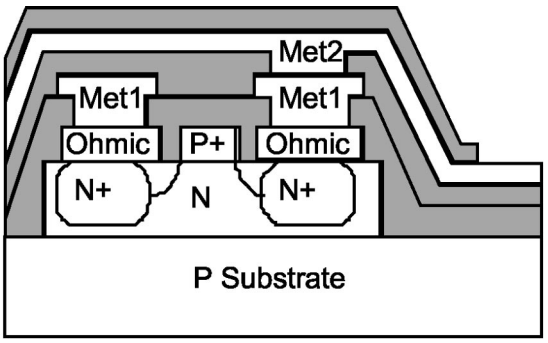

Fig. 1 Simplified (see text) cross-sectional representation of 6H-SiC epitaxial JFETs used to implement 600°C logic gates. The shaded regions are insulating silicon nitride dielectric.

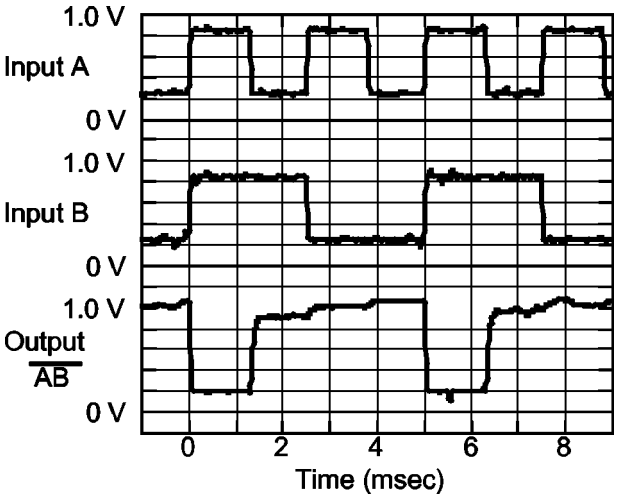

Fig. 2 NAND gate test waveforms at 600°C with $V_{DD}=2.5$ V, $V_{SS}=0$ V, $V_{substrate}=-1.4$ V

The operational lifetime of SiC-based transistors at 600°C is not limited by the semiconductor itself, but is instead largely governed by the reliability and stability of various interfaces with the SiC crystal surface. The physical degradation of the metal-semiconductor ohmic contact interface limits the 600°C operating lifetime of all devices, while high-temperature MOSFET operating lifetime is also limited by the electrical integrity of the oxide-semiconductor interface. Thus, junction-based transistors without gate insulators appear more feasible in the nearer term. Of the candidate junction-based transistor technologies that might be used to implement SiC integrated circuits, the pn junction gate JFET seems closest to demonstrating long-term operation at 600°C.

An example of the maturity of the JFET technology is the demonstration of 600°C digital logic using SiC JFET's [2]. A resistive load direct-coupled FET logic (DCFL) approach was adopted to demonstrate simple 600°C digital logic using SiC JFET's. The non-planar epitaxial gate JFET design shown in Fig. 1 was chosen over that of a planar ion-implanted structure, largely to alleviate the challenging process of sufficiently activating high-dose p^+ ion implants in SiC. The two-level interconnect approach uses oxidation-resistant silicon nitride as the dielectric passivation along with oxidation resistant gold for the metal interconnect. Contrary to the depiction of Fig. 1, the devices are laid out so that both the second and third layers of silicon nitride always covers the first via layer to the oxygen-sensitive metal-SiC ohmic contact interface. However, because non-optimized ohmic contact metals were employed in this experiment, long term 600°C operation was not obtained.

Figure 2 shows operation of a NAND gate at 600°C. The devices show good operation at these high temperatures. These circuits are the fundamental building blocks of more complex systems. However, adjustment of the substrate bias ($V_{substrate}$) and power supply bias (V_{DD}) was necessary to compensate for current-voltage property changes with temperature, as the circuit noise margins were not sufficient to absorb these changes while maintaining basic functionality. Therefore, they are not capable of operation over the desired 25°C to 600°C temperature range using fixed power supply voltages. Degradation of contacts to the device limited operational circuit testing at 600°C to less than 1 h.

Figure 3 shows a device following 600°C testing with visible evidence of contact degradation. This illustrates an area where additional technology development is necessary before 600°C SiC-based circuits can become useful. The operational lifetime of the circuit at 600°C could be extended by using separately optimized n-type and p-type ohmic contacts specifically designed to resist high-temperature degradation. These contacts, combined with the improved packaging of the device as a whole, could lead to implementation of complex electronics at high temperatures. Significant progress has been made in improving the reliability of high temperature contacts [3]. Advances in the development of high temperature packaging will be discussed in the following sections. Complete systems including SiC electronics are envisioned which include signal conditioning electronics and wireless communication.

Sensor Technology Development

Pressure Sensor Technology. One application that requires improved sensor technology is high temperature pressure sensing. Standard pressure sensors are temperature limited, while SiC-based pressure sensors have a much wider temperature range and have the added benefit that high-temperature SiC electronics can be integrated with the sensor. However, the difficulty of micromachining SiC to form a well-defined diaphragm structure, combined with the lack of reliable device packaging for these operating environments has largely prevented the application of these devices.

Progress has been made in both micromachining and packaging [4]. An approach using reactive ion etching (RIE) to form a well-defined diaphragm structure has been developed [5]. The SiC diaphragm is produced by patterning the starting wafer with nickel followed by a deep reactive ion etching process as described in [5] to form an array of 150 μm deep circular cavities in the SiC as shown in Fig. 4. The resulting diaphragm has well-defined side-

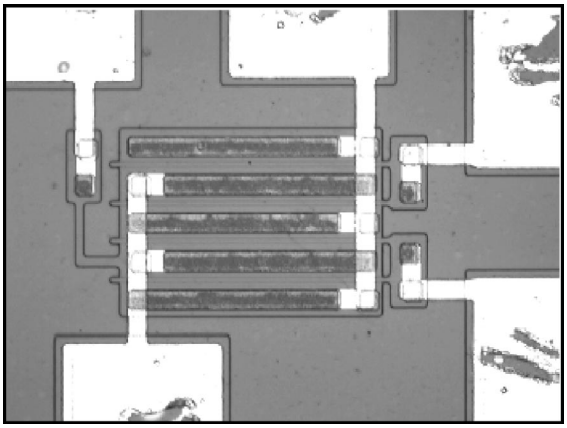

Fig. 3 Optical micrograph of 6H-SiC JFET gate following 600°C electrical testing. Each bondpad is 100×100 μm^2, and each of the four gate fingers is 3×150 μm. Degradation of the bondpads is clearly evident.

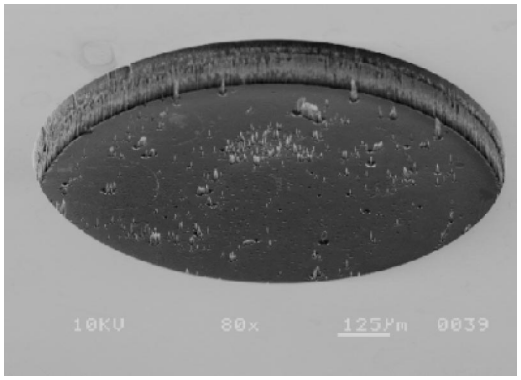

Fig. 4 Scanning electron microscopy (SEM) micrograph of cavity etched in 6H-SiC by deep reactive ion etching method

walls and does not exhibit curvature at the corners of the cavity present in cavities made by other etching processes. After formation of the cavity, piezoresistive mesas are formed [4] and a high temperature multilayer metallization stack [3] is deposited on the backside of the cavity. The piezoresistive mesas shown in Fig. 5 are configured in a Wheatstone bridge circuit. This structure completes the basic SiC pressure sensor.

A key challenge in fabricating a high-temperature pressure sensor is packaging. A forthcoming section discusses the general problems associated with high-temperature packaging. However, packaging for pressure sensors have their own challenges since the package itself can transmit stress to the sensor and cause the readings to deviate from predicted values. The packaging strategy adopted at NASA GRC for pressure sensors decouples thermomechanical interactions between the sensor and packaging components. The existence of stress during thermal cycling is generally recognized to induce fatigue at several critical areas of the system, such as at the wirebond/pad interface. The packaging methodology adopted here borrows from the traditional flip-chip bump packaging technology that allows a chip (or a chip array) to be intimately attached to another level of metallization via either a through-hole in the package substrate or directly on corresponding interconnects on the package substrate. The approach eliminates wirebonds, thereby making it possible to pack chips more densely than previously possible, and undesired effects caused by large differences in the coefficient of thermal expansion between stainless steel and sensor.

The basic components of the package are shown in Fig. 6(*a*).

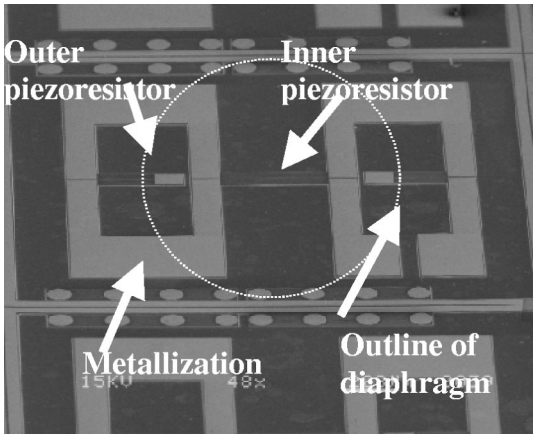

Fig. 5 SEM micrograph of top view of a 6H-SiC pressure sensor cell with patterned metallization and four piezoresistors. The circular patterns are ohmic contact test structures.

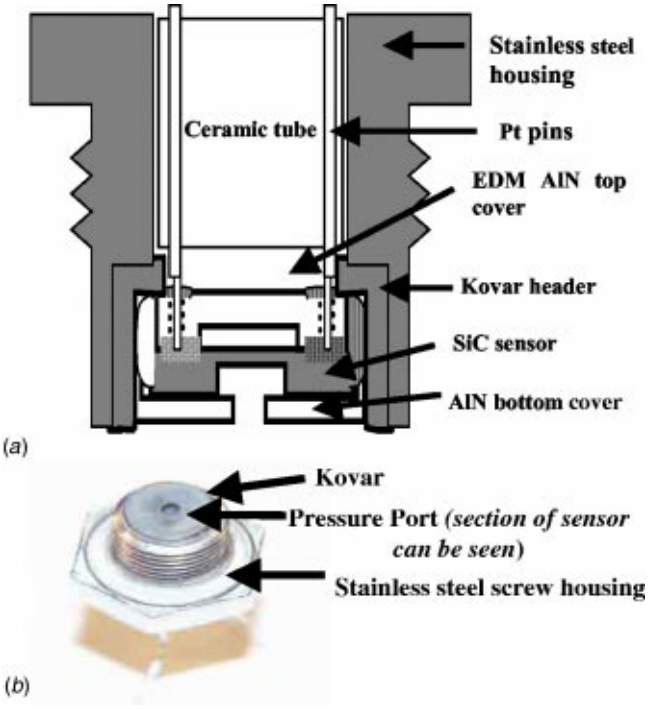

Fig. 6 (*a*) Sub-assembled 6H-SiC sensor unit for insertion into the stainless steel screw housing; (*b*) fully packaged 6H-SiC pressure transducer with pressure port and pins visible

The bottom substrate consists of an insulating dielectric material with thermomechanical properties similar to that of SiC (i.e., aluminum nitride). The top and bottom covers are chosen to minimize stress caused by coefficient of thermal expansion (CTE) mismatches. The packaging process also traps an air pocket within the reference cavity and provides hermetic sealing for the sensor after encasement between the top and bottom cover substrates. This direct chip attach (DCA) process eliminates the need for wirebonds and the associated failure mechanisms at high temperature. A representative fully packaged transducer is shown in Fig. 6(*b*).

The net output voltage as a function of applied pressure at various temperatures is shown in Fig. 7. The full-scale output (FSO) at a maximum applied absolute pressure of 200 psi was 32.5 mV at room temperature for an input voltage of 5V, which was in good agreement with prediction [4]. This indicated a sensitivity of 32.5 μV/V/psi. The excellent linearity obtained could

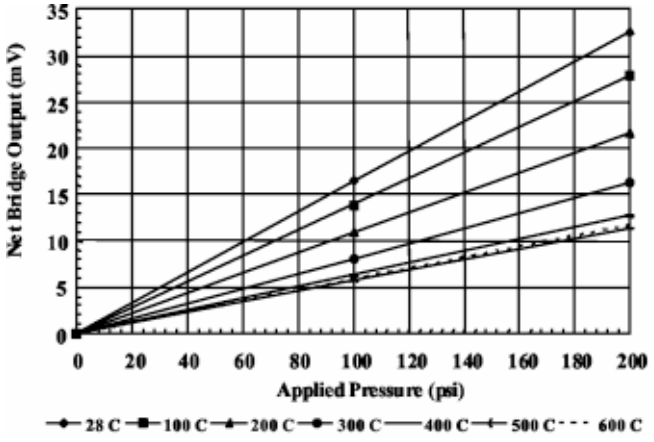

Fig. 7 Net bridge output voltage of 6H-SiC pressure sensor as function of pressure at various temperatures

be largely attributed to the thermomechanical stress management adopted with the packaging, however, more data points will be needed to improve the measurement resolution.

Thus, a hermetically sealed 6H-SiC pressure transducer operated at 600°C and at 200 psi has been demonstrated using this innovative packaging method. While this packaging method is expected to enable extended high-temperature device functionality, long-term reliability characterization will be performed in the future to validate such capability and demonstrate a new generation of single crystal SiC MEMS based pressure transducers potentially capable of long-term operation at 600°C in air.

High-Temperature Electronic Nose Technology. The detection of the chemical signature of the emissions of an engine may indicate the efficiency and health of the engine. Rapid or sudden changes in the emissions produced by combustion indicate changes in the engine combustion process. The automotive industry has made significant progress in emissions reduction as well as monitoring the health of the catalytic converter by including oxygen sensors in the engine exhaust stream and using these sensors for combustion control [6]. Ideally, an array of sensors placed in the emission stream close to the engine could provide information on the gases being emitted by the engine. However, there are very few sensors available commercially which are able to measure the components of the emissions in situ in harsh environments such as an engine. The harsh conditions and high temperatures inherent near the reaction chamber of the engine render most sensors inoperable. The notable exception to this is the automotive oxygen sensor. Thus, in order to detect the other species present in an emissions stream, the development of new high-temperature chemical sensor technology is necessary.

The development of sensors to measure emissions in harsh environments has been ongoing for a considerable time [7]. However, the characterization of a complex chemical environment is difficult with only one sensor. Thus, integration of a number of the individual high temperature gas sensors including hydrocarbons, oxygen, NO_x has begun. Development of such a microfabricated gas sensor array operable at high temperatures and high flow rates would be a dramatic step towards realizing the goal of monitoring/control of emissions produced by an engine, a power generation unit, or a chemical reactor. Such a gas sensor array would, in effect, be a *high-temperature* electronic nose and be able to detect a variety of gases of interest. Several of these arrays could be placed around the exit of the engine exhaust to monitor the emissions produced by the engine. The signals produced by this nose could be analyzed to determine the constituents of the emission stream and this information then could be used to monitor the health of the system producing those emissions.

The concept of an electronic nose has been in existence for a number of years [8]. Commercial electronic noses for near-room temperature applications presently exist and there are a number of efforts to develop other electronic noses. However, these electronic noses often depend significantly on the use of polymers and other lower temperature materials to detect the gases of interest. These polymers are generally unstable above 400°C, and thus would not be appropriate for use in harsh engine environments. Thus, a separate development is necessary for a high-temperature electronic nose.

The development of such a high-temperature electronic nose has begun using high-temperature gas sensors being developed for a range of applications [7,9]. There are three very different sensor types that constitute the high-temperature electronic nose: resistors, electrochemical cells, and Schottky diodes. Each sensor type provides qualitatively very different types of information on the environment being monitored. This is in contrast to a conventional array of sensors that generally consists of elements of the same type, e.g., SnO_2 resistors doped differently for different selectivities. Each sensor in this conventional system provides information available through the differently doped SnO_2 resistors (reactions occurring on the surface of the sensor film) but do not provide

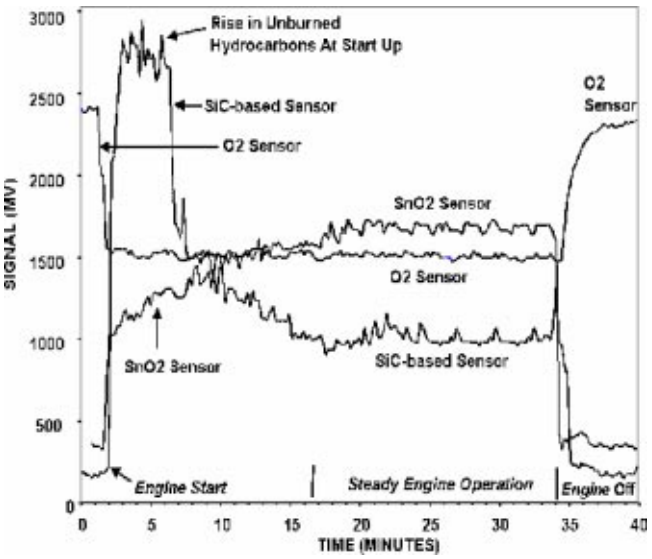

Fig. 8 The response of a sensor array composed of a tin oxide based sensor (doped for NO_x sensitivity), an oxygen sensor, and a SiC-based hydrocarbon sensor in an engine environment

information that can be determined by electrochemical cells or Schottky diodes. It is envisioned that the elements of the high-temperature electronic nose array (resistors, diodes, and electrochemical cells) will have very different responses to the individual gases in the environment. This information will be integrated and interpreted using neural net processing to allow a more accurate determination of the chemical constituents of harsh, high temperature environments.

A first-generation high-temperature electronic nose has been demonstrated on a modified automotive engine. Figure 8 shows the response of a tin oxide based sensor (doped for NO_x sensitivity), an oxygen (O_2) sensor, and a SiC-based hydrocarbon C_xH_y sensor. The figure shows the individual sensor responses during the initial start of the engine, a warm-up period, a steady state operation period, and at the engine turn-off. The sensors were operated at 400°C while the engine operating temperature was 337°C. Each sensor has a different characteristic response. The oxygen sensor shows a decrease in O_2 concentration while the NO_x and C_xH_y concentrations increase at start-up. The hydrocarbon concentrations decrease as the engine warms up to steady-state while the NO_x concentration increases before stabilizing. The O_2, NO_x, and C_xH_y concentrations all return to their start-up values after the engine is turned off. These results are qualitatively consistent with what would be expected for this type of engine. They also show the value of using sensors with very different response mechanisms in an electronic nose array: the information provided by each sensor was unique and monitored a different aspect of the engine's chemical behavior. Significant further work is necessary to achieve operation temperatures of 600°C.

Packaging of Harsh Environment Devices and Sensors

The operation of electronics and sensors in harsh environments requires packaging techniques beyond those of conventional lower temperature technology. For in-situ aerospace engine monitoring, electronics and sensors must operate at temperatures of at least 500°C and at gas turbine pressures up to 3000 lb psi. This is a chemically reactive gas environment composed of species such as oxygen in air, hydrocarbon/hydrogen in fuel, and catalytically poisoning species, such as NO_x and SO_x, in the combustion products. Additionally, the sensors and electronics may be exposed to high vibration. Thus, the packaging materials and basic components must withstand temperatures of at least 500°C, chemical corrosion (especially oxidizing and reducing), and potentially high

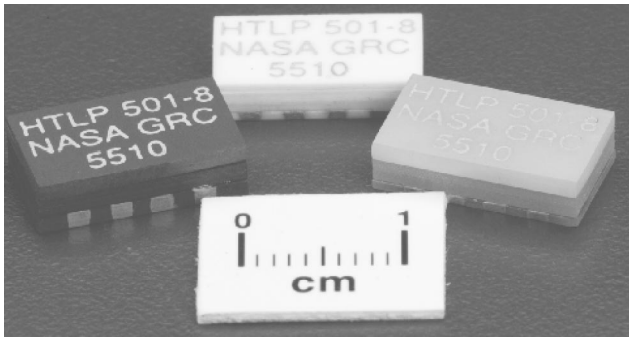

Fig. 9 Prototype high-temperature electronic package composed of ceramic substrates and Au thick-film metallization for harsh environment systems

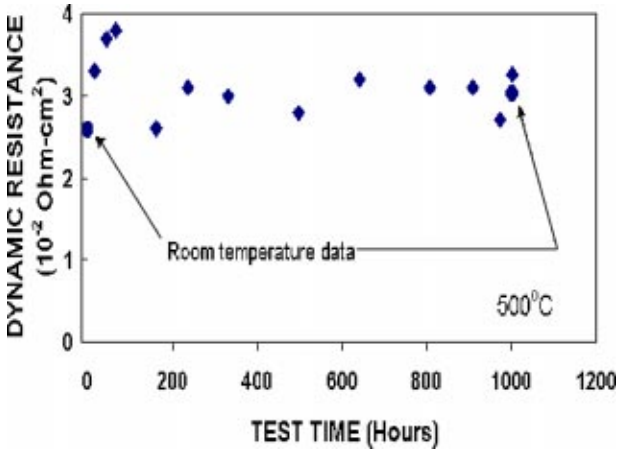

Fig. 10 Forward resistance of a packaged SiC Schottky diode at 500°C in an oxidizing environment for over 1000 h

dynamic pressure and high acceleration. These packaging materials and components include the substrate, metallization material(s), electrical interconnections (such as wire-bonds), and die-attach. These are far beyond standard operation conditions for most advanced (commercial) electronics/sensors, and thus new technology development is necessary.

The packaging technology also needs to be tailored for the device being packaged. The packaging needs of pressure sensor technology has been discussed earlier in this paper. Gas chemical sensors, gas flow sensors, and accelerometers are other sensors which each have their own packaging requirements. Further, SiC high-temperature electronic devices for signal processing and communication have their own packaging requirements. Therefore, as noted elsewhere in this paper, packaging technology for harsh environment operable devices has become a key issue for in-situ testing and the commercialization of harsh environment microsystems.

One of the major challenges of high temperature sensor packaging is to satisfy the requirements for mechanical operation of the systems. Both the operation and performance of microsystems based sensors can be very sensitive to external mechanical forces. One major undesired external force is the thermal mechanical stress generated in the die-attach structure due to the mismatch of coefficients of thermal expansion (CTE) between the die material (such as SiC), the substrate material, and the die-attaching material. The thermal stress of the dieattach structure must be suppressed in order to achieve precise and reliable device operation because the thermally induced stress may generate unwanted device outputs in response to the changes in thermal environment. In extreme cases, thermal stress can cause permanent mechanical damage to the die-attach due to the extremely wide temperature range experienced in these harsh environment applications. The thermal mechanical stability is one of most important criteria in die-attach material selection.

Ceramic substrates and precious metal thick-film metallizations have been proposed for hybrid [10] and chip-level packaging of high temperature, harsh environment operable microsystems [11] based on their excellent stabilities at high temperature and chemically reactive environment. Aluminum nitride was proposed to package high temperature SiC MEMS because this material possesses a low thermal expansion coefficient [11,12].

Recently, a chip-level electronic package has been designed, fabricated, and assembled for high-temperature harsh environment microelectronic systems using ceramic (aluminum nitride and aluminum oxide) substrates and gold (Au) thick-film metallization (see Fig. 9). The electrical interconnection system of this advanced packaging system, including the thick-film metallization and wirebond, has been successfully tested at 500°C in an oxidizing environment for over 5000 h. A compatible low resistance die-attach scheme using Au thick-film material as a conductive bonding material has also been developed to package SiC microsystems.

This complete electrical interconnection system was tested using an in-house-fabricated SiC semiconductor test chip (Schottky diode) in an oxidizing environment over a temperature range from room temperature to 500°C for more than 1000 h. The thick-film-based interconnection system demonstrated the required low (2.5 times of the room-temperature resistance of the Au conductor) and stable (3% decrease in the first 1500 hrs of continuous test) electrical resistance at 500°C in an oxidizing environment. Also, the electrical isolation impedance between the printed wires that were not electrically joined by a wirebond remained satisfactorily high (>0.4 GΩ) at 500°C in air. The attached SiC diode demonstrated low ($<3.8\times10^{-2}$ Ω-cm^2) and relatively consistent forward resistance from room temperature to 500°C, as shown in Fig. 10. This implies the operability of the die-attach between the room temperature and 500°C. Preliminary results from finite element analysis of a SiC die-attach with 1 mm^2 die on an aluminum nitride substrate show low thermal stress [13]. These results indicate that this prototype package and the compatible die-attach scheme meet the basic requirements for low-power long-term operation in high-temperature and chemically reactive environments.

Improved SiC Electronic Materials

Compared to silicon wafer standards, present-day SiC wafers are small, expensive, and generally of inferior quality. In addition to high densities of crystalline defects such as micropipes and closed-core screw dislocations, commercial SiC wafers of the 4H and 6H polytypes also exhibit significantly rougher surfaces, and larger warpage and bow than is typical for silicon wafers [14]. Further, problems with the quality of the oxide grown on SiC have led to difficulty in the application of Metal-Oxide-Semiconductor Field Effect Transistor (MOSFET) technology. The vast majority of semiconductor integrated circuit chips in use today in silicon rely on MOSFET technology. This disparity is not surprising considering that silicon technology has undergone several decades of commercial process refinement. While significant advances have nonetheless been made in the development of SiC electronics and sensors (as seen in this paper), the existence of improved SiC starting material should significantly enhance the development of these technologies.

Recent work has been aimed at improving the quality of the SiC starting material on which devices are fabricated by eliminating the defects and growing step-free SiC surfaces. The formation of SiC mesa surfaces as large 0.2×0.2 mm completely free of a single atomic step was recently reported [15]. As described in

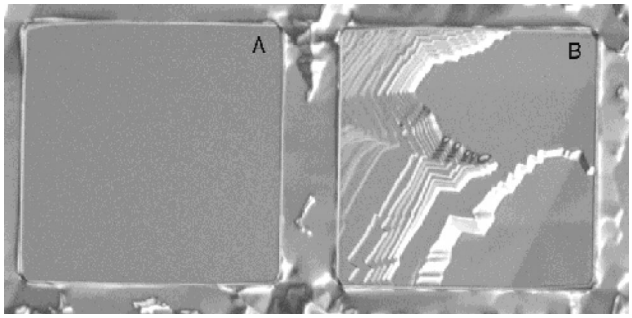

Fig. 11 Optical Nomarski images of two adjacent 200 mm square mesas on a 4H-SiC wafer. Mesa A is step-free and mesa B contains a screw dislocation which provided a continuous source of steps during growth.

[15], step-free surfaces are produced on commercially purchased on-axis 4H- or 6H-SiC wafers by first dry etching trench patterns into the wafer surface to form an array of isolated growth mesas. Pure stepflow epitaxial growth, carried out under conditions that suppress two-dimensional (2-D) terrace nucleation, is then used to grow all initial surface steps on top of the mesa over to the edge of the mesa, leaving behind a top mesa surface that is completely free of atomic steps.

Figure 11 is an optical image of a 4H wafer showing two adjacent 200 μm mesas fabricated using this process. Mesa A on the left is featureless and mesa B on the right contains a hillock which dominates the surface morphology. Mesas that initially contain screw dislocation (SD) defects cannot be flattened due to the continual spiral of new growth steps that emanate from screw dislocations during epitaxial growth. As reported in [15], the high density of screw dislocations (SDs) limited the yield and size of step free mesas.

Building from results such as those seen in Fig. 11, the achievement of 3C-SiC heteroepitaxial films completely free of double-positioning boundaries (DPB) and stacking fault (SF) defects on step-free 4H-SiC and 6H-SiC substrate mesas has been realized [16]. To overcome the mesa size limit imposed by screw dislocations, a lateral ''web-growth'' process has been developed. The process overgrows and thus terminates the c-axis propagation of screw dislocations, thereby enabling larger-area atomically flat surfaces to be realized on commercial SiC wafers. Figure 12 shows (a) pre-growth and (b) post-growth SEM image taken from a plus-shape (pre-growth) mesa. The epitaxially grown thin lateral cantilevers have completely spanned (or ''webbed'') the arms of the plus-shaped mesa, forming a seamless nearly hexagonal-shaped ''tabletop'' sitting on top of a plus-shaped support structure. The formation of this structure indicates that enhanced lateral web growth occurred at the inside (i.e., concave) corners of mesa shapes, which combined with hexagonal growth faceting to produce the result shown in Fig. 12.

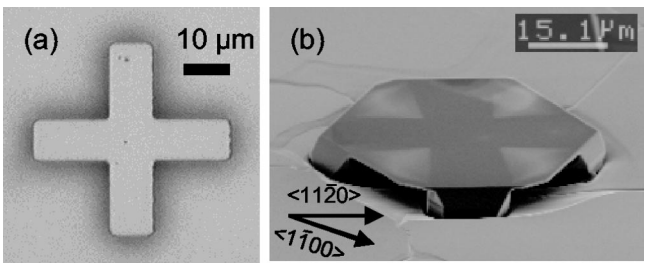

Fig. 12 (*a*) Pre-growth optical photo of cross-shaped mesa; (*b*) post-growth SEM image of "webbing" formed following 60-min growth

Step-free surfaces have also been proposed as being ideal for realizing greatly improved heteroepitaxial growth of films with much lower dislocation densities [16]. For example, previous efforts to grow heteroepitaxial films of the 3C-SiC polytype on Si and 4H/6H-SiC substrates have resulted in 3C-SiC films with extended crystal defects including DPB's and/or stacking faults SF's. The ability to reproducibly obtain 3C-SiC heteroepitaxial films free of extended crystal defects could enable advantageous new electrical devices.

Thus, significantly improved growth of SiC material has been achieved. This growth is not only of 4H and 6H-SiC on commercial SiC substrates but also the 3C-SiC polytype. Further work needs to be done to characterize these new growth mechanisms, but also to realize the advantages in device properties that use of these new materials can provide.

Summary

The realization of a future intelligent engine depends on the development of both hardware and software including electronics and sensors. The development of electronics and sensors for engine applications is problematic due to the harsh environments in which the devices must operate. NASA GRC is active in developing electronics and sensors for these environments. These include SiC-based electronics, high-temperature pressure sensors, a high-temperature electronic nose, and appropriate packaging technologies. The advent of improved electronic materials has the potential to significantly affect the quality and capabilities of the devices fabricated for these environments. The eventual goal of this work is the formation of high-temperature, integrated microsystems which sense, process, and communicate the information, and eventually modify engine conditions based on this information. When such smart components become available, an intelligent engine composed of smart components may become a reality.

Acknowledgments

We gratefully acknowledge the contributions of those whose made this review paper and its contents possible: Dr. L. Matus, Dr. M. Zeller, D. Sokolowski, Dr. J. Lei, P. Raitino, G. Fralick, J. Wrbanek, Dr. M. Lienhard, Dr. D. Larkin, E. Benavage, L. Keys, and Dr. P. Abel of NASA GRC, D. Androjna, B. Osborn, J. Heisler of Akima/NASA GRC, A. Trunek, D. Spry, and V. Thomas of OAI, D. Lukco of QSS, E. Savrun of Sienna Technologies, Inc., C. C. Liu and B. Ward of Case Western Reserve University, D. Makel of Makel Engineering, Inc., P. Dutta and B. Patton of the Ohio State University. The Glennan Microsystem Initiative activities mentioned in this paper have been funded in part by the UEET program.

References

[1] Neudeck P. G., 1999, *The VLSI Handbook*, CRC Press LLC, ed., Wai-Kai Chen, Ch. 6.
[2] Neudeck P. G., 2000, ''600°C Logic Gates Using Silicon Carbide JFET's,'' Government Microcircuit Applications Conference, March 20–23, Anaheim, CA., pp. 421–424.
[3] Okojie, R. S., Spry, D., Krotine, J., Salupo, C., and Wheeler, D. R., 2000, ''Stable Ti/$TaSi_2$/Pt Ohmic Contacts on N-Type 6H-SiC Epilayer at 600°C in Air,'' Mat. Res. Soc. Symp. Proc., 622, Wide-Bandgap Electronic Devices, R. J. Shul, F. Ren, M. Murakami, and W. Pletschen, eds., Materials Research Society, Warrandale, PA.
[4] Okojie, R. S., Beheim, G. M., Saad, G. J., and Savrun, E., 2001, ''Characteristics of a Hermetic 6H-SiC Pressure Sensor at 600°C,'' AIAA Pap., 2001–4652.
[5] Beheim, G. M., and Salupo, C. S., 2000, ''Deep RIE Process for Silicon Carbide Power Electronics and MEMS,'' Wide-Bandgap Electronic Devices, R. J. Shul, F. Ren, M. Murakami, and W. Pletschen, eds., Materials Research Society, Warrandale, PA.
[6] Logothetis, E. M., 1991, ''Automotive Oxygen Sensors,'' Chemical Sensor Technology, N. Yamazoe, ed., Kodansha Ltd., **3**, pp. 89–104.
[7] Hunter, G. W., Liu, C. C., and Makel, D., 2001, CRC Press LLC, ed., M. Gad-el-Hak, Ch. 22.
[8] Gardner, J. W., and Bartlett, P. N., 1994, ''A Brief History of Electronic Noses,'' Sens. Actuators B, **18**(1–3), pp. 211–220.
[9] Hunter, G. W., Neudeck, P. G., Fralick, G., Makel, D., Liu, C. C., Ward, B.,

Wu, Q. H., Thomas, V., and Hall, G., 2001, ''Microfabricated Chemical Sensors for Space Health Monitoring Applications,'' AIAA Pap., 2001–4689.
[10] Salmon, J. S., Johnson, R. W., and Palmer, M., 1998, ''Thick Film Hybrid Packaging Techniques for 500°C Operation,'' Trans. Fourth Int. High Temperature Electronics Conference (HiTEC), June 15–19, Albuquerque, NM.
[11] Chen, L.-Y., Okojie, R. S., Neudeck, P. G., and Hunter, G. W., 2001, ''Material System for Packaging 500°C MicroSystems,'' MRS Proc., Symposium N: Microelectronic, Optoelectronic, and MEMS Packaging, San Francisco, CA, April 16–20.
[12] Chen, L.-Y., Hunter, G. W., and Neudeck, P. G., 2000, ''Silicon Carbide Die Attach Scheme for 500°C Operation,'' MRS 2000 Spring Meeting Proceedings-Wide-Bandgap Electronic Devices (Symposium T), San Francisco, CA, April 10–14.
[13] Lin, S. T., 2001, ''Packaging Reliability of High Temperature SiC Devices,'' NASA Contract Report.
[14] Powell, J. A., and Larkin, D. J., 1997, ''Processed-Induced Morphological Defects in Epitaxial CVD Silicon Carbide,'' Phys. Status Solidi B, **202**, pp. 529–548.
[15] Powell, J. A., Neudeck, P. G., Trunek, A. J., Beheim, G. M., Matus, L. G., Hoffman, R. W. Jr., and Keys, L. J., 2000, ''Growth of Step-Free Surfaces on Device-Size—(0001)-SiC Mesas,'' Appl. Phys. Lett., **77**, pp. 1449–1451.
[16] Neudeck, P. G., Powell, J. A., Trunek, A. J., Huang, X. R., and Dudley, M., 2002, ''Growth of Defect-Free 3C-SiC on 4H- and 6H-SiC Mesas Using Step-Free Surface Heteroepitaxy,'' to be published in Silicon Carbide and Related Materials, Mater. Sci. Forum, **389–393**, pp. 311–314.

Heat Transfer and Friction Factors for Flows Inside Circular Tubes With Concavity Surfaces

Ronald S. Bunker
General Electric Research Center,
One Research Circle, ES-119,
Niskayuna, NY 12309
Fellow ASME

Katherine F. Donnellan
General Electric Power Systems,
Schenectady, NY 12345

Heat transfer and friction coefficients measurements have been obtained for fully developed, turbulent internal flows in circular tubes with six different concavity (dimple) surface array geometries. Two different concavity depths and three different concavity array densities were tested using tube bulk flow Reynolds numbers from 20,000 to 90,000. Liquid-crystal thermography was used to measure the temperature distributions on the outside of the concavity tubes. Using the average heat transfer coefficient for the fully developed region, the overall heat transfer enhancements are compared to baseline smooth tube results. Friction coefficients are also compared to values for a smooth tube. Dimple depths of 0.2–0.4 relative to the dimple surface diameter were used, with surface area densities ranging from 0.3 to 0.7. Dimple arrays were all in-line geometries. The results showed that heat transfer enhancements for dimpled internal surfaces of circular passages can reach factors of 2 or more when the relative dimple depth is greater than 0.3 and the dimple array density is about 0.5 or higher. The associated friction factor multipliers for such configurations are in the range of 4–6. The present study provides a first insight into the heat transfer and friction effects of various concavity arrays for turbulent flows. [DOI: 10.1115/1.1622713]

Introduction

The technology of cooling gas turbine components via internal convective flows of single-phase gases has developed over the years from simple smooth cooling passages to very complex geometries involving many differing surfaces. In many respects, the evolution of cooling passage geometries began in parallel with heat exchanger and fluid processing techniques, ''simply'' packaged into the constrained designs required of turbine airfoils; i.e., aerodynamics, mechanical strength, vibrational response, etc. The enhancement of internal convective flow surfaces for the augmentation of heat transfer was quickly improved through the introduction of rib rougheners or turbulators, and also pin banks or pin fins. These surface enhancement methods continue to play a large role in today's turbine cooling designs. With the advancements in materials and manufacturing technologies of the last decade, a drastically larger realm of surface enhancement techniques has become cost effective for use in the cooling of turbine airfoils. Turbulators and pins may now be of varying shape, orientation, segmentation, and size, essentially providing a continuous spectrum of possible geometries for achieving flow-surface interactions which serve to enhance local/global heat transfer coefficients. Such enhanced heat transfer comes at the inevitable price of increased pressure losses, though the range of methods now at a designers command allows a large degree of tailoring to take place. In all of these internal cooling methods which use modified surfaces, the enhancement features are projections from the surface into the flow, generally always substantially normal to the surface and the bulk flow direction.

Another class of surface enhancements results from the depression of features into the cooling channel walls, forming recesses rather than projections. Generically, such features are known as concavities, and may be formed in an infinite variation of geometries with various resulting heat transfer and friction characteristics. Concavity surfaces are commonly known for their drag reduction characteristics in external flows over bodies. The most famous example is golf balls, where they serve to delay the point of boundary layer separation, thereby reducing overall drag for the sphere, as shown by Bearman and Harvey [1]. Another example is external flow over a circular cylinder, for which Bearman and Harvey [2] show similar drag reduction effects to those of a sphere. Application of such concavity surfaces to external flows for marine vessels and airframes has been suggested by Kiknadze et al. [3], in which defined arrays of shallow concavities may cover the main hull or fuselage surfaces to prevent a thick boundary layer from forming, thereby reducing the drag. In a direct turbine application, Lake et al. [4] have demonstrated the use of discrete dimples placed on a model of a low-pressure turbine airfoil to reduce aerodynamic losses under low Reynolds number conditions.

Applications of concavity surfaces involving heat transfer were largely unknown until the recent dissolution of the Soviet Union, at which time Russian research from the 1980s began to surface. In the Russian nomenclature, concavity surfaces and the internal flows developed from them in confined geometries are alternately known as ''whirlwind'' cooling, ''tornadolike technology,'' ''orderly system of spherical hollows (OSSH),'' and ''orderly reliefs of spherical hollows (ORSH).'' In the broadest sense, these flows are one of a larger category known as ''vortex'' technologies, as described in the summary of Khalatov [5], which include various means for the formation of organized vortical or swirling flows in turbines.

The basic fluid dynamic condition for flow over concavities of spherical or cylindrical shape is well described in the study of Afanas'yev et al. [6]. A flow with boundary layer thickness less than the concavity surface diameter reacts with the cavity by flowing into the ''bowl,'' experiencing a separated region of some extent on the entry side. The spherical shape creates a pressure field within the bowl acting to collapse or concentrate the flow in the downstream portion of the recess, creating a vortex structure. In a steady flow over a symmetric spherical dimple, a pair of symmetric, counter-rotating vortices is ideally formed, as shown by the computational work of Isaev et al. [7]. In most real flow cases, only one vortex is created, and this vortex may move side-to-side with some frequency. This condition is said to ''expel'' flow from the cavity as an organized vortical structure. As the

Contributed by the International Gas Turbine Institute and presented at the International Gas Turbine and Aeroengine Congress and Exhibition, Atlanta, GA, June 16–19, 2003. Manuscript received by the IGTI December 2002; final revision March 2003. Paper No. 2003-GT-38053. Review Chair: H. R. Simmons.

vortex penetrates into and interacts with the mainstream flow, it provides a scrubbing action, which brings fresh core fluid to the surface for enhanced heat transfer. Because the motion is organized, rather than the more dissipative effect of shearing layers, the pressure loss is less than that observed with projecting obstructions such as turbulators. In fact, some cases of concavity surfaces have friction nearly the same as smooth surfaces.

Studies focusing on the heat transfer coefficients on a surface with a single hemispherical concavity show the fundamental potential of this method for thermal enhancement. Kesarev and Kozlov [8] show the detailed shear stress and heat transfer coefficient distributions relative to a flat surface for a single dimple in a wind tunnel wall with freestream turbulence levels from 7 to 22%. Overall heat transfer augmentations of up to 1.5 were observed. Schukin et al. [9] studied the effect of moderate freestream acceleration and deceleration over single dimples, showing that the dimpled surface resulted in approximately a 25% heat transfer improvement in all cases. Syred et al. [10] demonstrated the effects of surface curvature with a single dimple, yielding enhancements of more than 2 for concave surfaces.

The full potential for concavity surface heat transfer comes in the application of full-surface arrays of ordered concavities. Wind tunnel surface studies of Afanas'yev and Chudnovskiy [11] and also Afanas'yev et al. [12] for arrays of spacings from about 1 to 1.7 dimple diameters showed heat transfer enhancements of 30 to 40% with no increase in friction. Heat exchanger studies of Belen'kiy and co-workers [13,14] investigated the use of dimple arrays on the inner walls of annular passages and on tube surfaces of crossflow bundles, respectively. In some cases, as much as a 2.4 heat transfer enhancement was obtained with friction increases on the order of 2–4, relative to smooth surfaces. The variability of heat transfer and friction with dimple spacing and depth was pointed out, though not systematically investigated. Recent studies using arrays of hemispherical dimples in more confined channels with channel Reynolds numbers of up to 60,000 have been reported by Chyu et al. [15], Moon et al. [16], and Mahmood et al. [17]. In these studies, full-surface distributions of heat transfer coefficients were obtained showing the local cavity flow separation effects, and high thermal enhancement regions inside and downstream of the cavities. Heat transfer enhancements of 2–2.5 have been demonstrated with friction factor increases from about 1.5 to 4.

For application in turbine cooling, the summary of Nagoga [18] provides some insight into the effects of concavity array geometric parameters, namely the dimple depth-to-diameter ratio, the channel height-to-dimple diameter ratio, and the dimple spacing or surface density f. In general, shallow dimples yield lower heat transfer. A depth h/d of 0.5 at the limit of a hemisphere yields the highest heat transfer, but also a high friction factor. Higher density factors also result in higher heat transfer, with as much as a 2:1 improvement from f of 0.1 to 0.7. As the relative height decreases to close the distance between walls, the heat transfer increases. Enhancement of up to 200% is seen in very ''tight'' channels, but with more drastic increases in friction. An important feature to note about dimpled surfaces is the analogous form of the friction coefficient to that seen for rough surfaces, i.e., a decreasing magnitude of coefficient as Re increases, and a limiting value for a ''fully rough'' zone. A critical Re is demonstrated above which the friction coefficient does not change.

The foregoing literature summary shows that the reported studies concerning the thermohydraulics of surfaces with concavities have focused on flat plates, low aspect ratio channels, and certain external flow heat exchanger geometries. No investigations have been reported for the application of concavity arrays within circular tubes. The use of such arrays in the confined and axisymmetric flows of circular tubes has many potential applications, including the cooling of gas turbine components. The present study provides a first insight into the heat transfer and friction effects of various concavity arrays for turbulent flows.

Fig. 1 Sample test channel with machined concavities

Experimental Apparatus and Method

A test apparatus was designed to measure the local heat transfer coefficients and overall pressure drop across different dimpled (concavity array) tubes and one smooth tube. Six different dimple/dimple array geometries were machined inside aluminum tubes. An example of a test channel is shown in the photo of Fig. 1. Each channel was prepared by (1) first cutting the tubes in half to gain access to the interior surface, (2) machining the concavities with a 12.7-mm ball-nosed end mill, and (3) welding the tube halves together with an electron beam. Additional silicon sealant was applied to the exterior seams after welding to assure complete sealing of any pin holes or cracks. Any burrs were polished off the surface of the tubes in preparation for the assembly of the heater and liquid crystal sheets. All tubes had a 3.81-cm interior diameter. Two tube wall thicknesses were employed, 3.175 and 6.35 mm, to obtain concavity arrays of differing depths. Aluminum was selected to allow the local thermal response of the variable wall thickness (i.e., due to dimples) to be smoothed out, thereby providing surface averaged heat transfer coefficients as a function of axial location along the tube. This method also avoided severe viewing issues associated with the direct application of liquid crystals to the flow path concavities.

As shown in Table 1, two concavity surface diameters were used, as well as two concavity depths, which represent different sections of a full hemisphere. This resulted in two sets of tests with dimple diameter-to-tube diameter ratios d/D of 0.229 and 0.271, and dimple depth-to-diameter ratios h/d of 0.233 and 0.394. The dimple depth is that measured at the center of the concavity. For reference, the maximum h/d would be 0.5 for a full hemisphere. Figure 2 shows the cross section of each tube layout, including the angles between concavity centerlines and the number of concavities around the perimeter. All cases used in-line dimples axially. The dimple density f is defined as the ratio of projected dimple surface area on the tube ID to the smooth wall surface area. This density is a measure of the packing of the dimple array. By varying the axial spacing of the dimple rows, a range of f values from 0.339 to 0.704 was obtained.

The test facility as shown in Fig. 3 was composed of an air cooler, a plenum, an insulated developing flow section, the aluminum test section, a data acquisition system, and a liquid-crystal thermography system. A steady flow rate of air is supplied to the test by an in-house compressor, and metered through a calibrated sonic venturi. Flow is developed in a smooth section of insulated

Table 1 Test channel concavity specifications

Tube	Tube ID D (mm)	Concavity diameter d (mm)	Concavity depth h (mm)	h/d	d/D	Concavity density f
2	38.1	10.312	4.064	0.394	0.271	0.704
6	38.1	10.312	4.064	0.394	0.271	0.582
4	38.1	8.738	2.032	0.233	0.229	0.506
3	38.1	10.312	4.064	0.394	0.271	0.473
5	38.1	8.738	2.032	0.233	0.229	0.418
1	38.1	8.738	2.032	0.233	0.229	0.339

phenolic tubing attached to the aluminum test section by a rabbet fit and epoxy. The aluminum test section is wrapped with four layers of material as depicted in Fig. 4. The first layer is thin double-sided photo-mounting tape. The second layer consist of a thin-foil heater, which allows for a low-voltage, high dc current to distribute a uniform heat flux across the entire length of the test section. The heater consists of a 0.0127-mm layer of Inconel deposited on a 0.102-mm backing of Kapton. The third layer is another piece of double-sided tape. The final layer is a sheet of Hallcrest thermochromic liquid crystals (40C5W) with a wide-band response in the range between 40°C and 45°C. The current delivered to the Inconel heater was measured using a 50-mV, 100-amp shunt resistor. The power delivered to the test surface ranged from 50 to 250 W depending on the tube being tested. Thermocouples were used to measure the air temperature inside the tube, inside the plenum, and the ambient temperature. These thermocouples are used to measure the temperature increase of the flow inside the test section. A thermocouple was also taped to the middle of the test section on the outside of the liquid crystals for use in calculating heat losses to ambient. Pressure drop was measured using a static pressure wall tap located at the entrance of the dimpled test section. An inclined water manometer was used to measure the pressure in inches of H_2O as compared to atmospheric pressure. These values were used to calculate the Fanning friction factor for each dimple configuration.

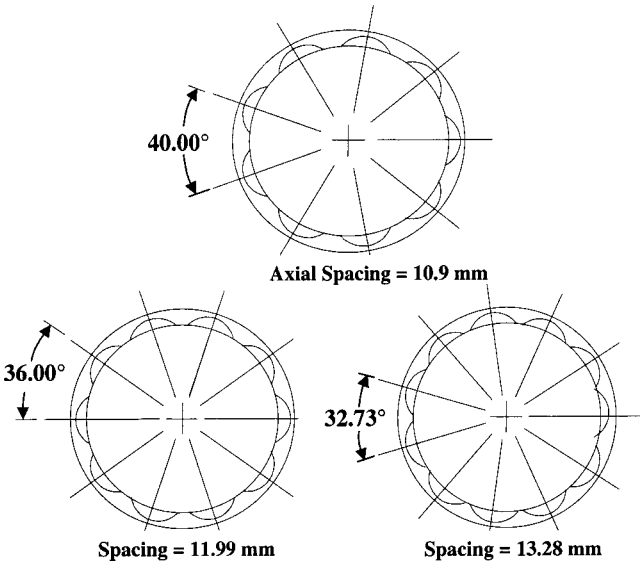

Fig. 2 Cross-sectional tube definitions

Convective heat losses to ambient were measured by filling the center and the outside of the aluminum and phenolic tubing with insulation. The test section was heated without any flow and monitored using four type-K thermocouples attached to the tube surface. Steady state was reached for three different power inputs covering the range of expected losses, 5, 10, and 15 W. The insulation on the outside of the test section was then removed and the test section was heated again until the liquid crystals (now visible as in an actual test) became completely colored using the same power levels. After curve fitting the two cases, the heat flux values were subtracted from each other to provide the overall convective ambient heat losses at the wall-to-ambient temperature ratios experienced during flow testing. The ratio of convective ambient heat losses to total power input was between 1.5% and 5% for the full range of test conditions with the dimpled tubes. The relative heat losses were from 5% to 16% for the smooth tube case, due to the much lower total power required without dimpled surfaces.

Surface temperature measurements were made using the steady-state liquid-crystal hue detection method of Farina et al. [19]. The liquid crystal sheet was calibrated by setting a temperature gradient across a 25.4-cm length copper bar with seven embedded thermocouples. An RGB (red-green-blue) image of the

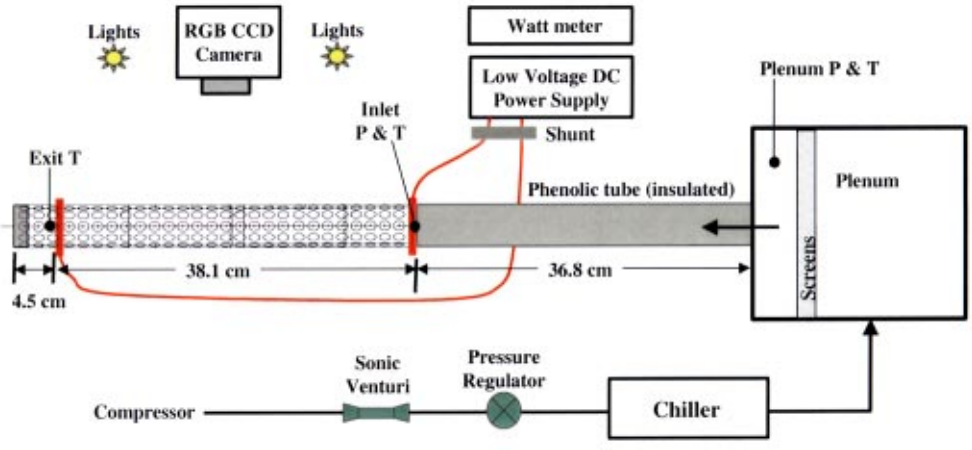

Fig. 3 Test facility and instrumentation

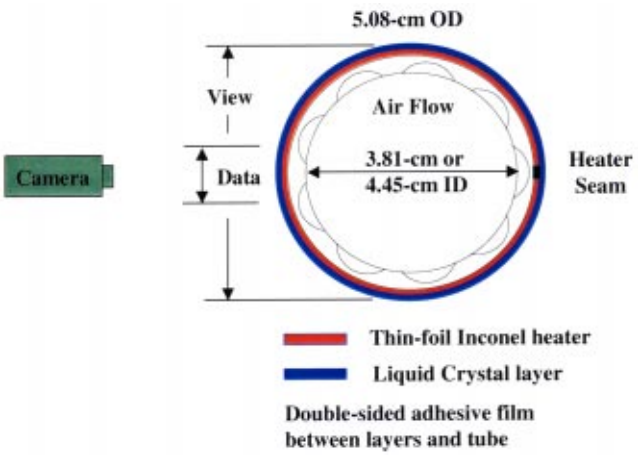

Fig. 4 Tube construction with heater

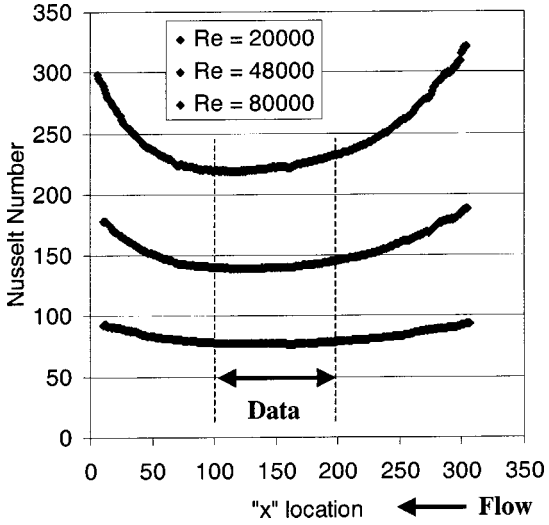

Fig. 6 Example of tube axial Nusselt number variation

heated bar was taken under the test lighting conditions and camera location, and the hue-temperature calibration extracted from a curve fit of the response.

The inlet bulk air temperature was measured with a thermocouple just prior to the heated section of tube, and the exit bulk air temperature just after the heated region. The average test channel air temperature was used as the representative air temperature for all heat transfer calculations, but most importantly for the middle third of the heated tube where fully developed conditions apply. The definition of the local heat transfer coefficient in this study is

$$h=(Q_{\text{total}}-Q_{\text{loss}})/A_{\text{smooth tube interior}}*(T_{\text{wall corrected}}-T_{\text{air average}}),$$

where Q_{wall} is the net input heater power $(Q_{\text{total}}-Q_{\text{loss}})$ per unit area after heat loss correction. $T_{\text{wall-corrected}}$ is the local interior aluminum wall temperature derived from the local liquid-crystal (heater) indicated temperature, with one-dimensional (1D) conduction corrections for the Kapton, adhesive, and average aluminum thickness. Inlet air temperatures were between 16°C and 19°C for all tests. Interior tube wall temperatures ranged between 30°C and 47°C for the various cases, providing wall-to-fluid temperature ratios from 1.048 to 1.095. For the range of test conditions encountered, the bulk air temperature rise through the whole test section is from 2°C to 10°C, and that for the fully developed data region only, 0.7°C to 3.5°C. In all tests, the minimum temperature potential between the heated surface and the bulk air was 14°C.

Figure 5 shows an example of the liquid-crystal display for a single heater setting and flow rate in one of the dimpled tubes. The color response is uniform in each axial location due to the aluminum, except for the inlet very near the power lead. To eliminate any concerns with viewing angle of the surface, only the center axial line of the images is used to provide data. The resulting Nu numbers, based upon smooth tube hydraulic diameter and surface area, are shown in Fig. 6 for three Re number examples in the same channel. The unheated upstream tube length is just under 10 hydraulic diameters. The total length to the center region of the aluminum tube then complies with the 10–15 diameters length for hydrodynamically developed flow. From the aluminum tube inlet at $x=300$ mm, the thermal entry region is clearly seen. The initial magnitude of this entry effect compared to the developed Nu region is about 1.4–1.5, very much in agreement with previous data such as that of Boelter et al. [20]. The present fully developed region is taken as that from $x=200-100$ mm, in accordance with the data of Ref. [20] that showed about 5 hydraulic diameters thermal entry length to reach within 10% of absolute fully developed Nu for a smooth tube. For the concavity tubes, the added turbulation is expected to reduce development lengths significantly. The results of this region are averaged to provide the overall Nu levels of this study. Downstream of $x=100$ mm, the effect of the exit conduction/convection loses is noted, with stronger magnitude as the overall internal Nu level is increased. This region is due primarily to the nonheated short section of channel at the exit. No corrections were made for these axial conduction inlet and exit effects. The only data used was that between x of 200 and 100 mm, such that very small variations in axial heat transfer coefficients resulted, leading to negligible axial conduction. Enhancement factors in this study are obtained by normalizing the measured Nu to that of a smooth tube, turbulent flow as determined by Dittus and Boelter [21] and shown in Holman [22].

The Fanning friction factor definition was used to calculate the friction coefficient for each test section in the unheated condition,

$$C_f=0.25*(D_h/L)*(\Delta P/0.5*\rho*V^2).$$

Normalized coefficient of friction, or enhancement factors, for the dimpled tubes were obtained using the measured smooth tube results at each Re number.

Using the single-sample methods of Kline and McClintock [23], the estimated uncertainty in local Nusselt numbers for these tests ranged from 11.5% to 12.5%. The higher uncertainty corre-

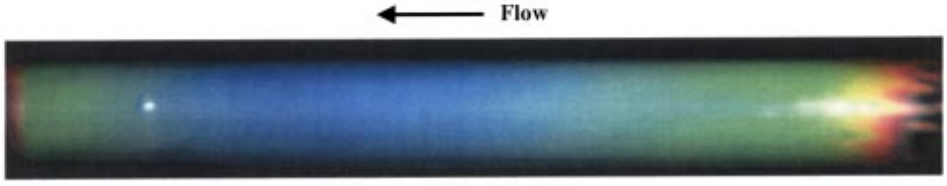

Fig. 5 Example of liquid crystal display on test section

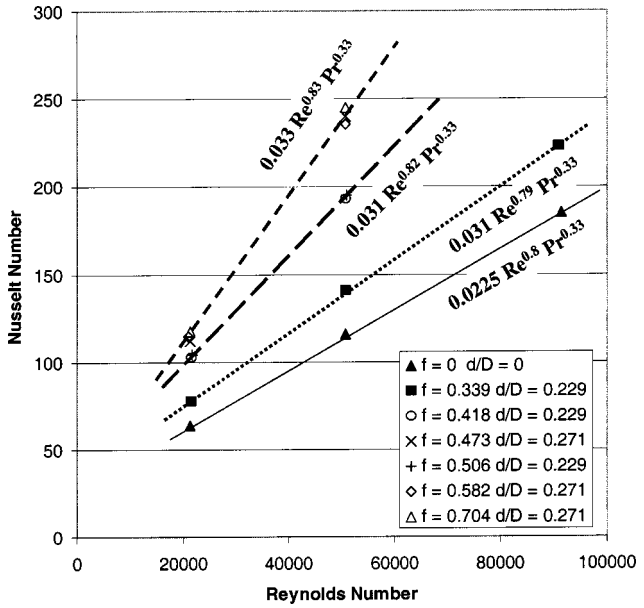

Fig. 7 Nusselt number correlations for all tests

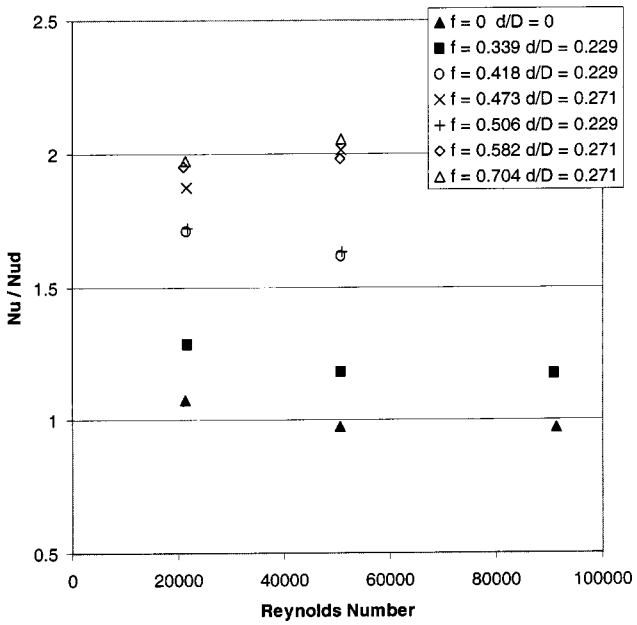

Fig. 8 Normalized Nusselt number all tests

sponds to high heat flux conditions at high power settings. The uncertainty in mass flow rate is 3%, which can lead to as much as 10% uncertainty in the coefficient of friction. The inclined manometer can result in as much as 15% uncertainty in pressure drop measurement at the very low Re for the smooth tube, declining to 1.2% at high values of Re. In the concavity tubes, the pressure drop uncertainty can be as high as 9% at lowest Re, but is typically under 1% for the majority of cases.

Results and Discussion

Heat Transfer. The smooth tube and concavity tube test results of the Nusselt number as a function of the Reynolds number are shown in Fig. 7. The characteristic dimension used in all cases for the Nusselt number and the Reynolds number is the smooth tube internal diameter. The data have been grouped according to several apparent curve-fitted relationships denoted in Fig. 7. The smooth tube Nu ($f=0$ and $d/D=0$) corresponds very nicely to the expected Re number dependence from previous literature. The least dense geometry of concavities $f=0.339$ and the shallowest depth case $d/D=0.229$ ($h/d=0.233$) exhibits very nearly the same Re dependence as the smooth tube, but with a somewhat enhanced magnitude.

Upon increasing the concavity density to greater than 0.4, the Re number dependence increases to $Re^{0.82}$ as shown by the greater line slope. This relationship holds for both higher density cases at the shallow depth. The highest Nu responses are shown for the three test cases of slightly deeper concavities. All concavity densities at the depth of $d/D=0.271$ ($h/d=0.394$) result in the same correlation of $Nu=0.033\ Re^{0.83}\ Pr^{0.33}$. It is intriguing that such seemingly small variations in depth and density should have so major an impact, though previous Russian investigations do follow this trend. Keep in mind that the present study also bases the Nu number on the smooth tube surface area, not the modified dimpled surface area. The added surface area of the dimples must play a role in the heat transfer enhancement, just as added turbulator surface area does for rib-roughened channels, but our interest is in the overall thermal augmentation which can be gained relative to a smooth tube.

Fig. 8 shows this same data in the Nusselt number enhancement format, where the normalizing Nu number is that of the smooth tube, fully developed turbulent flow Dittus-Boelter correlation provided above. The shallow and least dense concavity geometry provides an enhancement factor of about 1.2 over most of the Re range tested. Moving to more dense geometries increases the enhancement factor to 1.6 or 1.7, a very substantial amount. The slightly deeper concavity arrays all provide enhancement factors on the order of 2. From previous literature data in noncircular channels, these enhancement levels can be expected to hold at higher Re conditions (note that the present data do not all extend to Re of 90,000 due to power supply limitations).

The concavity array density dependence may be specifically highlighted as shown in Fig. 9. In this comparison, Re is seen to have a minor effect for each test case, but the two overall relative concavity depths used are clearly distinct from each other. For common density factors, the small increase in depth results in about 20% increased heat transfer. The density parameter shows the most overall effect on heat transfer augmentation from *f*

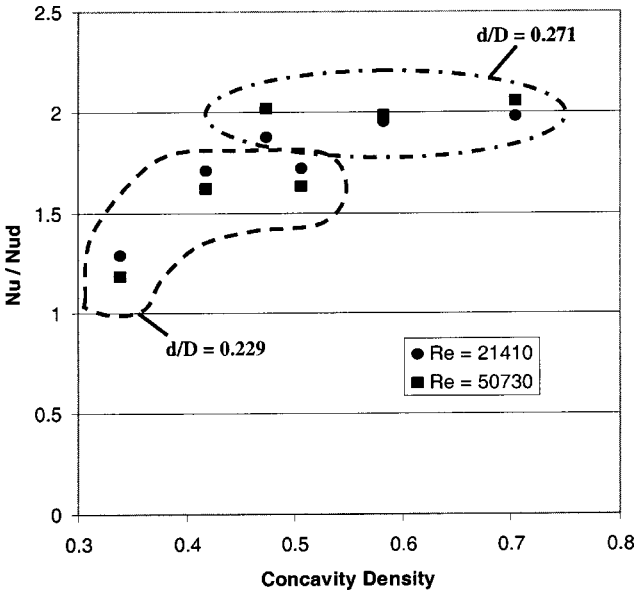

Fig. 9 Heat transfer enhancement with density *f*

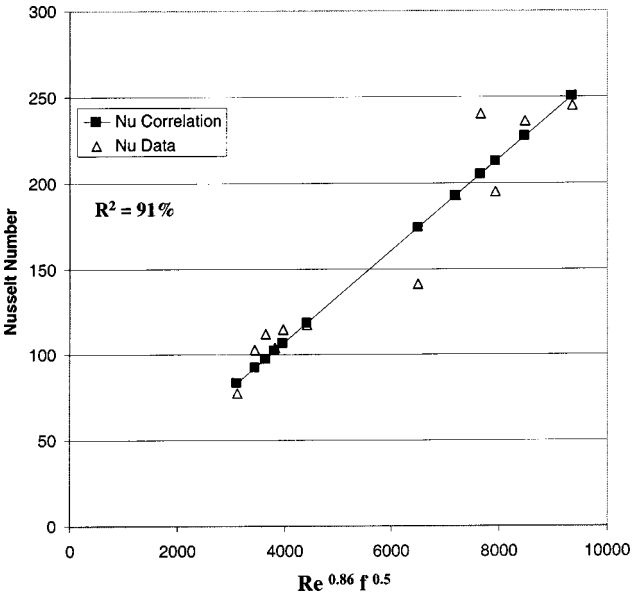

Fig. 10 General expression for Nu (Re, f)

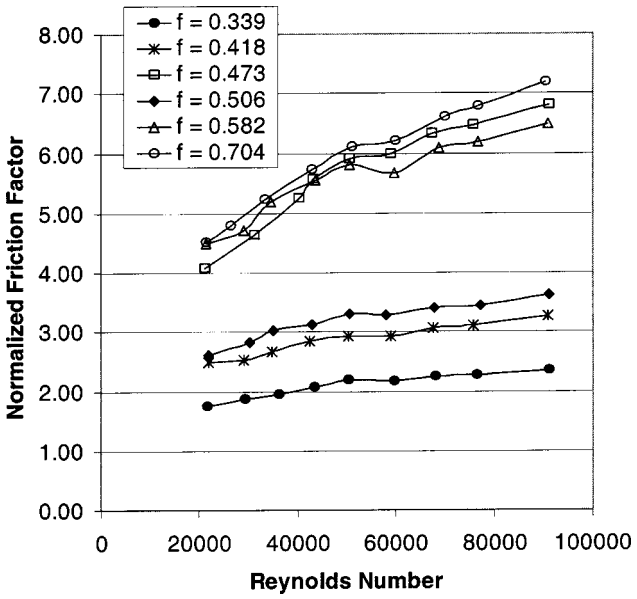

Fig. 12 Normalized friction factors

$=0.3-0.5$, but little effect above $f=0.5$. This indicates that additional enhancement may be obtained by making the concavities yet deeper.

The present data may be approximately fit to a correlation in terms of both Re and density f. Figure 10 shows this fit for the resulting dependence of $\mathrm{Re}^{0.86}\ f^{0.5}$. The parameter d/D (or h/d) does not appear in this form due to insufficient data at higher d/D values. Such data would help to further collapse the relationship into a compact expression with good fit.

Friction. The friction factor results somewhat mirror the heat transfer results in their variation with concavity depth and density. Figure 11 shows the Fanning friction factors for all tests, covering the full range from Re of 20,000 to 90,000. These data were all measured without wall heating. For comparison, the smooth tube correlation of Blasius is also shown as $C_f=0.079\ \mathrm{Re}^{-0.25}$. The present smooth tube data is about 25% above the Blasius correlation. This difference is attributed to measurement errors associated with mass flow and pressure drop. As in the heat transfer results, friction factor is greatest for the deeper concavity cases of $d/D=0.271$. In fact, these three test surfaces are essentially the same in terms of friction. For the shallower cases, again the least dense geometry shows the lowest friction of all concavity cases, while the other increased density surfaces are more elevated in effect.

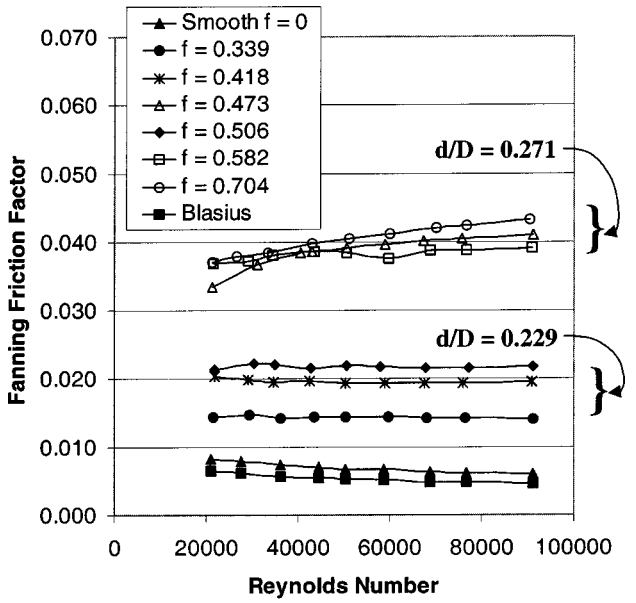

Fig. 11 Fanning friction factors

Figure 12 depicts this data as enhancement factors for friction, where for self-consistency the measured smooth tube data has been used as the normalization factor, not the Blasius correlation. At the shallow depth conditions, friction enhancement is relatively flat over the range of Re numbers, while the deeper cases all show a very strong dependence on Re number. Friction factor enhancements of 2–3 are observed for the shallow concavities, and 4–7 for the deeper concavities. The effect of concavity depth clearly dominates the friction factor enhancement.

Performance Comparison. Beyond the application of concavity tubes as an alternative heat transfer enhancement method, especially in cases where other forms of surface treatments may be difficult, the benefit of such surfaces must be shown in terms of performance. Figure 13 shows the normalized Nu number plotted directly against normalized friction factor, both for the present data and existing literature data.

In this comparison, the data of Chyu et al. [15] are for a rectangular channel with hemispherical concavities on the two wider sides. The channel aspect ratios were either 4 or 12. The concavity relative depth was $h/d=0.29$ and the density $f=0.5$. The channel Re number range of these tests was between 10,000 and 40,000. The data of Webb et al. [24] are for a circular tube with normal rib rougheners having blockages of 4% (i.e., 8% total blockage for the tube cross section). The turbulators are transverse to the bulk flow direction with a pitch-to-height ratio of 10. The large amount of other literature data for turbulated channels of various geometries and surface features is denoted by the general zone in which heat transfer is enhanced by 2–2.5, while friction is usually enhanced by 6–12 or more. Indeed, due to the very confined nature of the circular tube flow, the turbulated data of Ref. [24] shows a very high heat transfer enhancement, but with friction enhancements about four times as much as the heat transfer enhancement. The nature of flow and heat transfer for such turbulated channels is well documented for turbulent flows, showing significant flow separations and recirculating zones. While such flow disturbances lead to elevated heat transfer coefficients in the flow reattachment

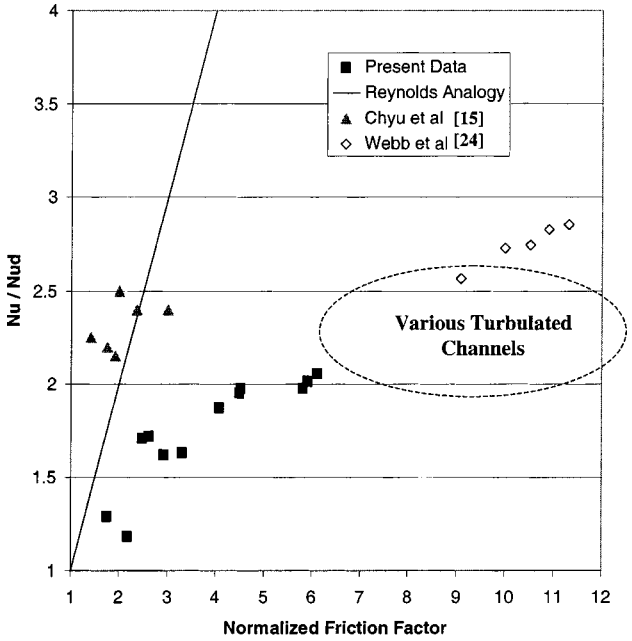

Fig. 13 Performance of concavity tubes

regions and on the rib top and forward faces, the mixing also causes very high friction coefficients. The concavity data of Ref. [15] are very encouraging, showing essentially a Reynolds analogy behavior. This is essentially the relationship between heat transfer and friction that many previous Russian studies have observed for flat plate concavity arrays. For turbine cooling purposes, this behavior is highly desirable in many situations. One cautionary note is appropriate though, in that data such as Ref. [15] are obtained with relatively large ratios of channel height to concavity depth (1.33 and greater for Ref. [15]). At such ratios, there is no significant interaction between concavity surfaces. Per Nagoga [18], at ratios of 0.5 and lower, interactions occur between the vortices expelled by each concavity, causing primarily an increase in friction coefficient with no additional heat transfer benefit.

The present circular tube concavity data lie between these two cases. The Reynolds analogy is not followed. The friction penalty, however, is not as high as that for turbulated circular channels. Just as the performance factor (normalized Nu divided by normalized Cf) is smaller for the turbulated circular tube than for a turbulated rectangular channel of equivalent blockage, so the performance factor for the concavity surface tube appears to be smaller than that for the concavity surface rectangular channel. From previous literature, it may be expected that deeper concavities will result in higher heat transfer, but also higher friction coefficient. Some of this pressure loss may be alleviated by rounding the edges of the concavities with little impact on the heat transfer coefficient.

Conclusion

The present study provides a first insight into the heat transfer and friction effects of various concavity arrays for turbulent flows in circular tubes. Heat transfer and friction coefficients measurements have been obtained for fully developed, turbulent internal flows in circular tubes with six different concavity (dimple) surface array geometries. Dimple depths of 0.2–0.4 relative to the dimple surface diameter were used, with surface area densities ranging from 0.3–0.7. The tube bulk flow Reynolds numbers were from 20,000 to 90,000. The results showed that heat transfer enhancements for dimpled internal surfaces of circular passages can reach factors of 2 or more when the relative dimple depth is greater than 0.3 and the dimple array density is about 0.5 or higher. Under such conditions, the fully developed Nusselt number may be correlated as $\mathrm{Nu}=0.033\,\mathrm{Re}^{0.83}\,\mathrm{Pr}^{0.33}$. The present data results in an overall Nu dependence of $\mathrm{Re}^{0.86}\,f^{0.5}$. The parameter h/d does not appear in this form due to insufficient current data at higher h/d values. The associated friction factor multipliers for such configurations are in the range of 4–6, resulting in a performance below that of Reynolds analogy behavior, but better than that due to rib rougheners within circular tubes.

Nomenclature

A = Smooth tube internal surface area
d = Concavity surface diameter
D_h = Smooth tube hydraulic diameter
f = Concavity array density, ratio of total projected concavity area on smooth tube to the total area of the smooth tube surface
C_f = Coefficient of friction, Fanning friction factor, $0.25*(D_h/L)*(\Delta P/0.5*\rho*V^2)$
h = Concavity depth at center
h = Heat transfer coefficient
k = Thermal conductivity
L = Test section pressure drop measurement length
Nu = Nusselt number, hD_h/k
$\mathrm{Nu_D}$ = Smooth tube $\mathrm{Nu}=.023\,\mathrm{Re}_{\mathrm{Dh}}^{0.8}\,\mathrm{Pr}^{1/3}$
P = Pressure
Pr = Prandtl number of air
$\mathrm{Re_D}$ = Flow Reynolds number, $\rho V D_\mathrm{h}/\mu$
T = Temperature
$T_{\text{ave wall}}$ = Average external test section temperature
T_{amb} = Ambient air temperature
$T_{\text{wall corrected}}$ = Interior corrected wall temperature
T_{air} = Measured air temperature, average of test region inlet and exit
V = Average flow velocity in tube
μ = Viscosity
ρ = Density

References

[1] Bearman, P. W., and Harvey, J. K., 1976, "Golf Ball Aerodynamics," Aeronaut. Q., **27**, May, pp. 112–122.
[2] Bearman, P. W., and Harvey, J. K., 1993, "Control of Circular Cylinder Flow by the Use of Dimples," AIAA J., **31**(10), pp. 1753–1756.
[3] Kiknadze, G. I., Gachechiladze, I. A., and Oleinikov, V. G., 2000, "Method and Apparatus for Controlling the Boundary or Wall Layer of a Continuous Medium," US Patent No. 6,119,987.
[4] Lake, J. P., King, P. I., and Rivir, R. B., 2000, "Low Reynolds Number Loss Reduction on Turbine Blades with Dimples and V-Grooves," AIAA Paper No. 00-0738, *38th AIAA Aerospace Sciences Meeting and Exhibit*, Reno.
[5] Khalatov, A. A., 2001, "Vortex Technologies in Aerospace Engineering," *Proceedings of the U.S.-Ukrainian Workshop on Innovative Combustion and Aerothermal Technologies in Energy and Power Systems*, May 20–25, Kiev.
[6] Afanas'yev, V. N., Veselkin, V. Yu., Leont'ev, A. I., Skibin, A. P., and Chudnovskiy, Ya. P., 1993, "Thermohydraulics of Flow Over Isolated Depressions (Pits, Grooves) in a Smooth Wall," Heat Transfer-Sov. Res., **25**(1), pp. 22–56.
[7] Isaev, S. A., Leont'ev, A. I., and Baranov, P. A., 2000, "Identification of Self-Organized Vortexlike Structures in Numerically Simulated Turbulent Flow of a Viscous Incompressible Liquid Streaming around a Well on a Plane," Tech. Phys. Lett., **26**(1), pp. 15–18.
[8] Kesarev, V. S., and Kozlov, A. P., 1993, "Convective Heat Transfer in Turbulized Flow Past a Hemispherical Cavity," Heat Transfer-Sov. Res., **25**, pp. 156–160.
[9] Schukin, A. V., Kozlov, A. P., and Agachev, R. S., 1995, "Study and Application for Hemispherical Cavities for Surface Heat Transfer Augmentation," IGTI Turbo Expo, Paper No. 95-GT-59, Houston.
[10] Syred, N., Khalatov, A., Kozlov, A., Shchukin, A., and Agachev, R., 2000, "Effect of Surface Curvature on Heat Transfer and Hydrodynamics within a Single Hemispherical Dimple," IGTI Turbo Expo, Paper No. 2000-GT-236, Munich.
[11] Afanas'yev, V. N., and Chudnovskiy, Ya. P., 1992, "Heat Transfer and Friction on Surfaces Contoured by Spherical Depressions," Heat Transfer-Sov. Res., **24**, pp. 24–104.
[12] Afanas'yev, V. N., Chudnovsky, Ya. P., Leont'ev, A. I., and Roganov, P. S., 1993, "Turbulent Flow Friction and Heat Transfer Characteristics for Spherical Cavities on a Flat Plate," Exp. Therm. Fluid Sci., **7**, pp. 1–8.

[13] Belen'kiy, M. Ya., Gotovskii, M. A., Lekakh, B. M., Fokin, B. S., and Khabenskii, V. B., 1992, ''Experimental Study of the Thermal and Hydraulic Characteristics of Heat Transfer Surfaces Formed by Spherical Cavities,'' Teplofiz. Vys. Temp., **29**(6), pp. 1142–1147.
[14] Belen'kiy, M. Ya., Gotovskii, M. A., Lekakh, B. M., Fokin, B. S., and Dolgushin, K. S., 1993, ''Heat Transfer Augmentation Using Surfaces Formed by a System of Spherical Cavities,'' Heat Transfer-Sov. Res., **25**, pp. 196–202.
[15] Chyu, M. K., Yu, Y., Ding, H., Downs, J. P., and Soechting, F. O., 1997, ''Concavity Enhanced Heat Transfer in an Internal Cooling Passage,'' IGTI Turbo Expo, Paper No. 97-GT-437, Orlando.
[16] Moon, H. K., O'Connell, T., and Glezer, B., 1999, ''Channel Height Effect on Heat Transfer and Friction in a Dimpled Passage,'' IGTI Turbo Expo, Paper No. 99-GT-163, Indianapolis.
[17] Mahmood, G. I., Hill, M. L., Nelson, D. L., Ligrani, P. M., Moon, H. K., and Glezer, B., 2000, ''Local Heat Transfer and Flow Structure On and Above a Dimpled Surface in a Channel,'' *IGTI Turbo Expo*, Paper No. 2000-GT-230, Munich.
[18] Nagoga, G. P., 1996, ''Effective Methods of Cooling of Blades of High Temperature Gas Turbines,'' Publishing House of Moscow Aerospace Institute (in Russian), p. 100.
[19] Farina, D. J., Hacker, J. M., Moffat, R. J., and Eaton, J. K., 1994, ''Illuminant Invariant Calibration of Thermochromic Liquid Crystals,'' Exp. Therm. Fluid Sci. **9**, pp. 1–9.
[20] Boelter, L. M. K., Young, G., and Iversen, H. W., 1948, ''An Investigation of Aircraft Heaters XXVII—Distribution of Heat Transfer Rate in the Entrance Region of a Tube,'' NACA TN 1451.
[21] Dittus, F. W., and Boelter, L. M. K., 1930, *University of California at Berkeley Publications in Engineering*, Vol. 2, p. 443.
[22] Holman, J. P., 1976, *Heat Transfer*, McGraw-Hill Book Co., 4th edition, p. 204.
[23] Kline, S. J., and McClintock, F. A., 1953, ''Describing Uncertainties in Single-Sample Experiments,'' Mech. Eng. (Am. Soc. Mech. Eng.), **Jan.**, pp. 3–8.
[24] Webb, R. L., Eckert, E. R. G., and Goldstein, R. J., 1971, ''Heat Transfer and Friction in Tubes with Repeated Rib Roughness,'' Int. J. Heat Mass Transfer, **14**, pp. 601–617.

Experimental Demonstration of Maximum Mistuned Bladed Disk Forced Response

J. A. Kenyon
Air Force Research Laboratory,
Propulsion Directorate,
Wright-Patterson AFB, OH 45433
e-mail: james.kenyon@wpafb.af.mil

J. H. Griffin
Department of Mechanical Engineering,
Carnegie Mellon University,
Pittsburgh, PA 15213
e-mail: jg9h@andrew.cmu.edu

A theory was previously developed for predicting robust maximum forced response in mistuned bladed disks from distortion of a structural mode. This paper describes an experiment to demonstrate the theory. A bladed disk is designed to be sufficiently sensitive to mistuning to obtain maximum response. The maximum amplitude magnification from mistuning is predicted using the theory, 1.918. The bladed disk is intentionally mistuned to obtain the maximum response, and the response to an engine order traveling wave excitation is measured. The measured amplitude magnification is in close agreement with the theory. The robustness of the maximum response is demonstrated.
[DOI: 10.1115/1.1624847]

1 Introduction

Mistuning of turbine engine bladed disks contributes to engine high cycle fatigue by increasing the vibration amplitudes of blades. Bladed disks in gas turbines are typically designed to be cyclically symmetric, so that each blade is identical and the disk or hub is perfectly periodic. Mistuning refers to variations in the blades or the disk/hub that arise as a result of manufacturing variations, wear, or damage. These variations lead to significant changes in the dynamic response of bladed disks. The vibration modes of a bladed disk can become localized, leading to large vibration amplitudes that contribute to accelerated fatigue and failure.

The variations in blade and hub properties are random in nature, making bladed disk forced response difficult to predict. In some instances, mistuning leads to excessively large vibration amplitudes that quickly lead to fatigue failure. Predicting the maximum response that a particular bladed disk design can experience has been a research area of interest for quite some time. Whitehead [1] first addressed this issue in 1966 by developing algebraic expressions for the maximum response based on the number of blades on a bladed disk, though he was not able to demonstrate that result numerically. Whitehead [2] later considered the special case of structural coupling, though he later asserted that this result was incorrect and that his original solution was applicable in all cases [3]. In his latest paper on maximum response [3], Whitehead considered example cases in which his proposed maximum would occur, though these cases were not demonstrated through numerical simulations or experiments.

A number of other approaches have been proposed for determining maximum response in a bladed disk design. Dye and Henry [4] used Monte Carlo simulations with a simple numerical model based on measured system properties to statistically estimate the maximum response of a bladed disk. A number of other researchers have proposed various methods to determine the statistical distribution of mistuned forced response amplitudes from which the maximum response can be estimated, for example, Refs. [5], [6]. Sinha [7] recently proposed an upper bound on maximum response using an infinity norm approach. Rivas-Guerra and Mignolet [8] and Petrov and Ewins [9] used numerical optimization techniques to obtain maximum response in bladed disk models.

A distinct approach to determining maximum response is to consider the physical effects of mistuning on the dynamic characteristics of a bladed disk and to determine how each of these physical effects influences the forced response. Kenyon and Griffin [10] identified two primary physical mechanisms associated with increases in forced response amplitudes due to mistuning in a single family of bladed disk modes, frequency splitting and mode distortion. Frequency splitting describes the separation of the repeated natural frequencies that occur in tuned bladed disks into two distinct natural frequencies. Mode distortion refers to harmonic content in the mode shape of a mistuned system in addition to the fundamental wave form of the nominally tuned mode. MacBain and Whaley [11] derived an analytical solution for the maximum response due to frequency splitting that agreed with the numerical results of Ewins [12]. Their result was later corroborated by Kenyon and Griffin [10]. Kenyon et al. [13] recently developed a theory for predicting the maximum forced response in a bladed disk from mode distortion in a single structural mode. It was also noted in Ref. [13] that the maximum response derived there was robust. In other words, if a bladed disk is intentionally mistuned to exhibit that maximum response, then small, unintentional random mistuning will not significantly affect the response amplitude of the bladed disk. These results were demonstrated numerically.

Mistuning makes experimental investigation of bladed disk dynamics especially challenging. The variations in system properties associated with mistuning may be smaller than the uncertainty in the measurements. As a result, correlation of experimental data to numerical or analytical models is difficult since there are undetermined variations in the system properties and uncertainty in how these variations will affect the response of a bladed disk that is being tested. In addition, measurement devices that contact the blades such as strain gages or accelerometers can actually contribute to mistuning. Qualitative studies of the effects of mistuning have been conducted experimentally, for example, Refs. [14], [15], and some researchers have reported some success in predicting and measuring the natural frequencies and mode shapes of mistuned bladed disks [16,17]. However, agreement between predicted and measured forced response amplitudes has remained elusive, for instance, Refs. [17], [18].

This paper describes an experiment in which the maximum response predicted by the theory in Ref. [13] is demonstrated. A bladed disk with simple geometry has been designed for sensitivity to mistuning in an isolated family of first bending modes. The tuned system is characterized, and the mistuning necessary to obtain maximum response is calculated. This mistuning is implemented on the bladed disk by varying masses attached to the blade tips. The forced response of the system to an engine order travel-

Contributed by the International Gas Turbine Institute and presented at the International Gas Turbine and Aeroengine Congress and Exhibition, Atlanta, GA, June 16–19, 2003. Manuscript received by the IGTI Dec. 2002; final revision Mar. 2003. Paper No. 2003-GT-38060. Review Chair: H. R. Simmons.

ing wave excitation is measured and compared to the tuned system response to demonstrate the maximum magnification of the response amplitude. In addition, small random mistuning is added to the system, and the response is measured to demonstrate that the maximum response is robust.

2 Review of Theory

This section briefly reviews the theory presented in Ref. [13]. Additional details about the derivation as well as a discussion of the physical implications of the results can be found in Ref. [13]. Consider the mass-spring-damper system shown in Fig. 1. The equation of motion for the jth mass is

$$m_j\ddot{x}_j+(c_j+2c_c)\dot{x}_j-c_c(\dot{x}_{j-1}+\dot{x}_{j+1})+(k_j+2k_c)x_j-k_c(x_{j-1}+x_{j+1})=f_j(t),\quad j=0,1,...,N-1, \tag{1}$$

where the "˙" superscript indicates differentiation with respect to time and N represents the number of blades on the disk. The system is cyclic such that $x_0=x_N$. The equations of motion for the entire system can be written in matrix form

$$\mathbf{M}\ddot{\mathbf{x}}+\mathbf{C}\dot{\mathbf{x}}+\mathbf{K}\mathbf{x}=\mathbf{f}(t). \tag{2}$$

This formulation allows for mistuning in both mass and stiffness parameters. Thus the mass matrix $\mathbf{M}=\mathbf{M}^\circ+\mathbf{\Delta M}$, where the superscript "°" indicates the tuned system matrix, and $\mathbf{\Delta M}$ is a diagonal matrix whose jth element represents a small perturbation in the mass of the jth sector m_j. Similarly, the stiffness matrix $\mathbf{K}=\mathbf{K}^\circ+\mathbf{\Delta K}$, where $\mathbf{\Delta K}$ is a diagonal matrix containing small perturbations in the blade stiffnesses k_j. Finally, it is assumed that the damping $\mathbf{C}$ is proportional to a linear combination of the tuned mass and stiffness matrices, $\mathbf{M}^\circ$ and $\mathbf{K}^\circ$.

The tuned modes are determined for $\mathbf{\Delta K}=\mathbf{\Delta M}=\mathbf{0}$ from the standard structural eigenvalue problem

$$\mathbf{K}^\circ\Phi^\circ=\mathbf{M}^\circ\Phi^\circ\Omega^{\circ 2}, \tag{3}$$

where Φ° is a matrix whose columns represent the tuned modes in real form and $\Omega^{\circ 2}$ is a diagonal matrix consisting of the squares of the tuned natural frequencies of the system. The tuned mode shapes are extended and wavelike in form, with m equally spaced nodal diameters. It is well known that the tuned system exhibits repeated natural frequencies for each m except $m=0$ and, in the case of N even, $m=N/2$. The modes corresponding to the repeated frequencies can be expressed as $\phi^{\circ S}_{mj}=b_m\sin m\theta_j$ and $\phi^{\circ C}_{mj}=b_m\cos m\theta_j$, where $\theta_j=2\pi j/N$. The modes for $m=0$ and $N/2$ have the form $b_m\cos m\theta_j$. The tuned modes are orthogonal with respect to the tuned mass, damping, and stiffness matrices, such that

$$\phi^\circ_m\mathbf{M}^\circ\phi^\circ_n=m_m\delta_{mn}, \tag{4}$$

$$\phi^\circ_m\mathbf{C}\phi^\circ_n=c_m\delta_{mn}, \tag{5}$$

$$\phi^\circ_m\mathbf{K}^\circ\phi^\circ_n=k_m\delta_{mn}, \tag{6}$$

where δ_{mn} is the Kronecker delta, and m and n now represent general mode indices, $\{m,n\}\in\{0,1,N-1\}$.

The forced response of the tuned system to an engine order traveling wave excitation is considered. The excitation of the jth mass can be described mathematically:

$$f_j(t)=f_0\cos(E\theta_j-\omega t). \tag{7}$$

Using standard modal analysis techniques, it can be shown that the amplitude of the steady-state response of each blade is the same, and at resonance ($\omega\approx\omega_{m=E}$ for small damping), this amplitude is

$$x_{\text{tuned}}=F_Eb_E/c_E\omega_E, \tag{8}$$

where F_E is the modal force in the mode corresponding to the engine order of the excitation, $F_E=b_Ef_0\eta_E$, and $\eta_E=N$ for $E\in\{0,N/2\}$ and $\eta_E=N/2$ otherwise.

The tuned modes form a complete basis spanning the same displacement space as the mistuned modes. Therefore the mistuned mode resulting in maximum response can be written as a linear combination of the tuned modes,

$$\phi=\sum_{m=0}^{M}\alpha_m\phi^{\circ S}_m+\beta_m\phi^{\circ C}_m \tag{9}$$

with $M=(N-1)/2$ for N odd or $M=N/2$ for N even. Each α_m and β_m is a real constant signifying the contribution of the mth tuned modes to the mistuned mode.

The blade that exhibits the highest response can be at any location on the disk. For mathematical convenience, this blade is assigned the reference coordinate $\theta=0$ (i.e., $j=0$), so that the contributions of the sine modes $\phi^{\circ S}_m$ at this blade location are zero. The component of the mode, Eq. (9), at $j=0$, denoted ϕ_0, will be used for this discussion. It is assumed that damping is sufficiently small and that the frequencies are sufficiently separated so that only the response of a single mode must be considered. Noting that b_m are the arbitrary coefficients of the tuned modes and scaling the β_m in Eq. (9) such that the contribution of the tuned mode corresponding to the engine order of the excitation $\beta_E=1$, the mode component at $\theta=0$ is written

$$\phi_0=b_E+\sum_{m\neq E}\beta_mb_m. \tag{10}$$

Examining the response in the mode, Eq. (9), and using similar modal analysis techniques as in the tuned analysis, the maximum mistuned forced response occurs at blade $j=0$ and can be shown to be

$$x_{\max}=F_E\phi_0/c^*_E\omega^*_E, \tag{11}$$

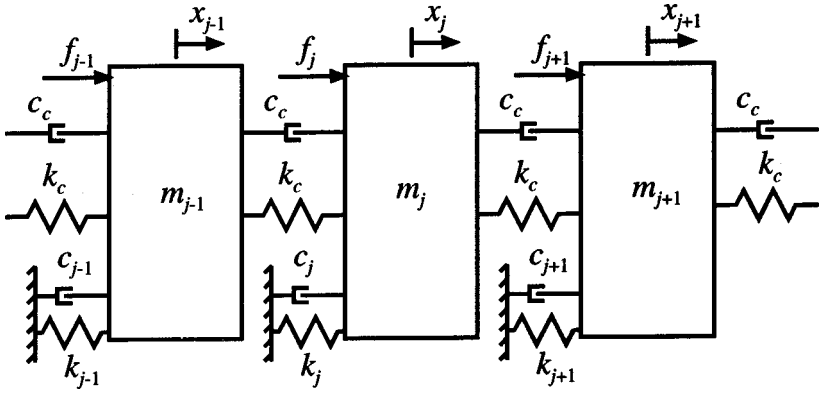

Fig. 1 Lumped parameter model of bladed disk dynamics

where the "*" superscript implies mistuned values. It can be shown that the modal force F_E remains the same as for the tuned case [13].

From Eqs. (8) and (11), it is clear that frequency changes can cause changes in forced response amplitude not generally associated with mistuning. Therefore it is assumed here that $\omega_E = \omega_E^*$. The tuned modes are scaled so that $b_E = 1$, and the magnification in the response amplitude due to mistuning is defined, $g = x_{\max}/x_{\text{tuned}}$. Thus from Eqs. (8) and (11),

$$g = \phi_0 c_E / c_E^*, \tag{12}$$

where the b_E in ϕ_0, Eq. (10), is unity. Using orthogonality, the mistuned modal damping c_E^* is written

$$c_E^* = c_E + \sum_{m \neq E} \beta_m^2 c_m. \tag{13}$$

It is convenient to choose the mode scaling factors b_m, so that all of the modes have the same modal damping c_m. Modes are commonly normalized so that the modal mass is unity. In this case, however, the tuned modes are normalized so that the modal damping equals c_E,

$$\phi_m^{\circ} \mathbf{C} \phi_m^{\circ} = c_E, \quad m = 0,1,...,N-1 \tag{14}$$

Using Eq. (14) with Eqs. (10) and (13), the amplitude magnification in Eq. (12) becomes

$$g = \frac{1 + \Sigma_{m \neq E} b_m \beta_m}{1 + \Sigma_{m \neq E} \beta_m^2}. \tag{15}$$

The maximum mistuned response of the bladed disk can be found by maximizing Eq. (15) with respect to all of the β_m simultaneously. After some algebra, it can be shown that a relationship exists between the β_m and the b_m at the maximum. Selecting one of the modes as a reference and labeling it the Rth mode, this relationship is expressed as

$$\beta_m^*/\beta_R^* = b_m/b_R, \tag{16}$$

where the "*" superscript now indicates optimum values. Using this result and defining

$$\gamma = \sum_{m \neq E} b_m^2/b_R^2, \tag{17}$$

Eq. (15) can be rewritten in terms of one variable, β_R^*. After some algebra, the maximum amplitude magnification factor is obtained,

$$g_{\max} = \frac{1 + \gamma b_R \beta_R^*}{1 + \gamma \beta_R^{*2}}. \tag{18}$$

Since b_R and γ are defined by the tuned system properties, Eq. (18) represents an optimization problem in only one variable, β_R^*. A simple expression for the optimum value of β_R^* can be found by setting the derivative of $g_{\max}$ equal to zero,

$$\beta_R^* = \frac{-1 + \sqrt{1 + \gamma b_R}}{\gamma b_R}. \tag{19}$$

It should be noted that the amplitude magnification factor in Eq. (15) can be maximized either directly or by using the simpler expressions in Eqs. (18) and (19).

3 Bladed Disk Characterization and Optimization

3.1 Bladed Disk Design. In order to obtain an appropriate test article to demonstrate the theory described in the previous section, a bladed disk was designed to have an isolated family of first bending modes. To achieve this, long slender blades were selected for the bladed disk. For ease of manufacture, the bladed disk was designed from steel sheet metal. An important design consideration was the sensitivity of the bladed disk to mistuning. The bladed disk could not be too sensitive to mode distortion from mistuning so that a reasonable estimate of the tuned response could be made even with small, inadvertent mistuning from manufacturing variations. However, the bladed disk had to be sensitive enough to obtain the maximum response with physically realizable mistuning.

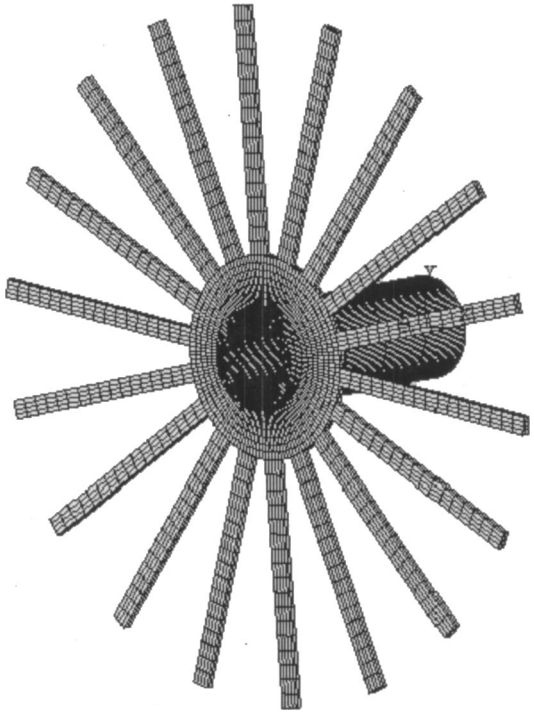

Fig. 2 Finite element model of experimental bladed disk

The bladed disk was fabricated from 0.125-in. steel sheet and had 18 blades. During the experiment, mistuning was applied to the bladed disk by adding masses to the blade tips. Therefore small steel blocks with equal masses were added to the tips of each of the blades in the nominally tuned system so that the frequency of the optimally mistuned mode would be approximately the same as the frequency of the tuned modes. For the tuned system, equal masses of 11.72 g were attached to each blade using accelerometer wax. The masses were measured to an accuracy of ± 0.02 g. In the optimized system, variable masses were attached to the blade tips according to the mistuning needed for maximum response.

To assist in design and analysis, a finite element model of the bladed disk was developed as shown in Fig. 2. The model consisted of 8-noded solid elements and had 91,692 degrees of freedom. Part of the fixture assembly used in the experiment, a cylindrical clamp, was included in the model to obtain a more accurate estimate of the boundary conditions on the bladed disk. The cylinder was fixed at an axial location consistent with the experimental setup. The masses at the blade tips of the actual system were modeled by increasing the density of the elements at the tips of the blades in the model.

3.2 Tuned System Characterization. The dynamic characteristics of the nominally tuned bladed disk were determined experimentally. The bladed disk was mounted in a fixture as shown in Fig. 3. The fixture consisted of a cylindrical clamp assembly that provided a uniform boundary condition on the inner diameter of the disk. The clamp was mounted in a four-jaw lathe chuck and secured on a multi-ton granite table to isolate the system from its surroundings. For reference, the blades were numbered sequentially from 1 to 18. A noncontacting eddy current probe was fixed

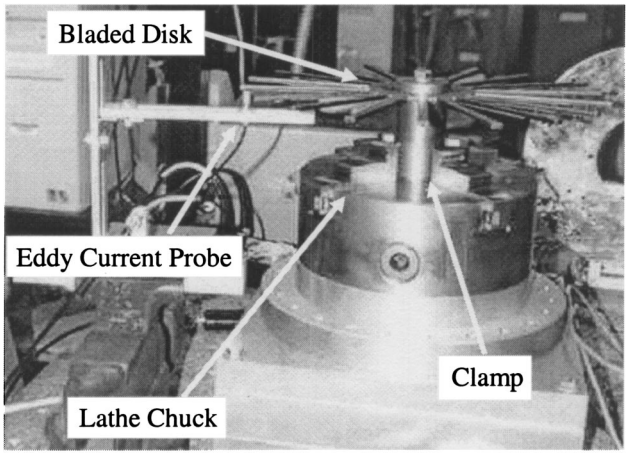

Fig. 3 Experimental setup for measuring natural frequencies, damping, and mode shapes of the bladed disk

under the tip of one of the blades (blade 17). The outputs from the probe and from an instrumented hammer were connected to a spectrum analyzer, which was in turn connected to a desktop computer with commercially available modal analysis software installed. During data acquisition, the transfer function between the displacement of the tip of the instrumented blade and the input force on each blade was determined. Ten transfer functions were acquired and averaged for each blade using Hanning windows for signal processing. Each modal test was performed twice to verify repeatability, and the results were averaged.

The natural frequencies, damping, and mode shapes of the first bending family of modes in the nominally tuned system were measured using a frequency resolution of 0.0625 Hz. The natural frequencies of the tuned system are plotted as a function of the number of nodal diameters in the mode shape in Fig. 4. The slight mistuning in the system caused some of the repeated frequency pairs to split. In this case, the average of the two frequencies in the pair was taken as the tuned (repeated) natural frequency. The three nodal diameter tuned modes were selected for optimization for maximum response. As seen in Fig. 4, the three nodal diameter modes were somewhat isolated from the other modes, reducing their sensitivity to distortion (see Ref. [19]). As a result, exciting these modes with a three engine order excitation will provide a reasonable estimate of the tuned system response. However, the overall spacing of the frequencies in the first bending mode family is still sufficiently close that the maximum response can be obtained with physically viable mistuning.

The mode shapes of the three nodal diameter modes were examined by splitting the nominally repeated frequency pair into

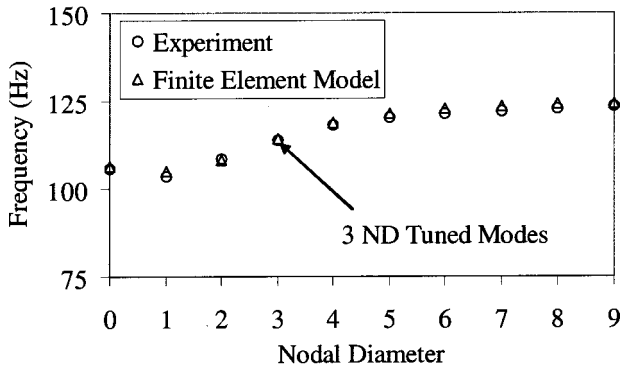

Fig. 4 Natural frequencies versus nodal diameters for the tuned bladed disk

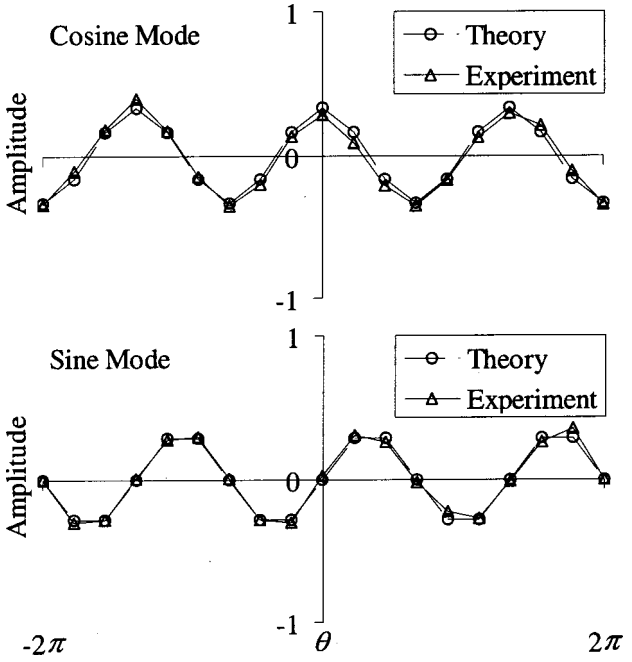

Fig. 5 Nominally tuned cosine (113.7 Hz) and sine (114.3 Hz) mode shapes

distinct natural frequencies. Six masses weighing 0.32 g each were added to the blades in an evenly spaced manner, resulting in a six harmonic mistuning pattern with blade 1 at $\theta=0$ (see Ref. [10] for a discussion of frequency splitting and the prescribed mistuning distribution). The mistuning split the three nodal diameter mode pair into individual cosine (113.7 Hz) and sine (114.3 Hz) modes, Fig. 5. The measured modes are compared with pure sine and cosine waves in the figure. The mode shapes agree well with the sine and cosine functions, indicating that even with the splitting in the natural frequencies, the modes are relatively undistorted. The lack of distortion in the tuned mode shapes verifies that an accurate estimate of the tuned forced response to an engine order traveling wave excitation can be obtained.

The damping measured in the tuned modes is shown in Table 1. The damping ratio in the three nodal diameter modes, or the modes of interest, was $\zeta_{\text{tuned}}=0.00063$. To obtain an accurate measurement of the damping values, the repeated frequency pairs were split as described previously, and the modal damping was taken as the average for the two modes in the pair. The damping values in Table 1 were used to optimize the mistuning for maximum response, as will be described in the next section.

3.3 Mistuning Optimization for Maximum Response. The bladed disk was optimized for maximum forced response according to the theory presented in Ref. [13] and in Sec. 2. For the optimization, the modal damping constants c_m were calculated from the measured damping ratios using

$$c_m = 4\pi m_m f_m \zeta_m, \tag{20}$$

where f_m is the measured frequency in cycles per second and ζ_m is the measured modal damping ratio of the mth tuned mode. The modal mass m_m is obtained from

Table 1 Modal damping in nominally tuned bladed disk

ND	0	1	2	3	4
Damping (ζ)	0.00079	0.00078	0.00067	0.00063	0.00067
ND	5	6	7	8	9
Damping (ζ)	0.00070	0.00068	0.00072	0.00068	0.00073

$$m_m = \phi_m^{\circ H} \mathbf{M}^\circ \phi_m^\circ, \tag{21}$$

where $\phi_{mj}^\circ = e^{i2\pi mj/N}/\sqrt{2}$, $m = 0,1,...,N-1$, and the operator H denotes the Hermitian. Here the tuned mass matrix $\mathbf{M}^\circ$ is a diagonal matrix whose elements are equivalent lumped masses for each blade, determined by treating each blade as a cantilevered beam and integrating the kinetic energy of the blade motion over the length of the blade [20]. The masses added to the blade tips in the experimental bladed disk are also added to the equivalent lumped masses from this calculation. The mode resulting in maximum response was determined from the optimization, and the predicted maximum amplitude magnification was calculated, 1.918.

The method presented in Ref. [13] for calculating the intentional mistuning for maximum response was extended to compute the mass mistuning needed for maximum response in the experimental bladed disk. The eigenvalue problem for the tuned natural frequencies and modes can be described in matrix form by

$$\mathbf{K}^\circ \Phi^\circ = \mathbf{M}^\circ \Phi^\circ \Omega^{\circ 2}, \tag{22}$$

where Φ° is a matrix whose columns are the tuned modes of the system written here in complex exponential form, and $\Omega^{\circ 2}$ is again a diagonal matrix consisting of the squares of the tuned natural frequencies of the system. The modes are normalized so that the modal mass of each tuned mode is unity,

$$\Phi^{\circ H} \mathbf{M}^\circ \Phi^\circ = \mathbf{I}, \tag{23}$$

$$\Phi^{\circ H} \mathbf{K}^\circ \Phi^\circ = \Omega^{\circ 2}. \tag{24}$$

Mistuning is assumed to occur in the mass matrix, so that the mistuned mass matrix $\mathbf{M} = \mathbf{M}^\circ + \mathbf{\Delta M}$, where $\mathbf{\Delta M}$ is a diagonal matrix consisting of the mistuning of each blade. The mistuned modes are written as a linear combination of the tuned modes, $\Phi = \Phi^\circ \mathbf{B}$, where the pqth element of $\mathbf{B}$ denotes the contribution of the pth tuned mode to the qth mistuned mode. Using Eqs. (23) and (24), the mistuned eigenvalue problem can be written,

$$\Omega^{\circ 2} \mathbf{B} = (\mathbf{I} + \hat{\mathbf{\Delta M}}) \mathbf{B} \Omega^2. \tag{25}$$

Here, Ω^2 is a diagonal matrix consisting of the squares of the mistuned natural frequencies, and the $\mathbf{\Delta M}$ matrix is derived by projecting the mistuning onto the tuned modes,

$$\hat{\mathbf{\Delta M}} = \Phi^{\circ H} \mathbf{\Delta M} \Phi^\circ. \tag{26}$$

Considering a mistuned mode with natural frequency ω for the optimization, Eq. (25) can be reduced to

$$-\omega^2 \hat{\mathbf{\Delta M}} \beta^c = (\omega^2 \mathbf{I} - \Omega^{\circ 2}) \beta^c, \tag{27}$$

where β^c is the column of $\mathbf{B}$ corresponding to ω and consists of the mode participation terms β_m described in Sec. 2 recast to correspond to the complex form of the tuned modes.

The matrix $\hat{\mathbf{\Delta M}}$ can be rearranged to obtain the mistuning needed for the mode described by β^c. This matrix consists of elements $\hat{\mathbf{\Delta M}}_{pq}$, where $\hat{\mathbf{\Delta M}}_{pq} = \phi_p^{\circ H} \mathbf{\Delta M} \phi_q^\circ$. Since the tuned system exhibits cyclic symmetry, $\hat{\mathbf{\Delta M}}_{pq}$ can be written as a summation over sectors j of the system,

$$\hat{\mathbf{\Delta M}}_{pq} = \sum_{j=0}^{N-1} \phi_p^{\circ(j)H} \mathbf{\Delta M}^{(j)} \phi_q^{\circ(j)}. \tag{28}$$

The mode at the jth sector can be written as the mode at the zero sector with a phase shift [21],

$$\phi_p^{\circ(j)} = e^{i2\pi pj/N} \phi_p^{\circ(0)}. \tag{29}$$

Therefore Eq. (28) can be recast,

$$\hat{\mathbf{\Delta M}}_{pq} = \sum_{j=0}^{N-1} e^{i2\pi(q-p)j/N} \phi_p^{\circ(0)H} \mathbf{\Delta M}^{(j)} \phi_q^{\circ(0)}. \tag{30}$$

Table 2 Mistuning distribution for experimental bladed disk

Blade	1	2	3	4	5	6
$\Delta\omega$	−2.1%	39.8%	−8.7%	−2.4%	3.5%	1.2%
Blade	7	8	9	10	11	12
$\Delta\omega$	−1.5%	1.6%	1.5%	−1.4%	1.5%	1.6%
Blade	13	14	15	16	17	18
$\Delta\omega$	−1.5%	1.2%	3.5%	−2.4%	−8.7%	39.8%

The family of modes being considered here consists of first bending blade modes. Therefore Eq. (30) can be simplified by considering only tip displacements,

$$\phi_p^{\circ(0)} \rightarrow b_p, \tag{31}$$

where b_p is the scalar complex displacement of the blade tip in the zero sector in the pth tuned mode. In addition, the sector mistuning $\mathbf{\Delta M}^{(j)}$ is reduced to a lumped mass δm_j at the blade tip. Thus

$$\hat{\mathbf{\Delta M}}_{pq} = b_p^* b_q \sum_{j=0}^{N-1} e^{i2\pi(q-p)j/N} \delta m_j, \tag{32}$$

where the "*" operator denotes the complex conjugate. Letting $r = q - p$,

$$\hat{\mathbf{\Delta M}}_{pq} = b_p^* b_q \overline{m}_r, \tag{33}$$

where

$$\overline{m}_r = \sum_{j=0}^{N-1} e^{i2\pi rj/N} \delta m_j \tag{34}$$

and $r = 0,1,...,N-1$ due to the periodic nature of the disk (see Ref. [13]). This expression is the rth element of the discrete Fourier transform of the mass mistuning at the blade tips.

The left side of Eq. (27) can be algebraically rearranged and expressed in terms of the $\overline{m}_r$,

$$-\omega^2 \hat{\mathbf{\Delta M}} \beta^c = -\omega^2 \mathbf{D} \overline{\mathbf{m}}, \tag{35}$$

where the matrix $\mathbf{D}$ reflects a regrouping of the known terms,

$$\mathbf{D} = \begin{bmatrix} b_0^* b_0 \beta_0^c & b_0^* b_1 \beta_1^c & \cdots & b_0^* b_{N-1} \beta_{N-1}^c \\ b_1^* b_1 \beta_1^c & b_1^* b_2 \beta_2^c & \cdots & b_1^* b_0 \beta_0^c \\ \vdots & \vdots & \ddots & \vdots \\ b_{N-1}^* b_{N-1} \beta_{N-1}^c & b_{N-1}^* b_0 \beta_0^c & \cdots & b_{N-1}^* b_{N-2} \beta_{N-2}^c \end{bmatrix}. \tag{36}$$

With Eqs. (35) and (36), Eq. (27) is rewritten,

$$-\omega^2 \mathbf{D} \overline{\mathbf{m}} = (\omega^2 \mathbf{I} - \Omega^{\circ 2}) \beta^c. \tag{37}$$

This expression is solved for $\overline{\mathbf{m}}$ using linear algebra techniques, and the physical mass mistuning for maximum response is calculated using the inverse Fourier transform of $\overline{\mathbf{m}}$,

$$\delta m_j = \frac{1}{N} \sum_{r=0}^{N-1} e^{-i2\pi rj/N} \overline{m}_r. \tag{38}$$

The method was applied to determine the mistuning necessary to obtain the optimum mode for maximum response. For the calculations, the mistuned natural frequency was selected to be the same as the tuned frequency for consistency with the maximum response theory in Sec. 2. To implement the intentional mistuning in the bladed disk, small steel blocks were fabricated and ground to the appropriate weight. These masses were accurate to ±0.02 g. The mistuning is shown in terms of blade frequency variations in Table 2. The maximum variation in an individual blade frequency was approximately 40%. The calculated mistuning for maximum response is significantly larger than what is typically observed or considered in gas turbine bladed disks, for instance Ref. [5]. How-

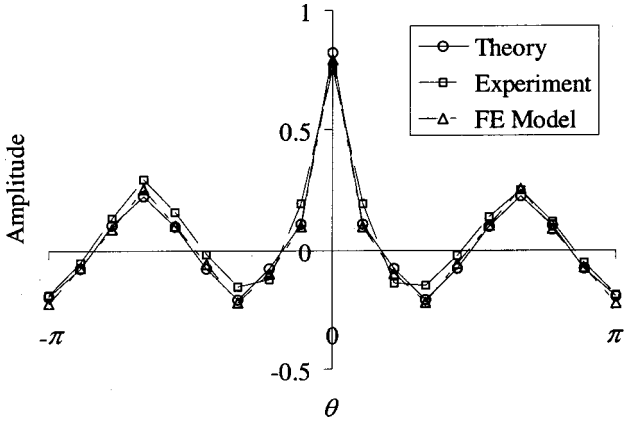

Fig. 6 Optimum mode shape for maximum response

ever, the large mistuning results from designing the experimental bladed disk to be insensitive to mode distortion so that the tuned response could be obtained. It should be noted that the intentional mistuning strategy derived here places no restrictions on the size of the mistuning. Furthermore, the theory on maximum response is derived in terms of mode shape and does not depend directly on the size of the mistuning. As a result, the predicted maximum response may often be achieved in bladed disks with different tuned system characteristics using smaller mistuning, see, for example, Ref. [13].

The optimized mode was measured using the experimental setup previously described. The measured mode shape in the optimum mode of interest is shown compared to the theoretically optimum mode in Fig. 6. The optimum mode shape calculated using the finite element model of the bladed disk is also shown. The modes are normalized to have unit length. As seen in the figure, the mode obtained experimentally agrees well with the theoretically predicted mode shape for maximum response. Blade 1 (θ=0) can be seen to demonstrate the largest response. Based on these results, the mistuning for maximum response was successfully calculated for the bladed disk, and the mode for maximum response was obtained.

Although the frequencies of the mistuned modes were split in the bladed disk, the frequencies of the optimum mode and its complement were too close to yield meaningful results in a forced response test with a traveling wave excitation. Therefore additional masses weighing 0.32 g were added in a six-harmonic pattern to split these frequencies by approximately 1 Hz. The natural frequency of the optimum mode after splitting was 113.0 Hz. The damping measured in the optimum mode was $\zeta_{opt}=0.00080$. The optimized mode shape did not change appreciably from that shown in Fig. 6 when frequency splitting was added to the system.

3.4 Numerical Simulations and Damping. A lumped parameter model (Fig. 1) of the experimental bladed disk was developed to perform forced response simulations. The equivalent lumped mass and stiffness parameters for the individual blades were obtained by treating the blades as cantilevered beams and integrating the kinetic and elastic strain energies over the length of the blade as described in the previous section and in Ref. [20]. The coupling stiffness, k_c in Fig. 1, was obtained by fitting the natural frequencies of the lumped parameter system to the measured frequencies in Fig. 4. Forced response simulations were performed using the lumped parameter model to verify the predicted amplitude magnification and optimization described in the previous section. The modal damping values measured in the tuned bladed disk were used in the forced response simulations. The predicted amplitude magnification was obtained in the numerical forced response simulations. Similar results were obtained using the finite element model for forced response simulations.

It was observed in numerical forced response simulations that the damping in the tuned modes and the optimized mode are predicted to be approximately the same in the application of the theory described here and in Ref. [13]. From the results presented here, this was not the case in the experiment. The measured damping in the three nodal diameter modes was $\zeta_{tuned}=0.00063$, and the damping in the optimum mistuned mode was $\zeta_{opt}=0.00080$. It was found that the measured damping depended on the amplitude of the response, and in turn, on the amplitude of the excitation. This result is not surprising given the clamped boundary condition at the disk inner diameter. This boundary condition introduces friction damping that depends on how strongly the disk vibrates. The damping values given in Table 1 were obtained using consistent excitation amplitudes. Therefore the relative damping values in the tuned system were essentially unaffected by the amplitude dependence, and the optimization and predicted amplitude magnification were considered accurate for this bladed disk. In the optimized mode, the strong response in blade 1 led to an increase in the damping for that mode. The damping will be discussed in more detail later with regard to the traveling wave forced response experiment.

4 Traveling Wave Forced Response Experiment

4.1 Description of Experiment. An experiment was conducted to measure the response of the bladed disk to an engine order traveling wave excitation. The traveling wave excitation was designed to simulate an excitation that may be experienced by a bladed disk in an engine. The test setup for the forced response test is shown in Fig. 7. The setup consists of the bladed disk mounted on a stand, with an electromagnet positioned behind each blade. The stand and the electromagnets were fixed at one end of a vibration isolation table. A single-point laser vibrometer was mounted on a two-dimensional traverse at the other end of the table, with the beam focused at the plane of the bladed disk surface. The electromagnets and the vibrometer were computer controlled using commercially available test control and data acquisition software. The traveling-wave excitation system is described in more detail in Ref. [22]. Transfer functions were measured for each blade over a frequency range of 100–200 Hz with a frequency increment of 0.0244 Hz. Blade tip velocities were determined for the transfer functions rather than tip displacements. However, the displacements are obtained by integrating the velocities in time. This results in division by the frequency of the response. Since the amplitude magnification, or the ratio of the maximum response to the tuned response, was to be determined and the system was designed to respond at approximately the same frequency in the tuned or optimized configuration, this cal-

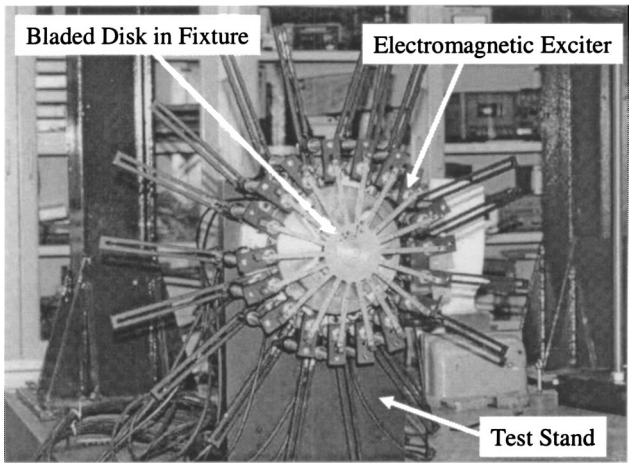

Fig. 7 Test setup for traveling wave forced response test

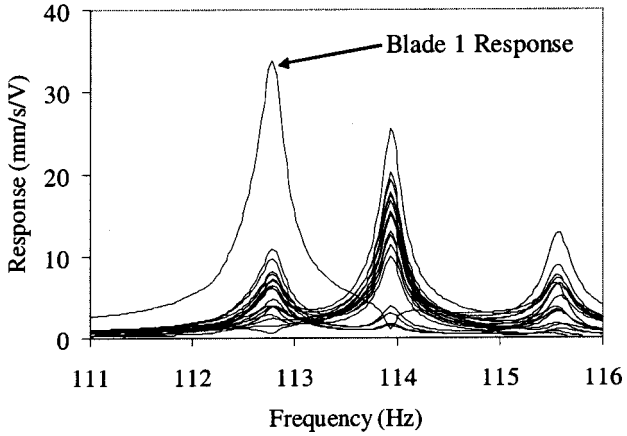

Fig. 8 Forced response of optimized bladed disk with maximum response

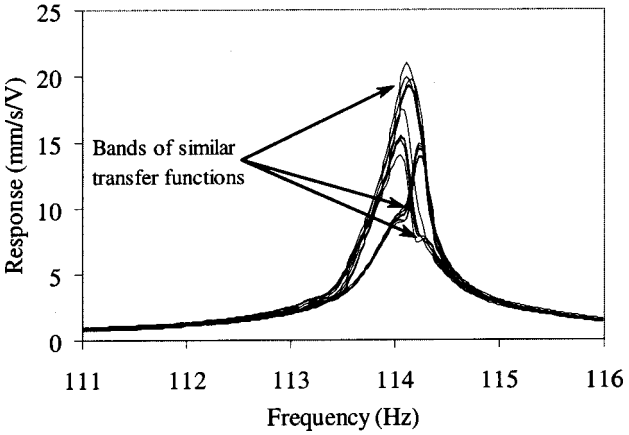

Fig. 9 Forced response of nominally tuned bladed disk

culation was omitted. The estimated uncertainty in the amplitude magnification factor for each blade in this experiment was ±4% [23].

It was pointed out previously that the damping in the bladed disk was nonlinear and amplitude dependent. This does not satisfy the damping assumption presented here and in Ref. [13]. However, the predicted maximum response from the theory can still be demonstrated if the damping in the system is equivalent to the damping that would occur if the theoretical assumption were satisfied. As pointed out in the previous section, this condition is satisfied if the damping ratios in the tuned and optimized systems are approximately equal. With amplitude dependent damping, this can be accomplished in the traveling wave experiment by adjusting the input force amplitudes for the tuned and optimized systems to achieve the same damping in both. The difference in the forces used to test the tuned and optimized systems is accounted for since transfer functions are measured. Thus an increase in the amplitude of the transfer function indicates an increase in the forced vibration response amplitude due to mistuning.

Experiments were performed in which the response of the bladed disk was measured for the tuned and optimized systems with various forcing amplitudes. The damping for the tuned and optimized systems was obtained using a half-power bandwidth estimate from the measured response data. It was found that with an excitation amplitude of 1 Vpp, the damping in the tuned system was $\zeta=0.0012$. It should be noted that the frequencies of the tuned modes were intentionally split for this measurement. With an excitation amplitude of 250 mVpp, the damping in the optimized system was also found to be $\zeta=0.0012$. Therefore these excitation levels (1 Vpp for the tuned system and 250 mVpp for the optimized system) were used to evaluate the theoretical prediction of maximum amplitude magnification.

4.2 Maximum Amplitude Magnification. With the excitation levels selected, the amplitude magnification in the optimized bladed disk was determined. For the optimized system, the response of the bladed disk to a third engine order traveling wave excitation with an amplitude of 250 mVpp was measured. The transfer functions for all 18 blades are shown in Fig. 8. As expected (see Fig. 6), the maximum response occurred in blade 1 ($\theta=0$). The other blades exhibited a relatively small amplitude in the mode with maximum response, indicating that the response was localized at blade 1. It should be noted that the resonant peaks in the transfer functions were well-separated, so that interaction between different modes was limited. The maximum response at this excitation was 33.73 mm/s/V at a frequency of 112.8 Hz.

To obtain the tuned system response, the tuned masses were attached to the blade tips, and the forced response of the system with an excitation amplitude of 1 Vpp was tested, as shown in Fig. 9. As can be observed in the figure, there was some mistuning inherent in the system. An initial approximation of the tuned response was calculated by taking the average of the resonant amplitudes of the individual blade responses. In this manner, the tuned response was estimated at 16.55 mm/s/V at a frequency of approximately 114.1 Hz. Based on these results, the amplitude magnification was 2.04, approximately 6% higher than the theoretical magnification of 1.918. However, a refinement in the tuned data analysis leads to improved agreement.

As in any bladed disk, small mistuning was present in the bladed disk described here. Since the bladed disk was designed to be relatively insensitive to mode distortion, the primary effect of this small mistuning was to split the frequencies of the three nodal diameter modes. Therefore the analytical result of MacBain and Whaley [11] was used to obtain a better estimate of the tuned response based on the measured response. To compare the analytical model to the experimental data, analytical transfer functions were calculated based on Ref. [11] and compared to the measured transfer functions. The analytical model predicted that there would be three distinct transfer functions that repeat cyclically in the blades. The experimental transfer functions occurred in three distinct bands of similar transfer functions that repeat in a cyclic fashion, Fig. 9. For each of these bands, an average transfer function was computed pointwise as a function of frequency. The three transfer functions that were obtained in this manner were compared to the three transfer functions from the analytical model.

The analysis in Ref. [11] depends on several key parameters. The damping in the system and the amount of frequency separa-

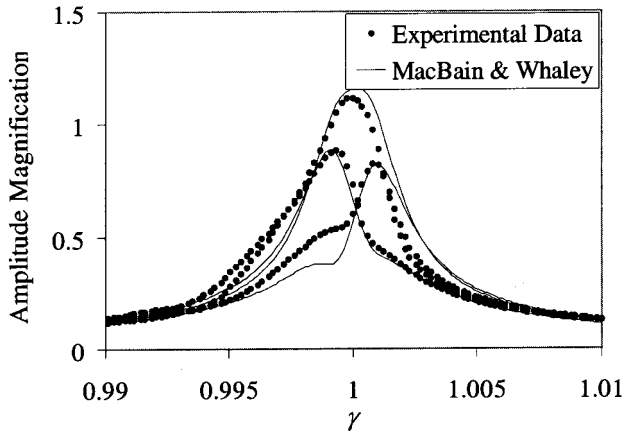

Fig. 10 Fit of experimental transfer functions to frequency splitting model of MacBain and Whaley [11]

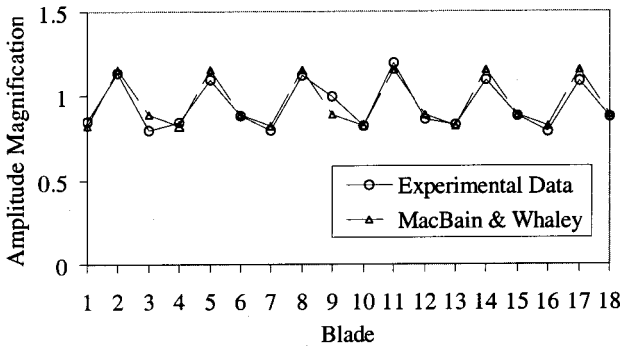

Fig. 11 Response distribution comparison between experimental results and MacBain and Whaley [11] model

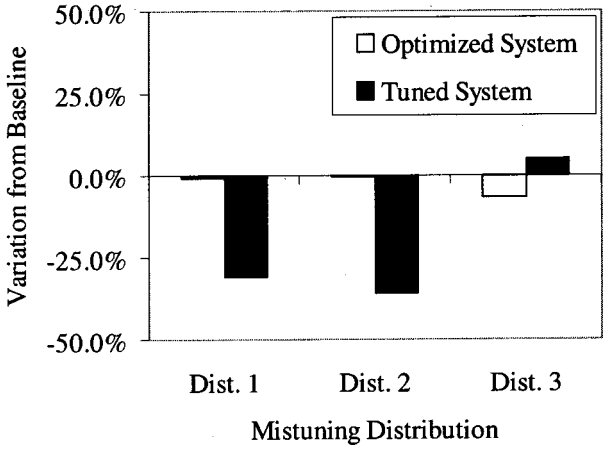

Fig. 12 Variation of blade 1 response due to small random mistuning

tion in the sine and cosine mode pair appear explicitly in the formulation. In addition, it is well-known that a six nodal diameter harmonic mistuning pattern will split the natural frequencies of the three nodal diameter mode pair, but to determine how particular blades will respond, the orientation of the mistuning pattern on the disk must be determined. Finally, the response amplitudes in Ref. [11] are normalized by the tuned system response. Therefore the tuned system response must be determined as a normalization factor. Determination of this last parameter, the tuned system response, provides the desired improved estimate of the tuned response.

The analytical frequency splitting model was fit to the experimental data by determining appropriate values of these parameters. The damping measured in the experiment was used, and the remaining parameters were systematically adjusted to obtain a best fit of the analytical transfer functions to the transfer functions obtained in the experiment. The frequencies from the experiment were normalized, γ, according to the convention in Ref. [11], and the response amplitudes were normalized by an assumed tuned response value of 17.58 mm/s/V. The frequency splitting and mistuning orientation were adjusted in the analytical model. The experimental transfer functions were compared to the analytical transfer functions, Fig. 10. Reasonable agreement can be seen between the measured and analytical transfer functions.

As a second check, the distribution of the response around the disk was examined. Here, the maximum response of each individual blade over the frequency range considered was determined and compared to the distribution predicted using Ref. [11]. Again, the experimental data were normalized by the assumed tuned response of 17.58 mm/s/V. The result is given in Fig. 11. The analytical result and the experimental result show good agreement. Therefore the assumed tuned response amplitude can be used to estimate the amplitude magnification. Using the improved estimate of the tuned system response of 17.58 mm/s/V, the amplitude magnification in the system is 1.92, which agrees very well with the theoretically predicted amplitude magnification of 1.918. It should be noted that the extraordinary agreement between the theory and the experimental results is fortuitous given that the uncertainty in the experiment is $\pm 4\%$. However, it is clear that the theory predicts the measured response within the practical limitation of experimental uncertainty.

5 Robustness of Maximum Response

As pointed out in Ref. [13], the maximum forced response derived in Sec. 2 is robust with respect to small random variations in the system properties. In other words, if a system is intentionally mistuned for maximum response, additional small random mistuning will not significantly change the maximum forced response amplitude. The robustness of the system response is a direct consequence of the process used to obtain the maximum response. The amplitude magnification factor, Eq. (15), can be thought of as a continuous function whose domain is an N-dimensional space spanned by the elements of the modal content vector $\{\beta_m\}$. The maximum of this function is found by setting the gradient of the function to zero and solving for the $\{\beta_m\}$ that satisfies this condition. The mapping of $\{\beta_m\}$ onto the mistuning space spanned by the elements of $\mathbf{\Delta M}$, $\{\delta m_j\}$, is a bijection except for an arbitrary rotation around the disk due to the periodicity of the system. As a consequence, the maximum in the forced response with respect to β_m implies a maximum with respect to δm_j. The gradient of the forced response function in the N-dimensional $\{\delta m_j\}$ space is zero and small variations in δm_j will have minimal impact on the forced response amplitude.

To observe the robustness of maximum response quantitatively in the experimental bladed disk would require a large number of tests in which a small random mistuning distribution is added to the masses on the blade tips. Such an experiment would be difficult and time consuming. However, the robustness of the optimized disk can be observed qualitatively using only a small number of tests with random mistuning. Here, the robustness of the system is illustrated by examining to what degree the responses of individual blades change when random mistuning is added.

A sensitivity study of the bladed disk was performed by adding small random mistuning to the nominally tuned bladed disk and to the intentionally mistuned bladed disk with maximum response. Three random mistuning patterns were computed using a random number generator. The random mistuning consisted of normally distributed sets of mass variations with a standard deviation of 1.75% of the nominal mass of a tuned blade. The additional mass mistuning was implemented on the bladed disk by moving the masses already on the blade tips a distance along the blade length that would result in the same kinetic energy change as the addition or removal of the mass specified in the mistuning pattern. The same random mistuning patterns were used for the optimized system and the nominally tuned system. The forced response of the system was measured, and the maximum response of each blade over the frequency range was determined.

To facilitate discussion, the response of blade 1 is considered. The results of the sensitivity study for blade 1 are shown in Fig. 12. For each of the three random mistuning patterns, the response amplitude of blade 1 is normalized by the appropriate "baseline" result, or the amplitude of blade 1 with the bladed disk in either the optimized or tuned configuration with no random mistuning. Thus the data shown in the figure indicate the amount by which the response amplitude of blade 1 changes as a result of small, random mistuning.

For the optimized system, the response amplitude of blade 1 changes little when small random mistuning is added. The maximum change from the baseline value is approximately 7%. In

contrast, the response amplitude of blade 1 on the nominally tuned bladed disk varies significantly with small random mistuning. The maximum change from the baseline value is 36%. It should be noted that this significant variation occurs despite the fact that the bladed disk was designed to be relatively insensitive to mode distortion from small mistuning. Thus it may be expected that even larger variations in the response of the nominally tuned system would occur if the bladed disk were more sensitive, i.e., the tuned frequencies were more closely spaced [19], as is typically the case in realistic bladed disk geometries. Furthermore, a reduction in the response amplitude is seen in Fig. 12 for the nominally tuned system, though in general an increase or a decrease may occur. Results similar to those shown here were observed for all the blades on the disk. Thus it is clear that the response of the optimized bladed disk is robust, particularly in comparison to the response of the nominally tuned system.

6 Conclusions

An experiment was conducted to demonstrate the theory developed in Ref. [13] for robust maximum bladed disk forced response from distortion of a structural mode. A bladed disk was designed to be sufficiently sensitive in the first bending family of modes so that the maximum forced response could be obtained. The nominally tuned system properties were measured, and based on the measured damping, the system response was optimized. The mistuning needed to obtain the optimal mode for maximum response was calculated and implemented on the bladed disk by varying the masses of small steel blocks attached to the blade tips. The mode shape obtained in this manner compared well to the theoretically predicted mode shape for maximum response.

With appropriate steps taken to account for a discrepancy between the assumed and actual damping in the system, the nominally tuned and optimized forced response of the bladed disk to a third engine order traveling wave excitation was measured. As an initial estimate, the tuned forced response was calculated by averaging the individual responses of the blades for the nominally tuned system. The amplitude magnification factor was 2.04, which was 6% higher than the theoretically predicted magnification of 1.918. The estimation of the tuned response was refined by applying an analytical frequency splitting model to the experimental data. Using this refinement, the amplitude magnification factor was 1.92, very close to the theoretical value.

The robustness of the optimized system was shown qualitatively. With three small random mistuning patterns added to the optimized system, the response of the system did not change significantly. However, the same mistuning patterns caused sizeable changes in the response of the nominally tuned system. These results indicate that the maximum response of the optimally mistuned bladed disk was robust, particularly in comparison to the nominally tuned system.

Acknowledgments

The authors would like to thank the staff of the Turbine Engine Fatigue Facility at Wright-Patterson Air Force Base, Ohio, and particularly Capt. Keith Jones, Air Force Research Laboratory, Propulsion Directorate, for their assistance in the traveling wave forced response experiment.

References

[1] Whitehead, D. S., 1966, ''Effect of Mistuning on the Vibration of Turbomachine Blades Induced by Wakes,'' J. Mech. Eng. Sci., **8**, pp. 15–21.
[2] Whitehead, D. S., 1976, ''Research Note: Effect of Mistuning on Forced Vibration of Blades With Mechanical Coupling,'' J. Mech. Eng. Sci., **18**, pp. 306–307.
[3] Whitehead, D. S., 1998, ''The Maximum Factor by Which Forced Vibration of Blades Can Increase Due to Mistuning,'' ASME J. Eng. Gas Turbines Power, **120**, pp. 115–119.
[4] Dye, R. C. F., and Henry, T. A., 1969, ''Vibration Amplitudes of Compressor Blades Resulting From Scatter in Blade Natural Frequencies,'' J. Eng. Power, **91**, pp. 182–187.
[5] Griffin, J. H., and Hoosac, T. M., 1984, ''Model Development and Statistical Investigation of Turbine Blade Mistuning,'' ASME J. Vibr. Acoust., **106**, pp. 204–210.
[6] Sinha, A., 1986, ''Calculating the Statistics of Forced Response of a Mistuned Bladed Disk Assembly,'' AIAA J., **24**, pp. 1797–1801.
[7] Sinha, A., 1997, ''Computation of the Maximum Amplitude of a Mistuned Bladed Disk Assembly via Infinity Norm,'' *Proc. of the 1997 ASME International Mechanical Engineering Congress and Exposition*, Dallas, TX, Vol. AD-55, pp. 427–432.
[8] Rivas-Guerra, A. J., and Mignolet, M. P., 2001, ''Local/Global Effects of Mistuning on the Forced Response of Bladed Disks,'' ASME Paper 2001-GT-0289, International Gas Turbine Institute Turbo Expo, New Orleans, LA.
[9] Petrov, E. P., and Ewins, D. J., 2001, ''Analysis of the Worst Mistuning Patterns in Bladed Disc Assemblies,'' ASME Paper 2001-GT-0292, International Gas Turbine Institute Turbo Expo, New Orleans, LA.
[10] Kenyon, J. A., and Griffin, J. H., 2003, ''Forced Response of Turbine Engine Bladed Disks and Sensitivity to Harmonic Mistuning,'' ASME J. Eng. Gas Turbines Power, **125**, pp. 113–120.
[11] MacBain, J. C., and Whaley, P. W., 1984, ''Maximum Resonant Response of Mistuned Bladed Disks,'' ASME J. Vibr. Acoust., **106**, pp. 218–223.
[12] Ewins, D. J., 1969, ''The Effects of Detuning Upon the Forced Vibrations of Bladed Disks,'' J. Sound Vib., **9**, pp. 65–79.
[13] Kenyon, J. A., Griffin, J. H., and Feiner, D. M., 2003, ''Maximum Bladed Disk Forced Response From Distortion of a Structural Mode,'' ASME J. Turbomach., **125**, pp. 352–363.
[14] Stange, W. A., and MacBain, J. C., 1983, ''An Investigation of Dual Mode Phenomena in a Mistuned Bladed Disk,'' ASME J. Vibr. Acoust., **105**, pp. 402–407.
[15] Kenyon, J. A., Cross, C. J., and Minkiewicz, G. R., 2000, ''Mechanical Coupling Effects on Turbomachine Mistuned Response,'' J. Propul. Power, **16**, pp. 1149–1154.
[16] Kruse, M. J., and Pierre, C., 1997, ''An Experimental Investigation of Vibration Localization in Bladed Disks, Part I: Free Response,'' ASME Paper 97-GT-501, International Gas Turbine Institute Turbo Expo, Orlando, FL.
[17] Kruse, M. J., and Pierre, C., 1997, ''An Experimental Investigation of Vibration Localization in Bladed Disks, Part II: Forced Response,'' ASME Paper 97-GT-502, International Gas Turbine Institute Turbo Expo, Orlando, FL.
[18] Judge, J., Pierre, C., and Mehmed, O., 2001, ''Experimental Investigation of Mode Localization and Forced Response Amplitude Magnification for a Mistuned Bladed Disk,'' ASME J. Eng. Gas Turbines Power, **123**, pp. 940–950.
[19] Yang, M.-T., and Griffin, J. H., 1997, ''A Normalized Eigenvalue Approach for Resolving Modal Interaction,'' ASME J. Eng. Gas Turbines Power, **119**, pp. 647–650.
[20] Rao, S. S., 1995, *Mechanical Vibrations*, 3rd Ed., Addison-Wesley Publishing Company, New York, front cover.
[21] Thomas, D. L., 1979, ''Dynamics of Rotationally Periodic Structures,'' Int. J. Numer. Methods Eng., **14**, pp. 81–102.
[22] Jones, K., and Cross, C., 2003, ''A Traveling Wave Excitation System for Bladed Disks,'' J. Propul. Power, **19**, pp. 135–141.
[23] Kenyon, J. A., 2002, ''Robust Maximum Forced Response in Mistuned Turbine Engine Bladed Disks,'' Ph.D. thesis, Carnegie Mellon University, Pittsburgh.

Experimental and Numerical Investigation of Impingement on a Rib-Roughened Leading-Edge Wall

M. E. Taslim

K. Bakhtari

H. Liu

Mechanical, Industrial, and Manufacturing Engineering Department, Northeastern University, Boston, MA 02115

Effective cooling of the airfoil leading edge is imperative in gas turbine designs. Among several methods of cooling the leading edge, impingement cooling has been utilized in many modern designs. In this method, the cooling air enters the leading edge cavity from the adjacent cavity through a series of crossover holes on the partition wall between the two cavities. The crossover jets impinge on a smooth leading-edge wall and exit through the film holes, and, in some cases, form a cross flow in the leading-edge cavity and move toward the end of the cavity. It was the main objective of this investigation to measure the heat transfer coefficient on a smooth as well as rib-roughened leading-edge wall. Experimental data for impingement on a leading-edge surface roughened with different conical bumps and radial ribs have been reported by the same authors previously. This investigation, however, deals with impingement on different horseshoe ribs and makes a comparison between the experimental and numerical results. Three geometries representing the leading-edge cooling cavity of a modern gas turbine airfoil with crossover jets impinging on (1) a smooth wall, (2) a wall roughened with horseshoe ribs, and (3) a wall roughened with notched-horseshoe ribs were investigated. The tests were run for a range of flow arrangements and jet Reynolds numbers. The major conclusions of this study were: (a) Impingement on the smooth target surface produced the highest overall heat transfer coefficients followed by the notched-horseshoe and horseshoe geometries. (b) There is, however, a heat transfer enhancement benefit in roughening the target surface. Among the three target surface geometries, the notched-horseshoe ribs produced the highest heat removal from the target surface, which was attributed entirely to the area increase of the target surface. (c) CFD could be considered as a viable tool for the prediction of impingement heat transfer coefficients on an airfoil leading-edge wall.
[DOI: 10.1115/1.1624848]

Introduction

Various methods have been developed over the years to keep the turbine airfoils temperatures below critical levels consistent with the required life for each component. Parallel with advances in airfoil material properties, advances in airfoil cooling schemes have also been remarkable. A main objective in turbine airfoil cooling design is to achieve maximum heat removal from the airfoil metal while minimizing the required coolant flow rate. One such method is to route coolant air through serpentine passages within the airfoil and convectively remove heat from the airfoil. The coolant is then ejected either at the tip of the airfoil, through the cooling slops along the trailing edge or the film holes on the airfoil surface at critical locations. To further enhance the heat transfer, the cooling channel walls are often roughened with ribs. Expensive research has been conducted on various aspects of the rib-roughened channels and it is concluded that geometric parameters such as passage aspect ratio (AR), rib height to passage hydraulic diameter or blockage ratio (e/D_h), rib angle of attack (α), the manner in which the ribs are positioned relative to one another (in-line, staggered, crisscross, etc.), rib pitch-to-height ratio (S/e) and rib shape (round versus sharp corners, fillets, rib aspect ratio (AR_{rib}), and skewness towards the flow direction) have pronounced effects on both local and overall heat transfer coefficients. The interested reader is referred to the work of investigators such as Burggraf [1], Chandra and Han [2], El-Husayni et al. [3], Han [4], Han et al. [5–7], Metzger et al. [8–10], Taslim and Spring [11,12], Taslim et al. [13–15], Webb et al. [16], and Zhang et al. [17].

Airfoil leading-edge surface, being exposed to very high gas temperatures, is often a life-limiting region and requires more complex cooling schemes especially in modern gas turbines with elevated turbine inlet temperatures. A combination of convective and film cooling is used in conventional designs to maintain the leading-edge metal temperature at levels consistent with airfoil design life. This study focuses on the leading-edge jet impingement and effects that roughening of the leading-edge surface has on the impingement heat transfer coefficient. In this flow arrangement, the coolant enters the leading-edge cooling cavity as jets from the adjacent cavity through a series of crossover holes on the partition wall between the two cavities. The crossover jets impinge on the leading-edge wall and exit through the leading-edge film holes on the pressure and suction sides, or form a cross flow in the leading-edge cavity and move toward the airfoil tip. A survey of many existing gas turbine airfoil geometries shows that, for analytical as well as experimental analyses, such cavities can be simplified by simulating the shape as a four-sided polygon with one curved side that simulates the leading-edge curvature, a rectangle with one curved side (often the smaller side) or a trapezoid, the smaller base of which is replaced with a curved wall. The available data in open literature is mostly for the jet impingement on flat surfaces that are smooth or rib roughened and a few cases of impingement on concave but smooth surfaces. These studies include the work of Chupp et al. [18], Metzger et al. [19], Kercher

Contributed by the International Gas Turbine Institute and presented at the International Gas Turbine and Aeroengine Congress and Exhibition, Atlanta, GA, June 16–19, 2003. Manuscript received by the IGTI Dec. 2002; final revision Mar. 2003. Paper No. 2003-GT-38118. Review Chair: H. R. Simmons.

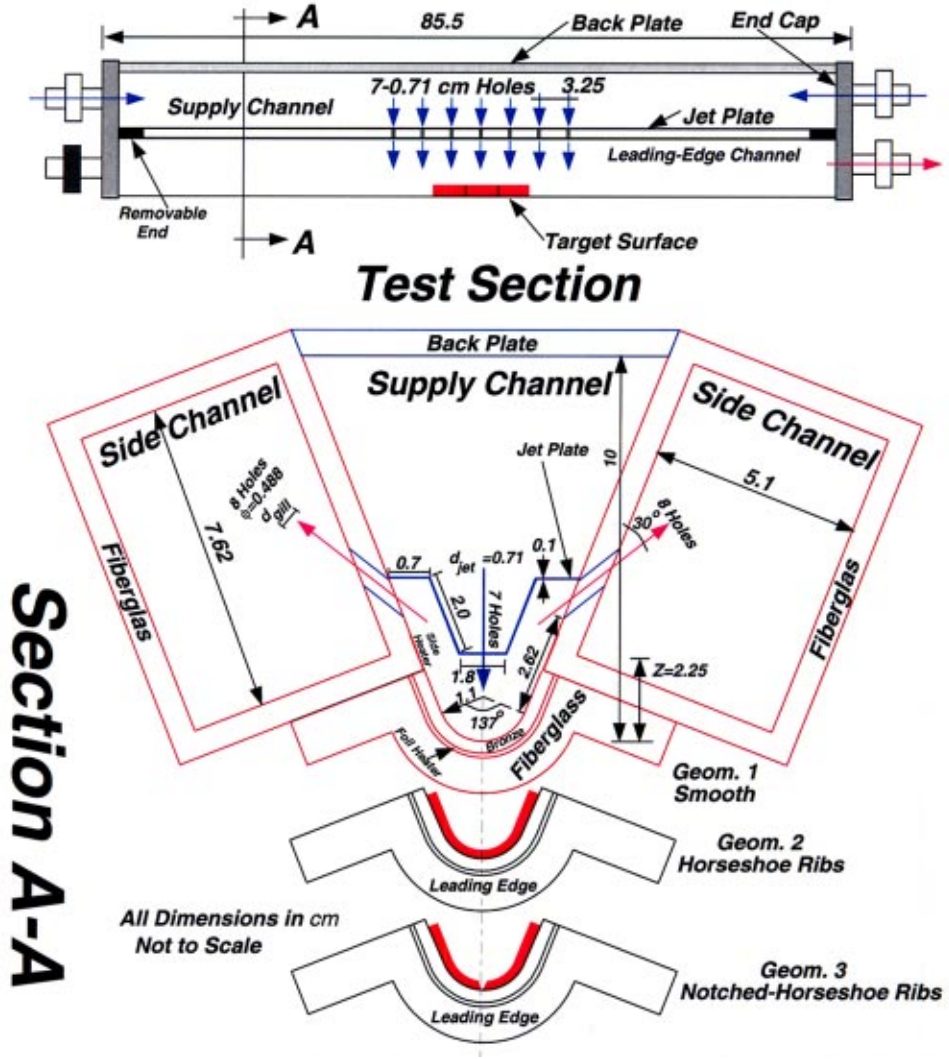

Fig. 1 Schematic of the test apparatus

and Tabakoff [20], Florschetz et al. [21–23], Metzger and Bunker [24], Bunker and Metzger [25], Van Treuren et al. [26], Chang et al. [27], Huang et al. [28], Akella and Han [29], and Ekkad et al. [30]. Taslim et al. [31–34] reported on impingement cooling of a smooth as well as roughened airfoil leading edge. They examined sandpaper roughness and different conical bump and radial rib geometries in a test section with a circular nose, two tapered sidewalls, and a flat fourth wall on which the crossover jets were positioned. Circular and racetrack-shaped crossover jets, at 0 and 45- deg angles with the channel's radial axis were compared. Results were also compared for leading-edge geometries with and without showerhead film holes. This paper, however, deals with impingement on an airfoil leading edge that is roughened with horseshoe ribs that are commonly used on the leading-edge surface in the traditional channel flow cooling of the leading-edge cavity. A numerical study was also conducted and the numerical results for representative cases are compared with the corresponding test results.

Test Sections

Figures 1 and 2 show schematically the layout, cross-sectional area, and the target surface geometries for the three test sections investigated in this project. A conventional technique of heated walls in conjunction with thermocouples was used to measure the heat transfer coefficient. The test wall, where all measurements were taken, consisted of three removable cast bronze pieces, which were heated by foil heaters attached on the back of the pieces. By proper adjustment of the ohmic power to the foil heater the desirable surface temperature was obtained. All test sections were 85.5 cm long. The circular wall simulating the leading-edge nose had an inner radius of 1.1 cm and an arc angle of 137 deg, was made up of fiberglass with a 9.9-cm-long recess in the middle to house the three bronze pieces. This circular recess along the inner radius with a depth of 3.2 mm allowed the bronze pieces to be fitted into the fiberglass shell. A flange on each side of the leading-edge piece facilitated the connections of the sidewalls. The two identical side channels with a cross-sectional area of 38.86 cm^2 (5.1×7.62 cm) and same length as the leading-edge piece were also made of fiberglass. The side channel's main function was to maintain the dump pressure to consequently control the amount of flow through the ''gill'' holes on the airfoil suction and pressure sides. Eight angled cylindrical holes with a diameter of 4.88 mm and a center-to-center distance of 3.25 cm were drilled on each side channel wall at an angle of 30 deg with the sidewall to simulate gill holes on the suction and pressure sides of an airfoil. These holes were staggered along the length of the test section with respect to the crossover jet holes on the jet plate.

Two removable 1-mm-thick jet plates corresponding to a $Z/d_{jet}=3.2$ were made of aluminum to produce the impinging jets for the symmetric and asymmetric impingement tests (Fig. 2*d*).

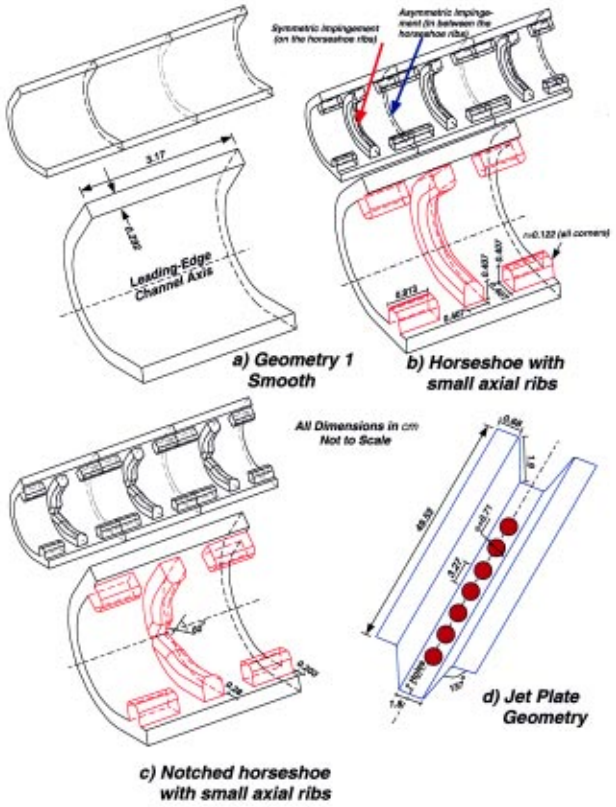

Fig. 2 Target surface and crossover hole geometries

Seven cylindrical holes with a diameter of 0.71 cm were drilled at a distance of 3.27 cm from each other (center to center) on each jet plate. The only difference between the two jet plates was the manner by which the crossover holes were drilled. For the symmetric impingement, the crossover holes were arranged such that the jets impinged on the horseshoe or notched-horseshoe ribs while for the asymmetric impingement tests, jets impinged in between the horseshoe or notched-horseshoe ribs. For the smooth wall, of course, the symmetric and asymmetric cases were identical. Therefore, for all smooth wall tests, jets impinged on the middle of the bronze pieces. The jet plate was attached and sealed to the side channel walls to simulate the partition wall between the leading edge and its adjacent cavities. The cylindrical holes were centered along both the length and width of the jet plate. The removable bronze pieces, installed in the fiberglass outer shell, provided the ability to change the impingement surface geometries in the test rig. Three different target geometries were manufactured and tested (Fig. 2):

(1) a smooth wall that served as a baseline,
(2) a roughened wall with horseshoe and straight ribs,
(3) a roughened wall with notched-horseshoe and straight ribs.

For each geometry, a Unigraphics® model was created for a LOM (laminated object model) machine. This LOM model was used to mold and create three cast bronze test pieces for each of the three geometries. A 3×6.1-cm custom-made thin etched-foil heater with a thickness of about 0.2 mm was glued around the outer curved surface of each bronze piece to provide the necessary heat flux. For each geometry, three identical bronze pieces, separated by a 1-mm-thick rubber insulator, were mounted next to each other. Heat transfer coefficients were measured on the middle piece while the other two pieces acted as guard heaters to minimize the heat losses to the adjacent walls. In addition, two custom-made thin etched-foil heaters were also mounted on the test section side channel walls next to the middle bronze piece free edges, again acting as guard heaters. The test section wall

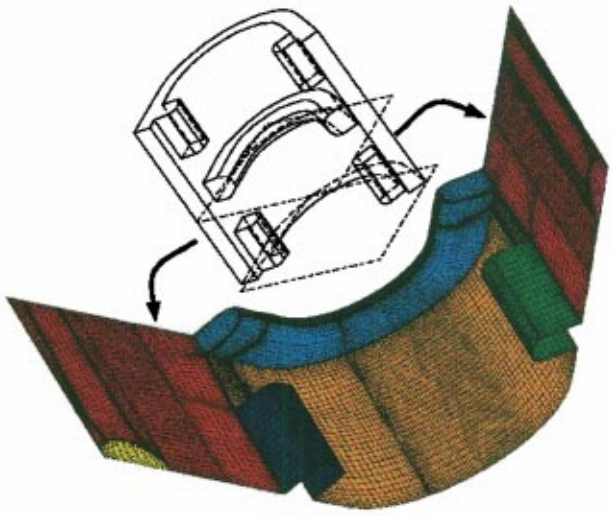

Fig. 3 Mesh arrangement on target and outer walls

temperature was adjusted to a desirable level by varying the Ohmic power to these heaters. Six thermocouples embedded in the middle bronze piece and three thermocouples embedded in each guard bronze piece measured the wall temperatures. The average of the six thermocouple readings in the middle bronze piece which, if different only differed by a fraction of a degree, was used as the surface temperature in the data reduction software for the average heat transfer coefficient. The selected nominal surface temperature was 45°C. With a jet temperature of about 20°C, a reasonable 25°C temperature difference between the wall surface and air was attained. Two thermocouples embedded in the wall behind the guard heaters were used to measure the side wall temperature adjacent to the middle bronze piece. By proper adjustment of the power to the side heaters, the wall temperature under the side heaters was set to be around 45°C. The conduction heat loss from the test piece to the fiberglass wall was calculated to be negligible (less than 0.02% of the total heat flux). ac power was supplied to individual heaters through an existing power panel with individual Variacs for each heater. Typical amperage and voltage levels for each heater varied from 0.23 to 0.4 A and 20 to 45 V, respectively. Air properties were evaluated at jet temperature. The supply channel was formed by the exterior walls of the side channels, the jet plate and a 1.27-cm-thick aluminum back plate. The end caps with throttling valves controlled the flow and pressure in each channel thus simulating many variations that may occur in a real airfoil. Static pressure taps and thermocouples in each channel measured the pressure and temperature at different locations. The test sections were covered on all sides, by 5-cm-thick glasswool sheets to minimize heat losses to the environment. The radiational heat loss from the heated wall to the unheated walls as well as losses to ambient air through the fiberglass nosepiece were taken into consideration when heat transfer coefficients were reduced. A contact micromanometer with an accuracy of 0.025 mm of water as well as a series of oil and mercury manometers measured the pressures and pressure differences between the static pressure taps mounted on both sides of the target wall for each geometry. For all cases, a critical venturimeter was used to measure the total air mass flow rate entering the supply channel.

Computational Models

The computational models were constructed for a representative repeated domain with two symmetric planes in each case. Figure 3 shows this representative domain for the horseshoe geometry and details of the mesh distribution on the surface of the domain. The computational domain size for the other two geometries were the same. The CFD analysis was performed using

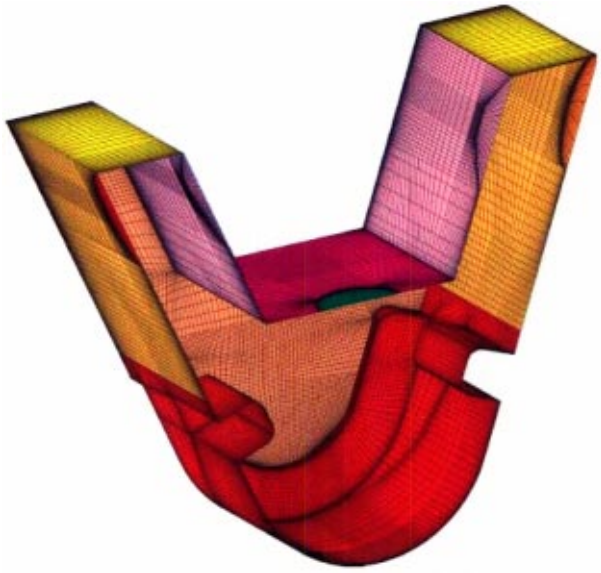

Fig. 4 Typical mesh arrangement around the computational domain periphery

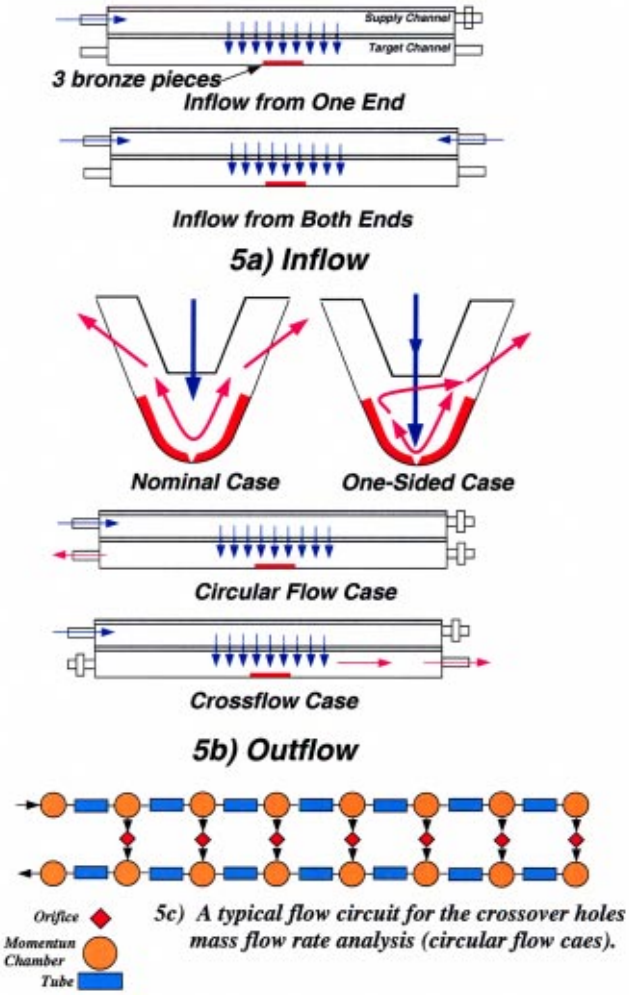

Fig. 5 Inflow and outflow arrangements

Fluent/UNS solver by Fluent, Inc., a pressure-correction based, multiblock, multigrid, unstructured/adaptive solver. Standard high Reynolds number κ-ε turbulence model in conjunction with the generalized wall function was used for turbulence closure. The average y^+ for the first layer of cells was calculated to vary between 4.5 and 10 for all cases. Other available turbulence models in this commercial code, short of two-layer model which required a change in mesh arrangement for each geometry and was beyond the scope of this investigation, were also tested and did not produce results significantly different from those of κ-ε model. Mesh independence was achieved at about 400,000 cells for a typical model. Cells in all models were entirely hexagonal, a preferred choice for CFD analyses, and were varied in size bi-geometrically from the boundaries to the center of the computational domain in order to have finer mesh close to the boundaries. Figure 4 shows the mesh distribution around the periphery of a typical model.

Results and Discussion

A total of 31 test setups each for seven jet Reynolds numbers ranging from 10,000 to 50,000 were run in this investigation. All tests had several common features described as follows. There were always seven impinging jets issuing from the jet plate. The middle jet (fourth) always impinged on the bronze test piece in the middle of the test section and the reported heat transfer results are always for that middle bronze test piece. The third and fifth jets impinged on the side bronze pieces that acted as guard heaters. The remaining four jets impinged on the fiberglass leading-edge wall to simulate the flow field in a typical leading-edge cavity. The jet Reynolds number is based on the air mass flow rate through the middle crossover hole. The nondimensional jet distance to the target surface, Z/d_{jet}, remained fixed at 3.2 for all target surface geometries.

Two inflow arrangements to the supply channel, as shown in Fig. 5*a*, where air either entered from one end or both ends were tested. The outflow arrangement, shown in Fig. 5*b*, was consisted of four different cases. For the ''nominal flow'' case the air, after impinging on the leading-edge wall, ejected equally through the side channel holes which simulate the gill holes on the pressure and suction sides of an airfoil. For the ''one-sided'' case the air, after impinging on the leading-edge wall, ejected through the gill holes on one side only. For the ''circular flow'' case the air, after impinging on the leading-edge wall, ejected from the same side of the test section as it entered while for the ''cross-flow'' case the air, after impinging on the leading-edge wall, ejected from the opposite side of the channel simulating exit flow through an airfoil tip. In the latter two flow arrangements, all side channel holes were plugged and valves were closed so that the only way out for the cooling air after impingement was through one end of the leading-edge channel. The three jets upstream of the middle jet (spent air) formed a cross flow that severely affected the impingement heat transfer coefficient. For a consistent comparison of heat transfer results for all these arrangements, the jet Reynolds number for all cases was calculated based on the air mass flow rate through the fourth crossover hole. To determine the air mass flow rate variation across the crossover holes, a one-dimensional flow circuit of each test setup consisting of appropriate orifices, tubes, momentum, and pressure chambers, shown in Fig. 5*c*, was built and analyzed. Appropriate discharge coefficients for the orifices were calculated from correlations for sharp-corner holes. The results, shown in Fig. 6, revealed that the air mass flow rate through the fourth crossover hole for the cases of flow entering the supply channel from one end or both ends and exiting through the side holes (on both sides or on one side) was very close to that of average mass flow through the seven holes, i.e., 14.28% each. The maximum difference was calculated to be 0.01%. It is also noted that the mass flow rates through other crossover holes are very close to the average percentage for these cases. For the circular and cross-flow arrangements, however, a 1% drop, compared to the average mass flow percentage of 14.28, was calculated for the mass flow rate through the fourth crossover hole and the jet Rey-

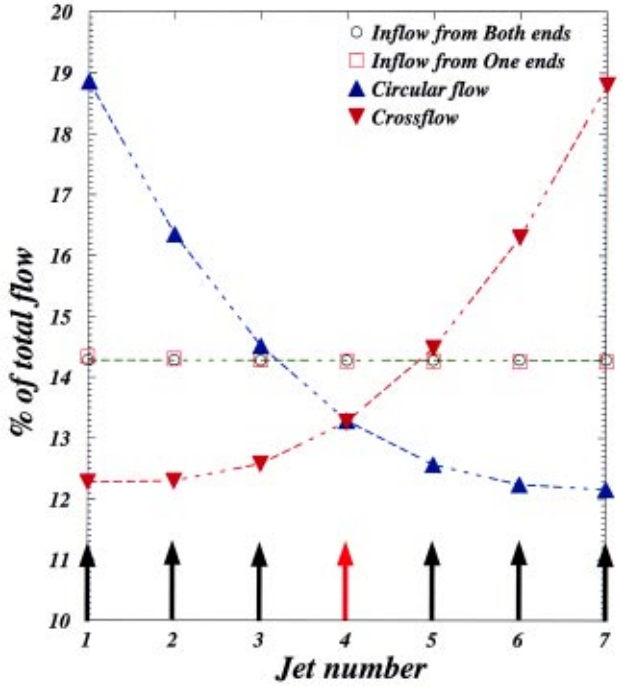

Fig. 6 Percentage of air flow rate through each crossover hole for all flow arrangements

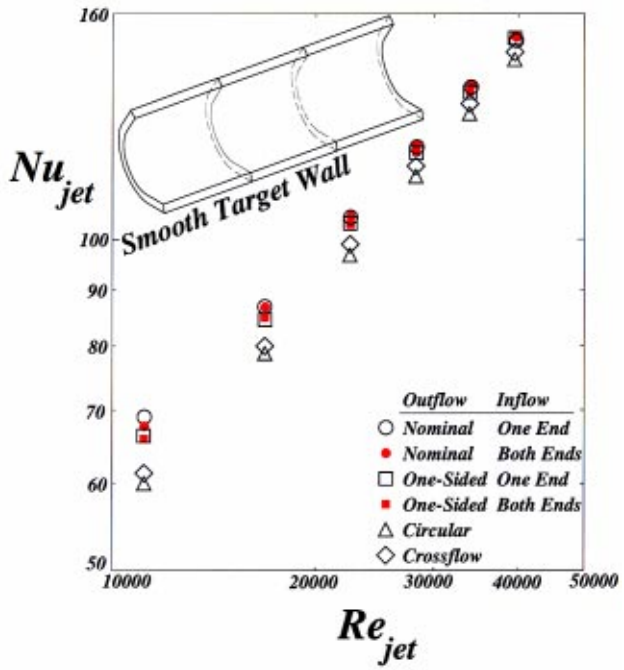

Fig. 7 Nusselt number variation with Reynolds number for the smooth surface (baseline) target geometry

nolds number was corrected accordingly. Static pressure taps in the middle and at each end of the supply channel did not measure a significant difference (about 1 cm of water column for a supply pressure ranging from 110 to 172 kPa, absolute). Experimental uncertainties in heat transfer coefficient and jet Reynolds number, following the method of Kline and McClintock [35], were determined to be 6% and 1.5%, respectively.

Geometry 1. Impingement on a smooth leading-edge wall, shown in Fig. 2*a*, was tested in this baseline geometry. Heat transfer results of this geometry are shown in Fig. 7. Several observations are made. Whether flow was entering the supply channel from one end or both ends, it had no significant effect on the impingement heat transfer coefficient because, as we showed in Fig. 6, the air mass flow rate through the fourth crossover hole for which the heat transfer results are reported, was nearly identical for both inflow arrangements. Other target surface geometries behaved similarly, as we will discuss shortly. The maximum calculated difference of 1.9% was for the nominal outflow at the lowest Reynolds number. Similarly, whether the jets, after impinging on the target surface, were exiting the leading-edge channel through one row of side holes or both rows, it had no significant effect on the impingement heat transfer coefficient. The maximum calculated difference of 3.9% was again at the lowest Reynolds number. The cross- and circular-flow arrangements, however, produced lower heat transfer coefficients. An explanation for this behavior is the presence of a cross flow (spent air), generated by the fifth, sixth, and seventh jets in the circular flow arrangement and by the first, second, and third jets for the cross-flow arrangement. This cross flow reduces the strength of the fourth jet before it impinges on the target surface which in turn reduces the impingement heat transfer coefficient. The maximum decrease compared with the nominal outflow case was calculated to be about 13% which occurred at the lowest jet Reynolds number. This difference decreased with increasing jet Reynolds number to about 2.5% at the highest jet Reynolds number.

Geometry 2. Horseshoe ribs are commonly used on the leading-edge surface of the airfoil cooling cavities in order to enhance the convective heat transfer coefficients on the leading-edge surface when the coolant is traveling in the cooling channels radially. Several investigators including the first author have reported experimental data on a variety of leading-edge rib geometries, often a critical area in airfoil life expectancy. Impingement on horseshoe ribs, however, is not reported by any investigator yet. The target wall for this geometry was roughened with two sets of ribs—a horseshoe rib that wrapped around the leading edge and two radial ribs in between the horseshoe ribs and on both sides of the airfoil stagnation line as shown in Fig. 2*b*. Compared to the baseline geometry, the total wetted heat transfer area was increased by about 40.5%. The two radial ribs were installed in between the horseshoe ribs because it was speculated that the jets, after impinging on the horseshoe ribs would interact with the radial ribs on their exit way through the gill holes, thereby increase the overall heat transfer coefficient.

To establish the superiority of the impingement cooling over the convective cooling, the heat transfer coefficient results for the two flow arrangements and for the same amount of cooling flow are compared in Fig. 8. The air mass flow rate and heat transfer coefficient were not nondimensionalized to the Reynolds and Nusselt numbers to make the comparison more realistic. The impingement heat transfer coefficient is about 2.6 times that of channel flow at the lowest cooling air mass flow rate and about 3.3 times at the highest air mass flow rate. It should be noted that these ratios are for the average heat transfer coefficient on the entire leading-edge surface (on the surface of the cast bronze piece). Local heat transfer coefficient ratios around the impingement point could be much higher than these values. This comparison proved that where high heat removal rates are desirable, impingement is a viable solution. Impingement tests for this geometry were conducted for all inflow and outflow arrangements shown in Fig. 5. The final results, however, are shown in Fig. 9 for one inflow case since, similar to the smooth target surface case, whether flow entered the supply channel from one end or both ends, the impingement heat transfer results did not show a significant change. Symmetric and asymmetric impingement cases, however, produced different results. For asymmetric impingement where jets impinged on the leading-edge area in between the

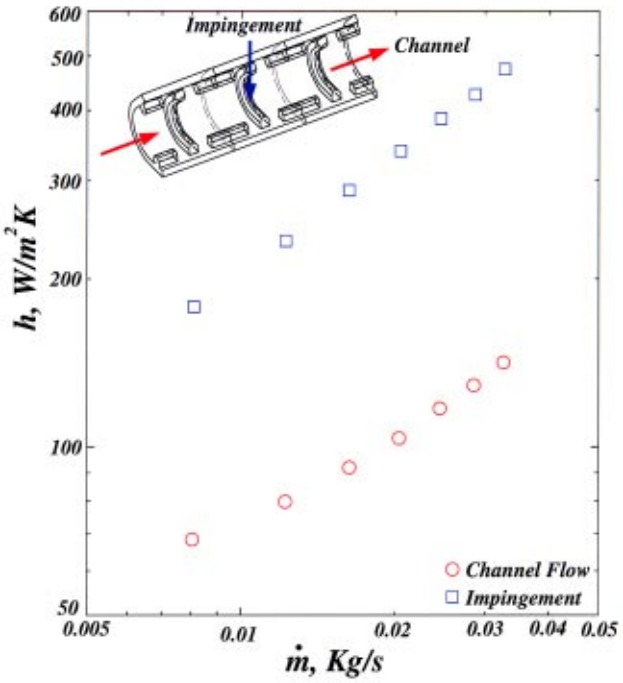

Fig. 8 Comparison between the heat transfer results of channel and impingement flows

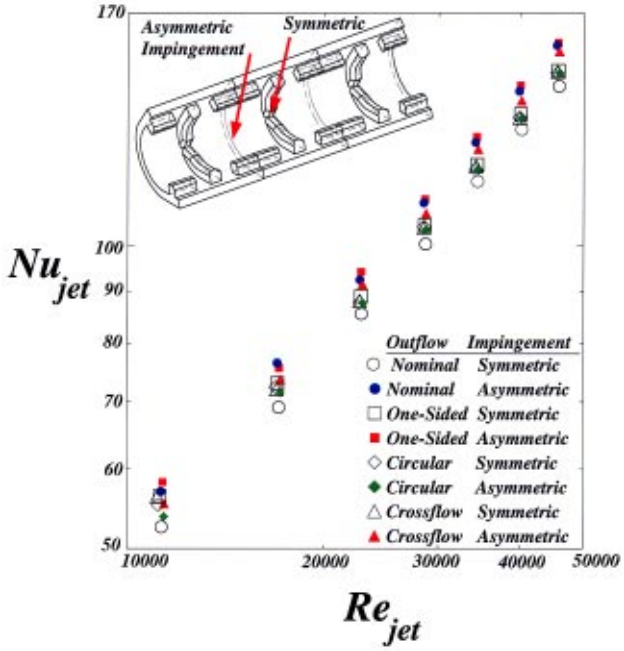

Fig. 10 Nusselt number variation with Reynolds number for the notched-horseshoe target surface geometry

horseshoe ribs, the nominal and one-sided outflow cases produced higher heat transfer coefficients compared with the symmetric impingement cases. The reason for this increase of up to 13% at low Reynolds numbers is the interaction of coolant with both horseshoe and radial ribs on its way to the side holes. The asymmetric impingements for the circular and cross-flow cases, however, produced lower heat transfer coefficients compared with the symmetric impingements. With the aid of Fig. 6 it can be reasoned that the share of the middle bronze piece from the cooling air in the asymmetric impingement case is two half jets that, with different amount of cross flow, are less effective than one full jet in the symmetric impingement case.

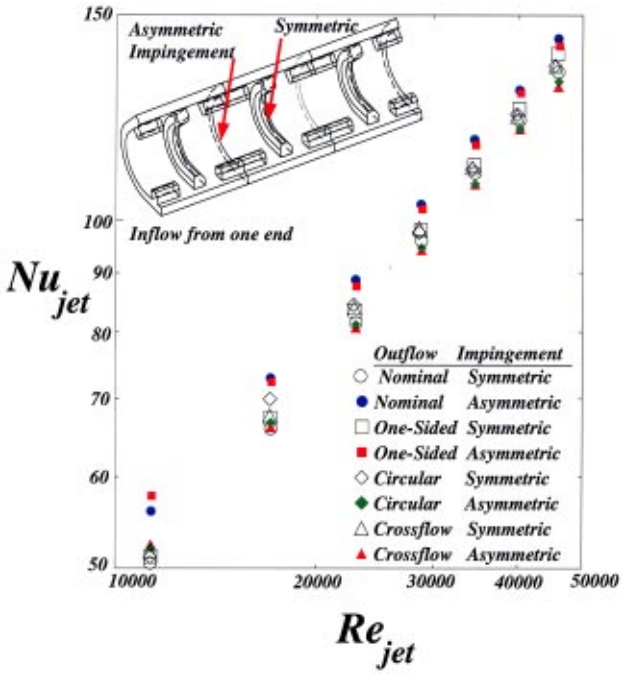

Fig. 9 Nusselt number variation with Reynolds number for the horseshoe-roughened target surface geometry

Geometry 3. The target wall for this geometry was identical to that of geometry 2 except that the horseshoe ribs had a 60 deg notch in the middle as shown in Fig. 2*c*. Based on our experience with notched ribs in rib-roughened axial-flow channels, it was expected that vortices shed off the notch in the cross- and circular-flow cases could improve the overall impingement heat transfer coefficients. Compared with the baseline geometry, the total wetted heat transfer area on the middle bronze piece was increased by about 40%. This geometry was also tested for all inflow and outflow arrangements the results of which are shown in Fig. 10. The asymmetric impingement produced higher heat transfer coefficients than those in the symmetric impingement for the nominal, one-sided, and cross-flow cases while it did not show a significant difference for the circular-flow case. When comparisons are made between the three-target surface geometries in Fig. 11, we see that in general when crossover jets impinge on the unroughened part of the target surface, they produce higher local heat transfer coefficients around the impingement area and the role of roughnesses is mostly to act as expended areas to increase the total heat pickup. That is why we notice higher heat transfer coefficients in most asymmetric cases.

Comparisons. Figures 11 and 12 compare the results of the three target surface geometries for symmetric impingement. Several observations are made. First, for all three target surface geometries, whether the cooling flow entered the supply channel from one end or both ends, the overall heat transfer coefficient did not change as shown in Fig. 12 for selected representative cases. A physical explanation based on Fig. 6 was given when the results of geometry 1 were discussed above. The same discussion holds for the other two target surface geometries. Second, smooth target surface geometry produced higher impingement heat transfer coefficients than roughened target surface with horseshoe or notched-horseshoe ribs, and notched-horseshoe ribs performed better than horseshoe ribs. Our CFD results showed the same behavior. The presence of horseshoe roughness directly under the

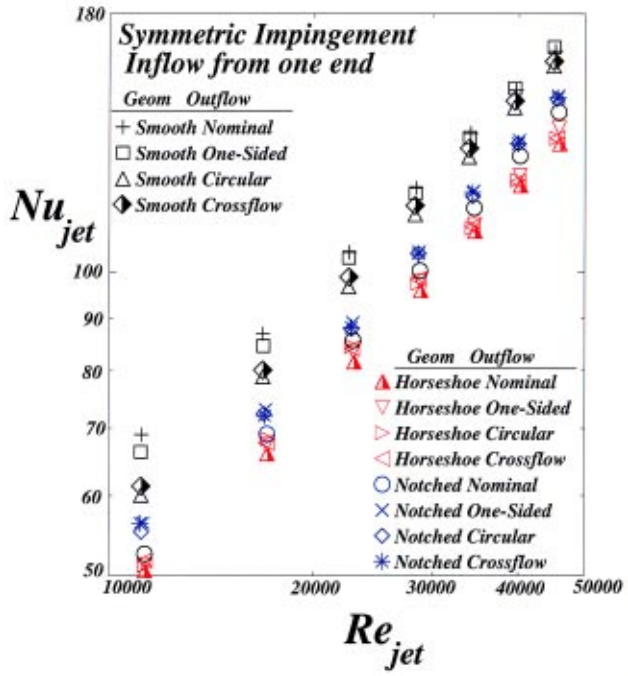

Fig. 11 Comparison between the heat transfer results of all target surface geometries

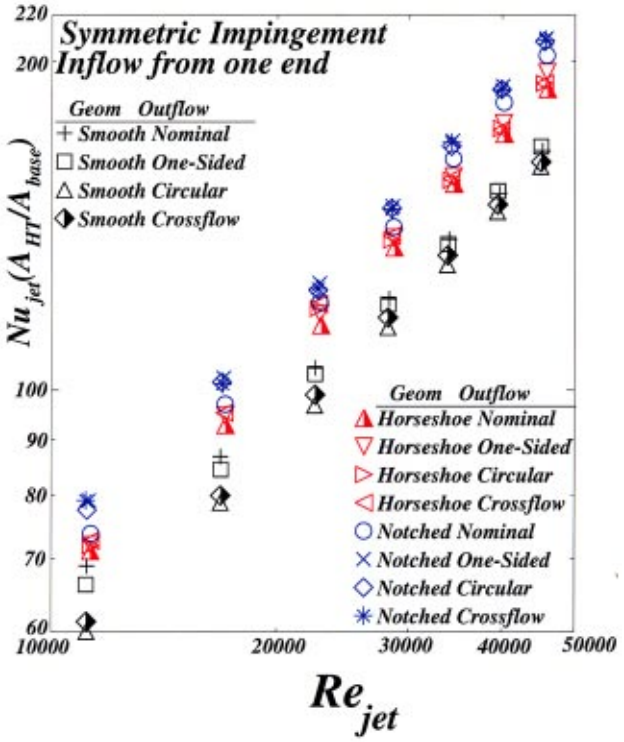

Fig. 13 Comparison between the area-augmented heat transfer results of all target surface geometries

impinging jet for the symmetric case seems to have reduced the effectiveness of the impingement for two reasons. One is that when the same jet was impinged on the smooth surface in between the horseshoe ribs, higher heat transfer coefficients were recorded and the other is that, based on the CFD velocity vectors shown in Fig. 16, the presence of radial ribs slows down the returning flow and creates recirculating zones that further reduce the overall heat transfer coefficients. Our previous work in this area dealing with impingement on target surfaces roughened with conical bumps of different sizes, sandpaper roughness and radials ribs showed the same results, i.e., the target surface roughnesses when they are smaller in size and more in numbers, at best, improve the impingement heat transfer coefficient by a few percent. A maximum reduction of 27% in heat transfer coefficient between the nominal cases of smooth and horseshoe geometries at the lowest Reynolds number was measured. However, what makes these roughnesses desirable is the area increase they introduce on the target surface which results in higher heat removal from the leading-edge surface which is often a critical area in turbine airfoil cooling design. Figure 13 includes the contribution of the increased area in the overall heat transfer from the target surface $[\mathrm{Nu}_{\mathrm{jet}}(A_{\mathrm{HT}}/A_{\mathrm{base}})]$ in the data reported in Fig. 11. The lower cluster of data represent the smooth geometry while the notched-horseshoe cases represent the highest area-augmented heat transfer. A maximum increase of about 32% in heat removal for the notched-horseshoe geometry, compared to the smooth target surface, was measured at the lowest Reynolds number which is entirely attributed to the increase in heat transfer area.

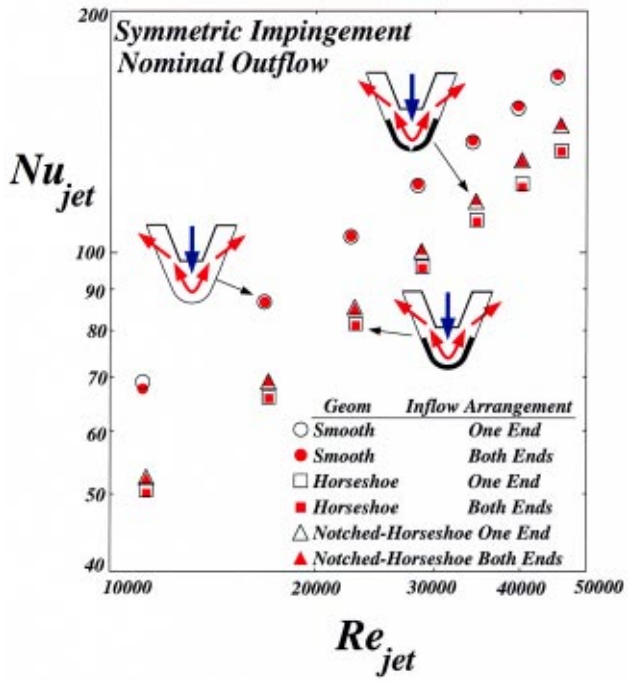

Fig. 12 Comparison between the heat transfer results of all target surface geometries for the two inflow arrangements

Static pressure ratios across the jet plate for all geometries and representative flow arrangements are shown in Fig. 14. At the lower Reynolds number range, different geometries and flow arrangements have almost the same pressure ratios across the crossover holes. At higher Reynolds numbers, however, a difference in pressure ratios across the crossover holes for different geometries is observed. Higher pressure ratios which did not go beyond 1.011, in general, correspond to the nominal cases in which there is a flow split after impingement. The small difference between the pressure ratios were mainly due to different inflow and outflow arrangements and not to target surface geometry.

CFD Results. Representative CFD results are compared with the experimental data in Fig. 15. CFD models with constant heat flux boundary conditions identical to the tested geometry for each case were run on PC Pentium 4, 1.6-GHz machines with 512 MB memory. A typical case took about 1000 iterations and about four

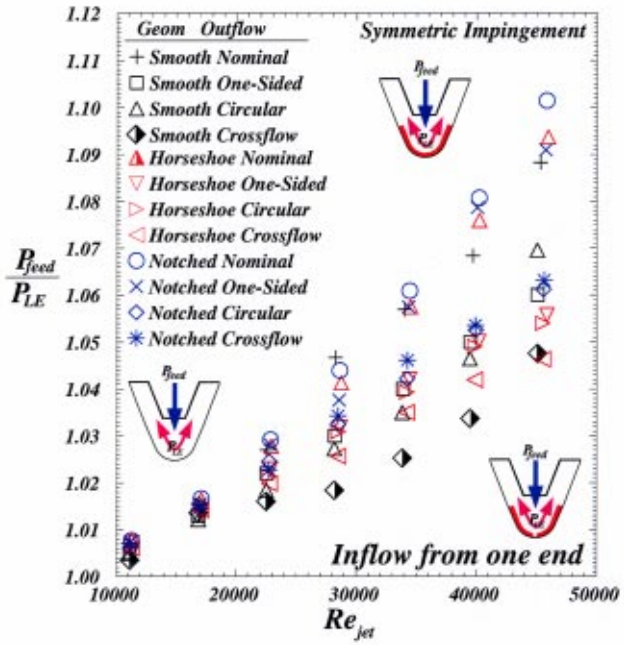

Fig. 14 Comparison between the pressure ratios across the crossover holes for all target surface geometries

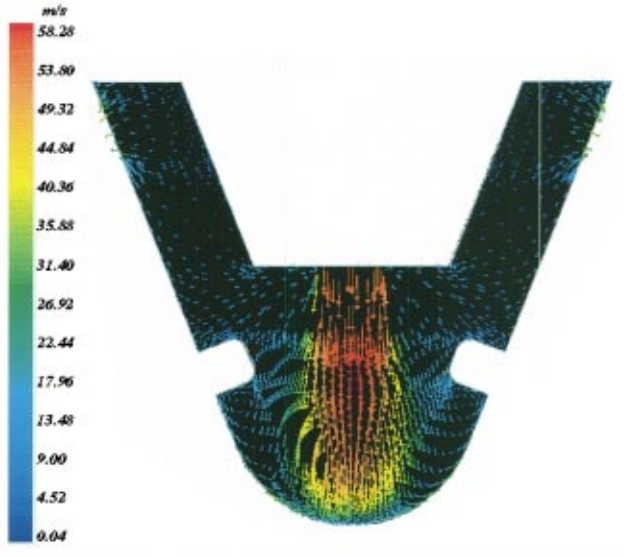

Fig. 16 Representative velocity vectors near the symmetry plane

to five hours to converge. Very good agreements between the measured and numerically calculated impingement heat transfer coefficients are observed. A small difference of 4%, at the most, for the smooth target wall makes these CFD packages viable tools in predicting the impingement heat transfer coefficient. For the roughened target surface cases, the difference is higher due to the presence of recirculating zones in the flow domain, as seen in Fig. 16 and generally more complex flow patterns around the horseshoe and straight ribs. A maximum difference of about 9% between the test and CFD results for the notched-horseshoe geometry is very encouraging. It is worth noticing that the numerical results also confirm that the smooth target surface produced higher impingement heat transfer coefficients followed by the notched-horseshoe and horseshoe geometries. Representative heat transfer coefficient and target surface temperature variations are shown in Figs. 17 and 18. As physically expected, the area directly under the jet shows the highest heat transfer coefficient and lowest surface temperature with the opposite behavior for the areas that are not directly affected by the jet.

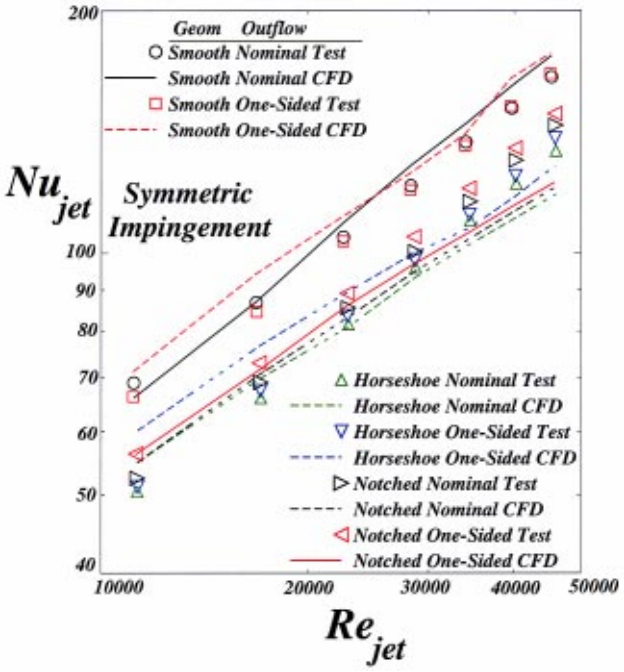

Fig. 15 Comparison between the experimental and numerical heat transfer results for all target surface geometries

Conclusions

Three leading-edge surface geometries, consisting of a baseline smooth surface and two surfaces roughened with a combination of horseshoe and straight radial ribs, were tested for impingement cooling. The smooth target surface produced the highest impingement heat transfer coefficients followed by the notched-horseshoe

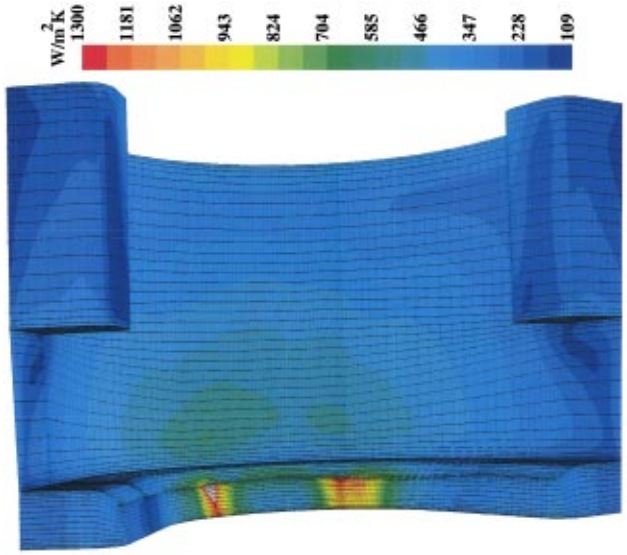

Fig. 17 Representative heat transfer coefficient variation on the heated surface

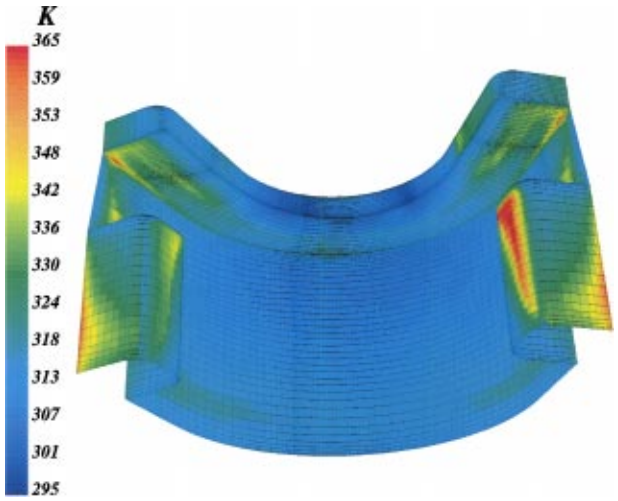

Fig. 18 Representative temperature variation on the heated surface

and horseshoe ribs. However, when the contribution of the increased area in the overall heat transfer is taken into consideration, the target surface roughed with notched-horseshoe ribs, for all inflow and outflow cases, proved to be the most effective geometry. An overall increase of about 27% in heat removal can be accomplished by roughening the leading-edge wall with these ribs. The increase is entirely attributed to the increase in the heat transfer area. A very good agreement between the numerical and experimental results, especially for the smooth target surface geometry, suggests that the CFD analyses are becoming a viable tool for the prediction of impingement heat transfer coefficients in turbine airfoil cooling.

Nomenclature

A_{base} = leading-edge base area for the smooth case
A_{hole} = crossover holes area
A_{HT} = total heat transfer area including the surface roughness
AR = cooling channel aspect ratio
AR_{rib} = rib aspect ratio
d_{jet} = jet diameter
D_h = cooling channel hydraulic diameter
e = roughness height
h = average heat transfer coefficient on the leading-edge wall, $[(vi/A_{HT})-q_{loss}]/(T_s-T_{jet})$
i = current through the foil heater on the middle bronze piece
k = air thermal conductivity
m = air mass flow rate through the middle (fourth) crossover hole
Nu_{jet} = average Nusselt number based on the jet diameter, hd_{jet}/k
P_{feed} = supply channel pressure
P_{LE} = leading-edge channel pressure
q_{loss} = heat losses from the middle bronze piece to the ambient by conduction and convection as well as the heat losses by radiation to the unheated walls
R_{nose} = channel radius at the leading edge
Re_{jet} = Reynolds number based on the jet diameter $(\rho U_{jet} d_{jet}/\mu)$
S = Rib pitch
T_{jet} = air jet temperature
T_s = surface temperature
U_{jet} = jet mean velocity, $m/\rho A_{hole}$
Z = jet plate distance to the target surface (Fig. 1)
v = voltage drop across the foil heater on the middle bronze piece
α = rib angle of attack
μ = air dynamic viscosity at jet temperature
ρ = air density at jet temperature and pressure

References

[1] Burggraf, F., 1970, "Experimental Heat Transfer and Pressure Drop With Two Dimensional Turbulence Promoters Applied to Two Opposite Walls of a Square Tube," *Augmentation of Convective Heat and Mass Transfer*, edited by A. E. Bergles and R. L. Webb, ASME, New York, pp. 70–79.
[2] Chandra, P. R., and Han, J. C., 1989, "Pressure Drop and Mass Transfer in Two-Pass Ribbed Channels," J. Thermophys. Heat Transfer, **3**, pp. 315–319.
[3] El-Husayni, H. A., Taslim, M. E., and Kercher, D. M., 1994, "An Experimental Investigation of Heat Transfer Coefficients in a Spanwise Rotating Channel With Two Opposite Rib-Roughened Walls," ASME J. Turbomach., **113**, pp. 75–82.
[4] Han, J. C., 1984, "Heat Transfer and Friction in Channels With Two Opposite Rib-Roughened Walls," ASME J. Heat Transfer, **106**, pp. 774–781.
[5] Han, J. C., Glicksman, L. R., and Rohsenow, W. M., 1978, "An Investigation of Heat Transfer and Friction for Rib Roughened Surfaces," Int. J. Heat Mass Transfer, **21**, 1143–1156.
[6] Han, J. C., Park, J. S., and Lei, C. K., 1985, "Heat Transfer Enhancement in Channels With Turbulence Promoters," ASME J. Eng. Gas Turbines Power, **107**, pp. 628–635.
[7] Han, J. C., Zhang, Y. M., and Lee, C. P., 1992, "Influence of Surface Heat Flux Ratio on Heat Transfer Augmentation in Square Channels With Parallel, Crossed, and V-Shaped Angled Ribs," ASME J. Turbomach., **114**, pp. 872–880.
[8] Metzger, D. E., Vedula, R. P., and Breen, D. D., 1987, "The Effect of Rib Angle and Length on Convection Heat Transfer in Rib-Roughened Triangular Ducts," *Proceedings of the ASME-JSME Thermal Engineering Joint Conference*, Vol. 3, pp. 327–333.
[9] Metzger, D. E., Chyu, M. K., and Bunker, R. S., 1988, "The Contribution of On-Rib Heat Transfer Coefficients to Total Heat Transfer From Rib-Roughened Surfaces," *Transport Phenomena in Rotating Machinery*, edited by J. H. Kim, Hemisphere Publishing Co., Washington, DC.
[10] Metzger, D. E., Fan, C. S., and Yu, Y., 1990, "Effects of Rib Angle and Orientation on Local Heat Transfer in Square Channels With Angled Roughness Ribs," *Compact Heat Exchangers: A Festschrift for A.L. London*, Hemisphere Publishing Co., Washington, DC, pp. 151–167.
[11] Taslim, M. E., and Spring, S. D., 1988, "An Experimental Investigation of Heat Transfer Coefficients and Friction Factors in Passages of Different Aspect Ratios Roughened With 45° Turbulators," *Proc. National Heat Conference*, Houston, TX.
[12] Taslim, M. E., and Spring, S. D., 1988, "Experimental Heat Transfer and Friction Factors in Turbulated Cooling Passages of Different Aspect Ratios, Where Turbulators are Staggered," Paper AIAA-88-3014.
[13] Taslim, M. E., Bondi, L. A., and Kercher, D. M., 1991, "An Experimental Investigation of Heat Transfer in an Orthogonally Rotating Channel Roughened 45 Degree Criss-Cross Ribs on Two Opposite Walls," ASME J. Turbomach., **113**, pp. 346–353.
[14] Taslim, M. E., and Spring, S. D., 1991, "An Experimental Investigation Into the Effects Turbulator Profile and Spacing Have on Heat Transfer Coefficients and Friction Factors in Small Cooled Turbine Airfoils," Paper AIAA-91-2033.
[15] Taslim, M. E., Rahman, A., and Spring, S. D., 1991, "An Experimental Investigation of Heat Transfer Coefficients in a Spanwise Rotating Channel With Two Opposite Rib-Roughened Walls," ASME J. Turbomach., **113**, pp. 75–82.
[16] Webb, R. L., Eckert, E. R. G., and Goldstein, R. J., 1971, "Heat Transfer and Friction in Tubes With Repeated-Rib-Roughness," Int. J. Heat Mass Transfer, **14**, pp. 601–617.
[17] Zhang, Y. M., Gu, W. Z., and Han, J. C., 1994, "Heat Transfer and Friction in Rectangular Channels With Ribbed or Ribbed-Grooved Walls," ASME J. Heat Transfer, **116**, pp. 58–65.
[18] Chupp, R. E., Helms, H. E., McFadden, P. W., and Brown, T. R., 1969, "Evaluation of Internal Heat Transfer Coefficients for Impingement Cooled Turbine Blades," J. Aircr., **6**, pp. 203–208.
[19] Metzger, D. E., Yamashita, T., and Jenkins, C. W., 1969, "Impingement Cooling of Concave Surfaces With Lines of Circular Air Jets," J. Eng. Power, **93**, pp. 149–155.
[20] Kercher, D. M., and Tabakoff, W., 1970, "Heat Transfer by a Square Array of Round Air Jets Impinging Perpendicular to a Flat Surface Including the Effect of Spent Air," J. Eng. Power, **92**, pp. 73–82.
[21] Florschetz, L. W., Berry, R. A., and Metzger, D. E., 1980, "Periodic Streamwise Variation of Heat Transfer Coefficients for Inline and Staggered of Circular Jets With Crossflow of Spent Air," ASME J. Heat Transfer, **102**, pp. 132–137.
[22] Florschetz, L. W., Truman, C. R., and Metzger, D. E., 1981, "Streamwise Flow and Heat Transfer Distribution for Jet Impingement With Crossflow," ASME J. Heat Transfer, **103**, pp. 337–342.
[23] Florschetz, L. W., Metzger, D. E., Su, C. C., Isoda, Y., and Tseng, H. H., 1984, "Heat Transfer Characteristics for Jet Arrays Impingement With Initial Crossflow," ASME J. Heat Transfer, **106**, pp. 34–41.
[24] Metzger, D. E., and Bunker, R. S., 1990, "Local Heat Transfer in Internally

Cooled Turbine Airfoil Leading Edge Regions: Part I—Impingement Cooling Without Film Coolant Extraction,'' ASME J. Turbomach., **112**, pp. 451–458.
[25] Bunker, R. S., and Metzger, D. E., 1990, ''Local Heat Transfer in Internally Cooled Turbine Airfoil Leading Edge Regions: Part II—Impingement Cooling With Film Coolant Extraction,'' ASME J. Turbomach., **112**, pp. 459–466.
[26] Van Treuren, K. W., Wang, Z., Ireland, P. T., and Jones, T. V., 1994, ''Detailed Measurements of Local Heat Transfer Coefficient and Adiabatic Wall Temperature Beneath an Array of Impinging Jets,'' ASME J. Turbomach., **116**, pp. 269–374.
[27] Chang, H., Zhang, D., and Huang, T., 1997, ''Impingement Heat Transfer From Rib Roughened Surface Within Arrays of Circular Jet: The Effect of the Relative Position of the Jet Hole to the Ribs,'' Paper 97-GT-331.
[28] Huang, Y., Ekkad, S. V., and Han, J. C., 1998, ''Detailed Heat Transfer Distributions Under an Array of Orthogonal Impinging Jets,'' J. Thermophys. Heat Transfer, **12**, pp. 73–79.
[29] Akella, K. V., and Han, J. C., 1999, ''Impingement Cooling in Rotating Two-Pass Rectangular Channels With Ribbed Walls,'' J. Thermophys. Heat Transfer, **13**, pp. 364–371.
[30] Ekkad, S. V., Huang, Y., and Han, J. C., 1999, ''Impingement Heat Transfer on a Target Plate With Film Holes,'' J. Thermophys. Heat Transfer, **13**, pp. 522–528.
[31] Taslim, M. E., Setayeshgar, L., and Spring, S. D., 2001, ''An Experimental Evaluation of Advanced Leading Edge Impingement Cooling Concepts,'' ASME J. Turbomach., **123**, pp. 147–153.
[32] Taslim, M. E., and Setayeshgar, L., 2001, ''Experimental Leading-Edge Impingement Cooling Through Racetrack Crossover Holes,'' Paper 2001-GT-0153.
[33] Taslim, M. E., Pan, Y., and Spring, S. D., 2001, ''An Experimental Study of Impingement on Roughened Airfoil Leading-Walls With Film Holes,'' ASME J. Turbomach., **123**, pp. 766–773.
[34] Taslim, M. E., Pan, Y., and Bakhtari, K., 2002, ''Experimental Racetrack Shaped Jet Impingement on a Roughened Leading-Edge Wall With Film Holes,'' Paper GT-2002-30477.
[35] Kline, S. J., and McClintock, F. A., 1953, ''Describing Uncertainty in Single-Sample Experiments,'' Mech. Eng. (Am. Soc. Mech. Eng.) **75**, Jan., pp. 3–8.

Impact of Geometric Variability on Axial Compressor Performance

Victor E. Garzon
Postdoctoral Associate
e-mail: vgarzon@mit.edu

David L. Darmofal
Associate Professor
e-mail: darmofal@mit.edu

Department of Aeronautics and Astronautics,
Massachusetts Institute of Technology,
77 Massachusetts Avenue,
Cambridge, MA 02139

A probabilistic methodology to quantify the impact of geometric variability on compressor aerodynamic performance is presented. High-fidelity probabilistic models of geometric variability are derived using a principal-component analysis of blade surface measurements. This probabilistic blade geometry model is then combined with a compressible, viscous blade-passage analysis to estimate the impact on the passage loss and turning using a Monte Carlo simulation. Finally, a mean-line multistage compressor model, with probabilistic loss and turning models from the blade-passage analysis, is developed to quantify the impact of the blade variability on overall compressor efficiency and pressure ratio. The methodology is applied to a flank-milled integrally bladed rotor. Results demonstrate that overall compressor efficiency can be reduced by approximately 1% due to blade-passage effects arising from representative manufacturing variability.
[DOI: 10.1115/1.1622715]

1 Motivation

Turbomachinery airfoils must perform reliably and efficiently in severe environments for prolonged periods of time. The optimal shapes of compressor and turbine airfoils have been the subject of a large body of research literature. Advances in numerical methods that allow prescribed velocity distributions for controlled diffusion and supercritical transonic operation have resulted in highly optimized airfoils and ever more efficient compression systems. Despite recent noteworthy advances in manufacturing techniques (e.g., electro-chemical machining, flank milling, etc.), finished airfoils always exhibit some deviation from their intended shape and size. The effect of such variations on compressor performance is poorly understood but generally thought to be detrimental.

Probabilistic techniques applied to structural design and analysis have been used in the aerospace industry for more than two decades [1]. In contrast, few similar endeavors have been undertaken in *aerothermal* analysis and design of turbomachinery components. Turbomachinery probabilistic aerothermal analysis is especially challenging because of the highly nonlinear mathematical models involved. A marked increase in computational requirements occurs in direct proportion to the physical complexity of the turbomachinery physics. Until recently, probabilistic treatments of turbomachinery aerothermal analysis and design have been deemed prohibitively expensive. The advent of relatively inexpensive parallel hardware has considerably increased the feasibility of such probabilistic studies.

In this work we present a methodology for estimating the impact of geometric variability on the aerodynamic performance of individual blade passages and, by a modeling extension, on the aerothermal performance of high-pressure axial compression systems. The methodology is applied to an integrally bladed rotor from a multistage axial compressor.

The paper is divided into three sections. The first section discusses the development of a probabilistic model for the geometric variability present in a set of compressor blade measurements. The second section illustrates the use of conventional computational fluid dynamics (CFD) analysis in combination with classical probabilistic simulation techniques to assess the impact of geometric variability on the aerodynamic performance of individual blade passages. In the third section, a probabilistic multistage mean-line compressor model is used to estimate the impact of airfoil geometric variability on overall compressor performance.

Contributed by the International Gas Turbine Institute and presented at the International Gas Turbine and Aeroengine Congress and Exhibition, Atlanta, GA, June 16–19, 2003. Manuscript received by the IGTI December 2002; final revision March 2003. Paper No. 2003-GT-38130. Review Chair: H. R. Simmons.

2 Geometric Characterization of Compressor Blade Variability

This section presents results from an application of principal-component analysis (PCA) to characterizing sets of compressor blade surface measurements. As discussed below, high fidelity models of geometric variability for use in probabilistic simulations can be readily constructed from the PCA results. Statistically based models of variability are clearly superior alternatives to heuristic models based on manufacturing tolerances or anecdotal evidence alone, as they represent the ''actual'' variability found in measurements.

2.1 Background. The nominal airfoil geometry is taken to be defined by p coordinate points $\mathbf{x}_j^0 \in \mathbb{R}^m$, $j=1,\ldots,p$ where m is typically 2 or 3. We consider a set of n coordinate measurements $\{\hat{\mathbf{x}}_{i,j} \in \mathbb{R}^m | i=1,\ldots,n; j=1,\ldots,p\}$ taken, for instance, with a coordinate-measuring machine. The measurements may correspond to single radial locations ($m=2$) or entire spanwise segments ($m=3$). Index j uniquely identifies specific nominal points and their measured counterparts. Similarly index i identifies a distinct set of measured points. The discrepancies in the coordinate measurements can then be expressed as

$$\mathbf{x}'_{i,j} = \hat{\mathbf{x}}_{i,j} - \mathbf{x}_j^0, \quad i=1,\ldots,n; \;\; j=1,\ldots,p.$$

Subtracting from these error vectors their ensemble average,

$$\overline{\mathbf{x}}_j = \frac{1}{n}\sum_{i=1}^{n} \mathbf{x}'_{i,j}, \quad j=1,\ldots,p,$$

gives a centered set of m-dimensional vectors, $\chi = \{\mathbf{x}_{i,j} = \hat{\mathbf{x}}_{i,j} - \overline{\mathbf{x}}_j | i=1,\ldots,n; j=1,\ldots,p\}$. Writing the m-dimensional measurements in vector form, $\mathbf{X}_j = [\mathbf{x}_{i,j}^T, \ldots, \mathbf{x}_{n,j}^T]^T$, the *scatter matrix* of set χ is given by

$$\mathbf{S} = \mathbf{X}^T\mathbf{X}.$$

The scatter matrix is related to the covariance matrix $\mathbf{C}$ via $\mathbf{C} = (n-1)^{-1}\mathbf{S}$.

It can be shown (see, for instance, Refs. [2] and [3]) that the directions along which the scatter is maximized correspond to nontrivial solutions of the eigenvalue problem,

$$\mathbf{S}\mathbf{v} = \lambda\mathbf{v}. \tag{1}$$

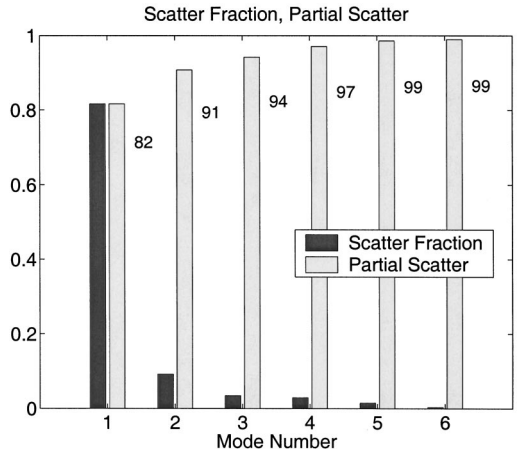

Fig. 1 IBR mid-span section: PCA modes

Since **S** is symmetric positive definite, it has in general *mp* orthonormal eigenvectors $\mathbf{v}_i \in \mathbb{R}^{mp}$, $i=1,\ldots,mp$ with corresponding real, non-negative eigenvalues λ_i, $i=1,\ldots,mp$. By construction, the variance of the geometric data corresponding to eigenvector $\mathbf{v}_i$ is $\lambda_i/(n-1)$. The eigenvector corresponding to the largest eigenvalue gives the direction along which the scatter of the data is maximized. The eigenvector corresponding to the next largest eigenvalue maximizes the scatter along a direction *normal* to the previous eigenvectors. It is in this sense that the eigenvectors of **S** are said to provide an *optimal* statistical basis for the decomposition of the scatter of the data.

The PCA synthesis of **S** can be shown to be equivalent to the *singular value decomposition* (SVD) of **X** in reduced form [4],

$$\mathbf{X}=\mathbf{U}\Sigma\mathbf{V}^T, \tag{2}$$

where $\Sigma=\mathrm{diag}(\hat{\sigma}_1,\ldots,\hat{\sigma}_{mp})$, $\hat{\sigma}_j=\sqrt{\lambda_j}$, $j=1,\ldots,mp$, and the columns of **V** are the corresponding eigenvectors of **S**. The standard deviation of the geometric data attributable to the *i*th mode is therefore $\sigma_i=(n-1)^{-1/2}\hat{\sigma}_i$. The columns of $\mathbf{A}=\mathbf{U}\Sigma$ are called the amplitude vectors or *principal components* of the data set χ. The SVD of **X** is made unique by requiring that $\{\hat{\sigma}_j\}_{j=1}^{mp}$ be a nonincreasing sequence.

2.2 Application. As an application of the PCA formalism outlined above, we consider an integrally bladed rotor (IBR) consisting of 56 blades. Surface measurements of 150 blades from four separate rotors were taken using a scanning coordinate-measuring machine. Each blade was measured at 13 different radial locations. The scanning measurements of each radial station were condensed to 103 points corresponding to those defining the nominal airfoil sections.

For the present application, the 13 separate cross-sectional measurements were stacked together to form a three-dimensional representation of the measured portion of the blade. Using bicubic spline interpolation, the nominal geometry, as well as each measured blade, were sliced along a mid-span axial streamline path of varying radius (see next section). In addition, the coordinate values were scaled by the blade tip radius.

Using the notation introduced above, the resulting set χ of two-dimensional centered measurement vectors can be written as $n \times mp$ matrix **X** where $n=150$, $m=2$, and $p=103$. Figure 1 shows the modal scatter fraction $\lambda_k/\Sigma_{i=1}^{mp}\lambda_i$ (decreasing) and the partial scatter $\Sigma_{i=1}^{k}\lambda_i/\Sigma_{i=1}^{mp}\lambda_i$ (increasing) of the first six eigenmodes of **S**. The first mode contains 82% of the total scatter in the original measurements and it clearly dwarfs the scatter fraction of the other modes. The scatter corresponding to the second-most energetic mode is roughly eight times smaller than the first.

Figures 2 and 3 depict the outlines of the first and third eigenmodes of **S** applied to the baseline geometry and scaled by their respective amplitude, that is,

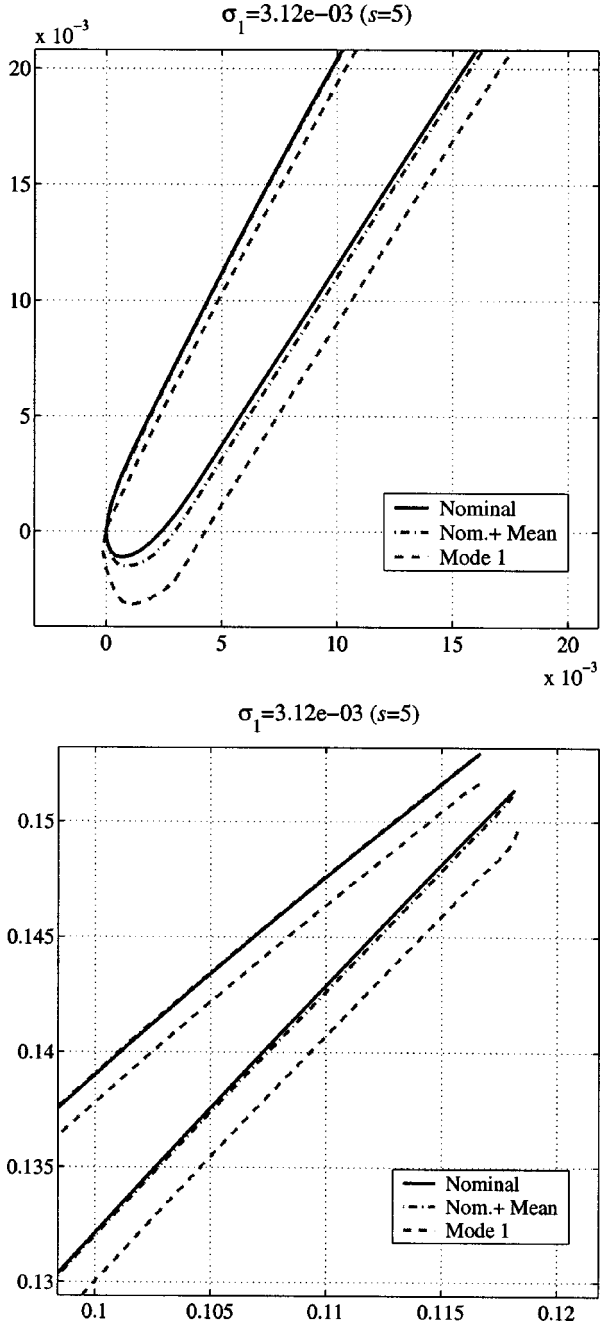

Fig. 2 IBR mid-span section: Scaled mode 1

$$\mathbf{x}_i=\mathbf{x}^0+\overline{\mathbf{x}}+s\sigma_i\mathbf{v}_i\,. \tag{3}$$

An additional scaling factor *s* has been used for plotting purposes to help distinguish the effect the eigenmodes from the mean geometry. Figure 2 indicates that the main effects of mode 1 are uniform thickening of the airfoil and azimuthal translation. Mode 3, on the other hand, exhibits a thinning of the airfoil on the suction surface away from the leading edge, with the shape of the latter being maintained. The perturbations to the airfoil nose are particularly noteworthy as the aerodynamic performance of transonic airfoils is known to be sensitive to leading-edge shape and thickness.

Figure 1(*a*) indicates that the first five modes, when combined, contain 99% of the total scatter present in the sample. The rapid

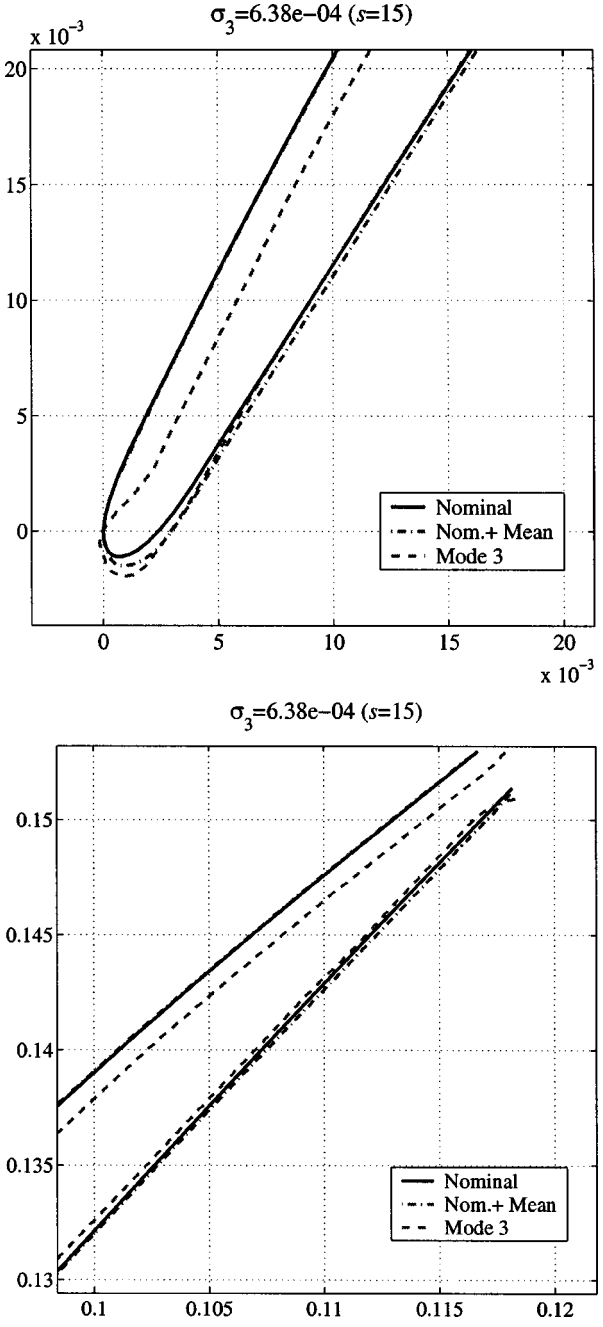

Fig. 3 IBR mid-span section: Scaled mode 3

decrease in relative energy of the higher modes suggests that a reduced-order model containing only the first few modes may be sufficient to represent most of the geometric variability contained in the original set of measurements.

The above description of modes 1 and 3 would suggest a decomposition into customary geometric features of known aerodynamic and structural importance. Table 1 summarizes percent changes in maximum thickness, maximum camber, leading-edge radius, chord length and cross-sectional area, as well as trailing-edge deflection angles, for the first six eigenmodes. In computing the parameters shown in the table, the modes were not scaled ($s=1$) and a positive amplitude was assumed.[1] The row labeled "mean" contains the changes corresponding to the average airfoil $\overline{\mathbf{x}}$. From Table 1, no single mode produces a dominant change in a particular feature; rather, each mode contributes to changes in all features. It follows that, in characterizing actual geometric variability, checking only for compliance of individual design tolerances based on customary geometric features may not be effective since these features show strong correlation.

2.3 PCA Results versus Number of Samples. In the application of PCA to compressor rotor blade measurements discussed above, all available samples (150) were used in the analysis. This section discusses how PCA results (covariance matrix eigenvalues) vary according to the number of samples being considered. Given n measurement samples, there are $\binom{n}{k}$ different ways of selecting $k \leqslant n$ among them.[2] Figure 4 depicts convergence trends of the first three eigenvalues of the covariance matrix for k measured samples. The average value and standard deviation of each eigenvalue are computed from $\min[\binom{n}{k},10^4]$ random permutations of the indices $\{1 \cdots n\}$. For each random permutation, the eigenvalues of the covariance matrix of the corresponding indexed measurements is computed via singular value decomposition. In Fig. 4 the average eigenvalues are shown as solid lines and a 2σ interval about the mean by dash-dot lines.

The uncertainty of the first covariance matrix eigenvalue is very large for small sample sizes and decreases monotonically as the sample size is increased. Since the $\pm 2\sigma$ bands are approximately the 95% confidence bands, the figures suggest that at least 130 blades would be required to have 95% confidence that the dominant eigenvalues deviate from their $k=n$ value by no more than 10% of the total variance.[3]

2.4 PCA-Based Reduced-Order Model of Geometric Variability. A reduced-order model of the geometric variability present in χ can be motivated as follows. Let Z_i, $i=1, \ldots, mp$ be independent, identically distributed random variables from $N(0,1)$ (normally distributed with zero mean and variance 1). By linearity, the random vector

[1] Geometric parameters computed with XFOIL [5].

[2] $\binom{n}{k}$ or "n choose k" is defined for $k \leqslant n$ by [6]: $\binom{n}{k} := n!/[(n-k)!k!]$.

[3] The total variance of the blade population is defined as $\Sigma_{i=1}^{mp}\sigma_i^2$ and for the data presented here it is roughly 1.2×10^{-5}.

Table 1 IBR mid-span section: geometric features of PCA modes

	Mode	Max thickness (%Δ)	Max camber (%Δ)	LE radius (%Δ)	TE angle (Δ deg)	Chord (%Δ)	Area (%Δ)
Mean (from $\mathbf{x}^0$)		−0.12	−0.98	18.33	0.06	−0.04	−1.03
From mean	1	−0.54	−0.06	−4.22	0.00	−0.04	−0.77
	2	−1.09	0.28	2.15	0.04	−0.04	−1.27
	3	0.53	0.04	1.83	−0.02	0.01	0.85
	4	−0.74	0.10	1.34	−0.07	0.02	−0.87
	5	−0.11	0.27	4.23	0.06	0.02	−0.01
	6	0.03	−0.01	−4.11	0.01	0.00	−0.08

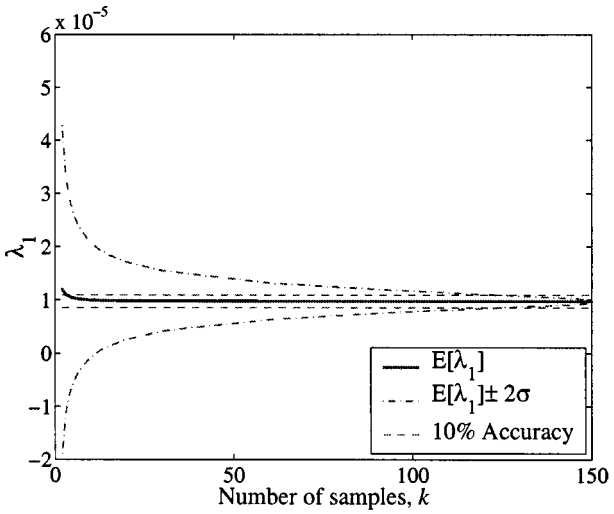

(a) λ_1

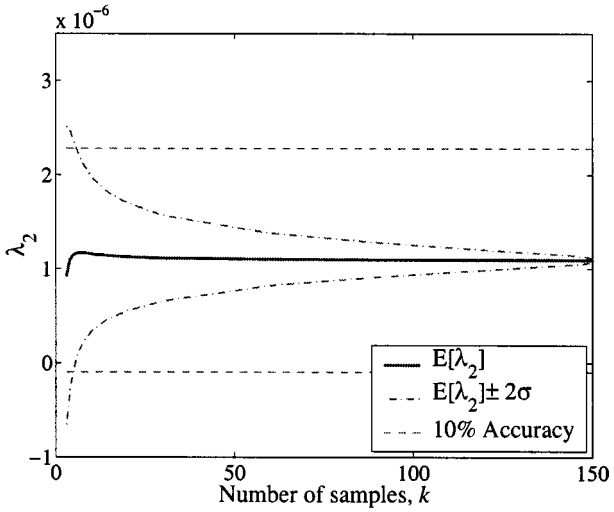

(b) λ_2

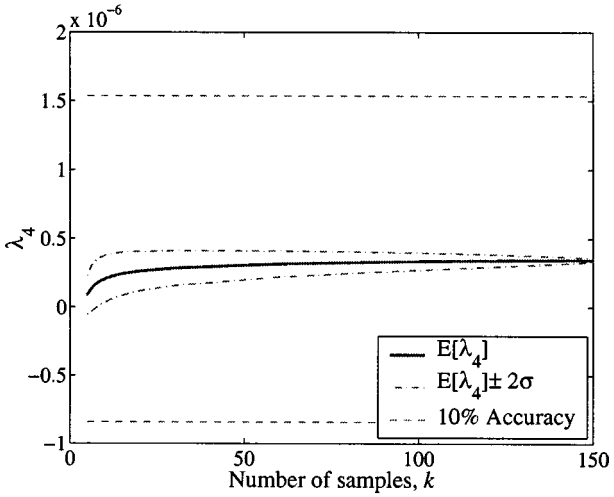

(c) λ_4

Fig. 4 Eigenvalues of covariance matrix versus number of samples. Average eigenvalues (—), $\pm 2\sigma$ interval about the mean (-.-) and ±10% accuracy bands (- - -).

$$X = \mathbf{x}^0 + \overline{\mathbf{x}} + \sum_{i=1}^{mp} \sigma_i Z_i \mathbf{v}_i$$

has mean $\mathbf{x}^0 + \overline{\mathbf{x}}$ and the same unbiased estimator of total variance as the set of measurements χ. This suggests a reduced-order model of the form

$$\tilde{X} = \mathbf{x}^0 + \overline{\mathbf{x}} + \sum_{i=1}^{K} \boldsymbol{\sigma}_i Z_i \mathbf{v}_i \tag{4}$$

where $K < mp$ is a free truncation parameter. For large enough n, as K increases the total variance of $\tilde{X}$ approaches that of X. In fact, the total scatter of a finite set of instances of X is bounded by $\Sigma_{i=1}^{K} \lambda_i \leqslant \Sigma_{i=1}^{mp} \lambda_i$.

3 Impact of Geometric Variability On Blade Passage Aerodynamics

3.1 Blade Passage Analysis: MISES. The transonic compressor blade analysis was carried out using MISES (multiple blade interacting streamtube Euler solver), an interactive viscous flow analysis package [7] widely used in turbomachinery analysis and design. MISES' flow solver, ISES can be used to analyze and design single- or multielement airfoils over a wide range of flow conditions. ISES incorporates a zonal approach in which the inviscid part of the flow is described by the projection of the steady-state three-dimensional (3D) Euler equations onto an axisymmetric stream surface of variable thickness and radius. The resulting two-dimensional equations are discretized in conservative form over a streamline grid. The viscous parts of the flow (boundary layers and wake) are modeled by a two-equation integral boundary layer formulation [8]. The viscous and inviscid parts of the flowfield are coupled through the displacement thickness and the resulting nonlinear system of equations is solved using the Newton-Raphson method [9]. A feature of MISES that is particularly relevant to probabilistic analysis is its speed. For the cases reported herein, typical execution times are three to ten sec per trial on a 1.8-GHz Pentium 4 processor.

The aerodynamic performance of an isolated compressor rotor passage may be summarized by the changes in total enthalpy and entropy in the flow across the passage, i.e., the amount of work done on the fluid and the losses accrued in the process. The dependence of total enthalpy change, Δh_t, on tangential momentum changes across the blade row is described by the Euler turbine equation,

$$\Delta h_t = \omega [r_1 u_1 \tan \beta_1 - r_2 u_2 \tan(\beta_1 - \vartheta)],$$

where ω, r, and u denote wheel speed, radius, and axial flow velocity, and the subscripts 1 and 2 denote inlet and exit, respectively. For small radial variation and axial velocity ratio (u_2/u_1) near unity, the enthalpy change depends primarily on the amount of flow turning, $\vartheta := \beta_2 - \beta_1$.

An appropriate choice for a measure of loss in an adiabatic machine is entropy generation [10]. The increase in entropy results in a decrease of the stagnation pressure rise when compared with the ideal (isentropic) value. In what follows, the loss coefficient is defined as the drop in total pressure at the passage exit scaled by the inlet dynamic pressure,

$$\varpi := \frac{p^0_{T_2} - \overline{p}_{T_2}}{p_{T_1} - p_1}. \tag{5}$$

Here $p^0_{T_2}$ is the ideal (isentropic) total pressure at the passage exit and $\overline{p}_{T_2}$ is the mass-averaged total pressure at the passage exit. Details of MISES' cascade loss calculation can be found in Appendix C of Ref. [9].

3.2 Probabilistic Analysis. Computed loss coefficient and turning values are taken to be functions of n independent variables representing the geometry of the flow passage and m variables representing other flow parameters,

$$\varpi = \varpi(x,y), \quad \vartheta = \vartheta(x,y),$$

where $x \in \mathbb{R}^n$ denotes the vector of geometric parameters and $y \in \mathbb{R}^m$ contains the remaining parameters. Both ϖ and ϑ are deterministic functions of x and y, i.e., for given x and y, there is a unique corresponding value of ϖ.

Consider next a continuous random vector X with joint probability density function f_X. For fixed flow parameters y, the expected value of $\varpi(X,y)$ is defined by

$$\mu_\varpi := \underset{x}{E}[\varpi(X,y)] = \int_{\mathbb{R}^n} \varpi(x,y) f_x(x) dx \tag{6}$$

and the variance of $\varpi(X,y)$ is given by

$$\sigma_\varpi^2 := \mathrm{Var}(\varpi(X,y)) = \underset{x}{E}[(\varpi(X,y) - \mu_\varpi)^2]. \tag{7}$$

Similar expressions follow for mean μ_ϑ and variance σ_ϑ^2 of turning.

In general, the functional dependence of ϖ on the geometric parameters x is too involved to allow for a closed form evaluation of the integrals in definitions (6) and (7). However, numerical approximations can be obtained via probabilistic analysis techniques. One such technique, the Monte Carlo method [11–13], is applied here to estimating the effect of geometric and inlet flow condition variability. Garzon and Darmofal [14] applied and compared other probabilistic analysis techniques (e.g., response surface methodology, probabilistic quadrature) to assessing the impact of geometric variability on aerodynamic performance. In that investigation, while the mean aerodynamic performance could be reasonably estimated using lower-fidelity probabilistic analysis techniques, the accurate prediction of the aerodynamic performance variability required Monte Carlo simulations (MCS). Thus, in the present work, we rely solely on Monte Carlo simulations for probabilistic analysis.

One of the attractive features of MCS is that parallelization of concurrent calculations can be readily implemented in shared memory parallel computers as well as across networks of heterogeneous workstations. In the present context, each function evaluation consisted of grid generation, flow-field analysis and post-processing steps that were automated and parallelized using command scripts. All probabilistic simulations reported in this paper were carried out on a 10-node Beowulf cluster at the MIT Aerospace Computational Design Laboratory. Each node was equipped with dual 1.8-GHz Xeon processors. For the present application, 2000 trials required about one hour of computing time using all ten nodes.

3.3 Application. The nominal rotor reported here was part of the sixth stage from an experimental core axial compression system. The following operating conditions were assumed in the through-flow analysis: mass flow rate of 20 kg/sec, wheel speed of 1200 rad/sec ($U_{\mathrm{tip}} = 301$ m/sec) and axial inlet flow (no swirl). In addition, the stage inlet static temperature and pressure were taken to be 390 K and 200 kPa resulting in an inlet Mach number of 0.43.

The axisymmetric viscous flow package MTFLOW was used to perform the initial through-flow calculation. MTFLOW implements a meridional streamline grid discretization of the axisymmetric Euler equations in conservative form. Total enthalpy at discrete flow field locations and constant mass along each streamtube are prescribed directly. The localized effects of swirl, entropy generation, and blockage due to rotating or static blade rows can also be modeled [15,16].

The inlet relative Mach number and flow angle were taken to be 0.90 and 62.6 degrees, respectively, and the Reynolds number based on inlet tip radius was 3×10^6. Figure 5 shows the pressure distribution on the suction and pressure surfaces of the airfoil. After a short precompression entry region, a shock appears on the suction surface followed by mild compression until about two-thirds of the chord length; from there the flow is further decelerated until the trailing edge is reached. On the concave side, an adverse pressure gradient exists until about midchord, followed by a plateau. The baseline loss coefficient and turning were computed by MISES to be 0.027 and 14.40 degrees, respectively.

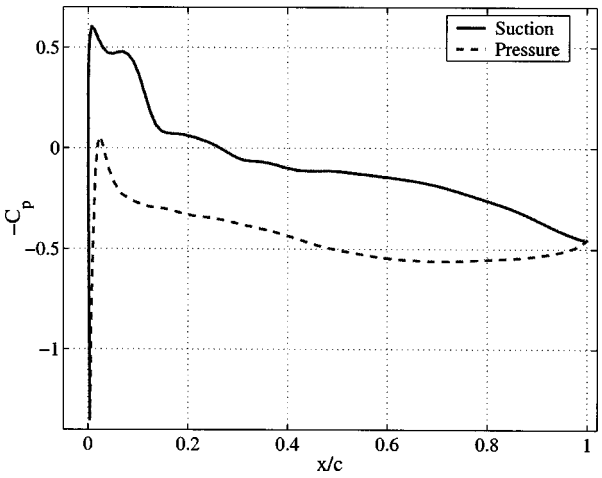

Fig. 5 IBR Pressure Coefficient, $M_1 = 0.90$, axial velocity-density ratio (AVDR): 1.27

The noise model employed in the probabilistic analysis is the PCA-based model described in a previous section. The model is defined by Eq. (4). The convergence criterion used for the Monte Carlo simulations was

$$|\hat{\sigma}_\varpi^N - \hat{\sigma}_\varpi^{N-n}| < \varepsilon,$$

where the superscripts indicate the number of samples taken. In the present study, $\varepsilon = 10^{-5}$ and $n = 10$ were used. Results from numerical experimentation suggested that $N = 2000$ trials were typically sufficient to achieve the required tolerance for the case reported here.

Figure 6 shows histograms of loss coefficient and turning. The abscissa represents the values of the output variable, while the ordinate indicates the relative number of trials that fall within each of the equal-length intervals subdividing the abscissa. In the limit of large number of trials, $N \to \infty$, the outline of the histogram bar plot approaches the continuous distribution of the output variable. The two vertical dashed lines indicate the nominal (baseline) and mean values. The estimated mean loss coefficient is about 4% higher than the baseline (noiseless) value, while the mean turning is about 1% lower than nominal. The standard deviation of loss coefficient is 0.0008, which is less than 3% of the mean loss. For the turning, the standard deviation is 0.087 degrees which is only about 0.6% of the mean turning.

The small impact of geometric variability on aerodynamic performance is not surprising given the small geometric variability present in the measurement samples. Production airfoils, manufactured with processes that are less tightly controlled than the current flank-milled IBR case, should be expected to exhibit higher levels of geometric variability. The Appendix illustrates the differences in shape variability between two IBR manufactured with point and flank milling, respectively. As discussed in the Appendix, the flank-milled IBR data being studied has approximately ten times less variability than can occur in other common manufacturing processes.

To explore the impact of increased manufacturing noise amplitude on the aerodynamic performance statistics, a series of Monte

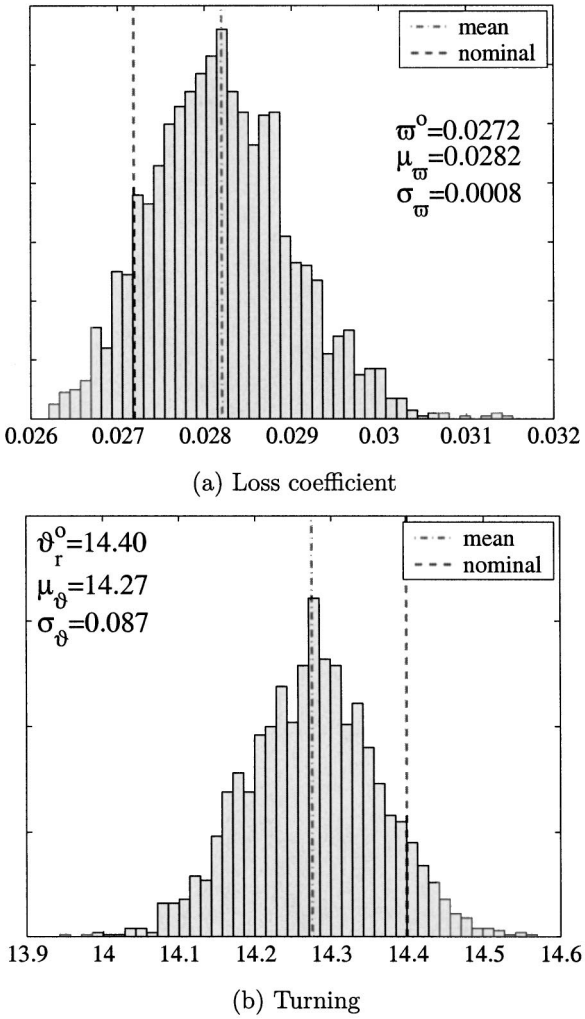

Fig. 6 IBR: Loss and turning histograms

Carlo simulations were performed with various levels of geometric noise. In those simulations, the geometric noise model was modified to take the form

$$\tilde{X} = \mathbf{x}^0 + \overline{\mathbf{x}} + a\sum_{i=1}^{K} \sigma_i Z_i \mathbf{v}_i, \tag{8}$$

where a is a geometric variability amplitude. Figure 7 summarizes the Monte Carlo estimates of mean and standard deviation of the outputs of interest for $a=1,\ldots,8$. In the figure, the horizontal dashed line indicates the loss and turning corresponding to the average geometry, $\mathbf{x}^0+\overline{\mathbf{x}}$. Similarly, the baseline loss and turning are indicated by solid lines. At the original noise level, $a=1$, the impact of the average geometry dominates the difference in loss coefficient and turning from the baseline values, i.e., the geometric variability about the average geometry has little effect on the "mean shift." For a noise amplitude of $a=2$, the effect of the geometric variability becomes noticeable; in the case of the loss coefficient, the noise contributes about half of the total shift. For $a=4$, the contribution of the average geometry to turning mean shift is about half of the total. For $a>4$, the shift from nominal in both loss and turning is dominated by the variability of the blade measurements, rather than by the average geometry. At $a=5$ the loss mean shift is about 23% of the nominal value, an increase of a factor of six from $a=1$. The standard deviation of loss coefficient increased by a factor of 6 from 0.0008 at $a=1$ to 0.005 at $a=5$. The turning mean shift at $a=5$ is roughly twice as large as

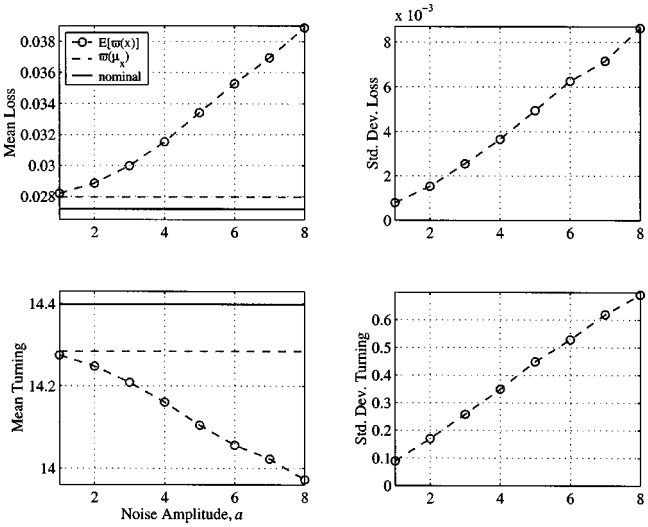

Fig. 7 IBR: Mean and standard deviation versus noise amplitude

the baseline value, while the standard deviation of turning increased by a factor of 5. One implication of the increase in relative importance of the scatter is that controlling the manufacturing process by "re-centering" the target geometry may not be sufficient to effectively improve the mean performance.

The mean loss coefficient and turning depicted in Fig. 7 do not vary linearly with geometric noise amplitude in the vicinity of $a=1$. Rather the amount of curvature indicates a higher-order dependence. The increase in loss and turning variability—a measured by their estimated standard deviation—increases nearly linearly with geometric noise amplitude, at the approximate rates of $0.001/a$ for loss and $0.1/a$ degrees for turning. This behavior can be explained by considering a quadratic approximation to the loss coefficient; namely,

$$\hat{\varpi}(x) = \hat{\varpi}_0 + c_1 x + c_2 x^2,$$

where x is a noise variable. In particular, consider a centered normal variable $X \in N(0, a\sigma_X^2)$ where a is the noise amplitude multiplying σ_X. Then, the expected value of ϖ is

$$E[\hat{\varpi}(X)] = \hat{\varpi}_0 + c_1 E[X] + c_2 E[X^2] = \hat{\varpi}_0 + c_2 a^2 \sigma_X^2.$$

Thus the mean-shift in loss coefficient is seen to depend quadratically on the amplitude of the noise. The variance of the assumed quadratic loss is

$$\mathrm{Var}(\hat{\varpi}_0(X)) = c_1^2 a^2 \sigma_X^2 \left[1 + 2\left(\frac{c_2 a \sigma_X}{c_1} \right) \right].$$

The nondimensional quantity $c_2 a \sigma_X / c_1$, is the ratio of the change in loss due to the quadratic term relative to the linear term for a $1-\sigma$ (after amplification by a) noise. Thus if the impact of the quadratic terms at this noise level is small compared to the linear terms, we would expect to see a largely linear dependence on the standard deviation of the loss with respect to the noise amplitude a. This linear dependence on a of the standard deviation of the turning angle is clearly seen in Fig. 9. The loss standard deviation is also fairly linear, but some curvature can be seen indicating that the quadratic terms are more important in the loss behavior.

Further understanding of how the amplitude of the noise impacts the cascade aerodynamic performance can be seen in Fig. 8 and 9 which show the cumulative distribution functions (CDF)[4] of loss and turning for values of a ranging from 1 to 8. The

[4]The distribution function $F:\mathbb{TR}\mapsto[0,1]$ of a random variable X is defined by $F(b)=P\{X\leqslant b\}$, i.e., the probability that X takes on a value smaller than or equal to b.

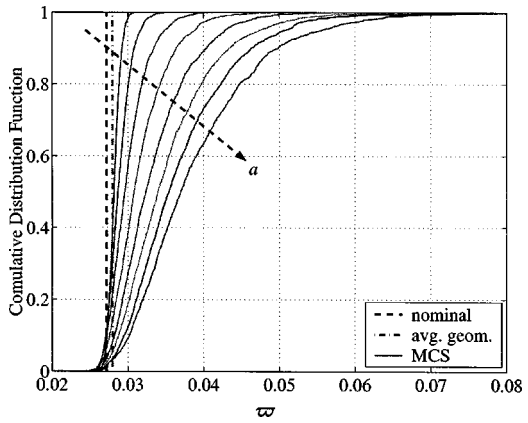

Fig. 8 IBR: Impact of geometric variability on loss coefficient distribution, $a=1,2,\ldots,8$

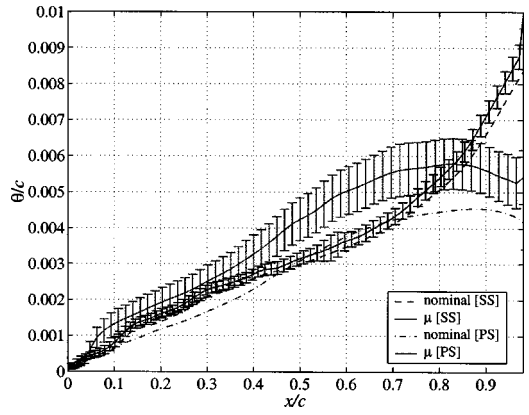

Fig. 10 IBR: Effect of geometric variability on momentum thickness. Mean indicated by solid lines, one-standard deviation interval by error bars. [SS]: suction side, [PS]: pressure side.

nominal and average-airfoil values are indicated by dashed and dash-dot vertical lines, respectively, and the arrows indicate the direction of increasing a. Figure 8 shows how the high-end ''tails'' of the loss distributions become thicker as a increases. For $a=1$ the probability that the loss coefficient will take on values smaller than nominal is only about 15%, while at $a=8$ that probability has dropped nearly to zero.

By comparison, the behavior of the turning distribution with increasing noise amplitude does not show a significant impact on mean turning (Fig. 9). The CDF of turning seem to all cross in the vicinity of the nominal value, indicating that the mean shift is small compared to the variability. This behavior of loss and turning has been consistently observed in a variety of compressor applications studied previously [17]. In particular, the mean loss is always increased as a result of geometric variability while the mean turning is relatively unaffected.

The impact of geometric variability on boundary layer thickness is illustrated in Fig. 10 for noise level $a=5$. The figure shows nominal and mean momentum thickness (θ/c) on the suction and pressure sides (indicated in the plots by SS and PS, respectively). The dashed and dot-dashed lines indicate the nominal values—i.e., without geometric noise—while the solid lines indicate the mean values from Monte Carlo simulation. The error bars indicate to a one-standard-deviation interval about the mean. The discrepancy between nominal and mean momentum thickness values is more pronounced on the pressure side, as is its variability. The growth in mean momentum thickness relative to the nominal is seen to occur most significantly at the leading edge (notably at about 5% chord) on the pressure surface.

As discussed by Cumpsty [18],[5] the momentum thickness itself does not necessarily point to the mechanism by which losses are created. A more appropriate quantity to consider is the boundary layer dissipation coefficient, defined by

$$C_d' = \int_0^{\delta} \frac{\tau}{\rho U_e^2} \frac{\partial}{\partial y}\left(\frac{u}{U_e}\right) dy, \tag{9}$$

where τ stands for shear stress, U_e is the boundary layer edge velocity, ρ stands for density, δ is the boundary layer thickness, and u is the component of the flow velocity along the dominant flow direction x (here x and its normal complement y are boundary layer coordinates). As shown by Denton [10] the cumulative value of $\rho U_e^3 C_d'$ over the interval $0 \leqslant x' \leqslant x$,

$$\int_0^x \rho U_e^3 C_d' dx', \tag{10}$$

is a measure of the rate of entropy generation per unit span[6] in the boundary layer.

Figure 11 shows cumulative values of $\rho U_e^3 C_d'$ as per Eq. (10) at geometric noise level $a=5$. The rate of entropy generation is about three times higher on the suction side than on the pressure side. The nominal-to-mean shift is more pronounced on the pressure side, as is the variability. As shown in the figure, the mean shift and variability in entropy generation rate increase rapidly in the first 10% chord and change little aft of the 25% chord location. This indicates that loss variability is accrued primarily at the leading edge and agrees with the observed growth of mean momentum thickness in this region.

While the PCA-based probabilistic model optimally describes the geometric variability, the impact of the geometric modes on the aerodynamic performance depends not only on the magnitude of the underlying geometric variability, but also on their aerodynamic sensitivity to that geometric perturbation. To quantify the relative importance of the PCA modes on aerodynamic performance, we have performed Monte Carlo simulations with increasing values of K (i.e., increasing numbers of PCA modes). Figure 12 presents statistics of loss and turning according to the number of PCA modes used in the geometric noise model (denoted K in Eq. (8)) for noise amplitude $a=5$. For each value of K, a Monte Carlo simulation with $N=5000$ trials was performed. Baseline

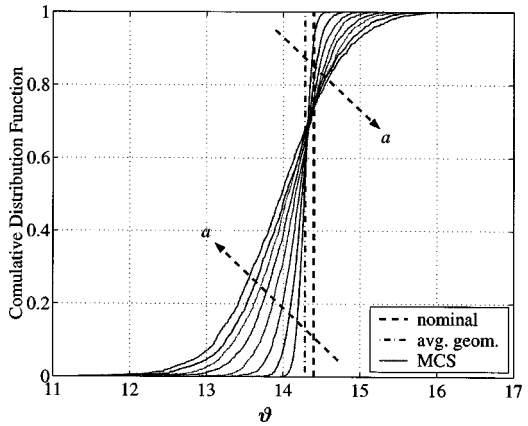

Fig. 9 IBR: Impact of geometric variability on turning distribution, $a=1,2,\ldots,8$

[5]Section 1.5; see also Denton [10].

[6]It is assumed here that the process takes place at constant temperature.

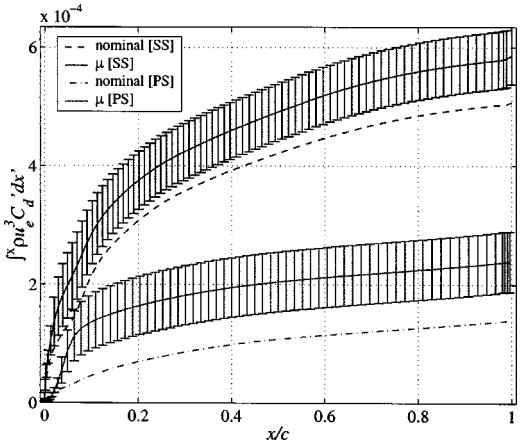

Fig. 11 IBR: Effect of geometric variability on boundary layer entropy generation as per Eq. (10). Mean indicated by solid lines, one-standard deviation interval by error bars. [SS]: suction side, [PS]: pressure side.

and average-geometry values are denoted by constant dashed lines, while the values corresponding to $K=mp$ (all modes) are shown by a solid line. The average-geometry contribution to mean loss constitutes a relatively small fraction of the total shift from nominal, as pointed out earlier. The geometric scatter of the first six modes is responsible for about 90% of the total mean shift in loss coefficient. Similarly, the first six modes taken together produce close to 90% of the turning mean shift obtained when all modes are considered. The first six modes are also the most influential on loss coefficient variability, as indicated by its standard deviation plot. The first two modes clearly dominate turning angle variability. Table 2 shows the percent differences between the statistics of the reduced-order and full-model simulations. Using only the first PCA mode, mean loss is underpredicted by 15% and the error in standard deviation of loss and turning is 56 and 71%, respectively. It takes 15 modes to reduce the error in standard deviation of loss coefficient to 7%. Beyond $K=15$, comparisons stop being meaningful due to lack of resolution in the Monte Carlo simulation.

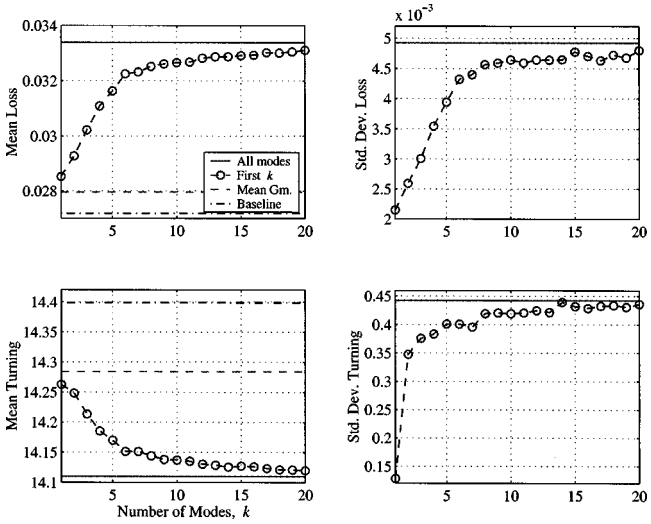

Fig. 12 IBR mid section: Statistics versus number of PCA modes, $a=5$

Table 2 Percent difference in statistics from reduced-order model (with K modes) and full model ($K=mp$) simulations, $a=5$

K	μ_ϖ	σ_ϖ	μ_ϑ	σ_ϑ
1	−14.5	−56.4	1.08	−71.1
5	−5.2	−20.0	0.43	−9.3
10	−2.2	−5.7	0.19	−5.2
15	−1.4	−3.0	0.12	−2.4
20	−0.8	−2.5	0.07	−1.4

4 Effect of Geometric Variability on Overall Compressor Performance

In this section, the impact of airfoil geometry variability on overall compressor performance is estimated. Compressor efficiency and pressure ratio are obtained by exercising a multistage mean-line compressor model in combination with probabilistic loss and turning models for the IBR blade discussed above.

A compressor stage mean-line model was derived from the following two observations. First, given the rotor total pressure loss coefficient ϕ_r, the flow turning ϑ_r, the outlet area, and the upstream flow conditions, the rotor outlet state is described by the nonlinear system

$$F := \Delta T_T - \frac{\omega}{c_p}(r_2 V_2 \sin\alpha_2 - r_1 V_1 \sin\alpha_1) = 0, \tag{11}$$

$$G := \frac{\dot{m}\sqrt{T_{T_2}}}{P_{T_2} A_2 \cos\alpha_2} - \sqrt{\frac{\gamma}{R}} \frac{M_2}{\left(1+\frac{\gamma-1}{2}M_2^2\right)^{(\gamma+1)[z(\gamma-1)]}} = 0, \tag{12}$$

$$H := V_2[\sin\alpha_2 + \cos\alpha_2 \tan(\beta_1 - \vartheta_r)] - \omega r_2 = 0, \tag{13}$$

where

$$T_{T_2}(\Delta T_T) = T_{T_1} + \Delta T_T,$$

$$V_2(\Delta T_T, M_2) = M_2 \left(\frac{\gamma R T_{T_2}}{1+\frac{\gamma-1}{2}M_2^2}\right)^{1/2},$$

$$P_{T_2}(\Delta T_T) = P_{T_{1R}} \left[1 - \phi_r \frac{\frac{1}{2}\gamma M_{1R}^2}{\left(1+\frac{\gamma-1}{2}M_{1R}^2\right)^{\gamma/(\gamma-1)}}\right] \left(\frac{T_{T_2}}{T_{T_{1R}}}\right)^{\gamma/(\gamma-1)}.$$

In the above equations, P, T, M, A, and R stand for temperature, pressure, Mach number, area, and gas constant, respectively; α denotes absolute and β relative flow angles; the subscripts 1, 2, and 3 denote rotor inlet, rotor exit/stator inlet, and stator exit; and the subscripts T and R denote "total" and "relative" quantities, respectively; ω stands for wheel speed, $\dot{m}$ for mass flow rate, and r for radius. The stator is described by similar equations with $\omega=0$, loss coefficient ϕ_s, and turning ϑ_s.

Equations (11)–(13) form a nonlinear system in the variables ΔT_T, M_2, and α_2, which was solved numerically using a Newton-Raphson solver. Equation (11) is simply a restatement of the Euler turbine equation for calorically perfect gases. Equation (12) is the flow parameter formula for quasi-one-dimensional flow of calorically perfect gases (Fligner's formula). Equation (13) states that the absolute and relative tangential velocities are related via the wheel speed.

The probabilistic mean-line calculations estimate only the impact of blade-to blade flow variability—caused by geometric noise—on compressor performance. Geometric variability leading to three dimensional flow effects (e.g., tip-clearance leakage, part-span losses, off-design radial imbalances, end-wall losses, etc.)

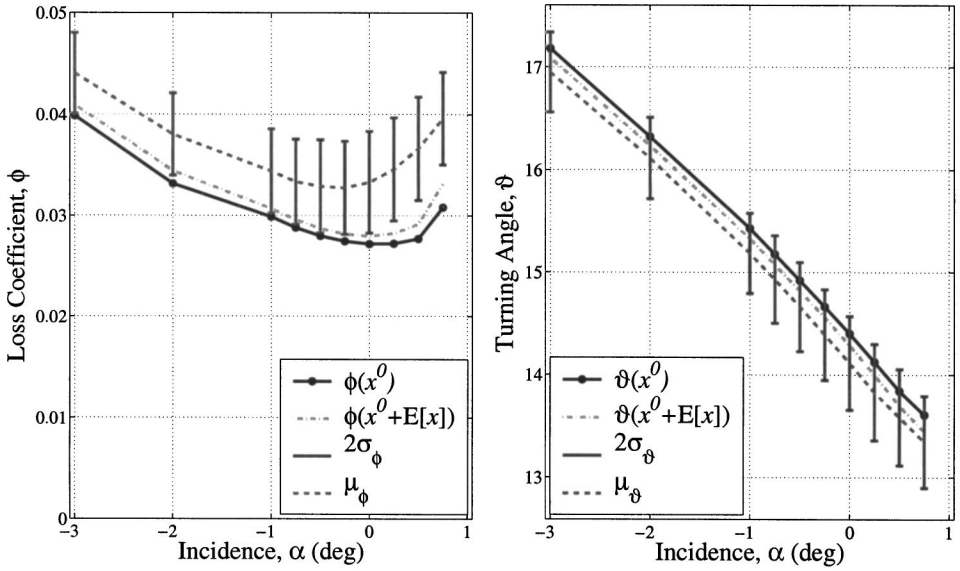

Fig. 13 IBR: Loss coefficient and turning angle versus incidence, $a=5$

are not considered. The present approach therefore is likely to underestimate the performance variability of actual compressors in the presence of geometric variability.

4.1 Loss Coefficient and Turning Angle Models. Conceptually, the loss coefficient and turning angle obtained from blade passage analyses may be taken to be deterministic functions of various geometric and flow parameters such as inlet flow angle, inlet Mach number, etc. In particular, let

$$\phi=\phi(\alpha,\mathbf{x}) \quad \text{and} \quad \vartheta=\vartheta(\alpha,\mathbf{x}),$$

where α is inlet flow incidence and $\mathbf{x}$ is a vector of parameters describing amplitudes of geometric noise modes such as those described above. In the present application, ''incidence'' is taken to mean the difference between the nominal inlet flow angle (here the minimum-loss angle) and the actual flow angle of the incoming stream. Other geometric and flow parameters are assumed to be fixed and their functional dependence is not explicitly modeled. Furthermore, we separate ϕ into nominal and noise terms,

$$\varphi(\alpha,\mathbf{x})=\varphi_0(\alpha)+\Delta\phi(\alpha,\mathbf{x}), \tag{14}$$

then define

$$\Delta\mu_\phi(\alpha) \coloneqq \underset{X}{E}[\Delta\phi(\alpha,X)], \quad \sigma^2_\phi(\alpha) \coloneqq \underset{X}{\mathrm{Var}}(\Delta\phi(\alpha,X)).$$

In general $\Delta\mu_\phi(\alpha)$ and $\sigma^2_\phi(\alpha)$ may not be available in closed form. Instead, let $\Delta\hat{\mu}_\phi(\alpha)$ and $\hat{\sigma}^2_\phi(\alpha)$ be models of loss ''mean shift'' (i.e., the difference between loss variance, respectively. Then

$$\underset{X}{E}[\phi(\alpha,X)]=\underset{X}{E}[\phi_0(\alpha)+\Delta\phi(\alpha,X)]\approx\phi_0(\alpha)+\Delta\hat{\mu}_\phi(\alpha),$$

$$\underset{X}{\mathrm{Var}}(\phi(\alpha,X))=\underset{X}{E}[(\Delta\phi(\alpha,X)-\Delta\mu_\phi(\alpha,X))^2]\approx\hat{\sigma}^2_\phi(\alpha).$$

For fixed α, it is further assumed that $\Delta\phi(\alpha,X)$ is normally distributed; that is,

$$\Delta\phi(\alpha,X)\in N(\Delta\hat{\mu}_\phi(\alpha),\hat{\sigma}^2_\phi(\alpha)).$$

Models of $\Delta\hat{\mu}_\phi(\alpha)$, $\hat{\sigma}^2_\phi(\alpha)$, $\Delta\hat{\mu}_\vartheta(\alpha)$, and $\hat{\sigma}^2_\vartheta(\alpha)$ were obtained from computed statistics of loss and turning at fixed values of incidence for isolated blade passages using the MISES blade passage analysis in a Monte Carlo simulation. Finally, an identical argument was applied to obtaining models for turning angle.

Figure 13 shows loss coefficient MCS results. The geometric noise assumed in the simulations was the PCA-based model as before, with noise amplitude $a=5$. The output statistics were computed for each fixed value of α from $N=2000$ trials. In Fig. 13, the solid line connects the computed nominal loss coefficient (i.e., in the absence of geometric noise); the dash-dot line connects the values computed for the average-geometry airfoil; the dashed line indicates the MCS mean values; and the error bars show two-standard-deviation intervals centered at the mean. The figure shows a typical ''loss bucket'' shape with minimum nominal loss approximately at zero incidence. The loss coefficient increases more steeply for positive values of incidence as does its variability. No points are plotted for $\alpha>1$ degree where numerical convergence of the Monte Carlo simulations was deficient (less than 80% of the MISES' runs in the Monte Carlo simulation converged).

The computed data points illustrated above are used to define piecewise-cubic interpolating splines with zero-second-derivative end conditions. To avoid dangerous extrapolation outside the incidence range for which computed data points were available, additional points were added at $\alpha=2$, 3, and 4 by linearly extrapolating the nominal loss and turning and replicating the mean-shift and variance values corresponding to the highest computed α.

4.2 Probabilistic Six-Stage Compressor Model. The starting point for the probabilistic analysis was a six-stage compressor model with nominal pressure ratio $\pi^0=10.8$ and polytropic efficiency $e^0=0.96$. The nominal rotor and stator loss coefficients were $\phi_r=\phi_s=0.03$, and the nominal rotor turning was $\vartheta_r=14.4$ deg. The high nominal efficiency is due to the absence of end-wall and tip-clearance losses in the model.

Stator nominal loss and turning, as well as their mean shift and standard deviation, were taken directly from the IBR incidence models discussed above. Stators are generally required to produce more flow turning than rotors. Therefore it should be expected that the stators will exhibit higher exit flow variability (e.g., more flow deflection) than the rotor. As a conservative estimate the same nominal, mean-shift and variance models for loss coefficient were used for the stator and for the rotor. The stator turning variability model was obtained by scaling the rotor model to the stator nominal turning—effectively using the same standard-deviation versus incidence model as for the rotor.

Monte Carlo simulation results ($N=2000$) show a 0.2% drop

Table 3 Impact of geometric noise amplitude on compressor performance. e_0 and π^0 are the efficiency and pressure ratio for the nominal compressor (no noise).

a	e^0	μ_e	$\sigma_e \times 100$	π^0	μ_π	σ_π
1		0.961	0.038		10.73	0.022
2	0.963	0.959	0.083	10.79	10.71	0.043
5		0.951	0.275		10.59	0.111

from nominal polytropic efficiency to the mean value, and a 0.5% decrease in total pressure ratio for the base noise level. At the baseline noise level the primary contribution to performance deviations comes from the average geometry rather than from the geometric variability.

The geometric variability present in the IBR coordinate measurements is quite small, due to the use of a highly controlled manufacturing process. The ''small'' geometric noise in the measurements translates to small loss and turning variability, which in turn result in small compressor performance uncertainty: the standard deviation of polytropic efficiency and pressure ratio are 0.04% and 0.02, respectively. The impact of increased noise level is reported next.

4.3 Impact of Geometric Noise Amplitude. Presumably, as the amount of geometric variability increases, so should its impact on compressor performance. This subsection attempts to quantify that trend within the limitations of the current mean-line model. Table 3 summarizes the polytropic efficiency and overall pressure ratio statistics for three noise variability levels: $a=1$, 2, and 5.

For $a=2$, the mean shift in polytropic efficiency and pressure ratio are 0.3% and 0.7%, respectively. The standard deviation of polytropic efficiency increases roughly by a factor of 2 when compared with its $a=1$ counterpart. At the $a=5$ level, the standard deviation of efficiency has risen to about 0.2%, a sevenfold increase from $a=1$. At this level of noise, the mean shift in polytropic efficiency also becomes noticeable at ~1% from nominal. When comparing the impact of geometric noise amplitude on pressure ratio variability, the increase is nearly linear with noise level, i.e., compared with the $a=1$ case, the standard deviation of pressure ratio at $a=2$ increases by a factor of 2 and at $a=5$ by a factor of 6.

4.4 Multiple-Blade Rows. In the calculations reported above, it was assumed that for a given bladed row, all passages behaved identically, i.e., that a single passage can be considered to represent each bladed row. In this section, multiple passages per blade row are considered. Loss and turning values for each passage are sampled from a normal distribution according to inlet incidence. Thus, for each passage instance, loss and turning values are in general different but have the same statistics prescribed by the loss and turning models. The corresponding system of stage equations [Eqs. (11)–(13)] is solved for each passage. The outlet conditions are area-averaged to initialize the inlet conditions of the next rotor or stator and the calculation is marched through the compressor.

Table 4 shows polytropic efficiency and pressure ratio statistics for the six-stage compressor model reported above but with 80 independent blades per row (rotor or stator). Statistics for three levels of geometric variability are reported. In comparing Table 4 to Table 3, it is seen that at $a=1$, the mean shifts for the baseline multiple-blade calculation are the same as for the single-blade case. The efficiency and pressure ratio standard deviations in the multiple-blade case are 13 and 77% lower, respectively, than in the single-blade case. At the $a=5$ noise level the efficiency mean shift is one percentage point, in contrast the 1.2% drop seen with the single-blade calculation. The standard deviations of efficiency and pressure ratio have decreased by 30 and 75%, respectively, compared to the single-blade results.

Table 4 Six-stage compressor, IBR airfoil-based loss and turning models, 80 blade passages per row. e^0 and π^0 are the efficiency and pressure ratio for the nominal compressor (no noise).

a	e^0	μ_e	$\sigma_e \times 100$	π^0	μ_π	σ_π
1		0.961	0.033		10.73	0.005
2	0.963	0.960	0.065	10.79	10.72	0.010
5		0.953	0.197		10.61	0.029

Table 5 Six-stage compressor, mean loss, and mean turning (no variability)

$a=1$		$a=2$		$a=5$	
e	π	e	π	e	π
0.961	10.73	0.960	10.71	0.954	10.62

The reduction in efficiency and pressure ratio mean shift can be explained in part by considering a deterministic compressor with loss and turning given by the mean values obtained from Monte Carlo simulation. As the number of blade passages is increased, the mean values of efficiency and pressure ratio converge to those obtained for mean loss and turning models. Table 5 shows the resulting polytropic efficiency and pressure ratio values using mean loss and turning for the three noise levels considered. Comparing the values in Table 5 to the mean polytropic efficiency and pressure ratio in Table 4 and taking into account their reduced variability, it can be concluded that the contribution of the mean values of loss and turning (for given incidence) dominates the mean shifts of polytropic efficiency and pressure ratio.

5 Conclusions

In this paper, we developed and applied a probabilistic methodology to quantify the impact of geometric variability on compressor aerodynamic performance. The methodology utilizes a principal-component analysis (PCA) to derive a high-fidelity probabilistic model of airfoil geometric variability. This probabilistic blade geometry model is then combined with a compressible, viscous blade-passage analysis to estimate the aerodynamic performance statistics using Monte Carlo simulation. Finally, a probabilistic mean-line multistage compressor model, with probabilistic loss and turning models from the blade-passage analysis, is developed to quantify the impact of the blade variability on compressor efficiency and pressure ratio.

The methodology was applied to a flank-milled integrally bladed rotor (IBR) with blade surface measurements taken by a coordinate measuring machine. The PCA model of the geometric variability demonstrates that 99% of the geometric scatter can be modeled with approximately the five strongest PCA modes. However, subsequent aerodynamic analysis of the blade passage demonstrates that approximately 15 modes are needed to model 99% of the overall aerodynamic impact on loss and turning.

At the blade passage level, the overall impact of the variability in the flank-milled IBR was found to be very low causing only a 4% shift (i.e., increase) of the mean loss compared to the loss of the design-intent blade, and an even smaller impact on the mean turning. The source of the change in mean performance was attributed to variability in the loss and turning. However, comparisons of the level of geometric variability in the flank-milled IBR data to other manufactured blades showed the flank-milled data in this study to have at least five times less variability than commonly observed in other situations. Thus a study of the aerodynamic impact of the variability was also performed at increased noise levels.

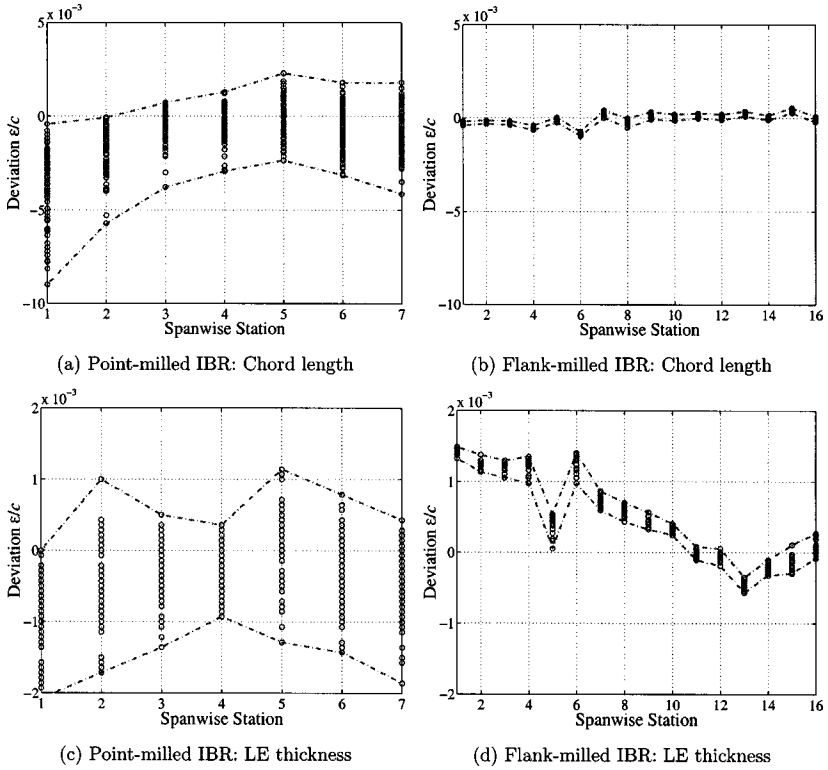

Fig. 14 Measured deviations for sample point and flank-milled IBR

At five times the actual IBR geometric noise level (which is considered representative of many manufacturing processes), the mean loss was approximately 20% larger than the nominal loss. In particular, for this application we note that:

- The majority of the mean shift in loss arises from the blade variability and only a small portion is due to errors in the mean geometry. Thus simply re-targeting the manufacturing process will not have a substantial impact on the mean aerodynamic performance of the blades.
- The major source of the increased mean and variance of the passage loss can be traced to the leading-edge of the blade, specifically in the first 5% of the chord on the pressure surface. In this region, substantial increases in mean dissipation and subsequently boundary layer momentum thickness were observed as a result of the geometric variability.
- Mean turning is not greatly impacted by geometric variability. At all the noise levels studied, the mean turning is similar to the nominal blade turning, though the variation of the turning increases with geometric noise level.

The impact of the blade variability was then studied for a multistage compressor using a mean-line model for a notional six-stage compressor. As observed in the blade-passage analysis, the actual noise in the flank-milled data has a small impact on the compressor efficiency (a 0.3% decrease in mean efficiency from nominal) and pressure ratio (a 0.7% decrease in mean pressure ratio from nominal). However, at the fivefold geometric noise level, the compressor mean efficiency drops by 1% indicating that geometric variability could have a significant impact on the compressor performance. Furthermore, the majority of this mean shift in compressor efficiency can be accounted for by the mean shift in the passage aerodynamic behavior.

Future work will include studies of other blades including those with larger manufacturing variability. Also, three-dimensional effects such as tip clearance are currently being investigated. Finally, robust aerothermal blade design has been applied to mitigate the impact of the geometric variability and will be reported in subsequent publications [17].

Acknowledgments

The authors wish to thank Professor M. Drela, Professor E. Greitzer, and Professor I. Waitz for their helpful comments and suggestions. Thanks also to Mr. Jeff Lancaster for helping us acquire geometric variability data. The support of NASA Glenn Research Center through Grant No. NAG3-2320 is thankfully acknowledged.

Appendix: Comparison With Production Manufacturing Variability

The flank-milled IBR considered in the main text exhibited geometric variability which is uncommonly low for production hardware. Point milling is a well understood and widely used method for manufacturing compressor blades. In this technique, a ball cutter removes material from a block of metal following computer-controlled paths. The main disadvantages of point milling are the time required to cut an entire blade surface in several passes and the resulting scalloped surface finish [19]. An alternative to point milling that is starting to become practical is flank milling, whereby a conical tool is used to cut the entire surface of a blade from the blank material in a single pass [19]. Flank milling poses a more challenging tool control problem than point milling, but can potentially be more time and cost effective. Another advantage of flank milling is that it produces a better surface finish than point milling, requiring less time for surface polishing. The geometric measurements reported above corresponded to an IBR manufactured via tightly controlled flank milling.

Figure 14 shows plots of measured deviations of two production compressor rotor blades, one manufactured with point milling and the other with flank milling. Deviations in chord length and

Table 6 Spanwise maximum deviation intervals (per unit chord) for point- and flank-milled IBR measurements

Dimension	Point ($\times 10^3$)	Flank ($\times 10^3$)	Ratio
Chord length	8.6	0.49	18
LE thickness	2.7	0.49	6.7
TE thickness	3.8	0.57	5.6

leading-edge thickness at various spanwise locations are shown. The deviations have been scaled with respect to the nominal spanwise average chord. Largest positive and negative deviations at each spanwise station are indicated by dashed lines, which in turn provides a rough measure of variability in each measured dimension. Table 6 shows maximum deviations (per unit chord) intervals in chord length, leading and trailing-edge thickness for the measurements shown in Fig. 14. The point-milled IBR exhibits roughly 18 times more variability in chord length than the flank-milled rotor. The variability in LE and TE thickness measurements for the point-milled IBR is roughly six times that of the flank-milled rotor. This comparison provides a justification for the higher geometric variability levels considered in the main text.

References

[1] Lykins, C., Thompson, D., and Pomfret, C., 1994, ''The Air Force's Application of Probabilistics to Gas Turbine Engines,'' AIAA paper 94-1440-CP.

[2] Preisendorfer, R. W., 1988, *Principal Component Analysis in Meteorology and Oceanography*, Elsevier, Amsterdam.

[3] Jolliffe, I. T., 1986, *Principal Component Analysis*, Springer Verlag, New York.

[4] Trefethen, L. N., and Bau, D., 1997, *Numerical Linear Algebra*, Society for Industrial and Applied Mathematics, Philadelphia, PA.

[5] Drela, M., and Youngren, H., 2001, *XFOIL 6.9 User Guide*, Dept. of Aeronautics and Astronautics, Massachusetts Institute of Technology, 77 Massachusetts Ave, Cambridge MA 02139.

[6] Ross, S., A *First Course in Probability*, 1997, Fifth Ed., Prentice Hall, Upper Saddle River, NJ.

[7] Drela, M., and Youngren, H., 1998, *A User's Guide to MISES 2.53*, Dept. of Aeronautics and Astronautics, Massachusetts Institute of Technology, 70 Vassar ST, Cambridge MA 02139.

[8] Drela, M., 1985, ''Two-Dimensional Transonic Aerodynamic Design and Analysis Using the Euler Equations,'' Ph.D. thesis, Massachusetts Institute of Technology.

[9] Youngren, H., 1991, ''Analysis and Design of Transonic Cascades With Splitter Vanes,'' Masters thesis, Massachusetts Institute of Technology.

[10] Denton, J. D., 1993, ''The 1998 IGTI Scholar Lecture: Loss Mechanisms in Turbomachines,'' ASME J. Turbomach., **115**, pp. 621–656.

[11] Hammersley, J. M., and Handscomb, D. C., 1965, *Monte Carlo Methods*, Methuen & Co., London, England.

[12] Thompson, James R., 2000, *Simulation: A Modeler's Approach*, John Wiley & Sons, Inc., New York.

[13] Fishman, George S., 1996, *Monte Carlo: Concepts, Algorithms and Applications*, Springer Verlag, New York.

[14] Garzon, V. E., and Darmofal, D. L., 2001, ''Using Computational Fluid Dynamics in Probabilistic Engineering Design,'' AIAA paper 2001-2526.

[15] Drela, M., 1997, *A User's Guide to MTFLOW 1.2*, Dept. of Aeronautics and Astronautics, Massachusetts Institute of Technology, 70 Vassar ST, Cambridge MA 02139.

[16] Merchant, A., 1999, ''Design and Analysis of Axial Aspirated Compressor Stages,'' Ph.D. thesis, Massachusetts Institute of Technology, 77 Massachusetts Ave, Cambridge MA 02139.

[17] Garzon, V. E., 2003, ''Probabilistics Aerothermal Design of Compressor Airfoils,'' Ph.D. thesis, Massachusetts Institute of Technology.

[18] Cumpsty, N. A., 1989, *Compressor Aerodynamics*, Longman, London.

[19] Wu, C. Y., 1995, ''Arbitrary Surface Flank Milling of Fan, Compressor and Impeller Blades,'' ASME J. Eng. Gas Turbines Power, **117**, pp. 534–539.

Experimental Investigation of Centrifugal Compressor Stabilization Techniques

Gary J. Skoch
U.S. Army Research Laboratory,
National Aeronautics and Space Administration,
Glenn Research Center,
Cleveland, OH 44135

Results from a series of experiments to investigate techniques for extending the stable flow range of a centrifugal compressor are reported. The research was conducted in a high-speed centrifugal compressor at the NASA Glenn Research Center. The stabilizing effect of steadily flowing air-streams injected into the vaneless region of a vane-island diffuser through the shroud surface is described. Parametric variations of injection angle, injection flow rate, number of injectors, injector spacing, and injection versus bleed were investigated for a range of impeller speeds and tip clearances. Both the compressor discharge and an external source were used for the injection air supply. The stabilizing effect of flow obstructions created by tubes that were inserted into the diffuser vaneless space through the shroud was also investigated. Tube immersion into the vaneless space was varied in the flow obstruction experiments. Results from testing done at impeller design speed and tip clearance are presented. Surge margin improved by 1.7 points using injection air that was supplied from within the compressor. Externally supplied injection air was used to return the compressor to stable operation after being throttled into surge. The tubes, which were capped to prevent mass flux, provided 6.5 points of additional surge margin over the baseline surge margin of 11.7 points. [DOI: 10.1115/1.1624846]

Introduction

The effort to determine the causes, precursors, and control mechanisms for stall and surge in both axial and centrifugal compressors has had many contributors over the years. Rodgers [1] tested numerous channel diffusers with back-swept impellers and found that diffuser initiated surge occurred at a nearly constant impeller to throat diffusion ratio of 1.8 for Mach numbers below unity. Rodgers concluded that a rapid accumulation of blockage near the diffuser throat limits the achievable diffusion ratio. The work was based in part on earlier work by Rundstadler and Dean [2] who demonstrated the importance of diffuser throat boundary layer blockage to the pressure recovery of the channel diffuser. Both works show the sensitivity of compressor performance to flow conditions in the vaneless and semivaneless regions of a channel diffuser.

A number of investigators have also demonstrated various strategies to extend the stable flow range of centrifugal compressors. Jansen et al. [3] reported the stabilizing effect of a slotted hub-wall treatment, beginning at the impeller exit and extending downstream of the diffuser throat, applied to a variable geometry vaned diffuser. Raw [4] demonstrated surge margin improvement in a conical pipe diffuser by using ''porous drillings'' to bleed flow from the region of the diffuser throat. Nelson et al. [5] reported a successful effort to stabilize the axial-centrifugal compressor of a turbo-shaft engine using both steady-flow and pulsed injection of air into the diffuser channels through slots in the suction side of the vanes.

Stein et al. [6] conducted three-dimensional (3D) time accurate simulations of a high-speed centrifugal impeller at surge conditions. Air injection at the impeller inlet was added to the model and several parametric variations of injection angle were analyzed. The computations showed that a flow reversal occurred on the leading edge of the impeller blades at reduced mass flow conditions. Air injection eliminated a local separation that was causing flow reversal and improved impeller stability.

Contributed by the International Gas Turbine Institute and presented at the International Gas Turbine and Aeroengine Congress and Exhibition, Atlanta, GA, June 16–19, 2003. Manuscript received by the IGTI December 2002; final revision March 2003. Paper No. 2003-GT-38524. Review Chair: H. R. Simmons.

Oakes et al. [7] worked to characterize the instability in a high-speed centrifugal compressor as it approached and entered surge. Arrays of high response pressure transducers were located upstream of the impeller inlet and in the endwall of the vaned diffuser. Two rotating stall modes were identified, a nine-cell mode that was a precursor to the initial surge cycle and a single cell mode that coincided with surge initiation. Both modes were found to be located near the diffuser.

Spakovszky [8] extended the Moore-Greitzer stability model for axial compression systems to centrifugal compressors by adding a radial duct to model the vaneless region between the impeller and vaned diffuser. The improved stability model also shows the importance of the vaneless space to compressor stability but from the viewpoint of system dynamics. The radial extent of the vaneless region and the amount of swirl in flow entering from the impeller discharge are important parameters that influence system stability. The improved model predicted a vaneless space disturbance rotating in a direction opposite the impeller. Working in the same compressor used for the experiments reported herein, Spakovszky verified the predicted disturbance and went on to demonstrate range improvement using small amounts of externally supplied air injected tangentially into the diffuser vaneless space in the direction of impeller rotation.

The motivation for the present work was to improve the stable flow range of centrifugal compressors by modifying flows in the vaneless and semi-vaneless regions of the diffuser. One strategy was to design a system of injectors that could provide variations in position, direction and flow rate to affect as many regions of the diffuser as possible. To implement that strategy, nozzles were installed through both the hub and shroud surfaces of the diffuser and air injection was tested at several impeller tip clearances and operating speeds. Another strategy implemented only on the shroud surface employed tubes that were inserted into the diffuser vaneless space to bleed low momentum flow discharging from the impeller tip.

This paper focuses on the techniques applied to the shroud-side of the diffuser. Results are presented from tests that were done at design speed with a constant tip clearance of 2.4% of impeller blade exit height.

Test Compressor

The test compressor is an Allison Engine Company design that was scaled up to a flow size of 10 lb_m/s (4.54 kg/s) from the original size of 3.655 lb_m/s (1.66 kg/s). McKain and Holbrook [9] give complete aerodynamic and mechanical design descriptions, including impeller and diffuser geometries.

The stage (impeller with vane-island diffuser) was designed to produce a pressure ratio of 4:1 at the design mass flow. The standard day corrected speed for the design flow condition is 21,789 rev/min with an exit tip speed of 1615 ft/s (492 m/s). The inlet relative Mach numbers on the suction surface range from 0.9 at the tip to 0.45 at the hub. The impeller contains 15 main blades and 15 splitter blades and has 50 degrees of backsweep from radial at the discharge. The splitter-blade leading edge, located at 20% of main blade chord, is offset slightly toward the main-blade suction surface in order to produce an even flow split. Both the main blades and splitter blades are formed from quasinormal straight-line elements between the hub and tip. The inlet tip diameter is 8.264 in. (210 mm) and the inlet blade height is 2.501 in. (64 mm). The exit diameter is 16.986 in. (431 mm) and the exit blade height is 0.671 in. (17 mm). All dimensions are for hot conditions at 100% of design speed.

The vane-island diffuser contains 24 passages. The vane leading edge is at a radius ratio of 1.08 and the mid pitch of the passage throat is at a radius ratio of 1.10. The diffuser exit is at a radius ratio of 1.68.

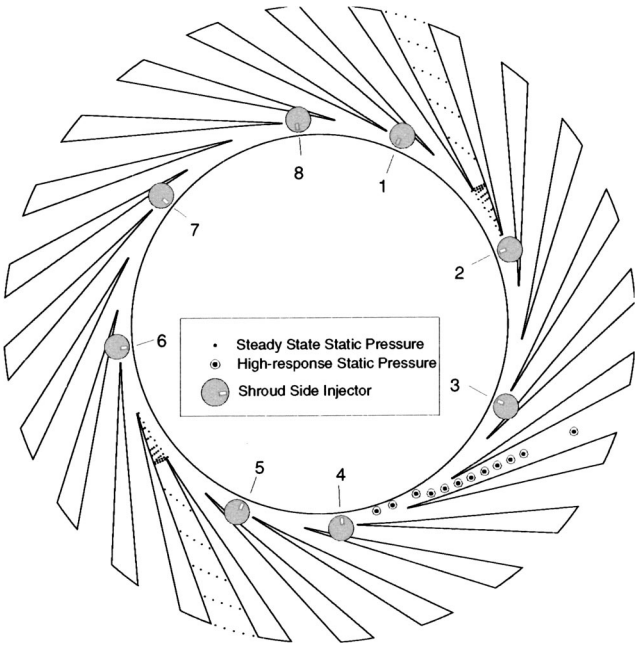

Fig. 2 Diffuser shroud instrumentation and injector locations

Surge Control Apparatus

Cross sections of the centrifugal compressor test rig, a shroud injector and the air supply system are shown in Fig. 1. Also shown is one of eight recirculation air pickups that were used for a configuration where recirculating air was supplied to the injectors.

Shroud Side Injectors. Eight injector nozzles were installed on the shroud side of the diffuser as shown in Fig. 2. The injector nozzles were contained in valve bodies that had been designed for pulsed-injection experiments where a voice-coil-type actuator drove an internal valve, hence the large size. The injection nozzles were interchangeable to permit testing of the wall-jet directions shown in Fig. 3.

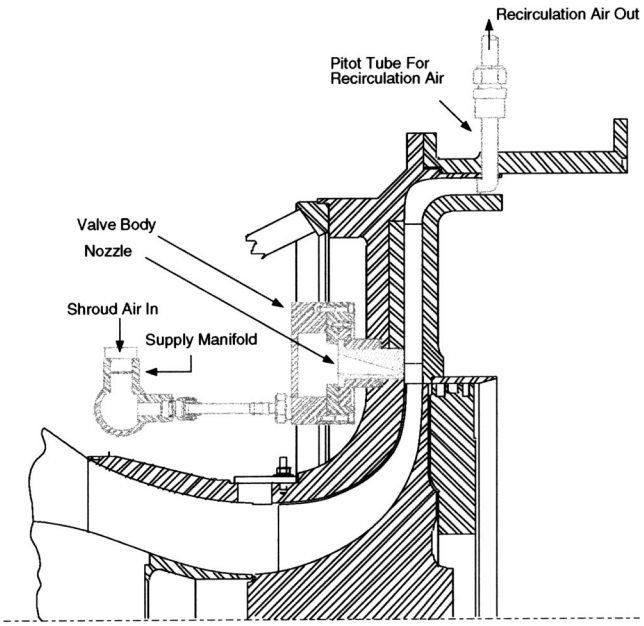

Fig. 1 Cross section of test compressor and air injection apparatus

Only steady flow injection was used in these experiments. Injection air was supplied to all eight valve bodies by an external manifold located around the circumference of the inlet. The manifold was supplied by an external air source or by recirculating flow collected through eight Pitot tube pickups located at the diffuser discharge (Fig. 1).

Control Tubes. Tubes were inserted through the shroud-side injector openings into the diffuser vaneless space as shown in Fig. 4. The tubes were fabricated from 0.375 in. (10 mm) diameter steel tubing that was bent to align the end residing inside the flow path with the local absolute velocity vector. The interior end was also partially recessed into the carrier plug to limit its immersion to 50% of diffuser span when the plug was fully seated without shims. Shims were placed under the exterior flange of the plug to achieve lesser immersions. Eight tubes could be installed using the same openings employed by the shroud side injectors (Fig. 2). The tubes provided a bleed path for the impeller discharge when the exterior ends were left open. However, the results reported here are from tests done with the external ends capped to prevent any mass flux through the tube.

Test Procedure, Instrumentation

Compressor stability experiments were completed over a speed range of 60–100% of design speed and at tip clearances of 2.4, 3.6, and 4.8% of exit blade height. Results from tests done at

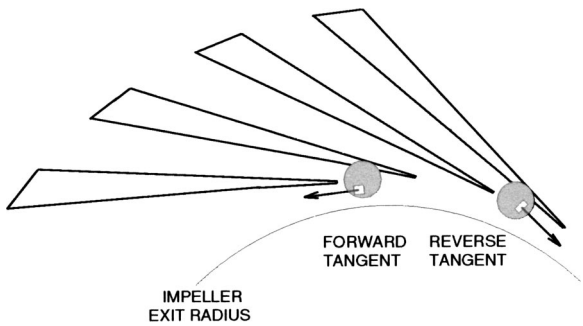

Fig. 3 Shroud side injector orientations

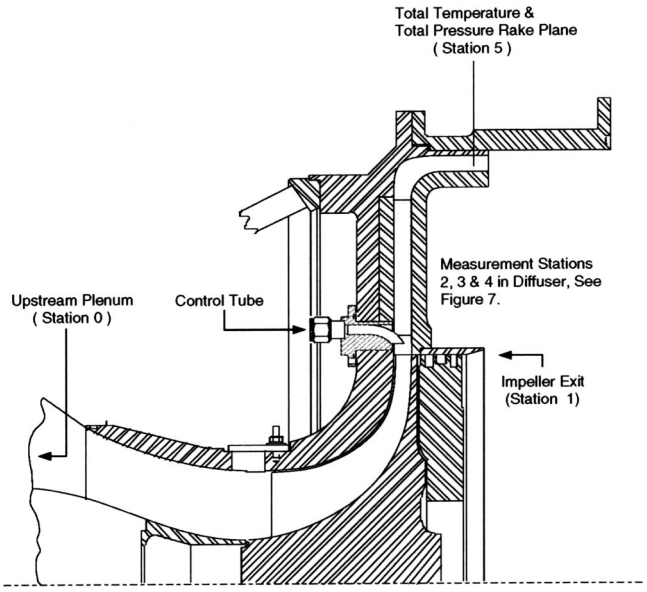

Fig. 4 Cross section of test compressor and control tube

100% of design speed with a tip clearance equal to 2.4% of exit blade height are reported here. At each condition, the compressor was throttled to a starting point on the operating characteristic that was near surge for the baseline compressor and then ramped into surge by closing the throttle slowly at a constant rate.

The flow rate where the compressor surged was determined by noting the flow rate where an audible change occurred in the sound emanating from the compressor. As a check on the audible indicator, the pressure delta across the main flow orifice was digitized during the ramps. A second surge flow rate was later determined from the digitized orifice data to verify the initial number. The computed surge flow rate was generally lower than the audible surge rate. The audible surge flow rates reported herein are within -0.05 and $+0.15$ lb_m/s (-24 and $+68$ g/s) of the computed value.

The surge flow rate was sensitive to changes in impeller tip clearance. Air injection changed the local metal temperature enough to change the clearance between the impeller trailing edge and the shroud. After arriving at a starting point on the characteristic that was near surge, the flow path dimensions were allowed to adjust to the temperature conditions created by air injection. The tip clearance was then adjusted to its initial value using a unique feature of the test rig that permits controlled axial movement of the impeller during operation. Tip clearance was measured during operation using a high-voltage touch-probe system.

High-response diffuser pressure data was collected using 50 psid (34.5 N/cm^2) Kulite pressure transducers. Data were recorded at a 2.5-kHz sampling rate with the raw signal filtered to a bandwidth of 1 kHz. The high-response transducers were located only on the shroud side of the diffuser as shown in Fig. 2. One passage was heavily instrumented with transducers located along a midpitch line extending from the vaneless space to a point near the passage exit.

Steady-state static pressure arrays were located in two passages on each of the shroud and hub surfaces. The shroud side static pressure arrays are shown in Fig. 2. Similar arrays were located on the hub. Stage total temperature and total pressure rise were determined from measurements collected in the upstream plenum and from rakes located in the discharge channel downstream of the diffuser. The downstream rake plane is marked in Fig. 4. Six four-element total pressure rakes and eight three-element total temperature rakes were located in the downstream plane. Five of the total temperature rakes and three of the total pressure rakes were replaced by Pitot tubes when recirculated air was used to supply injectors.

Steady-state data were collected using the test cell data system (Escort System) that records all steady-state pressure, temperature and speed data needed to determine compressor performance. Steady-state measurement uncertainties are pressure 0.1 psi (0.1 N/cm^2), temperature 1 R (0.6°C), and mass flow 0.05 lb_m/s (0.11 kg/s). The Escort System was also used to collect performance data while ramping toward surge since the throttle was being closed slowly. Data readings were taken at roughly 0.1 lb_m/s (50 g/s) flow increments between the ramp starting point and the surge point.

Experimental Results

Pressure rise characteristics, shown in Fig. 5, illustrate the range improvement provided by each shroud-side technique. Some of the results are shown as complete speed lines, others as partial speed lines beginning near the surge flow rate of the baseline characteristic.

All of the characteristics in Fig. 5 were obtained with injector nozzles installed on the hub surface. The hub nozzle air supply was closed for these experiments but a manifold between each nozzle and air supply lines permitted communication between nozzles. This communication improved the stable flow range of the compressor, as did the porous drillings described by Raw [4]. In the present work, the surge flow rate for the baseline compressor was approximately 0.1 lb_m/s (50 g/s) lower than it was for the same compressor with a solid diffuser hub surface.

The inlet corrected mass flow on each characteristic shown in Fig. 5 was adjusted to account for the air that was injected into the diffuser since it was injected downstream of the main flow orifice. Mass flow was adjusted by adding the absolute injection flow rate to the absolute flow rate at the compressor inlet and then correcting the sum to inlet conditions. The adjustment was made for both recirculated and external air supplies in order to determine the flow rate through the diffuser.

The final data point shown on each characteristic is at the flow rate determined from the audible surge indicator, adjusted for injection. The location of the data point on the ordinate was determined from a second order curve fit of three to six data points preceding surge.

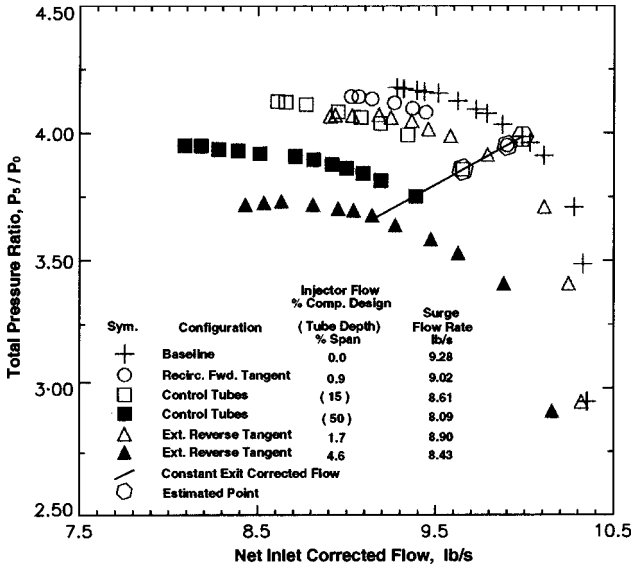

Fig. 5 Total pressure ratio characteristics at design speed and 2.4% tip clearance

Surge margin is typically used as an indicator of range improvement when comparing compressor designs, where surge margin is defined as

$$\mathrm{SM}=\left(1-\frac{\pi_{\mathrm{ref}}}{\pi_{\mathrm{surge}}}\cdot\frac{\dot{m}_{\mathrm{surge}}}{\dot{m}_{\mathrm{ref}}}\right)\times 100\% \qquad \text{and} \qquad \pi=\frac{P_5}{P_0}.$$

Each technique produced a unique pressure rise characteristic. A similar reference point on each characteristic is needed in order to compute surge margins that can be compared between the techniques. The reference points shown on each characteristic curve in Fig. 5 lie along a line of constant compressor-exit corrected flow computed at the design point of the baseline compressor. Reference points were estimated using second order curve fits of the measured points. Reference points in Fig. 5 that do not coincide with a measured point are indicated by a hexagon that surrounds the symbol.

Forward-Tangent Injection. The hardware configuration of forward-tangent injection is shown in Figs. 2 and 3. The injected air stream was in the direction of impeller rotation and coincident with the tangential component of the impeller discharge flow. The center of the injector opening was at a radius ratio of 1.04. The nozzles were sized to choke when 5% of compressor design mass flow was injected through eight nozzles (0.62% per nozzle) using air supplied at 80°F (27°C).

Spakovszky [8] first demonstrated the effectiveness of this configuration using externally supplied injection air. It was investigated again to determine whether the range improvement could be duplicated using an internal air supply. In the current work, injection air was taken from the diffuser discharge using the Pitot style pickups shown in Fig. 1. The open circles in Fig. 5 show results from forward-tangent injection using eight injectors.

Forward-tangent injection rates between 0.3 and 2.1% of design flow were tested. There was little variation in stage pressure ratio or flow range between the curves that were obtained. An injected flow rate of 0.9% produced the largest increase in stable flow range. The total pressure ratio at surge decreased by 1% compared to the baseline surge pressure ratio.

Design point surge margin on the baseline curve is 11.7%, computed using the design flow point of 10 $\mathrm{lb_m/s}$ (4.54 kg/s) as a reference. Surge margin improved to 13.4% with 0.9-percent forward-tangent injection. The improvement in surge margin is 14% ($\Delta\mathrm{SM}/\mathrm{SM_{Baseline}}$), which is much less than the 27% gain reported by Spakovszky [8]. However, baseline surge margin for the current configuration was higher due to the communication between hub injectors that was noted earlier.

Reverse-Tangent Injection. The reverse-tangent injector configuration is shown in Fig. 3. Eight injector nozzles were installed at the locations shown in Fig. 2. The injected stream was coincident with the tangential component of the impeller discharge flow at a radius ratio of 1.04, but the direction of the jet was opposed to impeller rotation. The total pressure at the injector opening had to be greater than the stagnation pressure of the impeller discharge to inject flow against impeller rotation. As such, an external air supply was used.

Injector flow rates ranging between 0.5 and 4.6% of compressor design flow were tested. The solid triangles in Fig. 5 are data from the highest injector flow rate. The open triangles are results from the middle of the injection flow-range at 1.7% of compressor design flow. Comparing the two characteristics shows that the stable flow range increased as injector flow rate increased, but the loss in total pressure ratio increased as well.

Reverse-tangent injection at 1.7% of compressor design flow provided a surge margin of 12.7%. When the injected flow rate was increased to 4.6% of design flow, the stable flow range increased but the pressure ratio at surge dropped substantially, losing 11% compared to the baseline pressure ratio. Surge margin decreased to 9.7% as a result.

Comparing the two reverse-tangent characteristics reveals part of the reason for the loss in pressure ratio. When the mass flow data along the 1.7% characteristic was adjusted to account for the effect of external air injection, the first operating point along the choked flow segment of the characteristic aligned with the first point on the baseline characteristic. A loss in pressure ratio is evident at subsequent points on the 1.7% characteristic that diminishes somewhat as surge is approached. Shifting the 4.6% characteristic did not produce the same choked flow alignment and the loss of pressure ratio is more substantial at low flow rates. Reverse-tangent injection reduces the tangential velocity component of flow entering the diffuser, beginning on the shroud surface and extending into some portion of the diffuser passage. At high injector flow rates the reverse-tangent process is inefficient and the dynamic head that could be recovered is lost instead. The resulting compressor characteristic appears to move down a constant throttle line as if compressor speed was being reduced.

Control Tubes. The final data set presented in Fig. 5 (squares) shows results from the control tube configuration where the outer ends were capped to prevent mass flux through the tubes. Only seven tubes were used in order to avoid a vibration mode in the impeller that could be excited by an eight per rev disturbance at design speed.

Laser anemometer surveys of this impeller (Skoch et al. [10]) showed that a region of fluid with low through flow velocity accumulates near the impeller tip along the suction surface of the blade. The low through-flow velocity fluid contributes to a jet-wake profile at the impeller exit. The original intent behind the control tube design was to bleed some of the low momentum fluid discharging from the impeller and re-inject that fluid at the impeller inlet, which was shown to benefit impeller stability in computations by Stein et al. [6]. However, a stabilizing influence was found to result simply from the presence of control tubes in the diffuser. It was not enhanced by bleed and, since the diffuser is the least stable element in this compressor, re-injection into the impeller did not impact the stable flow range.

Immersion into the vaneless space was varied during control tube experiments since bleed flow was not used. Figure 5 shows results obtained from two immersions. The open squares were obtained when the leading edge of the tube was immersed in the vaneless space to a depth of 15% of the local span. The solid squares represent data from a 50% immersion.

The 15% control-tube configuration provided a surge margin of 16.1% while losing only 1.4% in pressure ratio at surge. The 50% control-tubes provided a surge margin of 18.2% with a 5.5% decrease in pressure ratio at surge. The control tube configuration follows the pattern of reverse tangent injection where pressure ratio is traded for flow range. However, the level of pressure loss for a given improvement in range is much less with the control tubes.

Surge Mechanism. A surging flow condition in a centrifugal compressor is most likely the result of many factors that contribute individually or in combination to a final event that triggers surge. In this compressor, the event that precipitates surge occurs in the diffuser.

Figure 6 is an *X-T* diagram of high-response pressure measurements collected in the diffuser through one surge cycle in the baseline configuration. The operating condition was design speed with 2.4% impeller exit tip clearance. The pressure transducers used to construct the contours were located along the center of the diffuser passage as shown in Figs. 2 and 6. Measurements from two vaneless space transducers in line with the passage row are included. A pressure trace from the first vaneless space transducer is also shown in Fig. 6.

Wernet et al. [11] used Particle Image Velocimetry to visualize flow fields in this diffuser during surge and then connected the observations to a simultaneous measurement of pressure variation

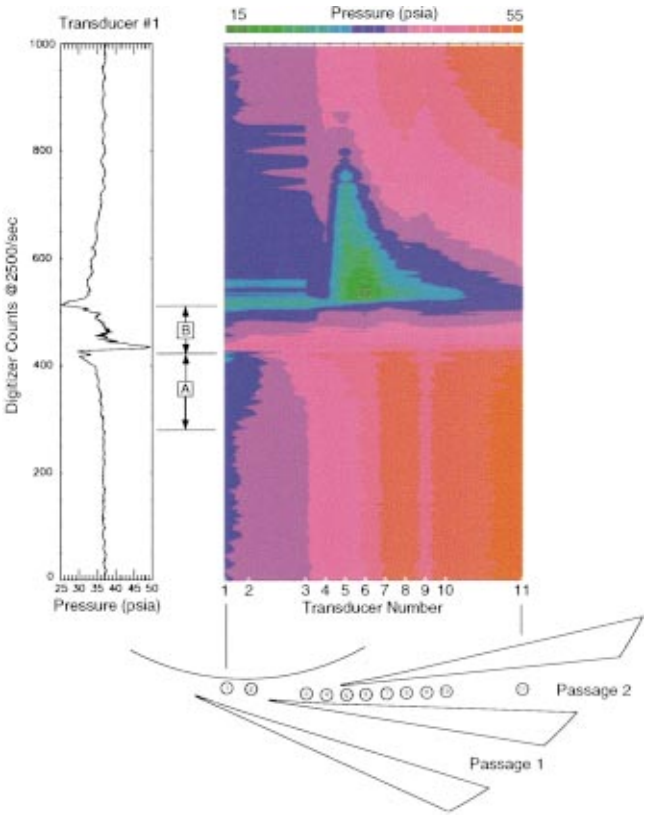

Fig. 6 ***X-T*** **diagram of diffuser passage pressures through one surge cycle**

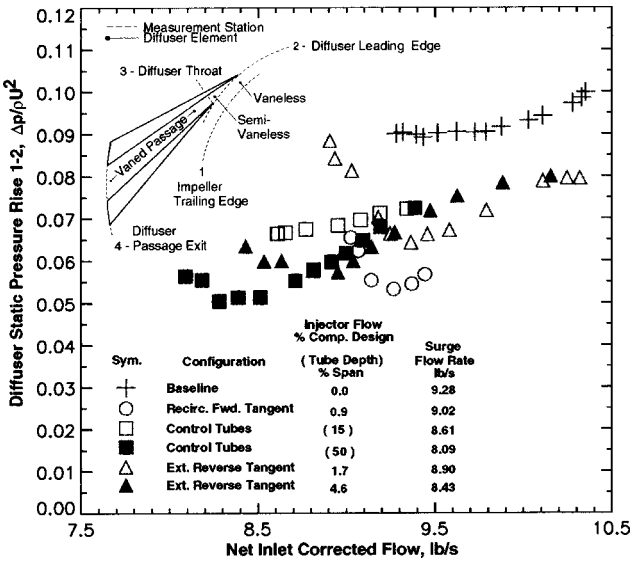

Fig. 7 Static pressure rise in the diffuser vaneless space at design speed and 2.4% tip clearance

in the diffuser throat. A reversal in flow direction through the diffuser was observed during the time interval indicated by region B in Fig. 6. A sudden spike in pressure at the diffuser throat marked the beginning of the reverse flow period, which continued until a subsequent minimum in pressure occurred. The pressure profile from transducer 1 shows the same characteristic spike in pressure followed by an immediate decrease to the minimum for the surge cycle.

Region A in Fig. 6 highlights a time interval just before surge. The pressures at transducers 1 and 2 are gradually decreasing, while the pressure at transducer 3 is gradually increasing. A rapid increase in vaneless space pressure occurs at surge, suggesting that a sudden collapse in diffusion is taking place upstream of the diffuser throat. Static pressure in the diffuser passage then drives a compression wave upstream into the vaneless space.

Blockage created by flow defects forming on either endwall of the vaneless space or near the leading edge of the lower vane in passage 1 could explain the observed condition. A reduction in flow area created by the defect would lower the static pressure in the leading edge region of the vaneless space requiring higher diffusion levels to support the existing static pressure gradient. Diffusion across the vaneless space eventually reaches a limit, existing downstream static pressure levels can no longer be supported, and diffuser flow suddenly reverses direction.

Surge Control Mechanisms. A significant interaction with the tangential component of velocity in flow entering the diffuser is a common element of the techniques that were tested here. Reverse-tangent injection and control tubes act directly against that component. A reduction in vaneless space tangential velocity and some mixing of the jet-wake profile on the shroud surface are likely to occur. At the same time, both injection and control tubes reduce the local through-flow area of the diffuser vaneless space and accelerate the through-flow component at lower spans. The combination results in lower average flow angles entering the diffuser.

When the flow angle at the diffuser entrance is reduced both diffusion ahead of the throat and incidence angles at the vane leading edge are also reduced. Rodgers [1] cites the level of diffusion taking place between the impeller trailing edge and the diffuser throat as a stability factor in a centrifugal compressor with a channel diffuser. Blockage growth increases with diffusion to the point that diffusion is reduced by accumulated blockage, leading to a positively sloped static pressure rise characteristic.

Spakovszky [8] developed a system model for centrifugal compressors to predict destabilizing flow resonance caused by unsteady interactions between the impeller and diffuser. Flow angle in the diffuser vaneless space was shown to influence the harmonic number of certain disturbances. Reducing flow angle in the vaneless space may have prevented the formation of one such backward rotating disturbance.

Diffuser performance, leading edge incidence, and backward rotating instability modes are discussed in more detail next.

Diffuser Performance. Diffusion occurring ahead of the throat was reduced for a given compressor flow rate by each technique. Diffuser static pressure rise coefficients are shown for the vaneless, semivaneless, and vaned-passage regions of the diffuser in Figs. 7–9. Static pressures measured on the hub and shroud at each element boundary were averaged before computing the static pressure rise across each element.

Vaneless Space. Figure 7 shows the static pressure rise coefficient across the diffuser vaneless space. The baseline configuration shows a slight decrease in pressure rise as the compressor is throttled. When the baseline configuration was tested with a solid hub surface the curve was increasing slightly as compressor flow was reduced. The opposite slope in this case is attributed to the communication between hub injectors that was noted earlier.

Data collected for the extended range configurations show a lower static pressure rise than the baseline at high through-flow rates. The decline in pressure rise at high through-flow is due to reduced flow area caused by injected air and to a loss of total pressure caused by interaction with the free-stream. Both reverse-tangent injection and control tubes act against the tangential component of velocity in the flow field so an increase in pressure loss is not unexpected.

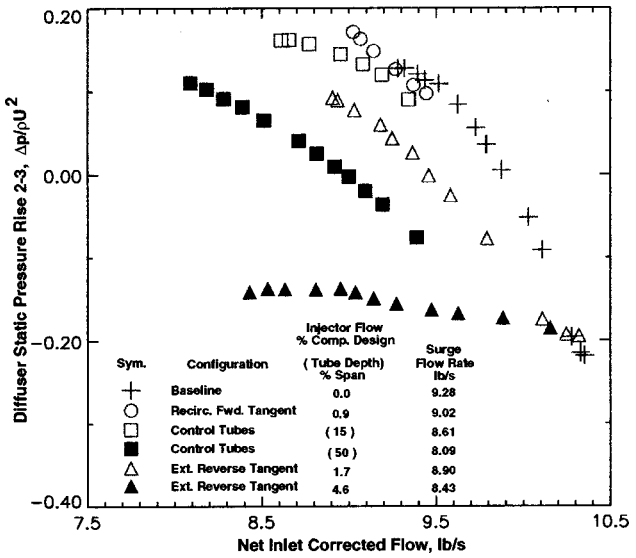

Fig. 8 Static pressure rise in the diffuser semivaneless region at design speed and 2.4% tip clearance

At high compressor through-flow rates, the tangential velocity component in air leaving the impeller is low and the losses associated with a head-on interaction between the injected jets or control tubes and the tangential component are small. As compressor through-flow is reduced the tangential component grows and the interaction produces increasing total pressure loss. Hence the further reduction in static pressure rise seen as compressor though-flow is reduced.

There is an inflection point on all but one of the characteristics where the slope turns negative and static pressure rise begins to increase. The maximum pressure loss caused by the interaction has been achieved at the inflection point and diffusion resumes as the compressor is throttled further.

The slope of the vaneless space characteristic is negative near surge on each of the characteristics shown in Fig. 7, except one, indicating that the vaneless space was becoming stable near surge. The 15% control-tube characteristic does not contain the inflection point seen on the other characteristics, suggesting that interaction losses developed more slowly in this configuration.

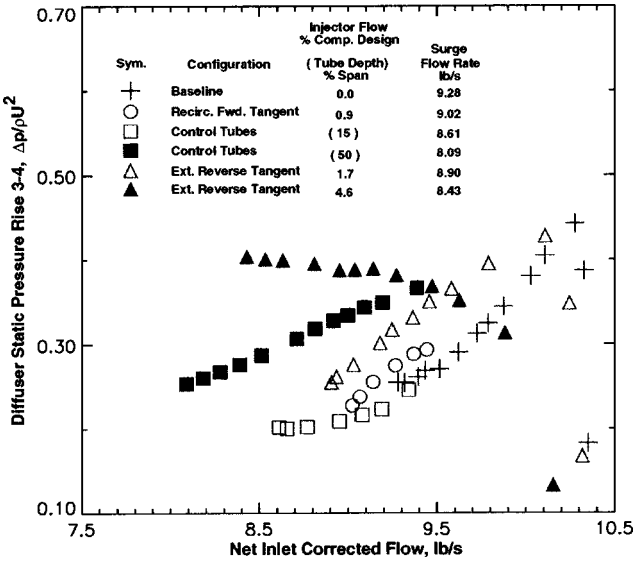

Fig. 9 Static pressure rise in the diffuser vaned passage at design speed and 2.4% tip clearance

Semivaneless Space. Figure 8 shows the static pressure rise measured across the semivaneless space. The characteristics generally maintain a negative slope over most of the flow range. The baseline characteristic exhibits a negative static pressure rise at high through-flow rates that is symptomatic of low swirl angle and negative incidence on the diffuser vanes. Low swirl angle decreases the effective throat area and diffusion across the element is reduced.

As the compressor is throttled, flow aligns with the throat and diffusion increases. This is demonstrated in Fig. 8 by the baseline characteristic as well as the extended range characteristics. The notable difference for the extended range characteristics is that the static pressure rise across this element is lower at a given rate of compressor through-flow. In the case of 4.6% reverse-tangent injection, the static pressure rise does not become positive anywhere on the characteristic.

The reasons for this behavior are twofold. First, when tangential velocity near the shroud is reduced and through-flow velocity at a lower span is increased, a lower average swirl angle is maintained to a lower compressor flow rate. Comparing characteristics from the same configuration illustrates this effect. The lower magnitude application in each pair is less effective at maintaining low swirl angle and produces more static pressure rise than its higher magnitude partner. For example, static-pressure rise on 15% control-tube characteristic is higher than it is on the 50% characteristic. The comparison also holds for the 1.7 and 4.6% reverse-tangent injection characteristics.

A total pressure loss is the second reason for the low static pressure observed in the semivaneless space. Losses in total pressure across the entire diffuser (shown later) were estimated for each of the range extension techniques tested. The loss across each element was not measured but it is reasonable to assume that a portion of the overall total pressure loss occurs in each element and is reflected in the static pressure rise coefficient across the element.

The 4.6% reverse-tangent injection characteristic shows negative static pressure rise along its entire characteristic. The loss coefficient measured across the diffuser was also largest for this configuration. The high momentum of the injected stream was directly opposed to the high tangential momentum of the impeller discharge flow. The injection process reduces the tangential velocity of the impeller discharge by mixing and the high losses produced by this process are not surprising.

Vaned Passage. Static pressure rise measurements from the vaned passage are shown in Fig. 9. The baseline static pressure rise characteristic exhibits a rapid increase at high compressor through-flow but quickly achieves an unstable positive slope as blockage growth limits diffusion in the passage and decreases static pressure rise at low compressor flow rates.

The extended range configurations, however, generally demonstrate higher static pressure rise than the baseline at low compressor flow rates. The slopes of the 4.6% reverse-tangent and 15% control-tube characteristics are negative or turning negative near surge, indicating an improvement in passage stability.

For the extreme case of 4.6% reverse-tangent injection, the characteristic in Fig. 9 has a negative slope over the entire flow range. This corresponds to a static pressure-rise characteristic in Fig. 8 that is below zero over the entire flow range. The conclusion drawn from this comparison is that reducing diffusion in the semivaneless region improves passage diffusion. Reduced blockage development in the passage or in the throat can account for this behavior since low momentum fluid resulting from throat blockage will diffuse less effectively.

Diffuser Total Pressure Loss. Figure 10 shows the diffuser loss coefficient for each configuration, where

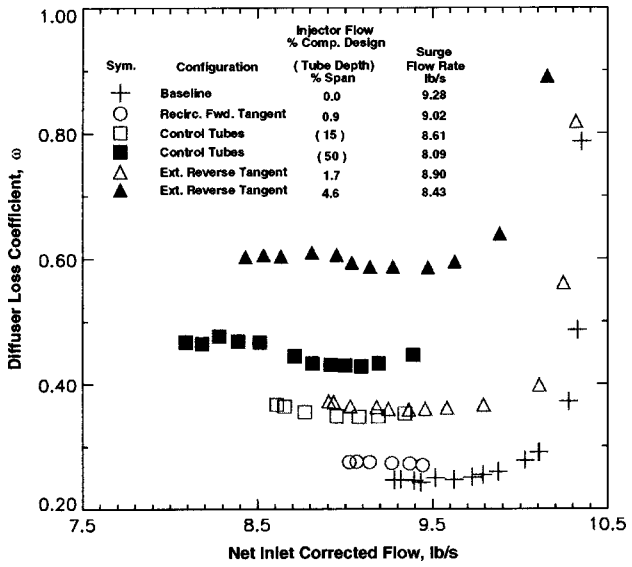

Fig. 10 Diffuser total pressure loss coefficient at design speed and 2.4% tip clearance

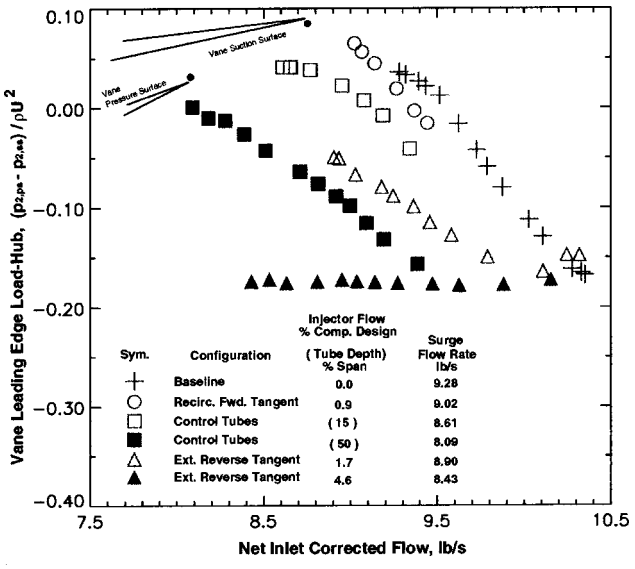

Fig. 11 Diffuser vane leading edge loading on the hub surface at design speed and 2.4% tip clearance

$$\omega = (P_1 - P_5)/(P_1 - p_1).$$

Total pressure at the impeller discharge (P_1) was estimated using the measured tip speed and stage total-temperature rise to find V_θ, where V_θ is the tangential velocity. The impeller tip static pressure (p_1) and mass flow were used to find the radial component of velocity V_r. An estimate of blockage at the impeller discharge was needed to estimate ρ and V_r. A 15% reduction of impeller discharge area was used in the estimate of impeller total pressure for all design speed conditions. The assumption of a constant 15-percent area reduction does not provide an exact representation of the actual flow area for each configuration; the goal was simply to provide a comparison of the losses generated by each technique.

The loss coefficient curves for the extended range configurations show that the level of total pressure loss across the diffuser is a function of control action magnitude for similar techniques. Lower loss was produced by 1.7% reverse-tangent injection than 4.6% reverse-tangent injection.

Stability may improve, even if surge margin does not, by creating losses in the vaneless space that increase corrected flow into the diffuser. However, a large pressure loss is not a necessary condition for significant flow range improvement. Total pressure loss produced by 4.6% reverse-tangent injection was much higher than the loss created by the 50% control tubes, yet the range improvement provided by the control tubes was greater.

Leading Edge Incidence. Diffuser vane leading edge incidence was reduced by each of the range improvement techniques that was tested. The change in pressure loading across the leading edge of a diffuser vane is an indicator of changes in leading edge incidence and is shown separately for the hub and shroud surfaces in Figs. 11 and 12, respectively.

Loading levels seen in Fig. 11 are generally negative at the hub surface, indicating negative incidence. Since there is not a strong jet-wake profile at the hub, flow discharging from the impeller hub has a lower time-averaged tangential velocity component and a higher through-flow component than flow discharging near the tip. When combined with the viscous drag generated by a transition from the rotating reference frame of the impeller to the stationary frame of the diffuser a significant reduction in swirl angle may result.

Further reductions in loading for a given compressor through-flow rate are demonstrated by the extended range configurations. This is indicative of increased negative hub incidence and shows that the range extension techniques employed on the shroud influenced the diffuser flow field across the entire span. For the extreme case of 4.6% reverse-tangent injection, negative incidence at the hub remained fairly constant as the throttle was closed. This is due to a significant reduction in V_θ coupled with an equally significant increase in V_r created by the reduction of through-flow area caused by the injected jet.

Leading edge loading at the shroud surface is plotted in Fig. 12. Loading levels on the baseline characteristic begin at a higher level and increase faster on the shroud than on the hub. Air discharges from the impeller tip with higher time-averaged swirl than air at the hub due to the low through-flow velocity fluid that has accumulated near the tip. The result is a more positive incidence on the vane leading edge and higher loading.

A reduction in swirl angle at a given flow rate is evident for each technique from the leading edge loading levels shown in Fig.

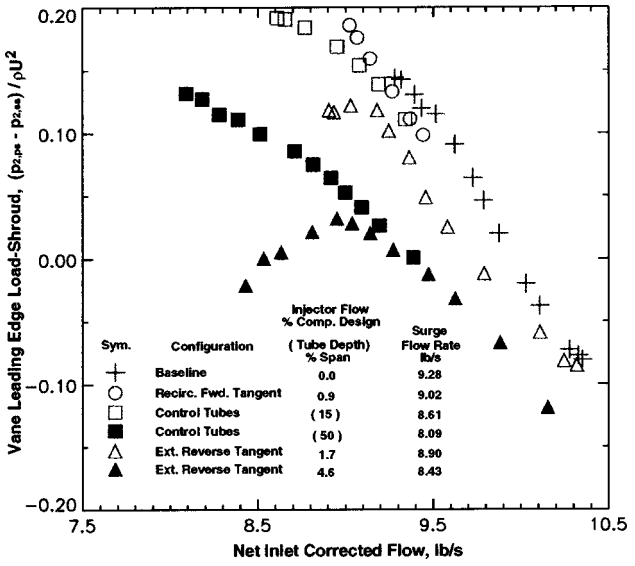

Fig. 12 Diffuser vane leading edge loading on the shroud surface at design speed and 2.4% tip clearance

12. Once again, the loading at a constant compressor flow rate is a function of the control action magnitude for similar methods.

The 15% control-tube and forward-tangent methods permitted the leading edge to support a higher loading level at surge than the baseline configuration. This effect was also seen at the hub and suggests that these configurations presented a more uniform flow field to the vane leading edge, permitting it to support a higher load. Reverse-tangent injection, however, reduced the pressure load supported at surge indicating a possible disruption in flow field uniformity.

Backward Rotating Instability Modes. Spakovszky [8] describes a relationship between compressor geometry and operating condition, repeated below, that can be used to determine the minimum harmonic of backward traveling instability waves that result from dynamic coupling between compressor blade rows,

$$\frac{\Delta\hat{x}}{R} > \frac{\pi}{n^2}\frac{1}{\tan\alpha}.$$

For a centrifugal compressor, $\Delta\hat{x}/R$ is a nondimensional distance between the impeller trailing edge and diffuser leading edge, n is the minimum harmonic for backward rotating disturbances, and α is the absolute swirl angle entering the diffuser.

When Spakovszky [8] applied the coupling criterion to this compressor it showed that backward traveling waves with harmonics of $n>2.8$ could be expected. His full compressor model predicted backward rotating third, fourth, fifth, and sixth harmonic disturbances, where disturbances with harmonic numbers above 4 were unstable over the entire characteristic and the fourth harmonic became unstable as the compressor was throttled to lower flow rates.

Spakovszky [8] also suggested that disturbances with harmonic numbers above 4 could not exist in this compressor because of a requirement that the disturbance cover at least two impeller blade passages, which left the fourth harmonic disturbance as the instability that contributed most to surge.

The coupling criterion indicates that for a fixed geometry the minimum harmonic of a backward traveling wave increases as swirl angle is reduced. It follows that if the minimum harmonic number for an unstable disturbance is increased to one that can not be supported by compressor geometry, then the contribution of that disturbance to surge is eliminated.

Two of the range improvement techniques tested here significantly reduced the absolute swirl angle in the diffuser vaneless space, which should have increased the minimum harmonic number for backward traveling disturbances. Pressure transducers were not available in sufficient quantity to detect disturbances with high harmonic numbers. However, it still follows that if the minimum harmonic of backward traveling instabilities was increased beyond 4, then backward rotating disturbances could not be maintained in the compressor and the contribution to surge of the original fourth harmonic disturbance would have been eliminated.

Impeller Performance and Stage Efficiency. Figure 13 shows temperature ratio versus diffuser through-flow for the baseline configuration and each of the extended range configurations. The total temperature measurements were corrected for the effect of injecting air into the system at a temperature that differed from the local flow. The following correction was applied to the measured total temperature:

$$T_5 \cdot \dot{m}_{\text{impeller}} = T_{5,\text{measured}} \cdot (\dot{m}_{\text{impeller}} + \dot{m}_{\text{injector}}) - T_{\text{injector}} \cdot \dot{m}_{\text{injector}}.$$

Impeller work input for each method generally follows the linear trend of the baseline curve and continues to rise as mass flow is reduced below the surge point of the baseline. The linear rise in temperature ratio indicates that V_θ is changing in proportion to V_r and impeller slip is not heavily influenced by the presence of the injected air streams or control tubes.

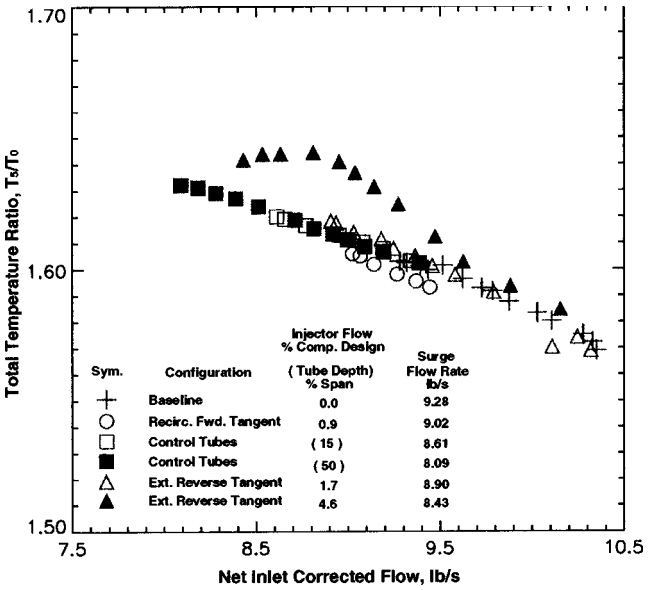

Fig. 13 Stage total temperature ratio at design speed and 2.4% tip clearance

A notable exception is the characteristic for reverse tangent injection at the 4.6% injector flow rate. This was the highest reverse-tangent flow rate tested and the increasing negative slope on the middle portion of the characteristic implies a net reduction in slip velocity.

Impeller static pressure ratio developed by the baseline compressor and each of the extended range configurations is shown in Fig. 14. The slope of the baseline characteristic is negative at the surge point, indicating that the impeller was stable at surge.

Except for the 15% control-tube configuration, the altered characteristics acquire a zero or positive slope prior to surge in Fig. 14. When this impeller was tested with a vaneless diffuser (Skoch et al. [10]) the stage did not surge until a flow rate of 7.2 lb_m/s (3.3 kg/s) was reached. The changing slopes seen here at flow rates above 7.2 lb_m/s suggest that each technique eventually

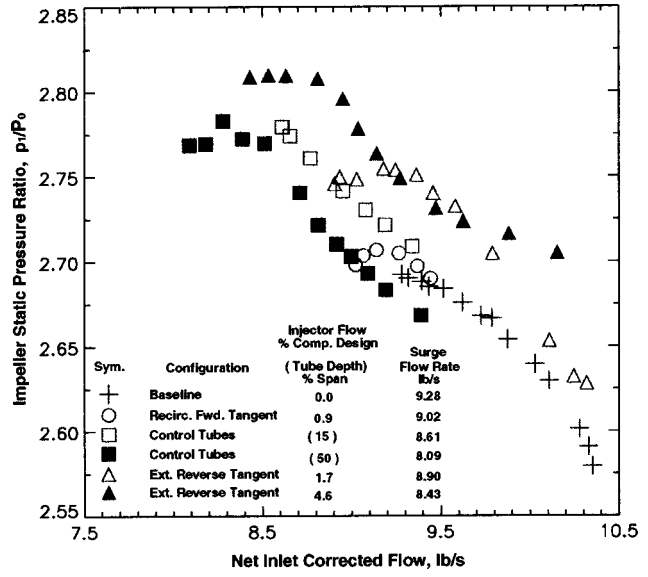

Fig. 14 Impeller static pressure ratio for the baseline and extended range configurations at design speed and 2.4% tip clearance

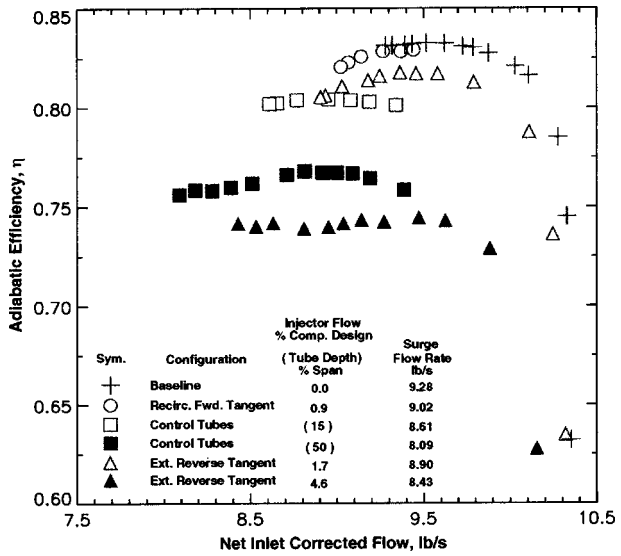

Fig. 15 Stage adiabatic efficiency at design speed and 2.4% tip clearance

began to destabilize the impeller. Forward-tangent injection destabilized the impeller much sooner in terms of compressor flow rate.

Increased impeller work input in the extended flow region of the characteristics produced higher total pressure at the impeller exit that mitigated somewhat, the effect of diffuser loss on stage pressure ratio. However, with increased impeller work input and a lower stage total pressure ratio, the stage efficiency is adversely impacted as seen in Fig. 15.

Practical Implications

Pressure loss incurred across the diffuser precludes the continuous use of any of the techniques described herein. However, it would make sense to employ these techniques if they can be used intermittently, turned on when the onset of compression system instability is detected and then turned off when stable operation returns. An intermittent operating strategy would make it possible to take advantage of improved stability provided by operating on the altered characteristics without enduring the penalty of a pressure loss during stable operation.

The feasibility of preventing surge by activating one of the techniques described above is demonstrated in Fig. 16 where reverse-tangent injection was used to bring the compressor out of surge. The figure shows the change in absolute compressor

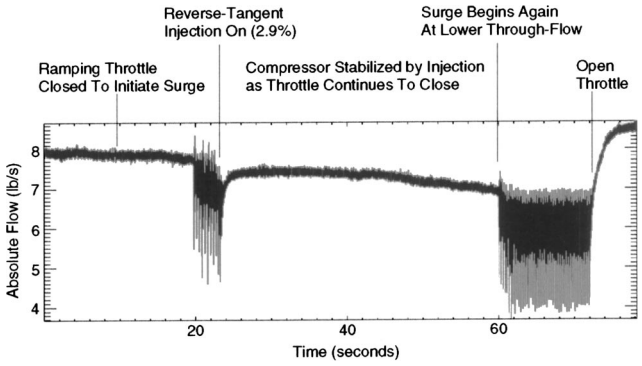

Fig. 16 Recovery from surge using reverse-tangent injectors 4 and 5 at 100% of design speed and 2.4% tip clearance

Table 1 Comparison of changes in surge margin and pressure ratio

Configuration	A surge margin, percent	B Δ surge margin, percent	C Δ PR at surge, percent
Baseline	11.7		
0.9% forward-tangent	13.4	1.7	−1.0
1.7% reverse-tangent	12.7	1.0	−2.6
4.6% reverse-tangent	9.7	−2.0	−11.0
15% control-tubes	16.1	4.4	−1.4
50% control-tubes	18.2	6.5	−5.5

through-flow with time, at design speed, as the throttle is closed to initiate surge and then as the compressor is stabilized using reverse-tangent injection.

Injection was initiated using a hand-operated valve when audible surge was detected. Only two injectors, 4 and 5 in Fig. 2, were used for this test. The total injected flow rate went from 0 to a value of 2.9% of design flow when the valve was first opened. As only two nozzles were in use, the flow through each nozzle was roughly equal to 1.5% of compressor design flow and both nozzles were choked.

Throttle closing continued, with injection stabilizing the compressor, until the compressor surged a second time. At the second surge point, both injectors were choked and additional supply pressure to raise injector mass flow was not available so a second recovery could not be accomplished. The throttle was then opened to bring the compressor out of surge.

If recovery from a fully developed surge condition can be accomplished then control actions taken at the first sign of instability should also stabilize the compressor. The test was not repeated using the control tubes or forward-tangent injection, since on-off control could not be done remotely. However, it seems reasonable that retractable control tubes and controllable recirculation valves could also be used to the limits of their effectiveness.

Summary

Three techniques to extend the stable flow range of a 4:1 pressure ratio centrifugal compressor have been demonstrated.

Table 1 summarizes the results obtained from each technique. Surge margin, computed along a line of constant compressor-exit corrected flow, is shown for each technique in column A. The improvement over the baseline surge margin ($SM - SM_{Baseline}$) is shown in column B. The change in stage pressure ratio at surge, $(PR - PR_{Baseline})/PR_{Baseline} \times 100\%$, is given in column C.

Forward-tangent injection using recirculated air caused very little pressure loss in the diffuser so an improvement in surge margin was demonstrated even though the stable flow range improvement was relatively small. Reverse-tangent injection produced the highest losses in stage pressure ratio for the increase in stable flow range that was achieved. It provided only a small improvement in surge margin and only at a low injected flow rate. Control tubes produced significant improvement in stable flow range with only moderate pressure loss in the diffuser, hence the greatest surge margin improvement.

The range improvement techniques acted on flow in the diffuser vaneless space and caused a reduction in average swirl angle across the span. Lower swirl angle produced the following results:

1. Diffusion between the impeller exit and diffuser throat was reduced.
2. Incidence on the diffuser vane leading edge was reduced.
3. Backward rotating instability modes may have been eliminated.

Each technique produced some loss of total pressure in the diffuser. Pressure losses created in the diffuser vaneless space helped

stabilize the compressor by throttling the diffuser but resulted in poor compressor performance and surge margin. Excessive pressure loss in the diffuser was not a necessary condition for stability improvement, however. Reducing the average swirl angle across the span of the vaneless space as the compressor approached surge was the important control action. If swirl angle reductions could be achieved with minimal pressure loss when approaching surge, then both performance and stability would be maintained.

The loss in total pressure across the diffuser precludes continuous operation using the techniques demonstrated here. However, an operating strategy that activates a particular technique when compression system instability is detected would be a practical alternative in order to take advantage of the significant stability improvement that is available.

Recovery from fully developed compressor surge using this strategy was demonstrated using reverse-tangent injection. However, based on measured surge margin improvement, retractable control tubes would be the best of the three methods tested here for an intermittent operating strategy.

Acknowledgments

The author would like to thank Thomas Jett, Winston Johnson, and Antonio Zaldana for test cell operation; Scott Panko, Edith Parrott, and Harry Fuller for electronics support; and Mark Stevens for hardware design. Special thanks also go to Dr. Anthony Strazisar for both programmatic and technical support of the project.

Nomenclature

P = total pressure
p = static pressure
T = total temperature
T_5 = total temperature at exit rake plane after correcting for injection
$T_{5,\text{measured}}$ = measured total temperature at exit rake plane
T_{injector} = total temperature of injector flow
$\dot{m}_{\text{ref}}$ = impeller net inlet corrected mass flow at constant exit corrected flow reference point
$\dot{m}_{\text{surge}}$ = impeller net inlet corrected mass flow at surge
$\dot{m}_{\text{impeller}}$ = impeller absolute mass flow
$\dot{m}_{\text{injector}}$ = injector absolute mass flow
π_{ref} = stage total pressure ratio at constant exit corrected flow reference point
π_{surge} = stage total pressure ratio at surge
SM = surge margin, $(1-(\pi_{\text{ref}}/\pi_{\text{surge}})\cdot(\dot{m}_{\text{surge}}/\dot{m}_{\text{ref}}))\times 100\%$
$\text{SM}_{\text{Baseline}}$ = surge margin on baseline characteristic
U = impeller exit tip speed
ρU^2 = impeller dynamic head
ΔH_{isen} = isentropic enthalpy rise
ΔH_{act} = actual enthalpy rise
η = adiabatic efficiency, $\Delta H_{\text{isen}}/\Delta H_{\text{act}}$

Measurement Station Subscripts

0 = upstream plenum
1 = impeller trailing edge
2 = diffuser vane leading edge
3 = diffuser throat
4 = diffuser exit
5 = rake plane in diffuser exit passage

References

[1] Rodgers, C., 1982, "The Performance of Centrifugal Compressor Channel Diffusers," ASME Paper No. 82-GT-10.
[2] Rundstadler, Jr., P. W., and Dean, Jr., R. C., 1969, "Straight Channel Diffuser Performance at High Inlet Mach Numbers," J. Basic Eng., **91**, pp. 397–422.
[3] Jansen, W., Carter, A. F., and Swarden, M. C., 1980, "Improvements in Surge Margin for Centrifugal Compressors," *Centrifugal Compressors, Flow Phenomena and Performance*, AGARD-CP-282, No. 19.
[4] Raw, J. A., 1986, "Surge Margin Enhancement by a Porous Throat Diffuser," Can. Aeronautics Space J., **32**, pp. 54–60.
[5] Nelson, E. B., Paduano, J. D., and Epstein, A. H., 2000, "Active Stabilization of Surge in an Axial Centrifugal Turboshaft Engine," ASME J. Turbomach., **122**, pp. 485–493.
[6] Stein, A., Saeid, N., and Sankar, L. N., 2000, "Numerical Analysis of Stall and Surge in a High-Speed Centrifugal Compressor," *38th Aerospace Sciences Meeting and Exhibit*, Reno, NV, AIAA paper No. 2000-0226.
[7] Oakes, W. C., Lawless, P. B., and Fleeter, S., 1999, "Instability Pathology of a High Speed Centrifugal Compressor," *ASME Turbo Expo*, Indianapolis, Indiana, ASME paper No. 99-GT-415.
[8] Spakovszky, Z. S., 2002, "Backward Traveling Rotating Stall Waves in Centrifugal Compressors," *ASME Turbo Expo*, Amsterdam, The Netherlands, ASME paper No. GT-2002-2039.
[9] McKain, T. F., and Holbrook, G. J., 1982, "Coordinates for a High Performance 4:1 Pressure Ratio Centrifugal Compressor," NASA CR-204134.
[10] Skoch, G. J., Prahst, P. S., Wernet, M. P., Wood, J. R., and Strazisar, A. J., 1997, "Laser Anemometer Measurements of the Flow Field in a 4:1 Pressure Ratio Centrifugal Impeller," *ASME Turbo Expo*, Orlando, Florida, ASME paper No. 97-GT-342.
[11] Wernet, M. P., Bright, M. M., and Skoch, G. J., 2001, "An Investigation of Surge in a High-Speed Centrifugal Compressor Using Digital PIV," Transactions of the ASME, **123**, pp. 418–428.

Average Passage Flow Field and Deterministic Stresses in the Tip and Hub Regions of a Multistage Turbomachine

Oguz Uzol
Yi-Chih Chow
Joseph Katz
Charles Meneveau

Department of Mechanical Engineering,
Johns Hopkins University,
Baltimore, MD 21218

This paper continues our effort to study the dynamics of deterministic stresses in a multistage turbomachine using experimental data. Here we focus on the tip and hub regions and compare them to midspan data obtained in previous studies. The analysis is based on data obtained in particle image velocimetry (PIV) measurements performed in the second stage of a two-stage turbomachine. A complete data set is obtained using blades and fluid with matched optical index of refraction. Previous measurements at midspan have shown that at midspan and close to design conditions, the deterministic kinetic energy is smaller than the turbulent kinetic energy. The primary contributor to the deterministic stresses at midspan is the interaction of a blade with the upstream wakes. Conversely, we find that the tip vortex is the dominant source of phase-dependent unsteadiness and deterministic stresses in the tip region. Along the trajectory of the tip vortex, the deterministic kinetic energy levels are more than one order of magnitude higher than the levels measured in the hub and midspan, and are of the same order of magnitude as the turbulent kinetic energy levels. Reasons for this trend are explained using a sample distribution of phase-averaged flow variables. Outside of the region affected by tip-vortex transport, within the rotor-stator gap and within the stator passages, the turbulent kinetic energy is still 3–4 times higher than the deterministic kinetic energy. The deterministic and turbulent shear stress levels are comparable in all spanwise locations, except for the wakes of the stator blades, where the turbulent stresses are higher. However, along the direction of tip-vortex transport, the deterministic shear stresses are about an order of magnitude higher than the turbulent shear stresses. The decay rates of deterministic kinetic energy in the hub and midspan regions are comparable to each other, whereas at the tip the decay rate is higher. The decay rates of turbulent kinetic energy are much smaller than those of the deterministic kinetic energy. The paper also examines terms in the deterministic kinetic energy transport equation. The data indicate that "deterministic production" and a new term, here called "dissipation due to turbulence," are the dominant source/sink terms. Regions with alternating signs of deterministic production indicate that the energy transfer between the phase-averaged and average-passage flow fields can occur in both directions. The divergence of the pressure-velocity correlation, obtained from a balance of all the other terms, is dominant and appears to be much larger than the deterministic production (source/sink) term. This trend indicates that there are substantial deterministic pressure fluctuations in the flow field, especially within the rotor-stator gap and within the stator passage. [DOI: 10.1115/1.1625692]

Introduction

The ''average-passage'' Reynolds-averaged Navier-Stokes (RANS) equations, introduced first by Adamczyk [1], enable computations of time-averaged flows within multistage turbomachines, while using steady boundary conditions, but still accounting for blade-rows interactions. This approach is especially important as a practical design tool for turbomachines with multiple blade rows and varying number of rotor and stator blades in consecutive stages. In this formulation each blade row has a steady average-passage flow field, which extends from the inlet to the exit of the machine. Neighboring blade rows are replaced with circumferentially uniform systems of body forces, energy sources, and (not necessarily uniform) deterministic stresses (Adamczyk [1], Adamczyk et al. [2], Adamczyk et al. [3], Rhie et al. [4], LeJambre et al. [5], Busby et al. [6]). The effects of phase-dependent unsteadiness on the average-passage flow field are accounted for through the deterministic stresses, which must be modeled in order to obtain a closed system of equations. Different models for the deterministic stresses have already been proposed (e.g., Adamczyk [2], Van de Wall [7], Meneveau and Katz, [8], He et al. [9]). However, unlike RANS closure models, there are no widely accepted and validated modeling tools. To develop such models one requires a database obtained either from experiments or from unsteady RANS involving multistages. The latter approach introduces uncertainties related to turbulence closure models.

In previous experimental studies, the deterministic stresses have been obtained either by traversing single point sensors (e.g., Prato et al. [10,11], Suryavamshi et al. [12,13]), or by particle image velocimetry (PIV) measurements in quasi two-dimensional (2D) centrifugal pumps (Sinha and Katz [14] and Sinha et al. [15]). In order to implement PIV in a multistage axial turbomachine, Uzol et al. [16] and Chow et al. [17] recently introduced a facility that enables unobstructed optical access using transparent rotor and stator blades operating in a liquid, which has the same optical

Contributed by the International Gas Turbine Institute and presented at the International Gas Turbine and Aeroengine Congress and Exhibition, Atlanta, GA, June 16–19, 2003. Manuscript received by the IGTI December 2002; final revision March 2003. Paper no. 2003-GT-38598. Review Chair: H. R. Simmons.

index of refraction as the blades. A brief description of this system is provided in the following chapter. Subsequent papers (Uzol et al. [18] and Chow et al. [19]) provided data on the distributions of phase-averaged and average-passage velocity distributions, along with the deterministic stresses and turbulence parameters in a midspan plane, covering the entire second stage of a two-stage axial turbomachine. The results showed substantial nonuniformities in distributions of deterministic stresses, which were caused by blade-wake and wake-wake interactions. At midspan and close to design conditions, the turbulent kinetic energy was higher than the deterministic kinetic energy, whereas the Reynolds stresses and deterministic stresses were of the same order of magnitudes, but followed completely different trends.

This paper continues our effort to study the dynamics of deterministic stresses in a multistage turbomachine using experimental data. However, this time we expand to the tip and hub regions. The analysis is based again on two-dimensional PIV measurements performed in three spanwise planes, which cover the entire second stage of a two-stage turbomachine. One plane is located close to the hub, the second is located at mid span, and the third is in the tip region, where the dynamics are dominated by the tip vortex. The data enable us to examine the effects of the tip-vortex and hub boundary layer on the phase-averaged and average-passage flow fields, as well as on the distributions of deterministic stresses. As will be demonstrated, for example, unsteady features of advection of the tip vortex results in very large deterministic kinetic energy. Furthermore, we also examine the decay rates of deterministic kinetic energy along the stator passage, and compare the results to the decay of average-passage turbulent kinetic energy. Finally, after introducing the evolution equations for the deterministic kinetic energy, we compare the magnitudes and spatial distributions of the dominant production and dissipation terms. A balance of all the terms also attempts to determine the effect of divergence in the deterministic pressure-velocity correlations.

Experimental Setup and Procedures

Facility. The axial turbomachine test facility enables us to perform detailed and unobstructed PIV measurements at any point within an entire stage including the rotor, stator, gap between them, inflow into the rotor, and the wake structure downstream of the stator. To generate such data using optical techniques one needs an unobstructed view of the entire domain at any phase angle. This unlimited optical access is facilitated using a rotor and stator made of a transparent material (acrylic) that has the same optical index of refraction as the working fluid, a concentrated solution, 62 percent–64 percent by weight, of NaI in water. This fluid has a specific gravity of 1.8 and a kinematic viscosity of 1.1×10^{-6} m^2/s, i.e., very close to that of water. Thus, the blades become almost invisible, do not obstruct the field of view, and do not alter the direction of the illuminating laser sheet required for PIV measurements. Information related to use and maintenance of the NaI solution can be found in Uzol et al. [16]. The two-stage axial turbomachine shown in Fig. 1 has four blade rows. There are 12 rotor blades, each with a chord length of 50 mm, span of 44.5 mm, thickness of 7.62 mm, and camber varying from 2.54 mm at the hub to 1.98 mm at the tip. The resulting Reynolds number based on the tip speed and rotor chord length is 3.7×10^5 at 500 rpm, the speed of the present tests. The stators have 17 blades, each with a chord length of 73.2 mm, span of 44.5 mm, thickness of 11 mm, and camber of 6.22 mm. The gap between the rotor and the stator is 50 mm. The system is driven by a 25 HP rim-driven motor, which drives the first rotor directly, and the two rotors are connected by a common shaft, supported by precision bearings. More details about the facility can be found in Uzol et al. [16,18] and Chow et al. [17,19].

PIV Setup and Experimental Procedure. The measurement domain covers the entire second stage. Data have been obtained at 500 rpm, for 10 rotor phases, every three degrees of blade orientation, covering an entire rotor blade passage of 30 deg. In this paper we focus on three spanwise planes (containing the streamwise and lateral velocity components), which are located at 3 percent, 50 percent, and 90 percent of the rotor span. At least one hundred instantaneous realizations are recorded for each phase and location. For selected cases we record 1000 image pairs in order to obtain converged statistics on the turbulence. We use a $2k\times2k$ camera and an Nd-YAG laser sheet, and the sample area is 50×50 mm^2, and each velocity distribution consists of 61×61 vectors. As a result, five data sets at different axial locations are needed to cover the entire second stage. The sample area (50×50 mm^2) covers 124 percent, 104 percent, and 92 percent of the stator pitch and 87 percent, 74 percent, and 65 percent of the rotor pitch at 3 percent, 50 percent, and 90 percent span locations, respectively. Data analysis includes image enhancement and cross-correlation analysis using in-house developed software and procedures (Roth et al. [20], Roth and Katz [21]). Adapting these procedures to the current geometry, including modifications to the image enhancement procedures, and removal of the blade trace/signature prior to velocity computations are discussed in Uzol et al. [16]. Additional details about the PIV setup and data acquisition system can be found in Chow et al. [17,19] and Uzol et al. [18]. A conservative estimate of the uncertainty in mean displacement in each interrogation window is 0.3 pixels, provided the window contains at least 5–10 particle pairs (Roth et al. [20], Roth and Katz [21]). For the typical displacement between exposures of 20 pixels, the resulting uncertainty in instantaneous velocity is about 1.5 percent. Slip due to the difference between the specific gravity of the particle (1.6) and that of the fluid (1.8) may cause an error of less than 0.2 percent, i.e., much less than other contributors (Sridhar and Katz [22]). Uncertainty related to inflow variations and timing errors is estimated to be less than 0.6 percent.

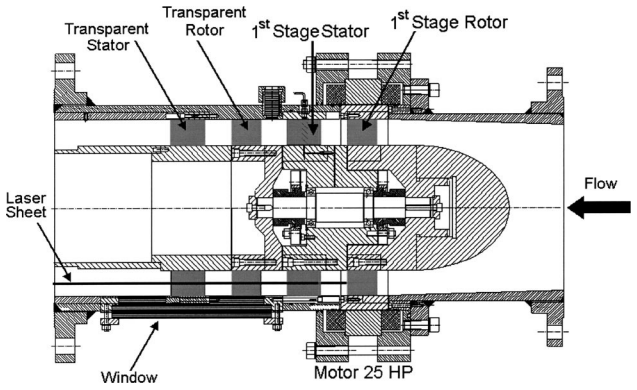

Fig. 1 Test section of the axial turbomachine. The second-stage rotors and stators are made of transparent acrylic.

Phase-Averaged Mean Flow and Turbulence

Using the instantaneous measurements, the phase-averaged parameters are calculated using

$$\overline{u_i}(x,y,\phi)=\frac{1}{N}\sum_{k=1}^{N}[u_i(x,y,\phi)]_k, \tag{1}$$

$$\overline{u_i'u_j'}(x,y,\phi)=\frac{1}{N}\sum_{k=1}^{N}\{[u_i(x,y,\phi)]_k-\overline{u_i}(x,y,\phi)\}\times\{[u_j(x,y,\phi)]_k-\overline{u_j}(x,y,\phi)\}, \tag{2}$$

$$k(x,y,\phi)=\tfrac{3}{4}[\overline{u_i'u_i'}(x,y,\phi)], \tag{3}$$

where $N=100$ is the number of instantaneous vector maps and for each phase, x and y are the axial lateral coordinates, respectively,

and ϕ is the phase angle. The subscripts i and j take values of 1 and 2, representing the axial ($u_1=u$) and lateral ($u_2=v$), almost circumferential (although the light sheet is flat) velocity components, respectively. The 3/4 coefficient of k, the ''turbulent kinetic energy,'' is selected to account for the contribution of the out of plane velocity component, assuming that it is an average of the available measured components. The phase-averaged flow angle and the z component of the vorticity are calculated using

$$\overline{\alpha}=\tan^{-1}\left(\frac{\overline{v}}{\overline{u}}\right), \tag{4}$$

$$\overline{\omega}=\frac{\partial\overline{v}}{\partial x}-\frac{\partial\overline{u}}{\partial y} \tag{5}$$

Detailed data and discussions on the characteristics of the phase dependent variations in flow structure and turbulence at the 50 percent span plane are presented in Uzol et al. [18] and Chow et al. [17,19]. Relevant phenomena include formation of a lattice of chopped-off rotor/stator wakes, wake-wake and wake-blade interactions leading to wake shearing and kinking, circumferential variations of work input, phase dependent variations in stator blade loading due to wake impingement, etc. In this section we compare the phase-averaged flow and turbulence in three planes, near the tip (90 percent span), near the hub (3 percent span), and at midspan (50 percent) span. Figure 2 shows the phase-averaged distributions of axial velocity ($\overline{u}$), lateral velocity ($\overline{v}$), absolute velocity magnitude ($|\overline{\vec{V}}|$), relative velocity magnitude ($|\overline{\vec{V}}|_{\mathrm{rel}}$), turbulent kinetic energy (k), and phase-averaged vorticity ($\overline{\omega}$) in the three planes, for one of the ten measured phases, $t/T=0.0$ (T is the rotor blade passing period). Figure 3 presents the vorticity distribution at a different phase in order to highlight certain phenomena, as follows.

Flow in the Tip Region. The flow field in the tip region (90 percent span) is dominated by the presence of the tip vortex. The vicinity of the tip vortex is characterized by low relative velocity magnitude [Fig. 2(d)], high turbulent kinetic energy [Fig. 2(e)], high lateral velocity [Fig. 2(b)], and in part, wake-like distribution of vorticity (streaks of opposite signs on opposite sides of the wake [Fig. 2(f)]. The turbulent kinetic energy levels as well as the phase-averaged axial and lateral velocity nonuniformities in the flow field are substantially higher than those at midspan. The tip vortex starts dissecting the 90 percent plane to the right (suction side) of the trailing edge of the blade that generates it (e.g., Fig. 3). The large structures on the pressure side of the blade, which occupy most of the rotor blade passage, are generated by the previous blades. In Fig. 2(f) one can see two such systems, the first near the pressure side of the blade, and the second in the rotor-stator gap. The ''blobs'' with high positive vorticity appear in regions, where the tip vortex dissects the 90 percent plane, as can be deduced from the sharp gradients in horizontal and lateral velocity [Figs. 2(a) and 2(b)]. Due to the vortex-induced velocity, $\overline{u}$ diminishes above (pitchwise) the vortex center, and $\overline{v}$ decreases sharply to the right of the center. The vortex center is also characterized by high turbulence level. The tip vortex impinges on the pressure side of the following rotor blade and then interacts with the wake of that blade. The impingement is evident in Fig. 2(f) at ($x/L_s=0.12$, $y/L_s=0.04$) $L_s=203$ mm is the stage length, as the concentrated positive vorticity regions comes into contact with the blade. At $t/T=0.7$ (Fig. 3) this very same region can be seen interacting with the wake of the rotor blade at (0.2, 0.16). During this interaction the rotor wake (of the subsequent blade) is split, and part of it is entrained by the tip vortex (of the previous blade). The split rotor wake segments merge with the tip vortex in the gap between the rotor and the stator [Fig. 2(f)], and the resulting complex structure is transported through the stator passages. Thus, the positive and negative vorticity regions within the stator passage in Fig. 2(f) are, in fact, combined tip vortex and (subsequent) rotor wake. It is not possible to distinguish the individual rotor wakes and the tip vortices in the stator passage once they merge together [unless one performs three-dimensional (3D) velocity measurements].

Upstream of the rotor ($x<0$) and within the rotor passage one can identify the wakes generated by the first stage. At the 50 percent plane [Fig. 2(f)], one can see the lower half of a first-stage stator wake with positive vorticity at (-0.05, 0.2), and the upper half of the following wake with negative vorticity at (-0.05, 0), as discussed in Uzol et al. [18]. The phase-dependent oscillations of the first-stage stator wakes in the tip region are substantial compared to the midspan, even upstream of the second-stage rotor, as is evident by comparing the corresponding vorticity plots in Figs. 2 and 3. At midspan the wakes do not change significantly, whereas at the tip the incoming stator wake is straight at $t/T=0.0$, and significantly distorted at $t/T=0.7$, most likely due to the flow field induced by the tip vortex. These periodic fluctuations of the first-stage stator wakes become clearly evident when all measured rotor phases are examined as a sequence. The first-stage rotor blade row does not generate a tip vortex since it is banded by an external ring containing the permanent magnets of the rim-driven motor, and there is no tip gap. The wakes of the first-stage rotor generates inclined vorticity layers with alternating signs (Uzol [18]). In Fig. 2(f) (50 percent), the second-stage rotor blade dissects such an inclined wake, creating a layer of negative vorticity on the pressure side of the blade, and positive vorticity on the suction side. Thus, the rotor is engulfed by the first-stage rotor wake. Due to spanwise variations in velocity, there are phase differences between the first-stage rotor wake at midspan and in the tip region (90 percent). Consequently, in the tip regions the first-stage rotor wake is located upstream of the blade. As a result, the inclined vorticity layers appear to have opposite signs, e.g., there is a positive vorticity layer on the pressure side of the blade in the tip region and a negative vorticity at midspan. The phase lag is also evident in Fig. 3, before the blade interacts with the inclined wakes. At midspan the blade is aligned with the positive vorticity layer with the negative layer slightly downstream, and the rotor blade is about to slice through this wake. In the tip region, the first-stage rotor wake is located upstream of the rotor blade. There are several possible reasons for delay, such as the effects of the boundary layer on the casing, both within the first-stage stator passage and in the gap between stages.

Although the flow field in the tip region is quite complicated, the interaction of the incoming first-stage stator wakes with the rotor blade and the tip vortex can still be depicted. The upstream stator wakes get chopped off by the rotor blades and then merge with the tip vortex. At $t/T=0.0$ [Figs. 2(e) and 2(f) at 90 percent], the rotor blade is about to cut through the stator wake. At this instant this stator wake intersects with the tip vortex of the previous rotor blade at (0.09, 0.2). As the wake gets chopped off, the wake segment and the tip vortex merge along the pressure side of the rotor blade, generating concentrated positive vorticity regions, identifiable, for example, in Fig. 3 at (0.27,0.06), (0.15,0.24), and in Fig. 2(f) at (0.32,0.12). These high vorticity ''blobs'' enter the second-stage stator passage along the suction side of the stator blade, and eventually become difficult to distinguish from the inclined structures generated by the tip vortices and entrained rotor wakes. These complex interactions near the tip create much wider, inclined patches of high vorticity in the tip region, as compared to the midspan. Note that these processes are easier to recognize as one examines all the ten phases in sequence (only two sample phases are presented in this paper).

In comparing the vorticity distributions at midspan to the tip region [Fig. 2(f)], one can also notice that the wake of the previous blade is located further downstream compared to the structures in the tip region. Furthermore, the angle between the wake and the streamwise direction at midspan is lower than the main orientation of structures in the tip region. These differences are caused by the lower axial velocity (presumably due to the casing boundary layer), and higher lateral velocities just downstream of

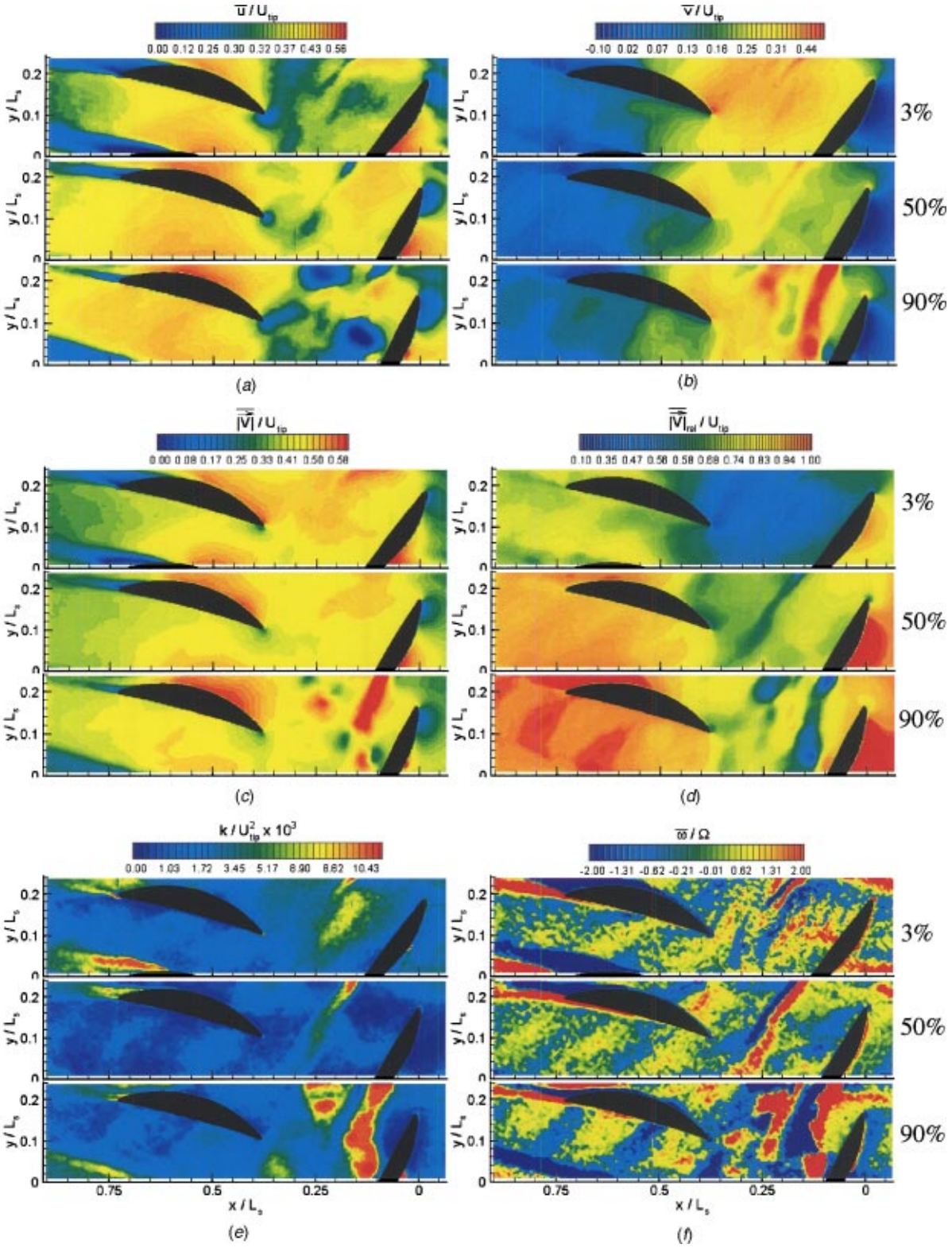

Fig. 2 Phase-averaged distributions for $t/T=0.0$ (*a*) axial velocity ($\overline{u}$); (*b*) lateral velocity ($\overline{v}$); (*c*) absolute velocity magnitude ($\overline{|\vec{V}|}$); (*d*) relative velocity magnitude ($\overline{|\vec{V}|}_{rel}$); (*e*) turbulent kinetic energy (k); and (*f*) vorticity ($\overline{\omega}$) at three spanwise planes. The plane location is indicated as percentage of the span. $U_{tip}=8$ m/s is the blade tip velocity at 500 rpm, $L_s=203$ mm is the stage length and $x=0$ is the rotor leading edge. $\Omega=52.36$ rad/s (500 rpm).

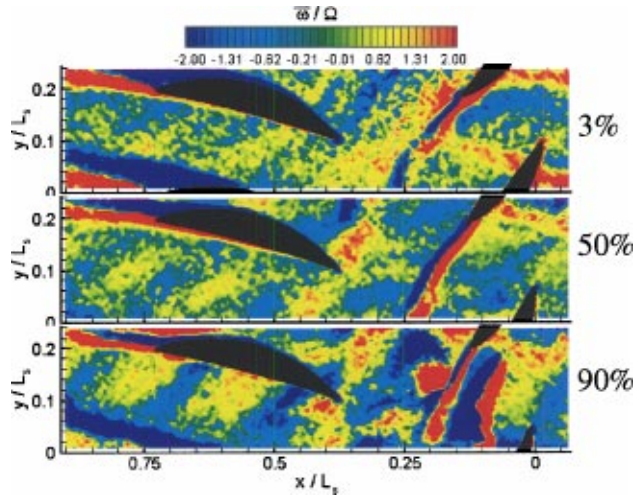

Fig. 3 Sample phase-averaged vorticity distributions at three spanwise locations at $t/T=0.7$

the rotor blade in the tip region. As the tip vortex is transported in the rotor-stator gap, its advection angle is initially very steep, about 60 deg at $x/L_s<0.2$. However, as it gets closer to the stator row, its advection angle decreases to about 40 deg, at $x/L_s>0.25$. The orientation of structures in the tip region remains higher than that at midspan throughout the entire stator passage.

The vorticity contours at the 90 percent span in Fig. 2(f) also reveal a wake-like zone just above (pitchwise) the second-stage stator wake. The positive vorticity layer can be seen above the stator wake at (0.7, 0.22), starting at midchord, and the negative layer (associated with a previous blade) can be seen on the bottom left side of the plot, along with parts of the positive vorticity layer at the (bottom left) corner. This phenomenon is most likely caused by some tip leakage flow at the stator blade tip. Although the stator blade is designed to come into contact with the window, the measurements indicate that there is some leakage. This leakage flow reduces the effective flow area at the exit from the stator, compared to the midspan [see distributions of $\overline{u}$, Fig. 2(a)]. This phenomenon occurs only in the three stator blades facing the window (and will be solved by sealing the gap in the future). The other blades of this stator, and all the blades of the first-stage stator are banded by an external ring, which is manufactured with the blades as one unit.

To recapitulate, at midspan, the spatial nonuniformities in velocity are associated with wake-blade and wake-wake interactions (Uzol et al. [18]). In the tip region, there are numerous additional interactions involving the upstream wakes, the rotor blade wake, and, most importantly, the tip vortex. The resulting nonuniformities and phase-dependent variations in the flow structure in the tip region are much higher than those at the midspan. For example, the axial velocities in Fig. 2(a) vary from very low (even negative) values at (0.15, 0.06) and (0.23, 0.23), just above the points of intersection between the tip vortices and the 90 percent plane, to very high values just below (pitchwise) the tip vortex intersections. The nonuniformities in the lateral velocity are also much higher than at midspan. Clearly, the largest spatial, phase-dependent variations are associated with the presence of the tip vortex. As the tip vortex is convected towards the stator passage, these phase-averaged nonuniformities sweep through the flow field, creating high phase-dependent velocity fluctuations. Thus, one should expect to find significantly higher levels of deterministic stresses in the tip region, as will be demonstrated in the next section.

Flow in the Hub Region. The flow field near the hub region is dominated by interactions between the rotor and stator wakes with the rotating and stationary hub boundary layers. (The rotating hub section is located at $-0.07<x/L_s<0.2$.) These interactions are the main causes of the phase-dependent unsteadiness and deterministic axial and lateral velocity fluctuations. Unlike the other spanwise planes, near the hub high lateral velocity is induced both by the blades and by the rotating hub. The levels of phase-averaged velocity nonuniformities appear to be lower than those at midspan or the tip. Conversely, in most hub regions the turbulence levels are substantially higher than the levels at midspan [Fig. 2(e)]. The 3 percent plane has a wide region with elevated turbulent kinetic energy, especially within the rotor passage and the rotor-stator gap. Figure 2(f) shows that the same domain contains several narrow vorticity layers, some with alternating signs (details follow). Inspection of all the available phase-averaged data reveals that the wide turbulent region is generated mainly within the rotor passages, presumably due to the rotating hub boundary layer (and its interaction with upstream structures), and are then convected through the stator passages while merging with the upstream rotor and stator wakes.

Chopping off and shearing of the first-stage stator wakes are also observed near the hub. At $t/T=0.0$ [Fig. 2(f)], the rotor blade is approaching the upper stator wake, while it has already sheared the lower stator wake, which intersects with the blade at (0.1, 0.1). Figure 3 shows an early stage of stator wake shearing. As noted before, at midspan the rotor is also engulfed by the wake of the first-stage rotor. In the hub region one finds instead several inclined vorticity layers, some with alternating signs that dominate the rotor-stator gap, extending diagonally from (0.1,0.2) to (0.25,0.04), but the trend seems to repeat itself on the other side of the short rotor-wake segment. Well-founded explanation for the formation of these structures requires analysis that is well beyond the scope of this paper, and would require 3D measurements. It seems, however, that a major contributor to this phenomenon is the transition from nonrotating to a rotating hub at $x/L_s=-0.07$, and the subsequent transition to a nonrotating hub at $x/L_s=0.2$. Such transitions generate a variety of three-dimensional flow structures on their own (e.g., Bouda et al., [23]), as well as stretch and realign upstream wakes. The negative inclined vorticity layer to the right of the rotor wake [Figs. 3 and 2(f)] exists already at the entrance to the rotating section, and may even be initially part of the first rotor wake. The layer turns slightly upward within the rotor passage, presumably by the rotating boundary layer, and is then turned downward while gaining strength (maybe due to stretching), in part by the rotor blade (Fig. 3), and in part by the transition to a nonrotating boundary. It is also possible that the increased strength is affected by the hub vortices on the rotor blade. The origin of the inclined structures with positive vorticity is not obvious. They may be a result of interaction of the first-stage stator wake segment (on the pressure side) with the combination of a rotating boundary layer and the pressure gradients in the rotor pressure side. Note that the positive inclined streaks are less evident in Fig. 3, shortly after the stator wake is chopped off by the rotor. The lateral velocity [Fig. 2(b)] peaks at the interface between the negative and positive vorticity layers, and consequently, the relative velocity [Fig. 2(d)] is minimal at the same location. The turbulent kinetic energy also peaks at this interface, giving it a wake-like structure, which migrates downstream, and overwhelms the rotor wake signature. In fact, the structures seen being advected in the stator passage are originated by this phenomenon, and not by the rotor wakes. Radially inward migration of the upstream stator wakes and secondary flows may also be an important factor. Clearly, analysis/explanation of this phenomenon requires additional extensive efforts.

Unlike midspan, where the rotor wake can be identified for a large distance, even after being deformed by upstream wakes (Chow et al., [19]), in the hub region, the wake of the upper rotor blade (which is out of the field of view at this phase) becomes much less distinct already at only a short distance downstream of

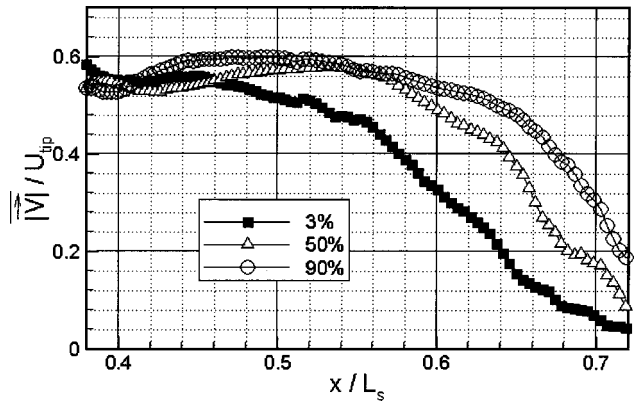

Fig. 4 Absolute velocity magnitude distributions along the suction side of the stator blade, 1 percent stator chord lengths away from the surface, for 3 percent, 50 percent, and 90 percent spanwise planes, all at $t/T=0.7$

the wake. In Fig. 2(*f*) the rotor wake can be identified only between (0.15, 0.23) and (0.2,0.18). The same rotor wake segment, with a similar length, can also be seen in Fig. 3 attached to the rotor. Breakup of this wake occurs due to nonuniformities in streamwise velocity associated with the first-stage stator wake, as discussed (for midspan) by Chow et al. [19]. The streamwise velocity is lower within the stator wakes and higher between them. When the rotor wake is exposed to these nonuniformities, it is sheared. At midspan the shearing generates kink with elevated turbulence levels (hot spots), whereas in the hub region the rotor wake becomes discontinuous, and the presence of other large structures makes it very difficult to identify the broken segments.

The elevated levels of lateral velocity in the rotor-stator gap in the hub region result in relatively high flow angles at the stator inlet. The average stator inlet flow angle at the hub is 47 deg, whereas it is only about 34 deg at midspan. (The stator inlet flow angle at the tip is also relatively high, about 47 deg, due to the effect of the tip vortex.) The high inlet flow angle at the hub affects the suction side boundary layer of the stator blade, especially on the downstream side. As is evident from the distributions of axial velocity, velocity magnitude, turbulent kinetic energy, and vorticity in Fig. 2, the boundary layer on the downstream side is much thicker than the corresponding layers in the other planes. Furthermore, expansion of the boundary layer starts much earlier near the hub, at about $x/L_s=0.55$, compared to $x/L_s=0.64$ and $x/L_s=0.66$ at the midspan and the tip, respectively. It is interesting to note that, although the average stator inlet flow angles are about the same at the tip and the hub, the suction side boundary layer starts to get thicker much later at the tip. This difference is most likely related to flows (and associated pressure gradients) induced by the tip vortex. Figure 4 compares the distributions of phase-averaged velocity magnitude along the suction side of the stator blade, 1 percent stator chord lengths away from the surface, for the hub, midspan, and tip regions, all at the same phase, $t/T=0.7$. The substantially higher momentum loss near the hub, especially at $x/L_s>0.55$, is evident. However, there is no reverse flow along the suction side of the upper stator blade in the 3 percent plane, namely there is no evidence of flow separation at this plane.

Although thickening of the boundary layer occurs on both stator blades that are within the field of view, there are slight differences between them. In fact, weak reverse flow develops along the suction side of the lower stator blade, starting from $x/L_s=0.65$. Thus, local boundary layer separation occurs on the lower blade, but does not occur on the upper blade at all phases. These circumferential differences are not caused by differences in flow fields. They are a result of using a flat 50×50 mm^2 measurement plane (laser sheet) that is perpendicular to the surface of the upper blade (which is located at the center of the window). Consequently, the upper blade is dissected at the 3 percent plane, whereas the lower blade is dissected at the 15 percent plane. We suspect that the 3 percent plane is located closer to the wall, and possibly below the hub vortex, whereas at the 15 percent plane we dissect the hub vortex, leading to differences in velocity distributions. The radial differences in the points of dissecting the blades exists also in these planes, but their impact is largest near the hub, in part due to the smaller radius of curvature, and in part due to large spanwise variations in flow structure near the hub. The deviations at midspan and the tip are 10 percent (50 percent and 60 percent on the upper and lower blades, respectively) and 8 percent (90 percent and 98 percent), respectively. Consequently, the lower blade seems to be affected more by the leakage at the tip of the stator blade.

Average-Passage Flow Fields, Turbulence, and Deterministic Stresses

The measured phase-averaged flow fields at ten different rotor phases, every 3 deg of rotor orientation, which cover the entire rotor passage, enable us to calculate the average-passage flow fields and distributions of deterministic stresses. Recall that each of the present phase-averaged flow fields is an ensemble average of 100 instantaneous realizations. Thus, the ''average-passage'' flow fields presented in this section are obtained by ''time averaging'' of the ''ensemble averaged'' parameters. We do not account for passage-to-passage variations. The average-passage velocity, $\tilde{u}_i$, $i=1,2$, deterministic stress, $\widetilde{u_i''u_j''}$, and deterministic kinetic energy, k_{det}, are calculated from

$$\tilde{u}_i(x,y)=\frac{1}{M}\sum_{k=1}^{M}[\overline{u_i}(x,y,\phi)]_k, \tag{6}$$

$$\widetilde{u_i''u_j''}(x,y)=\frac{1}{M}\sum_{k=1}^{M}\{[\overline{u_i}(x,y,\phi)]_k-\tilde{u}_i(x,y)\}\times\{[\overline{u_j}(x,y,\phi)]_k-\tilde{u}_j(x,y)\}, \tag{7}$$

$$k_{\text{det}}(x,y)=\tfrac{1}{2}[\widetilde{u_i''u_i''}(x,y)], \tag{8}$$

where M is the total number of phase-averaged realizations, covering an entire passage, the tilde denotes an average-passage quantity and the double prime represents the deterministic fluctuation, i.e., differences between average-passage and phase-averaged values. Average-passage values of all the phase-averaged parameters are calculated using the same procedure [Eqs. (6) and (7)], including the average-passage values of the turbulent kinetic energy and Reynolds stresses. For example, $\tilde{k}$, the average-passage turbulent kinetic energy, is calculated by replacing $\tilde{u}_i$ with $\tilde{k}$ in Eq. (6). Since the measurements provide a finite number of phases, the blades do not cover each point at the same frequency, and as a result the average-passage data becomes patchy, especially within the passages. To provide a smooth transition and prevent this patchiness, we have to construct additional interpolated fields every 0.75 deg of rotor orientation. The process is based on linear interpolation of the experimental data in points that are circumferentially shifted according to their phase, and using weighted averages based on their phase lags. The procedures are discussed in detail in Uzol et al. [18]. In this paper we focus on spanwise variations of the average-passage flow parameters in the stator frame of reference. Uzol et al. [18] presents results at midspan in both the rotor and stator reference frames.

Figure 5 shows the distributions of average-passage velocity magnitude, vorticity, turbulent kinetic energy, and Reynolds shear stress, as well as the distributions of deterministic kinetic energy and deterministic shear stress. As before, we compare the distributions in the 3 percent, 50 percent, and 90 percent spanwise planes. Several observations can readily be made:

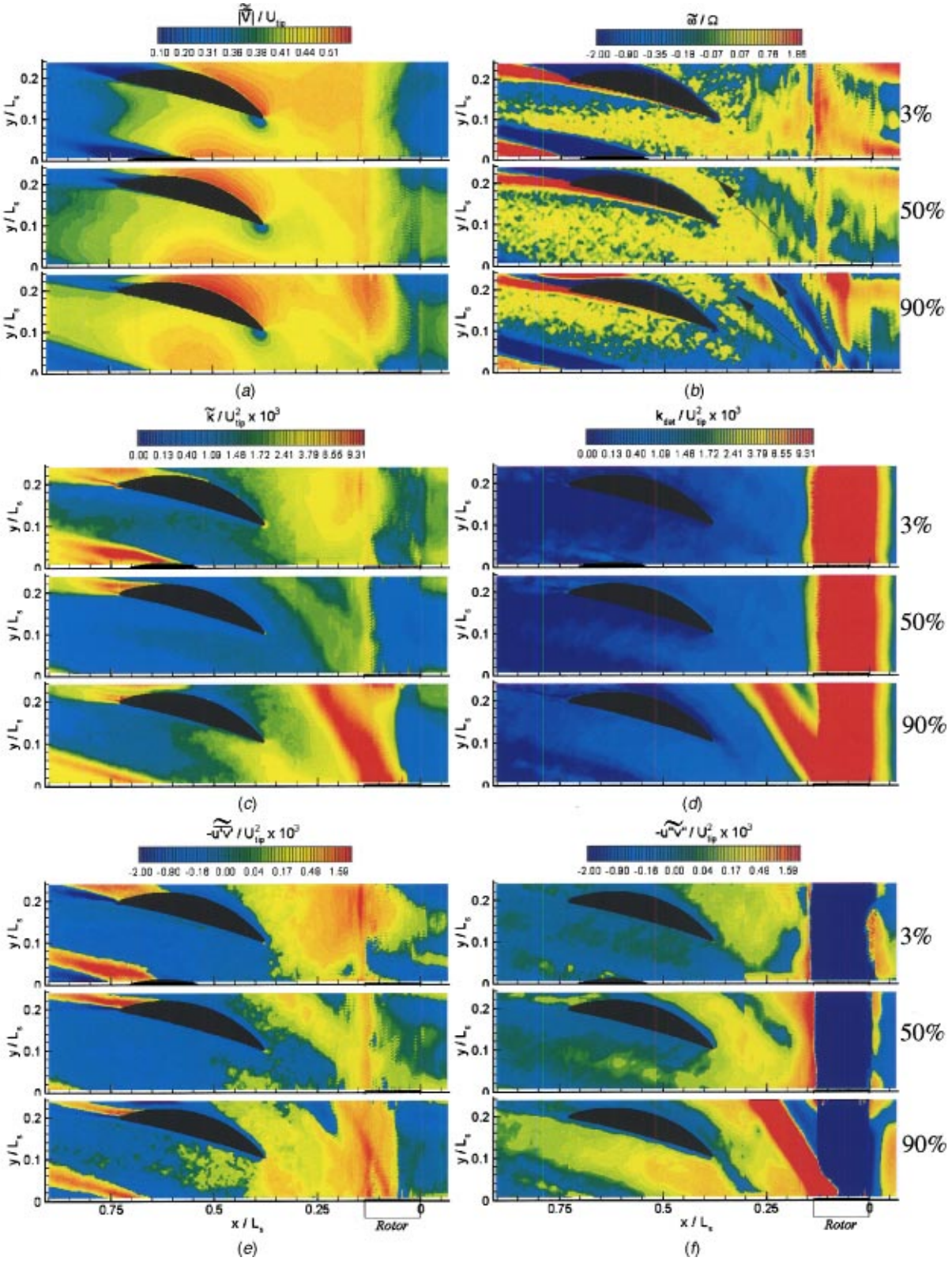

Fig. 5 Average-passage (*a*) velocity magnitude, (*b*) vorticity, (*c*) turbulent kinetic energy, (*d*) deterministic kinetic energy, (*e*) Reynolds shear stress, and (*f*) deterministic shear stress contours at 3 percent, 50 percent, and 90 percent spanwise locations in the stator frame of reference. In the vorticity plots, the arrow at 50 percent span and the arrow on the left at 90 percent span indicate upstream stator wake transport directions. The arrow on the right at 90 percent span vorticity plot shows the tip vortex transport direction.

Average-Passage Flow in the Tip Region. At 90 percent span, the average-passage vorticity contours [Fig. 5(*b*)] reveal two separate, inclined, wakelike vorticity distributions in the rotor-stator gap, both of which are marked by arrows. The structure with a steeper angle, about 55 deg, is associated with the trajectory and advection of the tip vortex. The arrow is aligned with the direction of tip-vortex transport. This region is also characterized by a very low axial and high lateral velocity components (not shown), very high average-passage turbulent kinetic energy [Fig. 5(*c*)], alternating signs of average-passage Reynolds shear stress that coincide with the regions with alternating vorticity signs [Fig. 5(*e*)], and extremely high deterministic kinetic energy [Fig. 5(*d*)]. The wake-like layers of alternating vorticity signs with a shallower angle, about 39 deg, are associated with advection of the chopped wake segments generated by the first-stage stator blade. This association was concluded from observations of phase-dependent distributions of vorticity. This wake transport direction also coincides with the low velocity magnitude region in Fig. 5(*a*) that extends diagonally from (0.15, 0.0) to (0.22, 0.1). As is evident, transport of the stator wake segments and advection of the tip vortex occur along different paths. Hence, they may even be transported through different passages in the stator blade row.

The transport direction of segments of the first-stage stator wake at 50 percent span is also indicated by an arrow in the corresponding vorticity plot in Fig. 5(*b*). The advection angle in this plane, 38 deg, is very close to that at the tip, but the wake occupies a wider region compared to the tip region, as is evident from the wide positive and negative vorticity zones on either side of the arrow. Near the tip the stator wake segments are ingested in part by the tip vortex, reducing the domain directly affected by their advection.

At the hub, the wake transport direction is not as distinct as the clear trajectories at the midspan or the tip regions. The complex flow structure generated by interaction of wakes with the rotating and stationary boundaries, as discussed before, are responsible for the reduced clarity. These interactions also contribute to the elevated levels of average-passage turbulent kinetic energy in the rotor-stator gap [Fig. 5(*c*)]. One can still identify regions with predominantly positive and negative vorticity, but the rotor-stator gap does not contain distinct wake-like layers with alternating signs. However, the corresponding distribution of deterministic kinetic energy within the gap [Fig. 5(*d*)] still shows a region with elevated levels that extends diagonally from (0.2,0.1) to (0.35,0.2), and continues within the stator passage. The elevated level of k_{det}, is associated with unsteadiness in the transport of the complex near-hub structures demonstrated in Figs. 2 and 3.

Average-Passage Flow Field Around the Stator. The previously discussed spanwise variation in the thickness of the boundary layer on the suction side of the stator, as well as the resulting effects on the wake thickness and effective exit flow area, are clearly evident from the average-passage velocity and vorticity distributions [Figs. 5(*a*) and 5(*b*)]. Substantial nonuniformities that exist in the average-passage velocity magnitude in the gap extend into the stator passage. They are caused by the complex wake-blade, wake-wake, wake-tip vortex and wake-hub interactions discussed in the previous section (and in Uzol et al. [18]). The average-passage velocity fields also reveal that the point of maximum velocity on the suction side of the stator shift downstream as we go from the hub to tip. This trend indicates that the stator blades are more front loaded close to the hub and more aft loaded in the vicinity of the tip.

Distributions of Deterministic Kinetic Energy. The highest deterministic kinetic energy levels develop immediately downstream of the rotor (except for the rotor passage). The decay process starts within the rotor-stator gap and extends into the stator passages. There are substantial circumferential nonuniformities in the distribution of k_{det} within the gap in any plane, but the most striking variations occur in the tip region. The highest levels of deterministic kinetic energy, and the only ones that exceed the turbulent kinetic energy, occur along the tip-vortex and wake trajectories (mostly the tip vortex) in the 90 percent plane. The origin of these high k_{det} values can be identified in the phase-dependent, spatially nonuniform velocity distributions associated with transport of the tip vortex and its interaction with the wakes that it encounters. Along the tip vortex trajectory, the levels of k_{det} are more than one order of magnitude higher than the levels at the hub and midspan, and are of the same order of magnitude as the turbulent kinetic energy [Fig. 5(*c*)]. From midspan to tip, the turbulent kinetic energy increases by about 5 times, whereas the deterministic kinetic energy increases by more than an order of magnitude. The high levels of k_{det} along the tip-vortex trajectory extend to the entrance and into the stator passage. Even within the passage they are still about four times higher than the levels at midspan and hub regions. Note that within the shown passage, the region with elevated level of k_{det} is an extension of the transport direction of a tip vortex generated by the rotor blade located below the sample area. The deterministic kinetic energy decays within the stator passage. This decay may be a result of vortex breakup due to interaction with other structures, or it can also be caused by the vortex migrating out of the 90 percent plane, but we cannot provide a substantiated explanation for this trend using the present data. Measurement in neighboring planes, as well as 3D measurements in an axial plane are needed to track the vortex trajectory. Outside the tip-vortex transport direction within the gap and the stator passages, the turbulent kinetic energy levels are still 3–4 times higher than the deterministic kinetic energy.

Other Trends of the Deterministic Kinetic Energy. In the rotor-stator gap the deterministic kinetic energy levels at midspan are about 30 percent higher than the levels at the hub within the gap. This difference can be attributed to the more spatially uniform phase-averaged velocity distributions in the hub (Fig. 2). A region of elevated deterministic kinetic energy exists also in the hub region, along the edge of the separated region on the suction side of the bottom stator blade. This phenomenon is associated with phase-dependent fluctuations in the boundary of the separated region, caused by transport of structures through the stator passage. Elevated levels can be observed near the trailing edges of the upper stator blade and near wake at midspan. This pattern is associated with modulation of the flow in the aft region by advected rotor and upstream stator wakes (Uzol et al. [18]).

In contrast to the distributions of k_{det}, the turbulent kinetic energy in the hub region is only 2–3 higher than the corresponding levels at midspan, especially in the region with complex interaction of wakes with the (fixed and rotating) boundaries. Recall that the rotating section extends to $x/L_s=0.2$. Within the tip-vortex region, the maximum turbulent kinetic energy is about 5 times than the levels at midspan.

Distributions of Deterministic Shear Stresses. The deterministic and (average-passage) turbulent shear stresses have comparable magnitudes, but different structures, in most areas, and in all spanwise locations. The only exceptions are the wakes of the stator blades where the turbulent stresses are much higher, and the tip-vortex region, where the deterministic stresses are substantially higher. The trajectory of the tip vortex is characterized by concentrated layers with positive and negative deterministic and Reynolds stresses with opposite signs. However, the deterministic shear stresses are about an order of magnitude higher than the average-passage Reynolds stresses. Quantitative demonstration of the differences in magnitudes and trends between Reynolds and deterministic stresses along an arbitrarily selected line in the rotor-stator gap is presented in Fig. 6. Other noted differences include higher turbulent shear stresses in the 3 percent plane and within the gap region. Conversely, at midspan the levels are close, but they have opposite signs. The negative and positive (deterministic and Reynolds) stress layers in the midspan gap are associated with transport of the upstream stator wake and its interaction with the

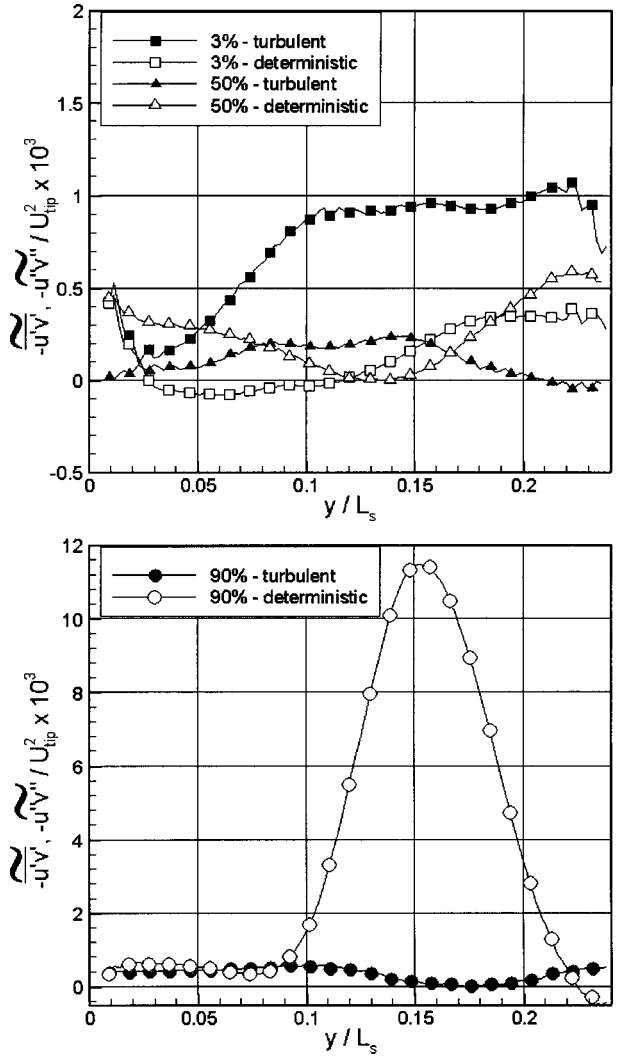

Fig. 6 Deterministic and turbulent shear stresses at $x/L_s = 0.2$ (in the rotor-stator gap) at the 3 percent, 50 percent (top), and 90 percent (bottom) spanwise planes. Solid symbols, Reynolds shear stresses; hollow symbols, deterministic shear stresses. Note the differences in scales.

rotor wake. In the middle of the stator passage, the deterministic shear stress is higher than the turbulent stress at the tip, but the trend is reversed in the hub and the midspan planes.

Along the suction side of the stator blade, there is a region with negative deterministic shear stress. This region is much wider at the tip, and it is narrowest at midspan. As will be shown in the next section, this region is characterized by negative deterministic energy production, i.e., flux of energy from the deterministic kinetic energy to the average-passage kinetic energy. Before concluding, one should note that there are many additional phenomena that can be observed by careful examination of the distributions in Fig. 5. We have only discussed those that have an impact on the dynamics of deterministic stresses.

Decay Rates of Deterministic and Turbulent Kinetic Energies

Figures 7(*a*) and 7(*b*) show the variations of the normalized deterministic and turbulent kinetic energies along the stator midpassage at the 3 percent, 50 percent, and 90 percent span locations. Since all levels are normalized with their respective inlet values, these distributions actually show the corresponding decay patterns. The x coordinate starts from $x/L_s = 0.38$, i.e., at the plane

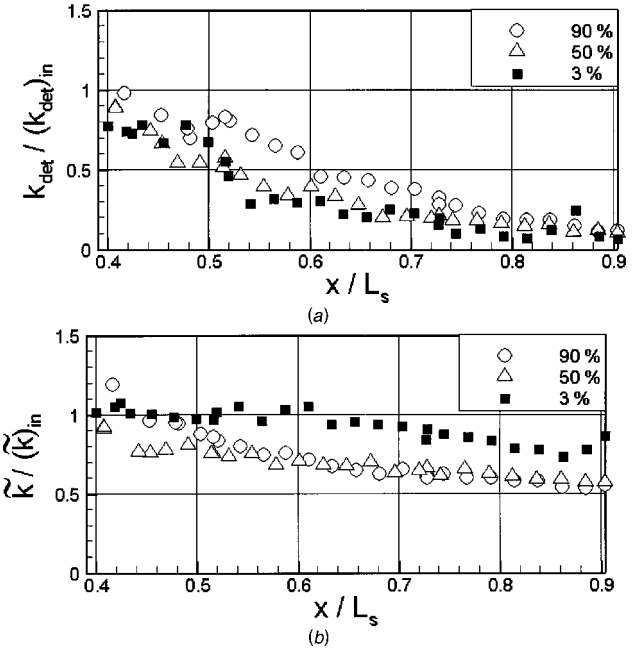

Fig. 7 Distributions of (*a*) deterministic and (*b*) average-passage turbulent kinetic energy along the stator midpassage at the 3 percent, 50 percent, and 90 percent spanwise planes. The levels are normalized by the respective inlet values. The x coordinate starts at the stator leading edge plane ($x/L_s = 0.38$), and the stator trailing edge is located at $x/L_s = 0.73$.

of the stator leading edge. The stator trailing edge is located at $x/L_s = 0.73$. Several observations can be made as follows:

The values k_{det} decrease gradually along the stator passage at all spanwise locations. At the exit of the stator blade row, 68 percent, 80 percent, and 82 percent of the inlet deterministic kinetic energy is already dissipated at the tip, midspan, and the hub planes, respectively. The decay continues downstream of the stator, and at $x/L_s = 0.9$, the levels are only about 5.6 percent, 10 percent, and 12.5 percent of the respective hub, midspan, and tip inlet values, i.e., there is one order of magnitude decay in all cases. The decay rates vary between planes, most likely due to variations in the local dominant flow phenomena (as discussed before). For example, in the hub region, the decay rate of k_{det} [Fig. 7(*a*)] is quite slow unit $x/L_s = 0.5$, and only about 30 percent of it is lost until that point. Just downstream of this point, there is a sudden drop to about 30 percent at $x/L_s = 0.54$. In the tip region, the values remain flat up to $x/L_s = 0.52$, and then decay at a faster pace.

Figure 7(*b*) demonstrates that the decay rates of the turbulent kinetic energy are much smaller than those of k_{det}. The decay rate at the tip and midspan planes are very close to each other, and at the exit from the stage only about 40 percent of the turbulent kinetic energy is dissipated. At the hub, the turbulent kinetic energy decay rate is even slower, and it is only 20 percent lower by $x/L_s = 0.9$. This lower decay rate is most likely associated with turbulence production in the hub boundary layer, which feeds turbulent kinetic energy into the 3 percent plane.

The fast decay of the deterministic kinetic energy within the stator points to the fact that significant amount of ''wake recovery'' may occur along stator passage. The term ''wake recovery'' refers to reduction in dissipation rate (mixing loss) of a turbulent wake due to reduction in its velocity deficit, caused by straining within the stator passage. This process was first suggested by Smith [24]. Adamczyk [25] showed, using a 2D perturbation analysis, that the difference in the mixing loss is equal to the change in the flux of deterministic kinetic energy from inlet to the exit. Therefore, when the ratio of the exit to inlet deterministic

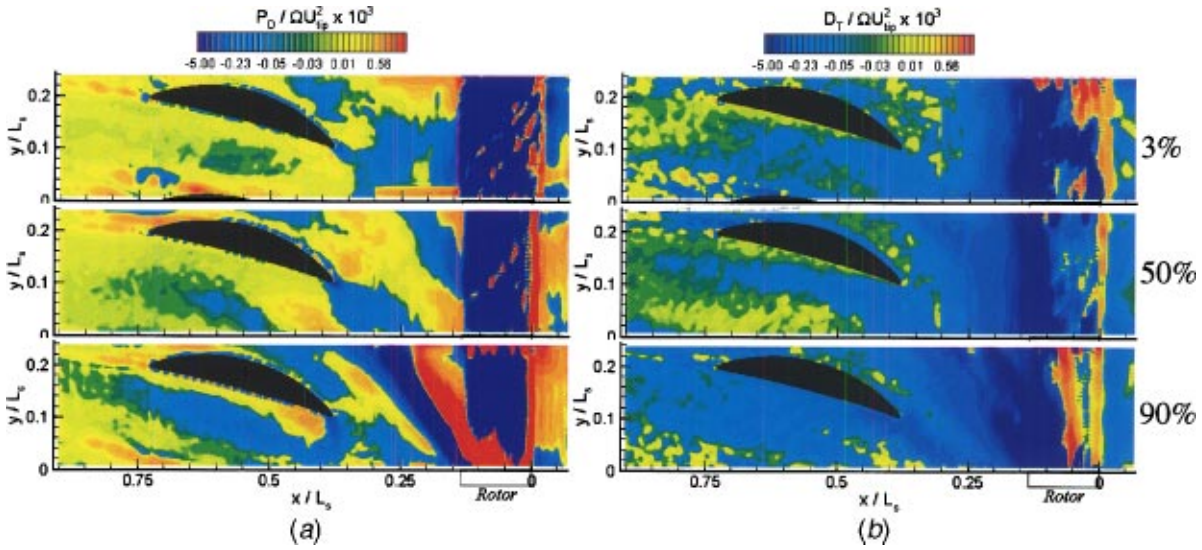

Fig. 8 Distribution of (*a*) deterministic production (P_D, term 1); (*b*) dissipation due to turbulence (D_T, term 2) on the right-hand side of the deterministic kinetic energy transport equation [Eq. (9)] at the 3 percent, 50 percent, and 90 percent spanwise planes.

kinetic energy fluxes is less than one, wake recovery process occurs, and the mixing loss of the upstream wake is reduced. In the present experiments, the ratios of exit to inlet deterministic kinetic energy flux are much less than one at all spanwise locations. Averaging the fluxes of deterministic kinetic energy at the inlet (leading edge) and the exit (trailing edge) of the stator passage, we obtain exit to inlet flux ratios of 29 percent, 17 percent, and 28 percent (i.e., reductions of 71 percent, 83 percent, and 72 percent) for the hub, midspan, and tip planes, respectively. These trends are consistent with previous experimental results obtained by Van Zante et al. [26] for NASA Stator37 at peak efficiency and 75 percent span, in which they reported a 71 percent reduction in the flux of deterministic kinetic energy.

Deterministic Kinetic Energy Budget

The momentum equations for the deterministic fluctuations, u_i'', are obtained by subtracting the average-passage RANS equations from the RANS equations. Then, a scalar product of u_j'' with the momentum equation for u_i'' and time averaging provides the transport equations for the deterministic stresses. The following deterministic kinetic energy transport equation is obtained as the trace of the equation of deterministic stresses:

$$\tilde{u}_k \frac{\partial}{\partial x_k}\left(\tfrac{1}{2}\widetilde{u_i'' u_i''}\right) = -\widetilde{u_i'' u_k''}\frac{\partial \tilde{u}_i}{\partial x_k} + \widetilde{(\overline{u_i' u_k'})''}\frac{\partial u_i''}{\partial x_k} - \nu \widetilde{\frac{\partial u_i''}{\partial x_k}\frac{\partial u_i''}{\partial x_k}} - \frac{\partial}{\partial x_k}\left[\frac{1}{2}\widetilde{u_i'' u_i'' u_k''} + \frac{1}{\rho}\widetilde{u_i'' p''}\delta_{ik} - \widetilde{u_i''(\overline{u_i' u_k'})''} - \nu \frac{\partial}{\partial x_k}\left(\frac{1}{2}\widetilde{u_i'' u_i''}\right)\right] \quad (9)$$

As before, the tilde denotes time-averaging over all phases (average-passage values) and the overbar denotes ensemble averaging. The double prime refers to deterministic fluctuation and a single prime is a turbulent fluctuation. The first three terms on the right-hand side are source/sink terms. The first one (including the minus) is a production/dissipation term due to deterministic stresses and will be called ''deterministic production (P_D)'' in the following discussion. This term also appears in the transport equation of the average-passage kinetic energy with a reversed sign, and determines the energy transfer between the phase-averaged and average-passage flow fields. The second term is production/dissipation due to the deterministic fluctuations of turbulent (Reynolds) stresses and will be called ''dissipation due to turbulence (D_T).'' The reason for defining this term as dissipation (instead of production) will become evident in this section. The third term is the viscous dissipation associated with gradients of deterministic velocity fluctuations. The last four terms involve spatial transport of deterministic kinetic energy, but do not participate in production or dissipation.

The present experimental data enable us to determine *in-plane* distributions of all terms on the right-hand side of Eq. (9), except for the pressure-velocity correlation term. Of course, one has to keep in mind that out-of plane (3D) effects may have a significant impact on the results, especially in the hub and tip regions. Nevertheless, as the following discussion shows, many interesting trends are revealed from the in-plane components. Distributions of the first two terms on the right-hand side of the deterministic kinetic energy transport equation, i.e., deterministic production and dissipation due to turbulence are presented in Fig. 8. Some observations can be summarized as follows.

First, P_D and D_T are the dominant source/sink terms in the Eq. (9). The third, viscous dissipation term is 3 to 4 orders of magnitude smaller. There are regions in the flow field where either P_D or D_T are substantially larger than one another, sometimes by orders of magnitude, and in other regions they are of the same order.

Second, as is evident from Fig. 8(*a*), there are distinct regions in the flow field with positive and negative deterministic production. Since this term is common to the average-passage and deterministic kinetic energy transport equations (with opposite signs), the results show that energy transfer between the phase-averaged and average-passage flow fields occurs in both direction. Adamczyk [25] showed that the sign of the volume integral of P_D determines whether the wake mixing loss is reduced or increased by passing through a blade row. Negative volume-averaged deterministic production indicates reduction in mixing losses (associated with a decrease in deterministic kinetic energy). However, Adamczyk's analysis does not account for the effect of D_T on the evolution of the deterministic kinetic energy. Since D_T is mostly negative, the deterministic kinetic energy my decrease in spite of the fact that P_D is positive.

Third, D_T is negative almost everywhere, and its magnitudes are particularly high downstream of the rotor, along the tip vortex trajectory (extending into the rotor-stator gap), and in parts of the

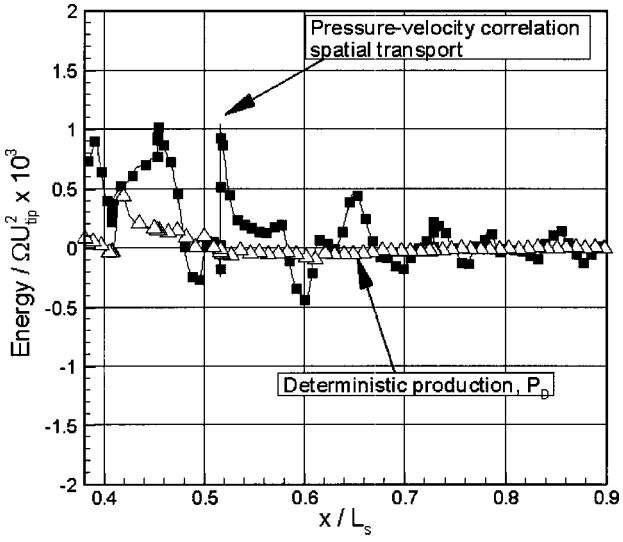

Fig. 9 Distributions at midspan of the deterministic production (P_D, term 1) and divergence of the deterministic pressure-velocity correlations (term 5) along the midpassage of the stator.

wake transport direction at mid span. Hence, we refer to this term as the ''dissipation due to turbulence.'' The loss of deterministic kinetic energy to turbulence should be accounted for, especially in these regions. At mid span, P_D is typically larger than D_T upstream of the stator passage, starting from $x/L_s=0.3$, and in the middle of the stator passage.

In the tip region, along the tip-vortex transport direction, there are parallel layers with high values of P_D with opposite signs. Thus, in part of the tip vortex, energy is transferred from deterministic kinetic energy to average-passage energy. However, adding the first two terms in Eq. (9) would still result in negative values, i.e., the deterministic kinetic energy decays over the entire tip region of the rotor-stator gap. One should also keep in mind that the flow in the tip region is highly three dimensional, and the missing out-of-plane terms may have a significant contribution to the overall balance.

Near the hub, in the rotor-stator gap, the deterministic production is predominantly negative, much more than at midspan. This trend is consistent with the higher average-passage velocity magnitude in the same region [Fig. 5(*a*)], and the faster decay of deterministic kinetic energy near the hub [Fig. 5(*d*)] compared to midspan.

There is also a wide negative deterministic production region upstream of the leading edge of the stator blade, and a narrower domain along the suction side of the stator boundary layer until about $x/L_s=0.45$. Further downstream, P_D becomes and remains positive through the trailing edge and the stator wake. A similar behavior occurs in the tip region, but the negative region is extended further downstream, ending at about $x/L_s=0.5$. This phenomenon does not occur at the hub and P_D is always positive along the suction side of the stator blade. High positive P_D values occupy substantial parts of the rotor-stator gap, especially the regions dominated by wake transport in the midspan and tip regions.

Spatial transport of deterministic kinetic energy due to deterministic fluctuations, term 4 on the right-hand side of Eq. (9), and the transport term due to Reynolds stress fluctuations (term 6), are usually of the same order of magnitude as the deterministic production and dissipation due to turbulence terms. Although not presented here, it is observed that term 4 is a dominant production term around the rotor leading edge region. It is about one order of magnitude higher than deterministic production and about 3 to 4 orders of magnitude higher than the other terms. The deterministic production itself is also positive in this region.

Since all the *in-plane* terms of Eq. (9) (including advection by the average-passage velocity on the left-hand side) except the pressure-velocity correlation can be calculated, it is possible to estimate the pressure-velocity correlation term from a balance of the other terms. Since one expects the three-dimensional effect to be minimal at midspan, such an estimate is more likely to yield reasonable results at midspan. Thus, we perform the analysis using the midspan data. Figure 9 compares the deterministic production term to the divergence of the pressure-velocity correlation term along the stator midpassage. As is evident, the pressure-velocity correlation term is much larger than the deterministic production term, especially within the rotor-stator gap and at the entrance of the stator passage. Considerable oscillations along the midpassage line may be due to lack of statistical convergence and the combination of many terms. However, an overall decreasing trend towards the exit of the stator appears visible in spite of the noise. This trend indicates that substantial deterministic pressure fluctuations occur within the gap, and at the entrance to the stator passage. These fluctuations are attenuated as the flow exits the stator row.

Conclusions

PIV measurements are performed covering the entire second stage of a two-stage axial turbomachine and near the hub and tip regions. Phase-averaged flow fields are obtained for 10 different rotor phases, and the results are then used to obtain the average-passage flow fields and distributions of deterministic stresses. The effects of the tip vortex and the hub boundary layer on the phase-averaged and average-passage flow fields, as well as on deterministic stresses are discussed, and the results are compared to the characteristics at midspan.

The tip vortex is a dominant source of phase-dependent unsteadiness and deterministic stresses near the tip region. The associated turbulent kinetic energy levels as well as the phase-averaged axial and lateral velocity nonuniformities are substantially higher than those at midspan. The transport direction of the upstream stator wakes is different than the transport direction of the tip vortex. Along this tip-vortex transport direction, the deterministic kinetic energy levels are more than one order of magnitude higher than the levels at the hub and at the midspan, and are about the same order of magnitude as the turbulent kinetic energy levels. Outside the tip-vortex trajectory, the turbulent kinetic energy levels are still 3–4 times higher than the deterministic kinetic energy levels. The deterministic and turbulent shear stress levels are comparable in all spanwise locations, except for the wakes of the stator blades, where the turbulent stresses are much higher. However, along the tip-vortex trajectory, the deterministic shear stress levels are about an order of magnitude higher than the turbulent shear stress levels.

The flow field near the hub is dominated by interaction between the rotor and stator wakes with the rotating and stationary hub boundary layers. These interactions are the main causes of the phase-dependent unsteadiness and deterministic axial and lateral velocity fluctuations. However, the levels of these phase-averaged velocity nonuniformities appear to be lower than those at midspan or the tip. Conversely, in most of the hub region, the turbulence levels are substantially higher than those at midspan. Also, both at the hub and at midspan, the turbulent kinetic energy is much higher than the deterministic kinetic energy.

The decay rates of deterministic kinetic energy in the hub and midspan regions are comparable to each other, whereas at the tip, the decay rate is higher. The decay rates of turbulent kinetic energy are much smaller than those of the deterministic kinetic energy. In the evolution equation for deterministic kinetic energy, the deterministic production, and newly introduced dissipation due to turbulence terms are found to be the dominant source/sink parameters. There are distinct regions in the flow field with positive and negative deterministic production. Since the deterministic production term is the common term between the average-passage

and deterministic kinetic energy transport equations (but with opposite sign), the results show that the energy transfer between the phase-averaged and average-passage flow fields can be in either direction. The divergence of the pressure-velocity correlation term, obtained from a balance of all the other terms, is dominant and appears to be much larger than the deterministic production term. This trend indicates that there are substantial deterministic pressure fluctuations in the flow field, especially within the rotor-stator gap and within the stator passage.

Acknowledgments

This project is sponsored in part by AFOSR under Grant No. F49620-01-1-0010. The program manager is Thomas Beutner. Partial support is also provided by ONR, under Grant No. N00014-99-1-0965. The program officers are Patrick Purtell and Ki-Han Kim. We would also like to thank Yury Ronzhes and Stephen King for their contribution to the construction of the facility and maintenance of the facility, and Khoon Ooi, for designing the rotor and stator blades.

Nomenclature

D_T = Dissipation of deterministic kinetic energy due to turbulence
k = Turbulent kinetic energy
k_{det} = Deterministic kinetic energy
M = Number of phase-averaged realizations
N = Number of instantaneous realizations
P_D = Deterministic production
t = Time
T = Rotor blade passing period
u = Axial velocity component
u_i' = Turbulent fluctuation
u_i'' = Deterministic fluctuation
$\overbrace{u_i' u_j'}$ = Turbulent stress
$u_i'' u_j''$ = Deterministic stress
v = Lateral velocity component (almost circumferential, but the laser sheet is flat)
$|\vec{V}|$ = Absolute velocity magnitude
$|V|_{rel}$ = Velocity magnitude in the rotor frame of reference
x = Axial coordinate
y = Lateral coordinate

Greek letters

α = Flow angle
ϕ = Rotor phase
ν = Kinematic viscosity
ω = Vorticity
Ω = Rotational speed of the turbomachine

References

[1] Adamczyk, J. J., 1985, "Model Equation for Simulating Flows in Multistage Turbomachinery," ASME paper No. 85-GT-226.
[2] Adamczyk, J. J., Mulac, R. A., and Celestina, M. L., 1986, "A Model for Closing the Inviscid Form of the Average-Passage Equation System," ASME paper No. 86-GT-227.
[3] Adamczyk, J. J., Celestina, M. L., Beach, T. A., and Barnett, M., 1990, "Simulation Of Three Dimensional Viscous Flow Within A Multistage Turbine," ASME J. Turbomach., **112**, p. 370.
[4] Rhie, C. M., Gleixner, A. J., Spear, D. A., Fischberg, C. J., and Zacharias, R. M., 1998, "Development and Application of a Multistage Navier-Stokes Solver. Part I: Multistage Modeling Using Body Forces and Deterministic Stresses," ASME J. Turbomach., **120**, p. 205.
[5] Lejambre, C. R., Zacharias, R. M., Biederman, B. P., Gleixner, A. J., and Yetka, C. J., 1998, "Development And Application of a Multistage Navier-Stokes Solver. Part II: Application to a High Pressure Compressor Design," ASME J. Turbomach., **120**, p. 215.
[6] Busby, J., Sondak, D., Staubach, B., and Davis, R., 2000, "Deterministic Stress Modeling of a Hot Gas Segregation in a Turbine," J. Turbomach., **122**, p. 62.
[7] Van de Wall, A. G., Kadambi, J. R., and Adamczyk, J. J., 2000, "A Transport Model for the Deterministic Stresses Associated with Turbomachinery Blade Row Interactions," ASME J. Turbomach., **122**, pp. 593–603.
[8] Meneveau, C., Katz, J., 2002, "A Deterministic Stress Model for Rotor-Stator Interactions in Simulations of Average-Passage Flow," J. Fluids Eng., **124**, pp. 550–554.
[9] He, L., Chen, T., Wells, R. G., Li, Y. S., and Ning, W., 2002, "Analysis of Rotor-Rotor and Stator-Stator Interferences in Multi-Stage Turbomachines," ASME J. Turbomach., **124**, pp. 564–571.
[10] Prato, J., Lakshminarayana, B., and Suryavamshi, N., 1997, "Exit Flow Field of an Embedded Stator in a Multi-Stage Compressor," J. Propul. Power, **13**, No. 2, pp. 169–177.
[11] Prato, J., Lakshminarayana B., and Suryavamshi N., 1998, "Steady and Unsteady Three-Dimensional Flow Field Downstream of an Embedded Stator in a Multi-Stage Axial Flow Compressor Part I: Unsteady Velocity Field," ASME paper No. 98-GT-521.
[12] Suryavamshi, N., Lakshminarayana, B., and Prato, J., 1998, "Steady and Unsteady Three-Dimensional Flow Field Downstream of an Embedded Stator in a Multi-Stage Axial Flow Compressor Part II: Composite Flow Field," ASME paper No. 98-GT-522.
[13] Suryavamshi, N., Lakshminarayana, B., and Prato, J., 1998, "Steady and Unsteady Three-Dimensional Flow Field Downstream of an Embedded Stator in a Multi-Stage Axial Flow Compressor Part III: Deterministic Stress and Heat Flux Distribution and Average-Passage Equation System," ASME paper No. 98-GT-523.
[14] Sinha, M., and Katz, J., 2000, "Quantitative Visualization of the Flow in a Centrifugal Pump With Diffuser Vanes—I: On Flow Structures and Turbulence," ASME J. Fluids Eng., **122**, pp. 97–107.
[15] Sinha, M., Katz, J., and Meneveau, C., 2000, "Quantitative Visualization of the Flow in a Centrifugal Pump With Diffuser Vanes—II: Addressing Passage-Averaged and Large-Eddy Simulation Modeling Issues in Turbomachinery Flows," ASME J. Fluids Eng., **122**, pp. 108–116.
[16] Uzol, O., Chow, Y. C., Katz J., and Meneveau, C., 2002, "Unobstructed PIV Measurements with in an Axial Turbo-pump Using Liquid and Blades with Matched Refractive Indices," *Experiments in Fluids*, **33**, pp. 909–918.
[17] Chow, Y. C., Uzol, O., Katz, J., and Meneveau C., 2002, "An Investigation of Axial Turbomachinery Flows Using PIV in an Optically-Unobstructed Facility," *Proceedings of the 9th International Symposium on Transport Phenomena and Dynamics of Rotating Machinery*, Honolulu, Hawaii, Feb. 10–14.
[18] Uzol, O., Chow, Y. C., Katz, J., and Meneveau, C., 2002, "Experimental Investigation of Unsteady Flow Field within a Two Stage Axial Turbomachine Using Particle Image Velocimetry," ASME J. Turbomach., **124**, pp. 542–552.
[19] Chow, Y. C., Uzol, O., and Katz, J., 2002, "Flow Non-Uniformities and Turbulent "Hot Spots" Due to Wake-Blade and Wake-Wake Interactions in a Multistage Turbomachine," ASME J. Turbomach., **124**, pp. 553–563.
[20] Roth, G. I., Mascenik, D. T., and Katz, J., 1999, "Measurements of The Flow Structure and Turbulence Within A Ship Bow Wave," Phys. Fluids, **11**, pp. 3512–3523.
[21] Roth, G. I., and Katz, J., 2001, "Five Techniques for Increasing the Speed and Accuracy of PIV Interrogation," Meas. Sci. Technol., **12**, pp. 238–245.
[22] Sridhar, G., and Katz, J., 1995, "Drag and Lift Forces on Microscopic Bubbles Entrained by a Vortex," Phys. Fluids, **7**, pp. 389–399.
[23] Bouda, N. N., Benabid, T., and Fulachier, L., 2002, "Relaxation of turbulent boundary layer submitted to sudden distortion at the wall," AIAA J., **40**, pp. 58–66.
[24] Smith, Jr., L. H., 1966, "Wake Dispersion in Turbomachines," J. Basic Eng., **1966**, September, pp. 688–690.
[25] Adamczyk J. J., 1996, "Wake Mixing in Axial Flow Compressors," ASME paper No. 96-GT-029.
[26] Van Zante, D. E., Adamczyk, J. J., Strazisar, A. J., and Okiishi, T. H., 2002, "Wake Recovery Performance Benefit in a High-Speed Axial Compressor," ASME J. Turbomach., **124**, pp. 275–284.

Heat Transfer in 1:4 Rectangular Passages With Rotation

Peeyush Agarwal

Sumanta Acharya

D. E. Nikitopoulos

Department of Mechanical Engineering,
Louisiana State University,
Baton Rouge, LA 70803

The paper presents an experimental study of heat/mass transfer coefficient in 1:4 rectangular channel with smooth or ribbed walls for Reynolds number in the range of 5000–40,000 and rotation numbers in the range of 0–0.12. Such passages are encountered close to the mid-chord sections of the turbine blade. Normal ribs ($e/D_h=0.3125$ and $P/e=8$) are placed on the leading and the trailing sides only. The experiments are conducted in a rotating two-pass coolant channel facility using the naphthalene sublimation technique. For purposes of comparison, selected measurements are also performed in a 1:1 cross section. The local mass-transfer data in the fully developed region is averaged to study the effect of the Reynolds and the rotation numbers. The spanwise mass transfer distributions in the smooth and the ribbed cases are also examined.
[DOI: 10.1115/1.1626683]

Introduction

Increasing the turbine inlet temperature can enhance the power output of a gas turbine engine, but this requires the development of advanced high-temperature materials or more effective internal and external blade cooling strategies. In internal cooling, the working fluid (typically compressed air) is circulated through smooth or ribbed serpentine passages and is discharged through the holes located at the trailing edge or the blade tip. Improved internal cooling designs rely on developing a better understanding of the flow and heat transfer in rotating ribbed passages. Important issues to be explored include the effect of aspect ratio and orientation of the coolant channel, and the effect of the rib turbulator shape and orientation. These issues need to be explored over parameter ranges of relevance to gas turbine engine applications.

In recent years, efforts directed at improving internal cooling have led to concepts that include the use of inclined ribs [1], vortex generators [2,3], profiled ribs [4,5], dimpled surfaces [6], etc. Most of these studies have been performed with square cross-section channels [1–12]. For example, Wagner et al. [7] examined the heat transfer characteristics of turbulent flow in rotating square, smooth serpentine passages, and were among the first to quantify in detail the role of Rotation number ($\mathrm{Ro}=\omega Dh/V$) and buoyancy parameter ($\mathrm{Bo}=(\Delta\rho/\rho)(R/Dh)\mathrm{Ro}^2$) in square cross-sectioned channels. Detailed distributions in rotating square channels were provided through mass transfer measurements by several investigators including Park et al. [1] and Kukreja et al. [10]. In real gas turbine blades, practical constraints often dictate the choice of the coolant passage cross section and orientation. Cross sections can have aspect ratios (AR's) that span the range from 1:4 (near the thickest portion of the blade) to 10:1 or higher (near the trailing edge), while the channel orientation can deviate significantly from the orthogonal orientation (90 degrees to the rotational axis). However, the literature dealing with low or high AR channels is quite limited compared to the square-aspect ratio channel. Han [11] and Han et al. [12] reported heat transfer, pressure drop, and the friction factor for ribbed rectangular channels of low aspect ratios ($=1:4$) under stationary conditions. Park et al. [13] investigated the effect of various rib configurations angled to the main flow direction in stationary channels with different AR's (1:4,1:2,1,2:1,4:1). Although computational [14,15] and analytical [16] efforts have been made in this area, the majority of the data published for low AR coolant channels are for stationary conditions, and there are little or no experimental data available under rotating conditions. Thus the main motivation of the present paper is to investigate the heat transfer behavior in a low aspect ratio coolant channels under conditions of rotation.

In the present study, a 1:4 aspect ratio channel has been selected, and both smooth and ribbed cases have been investigated. Results are compared with those of a square channel for both stationary and rotating cases. The study is conducted for a range of Reynolds number (5000–40,000) and rotation number (0–0.12). For the ribbed channel, $e/D_h=0.3125$ and $P/e=8$. The rib angle of attack is 90 deg. The value of $e/H=0.125$ and $e/W=0.5$.

The naphthalene sublimation technique [3–6,17,18] is used in the present study to obtain surface heat/mass transfer data for both stationary and rotational conditions. Mass transfer measurements permit the acquisition of detailed local distributions of the Sherwood number, which can be related to the Nusselt number using the heat-mass transfer analogy. The rotation of the channel creates coriolis forces, which, in turn, generate secondary flows orthogonal to the main flow direction. These secondary flows are important and are the principal reason for the differences in rotating and nonrotating flow cases. Note that with the naphthalene sublimation technique, centrifugal-buoyancy forces are not represented. However, as shown by Wagner et al. [7], heat transfer on the surfaces does not vary with density ratio for rotation numbers less than 0.12, and does not become significant until a rotation number of 0.35. Since the rotation numbers studied in this paper are all less than 0.12, and for the majority of the results presented $\mathrm{Ro}<0.05$, centrifugal buoyancy is not expected to play a major role for the parameter ranges studied in this paper. Therefore the use of the naphthalene sublimation technique is justified for the parameter ranges considered, and has the added advantage of providing detailed spatial distributions.

Experiments

Figure 1 shows a schematic diagram of the rotating rig facility. The test section is mounted on a rotating arm driven by a hydraulic motor. A dummy counterweight on the opposite end of the arm is used for balancing. The rotating arm is housed inside a pressure vessel for safety purposes. Compressed air is used as the working fluid for all experiments. The air is taken from large, exterior reservoirs in order to minimize flow disturbances caused by the compressor. A concentric bore orifice plate is used to measure the mass flow rate in the meter run. Naphthalene laden exhaust air is directed through flexible tubing to a fume hood.

Figure 2 shows the schematic of the two-pass test section and Fig. 3 shows the corresponding cross-sectional view. The aluminum alloy test section consists of a 69.85-mm tapered settling

Contributed by the International Gas Turbine Institute and presented at the International Gas Turbine and Aeroengine Congress and Exhibition, Atlanta, GA, June 16–19, 2003. Manuscript received by the IGTI December 2002; final revision March 2003. Paper No. 2003-GT-38615. Review Chair: H. R. Simmons.

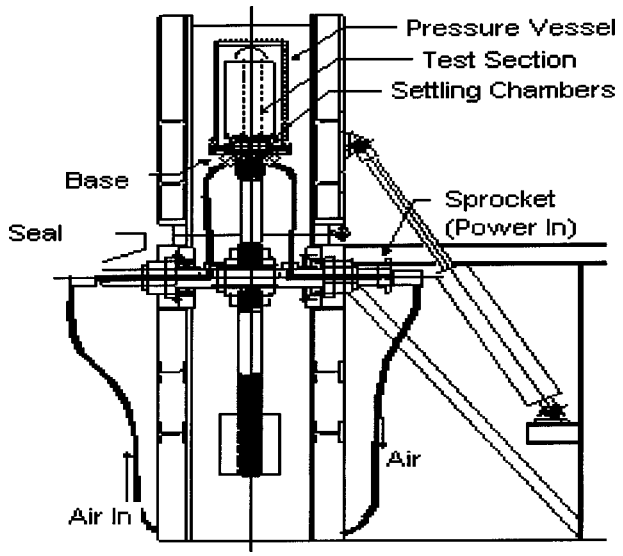

Fig. 1 Schematic of the rotating experimental facility

chamber; a frame that supports eight removable, wall frames; and a removable 180-degree bend. These major components are secured in a flangelike manner, using O rings between all parts to prevent air leakage. The ribs are placed using double-sided tape to prevent leaks and to prevent them from rattling. When assembled, the test section forms $6.35\times25.4\times304.8$-mm-long inlet and outlet sections 38.1 mm apart that are connected by the 180-degree, 6.35×25.4-mm square cross-section bend. For the ribbed duct, the aluminum ribs are $3.175\times3.175\times6.35$ mm long and have holes on either end for mounting. Steel 0.635-mm-diameter music wire is inserted into these holes to secure them to the sidewalls of the test section. The ribs are mounted only on opposite walls. All exposed surfaces except the ribs are coated with naphthalene.

Fresh 99% pure naphthalene crystals are melted in a heavy-walled glass beaker and molten naphthalene is quickly poured into the hollow cavity of the plate frame to fill completely the region between the walls. The cast plates stand for at least 8 h in a fume hood to attain thermal equilibrium with the laboratory. Test section assembly is begun by first inserting the two inner sidewalls and then attaching the bend. For ribbed surfaces, ribs are then attached to these walls and the two outer sidewalls are mounted.

Detailed surface profiles of the cast surfaces are required for local mass transfer results. These profiles are obtained by moving

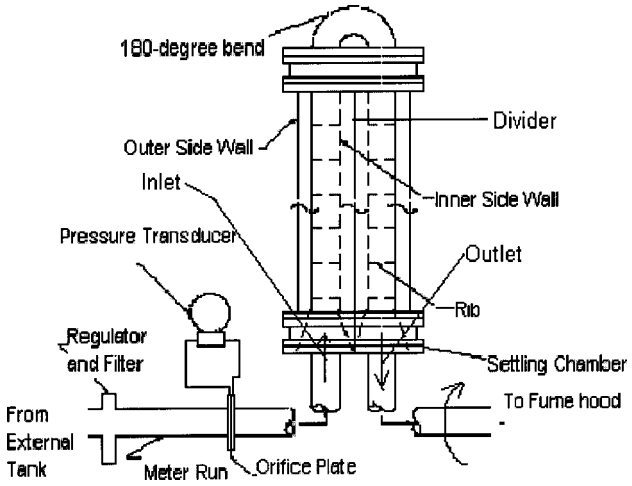

Fig. 2 Schematic of the test section and meter

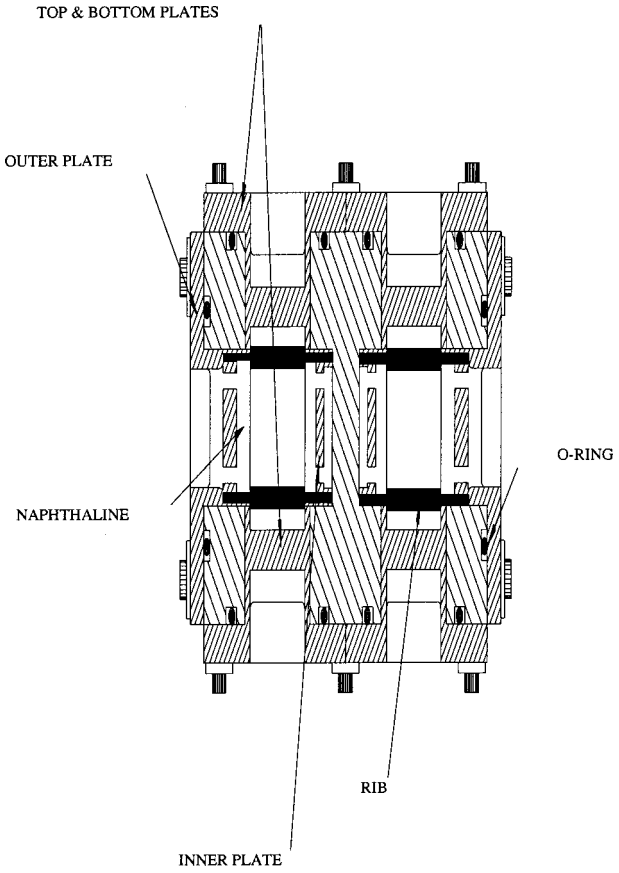

Fig. 3 Cross-stream section of the test section

the walls under a fixed, linear variable differential transducer (LVDT) type profilometer. A bi-directional traversing table is securely mounted to the platform of a milling machine. The plates are secured to a 15.875-mm-thick tooling aluminum plate, which is fixed to the traversing table. This mounting plate has been machined with an assortment of pin supports and machine screw taps to ensure the walls not only lie flat on the plate, but also are mounted in the same location for all scans. A custom written program run on a personal computer is used to control the motion of the traversing table through microstep drive motors with a 0.00127-mm step size.

Naphthalene sublimation depth is calculated from the two surface profiles for each wall. The surface scan of each plate takes about 25 min while the assembly time on the test section takes 8 min per plate. Except for the assembly and scanning time, each plate is kept in a sealed container with naphthalene-saturated atmosphere. Thus loss of naphthalene due to natural convection only occurs during approximately 58 min. This loss has been estimated to be less than the resolution of the surface measurement and verified experimentally. Nevertheless, this estimate is included in the uncertainty analysis. Each profile is normalized with respect to a reference plane computed from three points scanned on the aluminum surface of the walls. The difference between the normalized profiles gives the local sublimation depth. The local mass flux $\dot{m}''$ and the local mass transfer convection coefficient h_m at each location are then calculated from the following expressions:

$$\dot{m}''=\rho_s\delta/\Delta t; h_m=\dot{m}''/[\rho_w-\rho_b(x)], \quad (1)$$

where ρ_s is the density of solid naphthalene, δ is the local sublimation depth, Δt is the duration of the experiment, and ρ_w and $\rho_b(x)$ are the vapor density of the naphthalene at the wall (ob-

tained from equation of state) and in the bulk (obtained from mass balances). The local Sherwood number Sh is then calculated by

$$\mathrm{Sh} = h_m D_h / D_{n-a} = h_m D_h \mathrm{Sc}/\nu, \tag{2}$$

where the binary diffusion coefficient D_{n-a} for naphthalene sublimation in air is taken as the ratio of the kinematic viscosity of air ν to the Schmidt number for naphthalene-air (Sc=2.5). Sherwood number results presented in this study have been scaled with a correlation adapted from Ref. [21] for fully developed smooth wall pipe flow,

$$\mathrm{Sh}_o = 0.023 \mathrm{Re}^{0.8}\, \mathrm{Sc}^{0.4}, \tag{3}$$

where Re is the duct Reynolds number. Comparison of heat transfer and mass transfer results can be done through the use of the heat-mass transfer analogy [22]:

$$\mathrm{Nu} = \mathrm{Sh}(\mathrm{Pr}/\mathrm{Sc})^{0.4} \tag{4}$$

where Nu is the Nusselt number and Pr is the Prandtl number of air. Both local and area-averaged results are reported in this paper. Area averaging is performed as a simple arithmetic average of the 30×28 data points scanned over the region between consecutive ribs.

Uncertainties for all computed values are estimated using the second-power equation method [23]. Volume flow rate and duct Reynolds number (Re) uncertainties are estimated to be less than 10 percent for Re>6000. The uncertainty is higher for low Reynolds numbers due to the combined uncertainty in the gas expansion factor, and the generic calibration equation used for the orifice flow meter, which is not very accurate at low flow rates. The uncertainty is much less at higher Reynolds numbers.

For the stationary experiments, a thermocouple is imbedded in the naphthalene filled plate to measure wall temperature for the calculation of the vapor density of naphthalene, whereas in the rotating experiments the measured temperature of the incoming air is used. Since the temperature difference between inlet and exit temperature of the facility has been measured to be substantially less than a degree the effect is not significant and has been included in the uncertainty estimates. Significant viscous heating of the test section due to rotation-induced relative motion is insignificant because the test section is inside the small pressure vessel and exposed only to stagnant air.

The reported resolution of the LVDT is 0.00127 mm while the analog-to-digital (A/D) board is reported to have an accuracy of 0.002 mm in a 12-kHz acquisition rate, 16-bit resolution mode. Experimental tests of accuracy and repeatability for the entire acquisition system indicate a sublimation depth uncertainty of 0.0038 mm. Maximum sublimation depths are maintained at about 0.152 mm by varying the duration of the experiment. This target depth was selected to minimize uncertainties in both depth measurement and changes in duct cross-section area. These uncertainties were found to be 1 and 3 percent, respectively. The resulting experimental duration was between 120 min for Re=30,000 and 180 min for Re=5000. Overall uncertainty in Sherwood number calculation is about 8% and varies slightly with Reynolds number (<1%).

Results and Discussion

Smooth Channel Results.

Validation: A series of tests have been conducted to validate the experimental and analysis methods used. Figure 4 shows the centerline normalized Sherwood number ratio distribution for a 1:1 stationary channel at Re=30,000 along with published data [7,19]. Overall, comparisons show excellent agreement in the fully developed region of the inlet duct. Differences are seen in the developing region of the outlet duct, and are attributed to the differences in the bend region. In the present study, a smooth U bend is employed while in both Han et al. [19] and Wagner et al. [7] two successive 90-degree bends with zero bend radius have been used.

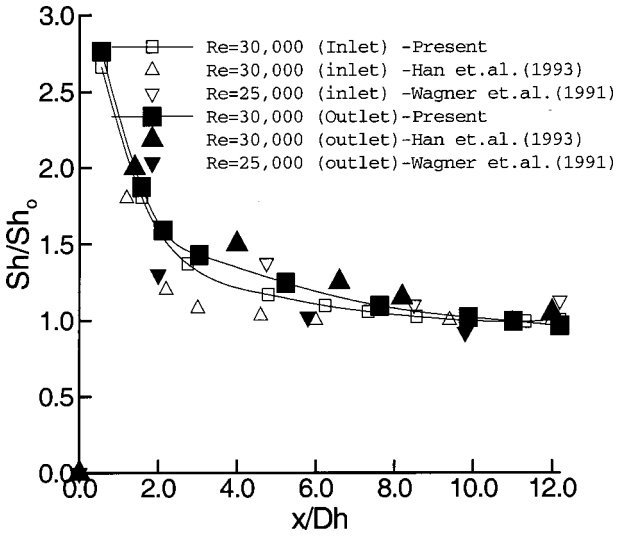

Fig. 4 Comparison of the present Sherwood number ratios with those published in the literature (AR=1:1)

Effect of Channel Aspect Ratio: Experiments have been conducted at Re=5760 and Ro=0.12 for both 1:1 and 1:4 aspect ratio channels in order to examine the effect of the aspect ratio. The comparison of the centerline normalized Sherwood number ratios are shown in Fig. 5, and the same qualitative trend is observed for the two aspect ratios. The scale on the *x* axis is different due to the difference in hydraulic diameter between AR=1:1 (=1 in.) and AR=1:4 (=0.4 in.).

In the inlet duct (radially outward flow), the trailing walls experience increased mass transfer while the leading-wall mass transfer is reduced because of the rotation-induced secondary flows. The opposite is true for the outlet duct where the flow is towards the axis of rotation. While the qualitative features are the same, quantitative differences are observed between the 1:1 and

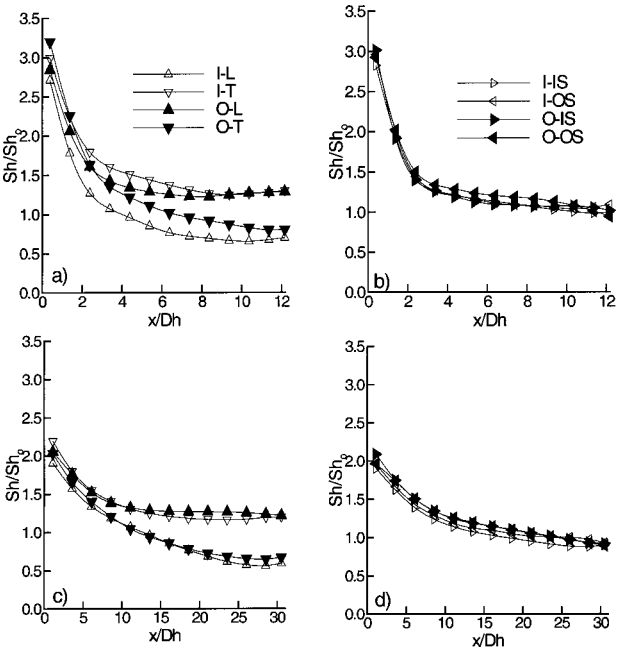

Fig. 5 Effect of aspect ratio on centerline normalized Sherwood number: Re=5760, Ro=0.12, (*a*) AR=1:1, leading and trailing walls, (*b*) AR=1:1, sidewalls, (*c*) AR=1:4, leading and trailing walls, (*d*) AR=1:4, sidewalls

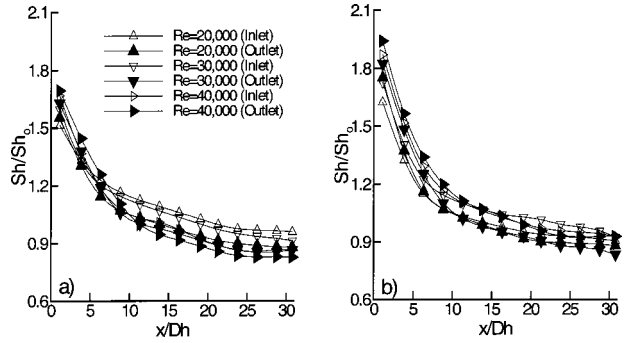

Fig. 6 Effect of Reynolds number on centerline normalized Sherwood number at Ro=0, AR=1:4, (*a*) leading and trailing wall average, (*b*) sidewalls average

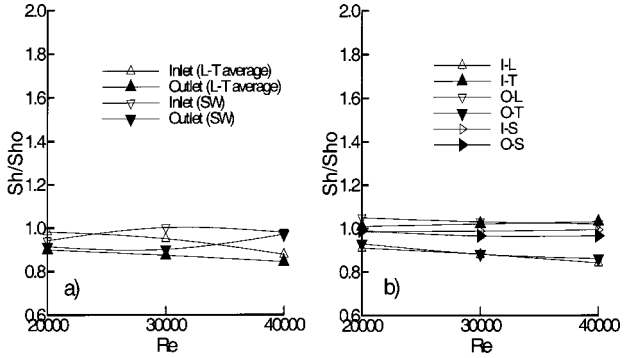

Fig. 7 Fully developed averaged normalized Sherwood number for AR=1:4 at (*a*) Ro=0, (*b*) Ro=0.025

1:4 aspect ratios, with the 1:4 case having lower values in the developing region. In the fully developed region of the 1:4 aspect ratio inlet channel, the rotation-induced increase in the mass transfer ratio is 17.5% on the trailing wall compared to 29% in the 1:1 channel. The rotation-induced decrease in the mass transfer ratio on the inlet leading side is 40% for the 1:4 case compared to 30% in the 1:1 channel. Thus with rotation the 1:4 channel shows a net degradation in the heat transfer on the leading and trailing surfaces combined, while the 1:1 channel does not exhibit a net change with rotation. In the outlet channel, the increase in mass transfer ratio on the leading side is 24% and the decrease on the trailing side is 20% for the 1:4 aspect ratio case. For the 1:1 channel the enhancement on the leading side is 30% while the degradation on the trailing side is only 12%. Thus for both aspect ratios the level of rotation-induced degradation is lower in the outlet channel relative to the inlet channel, and is presumably linked to the bend induced secondary flows increasing the mixing and heat transfer in the outlet channel. However, as in the inlet channel, the 1:4 aspect ratio channel still has lower net heat transfer enhancement relative to the 1:1 aspect ratio channel. On the sidewalls, the mass transfer ratio evolution is nearly identical for both aspect ratios, except for the lower values in the developing region for the 1:4 case.

Effect of Reynolds Number: To examine the effect of Reynolds number, experiments were conducted at three different Reynolds numbers under stationary conditions for both 1:1 and 1:4 channels. The comparison of the centerline normalized Sherwood number ratio of is shown in Fig. 6 for the 1:4 aspect ratio only. The fully developed normalized values for the 1:4 channel are slightly lower than 1, and are typically 9–12% lower than those of the 1:1 aspect ratio case (not shown in the interest of brevity). Figure 6 shows that as the Reynolds number is increased from 20,000 to 30,000, the fully developed ratio decreases slightly along the leading and trailing surfaces. No further decrease is observed when the Reynolds number is increased to 40,000. This is consistent with the expected asymptotic behavior in the fully developed region at high Reynolds numbers. In the developing region, the mass transfer ratio increases slightly with Reynolds number, with values in the range of 1.5–1.7 for the leading/trailing walls (Fig. 6(*a*)) and 1.62–1.92 for the sidewalls (Fig. 6(*b*)). The slightly higher values in the above-mentioned ranges correspond to the developing regions of the outlet duct and are presumably due to the secondary flows induced by the bend.

Figure 7 shows the average value of the fully developed mass transfer ratio with increasing Reynolds number at Ro=0 and Ro=0.025. In Fig. 7(*a*), for Ro=0, the dependence on Reynolds number appears to be relatively weak. In Fig. 7(*b*) the differences between the stabilized and de-stabilized surfaces are of the order of 10% for both the outward-flow and inward-flow passages, and this difference appears to increase marginally with Reynolds number. In fact, the heat transfer on the stabilized surface remains insensitive to Reynolds number while the heat transfer on the destabilized surface appears to decrease slightly with Reynolds number.

Effect of Rotation Number: A set of experiments has been conducted at three different rotation numbers at Re=30,000 for the 1:4 channel cross section. The results are shown in Fig. 8 for both inlet (flow radially outward) and outlet (flow radially inward) channels. The Sherwood number ratio on the leading wall is reduced by 10% relative to the stationary case by increasing the rotation number from 0 to 0.045, while on the trailing wall the Sherwood number ratio is increased by 12%. The Sherwood number ratio along the sidewall also generally exhibits an increase with rotation, with an increase of about 8% for Ro=0.045 relative to the stationary case (Ro=0). In the outlet channel the reverse behavior is expected on the leading and trailing walls relative to the inlet channel. However, only the destabilized wall is entirely consistent with expectations. It is observed that the rotation-induced mass transfer enhancement (20% relative to the stationary case) on the leading (destabilized) wall is much more pronounced than the degradation (6%) observed on the leading (stabilized) wall, which does not appear to change from Ro=0.025–0.045. A strong bend effect is a possible explanation for this behavior. The

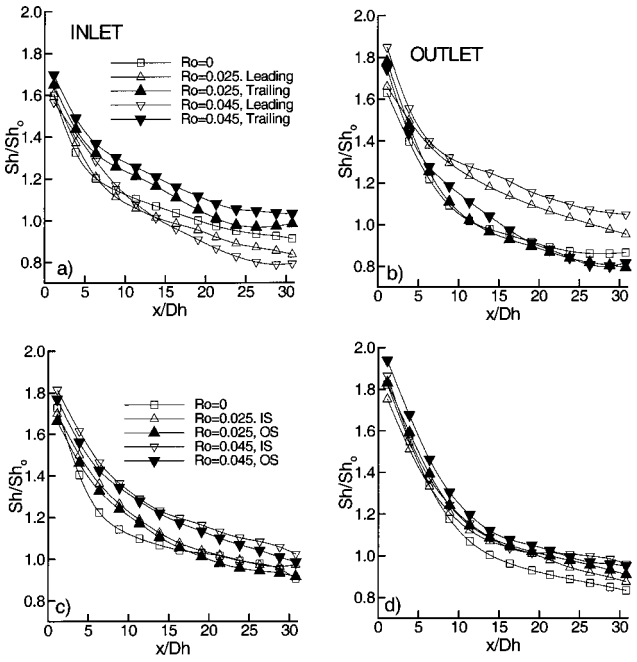

Fig. 8 Effect of rotation on centerline normalized Sherwood number at Re=30,000 for AR=1:4

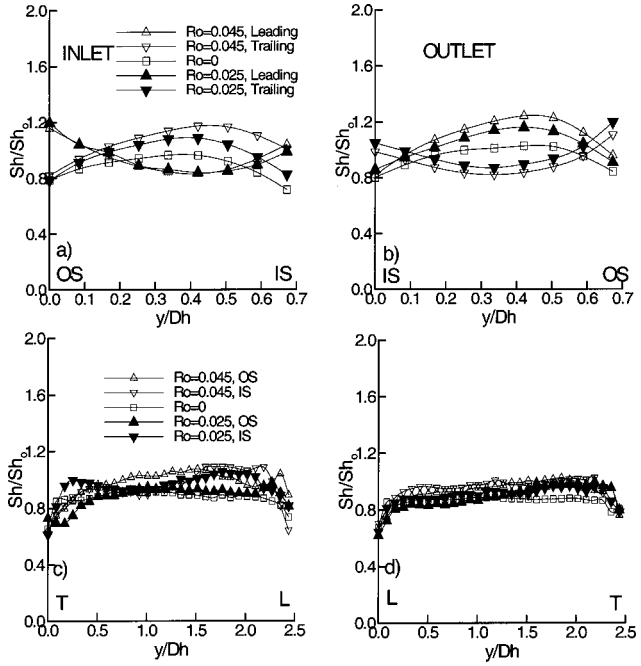

Fig. 9 Spanwise distributions at different rotation numbers in the fully developed region at Re=30,000 for AR=1:4, (*a*) and (*b*) leading and trailing, and (*c*) and (*d*) sidewalls

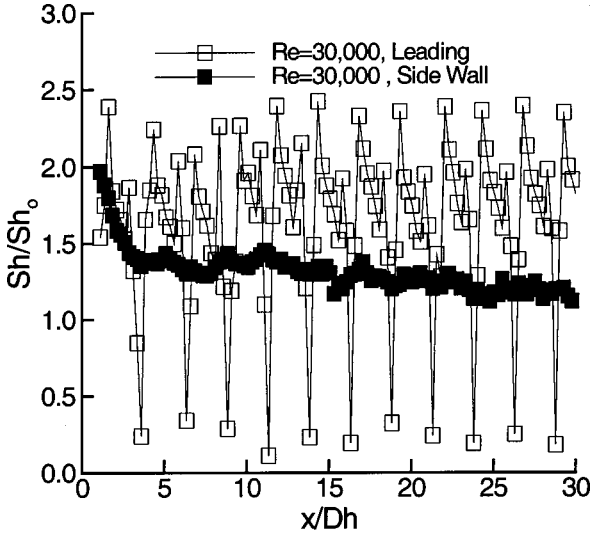

Fig. 10 Centerline distribution of the Sherwood number ratio along the ribbed and sidewall (inlet) for AR=1:4

sidewall mass transfer displays a modest monotonic increase with rotation, which is as high as 10% relative to the stationary case for the highest rotation number examined. No evidence of buoyancy-induced separation, as reported in Dutta et al. [16], has been observed in the present study. This is expected because the buoyancy in the mass transfer experiments is negligible ($Gr/Re \ll 1$ as per Ref. [16]).

Figure 9 shows the spanwise distributions for different rotation numbers in the fully developedregion at Re=30,000. These distributions are a result of averaging in the streamwise direction between successive ribs. Some level of asymmetry can be seen in the profiles and is indicative of the asymmetry in the flow induced by the bend and the asymmetry in the incoming flow. In smooth channels, these asymmetries do not wash out quickly, and persist well downstream. In general, the cross-stream profiles follow the expected patterns of reduction and enhancement of mass transfer along leading and trailing walls. For the destabilized surface, the peak heat transfer occurs close to the centerline where the Coriolis-induced secondary flows impinge, and decay outwards along the lateral direction. Along the stabilized surface, the minimum heat transfer occurs in the middle where the secondary flow lifts off the surface, and the peak heat transfer occurs close to the corners where the secondary flow moving down the sidewall impinges. Thus close to the corners, there is a crossover of the profiles along the stabilized and destabilized surfaces, with heat transfer along the stabilized surface actually being greater than the heat transfer along the destabilized surface. Note that close to the centerline, the differences in the Sherwood number ratio between the stabilized and destabilized surface can be a factor of 1.5 different at Ro=0.045. This is in contrast to the average Sherwood number ratio where the differences are much smaller and in the range of 10–20%. Along the sidewalls, enhancement is consistently noted with rotation, with the spanwise variation being relatively flat except close to the corners.

Results of Ribbed Channel, AR=1:4. For the ribbed channel, measurements are made with thermally inactive square cross-sectioned ribs, mounted on the leading and trailing surfaces in an in-line arrangement and 90 deg angle of attack ($e/D_h=0.3125$ and $P/e=8$). Figure 10 shows the centerline distribution of the Sherwood number along the leading surface and the average of the Sherwood number ratio along the sidewalls in the inlet channel for a nonrotating case. An obvious feature of the ribbed wall mass transfer profile is its periodic behavior.

Unlike the smooth channel, which did not attain truly fully developed conditions, the ribbed channel reaches periodically fully developed conditions shortly after the entrance (in the inlet channel) or after the bend (in the outlet channel). Inspection of the centerline mass transfer profiles (Fig. 10) indicates that there is a peak behind the rib where the flow reattaches and a peak immediately upstream of the rib due to a corner vortex. The lowest heat transfer occurs directly at the rib location, and this is a consequence of the rib being thermally inactive in the present study. The ribs also significantly enhance the mass transfer along the smooth sidewalls. This increase in mass transfer is believed to result from the acceleration of fluid between the ribs and an associated increase in turbulent kinetic energy. It is worth noting here that the ribs in the blade cooling application are usually not rectangular but rounded, in which case the flow supposedly remains more attached to the ribs, particularly on the upstream side. In the case of the square ribs that are usually studied in the laboratory and are the object of the present study, the flow separates very close to the upstream corner.

Effect of Reynolds Number: Figure 11 shows the average fully developed mass transfer ratio in the inlet and outlet channels for the ribbed leading and trailing walls and for the smooth sidewalls at different Reynolds numbers. The results for the stationary case are compared with Han and co-workers [11,12] for aspect ratio 1:4 and 1:1 channel, respectively. The present results for the stationary 1:4 aspect ratio case generally agree with those of Han and co-workers [11,12]. However, in the present results, a consistent Reynolds number effect is observed, with Sh/Sh_0 decreasing with Re (by nearly 20% on the ribbed surface and 13% on the smooth sidewall). With rotation (Fig. 11(*b*)) it is observed that for all the walls, the mass transfer ratio also decreases (in the range of 10–20%) with increasing Reynolds number. This dependence on Re for the rotational case is comparable to that observed for the nonrotating case. This behavior is surprising considering that the flow appears to be fully developed with consistently periodic modules. It should be noted that special care was given in verifying this trend through repeated experiments. One possibility is that the exponent of the Reynolds number (=0.8) with which the Sher-

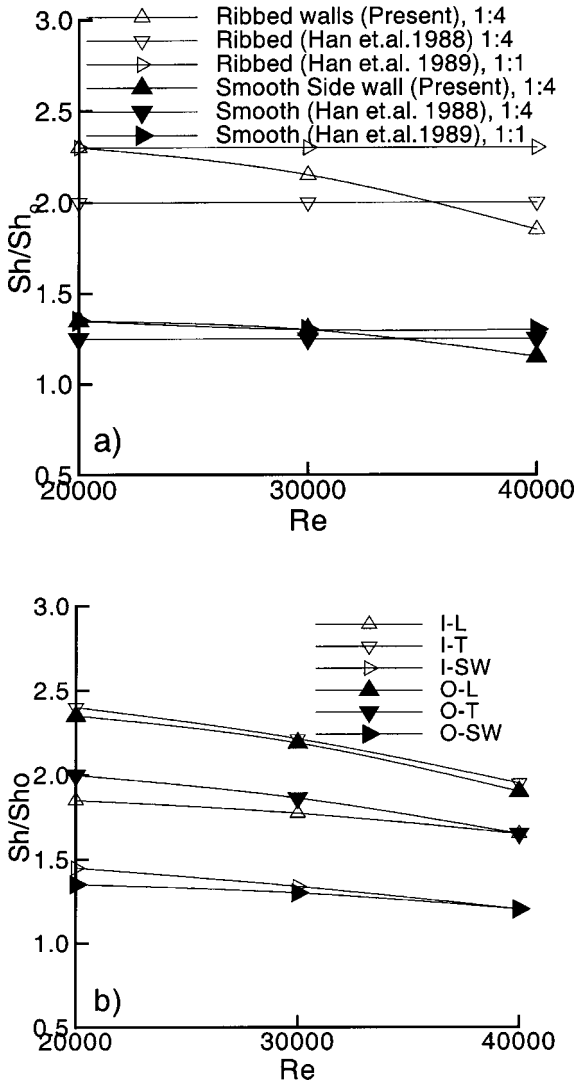

Fig. 11 Fully developed mass transfer ratio in the inlet and outlet ribbed channel, (*a*) Ro=0, (*b*) AR=1:4, Ro=0.025 (average of the inlet duct sidewalls and outlet duct sidewalls is plotted)

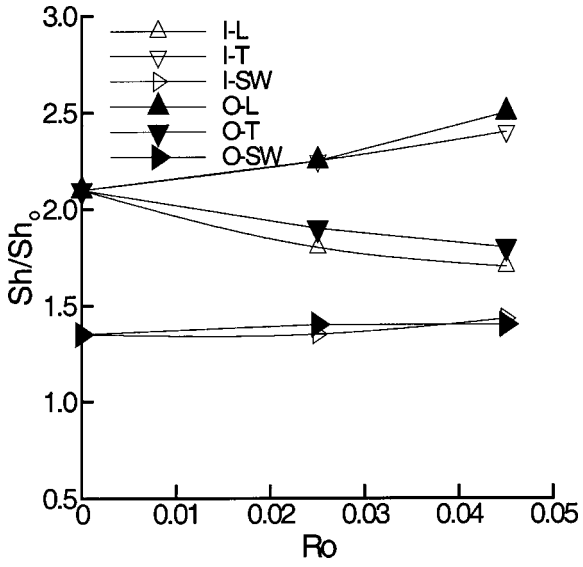

Fig. 12 Effect of rotation number at Re=30,000, AR=1:4 (fully developed averaged normalized Sherwood number)

wood number has been normalized is different. An attempt at estimating a corrected value was not done due to the limited number of Re values studied.

Effect of Rotation Number: Figure 12 shows the effect of the rotation number at Re=30,000. In the inlet (radially outward flow) passage, the trailing wall shows an increase of 18% and leading wall decreases by 18% when the rotation number is increased to 0.045. Correspondingly, in the outlet (radially inward flow) passage, the mass transfer ratio on the leading edge increases by 20% and decreases by 14% on the trailing edge. The sidewalls show a rather modest increase with Ro (within the experimental error range). For a 1:1 case at Re=25,000, Ro=0.05 (Wagner et al. [9]), the enhancements on the destabilized surfaces were observed to be nearly 10% and the degradation on the stabilized surfaces were nearly 20%. Therefore it is concluded that for the 1:4 case, the rotation effects are stronger and the enhancement is higher than the 1:1 rotating case. This is believed due to the effect of the stronger secondary flow formation in a 1:4 channel.

Figure 13(*a*) shows the centerline distribution of the normalized Sherwood number in a single periodically developed region between successive ribs in the inlet duct. The first peak corresponds to flow reattachment while the second peak corresponds to the corner vortex upstream of the rib. At Ro=0.045, the trailing surface shows roughly a 20% enhancement over the leading surface over most of the interrib module. Figure 13(*b*) shows the corresponding profiles for developing flow in the first inter-rib module following the bend in the outlet channel. Even in the first inter-rib module following the bend, there is an increase in the Sherwood number ratio (15–20%) on the leading surface relative to the trailing side. This indicates that in a 1:4 channel, the bend induced secondary flows are not strong enough to counter the rotation-induced secondary flows. The outer sidewall in the outlet channel has a slightly higher (less than 10%) Sherwood number ratio than inner sidewall. This is due to the bend effects and is associated with the accelerating flow on the outer sidewall. Note that unlike a 1:1 duct where a separation on the inner sidewall leads to low heat transfer values in this region, no such separation or region of significantly reduced heat transfer is along the inner sidewall immediately following the bend. This is to be expected, based on the fact that for the 1:1 channel the bend is effectively of a "shorter radius" compared to the 1:4 channel. This is also evidenced by the fact that for the 1:1 channel the Ito [24] curved-pipe similarity parameter $(\mathrm{Re}\{D_h/[2r]\}^2$, where r is the bend radius) is larger by a factor of 3 compared to that of the 1:4 channel.

Figure 14 shows the spanwise distribution along the ribbed trailing and leading surfaces (Figs. 14(*a*) and (*b*)) and smooth inner and outer side walls (Figs. 14(*c*) and (*d*)) for different rotation numbers in the fully developed region at Re=30,000. These distributions are a result of averaging in the streamwise direction

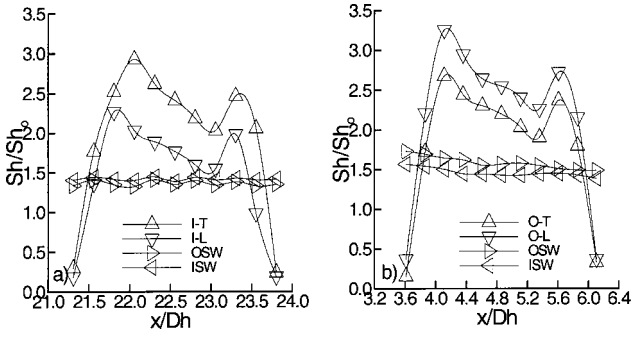

Fig. 13 Centerline normalized Sherwood number distribution in the inter-rib region at Re=30,000, Ro=0.045, AR=1:4, (a) inlet fully developed region, (*b*) outlet developing flow region

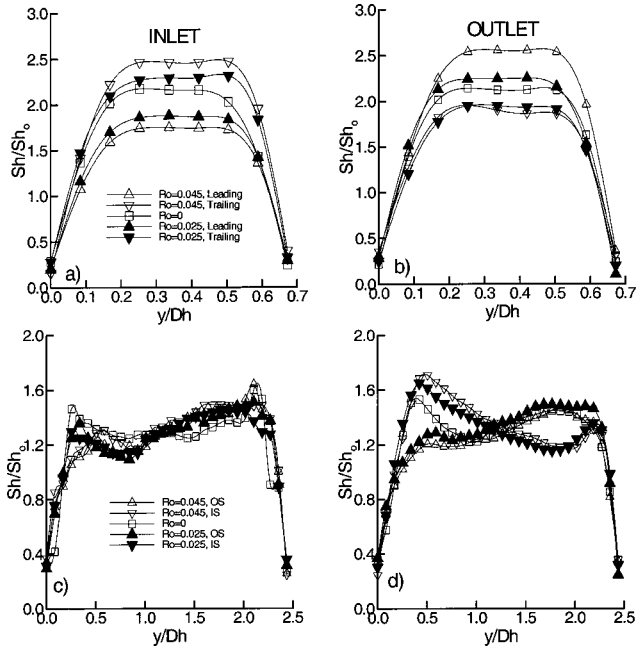

Fig. 14 Spanwise distribution for different rotation numbers in the fully developed region at Re=30,000, AR=1:4

between successive ribs. The profiles along the leading and trailing surfaces indicate a relatively uniform mass transfer distribution in the mid-span regions of the ribbed walls followed by a sharp dropoff toward the corners. Note that this behavior is distinctly different than the smooth channel (Fig. 9) where an increase in the Sherwood number was observed toward the corners. Along the smooth sidewalls (Figs. 14(*c*) and (*d*)), no significant variation is observed with rotation in the inlet duct (Fig. 14(*c*)). Slightly higher values (relative to the stationary case) are obtained close to the destabilized trailing-surface side where the rotation-induced secondary flows impinge, and correspondingly slightly lower values are obtained at the opposite end adjacent to the stabilized surface. In the outlet duct, larger differences are observed (Fig. 14(*d*)). Values are again higher closer to the destabilized surface (leading surface) and lower closer to the stabilized surface, but surprisingly this is only true along the inner wall. A plausible explanation for this is that the bend-induced acceleration along the outer wall skews the rotation induced secondary flow pattern toward the inner wall. Along the outer wall, a relatively uniform distribution is obtained with a mild increase toward the stabilized surface. With span-wise averaging however, the high and lows in the profiles average out, and the averaged values do not show a strong Ro number dependence as seen in Fig. 12.

It should be noted that the secondary flow effects after the bend are different with and without ribs. This is expected since the ribs induce secondary flows that are confined near the walls. The interaction of rib-induced and bend-induced secondary flows result in a different pattern with multiple rolls that causes enhanced mass transfer.

Concluding Remarks

Mass/heat transfer distributions have been obtained in a 1:4 smooth and ribbed channel under stationary and rotating conditions. The naphthalene sublimation technique has been used to obtain these measurements. These results have been compared with results for a 1:1 square cross-section channel. The following conclusions can be drawn:

1. For a smooth channel, the 1:4 cross section shows lower levels of enhancement along the destabilized surface, and higher levels of degradation along the stabilized surface compared to the 1:1 cross-section channel. Thus, for a specific parameter value, the 1:4 cross-section channel has lower heat transfer rates compared to the 1:1 channel.

2. For a smooth channel, the spanwise distributions along the destabilized surface show a peak at the center and decrease toward the corner. Along the stabilized surface, the center has the lowest heat transfer value and the values increase toward the corners. A crossover point is observed near the corners where the stabilized surface has higher heat transfer than the destabilized surface.

3. For the smooth duct, the Sherwood numbers are relatively insensitive to Re. For the ribbed duct, the Sherwood number ratios show a weak Re number dependence under stationary and rotating conditions, with Sherwood number ratios decreasing with Re.

4. At Re=30,000, as Ro is increased from 0 to 0.045, the 1:4 cross-section smooth duct shows roughly a 10–12% change in the inlet duct relative to the stationary case. For the ribbed duct, the corresponding change is about 18%. This observation is consistent with the square-aspect ratio results of Johnson et al. [20] who also show that 90-degree trips show a greater sensitivity to Ro compared to the smooth channel.

5. The spanwise distribution for the ribbed cases show fairly uniform distributions in the mid-span regions, and unlike the smooth channel case, the peak heat transfer rate on the stabilized surface is highest in the middle.

Acknowledgment

This research has been supported by the DOE-AGTSR program managed by the South Carolina Institute for Energy Studies. Their support is gratefully acknowledged.

Nomenclature

Re = Reynolds number (Re=$\rho VDh/\mu$)
Ro = Rotation number (Ro=$\omega Dh/V$)
AR = Aspect ratio (W/H)
e = Height of the rib
Dh = Hydraulic diameter
H = Distance between leading and trailing walls
p = Pitch (distance between the two consecutive ribs)
Sh = Sherwood number
Nu = Nusselt number
Sh$_o$ = Reference Sherwood number
Nu$_o$ = Reference Nusselt number
IS = Inner sidewall
OS = Outer sidewall
L = Leading side
T = Trailing side
IL = Inlet leading
IT = Inlet trailing
OL = Outlet leading
OT = Outlet trailing
OSW = Outlet sidewall
ISW = Inlet sidewall
SW = Sidewall
L-T average = Average of leading and trailing side
Sc = Schmidt number of naphthalene
ν = Viscosity of air
ρ_W = Density of naphthalene
ρ_b = Bulk density of naphthalene
D_{n-a} = Binary diffusion coefficient of naphthalene in air
Pr = Prandtl number (air)
ω = Rotation speed (RPM)
V = Velocity of air inside the channel
W = Distance between sidewalls
Bo = Buoyancy parameter (Bo=$(\Delta\rho/\rho)(R/Dh)$Ro^2)

References

[1] Park, C. W., Lau, S. C., and Kukreja, R. T., 1998, ''Heat/Mass Transfer in a Rotating Two-Pass Channel with Transverse Ribs,'' J. Thermophys. Heat Transfer, **12**, pp. 80–86.

[2] Myrum, T., Acharya, S., Sinha, S., and Qiu, X., 1996, ''The Effect of Placing Vortex Generators Above Ribs in Ribbed Ducts on the Flow, Flow Temperature, and Heat Transfer Behavior,'' ASME J. Heat Transfer, **118**, pp. 294–300.

[3] Eliades, V., Nikitopoulos, D. E., and Acharya, S., 2001, ''Mass Transfer Distribution in Rotating, Two-Pass Ribbed Channels with Vortex Generators,'' J. Thermophys. Heat Transfer, **15**, pp. 266–274.

[4] Acharya, S., Eliades, V., and Nikitopoulos, D. E., 2001, ''Heat Transfer Enhancements in Rotating Two-Pass Coolant Channels with Profiled Ribs: Average Results,'' ASME J. Turbomach., **23**, pp. 97–106.

[5] Nikitopoulos, D. E., Eliades, V., and Acharya, S., 2001, ''Heat Transfer Enhancements in Rotating Two-Pass Coolant Channels with Profiled Ribs: Detailed Measurements,'' ASME J. Turbomach., **23**, pp. 107–114.

[6] Zhou, F., and Acharya, S., 2001, ''Mass/Heat Transfer in Dimpled Turbine-Blade Coolant Passages,'' Ann. N.Y. Acad. Sci., **934**, pp. 424–431.

[7] Wagner, J. H., Johnson, B. V., and Kopper, F. C., 1991, ''Heat Transfer in Rotating Serpentine Passages with Smooth Walls,'' ASME J. Turbomach., **113**, pp. 321–330.

[8] Johnson, B. V., Wagner, J. H., Steuber, G. D., and Yeh, F. C., 1994, ''Heat Transfer in Rotating Serpentine Passages with Trips Skewed to the Flow,'' ASME J. Turbomach., **116**, pp. 113–123.

[9] Wagner, J. H., Johnson, B. V., Steuber, G. D., and Yeh, F. C., 1992, ''Heat Transfer in Rotating Serpentine Passages with Trips Normal to the Flow,'' ASME J. Turbomach., **114**, pp. 847–857.

[10] Kukreja, R. T., Park, C. W., and Lau, S. C., 1998, ''Heat (Mass) Transfer in a Rotating Two Pass Square Channel-Part-II: Local Transfer Coefficient, Smooth Channel,'' Int. J. Rotating Mach., **4**, pp. 1–15.

[11] Han, J. C., May, 1988, ''Heat Transfer and Friction Characteristics in Rectangular Channels with Rib Turbulators,'' ASME J. Heat Transfer, **110**, pp. 321–328.

[12] Han, J. C., Ou, S., Park, J. S., and Lei, C. K., 1989, ''Augmented Heat Transfer in Rectangular Channels of Narrow Aspect Ratios with Rib Turbulators,'' Int. J. Heat Mass Transfer, **32**, pp. 1699–1630.

[13] Park, J. S., Han, J. C., Huang, Y., and Ou, S., 1992, ''Heat Transfer Performance Comparisons of Five Different Rectangular Channels with Parallel Angled Ribs,'' Int. J. Heat Mass Transfer, **35**, pp. 2891–2903.

[14] Tekriwal, P., 1996, ''Effect of Aspect Ratio on Buoyancy Driven Reverse Flow Near the Leading Wall of Rotating Cooling Passages,'' *ASME Turbo Expo*, 96-GT-173.

[15] Dutta, S., Andrews, M. J., and Han, J. C., 1996, ''Prediction of Turbulent Heat Transfer in Rotating Smooth Square Ducts,'' Int. J. Heat Mass Transfer, **39**, pp. 2505–2514.

[16] Dutta, S., Andrews, M. J., and Han, J. C., 1996, ''On Flow Separation with Adverse Rotational Buoyancy,'' ASME J. Heat Transfer, **118**, pp. 977–979.

[17] Sparrow, E. M., and Taq, W. Q., 1984, ''Symmetric vs Asymmetric Periodic Disturbances at the Walls of a Heated Flow Passage,'' Int. J. Heat Mass Transfer, **27**, pp. 2133–2144.

[18] Souza Mendes, P. R., 1991, ''The Naphthalene Sublimation Technique,'' Exp. Therm. Fluid Sci., **4**, pp. 510–523.

[19] Han, J. C., Zhang, Y., and Kalluehler, K., 1993, ''Uneven Wall Temperature Effect on Local Heat Transfer in a Rotating Two Pass Square Channel with Smooth Walls,'' ASME J. Turbomach., **115**, pp. 912–920.

[20] Johnson, B. V., Wagner, J. H., and Steuber, G. D., 1993, ''Effects of Rotation on Coolant Passage Heat Transfer,'' NASA Contractor Report 4396, Vol. II.

[21] McAdams, W., 1954, ''Heat Transmission,'' 3rd Ed., McGraw-Hill Publishing Co., New York.

[22] Sogin, H., 1958, ''Sublimation from Disks to Air Streams Flowing Normal to their Surfaces,'' Trans. ASME, **80**, pp. 61–69.

[23] Kline, S. J., and McClintock, F. A., 1953, ''Describing Uncertainties in Single-Sample Experiments,'' Mech. Eng. (Am. Soc. Mech. Eng.), **75**, pp. 3–8.

[24] Ito, H., 1959, ''Friction Factors for Turbulent Flow in Curved Pipes,'' J. Basic Eng., **81**, pp. 123–134.

Large Eddy Simulation of Film Cooling Flow From an Inclined Cylindrical Jet

Mayank Tyagi[1]
Research Associate

Sumanta Acharya
Professor

Mechanical Engineering Department,
Louisiana State University,
Baton Rouge, LA 70803

Predictions of turbine blade film cooling have traditionally employed Reynolds-averaged Navier-Stokes solvers and two-equation models for turbulence. Evaluation of several versions of such models have revealed that the existing two-equation models fail to resolve the anisotropy and the dynamics of the highly complex flow field created by the jet-crossflow interaction. A more accurate prediction of the flow field can be obtained from large eddy simulations (LES) where the dynamics of the larger scales in the flow are directly resolved. In the present paper, such an approach has been used, and results are presented for a row of inclined cylindrical holes at blowing ratios of 0.5 and 1 and Reynolds numbers of 11,100 and 22,200, respectively, based on the jet velocity and hole diameter. Comparison of the time-averaged LES predictions with the flow measurements of Lavrich and Chiappetta (UTRC Report No. 90-04) shows that LES is able to predict the flow field with reasonable accuracy. The unsteady three-dimensional flow field is shown to be dominated by packets of hairpin-shaped vortices. The dynamics of the hairpin vortices in the wake region of the injected jet and their influence on the unsteady wall heat transfer are presented. Generation of "hot spots" and their migration on the film-cooled surface are associated with the entrainment induced by the hairpin structures. Several geometric properties of a "mixing interface" around hairpin coherent structures are presented to illustrate and quantify their impact on the entrainment rates and mixing processes in the wake region. [DOI: 10.1115/1.1625397]

Introduction

Advanced gas turbines are designed to operate at increasingly higher turbine inlet temperatures. This poses a greater challenge to design more effective blade cooling strategies. Film cooling is commonly used to cool the first-stage turbine blade and to maintain the blade temperatures below their melting point. In film cooling, coolant jets are injected at an angle into the heated crossflow that deflects these coolant jets over the blade surface to provide coolant film coverage. However, film-cooling air represents a reduction of the air in the main flow path through the combustor, and coolant injection introduces additional aerodynamic losses. Therefore, the goal of the turbine designer is to minimize coolant usage and maximize cooling effectiveness. This requires a complete and accurate understanding of the flow and heat transfer behavior associated with the film-cooling injection process.

Most of the computational studies on film cooling flow have been done using steady Reynolds-averaged Navier-Stokes (RANS) calculation procedures (Garg and Gaugler [1,2]; Berhe and Patankar [3]; Walters and Leylek [4]; Lakehal et al. [5]; Acharya et al. [6]). However, the turbulent stress field is highly anisotropic in the wake region of the coolant jet, and the inherent unsteadiness of the coolant jet-crossflow interactions may have important implications on the passive scalar entrainment process. In general, RANS calculations underpredict the lateral spread and mixing of the jet while they overpredict the vertical penetration of the coolant jet (Acharya et al. [6]). For a square jet injected vertically into a crossflow, comparisons of predictions and measurements (Hoda et al. [7]) reveal that RANS procedures with an array of turbulence models (from two-equation models to Reynolds stress models) significantly underpredict the lateral shear stress $u'w'$ (responsible for the lateral mixing and spreading), while large eddy simulation (LES) predictions are in excellent agreement with measurements. Clearly, RANS modeling either at the two-equation level or at the second-moment level is inaccurate for correctly predicting the turbulent stresses and the scalar mixing, while LES can more accurately capture the flow physics. In the present paper, LES for an inclined film-cooling jet is reported, and an effort is made to understand the flow physics associated with the coolant-jet–crossflow interaction. While limited comparisons with available experimental data are made in this paper to validate the calculation procedure and the subgrid scale models employed, the main goal of the paper is to focus on the large-scale unsteady dynamics of the coolant jet, and how these dynamics influence the mixing and heat transfer that control the cooling effectiveness of the jet.

Computational Procedure

In LES, the governing equations are spatially filtered, with the filter width (proportional to the size of each grid element) representing the scales in the flow field that are resolved (Vreman et al. [8]; Tyagi and Acharya [9]). The nondimensional filtered governing equations for the conservation of mass, momentum, and energy for an incompressible Newtonian fluid are given as

$$\frac{\partial U_j}{\partial x_j}=0,$$

$$\frac{\partial U_i}{\partial t}+\frac{\partial U_iU_j}{\partial x_j}=-\frac{\partial p}{\partial x_i}+\frac{1}{\mathrm{Re}}\frac{\partial^2 U_i}{\partial x_j^2}+\frac{\partial \tau_{ij}}{\partial x_j}+f_i,$$

$$\frac{\partial \Theta}{\partial t}=[1-\Phi]\left(-U_j\frac{\partial \Theta}{\partial x_j}+\frac{1}{\mathrm{Re\,Pr}}\frac{\partial^2\Theta}{\partial x_j^2}+\frac{\partial q_j}{\partial x_j}\right)+\Phi\frac{\Lambda}{\mathrm{Re\,Pr}}\frac{\partial^2\Theta}{\partial x_j^2}, \tag{1}$$

where U_i is the filtered velocity field, f_i is the body force term, and $\Theta=(T-T_\infty)/(T_j-T_\infty)$, where T_j is the coolant-jet temperature and T_∞ is the crossflow temperature. In the present calculation, a Cartesian grid is used, and an immersed boundary approach

[1]Author to whom correspondence should be addressed.

Contributed by the International Gas Turbine Institute and presented at the International Gas Turbine and Aeroengine Congress and Exhibition, Atlanta, GA, June 16–19, 2003. Manuscript received by the IGTI December 2002; final revision March 2003. Paper No. 2003-GT-38633. Review Chair: H. R. Simmons.

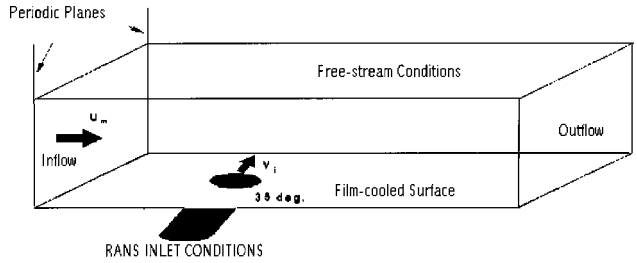

Fig. 1 Schematic of the computational domain and boundary conditions

(Yusof [10]; Fadlun et al. [11]; Tyagi and Acharya [9]) is utilized to resolve the inclined surfaces of the coolant delivery tube. With the immersed boundary method, grid points internal to a solid surface have body force terms added such that the no-slip boundary conditions at the interior surface is exactly satisfied. For temperature, a conjugate heat transfer problem is solved with Λ in the energy equation representing the ratio of thermal diffusivity of the immersed solid to thermal diffusivity of the fluid and Φ representing an indicator function that is 0 in the fluid region and 1 in the immersed solid region.

The subgrid scale (SGS) stress tensor and SGS scalar flux vector are represented by τ_{ij} and q_j, respectively, in the governing equation. In this study, a dynamic mixed model (DMM) is used to model the SGS stress tensor and the scalar flux vector (Moin et al. [12]; Vreman et al. [8]). The DMM can represent the backscatter of energy through the scale-similar part while it can drain the energy from the large scales to the small scales using an eddy viscosity part. This model is generally considered to be the simplest model that satisfies both the physical and mathematical requirements for SGS models. Box filters are used in the Germano identity for the calculation of the dynamic coefficient and for the calculation of Leonard stresses appearing in the subgrid stress term. The dynamic coefficient is test filtered to avoid numerical instabilities. Additional details of the procedure are given by Tyagi and Acharya [9].

The momentum equations are solved using a projection method. The temporal differencing is done using an explicit second-order accurate Adams-Bashforth scheme. The spatial descretization is done using a fourth-order central finite-difference scheme for all the terms except the convective term $(\partial U_\alpha U_\alpha / \partial x_\alpha)$ that is upwind-differenced with a third-order accurate scheme. The pressure-Poisson equation is solved using a direct solver based on a matrix diagonalization approach. The Laplacian operator in the pressure equation is approximated using a fourth-order central difference for the gradient operator and a second-order accurate central difference for the divergence operator. All the terms in energy equation are differenced using fourth-order central differences. Additional details of the numerical scheme used are given by Acharya et al. [6] and Tyagi and Acharya [9].

The computational domain of interest is shown in Fig. 1, and represents a spanwise-periodic module containing a single coolant delivery tube inclined at 35 deg to the streamwise direction. For this geometry, detailed flow measurements have been provided by Lavrich and Chiappetta [13] with a coolant delivery tube length of $6D$ (where D is the diameter of the coolant-jet delivery tube), and film-cooling effectiveness data are provided by Sinha et al. [14] with a coolant delivery tube length of $1.75D$. The LES results of the present study are compared with these reported measurements. A uniform grid of $172\times102\times62$ is used to model the computational domain of size $17D\times5D\times6D$. The film-cooled surface is placed at $1.0D$ from the bottom of the computational domain with the length of the coolant delivery tube being equal to $1.75D$. The center of the jet injection hole at the film-cooled surface is $5D$ downstream from the inlet plane. The origin of axes is placed at the center of hole on the film-cooled surface. Therefore, the domain is $[-5D,12D]\times[-1D,4D]\times[-3D,3D]$. The jet delivery tube is simulated as an inclined cylindrical surface, and as noted earlier, the immersed boundary method is utilized to enforce the no-slip conditions on the delivery tube surface (Yusof [10]).

At the inlet of the coolant delivery tube, flow boundary conditions must be provided that are consistent with the measurements. In most experimental studies, detailed velocity measurements at the inlet to the coolant delivery tube or the jet exit are not provided. Thus judicious choices must be made in this respect. It is generally accepted that since the crossflow influences the flow development in the delivery tube, the computational domain must include all or a portion of the coolant delivery tube. The present computations, with a $1.75D$ long delivery tube, are being compared with two sets of measurements with delivery tube lengths of $6D$ and $1.75D$, respectively. When comparing with the cooling effectiveness measurements of Sinha et al. [14] with a $1.75D$ long delivery tube and blowing ratio $M=0.5$, the correct delivery tube length was used in the calculations, and a large stagnation-type plenum was assumed in the computations upstream of the $1.75D$ delivery tube, with the plenum fed by air streams flowing parallel to the main crossflow. When comparing with the $6D$ delivery tube measurements of Lavrich and Chiappetta [13], instead of extending the delivery tube to be $6D$ long (due to the associated need for increasing the number of grid points significantly, and the limitations in the available computing resources), the delivery tube was maintained at $1.75D$, and mean velocities at the tube inlet were specified from a RANS calculation where a $6D$ long delivery tube fed by a large cylindrical plenum (as in the experiments) was used. Since LES requires the specification of instantaneous velocities, turbulent velocity fluctuations were added to the mean velocities. The velocity fluctuations were generated using a Gaussian random number generator (Box-Muller algorithm) with a variance corresponding to the RANS-computed turbulent kinetic energy.

The top boundary of the computational domain (located $4D$ from the surface) is treated as freestream boundary. At the inlet, a fully developed turbulent profile (1/7th law, boundary layer thickness $\sim1D$) is specified from the experimental data. At the outflow, a convective boundary condition is used where the convection speed is obtained from the mass flux balance. The spanwise direction (Z) is assumed to be periodic.

Results

Comparisons With Measurements. To validate the LES calculation procedure, the time-averaged LES results are compared with the velocity measurements of Lavrich and Chiappetta [13] and the film-cooling effectiveness data of Sinha et al. [14] Figures 2 and 3 present the velocity comparisons for blowing ratios (M) of 0.5 and 1.0, respectively. The streamwise (U) and vertical (V) components of the velocity are shown along the spanwise centerplane $(Z/D=0)$ at three axial locations $(X/D=0,\ 5,$ and $10)$, while the spanwise (W) component of velocity is presented at $Z/D=0.5$, which corresponds to the spanwise edge of the hole. The time-averaged statistics is obtained as the run-time average from the computations over approximately ten flow-through time periods (flow-through time is the time taken by the cross-flow to sweep the computational domain from the inlet plane to the exit plane). The velocity predictions at both blowing ratios are generally in good agreement with the experimental data. At $X/D=5$, the streamwise velocity underpredicts the measured data particularly for $M=1.0$. However, the spanwise and vertical velocity components are in excellent agreement with the data. These velocity components play a critical role in the spanwise and vertical penetration of the jet, respectively, and the good agreement with the data at $M=0.5$ and $M=1.0$ provides a measure of validation for the LES calculations.

Predictions of the centerline film-cooling effectiveness at a blowing ratio of 0.5 are shown in Fig. 4. Also shown are the data of Sinha et al. [14] at the same blowing ratio. In both experiments

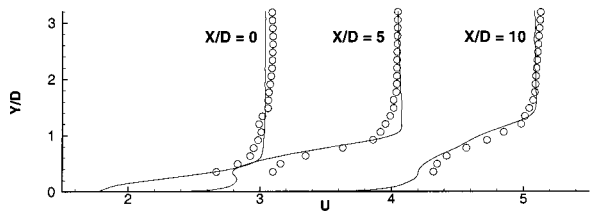

a) Streamwise component of velocity at Z/D = 0

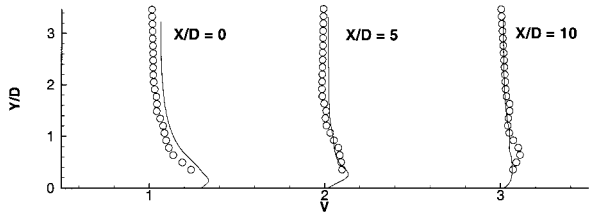

b) Vertical component of velocity at Z/D = 0

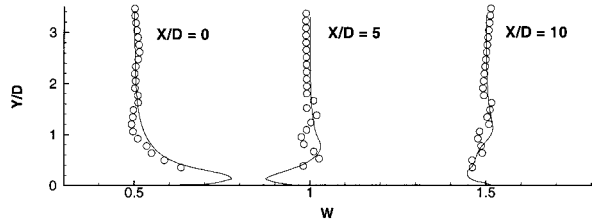

c) Spanwise component of velocity at Z/D = 0.5

Fig. 2 Comparison of predicted and measured (Lavrich and Chiapetta [13]) velocities at a blowing ratio $M=0.5$. (*a*) Streamwise component of velocity at $Z/D=0$. (*b*) Vertical component of velocity at $Z/D=0$. (*c*) Spanwise component of velocity at $Z/D=0.5$.

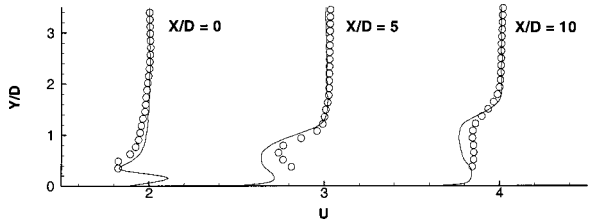

a) Streamwise component of velocity at Z/D = 0

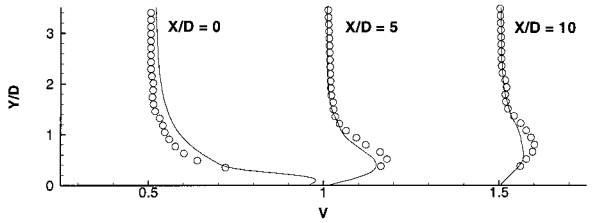

b) Vertical component of velocity at Z/D = 0

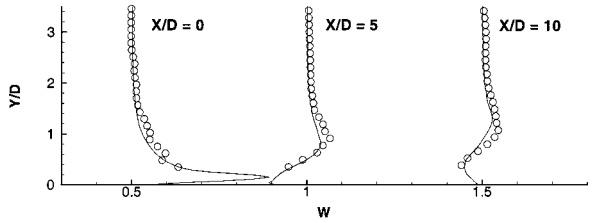

c) Spanwise component of velocity at Z/D = 0.5

Fig. 3 Comparison of predicted and measured (Lavrich and Chiapetta [13]) velocities at a blowing ratio $M=1.0$. (*a*) Streamwise component of velocity at $Z/D=0$. (*b*) Vertical component of velocity at $Z/D=0$. (*c*) Spanwise component of velocity at $Z/D=0.5$.

and computations the coolant delivery tube length was the same and equal to $1.75D$. The agreement between the predictions and the data is excellent with the predicted profile lying virtually on top of the data. The good agreement between the cooling effectiveness predictions and the data again confirms the predictive accuracy of LES.

Identification of Coherent Structures. The primary coherent structures for jets in crossflow (JICF) reported in the literature are the counter-rotating vortex pair (CVP), the horseshoe vortex, the upright wake vortices, and the jet-shear layer vortices. Most of these structures have been identified experimentally for normal jets injected at high blowing ratios, and the flow structures have been visualized using smoke-wire or dye-injection techniques (Fric and Roshko [15]; Kelso et al. [16]). There have been no studies, either experimental or computational, that have reported on the flow structures associated with an inclined jet injected into a crossflow at a moderate blowing ratio. Since inclined jets are of primary interest in film cooling, the present study attempts to identify the key flow structures and their dynamics for an inclined coolant jet at a moderate blowing ratio ($M=1.0$).

To simplify the understanding of the unsteady dynamics, different components of the vorticity field are presented at respective projection planes in Figs. 5(*a*)–5(*d*). The spanwise vorticity component ω_z at $Z/D=0$ shows shear layer or roller vortices (negative vorticity patches) along the leeward edge of coolant jet [Fig. 5(*a*)]. These roller vortices are shed regularly into the wake region and are convected downstream. The origin of the roller vortices appear to be linked to the corresponding boundary layer vorticity exiting the coolant hole. Vorticity generated along the windward surface of hole delivery tube is seen to be quickly dissipated. The absence of such rib- or roller-shaped vortices at the windward edge of the jet is primarily associated with the inclined jet injection, due to which the crossflow partially blocks the windward portion of the jet vortex ring issuing out of the delivery tube boundary layer. Note that no evidence of a horseshoe vortex is seen upstream of the inclined jet. This is in contrast to the normal jet injection studies (Fric and Roshko [15], Muldoon and Acharya [17]) where a horseshoe vortex pair was clearly generated immediately upstream of the jet hole. Inclining the jet reduces the pressure gradients immediately upstream of the hole exit that are responsible for the formation of the horseshoe vortex.

To visualize the upright vortices in the wake region, the vertical component ω_y is presented at a plane just above the surface ($Y/D=0.01$) in Fig. 5(*b*). In the near-wake region, a symmetric vortex pair, with opposite vorticity on either side of the centerline, is observed. This is clearly in contrast with the wake of a bluff body where the vortices are shed alternately on either side of the centerline, and positive and negative vortices are shifted in the streamwise direction relative to each other. Fric and Roshko [15] attribute the origin of these wake upright vortices to the entrainment and reorientation of the crossflow boundary layer in the wake region. Further downstream, the wake vortices are less organized, and seem to have spread outwards in the spanwise direction.

The streamwise vorticity component ω_x is presented at $X/D=5$ and 10 [Figs. 5(*c*)–5(*d*)] to illustrate the development of the counter-rotating vortex pair. This coherent structure persists in the far field of the jet, and is the only dominant organized pattern that

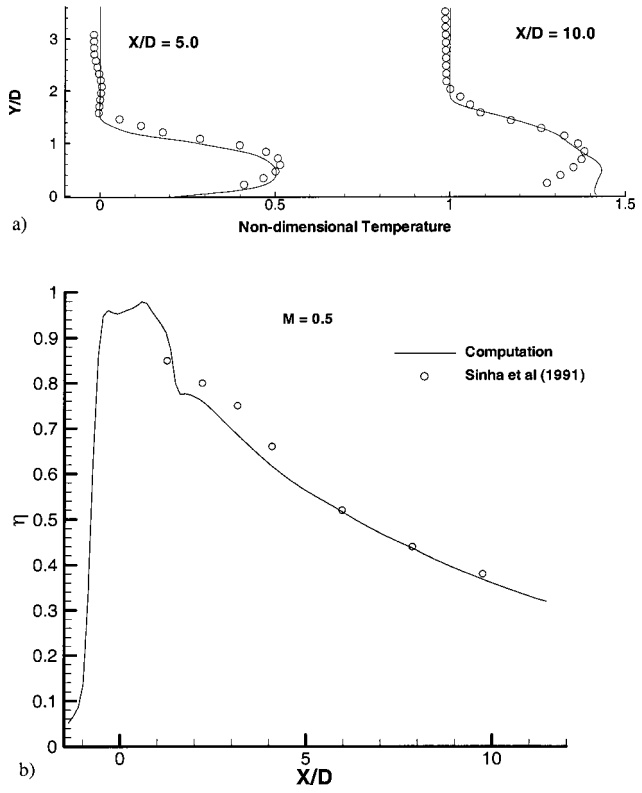

Fig. 4 Comparison of (*a*) predicted non-dimensional temperature with experimental data of Lavrich and Chiapetta [13] at $M=1.0$ and (*b*) predicted centerline film-cooling effectiveness (lines) with experimental data (symbols) of Sinha et al. [14] at $M=0.5$

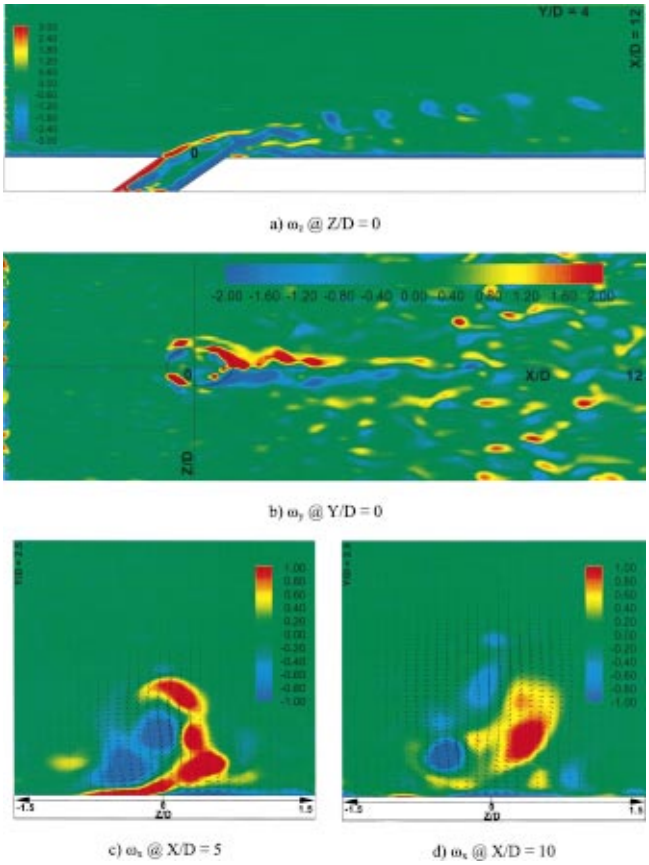

Fig. 5 (Color) Components of the instantaneous vorticity field on different projection planes ($M=1.0$)

can be observed in the time-averaged mean velocity field. The origin of the CVP is associated with the vorticity along the spanwise edges of the exiting coolant jet boundary layer. Figures 5(*c*) and 5(*d*) show that the instantaneous CVPs are somewhat asymmetric in nature, and consist of patches of positive and negative vorticity. When time averaged, a symmetric and organized CVP is observed.

Despite the large body of literature dealing with JICF, there is still no consensus on the generation mechanisms and evolutionary dynamics of the coherent structures (Fric and Roshko [15]; Eiff and Keffer [18]; Kelso et al. [16]; Blanchard et al. [19]). In an attempt to explain the flow physics better, coherent structures are extracted here using positive isosurfaces of the Laplacian of the pressure field (Wray and Hunt [20]; Tanaka and Kida [21]; Dubief and Delcayre [22]). Since the vortex cores are associated with strong vorticity and local pressure minima, it can be readily shown that positive surfaces of the Laplacian of pressure [$p_{,kk}=(\omega_i\omega_i)/2-S_{ij}S_{ji}$] can be used to identify coherent structures. For incompressible flows, $p_{,kk}$ is also directly related to the second invariant of the velocity gradient tensor. In Figs. 6 and 7, the isosurface corresponding to a positive value of 0.7 (of $p_{,kk}$) is plotted, and yields packets of hairpin coherent structures. Therefore, a coherent hairpin structure is identified here as the primary large-scale structure associated with the JICF. The evolution of this hairpin structure can explain the dynamics of the coherent eddies, and its structure projected on different planes can be related to the various vortical features observed in Fig. 5. Based on the present simulations, it is our premise that the various structures identified in Fig. 5 are all related to the evolution, growth and transport of the hairpin structures, and are not isolated, disparate structures with individual origins.

To explain the morphological details of the hairpin coherent structure, and its association with the various vortical structures identified in Fig. 5, a single hairpin vortex structure is presented in Fig. 6, along with several projected views and the corresponding vorticity in the X-Z, Y-Z, and X-Y planes. Superimposed on the hairpin structure are the velocity vectors at $X/D=5.7$, and the isosurface of helicity ($=U_i\omega_i$) associated with the legs of hairpin structure (shown as blue and red surfaces). Although helicity is a non-Galilean invariant property, it can be used to provide details of the flow physics in inertial frames (as is the case with present

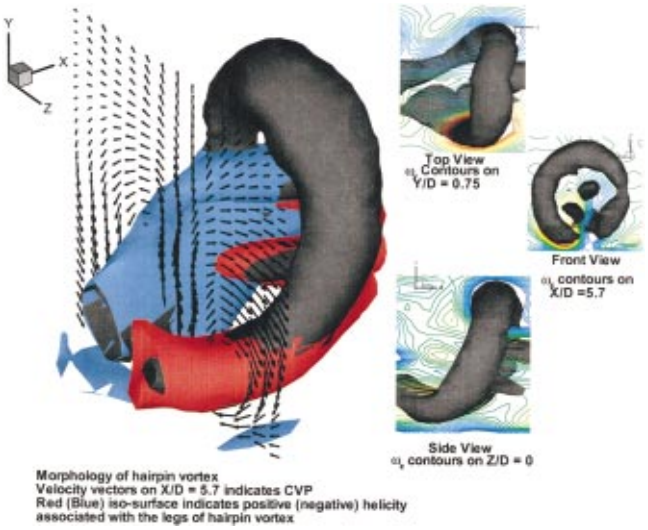

Fig. 6 (Color) Details of the flow field in the vicinity of a hairpin vortex ($M=1.0$)

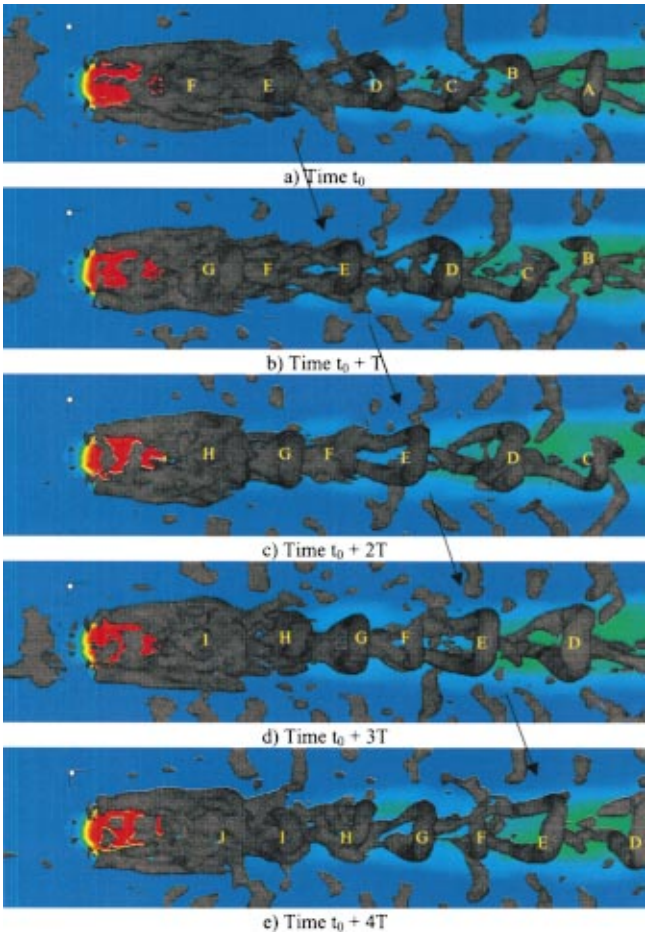

Fig. 7 (Color) Unsteady dynamics of coherent structures and their influence on wall heat transfer at different time instants (*a*) t_0 (arbitrary), (*b*) t_0+T, (*c*) t_0+2T, (*d*) T_0+3T, and (*e*) t_0 at $4T$. The time gap T is equal to 300 time steps ($=1.5D/U_j$). Arrows are tracking hairpin E from one snapshot to another ($M=1.0$).

computation). It provides the sense of rotation of fluid parcels as they move along with streamlines. The streamwise CVP is clearly associated with the horizontal legs (parallel to the surface) of hairpin structures. At almost all time instances, these legs are more or less located at similar (Y, Z) coordinates at a specific X/D plane. Therefore, time-averaging will distinctly capture the CVP as in many experimental and steady RANS studies. The helicity contour as well as the velocity vectors at the $X/D=5.7$ plane clearly define the CVP whose core is centered along the horizontal legs of the hairpin. The CVP structure is also seen in the ω_x contours on the projected plane at $X/D=5.7$ (front view), where the two legs of the hairpin structure are associated with streamwise vorticty of the opposite sign, and these are somewhat asymmetric in nature as seen in Fig. 5(*c*).

In the XZ projection plane (normal to the vertical direction, top view in Fig. 6), the wall normal vorticity is clearly associated with the upright legs of the hairpin structures. These upright legs are therefore most likely to be representative of the wake vortices observed in the flow visualization pictures of Fric and Roshko [15] and Kelso et al. [16]. These upright leg structures are oriented nearly parallel to the Y-Z plane, and help explain the symmetric shedding of vortices in the jet wake seen in Fig. 5(*b*). As noted earlier, this behavior is in distinct contrast to the alternate shedding of vortices behind a solid cylinder (or any bluff body). Note that these upright legs of the hairpin structures entrain flow from the crossflow boundary layer as they rotate in a horizontal plane normal to the surface. The entrained flow is then pulled upwards along the hairpin structure. This observation of crossflow entrainment and reorientation is consistent with the flow visualization studies of Fric and Roshko [15], who postulated this mechanism to be the origin of the wake vortices. The present simulations, however, reveal that the wake vortices are intrinsically related to the development of the hairpin structure, and the crossflow entrainment and reorientation are a consequence of the hairpin structure dynamics.

The train of roller vortices presented in Fig. 5(*a*) is also related to the hairpin structure. In fact it represents the signature of the heads of the various hairpin coherent structure packets in the wake region (see Fig. 7). The side view and the superimposed ω_z contoursshown in Fig. 6 clearly show that the hairpin head is associated with strong negative ω_x whose values match those of the roller vortices shown in Fig. 5(*a*). The entrainment of the crossflow fluid around the head of hairpin structures is expected to be a dominant contribution to the mixing processes in the wake region (shown in Fig. 9). Note that the velocity field induced by the arch of the hairpin (head and upright legs) generates a backflow between the legs and below the head of the hairpin. This backflow generated is the main mechanism associated with the velocity deficit in the wake region of coolant jet.

From the observations made in Figs. 5 and 6, it is clear that the structure and dynamics of the hairpin vortices can be used to rationalize many of the reported observations on flow structures in JICF. The hairpins are associated with Lagrangian disturbances issuing out of the jet representing hairpin-shaped loci of local pressure minima. The streamwise spacing of these disturbances and the Strouhal frequency of shedding of hairpin vortices can be related through the convection speed of these structures. The jet fluid wraps around the head and and the streamwise-oriented legs of these structures. The crossflow boundary layer is entrained by the horizontal and upright legs of the hairpins and is lifted upright (i.e., reoriented) around the upright legs of the hairpin structures. The experimental visualizations and measurements reported in the literature support the unified mechanism related to hairpin structures that has been discussed in this paper (Smith et al. [23]; Eiff and Keffer [18]; Blanchard et al. [19]; Rivero et al. [24]; Camussi et al. [25]; Fric and Roshko [15]; Kelso et al. [16]).

Dynamics of the Hairpin Structures. Hairpin structures evolve while convecting downstream in the wake region and control the entrainment and mixing of the crossflow fluid with the injected coolant fluid. Hairpin structures entrain crossflow fluid into the wake region of jet and can lead to the formation of ''hot spots'' on the film-cooled surface. The surface temperature of the adiabatic solid surface (at $Y/D=1.0$) is a measure of the film-cooling effectiveness. A time sequence of the coherent structures superimposed on the corresponding surface temperature is shown in Figs. 7(*a*)–7(*e*). The coherent structures are represented as a positive isosurface of the pressure Laplacian ($=0.7$) while the contours of the nondimensional temperature on the wall ($Y/D=0$) span the range from 1 (red) to 0 (blue). Since the jet fluid is heated in the present simulations, the wall temperature values can be directly interpreted as cooling effectiveness (with 1 representing perfect coolant coverage and 0 representing no coverage).

At $t=t_0$, five hairpin structures can be clearly identified (A–E), while hairpin structure F is in a nascent stage. Hairpins are labeled alphabetically in the time sequence of their generation. Thus, the last coherent structure in computational domain (exit plane $\sim 7D$) is labeled A and this convention is followed while identifying successive hairpins located closer to the coolant hole exit. Also, note that some of the hairpin structures (C and F) are not extracted completely by a single value of the pressure Laplacian isosurface. In examining the wall temperature values, low cooling effectiveness can be seen immediately below hairpin D (and upstream of it, which is obscured by the hairpins E and F) as evidenced by the blue color (low film-cooling effectiveness) in this region. This is associated with jet lift-off [see Figs. 8(*a*) and 8(*b*)] immediately downstream of the coolant hole. However, it should be noted that

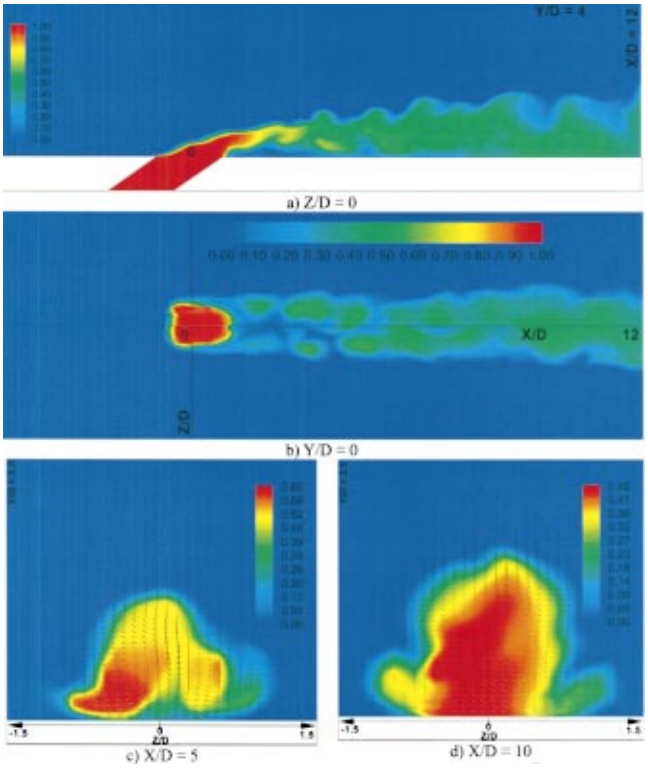

Fig. 8 (Color) Instantaneous non-dimensional temperature field on different projection planes ($M=1.0$)

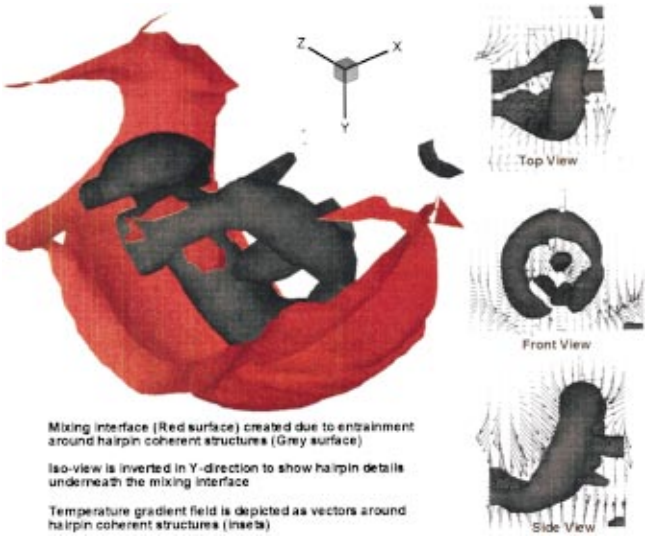

Fig. 9 (Color) Details of the "mixing interface" created by the hairpin coherent structure ($M=1.0$)

the horizontal legs of hairpin D are closer to the surface, and provide higher cooling effectiveness. Further downstream (beneath hairpins A–C), the coolant jet is attached to the surface, and higher cooling effectiveness values are obtained in the entire jet region.

At $t=t_0+T$, hairpin A has left the domain. The morphology of hairpins B and C have changed, while hairpin D has grown in size. Note that D in Fig. 8(*b*) is roughly at the same location as C in Fig. 8(*a*), but the cooling effectiveness at this spot is not exactly the same at the two time instances, reflecting the unsteadiness in the flow field. Further, as hairpin D traverses to the right, and moves closer to the surface, cooling effectiveness below the hairpin increases and high effectiveness values can now be seen in the core regions of the hairpin. Evidence of increased cooling effectiveness generating beneath the legs of hairpin E and head of hairpin F can now be seen. However, in the core regions of hairpin E, the effectiveness is low. Hairpin F has developed further and is followed by another hairpin G (at a nascent stage).

At $t=t_0+2T$, hairpin B has left the computational domain and hairpin C has moved close to the exit plane. Hairpin D has grown further in size and is associated with high cooling effectiveness. Hairpin E has grown in size and convected downstream. The low effectiveness region beneath it has not been ameliorated, although there is evidence of increased film-cooling effectiveness below the horizontal legs of hairpins E and F. Hairpin G has evolved to a well-formed structure and is followed closely by hairpin H.

At $t=t_0+3T$, hairpin C has left the computational domain. Hairpin E has convected to the right and has grown in size. There is evidence of increased cooling effectiveness below hairpin G and is presumably due to the downward migration of the G hairpin at this time instance. The cooling effectiveness below G is higher than the cooling effectiveness at this location at earlier time instances, and is a reflection of a low-frequency unsteadiness associated with the evolution and transport of the hairpin structures. In fact hairpin G appears to have lower effectiveness below it compared to hairpin F. Hairpin H closely follows hairpin G and there is another hairpin I forming around $1D$ downstream of the coolant hole exit.

At $t=t_0+4T$, hairpin D is at exit plane. The higher cooling effectiveness associated with hairpin G in Fig. 7(*d*) appears to be transported along with it in the next time instance [Fig. 7(*e*)]. Note that hairpin H is now at the same location as G in Fig. 7(*d*), but has a lower cooling effectiveness. It is interesting to note that generally large hairpins are followed by small hairpins that do not grow in size (there is evidence of a small ''unlabeled'' hairpin between D and E in all time instances). As explained earlier, large hairpin structures can generate substantial backflow and create velocity deficit in the wake region.

From Fig. 7, it can be clearly concluded that the cooling effectiveness is intrinsically linked to the dynamics of the hairpin structures. When the hairpins are formed, high cooling effectiveness is first seen below the horizontal legs of the hairpin structures. As the hairpins convect downstream and move closer to the surface, higher cooling effectiveness is also observed in the core regions of the hairpin immediately below the roller vortices. The cooling effectiveness on the surface does vary with time and is dictated by the dynamics of the evolution and growth of the hairpin structures.

Passive Scalar (Temperature) Mixing. The details of instantaneous temperature field are given at several projected planes of the computational domain [Figs. 8(*a*)–8(*d*)]. The center plane corresponds to $Z/D=0.0$ and shows the mixing of the main flow (nondimensional temperature of 0) and the injected jet (nondimensional temperature of 1). The jet temperature drops rapidly in the downstream direction, as it entrains and mixes with the crossflow. The injected jet is lifted off the surface downstream of the injection, and there is crossflow fluid entrained beneath the jet. The billows in the coolant–crossflow interface correspond to the heads of hairpin coherent structures. The temperature distribution on the wall is shown in Fig. 8(*b*), and as noted earlier, this temperature distribution also corresponds to the film-cooling effectiveness values. Again, an immediate decrease in film-cooling effectiveness is seen just downstream of the jet injection and is due to the jet lifting off the surface. Note that downstream of the jet injection, high cooling effectiveness is first noticed along the spanwise edges of the jet. This is associated with the horizontal legs of the hairpin structures that are closer to the surface. Evidence of this was presented in Fig. 7 earlier. The coolant jet is closer to the wall at further downstream stations ($X/D>5.0$) leading to a recovery

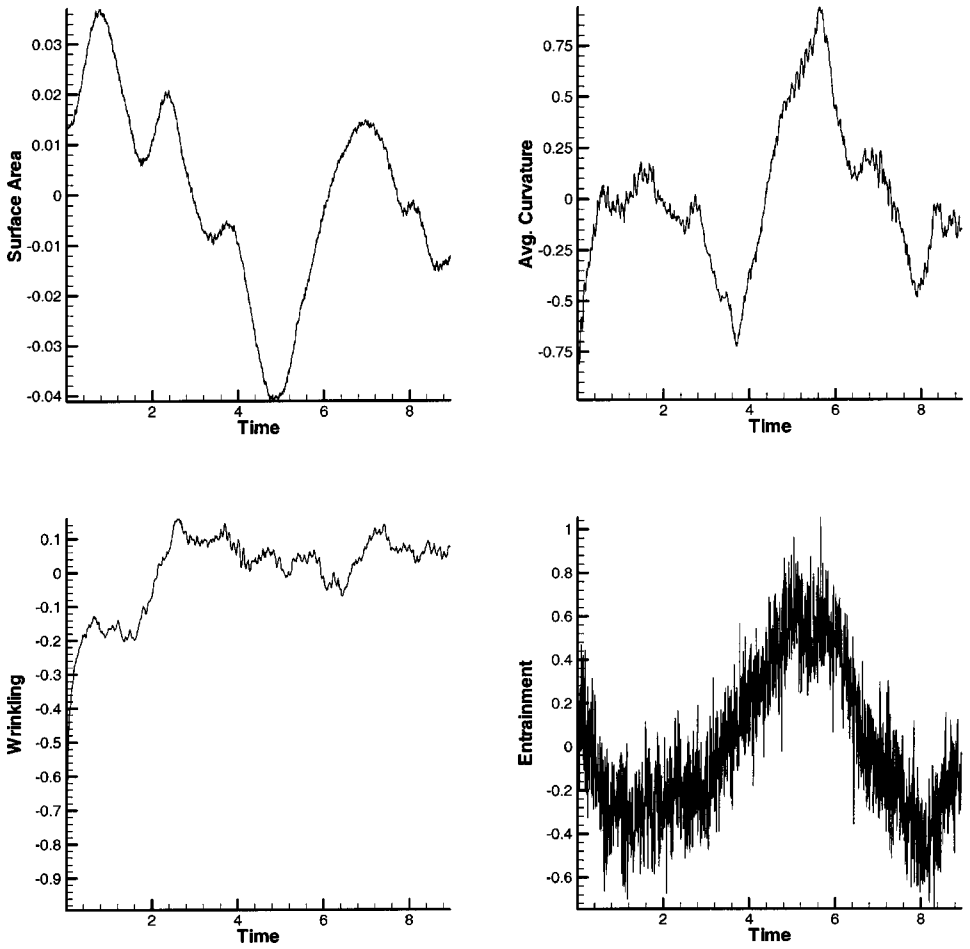

Fig. 10 Relative change in geometric properties from their respective mean value over observation period. (*a*) Surface Area. (*b*) Average Curvature. (*c*) Wrinkling. (*d*) Entrainment across the "mixing interface" versus time ($M=1.0$).

in film-cooling effectiveness in the entire jet region. The instantaneous temperature distributions at two X/D locations ($X/D=5$ and 10) are shown in Fig. 8(*d*), and reflect the vertical and lateral penetration of the jet. The coolant jet is observed to have a well-defined kidney-shaped structure with local maxima close to the core of the CVP and large gradients near the crossflow-coolant interface. The cross-plane mixing of scalars leads to the decrease in scalar value in the core of coolant jet at stations farther downstream. Close to the surface, there seems to be lobelike extensions of the CVP. These are associated with the enhanced scalar mixing induced by the horizontal legs of the hairpin vortical structures.

To further investigate the mixing and entrainment process due to a single hairpin structure, an isosurface of the scalar dissipation rate ($=\Theta_{,k}\Theta_{,k}$) is extracted and plotted in Fig. 9. The value ($=0.01$) is chosen such that this isosurface (shown in red) forms an envelope over a hairpin coherent structure (shown in gray). However, this measure of scalar dissipation rate does not account for subgrid stirring and mixing of scalar field and should be treated as a macroscale mixing measure (Southerland et al. [26]). Also the scaling factor [$=1/(\mathrm{Re}\,\mathrm{Pr})$] is omitted from the definition of the scalar dissipation rate since it does not change any interpretation of the results.

The contour of the scalar dissipation isosurface clearly follows the contour of the hairpin structure, indicating that scalar mixing is strongly influenced by the entrainment and mixing across the hairpin structures. The gradient of the scalar field ($=\Theta_{,i}$) is presented as vectors (representing heat flux vectors) on different projections of the hairpin structure. In the top view, these vectors are seen to be directed toward the region beneath the head of hairpin structure. Similarly, the vectors converge beneath the hairpin head in the side view. Clearly, the direction of heat flux vectors indicates that the heat flux is directed toward the core of the hairpin, and that scalar mixing is enhanced beneath the head of hairpin and between its upright legs. Absence of scalar gradients in the crossflow is observed in the front view representing a cross-stream projection across the hairpin legs.

A control volume of the size of a hairpin coherent structure is defined around $X/D=5$ over the film-cooled surface. As packets of hairpin structures convect through this control volume, they deform the scalar-dissipation isosurface. The geometric properties of this "mixing interface" are presented as a function of time in Figs. 10(*a*)–10(*d*). Different geometric properties such as the surface area of mixing interface [Fig. 10(*a*),] average curvature [Fig. 10(*b*),] wrinkling of the interface [Fig. 10(*c*),] and entrainment across the interface [Fig. 10(*d*)] are evaluated (Geurts [27]). The surface area of the "mixing interface" increases whenever the head of the hairpin structure is crossing through the fixed control volume. Hairpin packets usually are formed as clusters with smaller hairpins following large hairpin coherent structure and there is generally some gap between such clusters (Fig. 7). Such clusters would lead to peaks and valleys in the surface area of the "mixing interface" with a local minimum between such clusters [Fig. 10(*a*).] Note that local peaks of the surface area diminish in size as the hairpin cluster passes beneath this interface, suggesting that growth of following hairpin vortices may be hindered by the leading hairpin vortex in the cluster. The average curvature of this

surface (defined as the surface integral of local curvature) changes substantially (from -75% to $+75\%$ of the mean value) during this time interval corresponding to the passage of the hairpin vortex. The event that corresponds to this change in curvature is the relaxation of the ''mixing interface'' between two hairpin clusters followed by its subsequent stretching by the following hairpin cluster. The entrainment across this interface can be evaluated approximately from the difference in flux contributions using the surface integral over the control volume that encompasses the ''mixing interface'' around hairpin structures [This is simply a result of the Gauss divergence theorem to evaluate surface integral in a divergence-free (incompressible) flow field]. The change in curvature is associated with the reversal of the entrainment process across the interface [Fig. 10(*d*).] Also, the entrainment achieves a local maximum over the time interval between the passage of the hairpin clusters. Wrinkling (defined as the surface integral of absolute value of local curvature) is a relatively stable geometric property (usually varies between -10% to $+10\%$ of average mean value). It is a measure that is insensitive to ''convexity'' or ''concavity'' of mixing interface and implies that this interface maintains corrugations at almost all times. It is an important measure because small-scale mixing is insensitive to the curvature of mixing fronts and depends only on the absolute value of the curvature.

Conclusion

Large eddy simulations are performed for a simplified geometry representing film-cooling of a gas turbine blade surface and simulates an experimental study of Lavrich and Chiappetta [13]. The following remarks summarize this study:

- Comparison of time-averaged LES predictions with experimental data of Lavrich and Chiappetta [13] shows the adequacy of the LES approach for film-cooling flows. Few discrepancies are noted at stations farther downstream. Insufficient averaging of time-dependent fields as well as the uncertainty associated with boundary conditions can be regarded as the main reasons for these deviations.
- Flow physics is explained in terms of components of vorticity field on respective projection planes in the computational domain. All previously reported vortical structures, i.e., CVP, roller vortices, and upright wake vortices are identified (Kelso et al. [16]; Haven and Kurosaka [28]; Fric and Roshko [15]). Jet boundary layer vorticity is identified as the source of these vortices in the inclined jet in crossflow.
- Coherent structure extraction from instantaneous three-dimensional fields revealed packets of hairpin-shaped vortices in the coolant jet. A unified perspective of previously reported vortices on different projection planes in this flow field is presented in terms of these basic hairpin coherent structures. The CVP is shown to be associated with the legs of hairpin structure while roller vortices are linked to the head of hairpin structures. The upright legs are identified as the inception sites for wake vortices. Experimental visualizations and different coherent structure extraction techniques support this perspective (Smith et al. [23]; Eiff and Keffer [18]; Blanchard et al. [19]; Rivero et al. [24]; Camussi et al. [25]).
- The dynamics of packets of hairpins in the wake region of injected jet and their influence on the unsteady wall heat transfer is presented. Generation of ''hot spots'' and their migration on the film-cooled surface is associated with the entrainment due to hairpin structures. The transient behavior of wall heat transfer under the influence of coherent structures reveals the inadequacy of any steady state RANS simulation even if it matches time-averaged film-cooling effectiveness.
- Several geometric properties such as surface area, average curvature, and wrinkling of a ''mixing interface'' around hairpin coherent structures are presented to illustrate and quantify their impact on entrainment rates and mixing processes in the wake region.
- Scalar field distribution on different projection planes of computational domain revealed correspondence with large-scale coherent structures. Details of gradients of the scalar field around a hairpin coherent structure showed the dynamical significance of such large-scale vortices on the mixing process.

Acknowledgments

The authors would like to thank Mr. Asif Hoda for providing the RANS solution for LES boundary conditions and Dr. Raymond Jones for several fruitful discussions.

Nomenclature

U_i = Filtered velocity field
p = Pressure field divided by constant density
τ_{ij} = Subgrid scale (SGS) stress tensor
q_j = Subgrid scale (SGS) scalar flux vector
f_i = Body force terms arising due to immersed boundary
Θ = Nondimensional temperature $[\Theta=(T-T_\infty)/(T_j-T_\infty)]$
T_j = Coolant-jet temperature (dimensional)
T_∞ = Crossflow temperature (dimensional)
Φ = Indicator function
ν = Kinematic viscosity of fluid
Re = Reynolds number $(=U_\infty D/\nu)$
Pr = Prandtl number $(=0.71)$
D = Jet diameter
L = Coolant delivery tube length
M = Blowing ratio
SDR = Scalar dissipation rate $(=\Theta_{,k}\Theta_{,k})$
X = Streamwise direction
Y = Vertical direction (normal to the film-cooled surface)
Z = Spanwise direction (periodic)

References

[1] Garg, V. K., and Gaugler R. E., 1994, ''Prediction of Film Cooling on Gas Turbine Airfoils,'' ASME paper no. 94-GT-2.
[2] Garg, V. K., and Gaugler R. E., 1995, ''Effect of Velocity and Temperature Distribution at the Hole Exit on Film Cooling of Turbine Blades,'' ASME paper no. 95-GT-2.
[3] Berhe, M. K., and Patankar, S., 1996, ''A Numerical Study of Discrete-Hole Film Cooling,'' ASME paper 96-WA/HT-8.
[4] Walters, D. K. and Leylek, J. H., 1997, ''A Detailed Analysis of Film-Cooling Physics Part 1: Streamwise Injection with Cylindrical Holes,'' ASME paper no. 97-GT-269.
[5] Lakehal, D., Theodoridis, G. S., and Rodi, W., 1998, ''Computation of Film Cooling of a Flat Plate by Lateral Injection from a Row of Holes,'' Int. J. Heat Fluid Flow, **19**, pp. 418–430.
[6] Acharya, S., Tyagi, M., and Hoda, A., 2001, ''Flow and Heat Transfer Predictions for Film Cooling,'' Heat transfer in gas turbine systems, Ann. N.Y. Acad. Sci., **934**, pp. 110–125.
[7] Hoda, A., Acharya, S., and Tyagi, M., 2000, ''Predictions of a Jet-In-Crossflow with Reynolds Stress Transport Models and Large Eddy Simulations,'' ASME-IGTI00, Munich.
[8] Vreman, B., Geurts, B. J., and Kuerten, H., 1994, ''On the Formulation of the Dynamic Mixed Subgrid Scale Model,'' Phys. Fluids, **6**, pp. 4057–4059.
[9] Tyagi, M., and Acharya, S., 2001, ''Flow and Heat Transfer Predictions for the Film-Cooling Flow Using Large Eddy Simulations,'' *DNS/LES Progress and Challenges*, C. Liu, L. Sakell, and T. Beutner, eds., Gryden Press, Columbus, OH, pp. 799–806.
[10] Yusof, J. M., 1996, ''Interaction of Massive Particles with Turbulence,'' Ph.D. dissertation, Cornell University, Ithaca, NY.
[11] Fadlun, E., Verzicco, R., Orlandi, P., and Yusof, J. M., 2000, ''Combined Immersed Boundary Finite Difference Methods for Complex Flow Simulations,'' J. Comput. Phys., **161**, pp. 35–60.
[12] Moin, P., Squires, K., Cabot, W., and Lee, S., 1991, ''A Dynamic Subgrid-Scale Model for Compressible Turbulence and Scalar Transport,'' Phys. Fluids A, **11**, pp. 2746–2757.
[13] Lavrich, P. L., and Chiappetta, L. M., 1990, ''An Investigation of Jet in a Cross Flow for Turbine Film Cooling Applications,'' United Technologies Research Center, UTRC Report No. 90-04.
[14] Sinha, A. K., Bogard, D. G., and Crawford, M. E., 1991, ''Film-Cooling Effectiveness Downstream of a Single Row of Holes with Variable Density Ratio,'' ASME J. Turbomach., **113**, pp. 442–449.
[15] Fric, T. F., and Roshko, A., 1994, ''Vortical Structure in the Wake of a Transverse Jet,'' J. Fluid Mech., **279**, pp. 1–47.

[16] Kelso, R. M., Lim, T. T., and Perry, A. E., 1996, ''An Experimental Study of Round Jets in Crossflow,'' J. Fluid Mech., **306**, pp. 111–144.
[17] Muldoon, F., and Acharya, S., 1999, ''Numerical Investigation of the Dynamical Behavior of a Row of Square Jets in Crossflow Over a Surface,'' ASME-IGTI99.
[18] Eiff, O. S., and Keffer, J. F., 1997, ''On the Structures in the Near-Wake Region of an Elevated Turbulent Jet in a Crossflow,'' J. Fluid Mech., **333**, pp. 161–195.
[19] Blanchard, J. N., Brunet, Y., and Merlen, A., 1999, ''Influence of a Counter Rotating Vortex Pair on the Stability of a Jet in a Crossflow: An Experimental Study by Flow Visualizations,'' Exp. Fluids, **26**, pp. 63–74.
[20] Wray, A. A., and Hunt, J. C. R., 1989, ''Algorithms for Classification of Turbulent Structures,'' *Topological Fluid Mechanics*, H. K. Moffat and A. Tsinober, eds., Cambridge University Press, Cambridge, UK, pp. 95–104.
[21] Tanaka, M., and Kida, S., 1993, ''Characterization of Vortex Tubes and Sheets,'' Phys. Fluids A, **5**, pp. 2079–2082.
[22] Dubief, Y., and Delcayre, F., 2000, ''On Coherent-Vortex Identification in Turbulence,'' J. Turbulence, **1**, pp. 1–22.
[23] Smith, C. R., Walker, J. D. A., Haidari, A. H., and Soburn, U., 1991, ''On the Dynamics of Near-Wall Turbulence,'' Philos. Trans. R. Soc. London, **336**, pp. 131–175.
[24] Rivero, A., Ferre, J. A., and Giralt, F., 2001, ''Organized Motions in a Jet in Crossflow,'' J. Fluid Mech., **444**, pp. 117–149.
[25] Camussi, R., Guj, G., and Stella, A., 2002, ''Experimental Study of a Jet in Crossflow at Very Low Reynolds Number,'' J. Fluid Mech., **454**, pp. 113–144.
[26] Southerland, K. B., Frederikson, R. D., Dahm, W. J. A., and Dowling, D. R., 1995, ''Comparisons of Mixing in Chaotic and Turbulent Flows,'' *Chaos Applied to Fluid Mixing*, Pergamon, Oxford, UK, pp. 313–345.
[27] Geurts, B. J., 2002, ''Buoyant Turbulent Mixing in Shear Layers,'' *Advances Turbulence IX, Proceedings of the 9th European Turbulence Conference*, I. P. Castro, P. E. Hancock, and T. G. Thomas, eds., CIMNE, Barcelona.
[28] Haven, B. A., and Kurosaka, M., 1997, ''Kidney and Anti-Kidney Vortices in Crossflow Jets,'' J. Fluid Mech., **352**, pp. 27–64.

Influence of Clocking and Vane/Blade Spacing on the Unsteady Surface Pressure Loading for a Modern Stage and One-Half Transonic Turbine

C. W. Haldeman

M. L. Krumanaker

M. G. Dunn

Gas Turbine Laboratory,
The Ohio State University,
Columbus, OH 43235

This paper describes pressure measurements obtained for a modern one and one-half stage turbine. As part of the experimental effort, the position of the high-pressure turbine (HPT) vane was clocked relative to the downstream low-pressure turbine (LPT) vane to determine the influence of vane clocking on both the steady and unsteady pressure loadings on the LPT vane and the HPT blade. In addition, the axial location of the HPT vane relative to the HPT blade was changed to investigate the combined influence of vane/blade spacing and clocking on the unsteady pressure loading. Time-averaged and time-accurate surface-pressure results are presented for several spanwise locations on the vanes and blade. Results were obtained at four different HPT vane-clocking positions and at two different vane/blade axial spacings for three (of the four) clocking positions. For time-averaged results, the effect of clocking is small on the HPT blade and vane. The influence of clocking on the transition ducts and the LPT vane is slightly greater (on the order of ±1%). Reduced HPT vane/blade spacing has a larger effect than clocking on the HPT vanes and blades (±3%) depending upon the particular surface. Examining the data at blade passing and the first fundamental frequency, the effect of spacing does not produce a dramatic influence on the relative changes that occur between clocking positions. The results demonstrate that clocking and spacing effects on the surface pressure loading are very complex and may introduce problems if the results of measurements or analysis made at one span or location in the machine are extrapolated to other sections. [DOI: 10.1115/1.1625398]

1 Introduction

The need for improved durability, reliability, maintainability, and affordability for current and future propulsion systems has motivated exploration of ways to significantly improve design tools. The design tools of choice are generally simplifications of much more exotic tools that have been shown to be ''acceptably'' valid. The rapid increase in computational capability, driven by the ability to operate many computers in parallel, has significantly reduced the real time required to obtain predictions for turbomachinery applications. This has challenged the experimentalists to produce data sets that duplicate the design parameters to the greatest degree possible. These data sets are then used for modeling, code validation, and code development purposes.

Clocking (or indexing) is the technique of locating a downstream vane (or blade) row in different circumferential positions relative to an upstream row. It has been hypothesized in the literature [1–3] that clocking can increase performance by properly placing the downstream airfoils in the wakes of the upstream airfoils. Huber et al. [1] experimented with the Space Shuttle main engine (SSME) alternate turbopump design (ATD) at NASA's Marshal Space Flight Center (MSFC). The ATD turbine is a dual-stage machine with an equal number of blades and vanes in each row (54 vanes, 50 blades). The rig was operated at the aerodynamic design point and at off design conditions. At the design point condition, the stage pressure ratio for the first stage turbine was about 1.25 ($P_{T,\mathrm{in}}/P_{s,\mathrm{out}}$) and the stage pressure ratio for the combined two-stage turbine was about 1.42 ($P_{T,\mathrm{in}}/P_{T,\mathrm{out}}$), according to Dunn and Haldeman [4], who performed measurements with a similar SSME turbopump design. Huber et al. [1] clocked the upstream vane relative to the downstream vane in six circumferential positions in order to arrive at their conclusions. They determined the stage efficiency by measuring the inlet and exit total pressures and temperatures, rotor speed, and torque. Using this technique, efficiency gain of 0.8% was achieved by locating the first-stage vane so that its wake would impinge the second-stage vane's leading edge. They also determined that the least efficient location for the second vane was in the middle of the passage. This finding was in agreement with the calculations performed by Dorney and Sharma [3], who also found that maximum efficiency is obtained when the first-stage vane wake is aligned with the leading edge of the second-stage vane. Compressors blades and vanes can be clocked as well as turbines, as has been shown by Dorney and Gundy-Burlet [5] and Barankiewicz and Hathaway [6]. Hsu and Wo [7] use an experimental compressor in a rotor/stator/rotor rig to demonstrate that clocking can reduce the blade unsteady loading. More recently, Hummel [8] described the results of a study looking at the flow field behind the rotor of a transonic high-pressure turbine stage. The analysis used a two-dimensional Navier-Stokes code and concentrated on the midspan region downstream of the rotor. A slightly different investigation was done by Reinmoller et al. [9] using a Fauvre-averaged Navier-Stokes formulation coupled with experimental measurements. In this case clocking variations of less than 1% were observed both numerically and experimentally.

The drive to reduce weight and cost of gas turbine engines has led to the reduction in the number of stages, reduced spacing between blade rows, and more highly loaded airfoils. Single stage high-pressure turbines are becoming a standard in the industry. As a result, airfoil loading has increased, causing secondary flows

Contributed by the International Gas Turbine Institute and presented at the International Gas Turbine and Aeroengine Congress and Exhibition, Atlanta, GA, June 16–19, 2003. Manuscript received by the IGTI December 2002; final revision March 2003. Paper No. 2003-GT-38724. Review Chair: H. R. Simmons.

and shocks that arise from transonic passage flows to become more significant. This has also increased the potential for aerodynamic losses. Because of these factors, vane-blade interaction has become a concern in designing an efficient and durable machine.

One of the most widely used data sets for this type of analysis (reported Refs. [10–13]) comes from a turbine stage designed by Allison and then transitioned to researchers at Calspan Corporation (now at The Ohio State University). The stage is ideally designed for code verification since it has three blades for every two vanes. In addition, the stage can be made to easily operate at a vane exit Mach number of 0.8 or 1.1 and the vane/blade spacing was easily changed over the range from 20% to 60% of vane axial chord by the simple insertion of axial spacers. Research in the area of vane/blade spacing is also being done at the von Karman Institute by Denos et al. [14], which also includes trailing edge injection from the high-pressure vane of a coolant flow being compared with effects from rotational speed and axial spacing. They find that coolant ejection and rotational speed do not effect the magnitude of the unsteady pressure forces on the leading edge of the rotor blade as much as axial spacing.

This measurement program was performed in close cooperation with the people developing the advanced computing codes at Pratt and Whitney and at the United Technologies Research Center as indicated by previous publications of a portion of the experimental results associated with this work by Clark et al. [15], Davis et al. [16], and Clark et al. [17]. This experimental program was initiated to examine vane/blade interactions from various perspectives. Time-averaged and time-resolved data (for both surface pressures and heat flux) was examined under varying spacing/clocking combinations and operating points. This paper deals specifically with clocking and vane/blade spacing effects on pressure loadings at design speed.

Authors often present clocking results in terms of performance gain or loss. As part of this study, the upstream and downstream total pressure and total temperature rakes were used to obtain an estimate of the influence of clocking on performance. However, the results are inconclusive and are not pursued here. This may be because the turbine is a transonic machine with a S-duct configuration between the HPT rotor exit and the LPT vane entrance, resulting in significant mixing out of the potential performance effect, already a small variation. It is important to note that the clocking and spacing results are discussed here for the first time and were not reported in the earlier papers mentioned above. Heat transfer results from this effort are presented in Krumanker et al. [18].

2 Experimental Rig and Methodology

The machine used for this study is an early design version of the high-pressure stage of the PW6000 engine, at that time referred to as MTFE (mid-thrust family of engines). It is a transonic, stage and a one-half turbine designed so that many different aspects of the flow physics could be investigated experimentally and thus used to calibrate computational codes. Clark et al. [15] used results from this stage to study the applicability of airfoil scaling, while Davis et al. [16] used the results to help in the calibration of a major CFD code under development at Stanford University, and Clark et al. [17] used the experimental results to redesign the HPT vane. The instrumentation, its calibration, and data reduction techniques used in this paper are important topics and are covered in depth by Krumanaker [19], but the key points are reproduced below.

2.1 Experimental Facility and Model. The facility used to perform this experiment was previously described in detail in Dunn et al. [20]. Thus, only a brief summary will be given here. Figure 1 is a sketch of the facility with a sample turbine stage. The experiments described here were performed with the facility operating in blowdown mode. That is, the copper diaphragms are removed and the combined driver and the driven tubes [the entire shock tube, 0.47-m (18.5-in.) diameter by 30.5-m (100-ft) long]

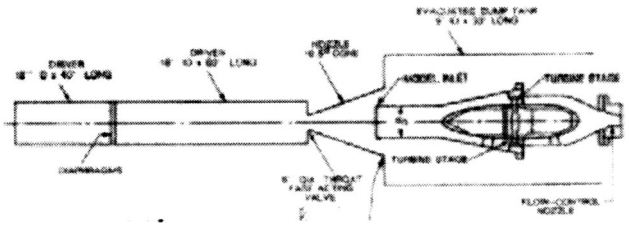

Fig. 1 Sketch of turbine stage located in OSU GTL shock tunnel

are pressurized with dry air to a predetermined pressure sufficient to produce the desired pressure at the turbine inlet. Pressure values are selected to duplicate the design flow conditions. The design flow function ($\dot{w}\sqrt{\theta}/\delta$), stage pressure ratio, and corrected speed are duplicated. In order to initiate an experiment the turbine is brought to approximately 98% of the desired physical speed in the evacuated test section immediately after the shock tube has been pressurized. A fast acting valve [0.254-m (10-in.) sleeve valve] initially separating the pressurized shock tube from the evacuated expansion nozzle is then opened (opening time on the order of 2 ms) to allow the test gas passage through the turbine stage. Utilizing the facility in this manner provides more test time than is available when operating in shock-tube mode and is significantly less expensive. However, this comes at a cost of a reduced total temperature making heat flux measurements on the low vane difficult. Thus, often the experiments are separated into those that can be done in a blowdown mode (aerodynamic measurements) and shock mode (heat-flux).

The turbine stage is housed in a device located in the expansion nozzle of the shock-tunnel facility as illustrated in Fig. 1. This device consists of an inlet duct, an exit nozzle designed to govern the flow through the turbine rig, a 200-channel slip ring to provide an electrical path to the laboratory data acquisition system, and an air motor drive system. A sketch of the stage and one-half turbine used for these measurements is shown in Fig. 2. The turbine configuration was 36 HPT vanes, 56 HPT blades, and 36 LPT vanes. The change in axial spacing was accomplished by removing a spacer located between the HPT vane and the HPT blade, as illustrated in Fig. 2. Removing the spacer creates a 22% reduction in axial gap between the HPT vane and HPT blade (from about 88% vane axial chord to about 69% vane axial chord). The rotating system remains fixed in space while the vane row is moved closer to the blade row. The axial distance between the HPT blade row and the LPT vane remains the same for both experimental conditions. The scale on the figure is intended to help orient the reader to the relative axial position of pressure transducers noted in various figures of the paper.

Surface-pressure measurements were performed for the shock-tube runs and were shown to be identical to those obtained for the blowdown runs. The time-averaged data comes directly from the

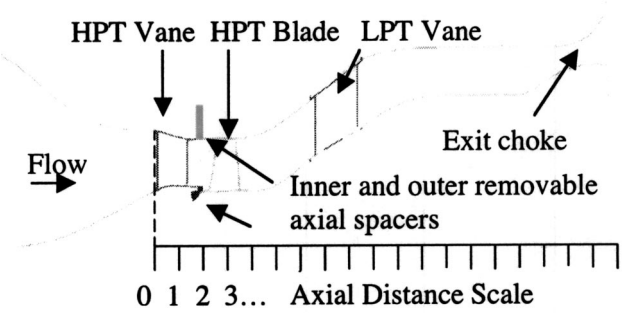

Fig. 2 Axial flow path of turbine stage

Table 1 Vane/blade interaction test matrix

Run no.	Vane/blade spacing	High vane clock position
4	Nominal	Pos. 1, no offset
5	Nominal	Pos. 1, no offset
15	Nominal	Pos. 2, 1/4 pitch
18	Nominal	Pos. 4, 3/4 pitch
19	Nominal	Pos. 4, 3/4 pitch
20	Nominal	Pos. 3, 1/2 pitch
21	Nominal	Pos. 3, 1/2 pitch
22	Nominal	Pos. 1, no offset
23	Nominal	Pos. 1, no offset
24	Closed	Pos. 1, no offset
25	Closed	Pos. 1, no offset
26	Closed	Pos. 2, 1/4 pitch
27	Closed	Pos. 2, 1/4 pitch
28	Closed	Pos. 4, 3/4 pitch

time-resolved data that was selected over one rotor revolution for which the values of the nondimensional parameters of flow function, stage pressure ratio, and corrected speed most closely duplicated the design values. The airfoils were highly loaded and the experiments were operated at conditions that had no predicted flow separation across the stage. For the clocking experimental results presented, the HPT vane was clocked relative to the LPT vane. Clocking position is based on the stacking axis of the HPT vane, which is placed at top dead center of the rig. Each clock position moves the stacking axis 2.5° counterclockwise. The spacing between two stacking axes is 10° so that four clock positions are needed to cover the entire vane passage. The axial spacing was changed by removing the spacers shown in Fig. 2 and moving the HPT vane row closer to the blade row. Results presented in this paper are from the runs listed in Table 1. Runs 4, 5, 22, and 23 represent the design point. These runs were all at design corrected speed, pressure ratio, and nominal spacing between the HPT vane and blade with the HPT vane set at clock position 1 (see Table 2; the error bars represent the maximum variation over all runs). For the clocking runs at nominal spacing, there were two runs done at each clocking position (other than position 2).

The data in all cases are treated as time-resolved. The time-average data presented represent a numerical average of the data over a set time range (as opposed to some other low-frequency response sensor). The time-resolved data could be presented in many different ways. This experiment was designed to look at the unsteadiness effect on blade life, so the natural tendency is to examine how the energy spectra vary for different key frequencies. In this case, these frequencies are the fundamental and first harmonic. However, one could use similar data to look at the integral effect of how the fundamentals and harmonics combine to change the shape and overall level of the unsteady envelope. This type of interpretation is of particular interest when examining issues related to film cooling and how overall cooling demands might be reduced by clocking. This topic will not be addressed in this paper due to length constraints, but will be the subject of future work.

The paper is split into two major sections. The first deals specifically with clocking effects at the nominal spacing condition. The second looks at the effects of reduced spacing. In both sections, there are subsections that present the time-averaged data and time-resolved data. A general description of the data reduction is given below, while specific details relevant to each section are given as needed throughout the text.

Table 2 Design properties

Property	Designed	Measured
$P_{\text{Total, inlet}}/P_{\text{static, exit}}$	5.19	$5.17\pm0.7\%$
Corrected speed ($\text{rpm}/K^{0.5}$)	421	$415.7\pm1\%$
Nominal spacing (% vane axial chord)		88%
Reduced spacing (% vane axial chord)		69%

2.2 Data Reduction and Error Analysis. Sections 3 and 4 of the paper (the nominal and reduced spacing data) have enough common data presentation and reduction that it is appropriate to examine these techniques together. The data are shown in six basic presentation styles or types:

a. *Time-averaged surface pressure*. For this case the pressure is normalized by the total inlet pressure. All of this is done in a time-accurate way, with the average being created over the period used (generally one revolution of data). No phase lagging was done to account for different axial positions (i.e., the total pressure measured by the rakes at time x was taken to be the total pressure at all the sensor at time x, where realistically one should account for the flow time required from the rakes to each sensor). This error is much less than the run-to-run variation, and removes a complicating factor from the reduction process. Figures 3–6 are of this type and are labeled on the ordinate as ''Normalized Pressure (P_L/P_{Total}).''

b. *Percent change from clock position 1 for time-averaged data*. Since small variations are examined, the changes between clock positions can best be seen by looking at the time-averaged data for clock position 1 [type (a)], and then looking at the variation from this clock position for the other clock positions. This provides both the general trend and the variations that would not be possible if just the normalized pressure data were plotted for all clock positions. This data and the error propagation are discussed in more detail below. Figures 7–9 are of this type and have ''% Change from Clock Position 1'' on the ordinate.

c. *Time-accurate data from FFTs*. For the time-accurate data, FFTs are performed to provide the amplitude as a function of frequency. The actual data presented, while referred to as FFTs, are really derived from a single-sided power spectrum. A conversion has occurred so that the data represent the peak value at a given frequency, as opposed to a more traditional RMS value. The data are also normalized by the inlet total pressure. Put another way, these data are the power spectrum (or normalized FFT) of type-(a) data. The FFT is performed over the same time range as that for the averaging, and runs at the same clock position were averaged together. Where multiple runs were done at the same clocking position, an uncertainty band was generated by calculating the maximum run-to-run variation. The FFT data were created using a Hamming window on the data selected to reduce spectral leakage and an interpolation routine was used to adjust the peak values to account for peaks, which occurred between frequencies resolved by the FFT directly. Only the amplitudes of the fundamental and first harmonic frequencies are plotted. Figures 10–16 are of this type and the ordinates are labeled as ''FFT Peak Amplitudes (Normalized by P_{total}).'' As an example, in Fig. 10 clock position 4 has an amplitude peak for the fundamental frequency (blade passing) of about 0.5% of the total inlet pressure at about 50% axial chord on the pressure side. The first harmonic ($2\times$blade passing) has a value of about 0.25% for the same clock position and gauge location.

d. *Change due to clocking, time-accurate data*. This is done to demonstrate the difference between the clocking positions for type-(c) data. This procedure takes the normalized FFT data for clock position 1 and subtracts it from the other clock positions. It is given as a percentage and is discussed below. The error represents the maximum range in the experimental variation of the normalized amplitude. Since these are normalized FFT amplitudes, both Z and ΔZ will be nondimensional. Figures 17–19 are of this type and the ordinates are

labeled as "Change due to Clocking at Nominal Spacing (%) (Clocking position X − Clocking position 1)." This is the time-accurate version of type-(b) data.

e. *Change due to reduced spacing*. This is used to show how spacing affects the data and is for any given clocking position, the nominal spacing data subtracted from the reduced spacing normalized pressure, divided by the nominal spacing data [or the percentage change in the type (a) data due to spacing]. Figures 20–22 are of this type and have ordinates of "% Variation (Clock (X) Reduced−Clock (X) Nominal)/ Clock (X) Nominal)." This is a similar method as was used for type-(b) data.

f. *Change due to spacing, time-accurate data*. This is the same as type-(d) data, except instead of comparing everything to clock position 1, the comparisons are made for one clock position at different spacings [such as in type (e)]. These are shown in Figs. 23–29. The ordinates are labeled as "Change due to Spacing (%) (Reduced−Nominal, Clock Pos. X)."

Looking at the data set in a more general manner, the basic figures are type (a) (the normalized pressure) and type (c) (the normalized FFT data over the same time range). The other figure types are ways of presenting the change from one configuration to another. The data are presented in this fashion, because the changes are so small that the variation between the cases of interest would be lost if data were just presented as types (a) and (c). However, it is important to realize that types (b) and (d)–(f) are given in terms of percent change; the actual value has different interpretations. For cases (b) and (e), the percentage change is from the nominal condition. In cases (d) and (f) the data show the change in the normalized FFT amplitudes due to changing conditions. It is only listed as a percent change because the input variable (P_L/P_{Total}) can be listed as a percent of the total inlet pressure. As a final note, Fig. 22, for example [type (e)], the scale of $\pm 4\%$ represents the percentage of the nominal case that is being changed, while in Fig. 24 [type (f)] the scale of $\pm 2\%$ represents the percent change in the total inlet pressure in each of the investigated frequencies as the spacing is changed.

The uncertainty propagation is specific to each type of data, although they clearly share similar roots. Several options were available to examine the repeatability of the measurements. Since four runs were available at the design point, the choice was made to look at the maximum deviations from the averages for the normalized pressure that were encountered over these runs for individual sensor locations. Plotting these maximum deviations as a percentage of reading and taking care to separate the positive from the negative deviations yielded remarkably consistent numbers for specific sensor locations (HPT vane, HPT blade, LPT vane, etc.) These variations were averaged to generate an "average variation" that was then used to create a range bar for the runs that had only one or two repeat conditions. This method leads towards a conservative estimate of the overall error for the runs. This method seems properly robust in that the average maximum positive and negative deviations tracked closely. Sensors were examined without regard to span location. The results are as follows:

HPT vane	±2%
HPT blade	±1.2%
LPT vane	±0.8%
Outer transition duct	±0.45%
Inner transition duct	±0.42%

Based on these ranges, the uncertainty was propagated using the following formulation for types (b) and (d) data, where for type (b) X = clock position x, Y = clock position 1, and for type (d) X = clock position x reduced spacing, Y = clock position x nominal spacing.

$$Z = \frac{\text{Clock}_x - \text{Clock}_y}{\text{Clock}_y},$$

$$\Delta Z = \left[\left(\frac{\text{Clock}_x}{Y}\right)^2\left\{\left(\frac{\Delta\text{Clock}_x}{\text{Clock}_x}\right)^2 + \left(\frac{\Delta\text{Clock}_y}{\text{Clock}_y}\right)^2\right\}\right]$$

For cases where a change in the percent of a reading is presented [cases (d) and (f)]; the error propagation is shown below:

$$Z = \text{Norm. FFT Amp}_{i.\text{Clock}(x)} - \text{Norm. FFT AMP}_{i,\text{Clock}(1)},$$

$$\text{Norm. FFT Amp} = \frac{\text{FFT Peak Amp.}}{\text{Time-Averaged Value}},$$

$$\Delta Z = [\{(\Delta\text{Norm. FFT AMP}_{i.\text{Clock}(x)})^2 + (\Delta\text{Norm. FFT Amp}_{i,\text{Clock}(1)})^2\}].$$

3 Nominal Axial Spacing Data

3.1 Time-Averaged Results. The time-averaged data are presented in terms of the normalized pressure, where the average inlet total pressure is used as the normalizing parameter. The first four plots show the nominal time-average data for different sections of the machine at the nominal spacing and at clocking position 1. The range bars (which are hard to see at these scales) represent the average maximum run-to-run variation, as experienced for this subset of data. Figure 3 shows the time-averaged data plotted for the HPT vane, HPT blade, and LPT vane at different sample spans (the high vane data at 50% does not have the spatial resolution of the 10% data, so it is not shown). This plot, as well as Figs. 4–6, is designed to show how the average value changes with position. It is important to note that the individual run-to-run variations are quite small. Figure 4 shows the inner and

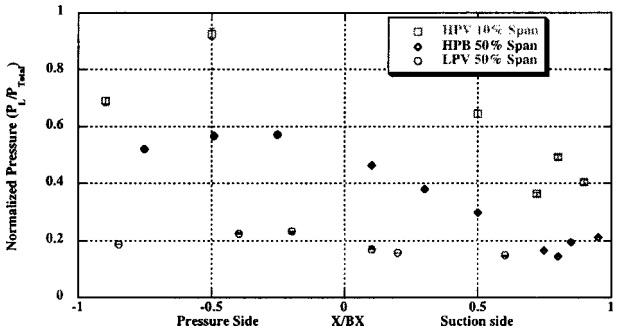

Fig. 3 Time-averaged normalized pressures, clocking position 1, for HPT vane, HPT blade, and LPT vane, various spans

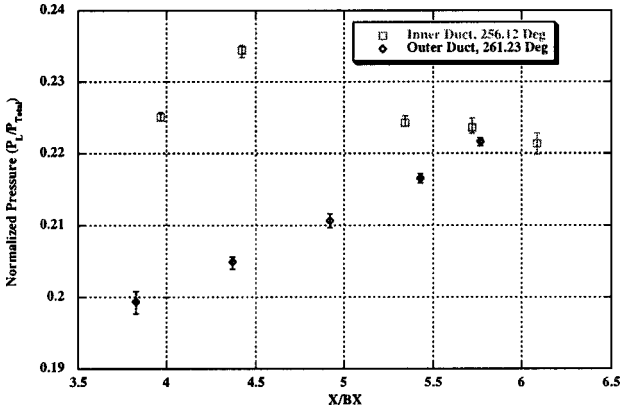

Fig. 4 Time-averaged normalized pressures, clock position 1 inner and outer transition ducts

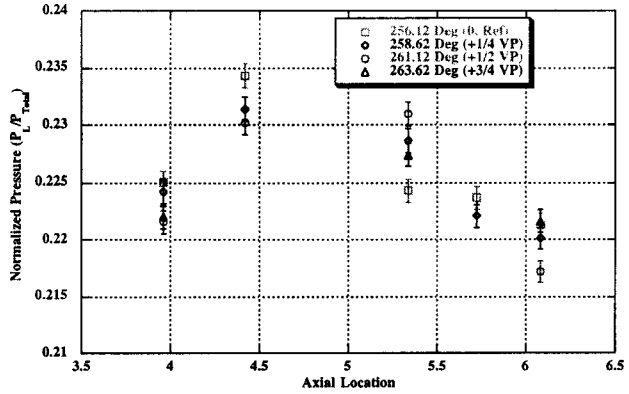

Fig. 5 Time-averaged normalized pressures for inner transition duct, clock position 1, various circumferential positions

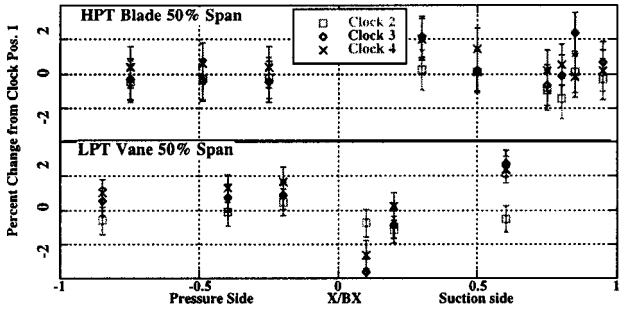

Fig. 7 Variation in normalized pressure due to clocking position for HPT blade and LPT vane at 50% span

outer transition ducts at representative circumferential positions. The main point of interest is the relatively different pressure distribution as seen by the two surfaces. Figures 5 and 6 show the variation that occurs at clocking position 1 with circumferential position on the ducts. Each circumferential location is 1/4 of a vane pitch from its predecessor. One can see that the effect of the upstream wakes (rotor and vane) are more noticeable on the outer transition duct close to the blade trailing edge, but damps out as one moves axially downstream. For the inner transition duct the difference is not as large as the outer ducts at the blade trailing edge, but the difference seems to be more consistent as one travels axially downstream.

The effect of the variation in clock position on the time-averaged values for the HPT blade, LPT vane, and transition duct are shown in Figs. 7–9 [type (b)]. Figure 7 for the midspan (50% span) location illustrates that clock position of the LPT vane relative to the HPT vane has little influence on the time-averaged pressure distributions for the HPT blade and the LPT vane. The variations observed are of the same magnitude with the possible exception being the LPT vane near the leading edge. The time-average pressure distributions for 10% and 90% spans were also analyzed and the result was consistent with that found at 50% span. The results just noted were anticipated, since from the rotor's perspective, it is passing through all the high vane wakes over a single revolution, no matter where the "first vane" is located. When the high vane is clocked relative to the low vane one might see some changes in the time-average pressures on the low vane, but only if the rotor is not dominating the flow field.

The effect is not as clear-cut on the transition ducts where the edge effects are more dominant and the rotor passing becomes less important. Figures 8 and 9 show how the time-averaged values vary with circumferential position for different clock positions. One item to note is that for both the inner and outer transition ducts, clock position 4 is consistently a lower pressure position than the other clock positions. On the outer duct, there is not much change between clock positions 2 and 3 (although they are both higher than clock position 1), once one moves away from the rotor trailing edge (TE) (the rotor TE is at about 3.4). For the inner duct (Fig. 8) clock positions 2 and 3 still seem to yield higher pressure than clock position 1, as was shown in the outer transition duct. Unlike the outer duct, there appears to be a measurable (although small) variation that occurs between clock positions 2 and 3 as one moves through the vane passage. This shows the effect from the HPT vane wakes propagating through the HPT blade and striking the downstream duct. The effect of

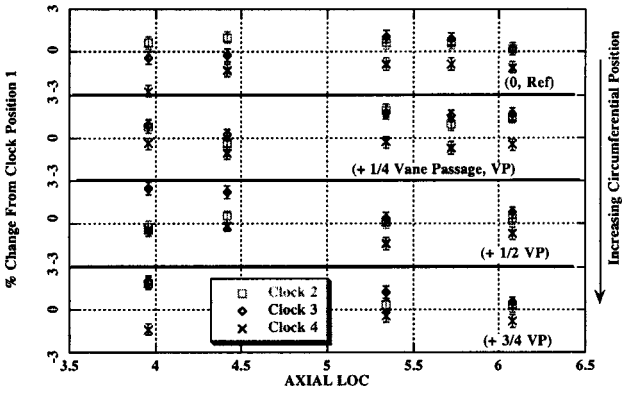

Fig. 8 Variation in normalized pressure due to clocking position for the inner transition duct at various circumferential positions

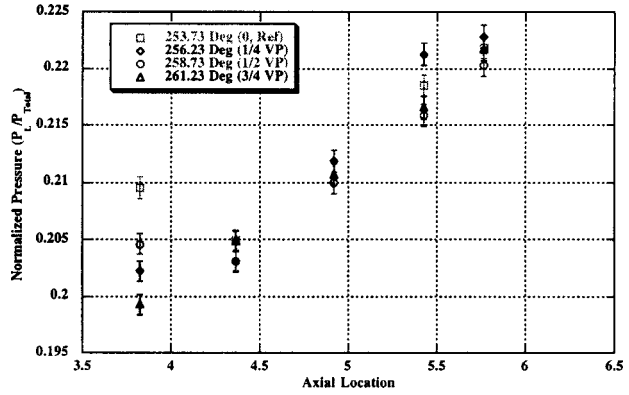

Fig. 6 Time-averaged normalized pressures for outer transition duct, clock position 1, various circumferential positions

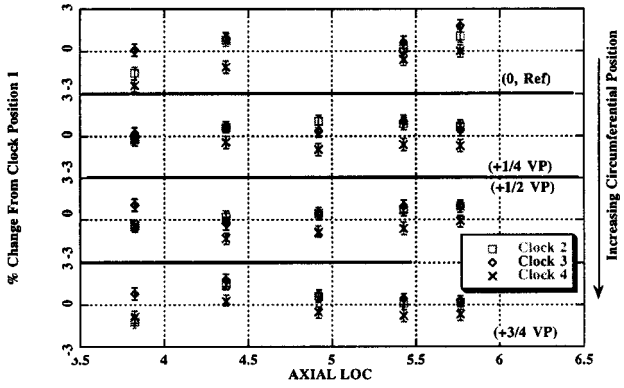

Fig. 9 Variation in normalized pressure due to clocking position for the outer transition duct at various circumferential positions

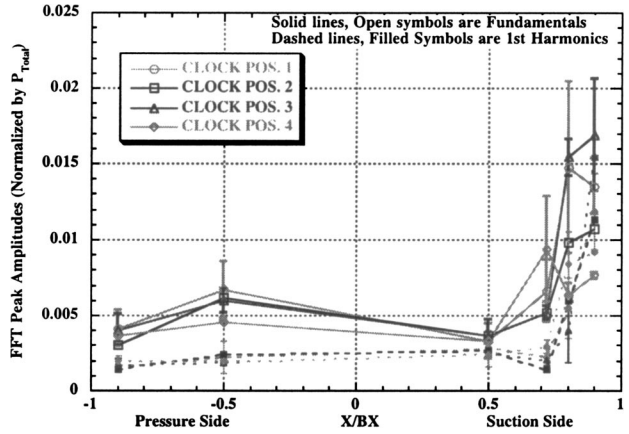

Fig. 10 Normalized pressure fundamental and first harmonic peaks, HPT vane at 10% span

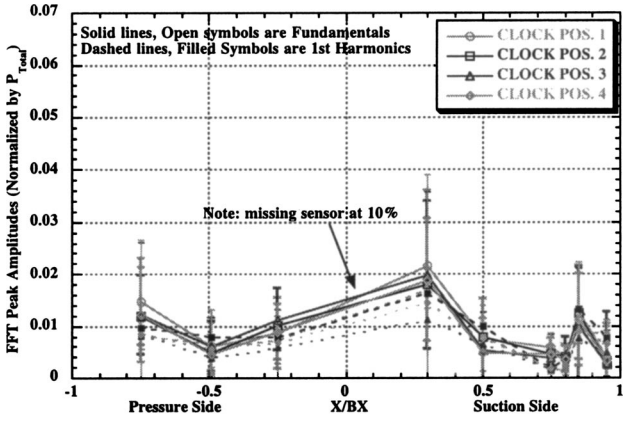

Fig. 12 Normalized pressure fundamental and first harmonic peaks, HPT blade at 50% span

clocking appears to be greater on this duct than that on the LPT vane. Therefore, one would expect that effects due to clocking are also a function of axial distance between the HPT vane and LPT vane. Figure 9 presents the results of the pressure distribution on the outer surface of the transition duct. Measurements were taken at circular locations of 253.73, 256.23, 258.73, and 261.23°, which correspond to changes in the vane passage (VP) of 0, 1/4VP, 1/2VP, and 3/4VP. Figure 9 shows that the effect from clocking is not as great on the outer surface as it is on the inner surface of the transition duct.

3.2 Time-Accurate Data for Nominal Spacing. The preceding section shows that the effects of clocking on the time-averaged values are small, but discernable, throughout the machine. The main impact of the clocking is seen in the transition duct. In this section, the unsteady nature of clocking changes is investigated by looking at the data in the frequency domain. To characterize the unsteadiness, both the fundamental and first harmonic amplitudes will be presented. For the vane data, these were taken at blade passing frequency, while for the blade data it was done at vane passing frequencies. The actual levels of both the fundamentals and the harmonics will be shown, since these show how the levels change with position on the blade surface [Figs. 10–16, type (c)]. However, quantifying the effects due to clocking is difficult with these plots, since the changes are small. In this section, the differences between the clocking positions will also be plotted for the LPT vane only [Figs. 17–19, (type (d)]. The equations for the error propagation were shown in Sec. 2.2.

3.2.1 High-Pressure Turbine Vane. High-pressure vane data are presented in the clocking case to show a complete picture of the interaction between the HPT vane and blade, although one would expect the interaction to be small. Figure 10 shows the fundamental and first harmonics for the HPT vane at 10% span. The interesting point to note here is the relative equivalent size of the fundamental and first harmonic over much of the airfoil. The measures are all grouped within the range bars until one gets to about 50% on the suction surface. At this point, the interaction becomes confused and noisy (note the large bars on these measurements). Clocking effects would not be expected at these locations, and they are not observed given the range of measurements at the trailing edge. At the trailing edge, the fundamentals and harmonics have both grown, but in comparison to the HPT blade leading edge (see Figs. 11 and 12), these values are still about 2.5 times less in magnitude.

3.2.2 HPT Blade. Figures 11–13 illustrate the magnitude of the fundamental and the first harmonic of the unsteady surface pressure at 10%, 50%, and 90% span on the HPT blade. All of these plots are on the same scale for ease of comparison. It is difficult to pick out trends by simply looking at the results. Clock position 2 has the lowest fundamental at 10% span by about 25%; however, when one looks at the 90% span data, the results for this clock position become the maximum. As is shown by the data range bars, most of the variation observed from clocking is contained within these bars, suggesting that if there is a clocking effect, it is small when compared with the experimental data

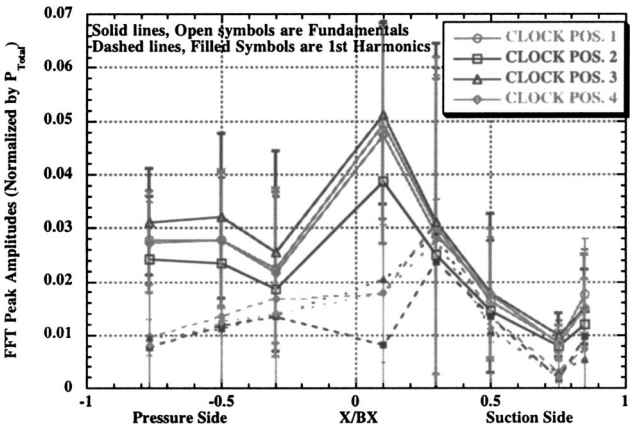

Fig. 11 Normalized pressure fundamental and first harmonic peaks, HPT blade at 10% span

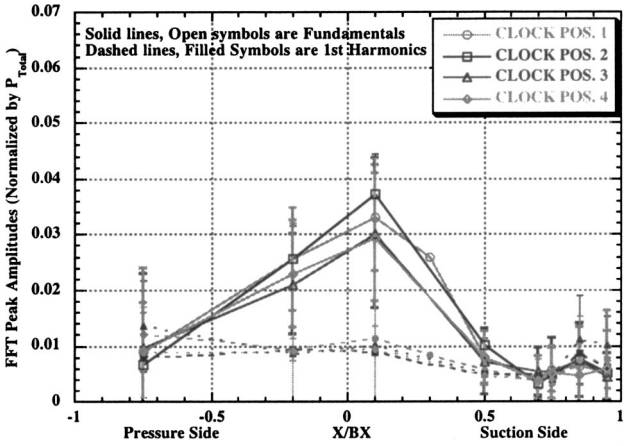

Fig. 13 Normalized pressure fundamental and first harmonic peaks, HPT blade at 90% span

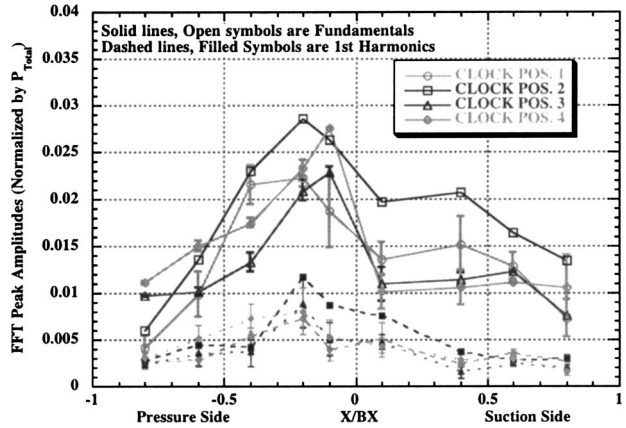

Fig. 14 Normalized pressure fundamental and first harmonic peaks, LPT vane at 10% span

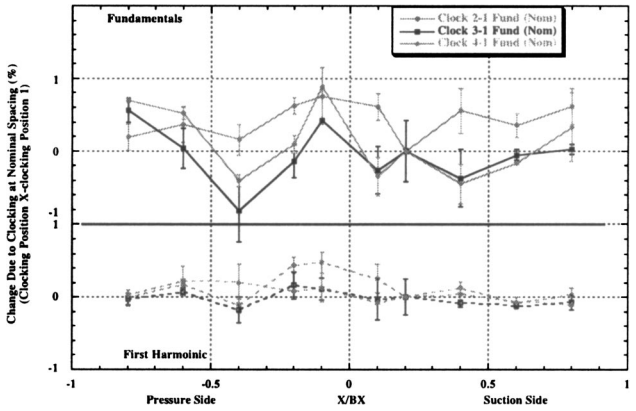

Fig. 17 Variation in normalized pressure fundamental and first harmonic peaks due to clocking position for LPT vane at 10% span

range. The fundamental on this HPT blade at 10% span was reported by Clark et al. [15] to be the cause of the redesign of the HPT vane for this turbine. What is perhaps more illustrative is the variation in harmonic and fundamental amplitudes as a function of span. At 50% span (Fig. 12), there is not much difference in magnitude between the fundamental and harmonic values along most of the blade. In addition, the clocking variation seems tightly bound; when compared to the 10% data (Fig. 11) or the 90% data (Fig. 13) the results suggest that at each spanwise location, there is a different clock position that has the peak magnitude for the fundamental. At 50% span, sensor mortality at the $+10\%$ x/b_x location makes determining the best clock position at that span impossible, since data from only clock position one were obtained. However, the single data point for $+10\%$ x/b_x and the

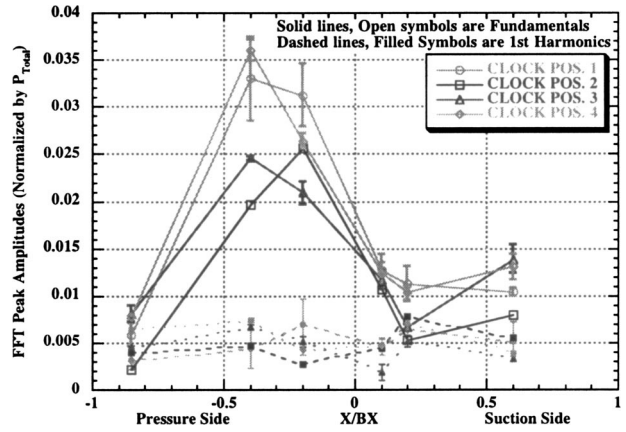

Fig. 15 Normalized pressure fundamental and first harmonic peaks, LPT vane at 50% span

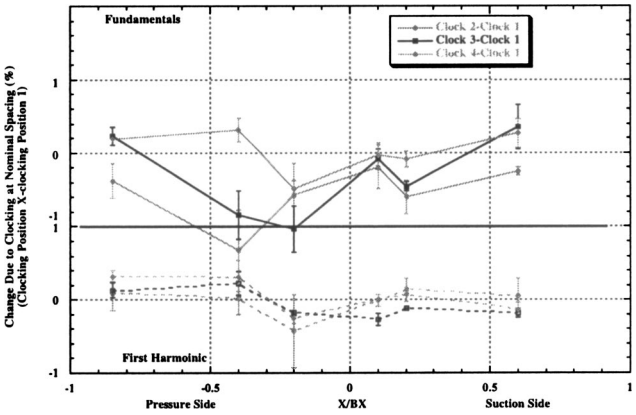

Fig. 18 Variation in normalized pressure fundamental and first harmonic peaks due to clocking position for LPT vane at 50% span

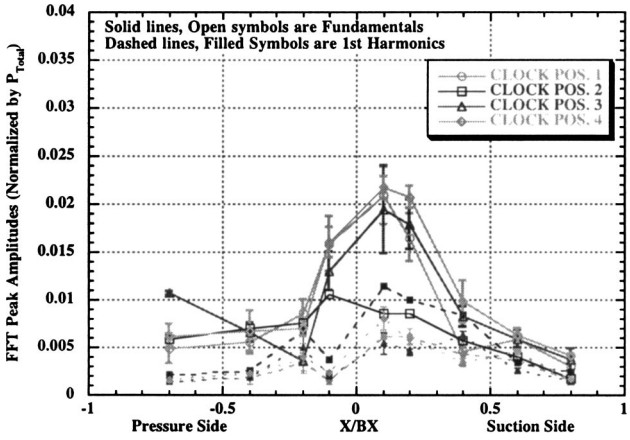

Fig. 16 Normalized pressure fundamental and first harmonic peaks, LPT vane at 90% span

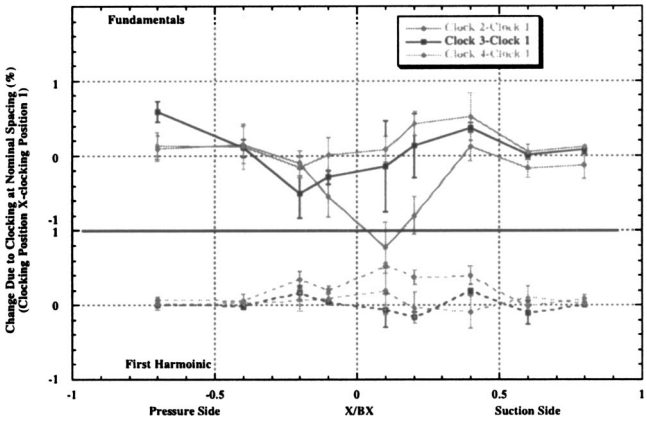

Fig. 19 Variation in normalized pressure fundamental and first harmonic peaks due to clocking position for LPT vane at 90% span

remaining pressure transducers do show that the magnitudes at 50% span are almost the same as those at 10% span. At 90% span, clock positions 3 and 4 have the lowest peak magnitudes, but the magnitude is 60% of the value at 10% span. The results obtained for the first harmonic also suggest that no single clock position consistently reduces the magnitudes at each of the spanwise measurement locations.

The results suggest a strong word of caution for those who are arriving at conclusions regarding the ''goodness'' of clocking based on measurements taken only at midspan. Results presented here illustrate a great deal of dependence on span and the complexities caused by the three-dimensional design of the airfoils.

3.2.3 Low-Pressure Turbine Vane. The frequency analysis is presented for the LPT vane at 10%, 50%, and 90% span in Figs. 14–16. In the low-pressure vane, the variation due to clocking is more noticeable due to several reasons. The first is that harmonic analysis shows that for all spans the fundamental is stronger than the harmonic with the exception being at the trailing edges. This implies that the fundamental blade passing frequency is dominating the unsteady results. In addition, when comparing the size of the fundamental on the low-pressure vane to the HPT blade, one sees that the normalized amplitudes are of the same order at the leading edges (about 0.03 on the vane to about 0.05 on the blade). However, referring to Fig. 3, one can see that the low-pressure vane is about 3 times less in actual pressure level; thus the proportional influence of the unsteadiness as a function of average local level is greatest in the low-pressure vane. General trends shown in the results for the fundamental obtained at 10%, 50%, and 90% span suggest that clock position 4 has a marginally higher level of unsteadiness. At 50% and 90% span, clock position 4 has the greatest peak magnitude, and at 10% span, it has the second highest peak magnitude.

Review of the results for the amplitude of the first harmonics of the pressure illustrates that clock position 2 clearly has the peak amplitude at all spans. This is different from the results presented for the HPT blade (see Figs. 11–13) that suggest clock position 2 could be the better position, but it may be the worst for the LPT vane. In general, the amplitudes of the first harmonic are about half of the fundamental, but could still be large enough to cause difficulty if the frequency of the harmonic happened to coincide with an excitation mode of the vane. Arguments could be made for a couple of the clock positions being the optimum, based upon results at selected spans.

Combining the results of the fundamental with those from the first harmonics, a clear-cut ''best clock position'' is difficult to find. However, what the results do illustrate is that trade-offs can be made with clock position to reduce the amplitudes at different spans of the vane. This is shown more clearly in Figs. 17–19, where the same data have been plotted as a relative change from clocking position 1. As one can see it is hard to make a claim of an absolute best clocking position when all three major variables (span, wetted distance, and harmonics) are considered.

4 Reduced Axial Spacing Data

4.1 Time-Average Data. In a manner similar to the time-averaged data at the nominal spacing, Figs. 20 and 21 show, as one would expect, that the effect of reducing the spacing by 22% is small on the time-averaged values on the HPT vane and blade with the exception of the vane trailing edge and the blade leading edge. Figure 22 shows the effect on the low-pressure vane, which as expected is much smaller than either the HPT vane or HPT blade.

4.2 Time-Accurate Data for Reduced HPT Vane/Blade Spacing. The figures presented in this section illustrate percentage change in the magnitude of the fundamental and first harmonic of the unsteady surface pressures as the spacing is reduced. The data are presented in a manner similar to the changes shown between clock positions in the preceding section.

4.2.1 HPT Vane and Blade. Figure 23 illustrates that the effect of spacing on the majority of the HPT vane at 10% span is negligible. Only at the trailing edge does one see some action. Figures 24–26 show that the effect of reducing spacing is not uniform across the different HPT blade spans. At 10% span, all the clocking positions have an increase in the fundamental value, whereas at 50% span, all clocking positions seem to be relatively unchanged (as compared to the 10% span). The harmonics also tend to be neutral to the spacing changes; no one position dominates. Clock position 4 seems to have the best mitigating effect on the blade overall.

4.2.2 LPT Vane. The results presented in this section illustrate the magnitude of the changes in the fundamental and first harmonic of the unsteady surface pressure at 10%, 50%, and 90% span on the LPT vane as the spacing is reduced. Figures 27–29

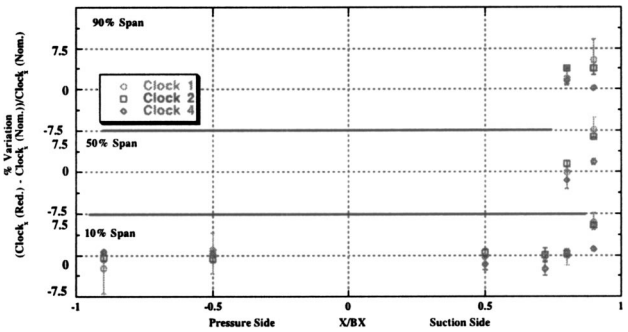

Fig. 20 Influence of reduced spacing on time-averaged normalized pressure as a function of clock position for the HPT vane

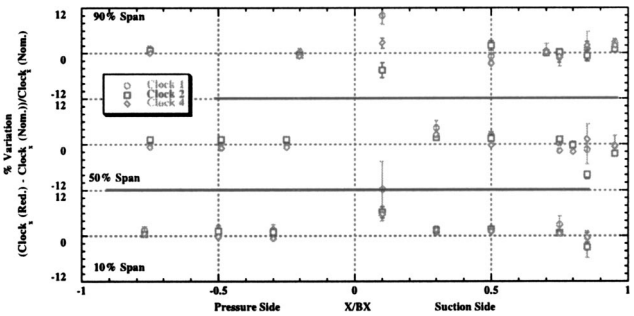

Fig. 21 Influence of reduced spacing on time-averaged normalized pressure as a function of clock position for the HPT blade

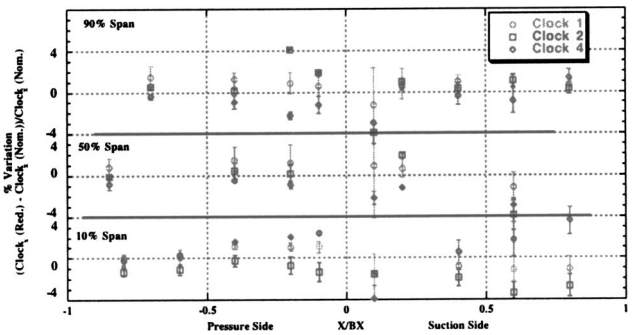

Fig. 22 Influence of reduced spacing on time-averaged normalized pressure as a function of clock position for the LPT vane

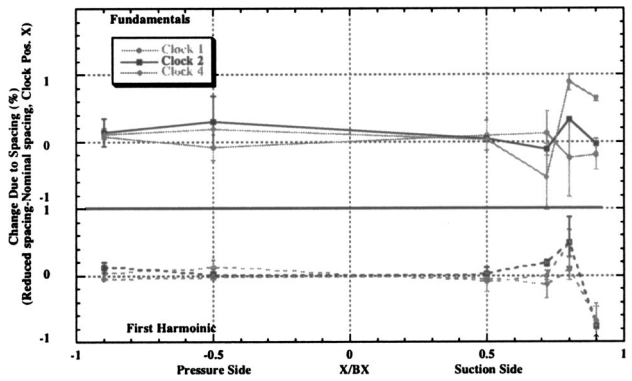

Fig. 23 Variation in normalized pressure fundamental and first harmonic peaks due to reduced HPT vane/blade spacing for HPT vane 10% span

suggest that the reduced spacing does not produce the same effects at each clock position for the fundamental. Examining the harmonics one sees a random effect, one for which the nominal and reduced spacing for each clock position intertwine and there is not one offset from the other. While one might make a case for clocking position 1 to reduce the fundamental on the blade, it seems to be the worse position for the low-pressure vane and the endwalls.

5 Conclusions

The results of these experiments suggest that the clocking position of the HPT vane has some effect on the time-averaged surface pressure distributions for the transition duct and LPT vane. It is also possible that reflections from the transition duct and/or the LPT vane at different HPT vane clocking positions have an effect

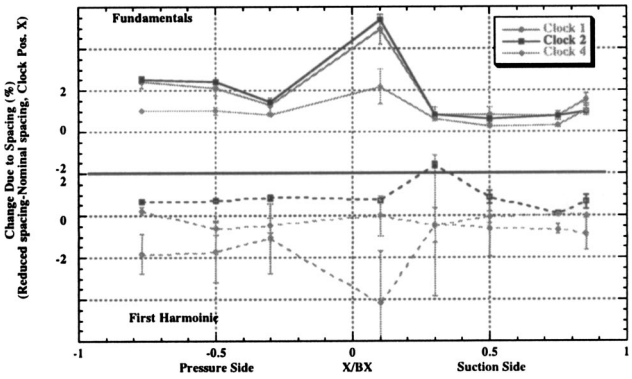

Fig. 24 Variation in normalized pressure fundamental and first harmonic peaks due to reduced HPT vane/blade spacing for HPT blade 10% span

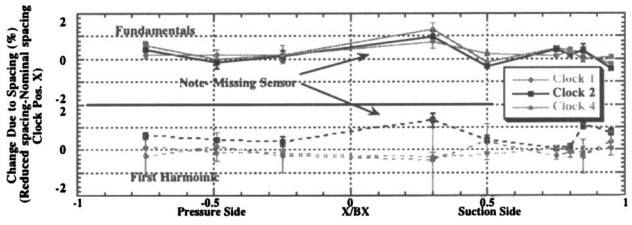

Fig. 25 Variation in normalized pressure fundamental and first harmonic peaks due to reduced HPT vane/blade spacing for HPT blade 50% span

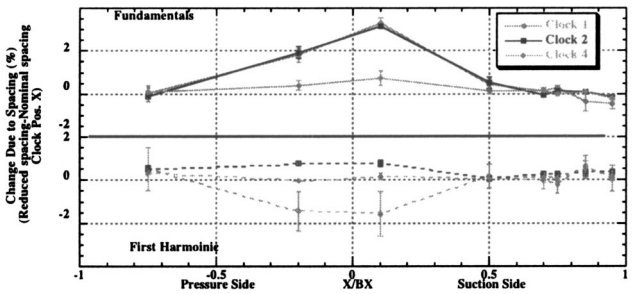

Fig. 26 Variation in normalized pressure fundamental and first harmonic peaks due to reduced HPT vane/blade spacing for HPT blade 90% span

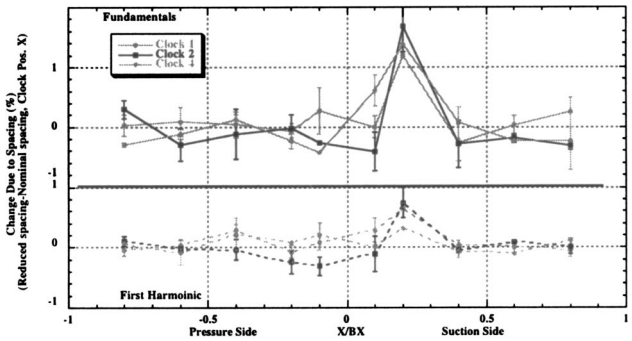

Fig. 27 Variation in normalized pressure fundamental and first harmonic peaks due to reduced HPT vane/blade spacing for LPT vane 10% span

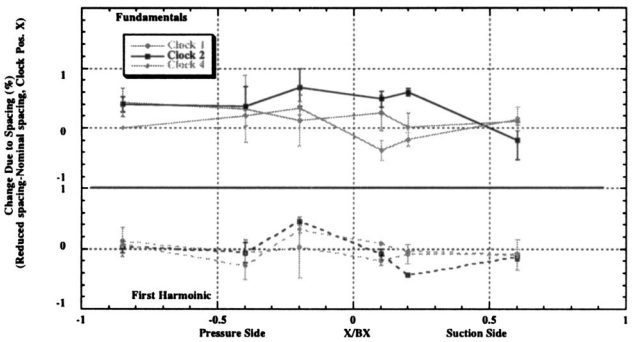

Fig. 28 Variation in normalized pressure fundamental and first harmonic peaks due to reduced HPT vane/blade spacing for LPT vane 50% span

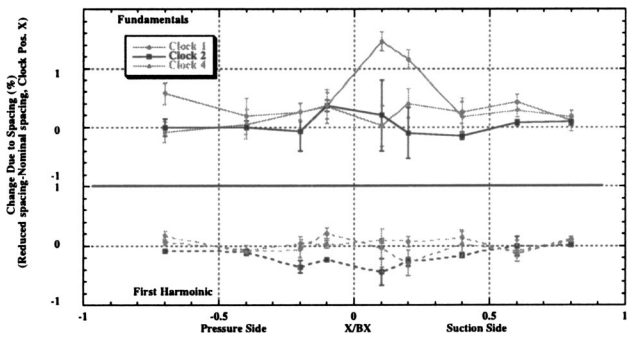

Fig. 29 Variation in normalized pressure fundamental and first harmonic peaks due to reduced HPT vane/blade spacing for LPT vane 90% span

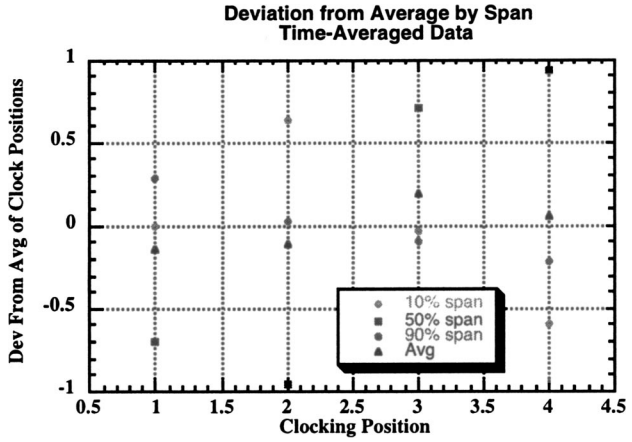

Fig. 30 Integral effects of clocking on LPV time-averaged pressure data

on the blade, but the effect is small and requires better resolution of the blade data. For the time-accurate pressure distributions, the effect is more apparent. In the time-accurate case, clocking shows the largest effect on the transition duct and the LPT vane. The effects are complex and suggest that it is difficult to select a single clock position that lowers the unsteadiness over the entire airfoil. The results suggest that there is no best clock position that uniformly reduces the unsteadiness on the transition duct or LPT vane, and certainly not simultaneously for both the duct and the vane. This can be verified by integrating the time-averaged pressure data on the low-pressure vane as a function of clocking position. There are many ways to perform this operation, but in this case the data were interpolated to fill in missing locations for the three different spans and then the overall clocking effect was created by integrating over the equal areas of the three different spans. The results are shown in Fig. 30.

Figure 30 shows the variation due to clocking for each span by subtracting the average for all clocking positions for that span. This removes the $\pm 5\%$ bias that occurs due to the three-dimensional effect across the spans but allows one to see the differences due to clocking more clearly. At 10% span, clocking position 2 has the highest pressure, whereas for 50% span, it is clearly clock position 4. The overall effect (shown in black) shows that clock position 3 has the highest pressure, but one can see that the overall effect is much smaller than that shown at any of the individual span locations. This once again shows that while the effect at a span may be large, the overall effect is generally small because the effect is different at each span, each favoring a different clocking location.

The results do illustrate that if there is a problem location on the airfoil for which the amplitude of the unsteady surface pressure is too great for the design, one alternative may be to employ clocking to locally reduce the level of unsteadiness. The measurements presented herein illustrated that the HPT vane design resulted in a problem with the magnitude of the unsteadiness at 10% span on the blade (Clark et al. [15]), which ultimately required a redesign.

Many very complex interactions occur, which cause a change of the spacing to influence the potential change caused by changing the clock positions. Reduced spacing does not have the same effect on the first harmonic of the unsteady surface pressure as it does on the fundamental. It has been demonstrated here that it may have the opposite effect. Reduced spacing increased the peak magnitudes of the fundamental by up to 30%, while the magnitude of the first harmonics was decreased by up to 30%.

Another important observation is that the effects at 50% span are significantly different from those at 10% and 90% span for the three-dimensional airfoils used in this study. Therefore, it would be an unwise decision to simply do a computational analysis at 50% span and extrapolate it to 10% and 90% spans. These measurements suggest that when the designer is determining the stage configuration, attention to all contributing factors must be assessed.

Acknowledgments

The authors would like to express our appreciation to United Technologies Pratt and Whitney for sponsoring this research activity at The Ohio State University Gas Turbine Laboratory. We would also like to express our appreciation to the technical monitor of this activity, Mr. Gary Stetson of Pratt and Whitney. Mr. Jeff Barton of the OSU GTL was instrumental in completing the experimental portion of the study and his work is greatly appreciated.

Nomenclature

HPT = high-pressure turbine
LPT = low-pressure turbine
CFD = computational fluid dynamics
FFT = fast Fourier transformation
x = axial distance
b_x = airfoil axial chord
P_s = static pressure
P_L = local static pressure
P_t = total pressure

References

[1] Huber, F. W., Johnson, P. D., Johnson, O. P., Staubach, J. B., and Gaddis, S. W., 1996, ''Performance Improvement Through Indexing of Turbine Airfoils: Part I—Experimental Investigation,'' ASME J. Turbomach., **118**, pp. 630–635.
[2] Griffin, L. W., and Sharma, O. P., 1996, ''Performance Improvement Through Indexing of Turbine Airfoils: Part 2-Numerical Simulation,'' ASME J. Turbomach., **118**, pp. 636–642.
[3] Dorney, D. J., and Sharma, O. P., 1996, ''A Study of Turbine Performance Increases Through Airfoil Clocking,'' AIAA paper no. 96-2816.
[4] Dunn, M. G., and Haldeman, C. W., 1995, ''Phase-Resolved Surface Pressure and Heat-Transfer Measurements on the Blade of a Two-Stage Turbine,'' ASME J. Fluids Eng., **117**, pp. 653–658.
[5] Dorney, D. J., and Gundy-Burlet, K., 1995, ''Hot-Streak Clocking Effects in a 1-1/2 Stage Turbine,'' ASME paper no. 95-GT-202.
[6] Barankiewicz, W. S., and Hathaway, M. D., ''Effects of Stator Indexing on Performance in a Low Speed Multistage Axial Compressor,'' ASME paper no. 97-GT-496.
[7] Hsu, S. T., and Wo, A. M., 1998, ''Reduction of Unsteady Blade Loading by Beneficial Use of Vortical and Potential Disturbances in an Axial compressor With Rotor Clocking,'' J. Turbomach., **120**, pp. 705–713.
[8] Hummel, F., 2001, ''Wake-Wake Interactions and its Potential for Clocking in a Transonic High Pressure Turbine,'' ASME paper no. 2001-GT-0302.
[9] Reinmoller, U., Stephan, B., Schmidt, S. and R. Niehuis, 2001, ''Clocking Effects in a 1.5 Stage Axial turbine-Steady and Unsteady Experimental Investigations Supported by Numerical simulations'' ASME paper no. 2001-GT-0304.
[10] Dunn, M. G., Bennett, W. A., Delaney, R. A., and Rao, K. V., 1992, ''Investigation of Unsteady Flow Through a Transonic Turbine Stage: Data/Prediction Comparison for Time-Averaged and Phase-Resolved Pressure Data,'' ASME J. Turbomach., **114**, pp. 91–99.
[11] Venable, B. L., Delaney, R. A., Busby, J. A., Davis, R. L., Dorney, D. J., Dunn, M. G., Haldeman, C. W., and Abhari, R. S., 1998, ''Influence of Vane-Blade Spacing on Transonic Turbine Stage Aerodynamics, Part I: Time-Averaged Data and Analysis,'' ASME paper no. 98-GT-481.
[12] Busby, J. A., Davis, R. L., Dorney, D. J., Dunn, M. G., Haldeman, C. W., Abhari, R. S., Venable, B. L., and Delaney, R. A., 1998, ''Influence of Vane-Blade Spacing on Transonic Turbine Stage Aerodynamics Part II: Time Resolved Data and Analysis,'' ASME paper no. 98-GT-482.
[13] Barter, J. W., Vitt, P. H., and Chen, J. P., 2000, ''Interaction Effects in a Transonic Stage,'' ASME paper no. 2000-GT-0376.
[14] Denos, R., Arts, T., Paniagua, G., Michelassi, V., and Martelli, F., 2000, ''Investigation of the Unsteady Rotor Aerodynamics in a Transonic Turbine Stage,'' ASME paper no. 2000-GT-435.
[15] Clark, J. P., Stetson, G. M., Magge, S. S., Ni, R. H., Haldeman, C. W., Jr., and Dunn, M. G., 2000 ''The Effect of Airfoil Scaling on the Predicted Unsteady Loading on the Blade of a 1 and 1/2 Stage Transonic Turbine and a Comparison with Experimental Results,'' ASME paper no. 2000-GT-0446.
[16] Davis, R. L., Yao, J., Clark, J. P., Stetson, G., Alonso, J. J., Jameson, A., Dunn, M. G., Haldeman, C. W., ''Unsteady Interaction Between a Transonic Turbine Stage and Downstream Components,'' ASME paper no. GT-2002-30364.
[17] Clark, J. P., Aggarwala, A. S., Velonis, M. A., Gacek, R. E., Magge, S. S., and Price, F. R., ''Using CFD to Reduce Resonant Stresses on a Single-Stage,

High-Pressure Turbine Blade,'' ASME paper no. GT-2002-30320.
[18] Krumanaker, M. L., Haldeman, C. W., and Dunn, M. G., 2003, ''Heat Transfer and Aerodynamic Measurements for a Modern Stage and One-Half Transonic Turbine,'' ASME paper no. GT2003-38725.
[19] Krumanaker, M. L., 2002, ''Aerodynamics and Heat Transfer for a Modern Stage and One-Half Turbine,'' OSU Masters thesis, GTL Doc. No. 2002-10-M7.
[20] Dunn, M. G., Moller, J. C., and Steel, R. C., 1989, ''Operating Point Verification for a Large Shock Tunnel Test Facility,'' Aeropropulsion and Power Laboratory, USAF, Report No. WRDC-TR-2027.

Passive Flow Control on Low-Pressure Turbine Airfoils

Ralph J. Volino
Department of Mechanical Engineering,
United State Naval Academy,
Annapolis, MD 21402
e-mail: volino@usna.edu

Two-dimensional rectangular bars have been used in an experimental study to control boundary layer transition and reattachment under low-pressure turbine conditions. Cases with Reynolds numbers (Re) ranging from 25,000 to 300,000 (based on suction surface length and exit velocity) have been considered at low (0.5%) and high (8.5% inlet) free-stream turbulence levels. Three different bars were considered, with heights ranging from 0.2% to 0.7% of suction surface length. Mean and fluctuating velocity and intermittency profiles are presented and compared to results of baseline cases from a previous study. Bar performance depends on the bar height and the location of the bar trailing edge. Bars located near the suction surface velocity maximum are most effective. Large bars trip the boundary layer to turbulent and prevent separation, but create unnecessarily high losses. Somewhat smaller bars had no immediate detectable effect on the boundary layer, but introduced small disturbances that caused transition and reattachment to move upstream from their locations in the corresponding baseline case. The smaller bars were effective under both high and low free-stream turbulence conditions, indicating that the high free-stream turbulence transition is not simply a bypass transition induced by the free stream. Losses appear to be minimized when a small separation bubble is present, so long as reattachment begins far enough upstream for the boundary layer to recover from the separation. Correlations for determining optimal bar height are presented. The bars appear to provide a simple and effective means of passive flow control. Bars that are large enough to induce reattachment at low Re, however, cause higher losses at the highest Re. Some compromise would, therefore, be needed when choosing a bar height for best overall performance. [DOI: 10.1115/1.1626685]

Introduction

Modern low-pressure turbine (LPT) airfoils are subject to increasingly stronger pressure gradients as designers impose higher loading in an effort to improve efficiency and lower cost by reducing the number of airfoils in an engine. If the adverse pressure gradient on the suction side of these airfoils becomes strong enough, the boundary layer will separate. Separation bubbles, particularly those that fail to reattach, can result in a significant loss of lift and a subsequent degradation of engine efficiency (e.g., Hourmouziadis [1], Mayle [2], and Sharma et al. [3]). The problem is particularly relevant in aircraft engines. Airfoils optimized to produce maximum power under takeoff conditions may still experience boundary layer separation at cruise conditions, due to the thinner air and lower Reynolds numbers at altitude. A component efficiency drop of 2% may occur between takeoff and cruise conditions in large commercial transport engines, and the difference could be as large as 7% in smaller engines operating at higher altitudes. Component life may also be affected by more than an order of magnitude (Hodson [4]). Because the LPT produces the bulk of the net power in many engines, changes in its component efficiency can result in nearly equal changes in overall engine efficiency (Wisler [5]). There are several sources for losses in an engine, including secondary flows, but the suction side boundary layer has been identified as the primary source of losses in the LPT (Curtis et al. [6]). Prediction and control of suction side separation, without sacrifice of the benefits of higher loading, are therefore, necessary for improved engine design.

Separation on LPT airfoils is complicated by boundary layer transition. Turbulent boundary layers are much more resistant to separation than laminar boundary layers. If transition occurs far enough upstream, it can prevent separation. If transition occurs in the shear layer over a separation bubble, it will tend to induce boundary layer reattachment. The lower the Reynolds number, the farther downstream transition will tend to occur and hence the problems associated with performance at altitude.

Separated flow transition has been studied extensively, and in recent years several studies have focused on transition in the LPT. Volino [7] provides a review of much of that work. Separation can be affected through naturally occurring phenomena in an engine and through deliberate attempts at flow control. Several studies have shown that high free-stream turbulence intensity (FSTI) tends to cause the transition to move upstream, resulting in a smaller separation bubble. Reducing the separation bubble size tends to result in thinner boundary layers after reattachment, thereby reducing losses. Moving the transition upstream, however, results in a longer turbulent region on the airfoil, which tends to increase losses. Volino [7] showed that the net result of these competing effects depends on the Reynolds number. High FSTI tends to reduce losses at low Re. At high Re, where separation bubbles are relatively small even with low FSTI, high FSTI results in higher losses. At very low Re, boundary layers may fail to reattach even with high FSTI (e.g., Volino [7] and Van Treuren et al. [8]). Unsteadiness caused by wakes generated upstream of an airfoil has been shown in several studies (e.g., Howell et al. [9]) to reduce the extent of separation bubbles and reduce losses. As with elevated FSTI, wake unsteadiness is most effective at reducing losses at lower Re, where the steady flow separation bubbles are largest. Stadtmüller et al. [10] found that at high Re, losses were higher with wakes than in steady flow.

Existing results suggest that separation bubbles should be kept small, but without producing an unnecessarily long turbulent region. Hourmouziadis [1] discussed ''controlled diffusion blading,'' in which an airfoil is designed so that a small separation bubble is present. The bubble itself is not thick enough to produce high losses, and its presence allows a shorter turbulent region near the trailing edge. This idea is discussed below in conjunction with the present results.

Capitalizing on the beneficial effects of unsteady wakes, Howell et al. [9] and Brunner et al. [11] studied airfoils modified for

Contributed by the International Gas Turbine Institute and presented at the International Gas Turbine and Aeroengine Congress and Exhibition, Atlanta, GA, June 16–19, 2003. Manuscript received by the IGTI Dec. 2002; final revision Mar. 2003. Paper No. 2003-GT-38728. Review Chair: H. R. Simmons.

higher lift. Losses increased with airfoil loading, as adverse pressure gradients became stronger and separation bubbles became larger. With wake passing, however, the magnitude of the loss increase was in some cases relatively small compared to the increase in lift. Aft loaded airfoils tended to have lower losses, since separation and transition occurred closer to the trailing edge, resulting in a shorter turbulent region.

While high FSTI and wakes help to mitigate separated flow problems, they clearly do not solve all problems, as evidenced by the known efficiency drop in modern engines at altitude. Howell et al. [9] indicated that their highly loaded airfoils might be close to a limit, and that higher loading could cause unacceptable separation problems even in the presence of wakes. Looking beyond FSTI and wakes, other types of flow control could prove useful. The literature contains numerous examples of separation control. Most have been applied to external flows over aircraft, but a few studies have considered passive devices added to LPT airfoils. Van Treuren et al. [8] utilized vortex generators on the suction surface of an LPT airfoil. The vortex generators caused reattachment at Re=50,000 (all Re in the present paper are based on exit velocity and suction surface length). Losses appeared to be slightly lower with the vortex generators. The vortex generators were not effective at Re=25,000, and the boundary layer did not reattach even with 8% FSTI. Van Treuren et al. [8] did not consider higher Re. In another study, Lake et al. [12] used various passive devices including dimples and boundary layer trips in an LPT cascade. They considered cases with Re above 100,000. Murawski and Vafai [13] added extensions to the trailing edges of the airfoils in their cascade. These extensions tended to move the separation location downstream. At low Re, they reduced the length of the separation bubble and reduced losses. At high Re, losses increased. Byerley et al. [14] used ''Gurney flaps'' to control separation. These devices were trips, near the trailing edge on the pressure side of the airfoils. They helped to keep the boundary layer attached on the suction side, but also increased losses in the cascade. Active separation control has also been employed. Bons et al. [15,16] used steady and pulsed vortex generator jets to successfully control separation under LPT conditions.

The studies listed above indicate that separation control should be possible under LPT conditions. Existing results are, however, limited both in the range of Reynolds numbers considered in each study and in the types of data acquired. More experiments are needed with various types of devices to expand the experimental data base. Detailed measurements will also help in the explanation of the physical mechanisms by which various devices affect the flow.

Passive flow control is considered in the present work. Thin bars of rectangular cross section are placed on the suction surface of an LPT airfoil near the suction surface velocity peak. Experiments were conducted in a single-passage cascade simulator, described in Volino [7]. The geometry of the passage corresponds to that of the ''Pak-B'' airfoil, which is an industry supplied research airfoil that is representative of a modern, aggressive LPT design. Volino [7] documented cases in the present facility without flow control. These serve as baseline cases for the present study.

Experiments

Experiments were conducted in a low speed wind tunnel, described by Volino et al. [17]. Briefly, air enters through blowers and passes through a honeycomb, a series of screens, two settling chambers, and a three-dimensional contraction before entering the test section. At the exit of the contraction, the mean velocity is uniform to within 1%. The FSTI is 0.5%±0.05%. Nearly all of this free-stream ''turbulence'' is actually streamwise unsteadiness at frequencies below 20 Hz and is not associated with turbulent eddies. The rms intensities of the three components of the unsteadiness are 0.7%, 0.2%, and 0.2% in the streamwise, pitchwise, and spanwise directions, respectively. For low-FSTI cases, the test section immediately follows the contraction. For high FSTI, a passive grid is installed at the contraction exit followed by a 1-m-long rectangular settling chamber. At the inlet to the test section the high-FSTI mean flow and turbulence are spatially uniform to within 3% and 6%, respectively. The free-stream turbulence is nearly isotropic with rms intensities of 8.8%, 8.9%, and 8.3% in the streamise, pitchwise, and spanwise directions. The integral length scales of these components are 3 cm, 1.6 cm and 1.4 cm. The integral scales were computed from the power spectra of each component.

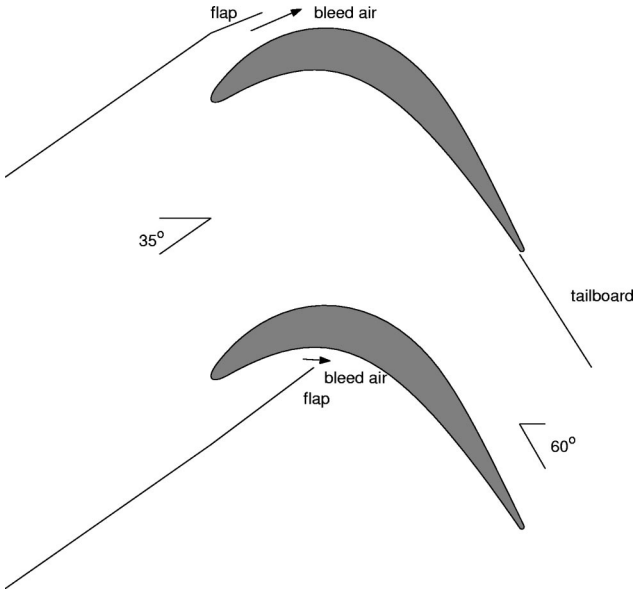

Fig. 1 Schematic of the test section

The test section, shown in Fig. 1, consists of the passage between two airfoils. Details are listed in Table 1 and more information is available in Ref. [7]. A large span-to-chord ratio of 4.3 was chosen to ensure two-dimensional flow at the spanwise centerline of the airfoils, where all measurements were made. Upstream of each airfoil are flaps, which control the amount of bleed air allowed to escape from the passage. The flaps, along with a tailboard on the pressure side of the passage, are adjusted to produce the correct leading edge flow and pressure gradient along the airfoils. The flow in the passage matches that in a multiblade cascade.

Experimental conditions match those of the ten baseline cases of Volino [7], who considered high- and low-FSTI cases at five Reynolds numbers (Re=25,000, 50,000, 100,000, 200,000, and 300,000). The Reynolds number range is representative of condi-

Table 1 Test section parameters

Axial chord (mm)	True chord (mm)	Pitch (mm)	Span (mm)	Suction side, L_s (mm)	Inlet flow angle	Exit flow angle
153.6	170.4	136.0	660.4	228.6	35°	60°

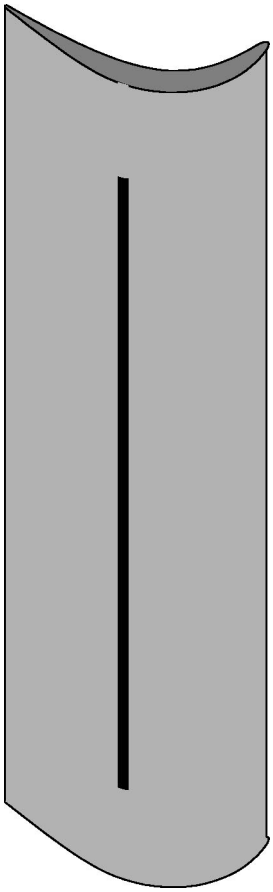

Fig. 2 Scale drawing of suction side airfoil showing location of bar

tions from cruise to takeoff. The FSTI levels in an engine may vary considerably, but the values in the present work are believed to span the range of most interest.

Prior to the detailed experiments of the present study, various devices were used in preliminary attempts at flow control. The devices included trip wires of various diameters, rectangular bars of various widths and thicknesses, and delta wing vortex generators of various heights, spacing, and angles with respect to the flow. All of these devices were tried at several streamwise locations along the suction surface. Documentation included streamwise pressure profiles and velocity profiles acquired near the trailing edge. Large devices of any type eliminated separation (as indicated by the pressure profiles), but caused large increases in losses (as indicated by large increases in momentum deficit at the trailing edge). As the size of the devices was reduced, it was found that all devices that were just large enough to induce boundary layer reattachment at Re=25,000 caused about the same increase in losses at higher Re. This was somewhat unexpected, as it was thought that the delta wings vortex generators might present less blockage, and more effectively promote mixing and inhibit separation than the trips or bars. Reasons for this unexpected finding are discussed with the results below. Since no device appeared to have a clear advantage, rectangular bars were chosen for further study because of their simplicity. The bars were of uniform rectangular cross section and extended along the airfoil span, as shown in Fig. 2. It should be noted that the tests described above were not exhaustive, and do not preclude the possible usefulness of vortex generators or other types of devices.

The results of the preliminary tests with the bars indicated that the streamwise width of a bar and the location of its leading edge were unimportant. The bar height and the location of its trailing edge were critical. Hence, it appeared that the backward-facing step at the trailing edge was most important for flow control. Bars were most effective when the trailing edge was near the location of the suction surface velocity peak. If the trailing edge was much farther downstream, it was located under the separation bubble and was ineffective. If the trailing edge was upstream in the favorable pressure gradient region, the stabilizing effect of the accelerating flow appeared to lessen the bar's effectiveness.

In the present study, rectangular bars were fabricated from multiple layers of vinyl tape. The trailing edge of the bar was located at $s/L_s=0.51$, near the suction surface velocity peak. All bars were 6 mm wide in the streamwise direction. Bar heights of 0.4 mm, 0.8 mm, and 1.6 mm were used. The bar heights were all less than 1% of L_s. They compare to local boundary layer thickness at the bar location of about 3.8 mm, 2.7 mm, 2.0 mm, 1.4 mm, and 1.2 mm in the baseline Re=25,000 through 300,000 cases, respectively. For each bar height, all 10 cases of the baseline study were redocumented, for a total of 30 new experimental cases.

Measurements. Pressure surveys were made for each case using a pressure transducer (0–870 Pa range Validyne transducer) and a Scanivalve. Stagnation pressure was measured with a pitot tube upstream of the passage inlet, and 11 pressure taps were located on each airfoil along their spanwise centerlines. Locations of the taps on the suction side are listed in Table 2 along with measured local FSTI components, and the Re K product at these stations based on a nonseparating, inviscid solution. The uncertainty in the suction side pressure coefficients was 7% at the lowest Re, and below 4% in other cases. Most of this uncertainty was due to bias error. Stochastic error was minimized by averaging pressure transducer readings over a 10-s period.

Velocity profiles on the suction surface were measured at streamwise stations corresponding to pressure taps 7–11, as given

Table 2 Measurement stations locations, local acceleration (inviscid solution), and measured local free-stream turbulence

Station	s/L_s	Re K	Low FSTI u'/U_∞ (%)	Low FSTI v'/U_∞ (%)	High FSTI u'/U_∞ (%)	High FSTI v'/U_∞ (%)
1	0.111	1.58	0.44		5.2	
2	0.194	1.20	0.39		4.6	
3	0.278	0.86	0.37		4.0	
4	0.361	0.75	0.38		3.5	
5	0.444	0.62	0.39		3.2	
6	0.528	−0.02	0.41		2.8	
7	0.611	−0.81	0.47	0.05	2.9	5.9
8	0.694	−0.95	0.47	0.12	3.0	6.2
9	0.777	−0.58	0.48	0.14	3.4	6.6
10	0.861	−0.53	0.54	0.11	3.8	6.8
11	0.944	−0.18	0.51	0.11	4.0	6.8

in Table 2. These stations are downstream of the bar. Profiles at stations 1–6 are fully documented for the baseline cases in Refs. [7,18], and show that the upstream boundary layer closely follows a laminar solution, even in the high-FSTI cases. Profiles were measured near but not at the spanwise centerline of the airfoil to insure that the pressure taps did not interfere with the velocity measurements. Profiles were acquired with a hot-wire anemometer (AA Lab Systems model AN-1003) and a single-sensor boundary layer probe (TSI model 1218-T1.5). The sensor diameter is 3.8 μm, and the active length is 1.27 mm. At each measurement location, data were acquired for 26 s at a 20-kHz sampling rate (2^{19} samples). All raw data were saved. The high sampling rate provides an essentially continuous signal, which is needed for intermittency and spectral postprocessing. The long sampling time results in low uncertainty in both statistical and spectral quantities. Data were acquired at 60 wall normal locations in each profile, extending from the wall to the free stream, with most points concentrated in the near-wall region. The closest point was within 0.1 mm of the wall, which corresponds to $y/L_s = 0.0004$ and between 0.01 and 0.2 boundary layer thicknesses. Flow direction in a separation bubble cannot be determined with a single-sensor hot-wire, but velocity magnitude can be measured and was found to be essentially zero within the bubbles of the present cases. Determining the direction was not, therefore, considered essential. Uncertainties in the mean velocity are 3–5% except in the very near wall region where near-wall corrections (Wills [19]) were applied to the mean velocity. Uncertainties in the momentum and displacement thicknesses computed from the mean profiles are 10%. Uncertainty in the shape factor, H, is 8%.

The uncertainty in the fluctuating streamwise velocity is below 10%, except in the very-near-wall region, where spatial averaging effects, due to the finite length of the hot-wire sensor, become important in some cases. For the present cases, as explained by Volino [7] based on the work of Ligrani and Bradshaw [20,21], spatial averaging should not be significant for the Re=25,000 and 50,000 cases, even near the wall. For the higher Re cases, spatial averaging should not be significant for $y>1$ mm ($y/L_s>0.004$), but may cause errors as high as 30% closer to the wall. It is not certain that the errors are this large, however. The estimates are based on the results of Ligrani and Bradshaw [20,21], who considered a boundary layer with $Re_\theta=2600$. The momentum thickness Reynolds numbers in the present cases are all below 1300. This may indicate less developed turbulence in the present study, which could imply fewer small-scale eddies and lower averaging errors.

The intermittency, γ, is the fraction of time the flow is turbulent within the transition region. It was determined at each measurement location based on the instantaneous streamwise velocity signal, using the technique described by Volino et al. [17]. The uncertainty in γ is 10%. As explained by Volino et al. [17], turbulent flow is defined here to include a range of large- and small-scale eddies, turbulence production, and dissipation. A boundary layer may be characterized by significant u' fluctuations but still be nonturbulent if these fluctuations are induced by an external source that does not also cause near-wall turbulence production. Such is often the case under high-FSTI conditions. Free-stream eddies buffet the boundary layer, inducing nonturbulent boundary layer fluctuations but very little momentum transport. Transition to turbulence is characterized not so much by large increases in u' levels, which may remain essentially constant, but by the appearance of higher frequencies. The higher frequencies signal the generation of turbulence in the near-wall region and are used to distinguish between turbulent and nonturbulent flow. Further discussion is available in Ref. [17].

Results

Velocity and Pressure Profiles. Pressure coefficients for the low-FSTI, Re=25,000 cases are shown in Fig. 3. Also shown is the inviscid solution for the present geometry. In all cases there is good agreement with the inviscid solution on the pressure side. On the suction side, the baseline case shows good agreement with the inviscid solution in the favorable pressure gradient region, but a large separation bubble in the adverse pressure gradient region. Separation is indicated by the nearly constant C_p values, which are well above the invisid solution. The C_p values remain high to the trailing edge, showing no sign of reattachment. With the 0.4-mm-thick bar, there is an increase in C_p over the baseline value at $s/L_s=0.53$. The pressure tap at this location is immediately downstream of the bar, and the flow over the tap is probably affected by the close proximity of the bar. The C_p values in this case remain high to the trailing edge, indicating that the boundary layer does not reattach. The same is true for the 0.8-mm bar case. With the 1.6-mm bar, C_p drops below the baseline values near the end of the favorable pressure gradient region. The larger bar is apparently enough of an obstruction to slow the near-wall flow upstream of the bar. Downstream of the 1.6-mm bar, C_p values are high, as in the other cases, but at the most downstream pressure tap C_p drops to near the inviscid solution value, indicating boundary layer reattachment.

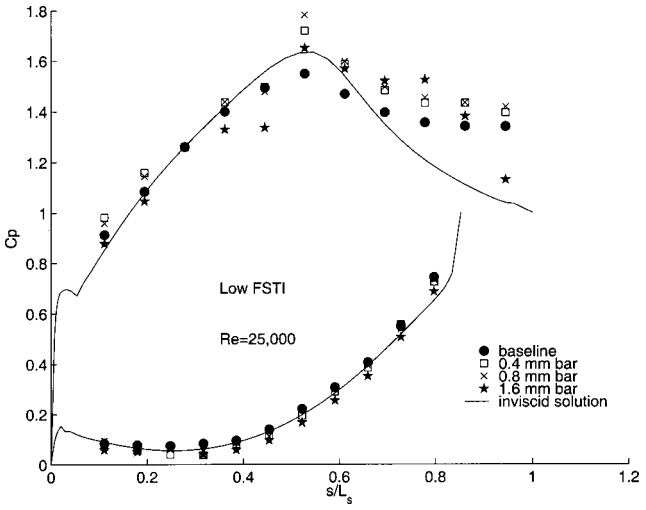

Fig. 3 C_p profiles, low FSTI, Re=25,000 cases

The velocity profiles for the low-FSTI, Re=25,000 cases are shown in Fig. 4. The top row of the figure shows dimensionless mean velocity profiles at stations 7–11. The baseline case shows a boundary layer near separation at station 7, a small separation bubble at station 8, and an increasingly larger bubble at stations 9–11. The mean profiles of the 0.4-mm and 0.8-mm bar cases are

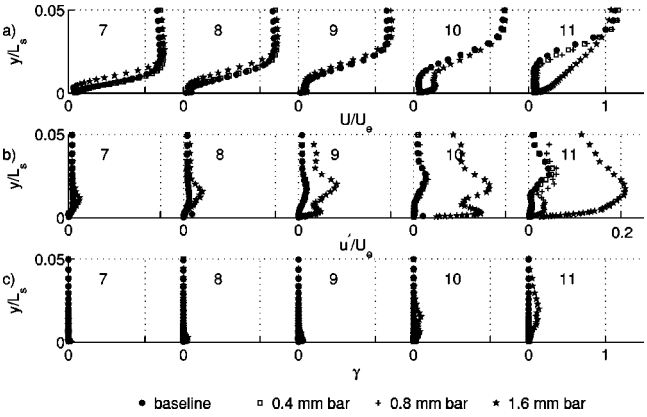

Fig. 4 Station 7–11 profiles, low FSTI, Re=25,000 cases: (*a*) mean velocity, (*b*) u', (*c*) intermittency

virtually indistinguishable from the baseline case. The 1.6-mm bar case shows a clear separation bubble at station 7, suggesting that the boundary layer has separated from the trailing edge of the bar. This bubble continues to grow, and at station 8 the separation bubble is larger with the 1.6-mm bar than in the other cases. At station 9 all cases appear similar. This agreement is really a crossing, as the shear layer in the 1.6-mm bar case is on the verge of reattaching, while the separation bubble is growing in the other cases. At station 10, the near-wall velocity in the 1.6-mm bar case has begun to rise, indicating incipient reattachment. By station 11, the boundary layer has clearly reattached in the 1.6-mm bar case, although the mean profile has not recovered to a fully developed turbulent shape. Dimensionless u' profiles are shown in the second row of Fig. 4. As with the mean profiles, the baseline case and the 0.4-mm and 0.8-mm bar cases are indistinguishable through station 10. All show a small u' peak growing in the shear layer over the separation bubble. As explained by Volino [7,18], this peak is not indicative of transition. It is caused primarily by low-frequency fluctuations that are amplified when they act across the region of high mean velocity gradient in the shear layer. At station 11, there is a slight increase in u' in the 0.8-mm bar case over the baseline case, and the high values extend into the near-wall region. These near-wall fluctuations suggest the beginning of transition and reattachment, but they are not large enough in this case to significantly affect the mean profile. The 1.6-mm bar case shows a larger u' peak than the other cases at stations 7 and 8. The peak is in the shear layer and is similar to the peaks at stations 9 and 10 of the other cases. It does not indicate transition. The peak becomes larger at station 9, and extends into the near-wall region, which is a sign of incipient transition. By station 10 u' is much larger with a clear double peak. This rise in u' corresponds to the beginning of reattachment observed in the mean profile. The third row of Fig. 4 shows the local intermittency. Its is zero in all cases through station 9, but begins to rise at stations 10 and 11 of the 1.6-mm bar case. The intermittency peak is in the shear layer, indicating that this is where transition begins. Intermittency only reaches about 13% at station 11. This is consistent with the mean velocity profile, which shows the boundary layer is reattached but not yet a fully developed turbulent profile. As the turbulence is intermittent, it is likely that the boundary layer is only intermittently reattached. The high u' peak at station 11 is also consistent with a transitional boundary layer. As a boundary layer becomes fully turbulent, the dimensionless u' peak will decrease in magnitude to about 0.1, and move close to the wall.

The behavior in the 1.6-mm bar case is interesting. The bar was not large enough to immediately trip the boundary layer to turbulent, but it did move the separation point upstream. This caused the transition to move upstream, and led to at least a partial reattachment by the trailing edge, which did not occur in the other cases. The 0.8-mm bar trip case is also very interesting. The bar in this case was so small that it had no immediate measurable affect on the mean or u' profiles. Well downstream at station 11, however, the effect of this bar became visible in the u' profile. Apparently this bar introduced a very small disturbance in the flow, which was too small to detect at first, but grew as it moved downstream.

The velocity profiles of Fig. 4 and the pressure profiles of Fig. 3 are in good agreement. Both show transition and reattachment at the same locations, and the measured static pressures agree with the local free-stream velocities of Fig. 4. The agreement between the pressure and velocity results was apparent in all cases. For brevity, the pressure profiles are not presented in the cases which follow.

Figure 5 shows the velocity profiles for the high-FSTI, Re $=25{,}000$ cases. The format is that same as in Fig. 4. As in the low-FSTI case, the baseline, 0.4-mm trip and 0.8-mm trip cases are nearly indistinguishable at the upstream stations. By station 11, some differences are apparent in the mean profiles for these cases. The separation bubble is less distinct in the cases with the

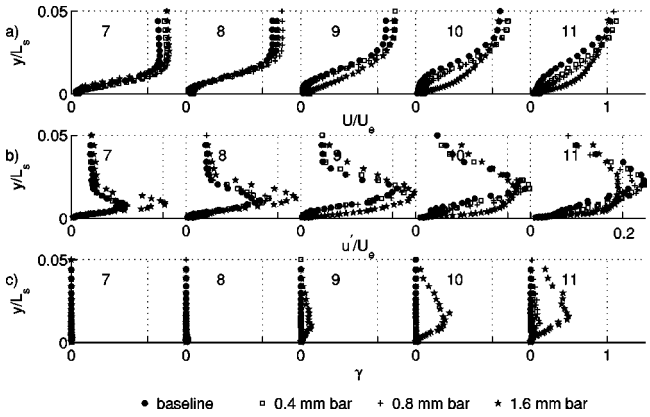

Fig. 5 Station 7—profiles, high FSTI, Re=25,000 cases: (*a*) mean velocity, (*b*) u', (*c*) intermittency

bars, but the boundary layer still does not appear fully reattached. Intermittency rises slightly above zero at station 11 of the 0.8-mm bar case, while remaining essentially at zero with the smaller bar and in the baseline case. The u' profiles show a large peak in the shear layer, which grows in the streamwise direction. As shown in Volino [7], this peak is caused by the action of the high FSTI on the shear layer, and does not indicate significant momentum transport. As in the low-FSTI cases of Fig. 4, the 1.6-mm bar case shows significant differences from the other cases in Fig. 5. The u' peak is significantly higher in this case at stations 7 and 8. At station 9, u' values are higher in the near-wall region, the intermittency rises above zero, and the mean profile appears to be reattached. At stations 10 and 11 the intermittency continues to increase. The mean profile adjusts toward a more turbulent shape between stations 9 and 11. The u' peak decreases somewhat by station 11, but still shows the relatively high values of a transitional boundary layer, rather than the somewhat lower values of a fully turbulent boundary layer. As in the low-FSTI, Re $=25{,}000$ case, the 1.6-mm bar is not large enough to immediately trip the boundary layer to turbulent, but it causes transition to move upstream and leads to a reattachment that did not occur in the baseline or smaller bar cases.

The velocity profiles of the low-FSTI, Re $=50{,}000$ case are shown in Fig. 6. The effects of the bars are clear. At station 7, the 1.6-mm bar has caused a relatively large separation bubble compared to the other cases and a small u' peak in the shear layer over this bubble. The smaller bar cases are indistinguishable from the baseline case, with mean profiles only on the verge of separation and u' near zero. By station 8, the 1.6-mm bar case has

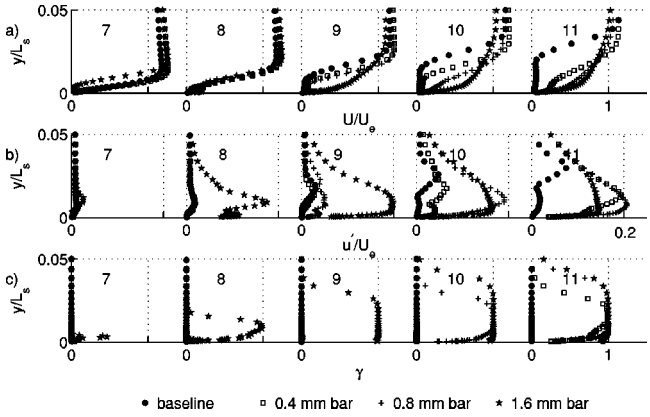

Fig. 6 Station 7–11 profiles, low FSTI, Re=50,000 cases: (*a*) mean velocity, (*b*) u', (*c*) intermittency

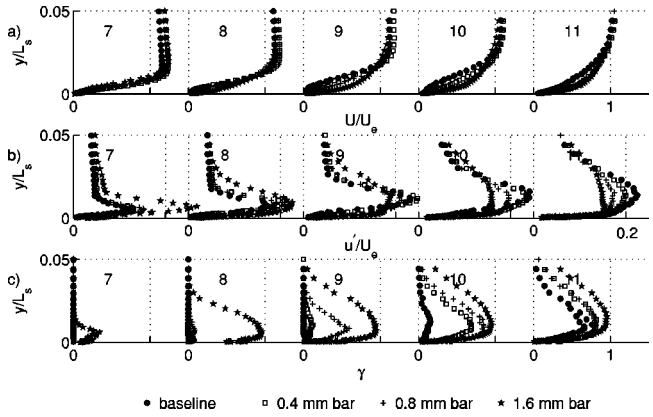

Fig. 7 Station 7–11 profiles, high FSTI, Re=50,000 cases: (*a*) mean velocity, (*b*) u', (*c*) intermittency

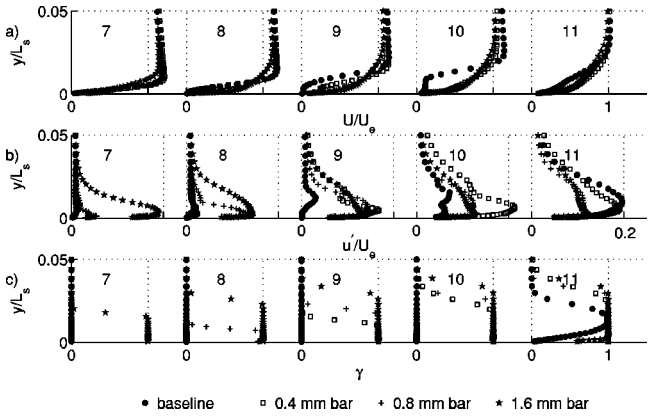

Fig. 8 Station 7–11 profiles, low FSTI, Re=100,000 cases: (*a*) mean velocity, (*b*) u', (*c*) intermittency

undergone a sudden transition, with $\gamma=1$, high u' levels in both the shear layer and near-wall regions, and the beginning of reattachment as indicated by nonzero mean velocity near the wall. The other cases are indistinguishable, exhibiting a small separation bubble and showing no sign of transition or reattachment. At station 9, the boundary layer is clearly reattached in the 1.6-mm bar case, and u' values are beginning to rise in the 0.8-mm bar case. At station 10 the intermittency indicates fully turbulent flow and the boundary layer has reattached in the 0.8-mm bar case. The 0.4-mm bar case is still separated with $\gamma=0$, but u' has begun to rise near the wall. By station 11 the 0.4-mm bar case has become turbulent and the boundary layer has started to reattach. The baseline case remains nonturbulent with a large separation bubble at station 11. As observed in the Re=25,000 cases, the 1.6-mm bar is not large enough to immediately trip the boundary layer to turbulent, but it does move separation upstream, which causes transition and reattachment to move significantly upstream. The smaller bars appear to have no immediate effect on the boundary layer, but they must introduce small disturbances that grow in the streamwise direction and have a significant effect in moving the transition and reattachment upstream. The 0.8-mm bar must introduce a larger disturbance than the 0.4-mm bar, since transition and reattachment occur one station farther upstream with the 0.8-mm bar.

Figure 7 shows the high-FSTI, Re=50,000 cases. With the larger bars, transition and reattachment move upstream. With the 1.6-mm bar, the intermittency is already nonzero by station 7, and the boundary layer is fully turbulent and attached by station 8. With the 0.8-mm bar, γ rises above zero at station 8 and is near fully turbulent by station 10. The mean profile appears to indicate reattachment by station 9. The intermittency rises above zero in the 0.4-mm bar case at station 9, and continues to rise at stations 10 and 11. The mean profile shows reattachment at station 10. In the baseline case, the intermittency begins to rise at station 10, and the boundary layer is reattached at station 11. At station 11 the mean profiles are indistinguishable in the cases with bars, and fuller than in the baseline case. In all cases, the transition begins upstream of the location in the corresponding low-FSTI case of Fig. 6, but the transition length is longer. Volino and Hultgren [22] also observed that transition begins farther upstream with high-FSTI, but is more abrupt in low-FSTI cases.

Figure 8 shows the low-FSTI, Re=100,000 cases. The 1.6-mm bar immediately trips the boundary layer to turbulent and eliminates the separation bubble. The 0.8-mm bar causes a small u' peak above the baseline values at station 7. The intermittency jumps from 0 to 1 between stations 7 and 8, and the separation bubble is effectively eliminated. As in the lower-Re cases, the 0.4-mm bar has no visible effect at station 7, and the mean and u' profiles are indistinguishable from the baseline case. The boundary layer separates, but by station 9 the shear layer has become fully turbulent and begun to reattach. In the baseline case, u' does not begin to show elevated near wall values until station 10, and transition and reattachment occur at station 11. The mean profiles at station 11 show the fullest profile and thinnest boundary layer in the 0.4-mm bar case. The larger bars result in thicker boundary layers. The mean profile in the baseline case has not yet recovered to a fully turbulent shape. As will be discussed below, the thinner attached boundary layer in the 0.4-mm bar case suggests that this case will have lower losses than the other cases.

The high-FSTI, Re=100,000 cases are shown in Fig. 9. As in the low-FSTI case, the 1.6-mm bar trips the boundary layer to turbulent and eliminates separation at this Re. The intermittency is nonzero at station 7 of the 0.8-mm bar case, and it continues to rise through station 10, indicating an extended transition zone. Because the transition begins so far upstream, the separation bubble is eliminated and transition occurs in an attached boundary layer. With the 0.4-mm bar, the intermittency indicates that the transition does not begin until station 8, so a small separation bubble forms, as in the baseline case. The boundary layer is reattached by station 9, however, and the transition is nearly complete by station 10. In the baseline case, the transition begins at station 9, and the boundary layer is reattached at station 10. Examining the mean profiles, the 1.6-mm bar causes an immediate thickening of the boundary layer, and the separation bubble in the baseline case also causes a thicker boundary layer. By station 11, the mean profiles for these two cases agree closely. The boundary layers are thinner in the cases with the smaller bars.

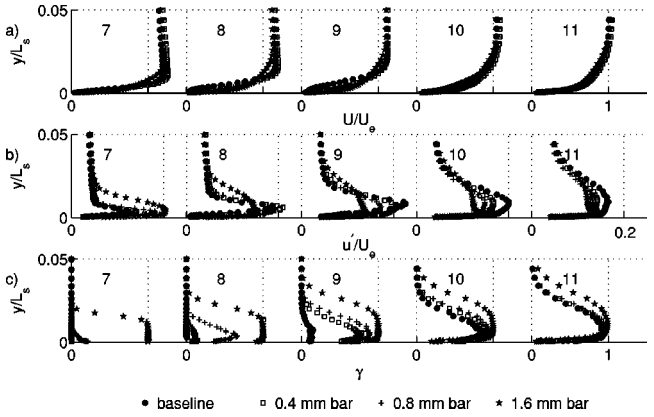

Fig. 9 Station 7–11 profiles, high FSTI, Re=100,000 cases: (*a*) mean velocity, (*b*) u', (*c*) intermittency

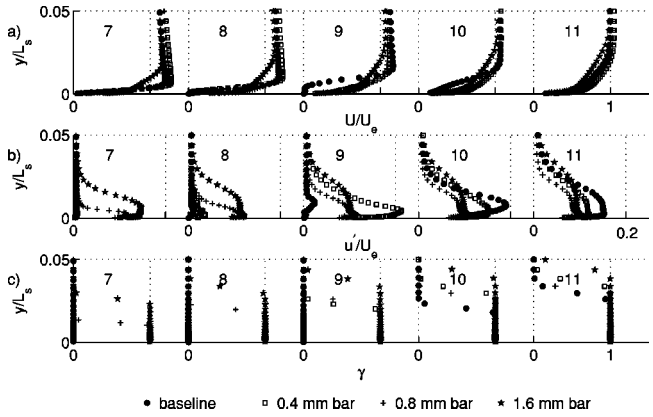

Fig. 10 Station 7–11 profiles, low FSTI, Re=200,000 cases: (*a*) mean velocity, (*b*) u', (*c*) intermittency

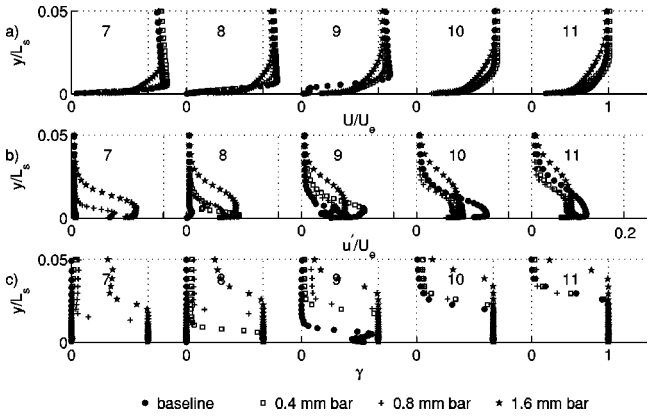

Fig. 12 Station 7–11 profiles, low FSTI, Re=300,000 cases: (*a*) mean velocity, (*b*) u', (*c*) intermittency

In the low-FSTI, Re=200,000 cases of Fig. 10, the intermittency profiles show that the 0.8-mm and 1.6-mm bars immediately trip the boundary layer to turbulent and eliminate the separation bubble. The 1.6-mm bar, which is the same thickness as the boundary layer at station 7 of the baseline case, results in a substantially thicker boundary layer than in all of the other cases. The 0.4-mm bar case shows a small separation bubble at station 8, but is fully turbulent and reattached by station 9. The baseline case exhibits a clear separation bubble at station 9, and is fully turbulent and reattached by station 10. The mean profiles at station 11 show that the growth of the bubble in the baseline case results in a thicker boundary layer than in the 0.8- and 0.4-mm bar cases.

Figure 11 shows the high-FSTI, Re=200,000 cases. As in the low-FSTI cases of Fig. 10, the 0.8- and 1.6-mm bars trip the boundary layer to turbulent. The transition has already started, as indicated by the nonzero intermittency, in the 0.4-mm bar case at station 7. In all of these cases, there is no separation. In the baseline case, γ does not rise above zero until station 9, and there may be a small separation bubble at station 8. At station 11, the mean, u', and intermittency profiles of the baseline, 0.4-mm, and 0.8-mm bar cases are all in good agreement, while the 1.6-mm bar case exhibits a noticeably thicker boundary layer.

The low FSTI, Re=300,000 cases are shown in Fig. 12. As in the Re=200,000 cases, the 0.8-mm and 1.6-mm bars trip the boundary layer to turbulent. The 0.4-mm bar appears to have no effect at station 7, where the mean and u' profiles agree with the baseline case and the intermittency is zero. By station 8, however, the boundary layer in the 0.4-mm bar case has become fully turbulent, while in the baseline case it is still laminar and has separated. By station 9 the shear layer in the baseline case is transitional, and it is fully turbulent and reattached by Station 10. At Station 11 the mean profiles for the four cases are all different, with the 0.4-mm bar and baseline cases having the thinnest boundary layers.

Figure 13 shows the high-FSTI, Re=300,000 cases. As in the low-FSTI cases, the 0.8-mm and 1.6-mm bars trip the boundary layer to fully turbulent, and the 0.4-mm bar causes the transition to start by station 7 and finish by station 8. Transition has started at station 8 of the baseline case and is complete near station 10. In all of these cases the transition begins far enough upstream to prevent separation. The mean profiles at all stations show that the boundary layer is thinnest in the baseline case and that the thickness increases with the bar size. With the 0.4-mm and 0.8-mm bars the boundary layer is only slightly thicker than in the baseline case, but it is substantially thicker in the 1.6-mm bar case.

Some consistent trends run through the data from all cases. If a bar is large enough, it will immediately trip the boundary layer to fully turbulent and prevent separation. As Reynolds number increases, the boundary layer thickness decreases as does the thickness of the bar required for tripping. If a bar is small enough, it initially appears to have no effect on the boundary layer. The boundary layer appears to proceed over the bar with no measurable change in the mean velocity or u' from the corresponding baseline case. The bars must, however, introduce some small disturbance into the boundary layer. The boundary layer is unstable against small disturbances in the adverse pressure gradient region, so the small disturbances grow and eventually cause transition. Larger bars must impart larger (albeit sometimes still undetect-

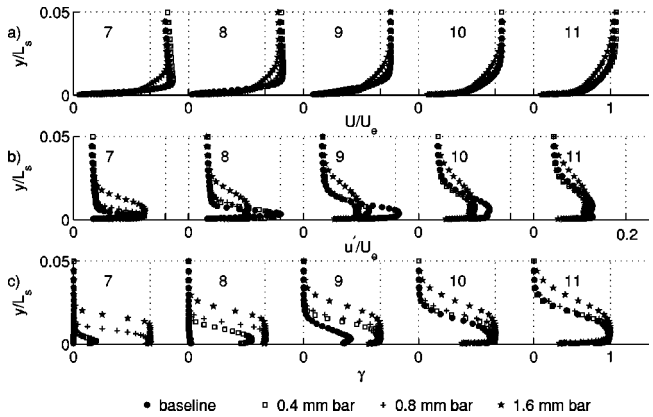

Fig. 11 Station 7–11 profiles, high FSTI, Re=200,000 cases: (*a*) mean velocity, (*b*) u', (*c*) intermittency

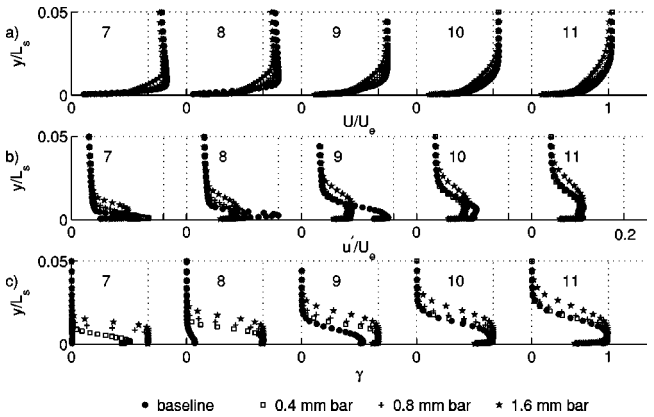

Fig. 13 Station 7–11 profiles, high FSTI, Re=300,000 cases: (*a*) mean velocity, (*b*) u', (*c*) intermittency

able) perturbations than the smaller bars, resulting in transition locations that move upstream as bar size is increased. The optimal bar size depends on the Reynolds number and is discussed further below.

The present results shed some light on the transition mechanism under both high- and low-FSTI conditions. Volino [18] examined spectra of the fluctuating velocity in the boundary layers and shear layers of the baseline cases. He observed sharp peaks in the spectra of the low-FSTI cases at frequencies that matched the most unstable frequencies for Tollmien-Schlicthing (TS) waves in the boundary layer just upstream of separation. He therefore concluded that the transition in the shear layer might be through a TS mechanism in these cases. In the high-FSTI cases, Volino [18] observed broadband peaks in the spectra and the relatively long transition regions noted above. Volino and Hultgren [22] made similar observations, and concluded that the high-FSTI separated flow transition was through a bypass mode, very similar to the high-FSTI transition in an attached boundary layer. Volino [18], however, noted that the broadband peaks in the high-FSTI case spectra were centered at the same frequencies as in the low-FSTI cases, suggesting a similar transition mechanism under high- and low-FSTI conditions. He concluded that disturbances that began to grow in the boundary layer prior to separation were causing a TS-type transition in the shear layer over the separation bubble in both the high- and low-FSTI cases. High-FSTI has a strong effect in moving the transition upstream, but the bars in the present cases had an equally strong or stronger effect in both the high- and low-FSTI cases. This confirms that the free-stream turbulence is not solely responsible for bypass transition in the high-FSTI cases.

The magnitude of the disturbances induced by the bars is too small to be quantified based on the mean or u' results presented above. Perhaps more can be learned from boundary layer spectra. Analyses of spectra based on u' fluctuations for the present cases show some interesting but inconclusive results. Volino [18] found that u' spectra are often characterized by low-frequency fluctuations that are induced by the free stream and have no direct effect on transition. In the early stages of transition, these low-frequency fluctuations can hide the very-low-amplitude fluctuations important for transition. Volino [18] found that spectra of the turbulent shear stress are less affected by the low-frequency unsteadiness and can provide a better means for detecting the early stages of transition. Acquisition and analysis of turbulent shear stress data for the cases of the present study may prove useful for explaining and quantifying the transition mechanism.

Shape Factor and Momentum Thickness. The shape factor and momentum thickness are useful parameters for evaluating the state of the boundary layer with respect to separation, transition, and losses. They provide a means for summarizing the information presented in the velocity profiles of Figs. 4–13. In the present cases, the boundary layer has a shape factor H of about 2.4 at the end of the favorable pressure gradient region. This is the expected value for this laminar, accelerated boundary layer. If the boundary layer separates, the displacement thickness grows rapidly, while the momentum thickness remains nearly constant. The result is a very high shape factor. If the boundary layer reattaches, the displacement thickness drops, and the momentum thickness begins to grow. The boundary layer eventually recovers to a fully turbulent shape, with a shape factor of about 1.6 in the present cases.

Stage losses in a multiblade turbine cascade can be determined through measurement of the momentum deficit in the wake downstream of the blade row. With the single-passage facility of the present study, wake measurements are not meaningful, since there is flow on only one side of the airfoils on each side of the passage. If a boundary layer separates and does not fully reattach, or reattaches near the trailing edge, momentum thickness will be relatively low at the trailing edge, and high losses will be generated in the wake downstream of the passage. While the losses in such a case cannot be quantified in the present study, it is safe to assume that they would be unacceptably high, and that there would be an unacceptable loss of lift from the airfoils. For those cases in which the boundary layer reattaches and recovers to a fully developed turbulent shape, the suction side profile loss is likely the dominant loss mechanism in the passage (Howell et al. [9]). As explained by Howell et al. [9], for a given shape factor and passage exit angle, the momentum thickness of the suction side boundary layer at the trailing edge is proportional to the suction side profile loss.

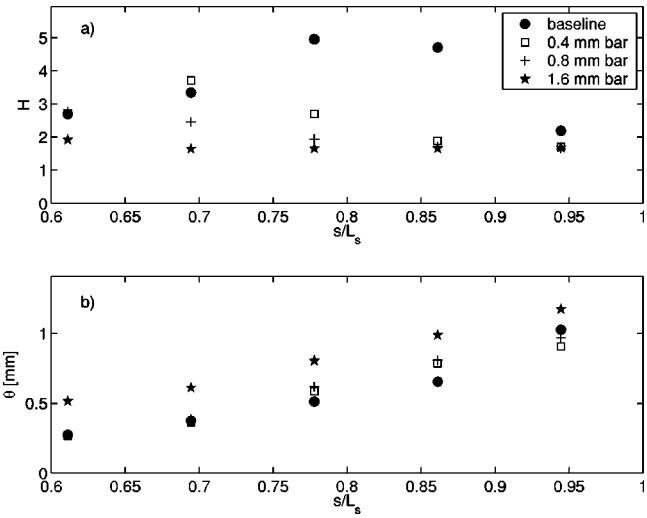

Fig. 14 Shape factor and momentum thickness versus streamwise location, low FSTI, Re=100,000: (*a*) H, (*b*) θ

Figure 14 provides an example of the development of the shape factor and momentum thickness, using the low-FSTI, Re $=100{,}000$ cases. In the baseline case, H increases from 2.4 to a high value of about 5 as the boundary layer separates. Reattachment occurs near the trailing edge, and H drops to about 2.2, which is still above the turbulent value of 1.6, indicating that recovery from the separation is not complete. In the 0.4-mm bar case, the boundary layer separates and H reaches a value of 3.7. The boundary layer then reattaches, and H gradually drops to a fully turbulent value by the trailing edge. With the 0.8-mm bar, transition occurs far enough upstream to prevent separation, and H drops continuously from a laminar value to a turbulent value as transition occurs. In the 1.6-mm bar case the boundary layer is tripped to turbulence, and H quickly reaches its turbulent value. The 1.6-mm bar causes an immediate thickening of the boundary layer, and the momentum thickness remains higher than in the other cases at all streamwise locations. The 0.4- and 0.8-mm bars appear to have no immediate effect on θ. When transition and reattachment occur, however, θ begins to rise. When reattachment occurs in the baseline case, it causes θ to increase to a higher value than in the 0.4- and 0.8-mm bar cases. Near the trailing edge θ is lowest in the 0.4-mm bar case. This would presumably be the case with the lowest profile losses. The larger bars force the transition to occur farther upstream than necessary, resulting in a longer turbulent region and higher losses. In the baseline case the separation bubble becomes relatively thick, resulting in a thick boundary layer after reattachment. The 0.4-mm bar case provides a good example of the controlled diffusion described by Hourmouziadis [1]. With the 0.4-mm bar, the separation bubble is relatively thin, and the turbulent region is relatively short, resulting in lower losses.

Figure 15 shows the shape factor and momentum thickness at station 11 ($s/L_s=0.94$), near the trailing edge, for all the low-FSTI cases. In the Re=25,000 cases, the shape factor indicates that the boundary layer only reattaches in the 1.6-mm bar case. The shape factor in this case is still above the expected turbulent value, indicating that recovery from the separation in not complete. Comparison of momentum thicknesses is not meaningful at

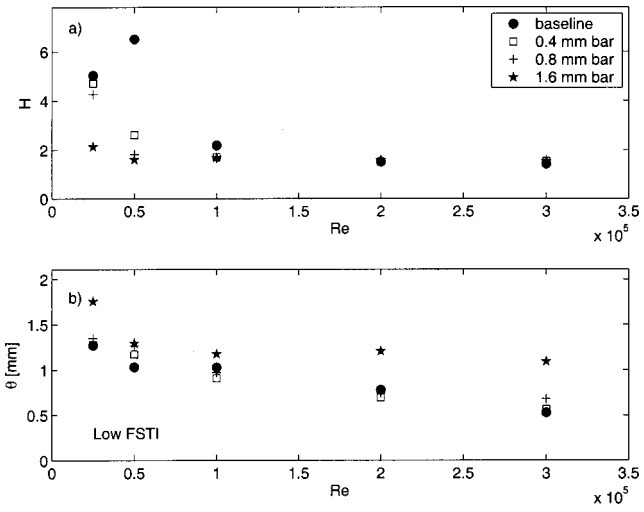

Fig. 15 Station 11 shape factor and momentum thickness versus Re, low-FSTI cases: (*a*) H, (*b*) θ

this Re. For the Re=50,000 cases, the 0.8- and 1.6-mm bars cause reattachment, while recovery from the separation is only partially complete in the 0.4-mm bar case and the shear layer remains separated in the baseline case. The 0.8- and 1.6-mm bar cases are, therefore, preferable at this Re, and both have about the same momentum thickness at station 11. At Re=100,000, already described in Fig. 14, the 0.4-mm bar produces the lowest losses. The 0.4-mm bar case is also best at Re=200,000, with slightly lower losses than with the 0.8-mm bar or in the baseline case. At Re =300,000, the transition occurs sufficiently far upstream in the baseline case to keep the separation bubble small and produce lower losses than in any of the cases with bars.

The station 11 shape factors and momentum thicknesses for the high-FSTI cases are shown in Fig. 16. As in the low-FSTI cases, only the 1.6-mm bar is large enough to force reattachment at Re=25,000, and it does not even quite result in full recovery to a turbulent profile. At Re=50,000, the shape factor shows that all of the bars cause reattachment, while the boundary layer in the baseline case has reattached but not fully recovered from the separation. The 0.4- and 0.8-mm bar cases have lower momentum thickness than the 1.6-mm bar case. At the higher Re, reattachment is complete in all cases, and the 1.6-mm bar cases have significantly

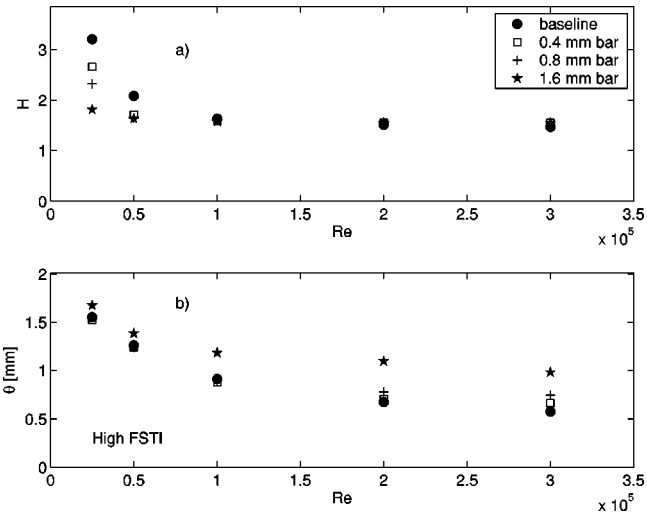

Fig. 16 Station 11 shape factor and momentum thickness versus Re, high-FSTI cases: (*a*) H, (*b*) θ

higher losses than the other cases. At Re=100,000, the 0.4- and 0.8-mm bar cases and the baseline case all have about the same losses. As Re increases to 200,000 and 300,000, the baseline case emerges as the case with lowest losses, in agreement with the low-FSTI cases of Fig. 15.

The optimal bar height clearly varies with the Reynolds number. As Re increases, the boundary layer becomes thinner and more prone to transition, so a smaller bar is needed. At Re =25,000, the 1.6-mm bar is needed, and a larger bar would be desirable to force a more complete reattachment. At Re=50,000, the 0.8-mm bar is best, since it is large enough to cause reattachment at low FSTI, but produces lower losses than the thicker bar at high FSTI. At Re=100,000 and 200,000, the 0.4-mm bar is best, since it is large enough to force complete reattachment at low FSTI, and results in equal or slightly lower losses than the baseline or 0.8-mm bar cases. At Re=300,000, the baseline case is best, although the losses are only slightly lower than those of the 0.4-mm bar case. If a bar is used for passive flow control, a single bar thickness must be chosen for optimal overall performance. The best size will depend on the operating range of the engine. If the operating range is large, a compromise between improved performance at cruise and higher losses at takeoff may be needed.

Correlation of Results. The size of a bar necessary to trip a boundary layer to turbulence can be predicted using the following correlation from Gibbings [23].

$$\mathrm{Re}_d = U_d d/\nu > 600, \tag{1}$$

where d is the bar thickness and U_d is the velocity in the untripped boundary layer at $y=d$ at the streamwise location of the bar. Equation (1) predicts that bar thicknesses of 4.7 mm, 2.3 mm, 1.3 mm, 0.68 mm, and 0.50 mm would be needed to immediately trip the boundary layer to turbulent in the Re=25,000 through 300,000 cases, respectively. In agreement with this prediction, the results above show that the boundary layer was only tripped in the Re=200,000 and 300,000 cases with the 0.8-mm and 1.6-mm bars, and in the Re=100,000 cases with the 1.6-mm bar. Since an optimal bar does not immediately trip the boundary layer; it will be thinner than indicated by Eq. (1).

The most effective bars in the present cases appear to be those that cause reattachment to begin between stations 8 and 9, at s/L_s of about 0.74. When reattachment begins by this location, there is sufficient distance downstream for the reattachment and recovery from the separation to be completed before the trailing edge. The beginning of reattachment and the start of transition are related and occur at approximately the same location. There are a few correlations in the literature for prediction of the distance from separation to transition onset. In general they are not very robust, but some give reasonable estimates. Mayle [2] provides the following correlations:

$$\mathrm{Re}_{st} = 300\,\mathrm{Re}_{\theta s}^{0.7} \quad \text{(short bubble)}, \tag{2}$$

$$\mathrm{Re}_{st} = 1000\,\mathrm{Re}_{\theta s}^{0.7} \quad \text{(long bubble)}. \tag{3}$$

Equations (2) and (3) apply to short and long separation bubbles, respectively. Volino [7] found that the present baseline case results lie between the predictions of Eqs. (2) and (3) tending toward the long bubble correlation at low FSTI and about midway between the two correlations at high FSTI. Although they differ by a factor of 3, Eqs. (2) and (3) provide at least a rough estimate of the reattachment location.

The following correlation provides an estimate of the effect of bar height on reattachment location. The equation is based on a curve fit of the present data:

$$(s_t - s_p)_m/(s_t - s_p)_b = [1 + 0.23(d/\theta_p)^{1.56}]^{-1}, \tag{4}$$

where $(s_t - s_p)_b$ is the distance from the suction side velocity maximum ($s/L_s = 0.53$) to the location of the beginning of reattachment in the baseline case, and $(s_t - s_p)_m$ is this distance with a bar in place. The present data along with Eq. (4) are shown in

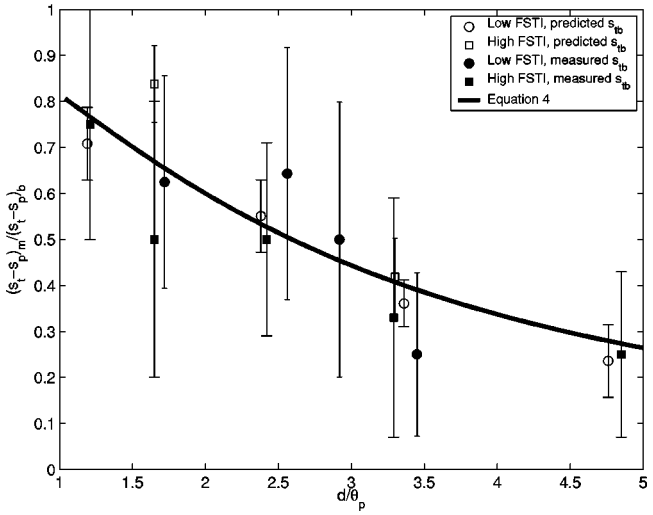

Fig. 17 Correlation of transition and reattachment start location to bar height; bars indicate range of possible values resulting from finite station spacing

Fig. 17. The finite spacing of the streamwise measurement stations results in some uncertainty in the transition start location, as indicated by the error bars in Fig. 17. Volino [7] showed that the boundary layer behavior upstream of the separation is predictable and laminar. To predict reattachment in a case with a bar, the laminar solution could be used to predict the separation location and the momentum thickness before separation. A correlation such as Eqs. (2) or (3) could then be used to estimate the distance to transition and reattachment in the baseline flow. This would give s_{tb}. Equation (4) could then be used to predict s_{tm} for a given bar thickness. Alternatively, the desired s_{tm} could be specified and used with Eq. (4) to predict the optimal bar thickness. Setting $s_{tm}=169$ mm ($s_{tm}/L_s=0.74$) and using the measured (when available) or predicted values for s_{tb} and θ_p for the baseline cases, optimal bar heights have been predicted for the present cases and are presented in Table 3.

Discussion. The above correlations are based only on the present data set, so it is doubtful that they are universally applicable. Still, they provide a start in the assessment of passive flow control devices. With more experiments with different airfoils, it may be possible to refine correlations such as Eq. (4), to make them more generally applicable.

Alternative passive devices such as vortex generators or dimples should also be considered. There is no guarantee, however, that these devices will provide improvement over the present bars. Dimples have been used in some applications such as internal blade cooling, to provide enhanced heat transfer with lower pressure drop than boundary layer trips. Dimples enhance heat transfer by promoting turbulence and mixing, which would also tend to promote boundary layer attachment. In the present application, however, we do not seek to enhance turbulence or heat transfer, or even to fully eliminate the separation bubble. Since the smaller bars in the present experiments did not increase losses or boundary layer thickness, or have any other immediate measurable effect on the boundary layer, it is not clear that any other device will be superior.

While the present bars have proven effective, it is clear from Table 3 and Figs. 15 and 16 that the optimal bar height varies with Re and FSTI. If applied passively, a single bar height would be selected for the entire operating range of the engine. If the operating range is large, a compromise will be necessary between improved performance at low Re and higher losses at high Re. Passive flow control has the distinct advantage of being relatively simple to implement in practice, but active flow control may provide a means for optimizing performance over a wider range of conditions. Unsteady active control also provides possibilities for further flexibility and improved performance not available with passive devices. Further consideration of active control is presented by Volino [24].

The present cases all involve steady inlet flow. In engine flows, the periodic wakes from upstream airfoils will make the flow unsteady. While steady flow experiments are necessary for building understanding of the flow and flow control devices, experiments should eventually be performed in flows with wakes.

Conclusions

1. Rectangular bars have been successfully employed as flow control devices on the suction side of a low-pressure turbine airfoil. Boundary layer reattachment was forced even in very-low-Reynolds-number cases.
2. Optimal bars are not large enough to immediately trip the boundary layer to turbulent or prevent separation, but rather induce very small disturbances that at first are essentially undetectable, but eventually promote transition in the shear layer at a downstream location.
3. Bars were effective under both high- and low-FSTI conditions, indicating that the high-FSTI transition is not simply a bypass transition induced by the free stream.
4. The optimal location for reattachment results in a relatively short turbulent region, but occurs sufficiently far upstream to prevent a large separation bubble and ensure complete recovery from the separation before the trailing edge. A bar height can be selected to induce reattachment at the desired location.
5. The optimal bar height varies with the Reynolds number and free-stream turbulence level. Bars that were large enough to induce reattachment at the lowest Re produced significantly higher losses at the higher Re. If a wide range of Reynolds numbers are encountered in practice, some compromise between improved performance at low Re and higher losses at high Re will be necessary in the choice of an overall best bar height.

Table 3 Baseline case boundary layer thickness at bar location ($s/L_s=0.53$), and predicted bar heights for tripping (d_{trip}) and for incipient reattachment (d_{opt}) at $s/L_s=0.74$ (all values in mm)

	Low FSTI				High FSTI			
$\mathrm{Re}\times10^{-3}$	$\delta_{99.5p}$	θ_p	d_{trip}	d_{opt}	$\delta_{99.5p}$	θ_p	d_{trip}	d_{opt}
25	3.8	0.48	4.7	2.4	3.9	0.48	4.7	1.5
50	2.7	0.34	2.3	1.2	2.8	0.33	2.3	0.6
100	1.9	0.23	1.3	0.4	2.2	0.24	1.3	0.2
200	1.3	0.16	0.7	0.2	1.6	0.16	0.7	0
300	1.2	0.14	0.5	0.1	1.4	0.14	0.5	0

Acknowledgments

This work was sponsored by the NASA Glenn Research Center. The grant monitor is Dr. David Ashpis. Additional matching support was provided through a U.S. Naval Academy Recognition Grant.

Nomenclature

C_p = $2(P_T-P)/\rho U_e^2$, pressure coefficient
d = Bar height
FSTI = Free-stream turbulence intensity
H = δ^*/θ, shape factor
K = $(\nu/U_\infty^2)(dU_\infty/ds)$, acceleration parameter
L_s = Suction surface length
P = Pressure
P_T = Upstream stagnation pressure
Re = $U_e L_s/\nu$, exit Reynolds number
Re_d = $U_d d/\nu$, Reynolds number based on bar height
Re_{st} = $U_\infty(s_t-s_s)/\nu$, separation to transition distance Reynolds number
Re_θ = Momentum thickness Reynolds number
s = Streamwise coordinate, distance from leading edge
U = Mean streamwise velocity
U_∞ = Local free-stream velocity
U_d = Mean velocity at bar height in baseline boundary layer
U_e = Nominal exit free-stream velocity, based on the inviscid solution
u' = rms streamwise fluctuating velocity
y = Cross-stream coordinate, distance from wall
$\delta_{99.5}$ = 99.5% boundary layer thickness
δ^* = Displacement thickness
γ = Intermittency, fraction of time flow is turbulent
ν = Kinematic viscosity
ρ = Density
θ = Momentum thickness

Subscripts

b = Baseline flow
m = Modified flow
p = Suction surface pressure minimum, velocity maximum
s = Separation location
t = Transition start location

References

[1] Hourmouziadis, J., 1989, "Aerodynamic Design of Low Pressure Turbines," AGARD Lecture Series 167.
[2] Mayle, R. E., 1991, "The Role of Laminar-Turbulent Transition in Gas Turbine Engines," ASME J. Turbomach., **113**, pp. 509–537.
[3] Sharma, O. P., Ni, R. H., and Tanrikut, S., 1994, "Unsteady Flow in Turbines," AGARD Lecture Series 195, Paper No. 5.
[4] Hodson, H. P., 1991, "Aspects of Unsteady Blade-Surface Boundary Layers and Transition in Axial Turbomachines," *Boundary Layers in Turbomachines*, VKI Lecture Series 1991-06.
[5] Wisler, D. C., 1998, "The Technical and Economic Relevance of Understanding Boundary Layer Transition in Gas Turbine Engines," in *Minnowbrook II, 1997 Workshop on Boundary Layer Transition in Turbomachines*, LaGraff, J. E., and Ashpis, D. E., eds., NASA/CP-1998-206958, NASA Glenn Research Center, Cleveland, OH, pp. 53–64.
[6] Curtis, E. M., Hodson, H. P., Banieghbal, M. R., Denton, J. D., Howell, R. J., and Harvey, N. W., 1997, "Development of Blade Profiles for Low-Pressure Turbine Applications," ASME J. Turbomach., **119**, pp. 531–538.
[7] Volino, R. J., 2002, "Separated Flow Transition Under Simulated Low-Pressure Turbine Airfoil Conditions: Part 1—Mean Flow and Turbulence Statistics," ASME J. Turbomach., **124**, pp. 645–655.
[8] Van Treuren, K. W., Simon, T., von Koller, M., Byerley, A. R., Baughn, J. W., and Rivir, R., 2002, "Measurements in a Turbine Cascade Flow Under Ultra Low Reynolds Number Conditions," ASME J. Turbomach., **124**, pp. 100–106.
[9] Howell, R. J., Ramesh, O. N., Hodson, H. P., Harvey, N. W., and Schulte, V., 2001, "High Lift and Aft-Loaded Profiles for Low-Pressure Turbines," ASME J. Turbomach., **123**, pp. 181–188.
[10] Stadtmüller, P., Fottner, L., and Fiala, A., 2000, "Experimental and Numerical Investigation of Wake-Induced Transition on a Highly Loaded LP Turbine at Low Reynolds Numbers," ASME paper no. 2000-GT-0269.
[11] Brunner, S., Fottner, L., and Schiffer, H.-P., 2000, "Comparison of Two Highly Loaded Low Pressure Turbine Cascades Under the Influence of Wake-Induced Transition," ASME paper no. 2000-GT-268.
[12] Lake, J. P., King, P. I., and Rivir, R. B., 2000, "Low Reynolds Number Loss Reduction on Turbine Blades With Dimples and V-Grooves," AIAA paper no. 00-738.
[13] Murawski, C. G., and Vafai, K., 1999, "Effect of Variable Axial Chord on a Low-Pressure Turbine Blade," J. Propul. Power, **15**, pp. 667–674.
[14] Byerley, A. R., Störmer, O., Baughn, J. W., Simon, T. W., Van Treuren, K. W., and List, J., 2002, "Using Gurney Flaps to Control Laminar Separation on Linear Cascade Blades," ASME J. Turbomach., **125**, pp. 114–120.
[15] Bons, J. P., Sondergaard, R., and Rivir, R. B., 2001, "Turbine Separation Control Using Pulsed Vortex Generator Jets," ASME J. Turbomach., **123**, pp. 198–206.
[16] Bons, J. P., Sondergaard, R., and Rivir, R. B., 2002, "The Fluid Dynamics of LPT Blade Separation Control Using Pulsed Jets," ASME J. Turbomach., **124**, pp. 77–85.
[17] Volino, R. J., Schultz, M. P., and Pratt, C. M., 2001, "Conditional Sampling in a Transitional Boundary Layer Under High Free-Stream Turbulence Conditions," ASME J. Fluids Eng., **125**, pp. 28–37.
[18] Volino, R. J., 2002, "Separated Flow Transition Under Simulated Low-Pressure Turbine Airfoil Conditions: Part 2—Turbulence Spectra," ASME J. Turbomach., **124**, pp. 656–664.
[19] Wills, J. A. B., 1962, "The Correction of Hot-Wire Readings for Proximity to a Solid Boundary," J. Fluid Mech., **12**, pp. 65–92.
[20] Ligrani, P. M., and Bradshaw, P., 1987, "Spatial Resolution and Measurement of Turbulence in the Viscous Sublayer Using Subminiature Hot-Wire Probes," Exp. Fluids, **5**, pp. 407–417.
[21] Ligrani, P. M., and Bradshaw, P., 1987, "Subminiature Hot-Wire Sensors: Development and Use," J. Phys. E, **20**, pp. 323–332.
[22] Volino, R. J., and Hultgren, L. S., 2001, "Measurements in Separated and Transitional Boundary Layers Under Low-Pressure Turbine Airfoil Conditions," ASME J. Turbomach., **123**, pp. 189–197.
[23] Gibbings, J. C., 1959, "On Boundary-Layer Transition Wires," Aeronautical Research Council, Current Papers 462.
[24] Volino, R. J., 2003, "Separation Control on Low-Pressure Turbine Airfoils Using Synthetic Vortex Generator Jets," ASME J. Turbomach., **125**, pp. 765–777.

Separation Control on Low-Pressure Turbine Airfoils Using Synthetic Vortex Generator Jets

Ralph J. Volino
Department of Mechanical Engineering,
United States Naval Academy,
Annapolis, MD 21402
e-mail: volino@usna.edu

Oscillating vortex generator jets have been used to control boundary layer separation from the suction side of a low-pressure turbine airfoil. A low Reynolds number (Re =25,000) case with low free-stream turbulence has been investigated with detailed measurements including profiles of mean and fluctuating velocity and turbulent shear stress. Ensemble averaged profiles are computed for times within the jet pulsing cycle, and integral parameters and local skin friction coefficients are computed from these profiles. The jets are injected into the mainflow at a compound angle through a spanwise row of holes in the suction surface. Preliminary tests showed that the jets were effective over a wide range of frequencies and amplitudes. Detailed tests were conducted with a maximum blowing ratio of 4.7 and a dimensionless oscillation frequency of 0.65. The outward pulse from the jets in each oscillation cycle causes a disturbance to move down the airfoil surface. The leading and trailing edge celerities for the disturbance match those expected for a turbulent spot. The disturbance is followed by a calmed region. Following the calmed region, the boundary layer does separate, but the separation bubble remains very thin. Results are compared to an uncontrolled baseline case in which the boundary layer separated and did not reattach, and a case controlled passively with a rectangular bar on the suction surface. The comparison indicates that losses will be substantially lower with the jets than in the baseline or passively controlled cases. [DOI: 10.1115/1.1626686]

Introduction

Modern low-pressure turbine (LPT) airfoils are subject to increasingly stronger pressure gradients as designers impose higher loading in an effort to improve efficiency and lower cost by reducing the number of airfoils in an engine. If the adverse pressure gradient on the suction side of these airfoils becomes strong enough, the boundary layer will separate. Separation bubbles, particularly those which fail to reattach, can result in a significant loss of lift and a subsequent degradation of engine efficiency (e.g., Hourmouziadis [1], Mayle [2], and Sharma et al. [3]). The problem is particularly relevant in aircraft engines. Airfoils optimized to produce maximum power under takeoff conditions may still experience boundary layer separation at cruise conditions, due to the thinner air and lower Reynolds numbers at altitude. A component efficiency drop of 2% may occur between takeoff and cruise conditions in large commercial transport engines, and the difference could be as large as 7% in smaller engines operating at higher altitudes.

Separation on LPT airfoils is complicated by boundary layer transition, which can prevent separation if it occurs far enough upstream, or induce boundary layer reattachment if it occurs in the shear layer over a separation bubble. At lower Reynolds numbers transition will tend to occur farther downstream, hence the problems associated with performance at altitude.

Separated flow transition has been studied extensively, and in recent years several studies have focused on transition in the LPT. Volino [4] provides a review of much of that work. Separation can be affected through naturally occurring phenomena such as high free-stream turbulence intensity (FSTI) or the unsteadiness caused by wakes generated upstream of an airfoil. Further discussion of these effects is available in Volino [5]. While high FSTI and wakes help to mitigate separated flow problems, they clearly do not solve all problems, as evidenced by the known efficiency drop in modern engines at altitude. Howell et al. [6], for example, studied airfoils modified for higher lift, noting that their highly loaded airfoils might be close to a limit, and that even higher loading could cause unacceptable separation problems even in the presence of wakes. Looking beyond free-stream turbulence and wakes, other types of separation control could prove useful. Gad-el-Hak [7] provides a recent review. Techniques include boundary layer tripping, vortex generation, suction, and injection of fluid normal to the wall to either increase the boundary layer momentum or promote turbulence.

While the general literature is extensive, only a few studies have considered separation control under LPT conditions. Some have utilized passive techniques. Lake et al. [8] considered dimples and boundary layer trips. Van Treuren et al. [9] considered vortex generators. Volino [5] used rectangular bars to impose disturbances in a boundary layer and move transition upstream. Passive flow control is appealing for its simplicity and the relative ease with which it might be implemented in gas turbine environments. It has its limitations, however. Volino [5] found that passive devices can successfully control separation even at the lowest Reynolds number of interest, but that these devices caused substantial increases in losses at higher Re. This is an important limitation for aircraft engines, where the Re range between takeoff and cruise is large. An active device could be turned off at high Re. Static passive devices are also unable to take advantage of the unsteadiness caused by wake passing. An active device might be timed to turn on and off in response to wake passing events. Unsteady devices might also take advantage of the calmed region following a transient turbulent event.

The literature contains several examples of active separation control. Lee et al. [10] used blowing in supersonic engine inlets to prevent or control separation. Sturm et al. [11] reported on blow-

Contributed by the International Gas Turbine Institute and presented at the International Gas Turbine and Aeroengine Congress and Exhibition, Atlanta, GA, June 16–19, 2003. Manuscript received by the IGTI December 2002; final revision March 2003. Paper No. 2003-GT-38729. Review Chair: H. R. Simmons.

ing in a compressor cascade. Johnston and Nishi [12] used vortex-generator-jets (VGJ's) to control separation in turbulent boundary layers. This method utilizes blowing from ''small, skewed, and pitched holes'' to create streamwise vortices similar to those created by solid vortex generators. Any jet injected into a flow will tend to produce some turbulence, and the turbulent mixing will tend to bring some high momentum fluid into the near wall region and inhibit separation. Streamwise vortices bring additional high momentum fluid into the near wall region. The most effective VGJ's enter the boundary layer at a relatively shallow pitch angle (typically 30–45°) relative to the wall and a high skew angle (45–90°) relative to the main flow. Compton and Johnston [13] showed that the co-rotating vortices produced by VGJ's are stronger and more effective for separation control than the counter-rotating vortices which form downstream of a normal jet. McManus et al. [14] and Raghunathan et al. [15] used pulsed VGJ's. Sinha and Pal [16] used acoustic excitation to perturb an unsteady separating flow. Jacobson and Reynolds [17] used piezoelectrically driven cantilevers to influence the near wall turbulence structure on a flat plate. They noted that the devices could be used in separation control. Miau et al. [18] used an oscillating fence to promote reattachment downstream of a backward facing step. Sinha et al. [19] used a driven flexible wall transducer to detect pressure fluctuations and then produce near wall vortices upstream of separation. Whitehead et al. [20] used a film transducer to produce airfoil vibrations and reduce separation at high angles of attack. Oscillatory blowing has been used in several studies to control separation on airfoils. Amitay and Glezer [21] provide one recent example. Oscillatory jets are often referred to as ''synthetic jets'' since they have no net mass flow. They are typically directed normal to a surface, meaning that they probably do not produce such strong streamwise vortices as VGJ's.

Only a few active control studies have been conducted under LPT conditions. Huang et al. [22] and Hultgren and Ashpis [23] employed high voltage electrodes to produce glow discharge plasma in a boundary layer to control separation. Bons et al. [24,25] used steady and pulsed VGJ's to successfully control separation on LPT airfoils. They used the ''Pak-B'' airfoil, which is an industry supplied research airfoil that is prone to separation problems at low Re. It has been used in numerous studies, as noted by Volino [4]. Bons et al. [24] used spanwise rows of VGJ's at several streamwise locations on the suction surface of the airfoil, and found that a row near the suction surface velocity maximum (pressure minimum) was most effective. The VGJ holes were oriented at 30° to the surface and 90° to the main flow. All holes were oriented in the same direction, to produce co-rotating vortices. Reynolds numbers as low as 60,000 (based on suction surface length and exit velocity) were considered. Bons et al. [25] found that both steady and pulsed jets were effective in controlling separation. The pulsed jets were fully effective even when the dimensionless pulsing frequency F^+ was as low as 0.1, where F^+ is a ratio of the transit time for flow between the VGJ hole and the trailing edge to the time interval between pulses. Ensemble averaged velocity profiles showed a long relaxation or ''calmed'' period following each jet pulse. During this calm period the boundary layer remained attached long after the turbulence generated by the pulse had moved downstream. Calmed regions have been observed following turbulent spots in transitional boundary layers (e.g., Gostelow et al. [26] and Schulte and Hodson [27]). The mean velocity profiles in the calmed region gradually relax from the turbulent shape associated with the turbulent spot they follow, to a laminar (and in some cases separated) profile shape. The calmed boundary layer is very resistant to separation, much like a turbulent boundary layer, but it is very laminarlike in terms of its fluctuation levels and low losses. The pulsed jets were more effective than continuous jets, even when the pulsed jet duty cycle was as low as 1%. This was believed to indicate that the starting vortex formed at the beginning of each jet pulse was responsible for most of the flow control in the pulsed jet cases.

Synthetic jets hold an advantage over continuous or pulsed jets in that they require no net mass flow. In the LPT environment, this means that no compressor bleed air is required. Use of bleed air for flow control or cooling comes at a cost in efficiency, although the small amount of air required for the pulsed jets of Bons et al. [25] might not be prohibitive if bleed air were already routed to the airfoils for cooling. Synthetic jets would not be useful for a cooled airfoil since ingestion of hot gas into the airfoil would be harmful. For uncooled LPT airfoils, however, the airfoil temperature will match the main flow temperature, and ingestion of hot gas should be acceptable. Routing of bleed air to uncooled airfoils for flow control may present a prohibitive addition of complexity and weight. With synthetic jets this problem could be avoided. In the present study, the oscillating flow of synthetic jets and the compound angle injection of vortex generator jets are combined to produce synthetic VGJ's. This is believed to be the first application of synthetic VGJ's. They are used to control the flow over a Pak-B airfoil. A survey of the literature indicates that the jet locations and angles chosen by Bons et al. [25] were likely optimal, so their geometry has been copied in the present study.

There are many parameters which could be varied in a synthetic jet study, including Reynolds number, FSTI, jet geometry, jet location, jet velocity, jet oscillation frequency, and jet waveform, to name a few. These are all potentially important parameters and should eventually be studied. The scope of the present study is more focused. A single experimental case is completely documented with detailed measurements including time resolved mean and fluctuating velocity and turbulent shear stress throughout the flow field. The goals of the study are to build an understanding of the physics of how synthetic VGJ's control separation and to generate questions for future parametric studies which may lead to optimized flow control for a broad range of flow conditions.

Volino [4,28] studied unmodified flow over the Pak-B airfoil at Reynolds numbers ranging from 25,000 to 300,000 under both high and low FSTI. In nearly all cases the boundary layer separated from the suction side of the airfoil. At all but the lowest Reynolds numbers it reattached before the trailing edge. The most severely separated case was the low FSTI, Re=25,000 case. This case has therefore been chosen as the test case for the present application of synthetic VGJ's. The unmodified case from Volino [4] is used as a baseline case for comparison to the new results. Also used for comparison is a case from Volino [5] in which a passive bar was employed to force reattachment. The bar was located at $s/L_s=0.51$, extending along the airfoil span. Its streamwise width was 6.35 mm and its height was 1.6 mm. The suction surface length was 228.6 mm. Bars of various heights were tested. The 1.6-mm bar was the smallest bar to cause reattachment at Re=25,000. Volino [5] found that the most effective bars in terms of minimizing losses were not large enough to immediately trip the boundary layer to turbulent. Rather, they induced small disturbances which grew and caused transition and reattachment downstream of a small separation bubble.

Experiment

Experiments were conducted in a low speed wind tunnel, described by Volino et al. [29]. Briefly, air enters through blowers and passes through a honeycomb, a series of screens, two settling chambers, and a three-dimensional contraction before entering the test section. At the exit of the contraction, the mean velocity is uniform to within 1%. The FSTI is 0.5%±0.05%. Nearly all of this free-stream ''turbulence'' is actually streamwise unsteadiness at frequencies below 20 Hz and is not associated with turbulent eddies. The rms intensities of the three components of the unsteadiness are 0.7%, 0.2%, and 0.2% in the streamwise, pitchwise and spanwise directions, respectively. The test section immediately follows the contraction.

The test section, shown in Fig. 1, consists of the passage between two airfoils. Details are listed in Table 1, and more information is available in Volino [4]. A large span-to-chord ratio of

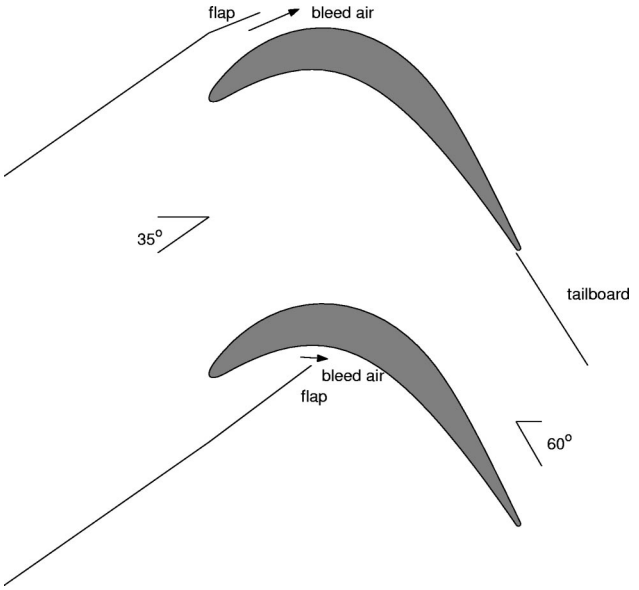

Fig. 1 Schematic of the test section

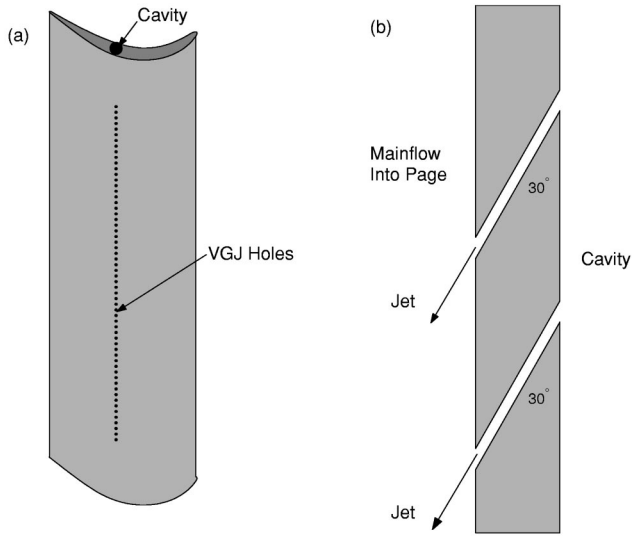

Fig. 2 Drawing of suction side airfoil with cavity and VGJ's: (*a*) full airfoil, (*b*) cross section of VGJ holes

4.3 was chosen to insure two-dimensional flow at the spanwise centerline of the airfoils, where all measurements were made. Upstream of each airfoil are flaps, which control the amount of bleed air allowed to escape from the passage. The flaps, along with a tailboard on the pressure side of the passage, are adjusted to produce the correct leading edge flow and pressure gradient along the airfoils. The flow in the passage matches that in a multiblade cascade. The single passage configuration allows for a large scale passage and better probe access than possible with a multiblade cascade in the same size wind tunnel. The wake downstream of the passage is not representative of a multiblade facility, however, since there is flow only on one side of each airfoil. Downstream effects that could influence the upstream flow in the passage are also potentially missed. Experimental conditions match those of the low FSTI, Re=25,000 baseline case of Volino [4] and the passive bar case of Volino [5].

The synthetic VGJ's were produced from a cavity within the suction side airfoil. The airfoils are machined from high density foam, which has a consistency much like hard wood. The surface of each airfoil was sanded smooth, painted, and sanded again to provide a smooth surface. A 1.27-cm-diameter hole was drilled through the airfoil span at about mid-chord, as shown in Fig. 2, to form a plenum. One end of the plenum is plugged, and the narrow end of a funnel is inserted in the other. A 20.3-cm-diameter loudspeaker (100-W subwoofer) is attached at the wide end of the funnel. The funnel is sealed to the speaker and to the airfoil with silicone RTV to prevent air leakage. The speaker is driven with a 200-W audio amplifier, which is in turn powered with a 12-V dc power supply and driven by a function generator. For the present study the function generator was set to output a sine wave. The amplitude of the signal from the function generator and the gain of the amplifier were adjusted to provide the desired input voltage to the speaker. Holes for the VGJ's were drilled into the suction surface in a spanwise line at $s/L_s=0.514$. The holes are 0.8 mm in diameter (0.35% of L_s) and are spaced 8.5 mm apart (3.7% of L_s). The holes are drilled at a 90° skew angle with respect to the main flow and a 30° pitch with respect to the surface, as shown in Fig. 2. Each hole extends from the suction surface into the cavity in the core of the airfoil. The length to diameter ratio of the holes is 7.5.

Table 1 Test section parameters

Axial Chord [mm]	True Chord [mm]	Pitch [mm]	Span [mm]	Suction side, L_s [mm]	Inlet flow angle	Exit flow angle
153.6	170.4	136.0	660.4	228.6	35°	60°

Measurements. Pressure surveys were made using a pressure transducer (0–870-Pa range Validyne transducer) and a Scanivalve. Stagnation pressure was measured with a pitot tube upstream of the passage inlet, and eleven pressure taps were located on each airfoil along their spanwise centerlines. Locations of the taps on the suction side are listed in Table 2 along with measured local FSTI components and the acceleration parameter K at these stations based on a nonseparating, inviscid solution. The uncertainty in the suction side pressure coefficients was 7%. Most of this uncertainty was due to bias error. Stochastic error was minimized by averaging pressure transducer readings over a 10-s period.

Velocity profiles on the suction surface were measured at streamwise stations corresponding to pressure taps 7–11, as given in Table 2, and at four additional stations, labeled 7.5, 8.5, 9.5, and 10.5, centered between the pressure taps. All stations are downstream of the VGJ holes. Stations 7, 8, 9, 10, and 11 correspond to stations documented in the baseline case in Volino [4,28]. Profiles at Stations 1–6 are fully documented for the baseline case in Volino [4,28], and show that the upstream boundary layer closely follows a laminar solution. Profiles were measured near but not at the spanwise centerline of the airfoil to insure that the pressure taps did not interfere with the velocity measurements.

Table 2 Measurement station locations, local acceleration (inviscid soln.), and measured local free-stream turbulence

Station	s/L_s	$K\times10^6$	$\overline{u'}/U_\infty$ [%]	$\overline{v'}/U_\infty$ [%]
1	0.111	6.32	0.44	
2	0.194	4.80	0.39	
3	0.278	3.44	0.37	
4	0.361	3.00	0.38	
5	0.444	2.48	0.39	
6	0.528	−0.08	0.41	
7	0.611	−3.24	0.47	0.05
8	0.694	−3.80	0.47	0.12
9	0.777	−2.32	0.48	0.14
10	0.861	−2.12	0.54	0.11
11	0.944	−0.72	0.51	0.11

Profiles were acquired with a hot-wire anemometer (AA Lab Systems model AN-1003) and a single sensor boundary layer probe (TSI model 1218-T 1.5). The sensor diameter is 3.8 μm, and the active length is 1.27 mm. At each measurement location, data were acquired for 26 s at a 20-kHz sampling rate (2^{19} samples). All raw data were saved. The high sampling rate provides an essentially continuous signal, and the long sampling time results in low uncertainty in both statistical and spectral quantities. Data were acquired at 60 wall normal locations in each profile, extending from the wall to the free stream, with most points concentrated in the near wall region. The closest point was within 0.1 mm of the wall, which corresponds to $y/L_s=0.0004$ and about 0.015 boundary layer thicknesses. Flow direction in a separation bubble cannot be determined with a single-sensor hot wire, but velocity magnitude can be measured and was found to be essentially zero within the bubbles of the present cases. Determining the direction was not therefore considered essential. Uncertainty in the mean velocity is 3–5% except in the very near wall region, where near-wall corrections (Wills [30]) were applied to the mean velocity. Uncertainties in the momentum and displacement thicknesses computed from the mean profiles are 10%. Uncertainty in the shape factor H is 8%. Local skin friction coefficients were computed from the near wall mean velocity profiles using the technique of Volino and Simon [31]. This technique accounts for streamwise pressure gradient effects on the mean profile. The uncertainty in C_f is 8%. The uncertainty in the fluctuating streamwise velocity is below 10%. As explained in Volino [4] based on the work of Ligrani and Bradshaw [32], spatial averaging effects due to the finite length of the hot-wire sensor should not be significant in the present case.

Profiles were also acquired using a cross-sensor boundary layer probe (TSI 1243-20). The sensors are 51-μm-diameter hot films with 1.02-mm active lengths. The probe is used to document the instantaneous turbulent shear stress, $-u'v'$. Profiles were acquired at the same stations as with the single-sensor probe. Data were acquired at 25 locations in each profile, extending from 1 mm from the wall to the free stream. Sampling rates and times were the same as for the single-sensor profiles. The vortices induced by the oscillating jets cause significant secondary velocity, particularly at the streamwise stations immediately downstream of the jet holes. The magnitude of these secondary velocity components remains below 20% of the local streamwise velocity, however, so they should not cause significant error in the hot-wire measurements. The uncertainty in $-u'v'$ is 10%.

The VGJ velocities were measured using a hot-film probe (TSI model 1210-10A) with a 0.25-mm active sensor length. The sensor was placed directly over the exit of the jet hole. During outflow from the hole, the jet was expected to blow directly across the sensor, providing an accurate measure of the jet velocity. Uncertainty in the velocity is 5% and results mainly from uncertainty in the position of the sensor, which could lead to a slightly lower velocity reading than the velocity at the jet exit plane. During inflow of the oscillating jet, the flow is expected to behave more like a sink flow than a jet. The measured velocity does not therefore provide an accurate indicator of the velocity inside the hole during inflow. The jet velocity was calibrated against the rms input voltage to the speaker with the main flow in the wind tunnel turned off, and the calibration was used to set the jet velocity in later experiments. The jet velocity is fixed by the frequency and amplitude of the displacement of the speaker diaphragm, which causes a pressurization of the cavity relative to the pressure at the jet exits. The dynamic pressure of the flow through the test section is about 2.4 Pa at the jet location. Since the test section exits to atmosphere, the dynamic pressure results in an average pressure of 2.4-Pa vacuum in the cavity, and a 2.4-Pa pressure difference across the speaker diaphragm. This pressure is much smaller than the pressure experienced by the speaker when driving the jets, and is not expected to influence its motion. If the amplitude of the diaphragm motion is unchanged by the presence of flow in the test section, the jets should drive approximately the same mass flow through the holes with the wind tunnel on or off. The jet velocity at the exit plane will presumably be affected by the mean flow, however.

The measured maximum jet exit velocity was 9.4 m/s for most of the cases presented below. Given the sensor length and the diameter of the holes, the measured velocity is an average over the middle 30% of the jet. The Reynolds number based on this velocity and the jet diameter is 500. At this Reynolds number, approximately 30 diameters would be needed to establish fully developed laminar flow inside the jet holes. Since the length to diameter ratio in only 7.5 and the jets are unsteady, the jet velocity is not expected to have a fully developed parabolic laminar profile, but rather a more flat profile. Given the averaging due to the sensor size and the expectation of a flat profile, the instantaneous mean velocity of the jet is assumed to approximately equal the measured velocity. Ideally this assumption would be checked with a survey of velocity across the jet exit plane, but the very small jet diameter precludes an accurate survey. The uncertainty in instantaneous mean velocity is, therefore, higher than the 5% uncertainty in the measured velocity. The uncertainty is estimated to be between 10 and 20%.

Data Processing. In addition to conventional time averaging, the velocity data were ensemble averaged relative to the time within each jet oscillation cycle. For this purpose, the speaker input voltage was digitized simultaneously along with the instantaneous velocity data. Data were ensemble averaged at 24 instances within the cycle. At each instance, data were averaged over 1/180th of the cycle. For each 26-s data trace, this results in roughly 3000 data points to average for each ensemble. With this many data points to average over a 26-s time record, the ensemble averaged results are well resolved and have uncertainties as low as those given above for the time averaged results. The start of the cycle was arbitrarily chosen as the instant when the speaker input voltage crossed from negative to positive. As will be shown below, this roughly corresponds to the beginning of the jets' outward pulse.

Results

Jet Velocity. Figure 3 shows a typical time trace of the measured jet velocity and the speaker input voltage. The frequency of the input signal was set to a nominal value of 10 Hz (actual value was 10.5 Hz). The maximum and average velocities in each outward pulse were 9.4 and 5.9 m/s, respectively. The jet velocity can be expressed as a blowing ratio B, defined as

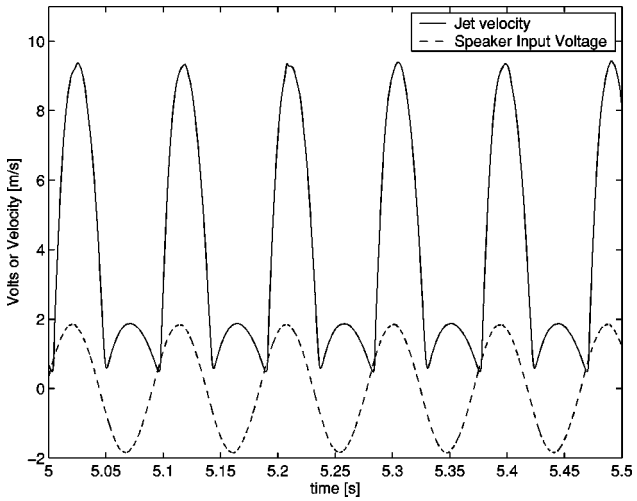

Fig. 3 Time trace of jet velocity and speaker input voltage, $F^+=0.65$

$$B = \rho_{jet} V_{jet} / \rho_\infty U_\infty ,$$

where $\rho_{jet} = \rho_\infty$ since the jet fluid comes from the boundary layer, and $U_\infty (= 2$ m/s) is the local free-stream velocity at the jet location. For the present cases $B_{max} = 4.7$ during each cycle and $B_{ave} = 3.0$ during the outward pulse. The mass flux of the jets can be compared to the velocity deficit in the boundary layer as

$$M = [\rho_{jet} V_{jet} (\pi D_{jet}^2/4) S]/[\rho_\infty U_\infty \delta^*],$$

where $S = 0.118$ holes/mm is the number of holes per unit span. The displacement thickness, $\delta^* (= 1.08$ mm) is the baseline case value at the jet location. This gives $M_{max} = 0.258$ and $M_{ave} = 0.162$. This could be interpreted to mean that 16% of the boundary layer in terms of displacement thickness is sucked off during the inflow half of each jet cycle, and then re-injected into the boundary layer during the outward pulse.

The momentum coefficient c_μ is defined as the ratio of the jet momentum to the free-stream dynamic pressure. Using the definition of Bons et al. [25],

$$c_\mu = [\rho_{jet} V_{jet}^2 (\pi D_{jet}^2/4) S]/[\rho_\infty U_\infty^2 \text{Chord}],$$

where the axial chord is 153.6 mm. The maximum value of c_μ in each cycle is 0.0085. The average value of V_{jet}^2 for the outpulse is 44 m^2/s^2. This gives an average $c_\mu = 0.0042$.

Figure 3 shows that the speaker input voltage and the jet velocity are slightly out of phase. The jets lag the input voltage by about 0.006 s, which is a dimensionless lag $\Delta t/T$ of 0.063, where T is the jet oscillation period of 0.095 s. The lag is expected, as the jets respond dynamically to the pressurizing of the cavity in the airfoil by the speaker, and there is no reason to expect the speaker voltage and the jet velocity to be exactly in phase. The finite distance from the speaker to the jet holes (of the order 0.5 m) and the finite speed of sound (340 m/s) will also lead to a time lag of the order 1 ms. The time lag increases with distance from the speaker along the airfoil span. At high jet frequencies, the time lag causes the jets along the span to be significantly out of phase with each other. Measurements, however, show that the jet amplitude along the span is uniform, regardless of the frequency. Variation in phase along the span could lead to difficulty in practice if attempts were made to time the jet pulsing to other cyclic events such as wake passing. It is not an issue in the present study. At the relatively low frequency of 10 Hz, the phase lag was not significant, and the jets were uniform in both phase and amplitude along the span.

Pressure Profiles. Pressure profiles were acquired for several jet amplitudes and jet frequencies. The general finding was that the jets were effective over a broad frequency range, so long as the amplitude was sufficiently high. Figure 4 shows Cp profiles for a range of jet amplitudes, with the jet frequency set to 10.5 Hz ($F^+ = 0.65$). In all cases there is good agreement between the data and an inviscid solution for the Pak-B airfoil on the pressure side and the upstream portion of the suction side. In the adverse pressure gradient region on the suction side, differences are clear. Without the jets the boundary layer separates and does not reattach, as indicated by the region of constant Cp values. With $B_{max} = 1.9$ the boundary layer still does not reattach, but there is some sign that Cp is starting to drop at the last pressure tap. For the cases with $B_{max} = 4.7$ and above, the boundary layer does not appear to separate. Significant case to case differences in Cp are present right at the suction peak, but these are likely due to the injection of the jets at this location and their effect on the flow over the adjacent pressure tap. The differences diminish rapidly and are essentially gone by the next downstream measurement station. Bons et al. [24] demonstrated effective flow control with B_{max} as low as 0.4 in their study. The significantly lower Re in the present study may explain the need for stronger jets. Figure 5 shows Cp profiles for several different jet frequencies with B_{max} held approximately constant at about 5. There does not appear to be any clear separated region in any of the cases with jets. The

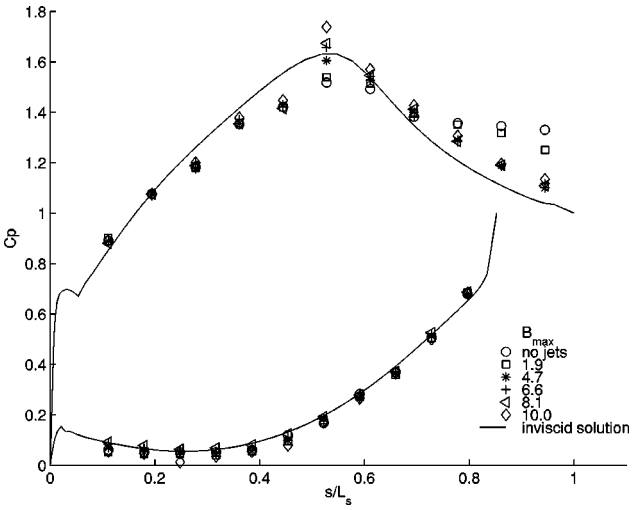

Fig. 4 *Cp* profiles, $F^+ = 0.65$, various blowing ratios

suction peak is higher in all the cases with jets than in the baseline case. This is an expected result, suggesting that the lift will be higher when the boundary layer is attached. The $F^+ = 0.65$ case appears to agree most closely with the inviscid solution. The broad range of effective frequencies agrees with the results of Bons et al. [25].

The objective of the present study is not to establish the optimal jet conditions for the present case, but to investigate in detail a case in which the jets provide effective flow control. The dimensionless frequency $F^+ = 0.65$ was chosen since it appeared to provide slightly better results than the other cases in Fig. 5, and $B_{max} = 4.7$ was chosen since it was the lowest effective blowing ratio tested. Figure 6 shows the Cp profile for the chosen case with jets along with the baseline case and the passive bar case of Volino [5].

Velocity Profiles. Figure 7 shows mean velocity $\overline{u'}$ and turbulent shear stress profiles for the present case, the baseline case, and the passive bar case. In the baseline case, the mean profiles show the boundary layer is on the verge of separating at station 7, is clearly separated at station 8, and the separation bubble grows through station 11. In the bar case, the boundary layer separates from the bar. The separation bubble is visible at station 7, and it grows through station 9. At station 10, the near wall velocities

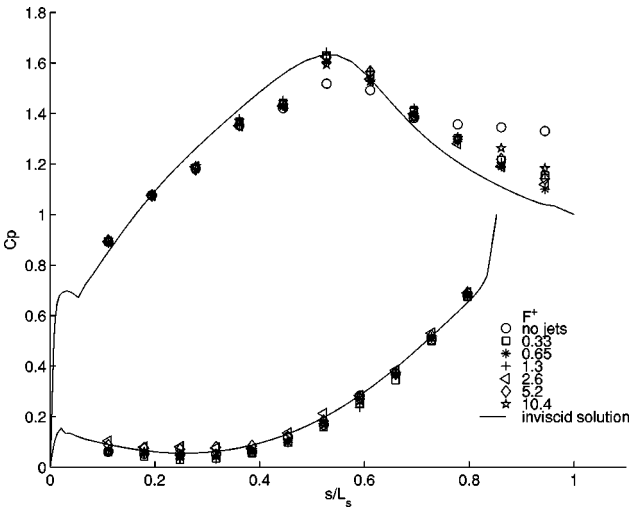

Fig. 5 *Cp* profiles, $B_{max} \approx 5$, various F^+

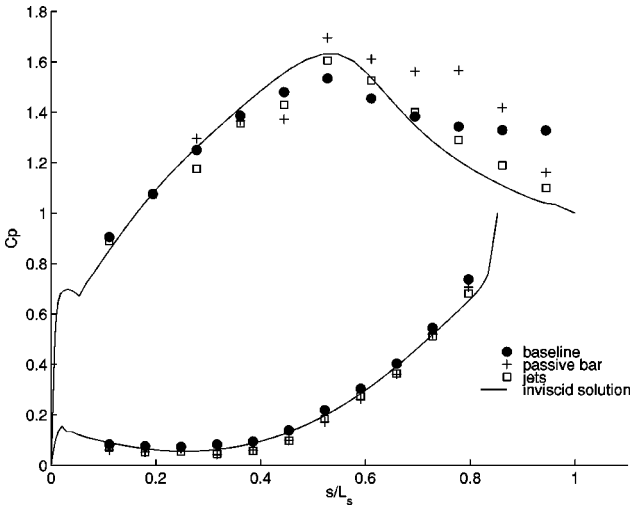

Fig. 6 *Cp* profiles, comparison of baseline, passive bar, and present jet case with $B_{max}=4.7$ and $F^+=0.65$

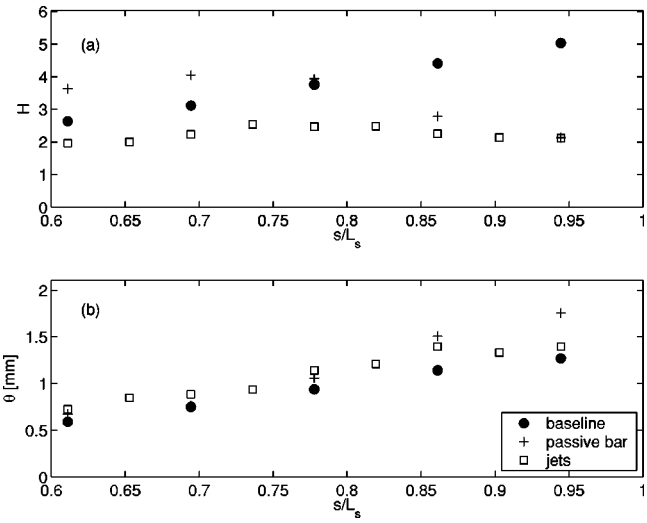

Fig. 8 Time averaged shape factor and momentum thickness verses streamwise location; comparison of baseline, passive bar and present jet cases: (*a*) H, (*b*) θ

begin to rise, indicating the beginning of reattachment, and the mean profile shows clear reattachment at station 11. With the VGJ's, the behavior is much different. There is no clear separation bubble. The mean profile appears to have an attached, laminarlike shape. The momentum deficit with the jets appears to be significantly lower at station 11 than in the case with the bars, indicating lower losses with the jets.

The $\overline{u'}$ values in the baseline and bar cases are very low at station 7, as expected since the boundary layer is still laminar. A peak appears downstream in the shear layer over the separation bubble. In the bar case, $\overline{u'}$ begins to rise in the near wall region at station 9, signaling imminent reattachment. At stations 10 and 11, $\overline{u'}$ in the bar case rises to the high values typical of a transitional boundary layer. In the jet case, $\overline{u'}$ is high at all stations. At the upstream locations it is much higher than would be expected for a turbulent boundary layer. As will be shown below, however, much of the contribution to $\overline{u'}$ is from 10-Hz unsteadiness associated with the jets and is not turbulence. The turbulent shear stress profiles show considerable momentum transport in the jet case at all stations, which helps to explain how the boundary layer remains attached. Unlike in a turbulent boundary layer, the $-\overline{u'v'}$ peak is well away from the wall. In the baseline case the shear layer does not transition to turbulent, and $-\overline{u'v'}$ remains near zero. In the bar case $-\overline{u'v'}$ profiles were not acquired.

Figure 8 shows shape factor and momentum thickness as computed from the mean profiles of Fig. 7. The shape factor H provides a measure of the state of the boundary layer with respect to separation and transition. The shape factor in the baseline and bar cases rises rapidly after separation, as δ^* increases while θ remains nearly constant. In the baseline case the boundary layer never reattaches. In the bar case, transition and reattachment occur, causing δ^* to fall and θ to rise. The shape factor begins to drop toward a turbulent value of about 1.6, but does not reach this value, indicating that the recovery from the separation is not com-

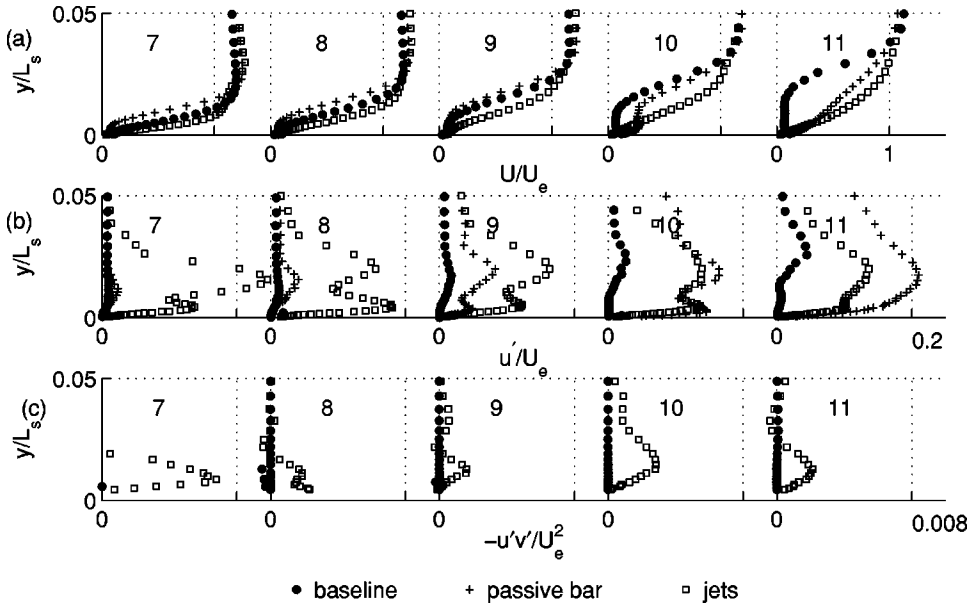

Fig. 7 Station 7–11 dimensionless time averaged profiles; comparison of baseline, passive bar and present jet cases: (*a*) mean velocity, (*b*) $\overline{u'}$, (*c*) turbulent shear stress

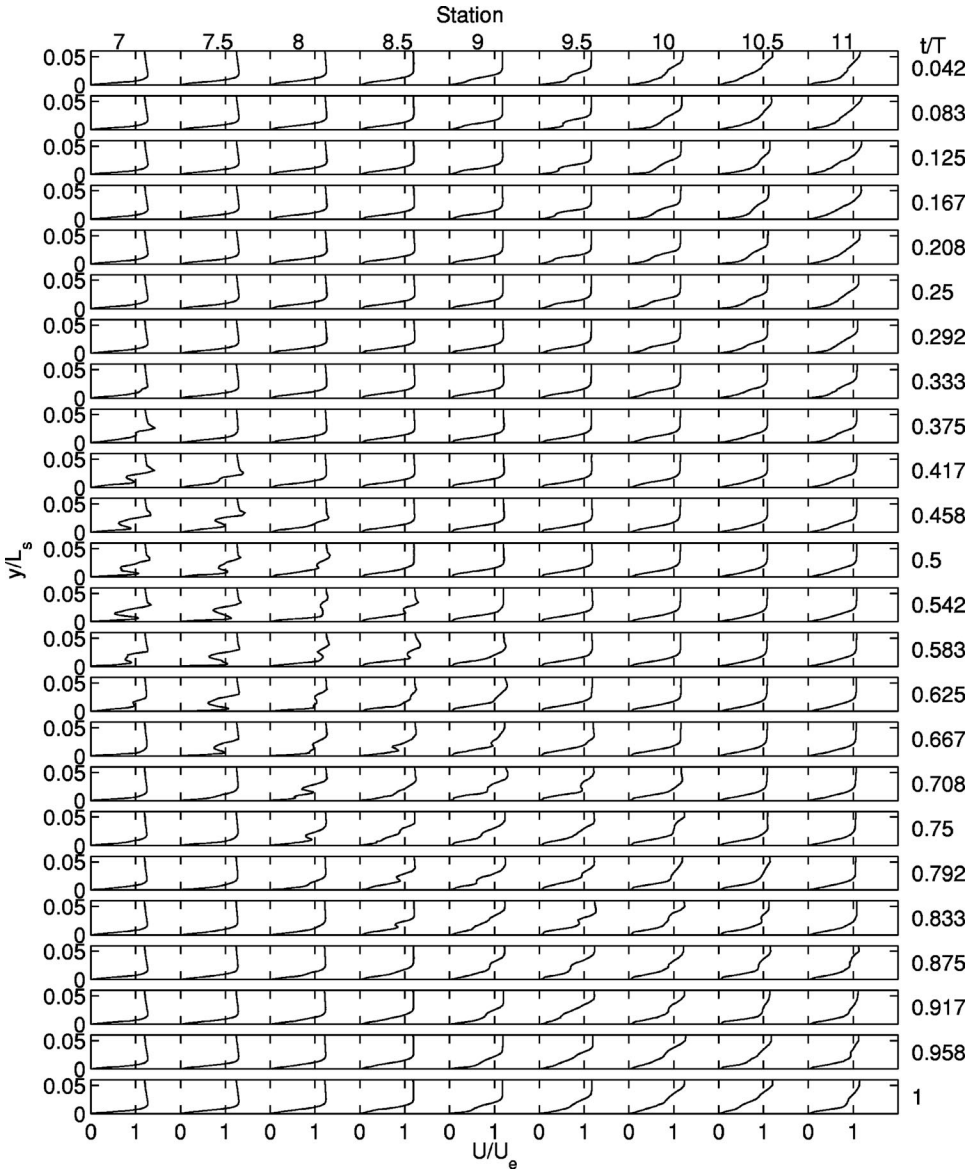

Fig. 9 Ensemble averaged dimensionless mean velocity ($\tilde{U}/U_e$) profiles

plete. In the jet case, the shape factor remains at a laminar value of about 2. It never rises to a separated flow value, nor does it drop to a turbulent value. The momentum thickness provides a measure of the losses in a boundary layer. If the boundary layer reattaches before the trailing edge, the suction side boundary layer losses will be the dominant losses in an LPT passage (Howell et al. [6]). In the baseline case the boundary layer does not reattach, so although θ remains low, high losses would be expected in the wake downstream of the airfoils. For the bar and jet cases, however, the boundary layer is attached at the trailing edge. Momentum thickness is about 20% higher in the bar case, indicating that the jets are better able to control separation, while causing lower losses.

Ensemble Average Velocity Profiles. The time averaged profiles of Fig. 7 indicate that the jets are effective in controlling the boundary layer, but they do not explain the mechanism by which the jets work. Figure 9 shows ensemble averaged mean velocity profiles. Profiles are shown for nine streamwise stations at 24 time increments within the jet oscillation cycle. Figures 10 and 11 show the corresponding $\tilde{u}'$ and $-\tilde{u}'\tilde{v}'$ profiles. Examining the profiles at station 7, the mean profile initially appears to be laminar and attached, and both the $\tilde{u}'$ and $-\tilde{u}'\tilde{v}'$ values are near zero, indicating again that the flow is laminar. Given the phase lag shown in Fig. 3 between the speaker input and the jets, and the finite convection time between the jet hole and station 7, one would expect that the disturbance created by the jet outpulse should arrive at station 7 at $t/T=0.18$. In fact, however, the disturbance is not seen in the mean profile until $t/T=0.333$. In agreement, the $\tilde{u}'$ and $-\tilde{u}'\tilde{v}'$ values also rise above zero at $t/T=0.333$. This may suggest that the rising jet velocity must reach a sufficiently high amplitude before it can significantly affect the boundary layer. Comparing the observed phase lag and the jet velocity of Fig. 3 suggests that the jet velocity must be about 8 m/s, corresponding to an instantaneous $B=4$, for the jets to be effective. Continuing forward in time at station 7, the jets cause a large disturbance in the mean profiles that continues until $t/T=0.667$. The time $t/T=0.667$ corresponds very closely with the end of the jet outpulse when the phase lag and convection time from the jet holes to station 7 are considered. The large local minima and maxima in the mean velocity profiles indicate the jets are not merely adding turbulence to the boundary layer, but are inducing some flow structure, most likely streamwise vortices.

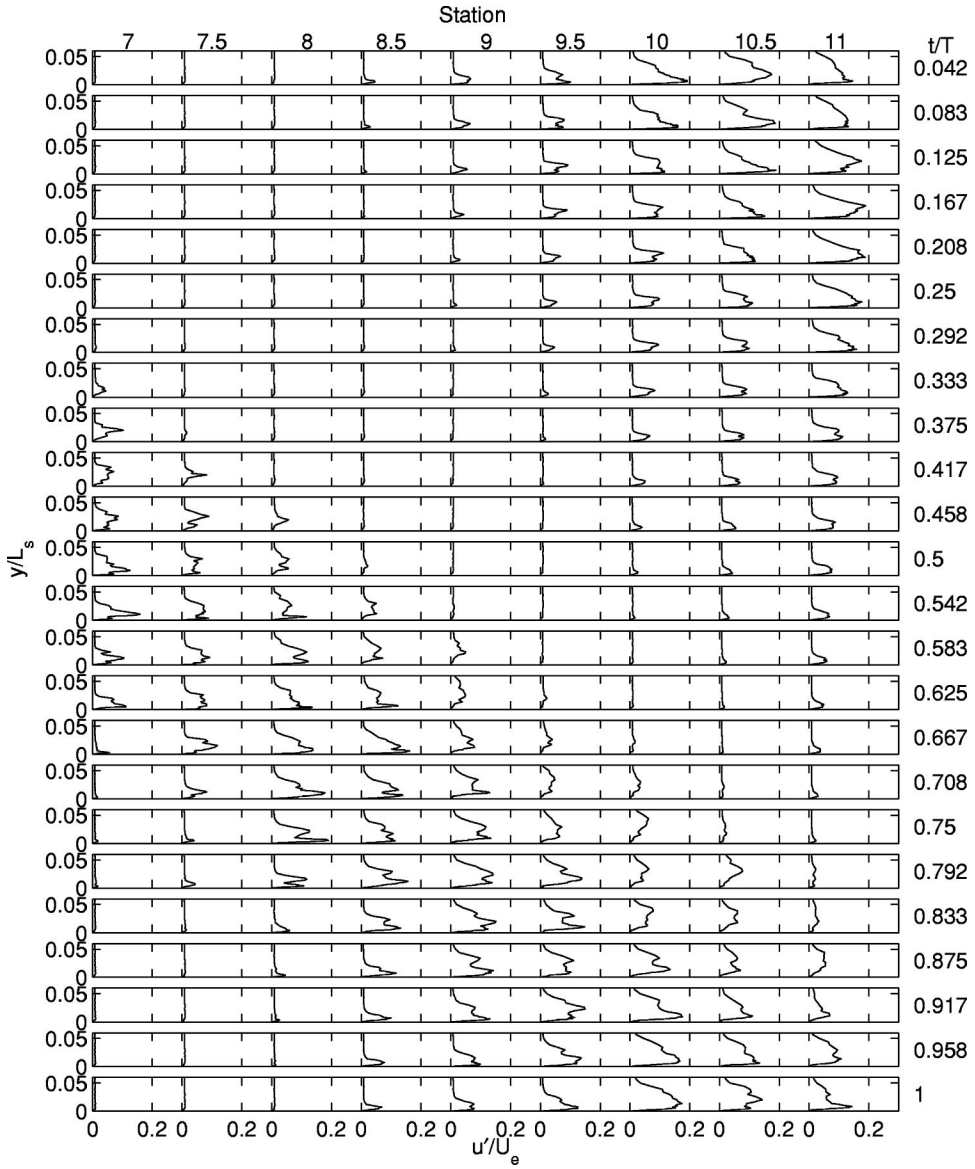

Fig. 10 Ensemble averaged rms value of dimensionless streamwise fluctuating velocity ($\tilde{u}'/U_e$) profiles

These vortices likely cause spanwise variation in the velocity, particularly at the stations nearest the jets. In the present study, data were only acquired at one spanwise location. Spanwise surveys should be considered in future work. The $\tilde{u}'$ and $-\tilde{u}'\tilde{v}'$ profiles exhibit large peaks in the regions where the mean velocity gradients are highest in Fig. 9. The $-\tilde{u}'\tilde{v}'$ values have the appropriate sign, corresponding to the sign of $d\tilde{U}/dy$ in the mean profiles. It should be noted that the magnitude of $\tilde{u}'$ is smaller in the ensemble averaged profiles of Fig. 10 than in the time averaged profiles of Fig. 7. This indicates that much of the contribution to $\overline{u'}$ in Fig. 7 is due to 10-Hz oscillations and not to turbulence. After $t/T=0.667$, the mean velocity profile resumes a laminar shape. There is no tendency toward boundary layer separation. The boundary layer did not separate in the baseline case at this station (Fig. 7), but the mean profile in the baseline case did appear closer to separation than in the present case.

Moving to the downstream stations, the leading edge of the disturbance, as observed in the mean profiles and the $\tilde{u}'$ and $-\tilde{u}'\tilde{v}'$ profiles moves to later values of t/T, as expected since the disturbance takes some time to convect downstream. The leading edge of the disturbance appears to move at about 90% of the local free-stream velocity, which corresponds with the expected leading edge celerity of a turbulent spot (e.g., Gostelow et al. [26], Schulte and Hodson [27]). The trailing edge of the disturbance appears to move at about 45% of the local free-stream velocity, agreeing with the expected trailing edge celerity of a turbulent spot. Because the leading and trailing edge celerities are different, the boundary layer is only disturbed by the jets during approximately 30% of the cycle at station 7, but is disturbed during approximately 70% of the cycle at station 11. The beginning of the disturbance at each station is seen simultaneously in the mean profile and the $\tilde{u}'$ and $-\tilde{u}'\tilde{v}'$ profiles of Figs. 9–11. At the trailing edge of the disturbance, return of the mean velocity profile to a smooth shape corresponds closely with the return of $-\tilde{u}'\tilde{v}'$ to near zero (see, for example, the profiles at station 8 at $t/T=0.833$ or station 10.5 at $t/T=0.417$). The $\tilde{u}'$ profiles, in contrast, take somewhat longer to return to an undisturbed condition. At station 11, for example, there is at least a small near wall $\tilde{u}'$ peak at all times, while the $-\tilde{u}'\tilde{v}'$ values are essentially zero between $t/T=0.625$ and 0.792.

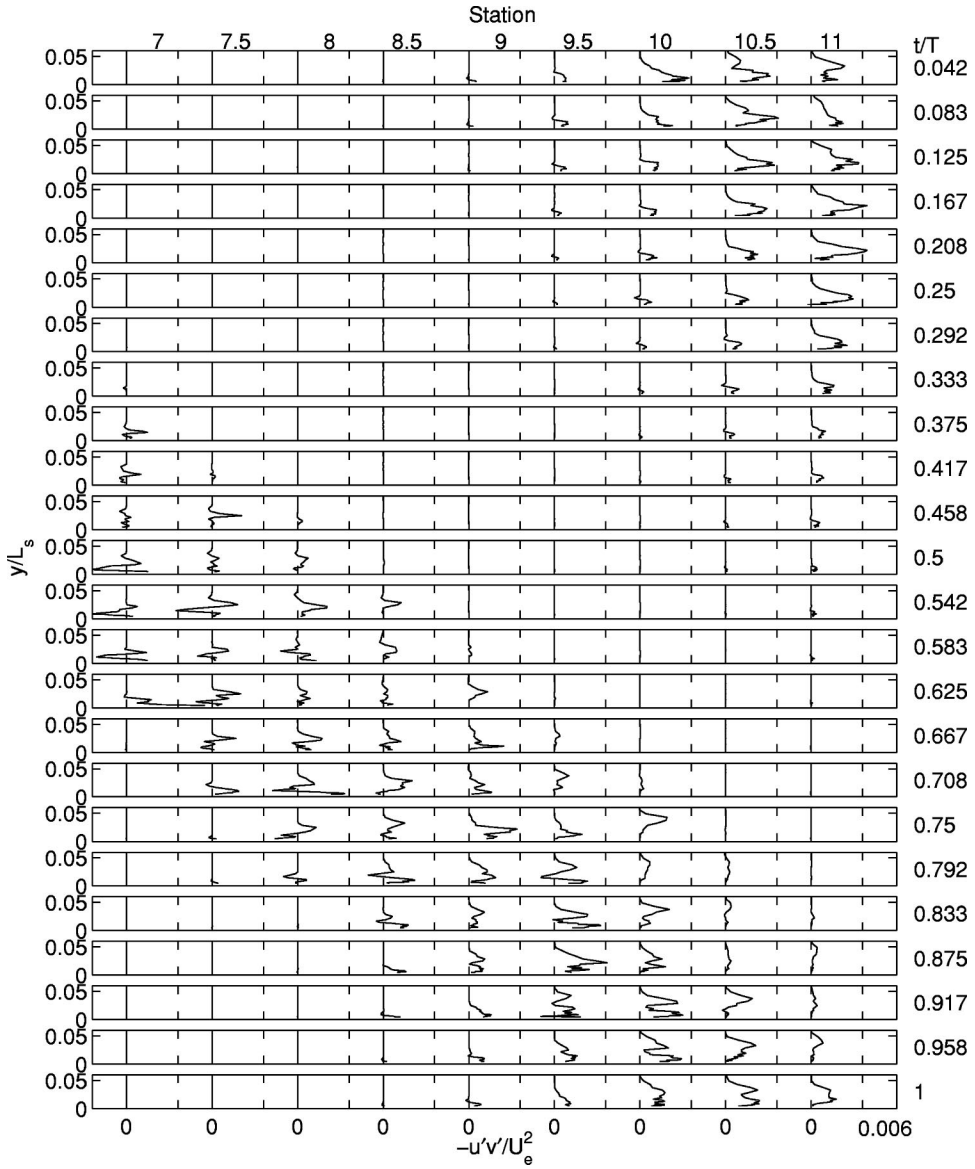

Fig. 11 Ensemble averaged dimensionless turbulent shear stress ($-\tilde{u}'\tilde{v}'/U_e^2$) profiles

The flow structure at the downstream stations appears to be less distinct than at stations 7 and 7.5. Inflection points are still present in the mean profiles, but the local minima and maxima in the mean profiles are less sharp. Still, the mean profile shapes and the multiple peaks in the $\tilde{u}'$ and $-\tilde{u}'\tilde{v}'$ profiles, particularly those far from the wall (see for example the station 10 profiles of Figs. 10 and 11 between $t/T=0.75$ and 0.958) are evidence that the flow structures induced by the jets persist downstream.

After the disturbance caused by the jets passes, the boundary layer eventually separates at locations between stations 8 and 11. At station 8.5, for example, the trailing edge of the disturbance passes at about $t/T=0.9$. By $t/T=0.1$ the near wall profile appears separated. The separation appears to coincide with the return of $\tilde{u}'$ to near zero. The separation appears to persist until about $t/T=0.6$, after the start of the next disturbance event. The reattachment within the disturbance event corresponds to the motion of high $\tilde{u}'$ and $-\tilde{u}'\tilde{v}'$ into the near wall region at $t/T=0.667$. The same sequence of events is visible at downstream stations. At station 10.5, for example, the trailing edge of the disturbance has passed by $t/T=0.4$, but the boundary layer remains attached until about $t/T=0.75$. Reattachment is visible at $t/T=1$, and a near wall peak emerges at the same time in $-\tilde{u}'\tilde{v}'$. It should be noted that the separation bubble remains thin at all stations, and never begins to approach the thickness observed in the baseline flow of Fig. 7.

The period between the passage of the disturbance and boundary layer separation is believed to indicate a "calmed" region. Calmed regions have been observed in previous studies to follow turbulent spots and wake induced turbulent strips. The duration of the calmed region increases at the downstream stations, since the trailing edge celerity of the calmed region, shown in Fig. 9 to be about 0.3 the local free-stream velocity (in agreement with previous studies of calmed regions), is slower than the trailing edge celerity of the disturbed region. Hence at station 8.5 the calmed region extends for $\Delta t/T$ of about 0.2, while at station 10.5 it extends for $\Delta t/T$ of about 0.4. The presence of the calmed region may help to limit the separation bubble thickness.

Figure 12 shows the ensemble $\tilde{u}'$ data in a different format. Contours of near wall $\tilde{u}'$ at $y=0.095$ mm ($y/L_s=0.0004$) are shown in a time-space plot. The horizontal axis shows the dimensionless streamwise location, and the vertical axis indicates the dimensionless time within the cycle. Two complete cycles are

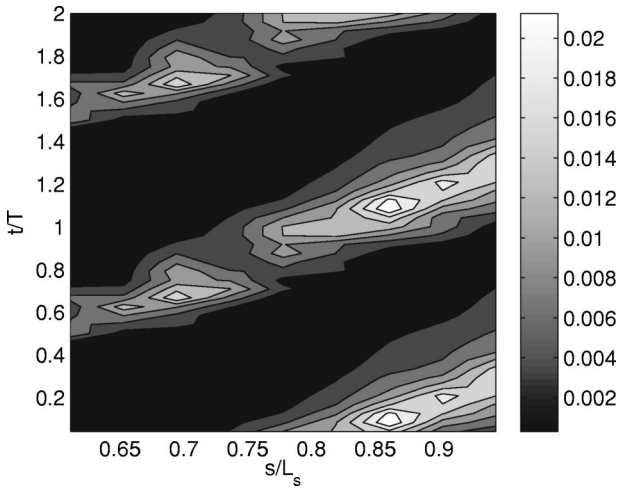

Fig. 12 Time-space plot of ensemble averaged $\tilde{u}'/U_e$ at $y/L_s = 0.0004$

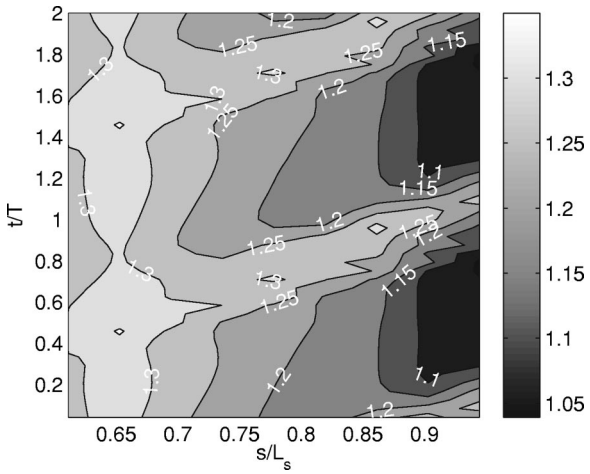

Fig. 14 Time-space plot of ensemble averaged dimensionless free-stream velocity $\tilde{U}_\infty/U_e$

shown to better illustrate the periodicity of the event. The data in the bottom half of the figure is shown again in the top half. In this format, it is clear that the jet outpulse causes a high $\tilde{u}'$ event to appear at $s/L_s = 0.6$ (station 7) and $t/T = 0.6$. This event then proceeds downstream in a widening wedge of turbulence. The lower and upper slopes of the wedge indicate its leading and trailing edge celerities, respectively. Within the wedge, a local $\tilde{u}'$ peak is visible at $s/L_s = 0.7$ (station 8). This peak indicates that the flow structure produced by the jets has penetrated very near the wall. Slightly farther downstream at $s/L_s = 0.75$ (station 8.5) a local minimum is visible in the $\tilde{u}'$ contours. This may indicate that the flow structure induced by the jets has lifted off the wall slightly. The mean profiles of Fig. 9, support this, showing lower near wall mean velocity gradients at station 8.5, which indicates that high speed fluid is not as effectively brought into the near wall region at this station. Farther downstream in Fig. 12, the $\tilde{u}'$ level in the turbulent wedge rises again as a fully turbulent boundary layer begins to develop. Outside of the wedge the $\tilde{u}'$ level is very low, indicating laminar flow.

Figure 13 shows ensemble averaged $-\tilde{u}'\tilde{v}'$ contours at $y/L_s = 0.0128$ in the format of Fig. 12. As in Fig. 12, the wedge of turbulence is clear. Within the wedge momentum transport is high, but outside the wedge the flow appears to be laminar.

Figure 14 shows a time-space plot of the local ensemble averaged free-stream velocity. The free-stream velocity varies both spatially and temporally. Spatially, the shape of the airfoil passage causes the flow to decelerate. Temporally, when the jets cause a turbulent event to moves down the surface, it causes the boundary layer to thicken and accelerates the free-stream. During the laminar and calmed periods the boundary layer is thinner and the free-stream velocity is lower. Figure 15 shows the local Thwaites parameter, λ_θ, as computed from the free-stream velocity data of Fig. 14. In a laminar boundary layer, separation is expected when λ_θ is less than -0.082. With the exception of the turbulent strip, where the boundary layer is locally accelerated, λ_θ is below -0.082 at most times and locations on the surface, and at some times is below -2. Hence it is not a surprise that the boundary layer tends to separate when not controlled by turbulence or a calmed region.

Integral Parameters. Local displacement and momentum thickness values can be computed from the ensemble mean velocity profiles of Fig. 9. Momentum thickness is shown in Fig. 16. Both δ^* and θ grow in the streamwise direction and are about twice as large in the turbulent region than in the laminar flow region. The slow growth of the momentum thickness in the nonturbulent flow indicates that losses should be low in this region, as might be expected based on the low $\tilde{u}'$ and $-\tilde{u}'\tilde{v}'$ values of Figs.

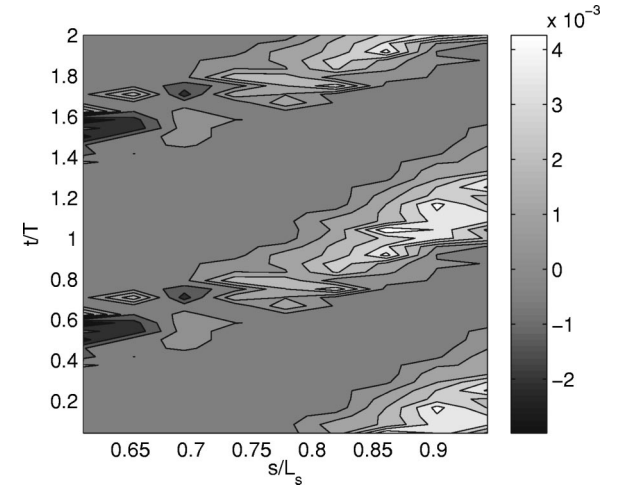

Fig. 13 Time-space plot of ensemble averaged $-\tilde{u}'\tilde{v}'/U_e^2$ at $y/L_s = 0.0128$

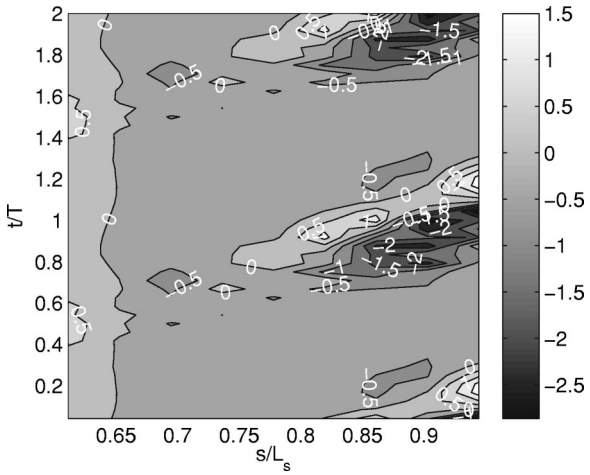

Fig. 15 Time-space plot of ensemble averaged Thwaites acceleration parameter λ_θ

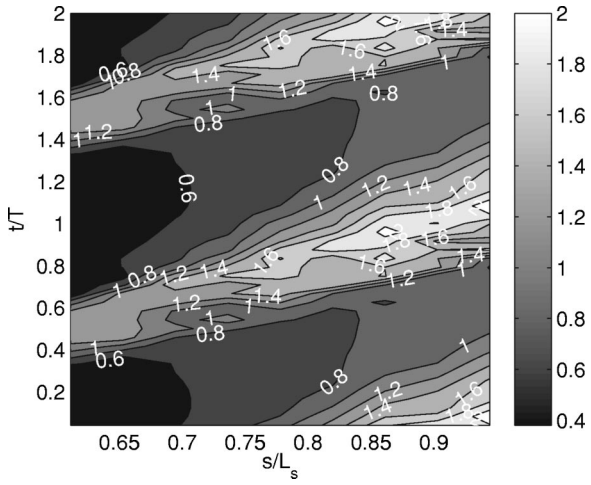

Fig. 16 Time-space plot of ensemble averaged momentum thickness θ in mm

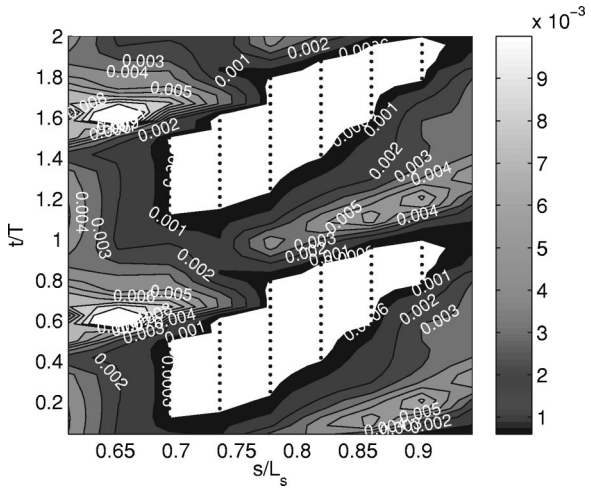

Fig. 18 Time-space plot of ensemble averaged skin friction coefficient C_f; white areas with dots indicate separated flow

10 and 11. At $s/L_s=0.6$ (station 7), δ^* and θ in the laminar flow are both roughly 67% of their values in the baseline case of Volino [4]. The lower values in the present case may be due to the suppression of the large separation bubble downstream, which changes the local pressure gradient at station 7. The suction during the inflow portion of the jet cycle could also be an explanation, but δ^* and θ are uniformly low in the laminar flow at station 7. If the suction were causing a thinner boundary layer, one would expect the effect to be stronger during the time of strongest inflow into the jet holes. Figure 17 shows the local shape factor H, computed from the δ^* and θ values. Within the turbulent region, the shape factor remains between 2 and 2.4, which is well above the expected value of 1.6 for a fully turbulent boundary layer subject to the strong adverse pressure gradient of the present case. In the nonturbulent flow, H reaches values as high as 3.4, which is consistent with the observed flow separation.

Skin Friction Coefficient. It is clear from the mean profiles of Fig. 9 that the local wall shear stress varies greatly during the jet oscillation cycle. At the upstream stations at $t/T=0.6$, for example, the jets bring high speed fluid very close to the wall, producing a very high mean velocity gradient at the wall. At other times at all stations, the boundary layer appears very laminarlike, indicating a relatively low wall shear stress. When the boundary layer is separated the wall shear goes to zero. Figure 18 shows the local skin friction coefficients C_f. The white regions with dots indicate where the flow is separated and the local skin friction is essentially zero. At $s/L_s=0.6$ (station 7) there is a laminar boundary layer with $C_f=0.005$ between jet outward pulses. The corresponding momentum thickness Reynolds is about 60. The skin friction drops in the streamwise direction and the boundary layer separates at $s/L_s=0.7$ (station 8). At $t/T=0.6$ and $s/L_s=0.6$, the skin friction is much higher, following the jet outpulse. The momentum thickness Reynolds number is as high as 180, and C_f reaches values as high as 0.014. Moving downstream along this turbulent region, C_f rapidly drops to 0.001 at $t/T=0.8$ and $s/L_s=0.75$ (station 8.5). The turbulence at this time and position is also low (Fig. 10). As stated above, the vortices produced by the jets appear to quickly bring high speed fluid near the wall, resulting in high skin friction and turbulence, but by $s/L_s=0.75$ this effect may weaken, resulting in lower C_f and $\tilde{u}'$. Moving farther downstream to $t/T=1.1$ and $s/L_s=0.85$, C_f rises again to as high as 0.007. The corresponding Re_θ is about 200 at this time and location. $C_f=0.007$ is about what one would expect for a fully turbulent boundary layer with $\mathrm{Re}_\theta=200$, based on the standard correlation $C_f=0.0256/\mathrm{Re}_\theta^{0.25}$ (Schlichting [33]).

Figure 18 clearly shows the calmed region described above. It is the triangular shaped region centered at $t/T=0.4$ and $s/L_s=0.9$ that in the figure is bounded below by the strip of high C_f and above by the separated flow region. Comparing Figs. 12, 13, 16, and 18 shows that the calmed region has low skin friction, low momentum thickness, and low turbulence. Losses should therefore be low for the calmed region, as expected.

A comparison of the momentum thickness and skin friction in Figs. 16 and 18 is interesting. The wedge of high θ overlaps both the upper portion of the separated flow region and the strip of high C_f. As shown in the profiles of Figs. 10 and 11, downstream of $s/L_s=0.75$ (station 8.5), the turbulence and mixing induced by the jet outpulse initially affects the outer part of the boundary layer and does not immediately eliminate the separation bubble. Figure 16 shows that this outer region mixing causes a rise in the momentum thickness. It is only somewhat later and farther downstream that this mixing moves into the near wall region, causing reattachment and high C_f. Kaszeta et al. [34] reported a similar result for flow over the Pak-B airfoil subject to wake passing events. They observed a time lag between the wake arrival and near wall transition.

Kaszeta et al. [34] also observed a relation between the temporal acceleration and deceleration of the flow associated with the wake passing, and its relation to transition and the thickening and thinning of the boundary layer. Similarly, a comparison of Figs.

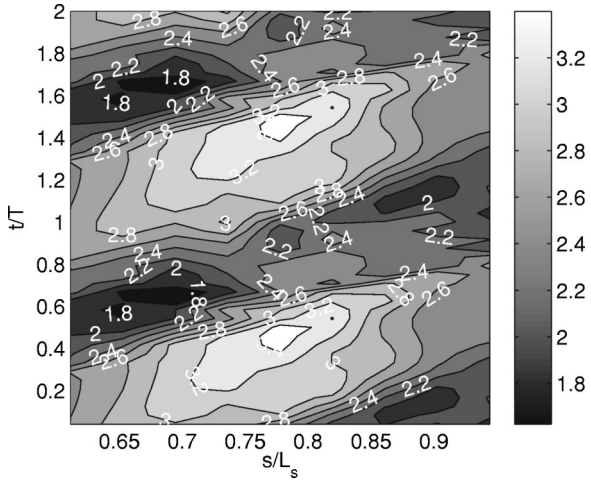

Fig. 17 Time-space plot of ensemble averaged shape factor H

15, 16, and 18 show the relation between the local acceleration, θ and C_f. The region of overlap between high θ and separated flow corresponds to the region of strong deceleration centered at $s/L_s = 0.9$ and $t/T = 0.85$. One could argue that the deceleration inhibits reattachment in spite of the mixing in the outer part of the boundary layer. At slightly later t/T, the flow is accelerated. Under the combination of acceleration and high $-\tilde{u}'\tilde{v}'$ the boundary layer reattaches.

Open Questions. The first objective of the present study was to assess the effectiveness of synthetic VGJ's on separation control for an LPT airfoil and provide some description of the mechanisms through which the jets work. This has been addressed above. The second objective was to use these results to generate questions for further consideration. These are discussed below.

What is the effect of jet frequency on flow control? In the present case, with $F^+ = 0.65$, the airfoil boundary layer at any given time was approximately half disturbed by the jets and half laminar or calmed. The effects of one jet outpulse are present in the boundary layer at all times. Separation occurred, but the separation bubble was small and did not appear to result in any harmful effects. How thick a separation bubble is tolerable? If F^+ were increased, the duration of each event would be reduced, but more events would be present in the boundary layer at any given time. It is not clear what effect this would have. In other studies with synthetic jets, some have found that F^+ of the order 1, as in the present study, is most effective (e.g., Seifert and Pack [35]). Others, such as Amitay and Glezer [21] report that under some conditions jets with F^+ of the order 10 are more effective. Lowering the jet frequency might be beneficial. Losses appear to be generated primarily in the flow disturbed by the jets, while the flow between these events is laminar or calmed with low losses. Reducing F^+ could presumably result in a smaller fraction of the airfoil covered by disturbed flow at any time. At some point, however, if the jets are too widely spaced, the flow will become uncontrolled at times and revert to the large separation bubble of the baseline case. Based on the trailing edge celerity of the disturbed flow, if F^+ were reduced below 0.45, there would be instances within the jet cycle when no disturbances would be present in the boundary layer. If F^+ were reduced below 0.3, there would be times when neither disturbed or calmed flow would be present. In flow around a single airfoil, Seifert and Pack [35] found that jets with F^+ between 0.5 and 1.5 were most effective at all Re, but that with $F^+ = 0.25$ the jets were ineffective. Bons et al. [25], in contrast, found that their VGJ's were effective at F^+ as low as 0.1. They suggested that the more controlled nature of the LPT flow, where adjacent airfoils provide covered turning, might explain the lower effective F^+ in their study. It should be noted that the Bons et al. [25] experiments were conducted at a Reynolds number of 60,000, where separation effects are not as severe as in the present case with Re=25,000.

What is the effect of jet amplitude on flow control? The pressure profiles of Fig. 4 indicate that the jet amplitude must be sufficiently high for the jets to be effective. It is expected that using a higher amplitude than necessary will result in higher losses, but the extent to which the losses would increase is not known. Volino [5] using passive bars found that cases with a small separation bubble followed by reattachment had lower losses than cases in which the boundary layer was tripped to turbulent to prevent separation. Low amplitude jets could potentially produce a similar effect.

What is the effect of jet wave form? In the present case the speaker was driven with a sine wave input. A square wave with a short duty cycle, as in the study of Bons et al. [25], might be better. By keeping the duty cycle short, the amount of calmed flow relative to disturbed flow could be increased. This might allow a reduction of losses without a sacrifice of separation control.

What is the effect of jet inflow? The outward flow portion of each jet cycle appears to dominate the flow control. It is possible, however, that the inflow may help reduce the boundary layer thickness in the undisturbed flow periods and help reduce separation effects. A direct comparison of cases at the same Re using synthetic VGJ's and pulsed VGJ's could help answer this question.

What is the effect of jet geometry? The VGJ's are clearly effective. Through the generation of streamwise vortices they appear to provide more mixing than would be produced with normal jets that simply produced turbulence. The relative magnitudes of the effects of turbulence and streamwise vortices in enhancing mixing are uncertain. Might the generation of turbulent spots with a normal jet be sufficient? Which would result in lower losses?

What are the effect of Reynolds number and free-stream turbulence level? The baseline cases of Volino [4] show that at higher Re and higher FSTI the boundary layer is more likely to transition and reattach even without flow control. The generation of calmed attached flow between jet events could still prove beneficial at higher Re, however. There would be a tradeoff between the losses generated by the jets themselves and the reduction in losses the jets might provide by reducing the separation bubble thickness and producing low-loss calmed regions. It might be possible to control the flow at higher Re with significantly lower blowing ratios than in the present case. Natural transition in the undisturbed flow between jet events and its interaction with calmed regions would be an added complication at higher Re not seen in the present study. If the Re were sufficiently high so that separation did not occur in the uncontrolled case, it is unlikely that the jets would provide any benefit. Schulte and Hodson [27] noted that the presence of calmed regions produced by unsteady wake passing could not significantly lower the losses in an already attached boundary layer.

Conclusions

1. Synthetic vortex generator jets proved effective for controlling boundary layer separation on an LPT airfoil at very low Reynolds numbers. The separation bubble was effectively eliminated, and losses were lower than in a similar case with passive flow control.
2. The VGJ's prevent separation by bringing high momentum fluid into the near wall region and by promoting momentum transport through turbulent mixing.
3. The disturbance produced by the VGJ's behaves in many ways like the disturbance associated with a turbulent spot or a wake induced turbulent strip. The leading edge celerity of the disturbance is approximately $0.9U_\infty$, and the trailing edge celerity is about $0.45U_\infty$. A calmed region with a trailing edge celerity of $0.3U_\infty$ follows the disturbance. The calmed region is resistant to separation.
4. The adverse pressure gradient in the present case was strong enough so that the boundary layer did separate after the passage of the calmed flow. The separation bubble remained thin, however. The appearance of a disturbance did not immediately induce reattachment. The disturbance appeared initially in the outer part of the boundary layer. After some lag time the disturbance spread into the near wall region and caused reattachment.
5. While much has been learned regarding the effectiveness and physics of synthetic VGJ's in LPT flows, many questions remain regarding their applicability under different flow conditions and their optimal design. These questions have been discussed.

Acknowledgments

This work was sponsored by the NASA Glenn Research Center. The grant monitor is Dr. David Ashpis. Additional matching support was provided through a U.S. Naval Academy Recognition Grant. Mr. Dale Boyer of the Technical Support Department at the

Naval Academy fabricated the test section and the airfoils. Midshipman Dirk Heron conducted preliminary tests which led into the present study.

Nomenclature

B = blowing ratio
C_f = skin friction coefficient
C_p = $2(P_T - P)/\rho U_e^2$, pressure coefficient
c_μ = momentum coefficient
D = diameter
F^+ = $(0.442L_s)/(U_e T)$, dimensionless frequency
FSTI = free-stream turbulence intensity
H = δ^*/θ, shape factor
K = $(\nu/U_\infty^2)(dU_\infty/ds)$, acceleration parameter
L_s = suction surface length
M = jet to boundary layer mass flux ratio
P = pressure
P_T = upstream stagnation pressure
Re = $U_e L_s/\nu$, exit Reynolds number
Re_θ = momentum thickness Reynolds number
S = jet holes per unit span
s = streamwise coordinate, distance from leading edge
T = jet oscillation period
t = time
U = mean streamwise velocity
U_∞ = local free-stream velocity
U_e = nominal exit free-stream velocity, based on inviscid solution
V_{jet} = jet velocity
u' = time averaged rms streamwise fluctuating velocity
$\tilde{u}'$ = ensemble averaged rms streamwise fluctuating velocity
$-\overline{u'v'}$ = time averaged turbulent shear stress
$-\tilde{u}'\tilde{v}'$ = ensemble averaged turbulent shear stress
y = cross-stream coordinate, distance from wall
δ^* = displacement thickness
λ_θ = $\mathrm{Re}_\theta^2 K$, Thwaites parameter
ν = kinematic viscosity
ρ = density
θ = momentum thickness

Subscripts

ave = average over jet outpulse
jet = jet condition
max = maximum in jet cycle
∞ = free stream

References

[1] Hourmouziadis, J., 1989, "Aerodynamic Design of Low Pressure Turbines," AGARD Lecture Series 167.
[2] Mayle, R. E., 1991, "The Role of Laminar-Turbulent Transition in Gas Turbine Engines," ASME J. Turbomach., **113**, pp. 509–537.
[3] Sharma, O. P., Ni, R. H., and Tanrikut, S., 1994, "Unsteady Flow in Turbines," AGARD Lecture Series 195, Paper No. 5.
[4] Volino, R. J., 2002, "Separated Flow Transition Under Simulated Low-Pressure Turbine Airfoil Conditions: Part 1—Mean Flow and Turbulence Statistics," ASME J. Turbomach., **124**, pp. 645–655.
[5] Volino, R. J., 2003, "Passive Flow Control on Low-Pressure Turbine Airfoils," ASME J. Turbomach., **125**, pp. 754–764.
[6] Howell, R. J., Ramesh, O. N., Hodson, H. P., Harvey, N. W., and Schulte, V., 2001, "High Lift and Aft-Loaded Profiles for Low-Pressure Turbines," ASME J. Turbomach., **123**, pp. 181–188.
[7] Gad-el-Hak, M., 2000, *Flow Control, Passive, Active, and Reactive Flow Management*, Cambridge University Press, Cambridge.
[8] Lake, J. P., King, P. I., and Rivir, R. B., 2000, "Low Reynolds Number Loss Reduction on Turbine Blades With Dimples and V-Grooves," AIAA Paper 00-738.
[9] Van Treuren, K. W., Simon, T., von Koller, M., Byerley, A. R., Baughn, J. W., and Rivir, R., 2001, "Measurements in a Turbine Cascade Flow Under Ultra Low Reynolds Number Conditions," ASME J. Turbomach., **124**, pp. 100–106.
[10] Lee, J., Sloan, M. L., and Paynter, G. C., 1994, "Lag Model for Turbulent Boundary Layers Over Rough Bleed Surfaces," J. Propul. Power, **10**, pp. 562–568.
[11] Sturm, W., Schcugenpflug, H., and Fottner, L., 1992, "Performance Improvements of Compressor Cascades by Controlling the Profile and Sidewall Boundary Layers," ASME J. Turbomach., **114**, pp. 477–486.
[12] Johnston, J. P., and Nishi, M., 1990, "Vortex Generator Jets. Means for Flow Separation Control," AIAA J., **28**, pp. 989–994.
[13] Compton, D. A., and Johnston, J. P., 1992, "Streamwise Vortex Production by Pitched and Skewed Jets in a Turbulent Boundary Layer," AIAA J., **30**, pp. 640–647.
[14] McManus, K., Legner, H., and Davis, S., 1994, "Pulsed Vortex Generator Jets for Active Control of Flow Separation," AIAA Paper 94-2218.
[15] Raghunathan, S., Watterson, J., Cooper, R., and Lee, S., 1999, "Short Wide Angle Diffuser With Pulse Jet Control," AIAA Paper 99-0280.
[16] Sinha, S. K., and Pal, D., 1993, "Optimizing the Use of Acoustic Perturbation to Control Unsteady Boundary Layer Separation," FED (Am. Soc. Mech. Eng.), **157**, pp. 253–263.
[17] Jacobson, S. A., and Reynolds, W. C., 1998, "Active Control of Streamwise Vortices and Streaks in Boundary Layers," J. Fluid Mech., **360**, pp. 179–211.
[18] Miau, J. J., Lee, K. C., Chen, M. H., and Chou, J. H., 1991, "Control of Separated Flow by a Two-Dimensional Oscillating Fence," AIAA J., **29**, pp. 1140–1148.
[19] Sinha, S. K., Pal, D., and Banerjee, D., 1996, "Control of Flow Separation Using the EMEMS Approach: Proof of Concept Experiments," DSC (Am. Soc. Mech. Eng.), **59**, pp. 253–263.
[20] Whitehead, L. A., Graham, D. J., Moore, F. A., Bolleman, B. J., Lake, R., and Dunwoody, A. B., 1996, "Investigation of Boundary Layer Flow Separation Control by Airfoil Surface Vibration," Can. Aeronautics Space J., **42**, pp. 213–219.
[21] Amitay, M., and Glezer, A., 2002, "Role of Actuation Frequency in Controlled Flow Reattachment Over a Stalled Airfoil," AIAA J., **40**, pp. 209–216.
[22] Huang, J., Corke, T. C., and Thomas, F. O., 2002, "Separation Control Over Low Pressure Turbine Blades," Bull. Am. Phys. Soc., DFD2002, **47**(10), p. 167.
[23] Hultgren, L. S., and Ashpis, D. E., 2002, "Glow Discharge Plasma Active Control of Separation at Low Pressure Turbine Conditions," Bull. Am. Phys. Soc., DFD2002, **47**(10), pp. 167–168.
[24] Bons, J. P., Sondergaard, R., and Rivir, R. B., 2001, "Turbine Separation Control Using Pulsed Vortex Generator Jets," ASME J. Turbomach., **123**, pp. 198–206.
[25] Bons, J. P., Sondergaard, R., and Rivir, R. B., 2002, "The Fluid Dynamics of LPT Blade Separation Control Using Pulsed Jets," ASME J. Turbomach., **124**, pp. 77–85.
[26] Gostelow, J. P., Walker, G. J., Solomon, W. J., Hong, G., and Melwani, N., 1997, "Investigation of the Calmed Region Behind a Turbulent Spot," ASME J. Turbomach., **119**, pp. 802–809.
[27] Schulte, V., and Hodson, H. P., 1998, "Prediction of the Becalmed Region for LP Turbine Profile Design," ASME J. Turbomach., **120**, pp. 839–846.
[28] Volino, R. J., 2002, "Separated Flow Transition Under Simulated Low-Pressure Turbine Airfoil Conditions: Part 2—Turbulence Spectra," ASME J. Turbomach., **124**, pp. 656–664.
[29] Volino, R. J., Schultz, M. P., and Pratt, C. M., 2001, "Conditional Sampling in a Transitional Boundary Layer Under High Free-Stream Turbulence Conditions," ASME J. Fluids Eng., **125**, pp. 28–37.
[30] Wills, J. A. B., 1962, "The Correction of Hot-Wire Readings for Proximity to a Solid Boundary," J. Fluid Mech., **12**, pp. 65–92.
[31] Volino, R. J., and Simon, T. W., 1997, "Velocity and Temperature Profiles in Turbulent Boundary Layers Experiencing Streamwise Pressure Gradients," ASME J. Heat Transfer, **119**, pp. 433–439.
[32] Ligrani, P. M., and Bradshaw, P., 1987, "Spatial Resolution and Measurement of Turbulence in the Viscous Sublayer Using Subminiature Hot-Wire Probes," Exp. Fluids, **5**, pp. 407–417.
[33] Schlichting, H., 1979, *Boundary Layer Theory*, 7th ed. McGraw-Hill, New York.
[34] Kaszeta, R. W., Simon, T. W., and Ashpis, D. E., 2001, "Experimental Investigation of Transition to Turbulence as Affected by Passing Wakes," ASME Paper 2001-GT-195.
[35] Seifert, A., and Pack, L. G., 1999, "Oscillatory Control of Separation at High Reynolds Numbers," AIAA J., **37**, pp. 1062–1071.

Jae Su Kwak[1]

Jaeyong Ahn

Je-Chin Han
e-mail: jchan@mengr.tamu.edu

Turbine Heat Transfer Laboratory,
Department of Mechanical Engineering,
Texas A&M University,
College Station, TX 77843-3123

C. Pang Lee
GE Aircraft Engines,
1 Neumann Way, MD A406,
Cincinnati, OH 45215-6301

Ronald S. Bunker
GE Corporate R&D,
K-1, ES-119, P.O. Box 8,
Schenecetady, NY 12301

Robert Boyle

Raymond Gaugler

NASA Research Center,
21000 Brookpark Road, MS 5-11,
Cleveland, OH 44135

Heat Transfer Coefficients on the Squealer Tip and Near-Tip Regions of a Gas Turbine Blade With Single or Double Squealer

Detailed heat transfer coefficient distributions on a gas turbine squealer tip blade were measured using a hue detection based transient liquid-crystals technique. The heat transfer coefficients on the shroud and near tip regions of the pressure and suction sides of a blade were also measured. Squealer rims were located along (a) the camber line, (b) the pressure side, (c) the suction side, (d) the pressure and suction sides, (e) the camber line and the pressure side, and (f) the camber line and the suction side, respectively. Tests were performed on a five-bladed linear cascade with a blow down facility. The Reynolds number based on the cascade exit velocity and the axial chord length of a blade was 1.1 $\times 10^6$ *and the overall pressure ratio was 1.2. Heat transfer measurements were taken at the three tip gap clearances of 1.0%, 1.5%, and 2.5% of blade span. Results show that the heat transfer coefficients on the blade tip and the shroud were significantly reduced by using a squealer tip blade. Results also showed that a different squealer geometry arrangement changed the leakage flow path and resulted in different heat transfer coefficient distributions. The suction side squealer tip provided the lowest heat transfer coefficient on the blade tip and near tip regions compared to the other squealer geometry arrangements.* [DOI: 10.1115/1.1626684]

Introduction

Due to the pressure difference between the blade pressure and suction side, hot gas leaks through the gap between the blade tip and the shroud. This flow, called leakage flow, causes thin boundary layer and high heat transfer coefficient on the blade tip. The hot leakage flow is the major cause of blade tip failures. To reduce the leakage flow and heat transfer on the tip, the blades of modern gas turbines typically have a recessed cavity at the tip and are called squealer tip blades. The cavity acts as a labyrinth seal to increase flow resistance and thus reduces leakage flow.

Recently, many experimental studies for the squealer tip blade have been conducted in a cascade environment. Azad et al. [1,2] studied the heat transfer on the first stage blade tip of an aircraft engine turbine (GE-E^3). They presented the effects of tip gap clearance and free-stream turbulence intensity level on the detailed heat transfer coefficient distributions for both plane and squealer tips under engine representative flow conditions. Azad et al. [3] also studied the effect of squealer geometry arrangement on gas turbine blade tip heat transfer and found that the location of the squealer rim could change the leakage flow and result in different heat loads to the blade tip. They also found that the suction side squealer provided best sealing to leakage flow among all the cases they studied. Kwak and Han [4,5] presented heat transfer coefficients on the tip and near tip regions of both plane and squealer tip blades. They showed that the squealer tip could reduce heat transfer coefficients on the tip and near tip regions. Kwak and Han [6,7] also studied heat transfer and film cooling effectiveness on both plane and squealer tip blades. Their results showed that the film cooling effectiveness on the squealer tip was much higher than that on the plane tip. Dunn and Haldeman [8] measured time averaged heat flux at a recessed blade tip for a full-scale rotating turbine stage at transonic vane exit conditions. Their results showed that the heat transfer coefficient (Nusselt number) at the mid and rear portion of the cavity floor is on the same order as the blade leading edge value. Yang and Diller [9] studied local heat transfer coefficients at several locations on a turbine blade tip model with a recessed cavity (squealer tip) in a stationary linear cascade. Papa et al. [10] measured average and local mass transfer coefficients on a squealer tip and winglet-squealer tip using the naphthalene sublimation technique. They also presented the flow visualization on the tip surface using an oil dot technique. Metzger et al. [11] and Chyu et al. [12] investigated heat transfer in a rectangular grooved tip model. They showed that the heat transfer in the upstream end of the cavity was greatly reduced compared to the flat tip, however, at the downstream of the cavity, the heat transfer levels for the grooved tip were higher due to flow reattachment inside the cavity. They also showed that the effect of the shroud velocity on the heat transfer coefficient was very small. Heyes et al. [13] studied tip leakage flow on plane and squealer tips in a linear cascade and concluded that the use of a squealer tip, especially a suction-side squealer tip, was more beneficial than a flat tip. Kim et al. [14] and Kim and Metzger [15] studied heat transfer and film cooling effectiveness using a two-dimensional (2D) rectangular tip model.

Researchers have also studied heat transfer on the plane tip blade. Mayle and Metzger [16], Metzger and Rued [17], and Rued and Metzger [18] performed heat transfer studies using a simplified tip-simulated model. Metzger et al. [19] measured local heat

[1]Currently Senior Researcher, Aeropropulsion Department, Korea Aerospace Research Institute, Daejeon, Korea.

Contributed by the International Gas Turbine Institute and presented at the International Gas Turbine and Aeroengine Congress and Exhibition, Atlanta, GA, June 16–19, 2003. Manuscript received by the IGTI December 2002; final revision March 2003. Paper No. 2003-GT-38907. Review Chair: H. R. Simmons.

flux using heat flux sensors in a rotating turbine rig with two different tip gaps. Bunker et al. [20] investigated the detailed heat transfer coefficient distribution on the blade tip surface using hue detection based liquid crystal technique. They measured the heat transfer coefficient at three tip gaps and two free-stream turbulence levels with both sharp and rounded edges. Bunker and Bailey [21] studied the effect of squealer cavity depth and oxidation on turbine blade tip heat transfer. They showed that the effect of cavity depth is not uniform over the entire tip cavity surface, but generally a deeper cavity produced lower heat transfer coefficients. Their results also showed that blade tip heat transfer had low sensitivity to clearance gap magnitude. Teng et al. [22] measured the heat transfer coefficients and static pressure distributions of a turbine blade tip region in a large-scale low-speed wind tunnel facility using a transient liquid crystals technique. Rhee et al. [23] studied the local heat/mass transfer on the stationary shroud with blade tip clearances for flat tip geometry. They used the naphthalene sublimation method and concluded that the heat/mass transfer characteristics changed significantly with the gap clearance. Jin and Goldstein [24,25] measured local mass transfer on a simulated high pressure turbine blade and near tip surfaces. They showed that the averaged mass transfer rate on the tip surface was much higher than that on the suction and the pressure surface.

Numerical studies to investigate blade tip heat transfer also have been conducted. Ameri and Steinthorsson [26,27] predicted heat transfer on the tip of the SSME (Space Shuttle Main Engine) rotor blade. Ameri et al. [28] also predicted the effects of tip gap clearance and casing recess on heat transfer and stage efficiency for several squealer blade tip geometries. Ameri and Bunker [29] performed a computational study to investigate the detailed heat transfer distributions on blade tip surfaces for a large power generation turbine and compared the result with the experimental data of Bunker et al. [20]. Ameri and Rigby [30] also calculated heat transfer and film-cooling effectiveness on film cooled turbine blade models. Ameri [31] predicted heat transfer and flow on the blade tip of a gas turbine equipped with a mean-camber line strip. Numerical studies to investigate the heat transfer on the squealer tip blade also have been conducted by Ameri et al. [32] and Yang et al. [33,34]

Most of the above referenced studies focused on the heat transfer coefficient on the blade tip surface only. The present study applies a hue detection based transient liquid-crystals technique to obtain the heat transfer coefficient on the tip surface, shroud, and near tip region of the blade pressure and suction side of the blade with a single or double squealer. This study provides comprehensive information about the heat transfer coefficient on the tip and near the tip regions with the single or double squealer blade tip. The effect of the squealer rim arrangement on the heat transfer coefficient is also presented. The results are compared with the plane tip and the double squealer tip results (Kwak and Han [4,5]).

Experimental Setup

Figure 1 shows the schematic of the test facility. The detailed description of the test facility can be found in Kwak and Han [4,5]. The turbulence intensity measured 6 cm upstream of the center was 9.7%. The turbulence length scale was estimated to be 1.5 cm. The tip gaps used for this study were about 1.0%, 1.5%, and 2.5% of the blade span (12.2 cm). The definitions of blade tip and shroud are also shown in the upper part of Fig. 2.

The blade had a 12.2-cm span and an 8.61-cm axial chord length. This was three times larger than the dimension of a GE-E^3 blade tip profile. Each blade had a constant cross section for the entire span as shown in the lower part of Fig. 2. Figure 3 shows the heat transfer measurement blade. The lower portion of the blade was made of aluminum, and the upper portion consisted of an inner aluminum rim with a cavity. The outer removal shells were made of a polycarbonate with low thermal conductivity. Cartridge heaters were inserted into the blade to heat the aluminum

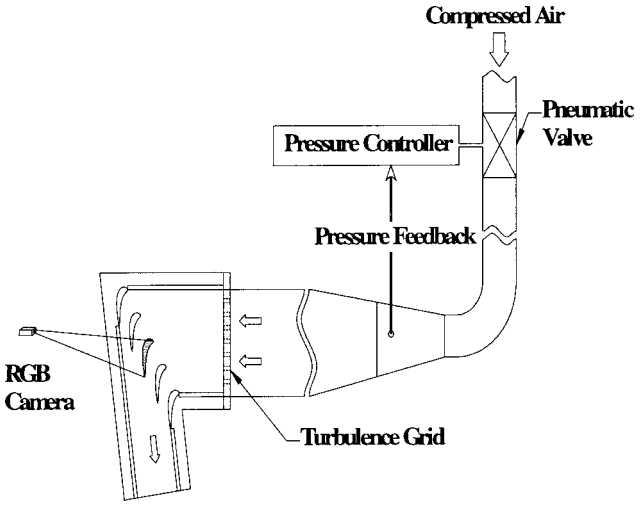

Fig. 1 Schematic of blow down facility

core and consequently the outer polycarbonate shell. For the heat transfer measurement on the shroud, a 300-W plate heater was used to heat the shroud plate and was removed before the test. Figure 4 shows a detailed view of the removable blade tips with different squealer arrangements. A squealer rim was placed along (*a*) the camber line (CL), (*b*) the pressure side (PS), (*c*) the suction side (SS), (*d*) the pressure and suction sides (PS+SS), (*e*) the camber line and the pressure side (CL+PS), and (*f*) the camber line and the suction side (CL+SS), respectively. The thickness and height (*H*) of the squealer rim is 0.229 and 0.508 cm, respectively. The height of the squealer rim is about 4.2% of the blade span.

During the blow down test, the cascade inlet and exit air velocities were 85 and 199 m/s, respectively, and the inlet and exit

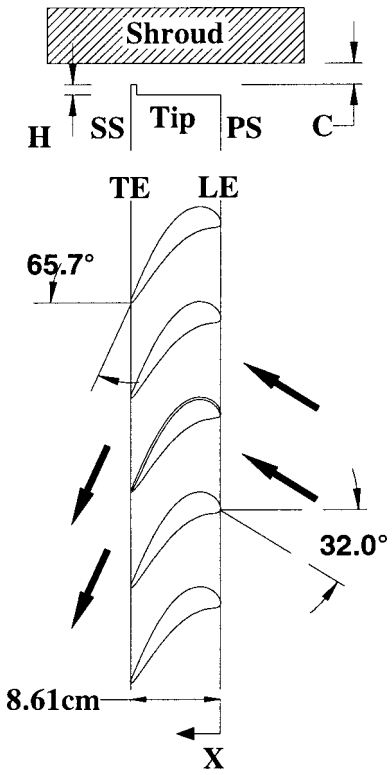

Fig. 2 Definition of blade tip and shroud

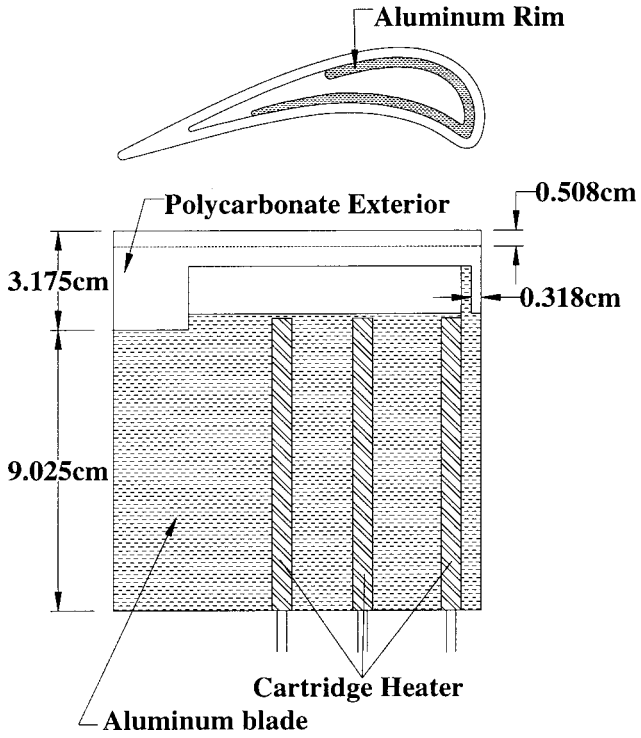

Fig. 3 Heat transfer measurement blade

Mach numbers were 0.25 and 0.59, respectively. The Reynolds number based on axial chord length and exit velocity was 1.1×10^6. The inlet total pressure (P_t) was 126.9 kPa, and the exit static pressure (P) was 102.7 kPa, which gave an overall pressure ratio (P_t/P) of 1.2. Azad et al. [1,2] described the detailed flow conditions, including the flow periodicity in cascade.

Heat Transfer Measurement Theory

A hue detection based transient liquid-crystals technique was used to measure the heat transfer coefficient on the blade tip. The local heat transfer coefficient over a liquid-crystals coated surface can be obtained using a one-dimensional semi-infinite solid assumption with convective boundary condition at the test surface. The solution for the 1D transient conduction equation at the surface ($x=0$) is

$$\frac{T_w - T_i}{T_m - T_i} = 1 - \exp\left(\frac{h^2 \alpha t}{k^2}\right) \operatorname{erfc}\left(\frac{h\sqrt{\alpha t}}{k}\right). \tag{1}$$

By knowing the initial temperature (T_i) of the test surface, the mainstream (recovery) temperature (T_m) at the cascade inlet, and the color change temperature (T_w) at time t, the local heat transfer coefficient (h) can be calculated from Eq. (1). If the mainstream temperature changes with time, the varying temperature can be represented as a series of step changes. Using Duhamel's superposition theorem, Eq. (1) can be written as follows:

$$T_w - T_i = \{T_{m,0} - T_i\} \times F\left(\frac{h\sqrt{\alpha t}}{k}\right) + \sum_{i=1}^{n} \left[F\left(\frac{h\sqrt{\alpha(t-\tau_i)}}{k}\right) \Delta T_{m,i} \right] \tag{2}$$

where $F(x) = 1 - \exp(x^2)\operatorname{erfc}(x)$, and ΔT_m is step changes in the mainstream.

The experimental uncertainty was calculated by the methods of Kline and McClintock [35]. Note that the blade tip material (polycarbonate) has a very low thermal conductivity of 0.18 W/m K. The liquid crystals color change transition occurs at the surface which is kept at a uniform initial temperature. Test duration is smaller (10–30 sec) than the time required for the temperature to penetrate the full thickness of the blade tip material. Thus a 1D transition, semi-infinite solid assumption is valid throughout the surface, except near the tip edges. The individual uncertainties in the measurement of the time of color change ($\Delta t = \pm 0.5$ sec), the mainstream temperature ($\Delta T_m = \pm 0.5°C$), the color change temperature ($\Delta T_w = \pm 0.2°C$), the initial temperature ($\Delta T_i = \pm 1°C$), and the blade tip material properties ($\Delta \alpha / k^2 = \pm 5\%$) were included in the calculation of the overall uncertainty of heat transfer coefficient. The uncertainty for the local heat transfer coefficient was estimated to be $\pm 8\%$. However, the uncertainty near the blade tip edge might be much greater up to 15% due to the 2D heat conduction effect. The uncertainty in the high heat transfer region also might be higher due to the short color change time.

Heat Transfer Measurement and Results

Two different liquid crystals were used in this study. The 20°C bandwidth liquid crystals (R34C20W, Hallcrest) were used to measure the initial temperature of the test surface, and the 4°C bandwidth liquid crystals (R29C4W, Hallcrest) were used to measure the color changing time. Figure 5(*a*) shows the results of the calibration for both liquid crystals.

Before the transient test, the initial temperature of the test surface was measured using the 20°C bandwidth liquid crystals and Fig. 5(*b*) presents the initial temperature on the tip ($C = 1.5\%$, squealer along the suction side case).

After the initial temperature measurement on the test surface, the transient time t in Eq. (2) was measured using the 4°C bandwidth liquid crystals and the local heat transfer coefficient h was calculated from Eq. (2). The test duration time was short enough (10–30 sec) to make a 1D semi-infinite solid assumption. The detailed experimental procedure was described by Kwak and Han [4,5].

Heat Transfer Coefficient on the Blade Tip. Figure 6 shows the heat transfer coefficient on the blade tip with different tip geometries. The squealer along the PS+SS case and the plane tip case (Figs. 6(*d*) and (*g*)) are presented for comparison. The detailed results of the plane tip and the squealer along the PS+SS

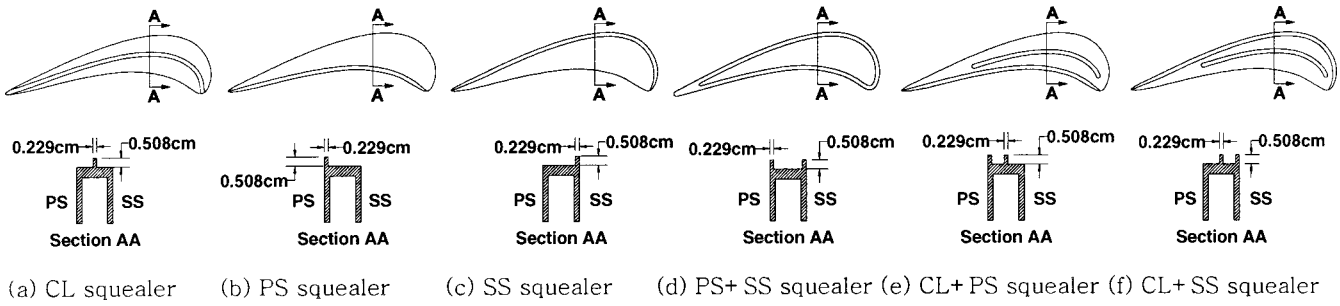

Fig. 4 Geometry of squealer tips

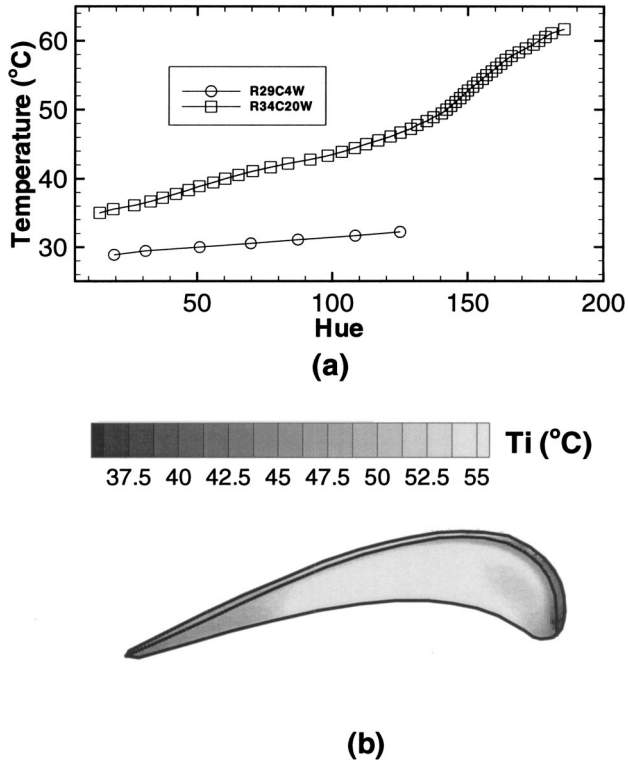

Fig. 5 (*a*) **The relation between hue and temperature** (*b*) **Initial temperature on the tip for the squealer along suction side and** $C=1.5\%$ **case**

cases are discussed by Kwak and Han [4,5]. Due to the shadow of the squealer rim, data near the squealer rim could not be obtained. Compared to the plane tip case (Fig. 6(*g*)), the squealer tip cases (Figs. 6(*a*)–(*f*)) show much lower heat transfer coefficient. However, the heat transfer coefficient on the squealer rim is comparable to the high heat transfer coefficient of the plane tip case. For the squealer tip cases, the heat transfer coefficient on the squealer rim is generally higher than on the tip surface.

For the squealer along the camber line case (Fig. 6(*a*)), the heat transfer coefficient between the suction side and the squealer rim is higher than between the pressure side and the squealer rim. This is caused by reattachment of the leakage flow. The leakage flow reattaches to the tip surface as shown in Fig. 7(*a*) and results in a high heat transfer coefficient. Figure 7 shows the conceptual view of the flow leakage near the tip region. If the squealer is located along the camber line as shown in Fig. 7(*a*), the leakage flow reattaches to the tip surface near the suction side and results in a high heat transfer coefficient in that region. A leakage vortex exists near the blade suction side. For the squealer along the pressure side case (Fig. 7(*b*)), a recirculation flow exists near the pressure side squealer rim, which results in a low heat transfer coefficient on the tip surface near the pressure side squealer rim. A reattachment exists between the suction side and the squealer rim and causes a higher heat transfer coefficient. If the squealer is located along the suction side (Fig. 7(*c*)), a recirculation region exists near the squealer rim. For the double squealer case (Fig. 7(*d*)), the leakage flow reattaches to the tip surface near the suction side or to the suction side squealer rim, which results in a higher heat transfer coefficient on the tip surface near the suction side. The recirculation flow exists near the pressure side squealer rim and causes a relatively low heat transfer coefficient on the cavity sur-

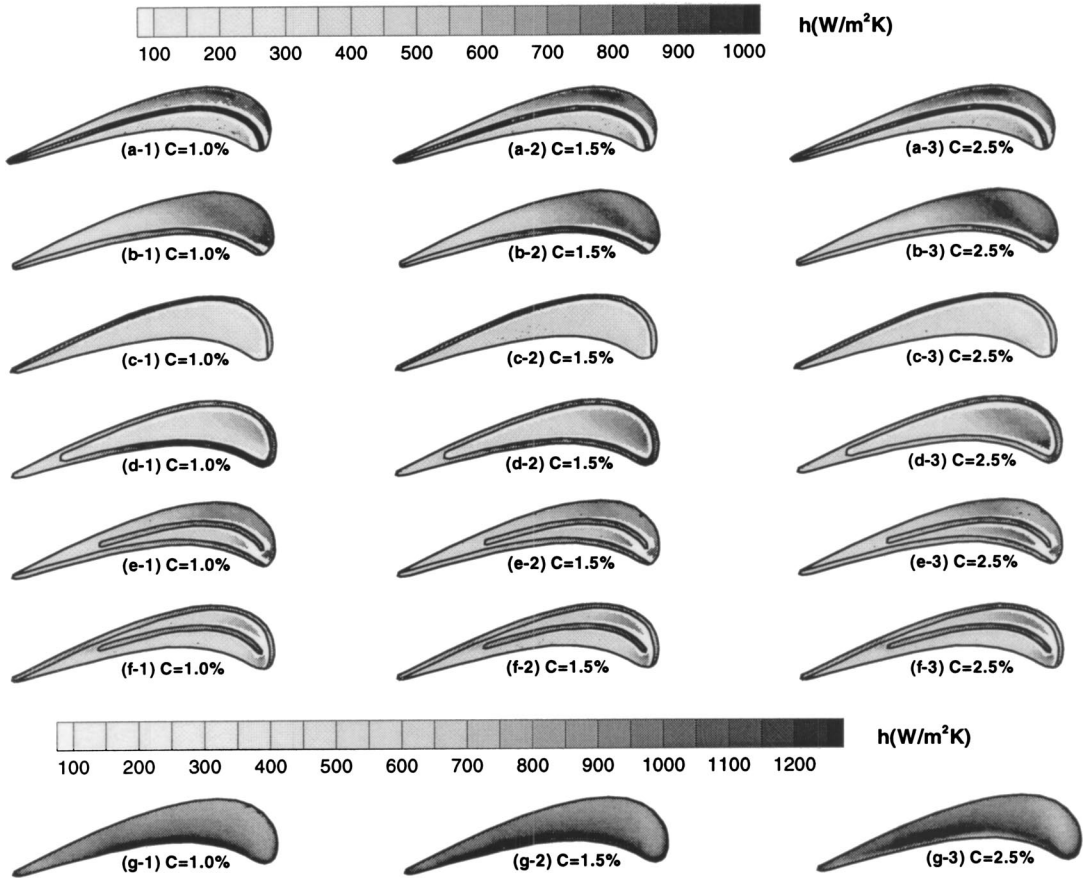

Fig. 6 Heat transfer coefficient on the tip, (*a*) **squealer along CL;** (*b*) **squealer along PS;** (*c*) **squealer along SS;** (*d*) **squealer along PS+SS (Kwak and Han [5]);** (*e*) **squealer along CL+PS;** (*f*) **squealer along CL +SS;** (*g*) **plane tip (Kwak and Han [4])**

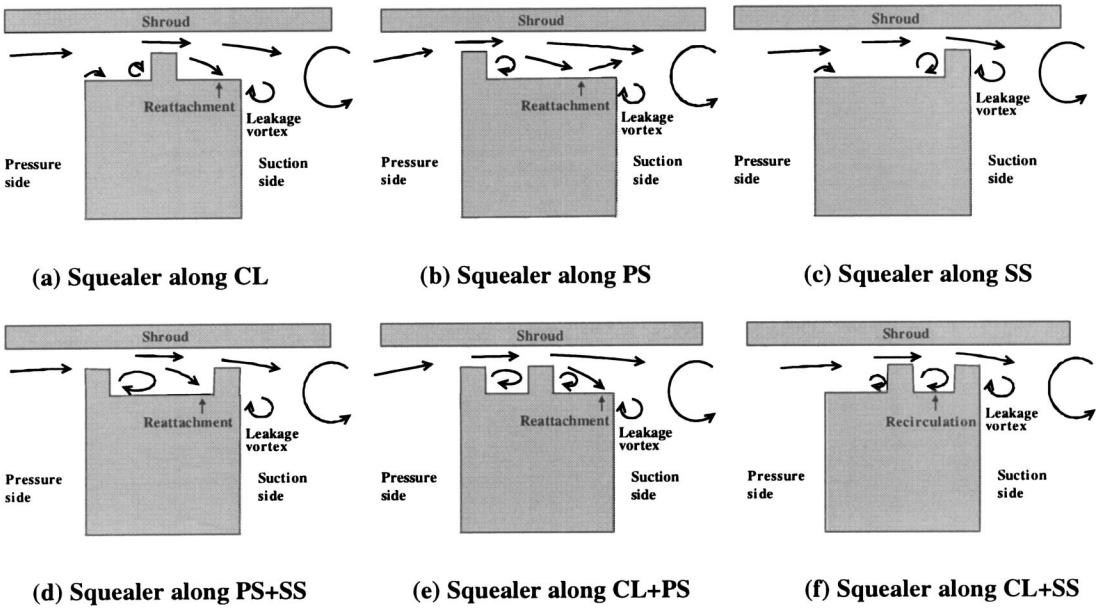

Fig. 7 The conceptual view of the flow leakage near the tip region

face near the pressure side. For the squealer along the camber line and the pressure side case (Fig. 7(*e*)), the leakage flow reattaches to the tip surface between the camber line squealer and the suction side edge. Between the two squealer rims, a recirculation flow exists. If the squealer rims are located along the camber line and the suction side as shown in Fig. 7(*f*), a recirculation flow exists between two squealer rims.

For the squealer along camber line case (Fig. 6(*a*)), as the tip gap clearance increases, the heat transfer coefficient on the tip increases. Figure 6(*b*) shows heat transfer coefficient on the tip with a squealer along the pressure side. The overall heat transfer coefficient for this case is smaller than in the plane tip case (Fig. 6(*g*)), but larger than in the squealer along the camber line case (Fig. 6(*a*)) or the double squealer cases (Figs. 6(*d*)–(*f*)). There is a high heat transfer coefficient region near 20–30% of the blade chord, and this could be caused by the reattachment of the leakage flow. Near the trailing edge, the separated leakage flow creates a recirculation zone near the squealer rim, which results in a low heat transfer coefficient near the trailing edge. As the tip gap increases, the heat transfer coefficient on the tip increases. Figure 6(*c*) presents the heat transfer coefficient on the tip with a squealer along the suction side. The overall heat transfer coefficient on the tip for this case is smaller than in the other cases. There is a relatively low heat transfer coefficient region on the tip surface near the squealer rim close to the leading edge. This is caused by recirculation of the flow near the squealer rim as shown in Fig. 7(*c*). As the tip gap increases, the overall heat transfer coefficient on the tip surface slightly increases. Figure 6(*e*) shows the heat transfer coefficient on the tip with squealer along the camber line and the pressure side. A high heat transfer coefficient region exists near the blade leading edge. A relatively high heat transfer region also can be seen near the blade suction side of about 20–40% of the blade chord. This region is caused by the reattachment of the leakage flow as shown in Fig. 7(*e*). The heat transfer coefficients near the trailing edge are low because of the flow recirculation near the pressure side squealer. As the tip gap clearance increases, the heat transfer coefficients between the two squealer rims near 20–30% of the blade chord increases. The overall heat transfer coefficient slightly increases as the tip gap clearance increases. Figure 6(*f*) presents heat transfer coefficients on the tip with squealer along the camber line and the suction side. A relative high heat transfer coefficient exists near the leading edge and between the two squealer rims near 20% of the blade chord. A higher heat transfer coefficient can be found near the camber line squealer close to the trailing edge. As the recirculation flow between the two squealer rims exits near this region, the heat transfer coefficient in the region is increased. The overall heat transfer coefficient on the tip with squealer along the camber line and the suction side provides the lower value compared with the other double squealer cases.

Heat Transfer Coefficient on the Shroud Surface. Figure 8 presents the heat transfer coefficient distribution on the shroud. The squealer along the PS+SS case and the plane tip case (Figs. 8(*d*) and (*g*)) are presented for comparison. The detailed results of the plane tip and the squealer along the PS+SS cases are discussed by Kwak and Han [4,5]. Compared to the plane tip case (Fig. 8(*g*)), the squealer tip cases (Figs. 8(*a*)–(*f*)) show much lower heat transfer coefficients.

For all cases, the heat transfer coefficient on the shroud above the suction side is higher than above the pressure side. For the plane tip case, the high heat transfer coefficient region begins above the pressure side edge of the blade tip and extends downstream from the suction side. For the squealer tip cases (Figs. 8(*a*)–(*f*)), however, the high heat transfer coefficient region begins above the squealer rim. The flow leaked between the rim and the shroud can impinge on the shroud and results in a high heat transfer coefficient downstream from the squealer rim. Generally, the overall heat transfer coefficient increases as the tip gap clearance increases.

The overall heat transfer coefficient on the shroud above the blade tip is lowest for the squealer along the suction side case (Fig. 8(*c*)).

Heat Transfer Coefficient on the Near Tip Region of the Pressure Side. Figure 9 shows the heat transfer coefficient distribution on the near tip region of the pressure side. The height of the test area was about 2.5 cm from the tip (about 20% of the blade span). The squealer along the PS+SS case and the plane tip case (Figs. 9(*d*) and (*g*)) are presented for comparison. The detailed results of the plane tip and the double squealer tip cases are discussed by Kwak and Han [4,5].

All cases show that the heat transfer coefficient near the trailing edge is higher than near the mid chord region. This can be caused by the boundary layer transition on the pressure side surface. The heat transfer coefficient very near the blade tip is higher than far

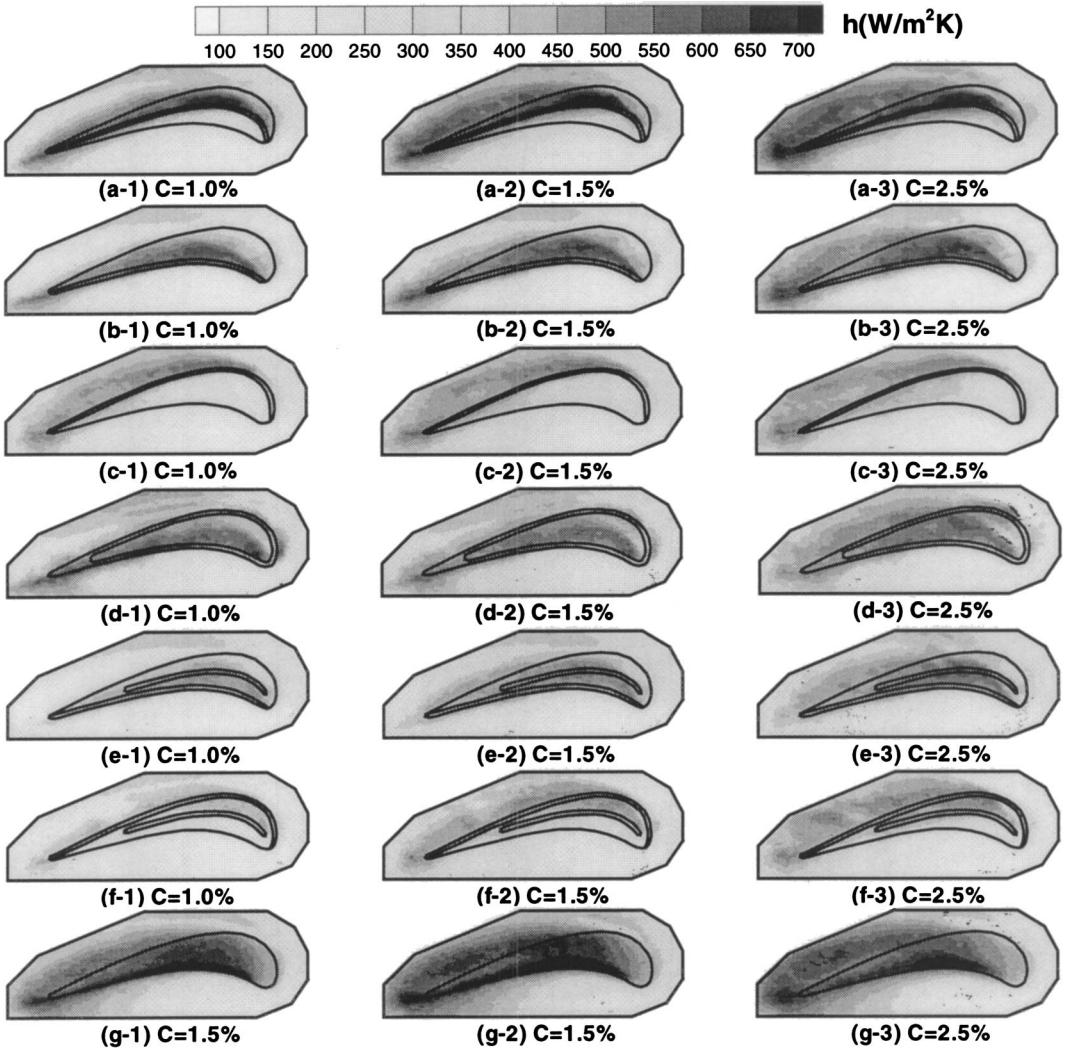

Fig. 8 Heat transfer coefficient on the shroud, (*a*) squealer along CL; (*b*) squealer along PS; (*c*) squealer along SS; (*d*) squealer along PS+SS (Kwak and Han [5]); (*e*) squealer along CL+PS; (*f*) squealer along CL+SS; (*g*) plane tip (Kwak and Han [4])

below the blade tip. The entrance effect of the leakage flow increases the heat transfer coefficient on the near tip region as shown in Fig. 7.

The heat transfer on the pressure side is not affected much by squealer arrangement or tip gap clearance. All cases show a similar trend and value of the heat transfer coefficient.

The maximum value of the heat transfer coefficient on the near tip of the pressure side is about 500 W/m^2 K, which is about 50% of the maximum value on the tip surface. The overall heat transfer coefficient on the pressure side is generally lower than on the tip or the shroud surface.

Heat Transfer Coefficient on the Near Tip Region of the Suction Side. Figure 10 shows the heat transfer coefficient distribution on the near tip region of the suction side. The height of the measurement region was about 20% of the blade span. The squealer along the PS+SS case and the plane tip case (Figs. 10(*d*) and (*g*)) are presented for comparison. The detailed results of the plane tip and the double squealer tip cases are discussed by Kwak and Han [4,5].

All cases show a high heat transfer coefficient region along the suction side tip. The high heat transfer coefficient in the region is caused by the leakage vortex. As the leakage flow exits from the tip gap, the leakage flow separates from the tip surface or the squealer rim and forms a leakage vortex due to the interaction with the mainstream flow. For the plane tip case (Fig. 10(*g*)), the path of the leakage vortex can be seen clearly. There is a lower heat transfer coefficient region between the suction side tip and the trace of leakage vortex due to separation of the leakage flow. For the camber line squealer case (Fig. 10(*a*)) and the pressure side squealer case (Fig. 10(*b*)), the heat transfer coefficient in the trace of the leakage vortex is higher than for the plane tip case and the trace of the leakage vortex is very close to the tip. The leakage flow separated from the squealer rim forms the leakage vortex earlier than in the plane tip case and results in a stronger leakage vortex near the suction side surface. The heat transfer coefficient in the trace of the leakage vortex is highest for the pressure side squealer case. The pressure side squealer case has a longer distance between the squealer rim and the suction side, which may increase the possibility of a leakage vortex to develop. The stronger vortex results in a higher heat transfer coefficient on the suction side surface. For the suction side squealer case (Fig. 10(*c*)), the peak heat transfer coefficient in the trace of the leakage vortex is smaller than in the other single squealer cases. The heat transfer coefficients on the tip and the shroud for this case show lower values than for the other cases, and this indicates that the amount of the leakage flow for the suction side squealer case is less than that of the other cases. The reduced leakage flow results in a weaker leakage vortex on the blade suction side. Also, the sepa-

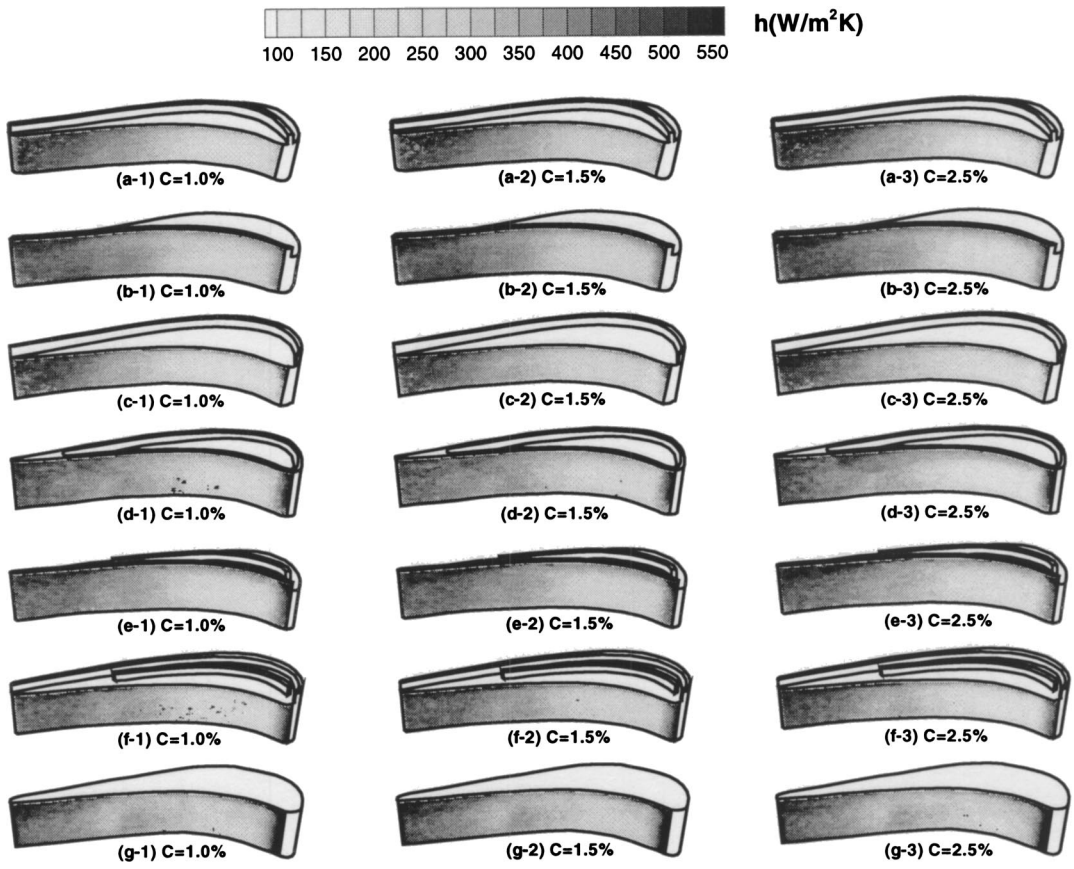

Fig. 9 Heat transfer coefficient on the near tip region of the pressure side, (*a*) squealer along CL; (*b*) squealer along PS; (*c*) squealer along SS; (*d*) squealer along PS+SS (Kwak and Han [5]); (*e*) squealer along CL+PS; (*f*) squealer along CL+SS; (*g*) plane tip (Kwak and Han [4])

ration of the leakage vortex on the suction side squealer rim decreases the possibility of leakage flow development. For the squealer along the pressure side and the suction side case (Fig. 10(*d*)), the heat transfer coefficient on the suction side near the tip is not sensitive to the tip gap clearance. The heat transfer coefficients for all the tip gap cases show a similar trend and value. For the squealer along the camber line and the pressure side case (Fig. 10(*e*)), the heat transfer coefficient on the suction side near the tip increases as the tip gap clearance increases. The trace of the leakage vortex is very close to the tip, and the heat transfer coefficient in that corner region is higher than for the other double squealer cases. In this case, the leakage flow separated from the squealer rim may form the leakage vortex earlier than in the other double squealer cases and results in a stronger leakage vortex. A stronger leakage vortex results in a higher heat transfer coefficient on the suction side. The squealer along the camber line and the suction side case (Fig. 10(*f*)) shows a similar distribution of the heat transfer coefficient to the squealer along the camber line and the pressure side case.

For all cases, the heat transfer coefficient decreases toward the trailing edge as the leakage vortex becomes weaker.

The overall heat transfer coefficient on the suction side is highest for the pressure side squealer case and lowest for the squealer along the pressure and suction sides case. The maximum value of the heat transfer coefficient is about 70% of that on the tip and is comparable with a maximum value on the shroud surface.

Averaged Heat Transfer Coefficient. Figures 11 and 12(*a*)–(*c*) present the averaged heat transfer coefficient on the tip, the shroud, the pressure side and the suction side, respectively. The local heat transfer coefficients are averaged at the given X/C_x location.

On the tip (Fig. 11), the averaged heat transfer coefficient on the squealer rim is generally higher than on the tip surface. Generally, the averaged heat transfer coefficient decreases as X/C_x increases for the camber line squealer case and the pressure side squealer case. However, the suction side squealer case shows a reverse trend. For the shroud (Fig. 12(*a*)), the averaged heat transfer coefficient increases as X/C_x increases, while the averaged heat transfer coefficient on the suction side (Fig. 12(*c*)) decreases as X/C_x increases. The averaged heat transfer coefficient on the pressure side shows a high value near the leading edge ($X/C_x=0$) and a minimum near $X/C_x=0.1$. Between $X/C_x=0.1$ and $X/C_x=1$, the averaged heat transfer coefficient gradually increases as X/C_x increases due to the boundary layer transition.

Conclusions

The major findings based on the experimental results are as follows:

1. By using a squealer tip blade, the heat transfer coefficient on the blade tip and the shroud was significantly reduced. However, the reduction in the heat transfer coefficient on the blade pressure and suction side was not remarkable.
2. The location of the high heat transfer region varied by changing the arrangement of the squealer rim. Generally, the heat transfer coefficient on the rim is higher than on the tip surface.
3. The overall heat transfer coefficient on the tip for the suction side squealer case was lower than other squealer tip arrangement cases.

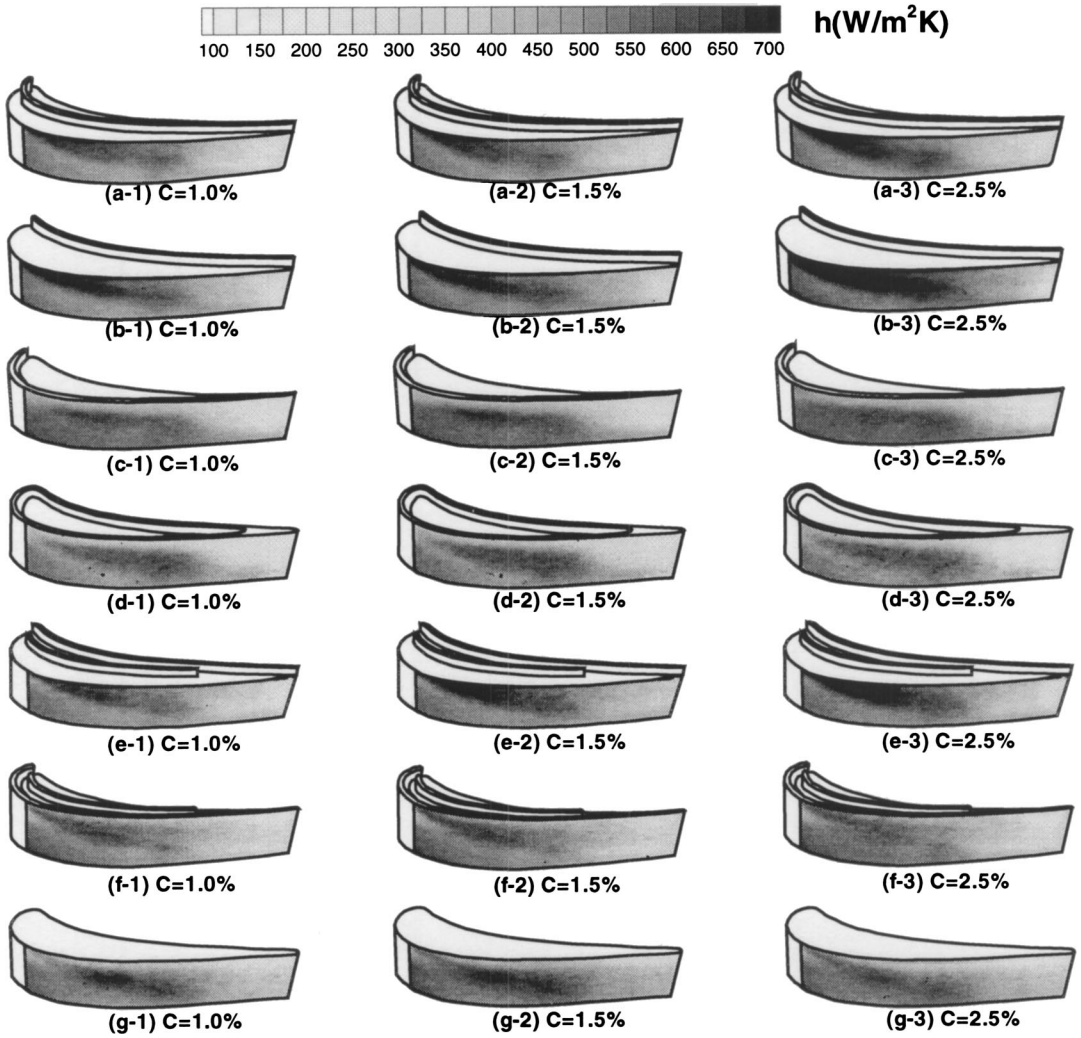

Fig. 10 Heat transfer coefficient on the near tip region of the suction side, (*a*) squealer along CL; (*b*) squealer along PS; (*c*) squealer along SS; (*d*) squealer along PS+SS (Kwak and Han [5]); (*e*) squealer along CL+PS; (*f*) squealer along CL+SS; (*g*) plane tip (Kwak and Han [4])

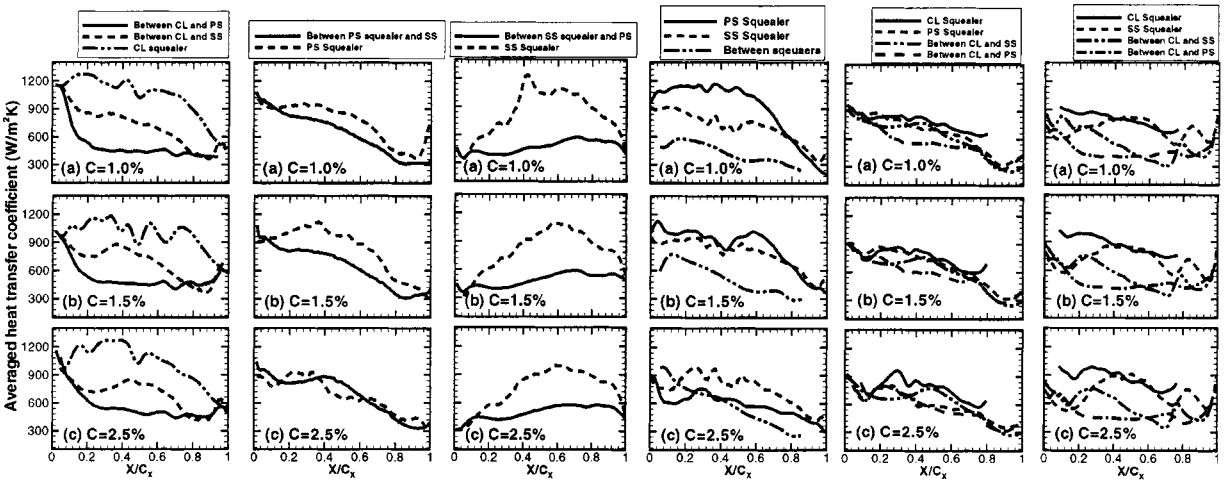

(a) squealer along CL (b) squealer along PS (c) squealer along SS (d) squealer along PS+SS (e) squealer along CL+PS (f) squealer along CL+SS

Fig. 11 Averaged heat transfer coefficient on the tip

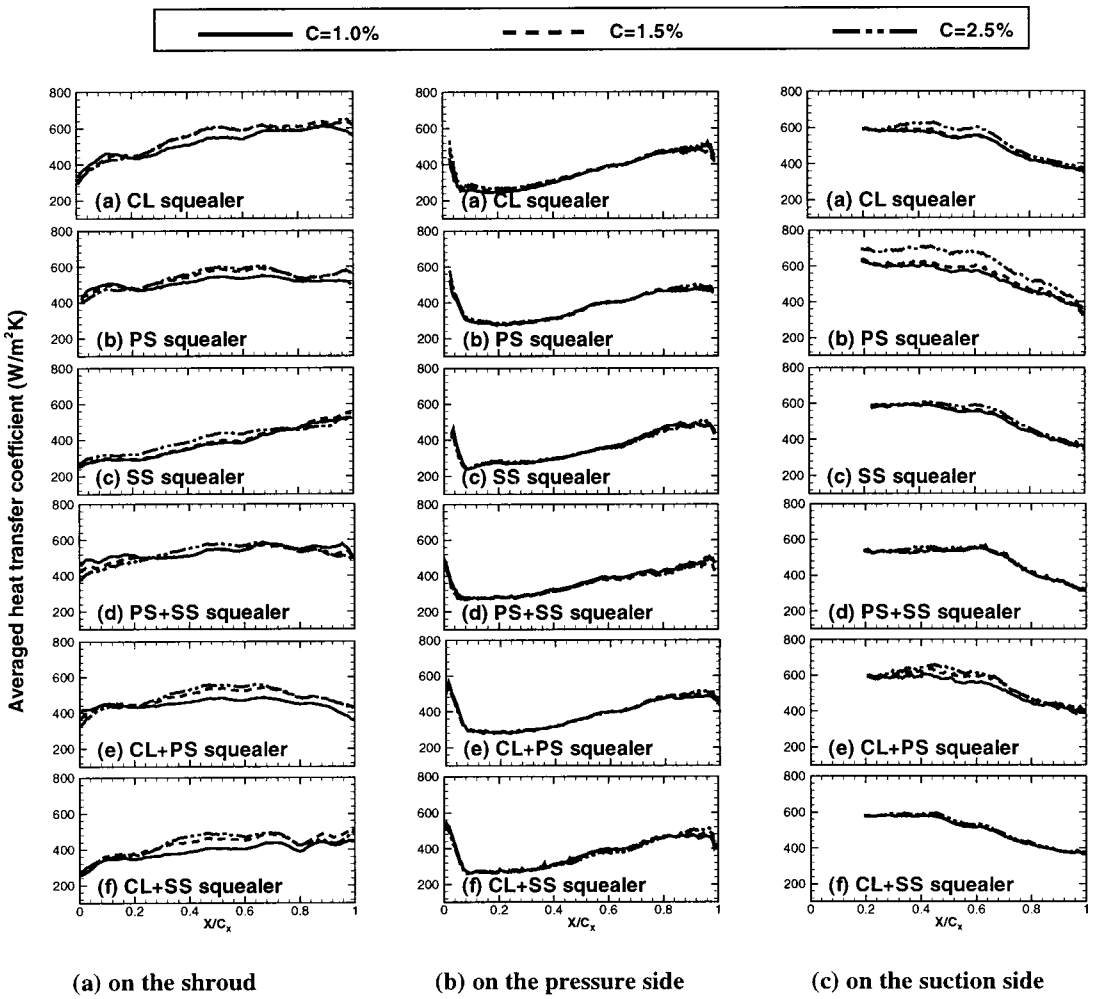

Fig. 12 Averaged heat transfer coefficient on the shroud, the pressure side and the suction side

4. The heat transfer coefficient on the shroud upstream from the squealer rim was much lower than on the shroud downstream from the squealer rim.
5. Generally, the heat transfer coefficient on the pressure side was laterally uniform. The effect of tip gap clearance and the arrangement of the squealer rim on the pressure side heat transfer coefficient was small. The overall heat transfer coefficient on the pressure side was lower than on the other surfaces.
6. The trace of the leakage vortex can be seen on the suction side and the overall heat transfer coefficient on the suction side was comparable with that on the shroud. The distribution of the heat transfer coefficient on the suction side varied as the geometry of the blade tip changed, but it was insensitive to the tip gap clearance.
7. Generally, the heat transfer coefficients on the tip surface, the shroud, and suction side increased slightly as the tip gap clearance increased. However, the heat transfer coefficient on the blade pressure side was insensitive to the tip gap clearance.

The observations and conclusions from this study are limited to stationary blades. Cautions should be exercised in extending the results to rotating blades. In addition, the overall pressure ratio in this study was lower than in real engine conditions.

Acknowledgment

This work was prepared with the support of the NASA Glenn Research Center under Grant Number NAG3-2002. Their support is greatly appreciated.

Nomenclature

C = Tip clearance gap (% of the blade span)
CL = Blade camber line
C_x = Axial chord length of the blade (8.61 cm)
h = Local convective heat transfer coefficient (W/m^2 K)
H = Height of the squealer rim (4.2% of the blade span)
k = Thermal conductivity of blade tip material (0.18 W/m K)
LE = Leading edge of the blade
PS = Blade pressure side
t = Transition time for liquid crystals color change
TE = Trailing edge of the blade
T_i = Initial temperature of the test surface
T_m = Temperature of the mainstream at the cascade inlet (recovery temperature)
T_w = Color change temperature of the liquid crystals
SS = Blade suction side
X = Axial distance (cm)
α = Thermal diffusivity of blade tip material (1.25×10^{-7} m^2/s)
τ_i = Step change of time

References

[1] Azad, GM S., Han, J. C., Teng, S., and Boyle, R., 2000, "Heat Transfer and Pressure Distributions on a Gas Turbine Blade Tip," ASME J. Turbomach., **122**, pp. 717–724.
[2] Azad, GM S., Han, J. C., and Boyle, R., 2000, "Heat Transfer and Pressure Distributions on the Squealer Tip of a Gas Turbine Blade," ASME J. Turbomach., **122**, pp. 725–732.

[3] Azad, GM S., Han, J. C., Bunker, R. S., and Lee, C. P., 2002, ''Effect of Squealer Geometry Arrangement on a Gas Turbine Blade Tip Heat Transfer,'' ASME J. Heat Transfer, **124**, pp. 452–459.
[4] Kwak, J. S., and Han, J. C., 2003, ''Heat Transfer Coefficient on a Gas Turbine Blade Tip and Near Tip Regions,'' J. Thermophys. Heat Transfer, **17**, pp. 297–303.
[5] Kwak, J. S., and Han, J. C., 2003, ''Heat Transfer Coefficient on the Squealer Tip and Near Squealer Tip Regions of a Gas Turbine Blade,'' ASME J. Heat Transfer, **125**, pp. 669–677.
[6] Kwak, J. S., and Han, J. C., 2003, ''Heat Transfer Coefficients and Film-Cooling Effectiveness on a Gas Turbine Blade Tip,'' ASME J. Heat Transfer, **125**, pp. 494–502.
[7] Kwak, J. S., and Han, J. C., 2003 ''Heat Transfer Coefficient and Film-Cooling Effectiveness on the Squealer Tip of a Gas Turbine Blade,'' ASME J. Turbomach. **125**, pp. 648–657.
[8] Dunn, M. G., and Haldeman, C. W., 2000, ''Time-Averaged Heat Flux for a Recessed Tip, Lip, and Platform of a Transonic Turbine Blade,'' ASME J. Turbomach., **122**, pp. 692–697.
[9] Yang, T. T., and Diller, T. E., 1995, ''Heat Transfer and Flow for a Grooved Turbine Blade Tip in a Transonic Cascade,'' ASME-95-WA/HT-29.
[10] Papa, M., Goldstein, R. J., and Gori, F., 2002, ''Effects of Tip Geometry and Tip Clearance on the Mass/Heat Transfer From a Large-Scale Gas Turbine Blade,'' ASME Paper GT-2002-30192.
[11] Metzger, D. E., Bunker, R. S., and Chyu, M. K., 1989, ''Cavity Heat Transfer on a Transverse Grooved Wall in a Narrow Flow Channel,'' ASME J. Heat Transfer, **111**, pp. 73–79.
[12] Chyu, M. K., Moon, H. K., and Metzger, D. E., 1989, ''Heat Transfer in the Tip Region of Grooved Turbine Blades,'' ASME J. Turbomach., **111**, pp. 131–138.
[13] Heyes, F. J. G., Hodson, H. P., and Dailey, G. M., 1991, ''The Effect of Blade Tip Geometry on the Tip Leakage Flow in Axial Turbine Cascades,'' ASME 91-GT-135.
[14] Kim, Y. W., and Metzger, D. E., 1995, ''Heat Transfer and Effectiveness on Film Cooled Turbine Blade Tip Model,'' ASME J. Turbomach., **117**, pp. 12–21.
[15] Metzger, D. E., Bunker, R. S., and Chyu, M. K., 1989, ''Cavity Heat Transfer on a Transverse Grooved Wall in a Narrow Flow Channel,'' ASME J. Heat Transfer, **111**, pp. 73–79.
[16] Mayle, R. E., and Metzger D. E., 1982, ''Heat Transfer at the Tip of an Unshrouded Turbine Blade,'' *Proc. Seventh Int. Heat Transfer Conf.*, Hemisphere Publishing, pp. 87–92.
[17] Metzger, D. E., and Rued, K., 1989, ''The Influence of Turbine Clearance Gap Leakage on Passage Velocity and Heat Transfer Near Blade Tips. Part I: Sink Flow Effects on Blade Pressure Side,'' ASME J. Turbomach., **111**, pp. 284–292.
[18] Rued, K., and Metzger, D. E., 1989, ''The Influence of Turbine Clearance Gap Leakage on Passage Velocity and Heat Transfer Near Blade Tips. Part II: Source Flow Effects on Blade Pressure Side,'' ASME J. Turbomach., **111**, pp. 293–300.
[19] Metzger, D. E., Dunn, M. G., and Hah, C., 1991, ''Turbine Tip and Shroud Heat Transfer,'' ASME J. Turbomach., **113**, pp. 502–507.
[20] Bunker, R. S., Baily, J. C., and Ameri, A. A., 2000, ''Heat Transfer and Flow on the First Stage Blade Tip of a Power Generation Gas Turbine: Part 1: Experimental Results,'' ASME J. Turbomach., **122**, pp. 272–277.
[21] Bunker, R. S., and Baily, J. C., 2001, ''Effect of Squealer Cavity Depth and Oxidation on Turbine Blade Tip Heat Transfer,'' ASME Paper No. 2001-GT-0155.
[22] Teng, S., Han, J. C., and Azad, GM S., 2001, ''Derailed Heat Transfer Coefficient Distributions on a Large-Scale Gas Turbine Blade Tip,'' ASME J. Heat Transfer, **123**, pp. 803–809.
[23] Rhee, D. H., Choi, J. H., and Cho, H. H., 2001, ''Effect of Blade Tip Clearance on Turbine Shroud Heat/Mass Transfer,'' ASME Paper 2001-GT-0158.
[24] Jin, P., and Goldstein, R. J., 2002, ''Local Mass/Heat Transfer on a Turbine Blade Tip,'' *9th International Symposium on Transport Phenomena and Dynamics of Rotating Machinery*, Honolulu, February.
[25] Jin, P., and Goldstein, R. J., 2002, ''Local Mass/Heat Transfer on Turbine Blade Near-Tip Surfaces,'' ASME Paper GT-2002-30556.
[26] Ameri, A. A., and Steinthorsson, E., 1995, ''Prediction of Unshrouded Rotor Blade Tip Heat Transfer,'' ASME 95-GT-142.
[27] Ameri, A. A., and Steinthorsson, E., 1996, ''Analysis of Gas Turbine Rotor Blade Tip and Shroud Heat Transfer,'' ASME 96-GT-189.
[28] Ameri, A. A., Steinthorsson, E., and Rigby, L. David, 1999, ''Effects of Tip Clearance and Casing Recess on Heat Transfer and Stage Efficiency in Axial Turbines,'' ASME J. Turbomach., **121**, pp. 683–693.
[29] Ameri, A. A., and Bunker, R. S., 2000, ''Heat Transfer and Flow on the First Stage Blade Tip of a Power Generation Gas Turbine: Part 2: Simulation Results,'' ASME J. Turbomach., **122**, pp. 272–277.
[30] Ameri, A. A., and Rigby, D. L., 1999, ''A Numerical Analysis of Heat Transfer and Effectiveness on Film Cooled Turbine Blade Tip Models,'' NASA/CR 1999-209165.
[31] Ameri, A. A., 2001, ''Heat Transfer and Flow on the Blade Tip of a Gas Turbine Equipped With a Mean-Camberline Strip,'' ASME J. Turbomach., **123**, pp. 704–708.
[32] Ameri, A. A., Steinthorsson, E., and Rigby, L. David, 1997, ''Effect of Squealer Tip on Rotor Heat Transfer and Efficiency,'' ASME 97-GT-128.
[33] Yang, H., Acharya, S., Ekkad, S. V., Prakash, C., and Bunker, R., 2002, ''Flow and Heat Transfer Predictions for a Flat-Tip Turbine Blade,'' ASME Paper GT-2002-30190.
[34] Yang, H., Acharya, S., Ekkad, S. V., Prakash, C., and Bunker, R., 2002, ''Numerical Simulation of Flow and Heat Transfer Past a Turbine Blade with a Squealer-Tip,'' ASME Paper GT-2002-30193.
[35] Kline, S. J., and McClintock, F. A., 1953, ''Describing Uncertainties in Single Sample Experiments,'' Mech. Eng. (Am. Soc. Mech. Eng.), **75**, pp. 3–8.

Journal of Turbomachinery

Technical Brief

Heat Transfer Enhancement in Square Ducts With V-Shaped Ribs

Rongguang Jia, Arash Saidi, and Bengt Sunden
Division of Heat Transfer, Lund Institute of Technology, P. O. Box 118, 221 00 Lund, Sweden

This paper concerns a numerical investigation of the heat and fluid flow in V-shaped ribbed ducts. The Navier-Stokes equations and the energy equation are solved in conjunction with a low Reynolds number k–ε turbulence model. The Reynolds turbulent stresses are computed with an explicit algebraic stress model (EASM) while the turbulent heat fluxes are calculated with a simple eddy diffusivity model (SED). Detailed velocity and thermal field results have been used to explain the effects of the V-shaped ribs and the mechanisms of the heat transfer enhancement. [DOI: 10.1115/1.1622708]

1 Introduction

Introduction of roughness by ribs in flow passages is a popular method of enhancing heat transfer in the cooling passages, e.g., of turbine blades and combustors. The heat transfer and fluid flow in ribbed ducts have been extensively studied both experimentally and numerically. A good review can be found in Sundén [1].

Experimental studies have revealed that both downstream and upstream pointing V-shaped ribs result in better heat transfer enhancement than transverse straight ribs of the same geometry. Secondary flows induced by the angled ribs are believed to be responsible for this higher heat transfer enhancement. However, contradiction exists on which pointing direction is the better for V-shaped ribs [2–5]. Further investigations are thus necessary to understand this. This paper reports the authors' efforts to further improve the understanding of the internal cooling of turbine blades roughened with V ribs, especially to clarify the contradictions in different experiments.

In this study, the computations are carried out for the 45-deg V-shaped ribs, which are arranged both inline and staggered. The rib size to duct height (e/D_h) is 0.0625, with Reynolds number ranging from 15,000 to 32,000.

2 Governing Equations and Numerical Procedure

The time-averaged incompressible fluid flow is solved using the steady incompressible Reynolds-averaged Navier-Stokes (RANS) equations, with periodic boundary conditions, which prevailed in the experimental setups [2–5]. The turbulent Reynolds stresses are modeled by a low-Reynolds-number explicit algebraic stress model (EASM) turbulence model and the turbulent heat fluxes are modeled using the simple eddy diffusivity (SED) model.

An in-house multiblock parallel computer code, CALC-MP [6], is applied to solve the governing equations. The code uses a collocated mesh arrangement. The SIMPLEC algorithm couples the pressure and velocity. Coefficients are determined by the QUICK scheme for the momentum equations, while the hybrid scheme is used for all the discretized energy and turbulence equations.

Nonuniform body-fitted grids were generated, and grid refinement close to the wall was applied. Several successive grid refinements have been carried out in every considered case to make sure that negligible effects of the mesh on the solutions prevail. For the ducts roughened with inline V ribs (IV), $82\times56\times32$ grid points were used, due to the symmetry characteristics in both the y and z directions of the IV ribbed case. A $98\times118\times32$ grid was used for the staggered V ribs (SV) cases.

3 Results and Discussion

Basically, the present models and code have been validated by our previous studies with the detailed experimental data, including the one-sided-ribbed (1s) cases with $e/D_h=0.1$, and $P/e=9$ and 12, and the two-sided-ribbed (2s) case with $P/e=9$, and Re $=30{,}000$. The overall thermal and flow field features were predicted reasonably well.

The computations are conducted to make clear which of the following parameters leading to contradictory conclusions: (1) rib alignment, inline or staggered; (2) heating of the smooth-sided wall (SSW) or not.

3.2 Straight Duct with Two-Sided V Ribs

3.2.1 IV Ribs (Inline, $e/D_h=0.0625$). Figure 1 shows the normalized average Nusselt number (Nu) on the smooth side-walls (SSW's) and ribbed side-walls (RSW's) of one period versus Re for IV ribs, and the Fanning friction factor. The results for the ‖ ribs are also enclosed for comparison purpose. The thermal results show that the « ribs provide higher Nusselt number than ‖ ribs and » ribs, on both the SSW and RSW. In addition, the » ribs have better heat transfer enhancement than ‖ ribs. All of these trends are in consistence with the experiments of Han et al. The errors are shown in Table 1, and are explained in the following paragraph.

The sampling locations are different between the present simulation and the experiments of Han et al. The present simulation is carried out at the fully developed fluid flow and heat transfer region, and periodic boundary conditions are assumed in the main flow direction. In a V-ribbed duct, the rib-induced secondary flow grows continuously along the duct, which results in a continuous growth of the Nusselt number and friction factor. Therefore the Nusselt number and Fanning friction factor based on the whole channel (including the developing region) will be lower than those based on one fully developed period. This can be confirmed in the paper of Han et al., a steep Nusselt number increase downstream $x/D_h=16$ for the V ribs, which is explained by the authors as aneffect of favorable secondary flow induced by the rib orienta-

Contributed by the International Gas Turbine Institute for publication in the JOURNAL OF TURBOMACHINERY. Manuscript received by the IGTI May 20, 2002, revised manuscript received May 17, 2003. Associate Editor: R. S. Bunker.

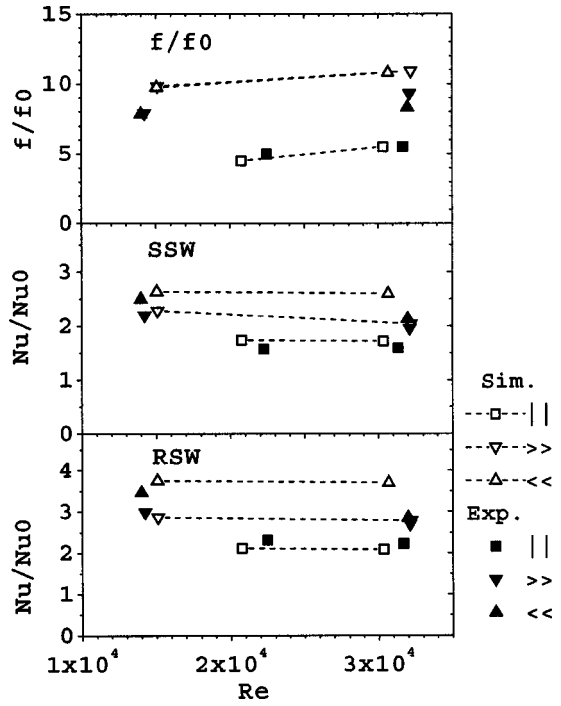

Fig. 1 Normalized Fanning friction factors, and average Nusselt number of different rib configurations and Reynolds number at the ribbed and smooth side-walls of the inline V ribs

tion. This partly clarifies why the Fanning friction factors for V ribs predicted by the present simulation are around 25 percent (cf. Table 1) higher than the experimental ones by Han et al., which also applies to the overprediction of the Nusselt number. For ‖ ribs, however, the whole-channel averaging value (Nu or f) may be very similar to that based on one fully developed period, because the secondary flows for ‖ ribs are much weaker than those for V ribs.

3.2.1.2 Explanation of the heat transfer enhancement on the ribbed side wall. First, the secondary flow directions induced by different pointing ribs make a difference. It can be observed that » ribs brings fluid heated by the smooth side wall to the ribbed side wall, while « ribs bring fluids from the cool main stream flow to the ribbed side wall. The cooler fluid in contact with the hot ribbed floor will result in lower local wall temperatures (T_w), because the heat flux is kept equal and constant for both cases. The lower wall temperature will lead to higher heat transfer coefficients because the bulk temperature (T_b) is the same for both cases in each cross section.

Second, the higher heat transfer coefficient on the ribbed side wall for the « ribs can also be explained by the vortex line stretching near the wall, as shown in Fig. 2. As discussed by Olsson and Sundén [4], vortex line is bent to a V-shaped form similar to the ribs if the vortex line is close to the wall. This can be identified in the streamline traces. The vortex line will be stretched and the vorticity amplified by the velocity gradients in the vicinity of the ribs. Consequently, the vortex line now has both axial and spanwise components. The axial component is associated with the secondary flow, while the spanwise component has similar behavior as the original vortex line. For the « ribs, the axial vorticity components will act as an inflow pair of vortices resulting in thinning of the boundary layer, consequently higher turbulence ($\mu_T^+ = \mu_T/\rho D_h U_b = 0.061$ at $y/e = 0.1$) at the close RSW region than the » ribs ($\mu_T^+ = 0.049$ at $y/e = 0.1$), and enhancement of the heat transfer on RSW. For the » ribs, an outflow vortex pair will occur and the boundary layer thickness is increased, which decreases the local heat transfer.

Third, the higher heat transfer coefficient on the RSW for the « ribs can be explained by the longitudinal vortex-pair directions, as shown in Fig. 2. The « ribs induce an inflow vortex pair. The inflow vortex pair will stretch and thin the boundary layer be-

Table 1 The results from the present simulation for $e/D_h = 0.0625$ ribs with inline arrangement, in comparison with the experimental data of Han et al. [1]

		f/f_0			Nu/Nu_0 (RSW)			Nu/Nu_0 (SSW)		
Rib	Re	Sim.	Expt.	Error	Sim.	Expt.	Error	Sim.	Expt.	Error
«	15,000	9.75	7.85	24.0%	3.75	3.48	8.2%	2.63	2.50	5.3%
	30,000	10.80	8.30	30.0%	3.68	2.85	29.0%	2.58	2.13	22.0%
»	15,000	9.83	7.89	24.0%	2.86	2.98	−4.2%	2.28	2.20	3.8%
	30,000	10.90	9.30	24.7%	2.77	2.69	3.2%	2.03	1.96	4.4%

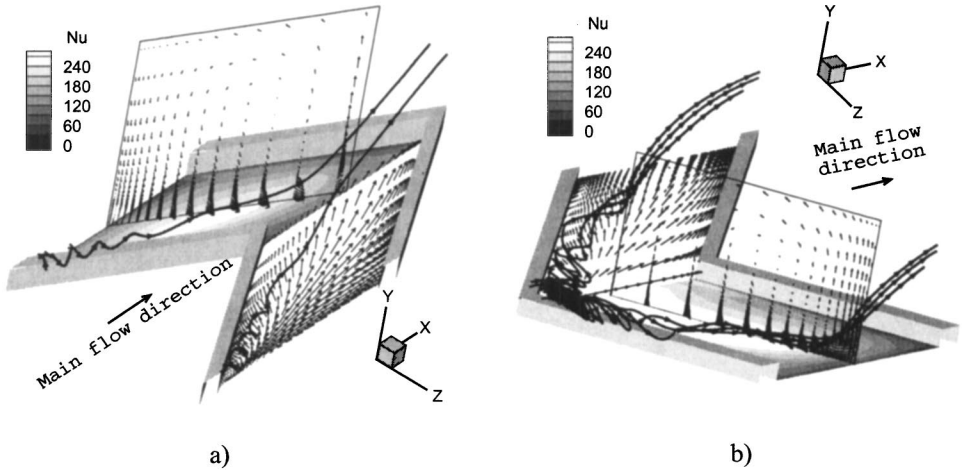

Fig. 2 The simulated fluid flow and heat transfer structure in ducts ribbed with inline V ribs at Re=15,000, (*a*) » ribs, (*b*) « ribs

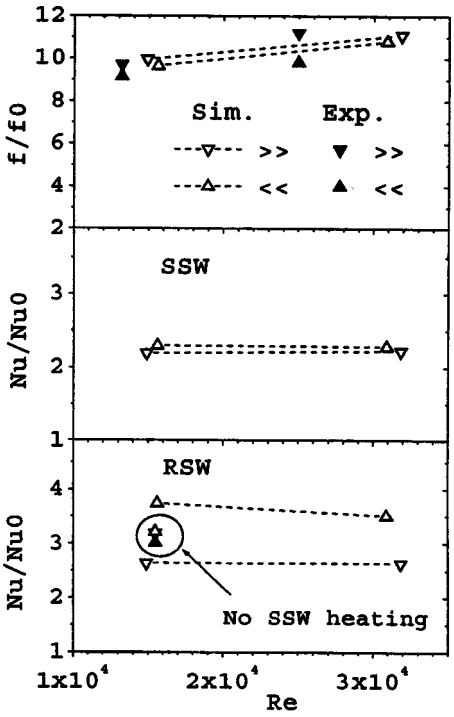

Fig. 3 Normalized Fanning friction factors, and average Nusselt number of different rib configurations and Reynolds numbers at the ribbed and smooth side walls of the staggered V ribs with $e/D_h=0.0625$

tween the two vortices, resulting in higher heat transfer coefficients there. However, the secondary flow induced by » ribs acts in a contrary manner, inducing outflow.

3.2.1.3 Heat transfer enhancement on the smooth side wall. At the close SSW region, the » ribs induce slightly higher (about 3%) turbulence ($\mu_T^+=0.043$) than the « ribs ($\mu_T^+=0.041$), which is not consistent with the higher Nu achieved by the « ribs. This higher turbulence intensity is because of the inflow vortex pair on the SSW induced by the » ribs. The strong secondary motion induced by « ribs impinges on the smooth side wall, after cooling the ribbed side wall. This impingement provides a pretty high heat transfer rate (probably two to three times higher than pure forced convection along the wall), which can basically serve as the explanation why higher heat transfer is also achieved on the SSW from « ribs.

3.2.2 The Staggered V-Shaped Ribs (Staggered, $e/D_h=0.0625$). As shown in Fig. 3 and Table 2, generally speaking, there is no large difference in the numerical Nu results on the RSW's between the inline and staggered ribs. However, a lower Nu on the SSW's of staggered ribs is found. In addition, the difference of the Nu on the SSW's between the » and « ribs becomes smaller than for the IV ribs.

The predicted friction factors are very similar to those of IV ribs, although the influence of the rib pointing directions is somewhat larger than for the IV ribs. They are also in decent agreement with the experiments of Taslim et al. [3]. For this staggered arrangement, the agreement between the numerical prediction of the friction factor and that of the experiments seems much better.

3.2.3 Effect of Heating of SSW's. SSW heating could be the reason for the contradictory conclusions, because the two experiments [2,4] with SSW heating demonstrated the superior of the « ribs, while contrary conclusions are reached with the two experiments [3,5] without SSW heating. From the present study, the difference between the two pointing directions become smaller without SSW heating, which is clearly shown in the numerical results in Fig. 3 and Table 2. The following paragraphs provide the explanations.

From Fig. 2, one can observe the secondary flow directions at the corners between the SSW's and RSW's of the » and « ribs. For » ribs, the fluid from the mainstream is heated by the SSW before it reaches the RSW, while the secondary flow has an opposite direction for « ribs. This serves as one of the explanations for better performance of the « ribs with SSW heating.

Without heating the SSW, the temperature of the fluid passing the RSW of the » ribs will be lower. Consequently, a lower T_w appears. Thus a higher Nu is obtained on the RSW, although T_b will also be lower due to the less total heat input, which is not favorable for a high Nu. In fact, this lower T_b weakens the heat transfer on the RSW of the « ribs, where T_w is not affected by the heating of SSW due to the secondary flow direction, as shown in Fig. 2(*b*). All these changes can be clearly observed in Fig. 3, i.e., the Nu on the RSW is higher for » ribs without SSW heating than that with SSW heating. The Nu on the RSW of the « ribs behaves contrarily.

There is no SSW heating in the experiments of Taslim et al., which results in a lower T_b due to the less heat input. Also the heating of the side wall has a very minor effect on T_w, because the secondary flow direction of the ‖ ribs is the same as « ribs (Fig. 2(*b*)). According to the definition of Nu, this decrease of T_b results in a lower Nu. Therefore, the difference between [2] and [3] in the Nu on the RSW of ‖ ribs might be because of the SSW heating.

Consider now carefully the heat transfer coefficient distribution provided by Taslim et al. One finds that the Nu_{RSW} is very large even very close to the SSW which is not heated. If the SSW is heated, however, this is not true, but a very small Nu is obtained at the vicinity of the wall. This is because without SSW heating cooler air first comes in contact with the corner. Although Taslim et al. claimed that the heating of the other walls will not have a big effect on the heat transfer of the RSW, care should be taken and a deeper analysis might be necessary.

In summary, the results from the present simulation show that « ribs perform better with and without SSW heating, although the difference is very weak without SSW heating

Table 2 The results from the present simulation for $e/D_h=0.0625$ ribs with staggered arrangement and Re=15,000, in comparison with the experimental data of Taslim et al. [3]

Rib	SSW heating	f/f_0			Nu/Nu_0 (RSW)			Nu/Nu_0 (SSW)		
		Sim.	Expt.	Error	Sim.	Expt.	Error	Sim.	Expt.	Error
«	*Y*	9.65	9.15		3.741			2.292		
	N				3.215	3.011	6.8%			
»	*Y*	9.95	9.69	2.7%	2.633			2.19		
	N				3.191	3.187	1.2%			

4 Concluding Remarks

The contradiction in the four experiments is mainly caused by the heating of the SSW's or not, because the drop of heating the SSW's will decrease the difference between the Nu on the RSW's of the « and » ribs. This is consistent with the four experiments, i.e., the two experiments [2,4] with SSW heating concluding the superiority of the « ribs, while contrary conclusions are reached with the two experiments [3,5] without SSW heating.

The « ribs performed superior compared to the » and ‖ ribs. This better performance is mainly due to the secondary flow induced by the angled ribs. The main objective of creating a secondary flow is to establish or improve the exchange of fluid between the core region (main stream) and the wall region, and/or make the boundary layer thinner near the walls, thus to increase the temperature gradient at the walls. The « ribs fulfill both of these criteria properly, because they induce inflow vortex pairs near the ribbed side wall, and the secondary flows impinge on the smooth side-wall to increase the turbulence intensity near the walls.

Acknowledgment

The Swedish Energy Agency (STEM) financially supported this research work.

References

[1] Sundén, B., 1999, "Enhancement of Convective Heat Transfer in Rib-roughened Rectangular Ducts," J. Enhanced Heat Transfer, **6**, pp. 89–103.

[2] Han, J. C., Zhang, Y. M., and Lee, C. P., 1991, "Augmented Heat Transfer in Square Channels with Parallel, Crossed, and V-shaped Angled Ribs," ASME J. Heat Transfer, **113**, pp. 590–596.

[3] Taslim, M. E., Liu, T., and Kercher, D. M., 1996, "Experimental Heat Transfer and Friction in Channels Roughened with Angled, V-shaped, and Discrete Ribs on Two Opposite Walls," ASME J. Turbomach., **118**(1), pp. 20–28.

[4] Olsson, C. O., and Sundén, B., 1998, "Experimental Study of Flow and Heat Transfer in Rib-Roughened Rectangular Channels," Exp. Therm. Fluid Sci., **16**(4), pp. 349–365.

[5] Gao, X., and Sundén, B., 2001, "Heat Transfer and Pressure Drop Measurements in Rib-Roughened Rectangular Ducts," Exp. Therm. Fluid Sci., **24**(1–2), pp. 25–34.

[6] Jia, R., and Sundén, B., 2003, "Parallelization of a Multi-Blocked CFD Code via Three Strategies for Fluid Flow and Heat Transfer Analysis," Comput. Fluids, **33**, pp. 57–80.